Surv Geophys (2011) 32:315–317
DOI 10.1007/s10712-011-9136-0

EDITORIAL

Foreword: International Space Science Institute (ISSI) Workshop on the Earth's Cryosphere and Sea Level Change

Lennart Bengtsson

Received: 23 May 2011 / Accepted: 25 May 2011 / Published online: 30 June 2011

Rising sea level is perhaps the most severe consequence of climate warming, as much of the world's population and infrastructure is located near current sea level (Lemke et al. 2007). A major rise of a metre or more would cause serious problems. Such possibilities have been suggested by Hansen and Sato (2011) who pointed out that sea level was several metres higher than now during the Holsteinian and Eemian interglacials (about 250,000 and 120,000 years ago, respectively), even though the global temperature was then only slightly higher than it is nowadays. It is consequently of the utmost importance to determine whether such a sea level rise could occur and, if so, how fast it might happen.

Sea level undergoes considerable changes due to natural processes such as the wind, ocean currents and tidal motions. On longer time scales, the sea level is influenced by *steric* effects (sea water expansion caused by temperature and salinity changes of the ocean) and by *eustatic* effects caused by changes in ocean mass. Changes in the Earth's cryosphere, such as the retreat or expansion of glaciers and land ice areas, have been the dominant cause of sea level change during the Earth's recent history. During the glacial cycles of the last million years, the sea level varied by a large amount, of the order of 100 m. If the Earth's cryosphere were to disappear completely, the sea level would rise by some 65 m.

The scientific papers in the present volume address the different aspects of the Earth's cryosphere and how the different changes in the cryosphere affect sea level change. It represents the outcome of the first workshop held within the new ISSI Earth Science Programme. The workshop took place from 22 to 26 March, 2010, in Bern, Switzerland, with the objective of providing an in-depth insight into the future of mountain glaciers and the large land ice areas of Antarctica and Greenland, which are exposed to natural and anthropogenic climate influences, and their effects on sea level change. The participants of the workshop are experts in different fields including meteorology, climatology, oceanography, glaciology and geodesy; they use advanced space-based observational studies and state-of-the-art numerical modelling.

Present assessments of sea level height reported in this volume (Church and White 2011; Woodworth et al. 2011) show that sea level rise has been going on at least since the

L. Bengtsson (✉)
International Space Science Institute, Hallerstrasse 6, 3012 Bern, Switzerland
e-mail: Bengtsson@issibern.ch

middle of the nineteenth century, with a tendency towards an acceleration during the last decades. The global averaged increase in sea level during the last 150 years amounts to 20–25 cm. The sparse and irregular observational records and difficult sampling due to local variations, such as caused by wind and ocean currents, complicate the accuracy of this estimate. Accurate estimates are also compromised by geodetic changes, including an ongoing rise of the land, especially in areas that were glaciated during the last ice age.

Since 1993, sea level height has been monitored from space by radar altimetry measurements that have led to a significant improvement in accuracy. There is a general agreement (e.g., Nicholls and Cazenave 2010; Church and White 2011) that the mean sea level rise during the last 17 years is approximately 3 mm/year. There are minor variations from year to year, but no significant change in the trend has been determined for the period during which we have space observations. Thanks to the recent development of gravity measurements made from space and vertical temperature soundings of the oceans, it has been possible to identify separately the mass and volume changes of the oceans; the steric and eustatic components of sea level change have thus been quantitatively determined.

Observations show that sea level rise is slowly accelerating, and the present trend is well above the mean trend of the last century. The latest results, including those obtained using space-based gravity techniques, show in fact that the present sea level rise is dominated by the increase in ocean mass due to melt water (about two-thirds) and the remaining third by thermal expansion of seawater. The melt water comes from mountain and coastal glaciers and parts of the large land ice masses. Present observations and model studies show ongoing mass losses of glaciers worldwide, together with a net loss of mass of the land ice from both Greenland and Antarctica. Whether this is only a temporary effect cannot yet be determined because of the short observational record. The storage of water on land in lakes, dams and aquifers also undergoes changes, but the gains and losses broadly compensate each other.

A particular concern in recent years has been the indications of the rapid acceleration of some of the large glaciers on Greenland and Antarctica which suggest larger net losses than previously estimated. These indications have been supported by different space measurements including those from ICESat and GRACE. Although the mechanisms are not fully understood, it appears that higher ocean temperatures at the outlet of the glaciers at the coast is a dominant process, while the percolation of melt water through the land ice is seen as being of secondary importance.

Recent modelling results with a more detailed representation of non-linear dynamical effects influencing the deformation of the ice flow seem to imply counteracting processes that swiftly can decelerate the flow. Thus, *periodically accelerating and decelerating glaciers might be part of their natural behaviours*. Needless to say, this must be further explored; it justifies the continuous monitoring of the dynamics of the land ice masses as well as their detailed modelling.

Under the assumption of a continued warming as a consequence of increasing concentrations of greenhouse gases in the atmosphere, the sea level is expected to continue to rise. Most model estimates suggest a modest acceleration of sea level rise towards the end of the twenty-first century compared to now. In this respect, recent studies reported at the workshop support the IPCC report (2007) giving likely values for a middle-of-the-line-scenario of 20–50 cm. The view of the workshop is that detailed numbers are difficult to justify as both climate models and the scenarios are changing. There are no scientific reasons that the range might narrow; rather it might widen as more aspects of the climate system are considered. *Instead, it is more sensible to make risk assessments, not predictions.*

However, there are severe worries what might happen in the next century and later. In the case of Greenland, model studies indicate several equilibria, with different amounts of land ice maintained at higher temperatures but also *different thresholds of irreversibility* where the land ice after a major melt is unable to recover. It is thought that the first of such thresholds might occur after a 10% loss of the mass of ice on Greenland.

While global sea level rise is an integrated measure of climate change, the concern of sea level change is foremost an issue affecting specific local areas that could be a consequence of natural processes. Here, sea level is influenced by ocean currents and wind patterns as well as by ongoing tectonic processes. There are regions where sea level has been rising and others where the sea level has been falling over longer periods of time. Such local trends over the last decades might be *several times larger* than the global mean trend of 3 mm/year.

A fundamental problem facing virtually all Earth system studies today is the need for long-term observations and monitoring as well as better and more relevant observations. *The dilemma is that the time scale of the internal mode of variability of the system is significantly longer that the lifetime of a dedicated space mission, which makes it extremely difficult to separate a climate signal from the noise of natural processes*. We are, for example, not able to establish whether the recent marked mass losses noted by GRACE and ICESat on Greenland are robust signals or not. This calls for a dual strategy combining new space missions with continued and extended measurements by space instruments whose performance and value has already been proved.

References

Church JA, White NJ (2011) Sea-level rise from the late nineteenth to the early twenty-first century. Surv Geophys 32, this issue. doi:10.1007/s10712-011-91191-1

Hansen JE, Sato M (2011) Paleoclimate implications for human-made climate change. Atmospheric Ocean Phys arXiv:1105.0968v1

Intergovernmental Panel on Climate Change (IPCC) (2007) Climate change 2007: the physical science basis. In: Solomon S, Qin D, Manning M, Chen Z, Marquis M, Avery KB, Tignor M, Miller HL (eds) Climate Cambridge University Press, Cambridge

Lemke P, Ren J, Alley RB, Allison I, Carrasco J, Flato G, Fujii Y, Kaser G, Mote P, Thomas RH, Zhang T (2007) Observations: changes in snow, ice and frozen ground. In: Solomon S, Qin D, Manning M, Chen Z, Marquis M, Avery KB, Tignor M, Miller HL (eds) Climate change 2007: the physical science basis. Contribution of working group I to the fourth assessment report of the intergovernmental panel on climate change. Cambridge University Press, Cambridge

Nicholls R, Cazenave A (2010) Sea level change and the impacts in coastal zones. Science 328:1517–1520. doi:10.1126/science.1185782

Woodworth PL, Menéndez M, Gehrels WR (2011) Evidence for century-timescale acceleration in mean sea levels and for recent changes in extreme sea levels. Surv Geophys 32, this issue. doi:10.1007/s10712-011-9112-8

Surv Geophys (2011) 32:319–328
DOI 10.1007/s10712-011-9129-z

Climate Change Challenges

Hartmut Grassl

Received: 23 December 2010 / Accepted: 12 May 2011 / Published online: 10 June 2011

Abstract Anthropogenic climate change has emerged as one of the major challenges for mankind in the centuries to come. The strongly modified composition of the atmosphere, due to emissions of greenhouse gases and aerosol particles, leads to an enhanced greenhouse effect and also intensified backscattering of solar radiation by aerosol particles. The resulting global mean warming will have a major impact on the entire cryosphere, with global consequences via mean sea level rise and redistributed precipitation. This introductory presentation will summarize the emergence of the topic, its already observed consequences for the cryosphere, and it will also discuss issues in climate policy making when dealing with the climate change challenge.

Keywords Climate change · Cryosphere · Sea level

1 Introduction

Anthropogenic climate change has emerged as one of the key challenges for humankind in the twenty-first century besides biodiversity loss and the development of less developed countries. This contribution is meant to show the overall facets of climate change while the workshop itself concentrated on the Earth's cryosphere and its associated sea level change, which is part of a strong positive feedback in the water cycle, the so-called albedo-temperature feedback. This contribution will also show how difficult it will be to reach the 2°C goal. This maximum tolerable mean global warming until the end of the twenty-first century, in comparison to the preindustrial value, was already taken note of at the 15th Conference of the Parties (COP 15) to the United Nations Framework Convention on Climate Change (UNFCCC) in Copenhagen in December 2009 and was made an accepted global goal (only Bolivia did not agree) at COP 16 in Cancun in December 2010. At the same time I will show that this stringent goal might not be sufficient to avoid a dangerous interference with the climate system as stipulated in the UNFCCC. In Sect. 2 I will report

H. Grassl (✉)
Max Planck Institute for Meteorology, Hamburg, Germany
e-mail: hartmut.grassl@zmaw.de

about the emergence of the knowledge about the greenhouse effect of the atmosphere and then in Sect. 3 about the observation (better called estimate) of the fundamental climate parameter, the solar radiation flux density. In Sect. 4 I repeat the IPCC projections of mean global warming and the redistribution of precipitation. A main consequence of this global mean warming, very often forgotten in the climate change debate, is the growing injustice due to stronger impacts for those not having considerably contributed to it. In Sect. 5 observed reactions of the cryosphere are summarized and Sect. 6 shows which climate change impacts a 2°C goal will still not be able to avoid and points to the uniqueness of the present situation in recent Earth history with its consequences for policy making.

2 Development of the Knowledge about the Greenhouse Effect

The famous French scientist Joseph Baptiste Fourier was the first to describe what is now called the greenhouse effect (Fourier 1824): "La transparence des eaux et celle de l'air paraissent concourir à augmenter le degré de chaleur acquise, parce que la chaleur lumineuse affluente pénètre assez facilement dans l'intérieur de la masse, et que la chaleur obscure sort plus difficilement suivant une route contraire" (Translation by the author: Both the transparency of water and air seem to augment the heat absorbed because the incoming visible heat penetrates rather easily into the interior of the mass but the invisible heat escapes more difficult).

The first clear description of the greenhouse effect of the Earth's atmosphere was published about 40 years later by John Tyndall. In 1863 he wrote: "The solar heat possesses the power of crossing an atmosphere, but, when the heat is absorbed by the planet, it is so changed in quality that the rays emanating from the planet cannot get with the same freedom back into space. Thus the atmosphere admits the entrance of the solar heat but checks its exit, and the result is a tendency to accumulate heat at the surface of the planet" (Tyndall 1863). The first to talk about anthropogenic climate change caused by an enhanced greenhouse effect of the atmosphere was Svante Arrhenius. He used the knowledge of carbon dioxide absorption bands published by Langley to argue that increased combustion of coal may lead to higher surface temperatures. He stated: '[…] if the quantity of carbonic acid [i.e. carbon dioxide] increases in geometric progression, the augmentation of the temperature will increase nearly in arithmetic progression' (Arrhenius 1896). In other words he knew that the growth of the greenhouse effect by carbon dioxide depends at present concentration ranges on the logarithm of the concentration increase.

The full theory of anthropogenic climate change caused by changed atmospheric composition was established by Guy Stuart Callendar. He stated: 'As man is now changing the composition of the atmosphere at a rate which must be very exceptional on the geological time scale, it is natural to seek for the probable effects of such a change. From the best laboratory observations it appears that the principal result of increasing carbon dioxide […] would be a gradual increase in the mean temperature of the colder regions of the Earth' (Callendar 1939). Even the stronger temperature changes at high latitudes—in comparison to the low latitudes—was part of his reasoning. Implicitly he talked about the positive albedo-temperature-feedback, which is estimated to cause half of the temperature difference between a glacial and the following interglacial period. If expressed in terms of radiative forcing about 3.5 ± 1 W/m^2 are due to this positive feedback of the water cycle based largely on the extreme albedo difference between snow and liquid water or bare soil (Hansen et al. 2007).

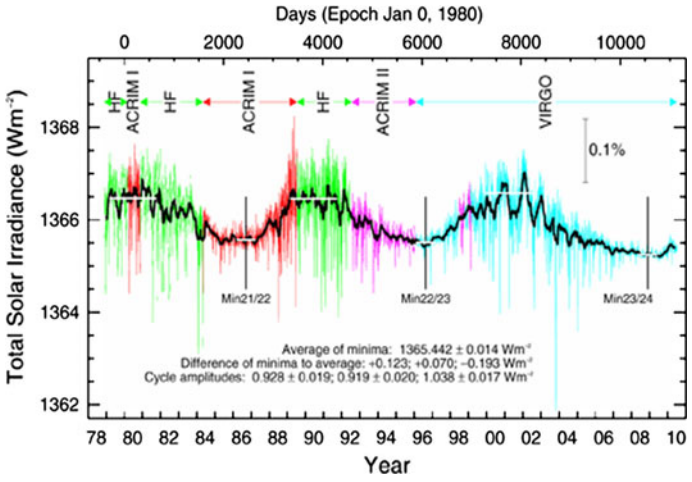

Fig. 1 Daily total solar irradiance of the PMOD composite (updated until end of March 2010, Version 41 62 1003a) and extrapolated with a proxy model *back* to 1976. The amplitudes of the three cycles decrease first and then increase again. The three *horizontal lines* indicate the minima in 1986, 1996 and 2008, respectively. Note the low value of the 2008/9 minimum, which is 0.22 Wm^{-2} lower than the previous one, or 25% in terms of the mean cycle amplitude. *Source*: Fröhlich (2010)

3 Observed Solar Irradiance Changes

One of the key climate parameters is the radiation flux density or solar irradiance at the top of the atmosphere, formerly often called the solar constant. Fortunately, we have satellite observations of this quantity since 1978. As Fig. 1 clarifies, there is no significant trend in solar radiation output since then. The period with the largest mean global warming rate at the Earth's surface since direct observations began in the mid nineteenth century is thus accompanied by a statistically insignificant negative trend of solar radiation flux density.

Also the often discussed influence of solar activity on cloud formation via a modulation of ionization of the atmosphere caused by cosmic radiation, as postulated by Svensmark and Friis-Christensen (1997), is not detectable in cloud observations of the recent few solar activity cycles. If there would be a strong one, the different solar cycles should also be detectable in significant oscillations of surface climate parameters like temperature and precipitation, for which we have long homogenized time series in larger parts of the earth surface (IPCC 2007a). Unfortunately such long time series do not exist for cloud cover. However, in the stratosphere clear signals of a solar cycle influence on ozone concentration profiles have been detected for the recent decades.

4 Projections of Anthropogenic Climate Change

After the scientists and governments had accepted the now famous sentence "The balance of evidence suggests a discernible human influence on global climate" (IPCC 2007a), the main scientific debate is about answers to the following still in parts open question: "When and where will climate change, by which amount for which climate parameter, given a distinct behaviour of humankind". The main answer so far is contained in Fig. 2 (taken

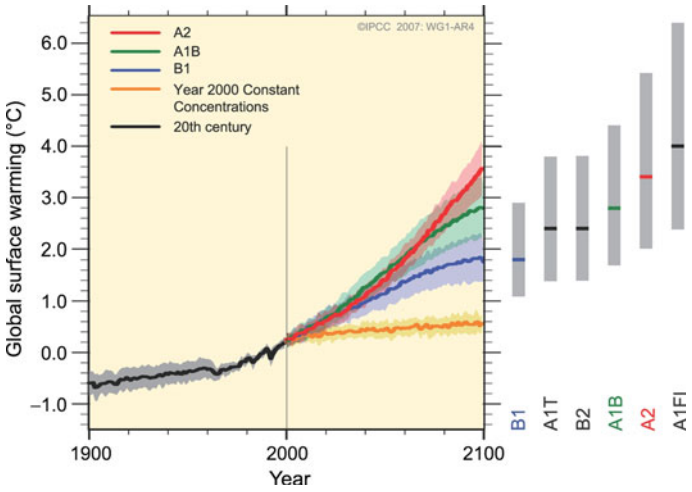

Fig. 2 Mean global warming projected with climate models. *Solid lines* are multi-model global averages of surface warming (relative to 1980–1999) for the scenarios A2, A1B and B1, shown as continuations of the twentieth century simulations. Shading denotes the ±1 standard deviation range of individual model annual averages. The *orange line* is for the experiment where concentrations were held constant at year 2000 values. The *grey bars* at right indicate the best estimate (*solid line* within each *bar*) and the likely range assessed for the six SRES marker scenarios. The assessment of the best estimate and likely ranges in the *grey bars* includes the AOGCMs in the *left* part of the figure, as well as results from a hierarchy of independent models and observational constraints

from the Fourth Assessment Report (AR4) of IPCC (2007b). Would one draw two horizontal lines in this figure showing the highest temperature ever experienced by *homo sapiens* (1.0–1.5°C above preindustrial levels) and the 2°C goal (maximum tolerable temperature increase in the twenty-first century compared to the preindustrial level) both lines would lie below all scenarios in a few decades from now. Without strong climate policy we will enter with very high probability into a climate never experienced by mankind.

For most people in low geographical latitudes the key climate parameter is precipitation. Because mean global warming is not uniform, showing strong latitudinal and also longitudinal gradients, there must be a change of atmospheric circulation and thus a redistribution of precipitation as well. For one of the scenarios in Fig. 2, namely A1B, standing for a balanced energy supply system using all conventional and also renewable sources, if economically competitive, in a world with continuing globalisation, the redistribution of precipitation is presented in Fig. 3 IPCC (2007b). Both for boreal winter and summer a systematic change becomes visible: More precipitation in high latitudes and also large parts of the inner tropics and much less in most semi-arid and sub-humid climates of the tropics and subtropics. Slightly exaggerated: Areas with enough water get more and those with present water scarcity get often even less. In other words: Climate change impacts more on those not having caused the bulk of climate change, hence leading to growing injustice. There is a simple physical explanation for the redistribution of precipitation: Because of stronger warming in high latitudes the latitudinal temperature gradients, the reason for mid-latitude cyclones, shrink, enlarging the Hadley cell and thus moving the storm tracks slightly polewards. Whether these storms become weaker or stronger is the

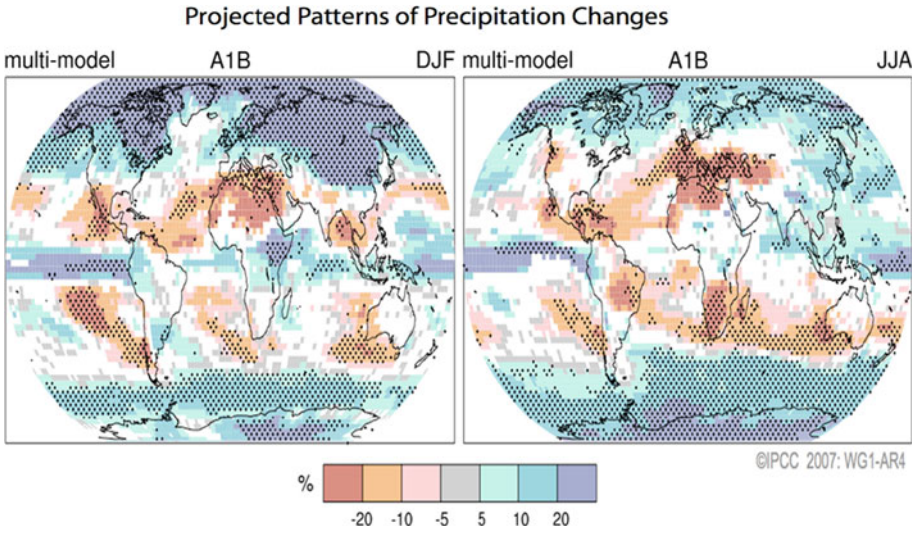

Fig. 3 Relative changes in precipitation (in percent) for the period 2090–2099, relative to 1980–1999. Values are multi-model averages based on the SRES A1B scenario for December to February (*left*) and June to August (*right*). *White areas* are where less than 66% of the models agree in the sign of the change and stippled areas are where more than 90% of the models agree in the sign of the change

result of two opposing processes, namely the reduced temperature gradient which reduces and the intensified water cycle in the cyclones at higher temperatures which increases storm intensity. Therefore maximum wind speed changes might remain small while maximum rain intensity will grow; for details see Bengtsson et al. (2006) and (2009).

5 Observations of the Reactions of the Cryosphere

The cryosphere is the climate system component reacting with maybe the strongest positive feedback of the water cycle. The strong difference between the albedo of a snow surface and the underlying ground or the ocean—in extreme cases powder snow on sea ice with nearly 90 percent shortwave albedo is replaced by ocean water with a very low albedo of typically only 4–7 percent, depending on solar zenith angle, cloudiness and phyto-plankton concentration. Therefore, any modest change in atmospheric composition leading to a warming or cooling will inevitably result in an amplified effect by this feedback and also the positive water vapour feedback, if other negative feedbacks are not counteracting more strongly. Such a counteracting feedback could be related to changes in cloud albedo and/or cloud amount stimulated by a global warming or cooling tendency. However, the cloud feedback is not yet determined with high enough accuracy to be able to speak about the sign of the feedback. As stated by IPCC (2007b), the result of all anthropogenic climate influencing factors is a mean global warming, i.e., cloud feedbacks both to an enhanced greenhouse effect and/or the increased atmospheric turbidity—if overall negative—must be weaker than the sum of the two positive ones in the water cycle for the present climate change rate.

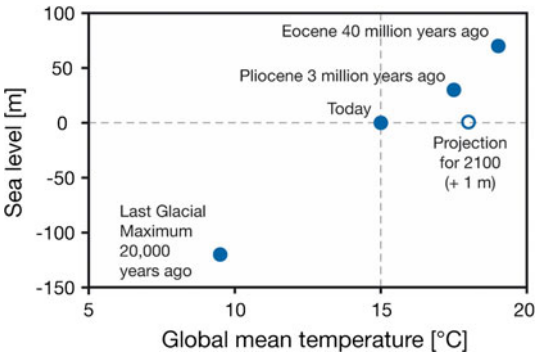

Fig. 4 Mean global temperature and sea level (relative to today's) at different times in Earth's history, with the maximum projection for the year 2100 (1 m above today's sea level). For the long term a much higher sea-level rise probably has to be assumed than that predicted for 2100. *Source*: WBGU (2006) and Archer (2006)

5.1 Observed Sea Level Changes in the Past

Mean sea level changes in the last about 50 million years are the result of many factors: ocean bottom topography changes caused by plate tectonics, land ice volume, fresh water volume in lakes, permafrost and rivers, and ocean temperature changes. As demonstrated in Fig. 4, long-term sea level reached a minimum of −120 m during the last glacial maximum and about +75 m in a period without inland ice sheets, like in the Eocene about 40 million years ago. Figure 4 also points to a major question mark of today's discussions: A sea level rise by only 1 m, as projected as the uppermost value for the twenty-first century, is a very low estimate compared to the changes in Earth history for the same amount of long lasting warming, when time scales of thousands of years allowed for a nearly complete adaptation of the climate system to changed boundary conditions. In other words: Will the anthropogenic climate change due to an enhanced greenhouse effect last long enough to trigger the irreversible (for timescales of human cultures) melting of the Greenland ice sheet (see Ridley et al. (2005) and Ridley et al. (2010)) Or in even other words: Is the 2°C goal already too high and will it trigger the melting of the main ice sheets? Several scientists believe that this might happen but more evidence is still required.

5.2 Observed Recent Sea Level Changes

Since 1993 satellite altimeters (radars measuring the distance between satellite and ocean surface with an accuracy of about 1 cm per radar pulse) allow the determination of regionalized sea level height for the world ocean with unprecedented accuracy. Therefore we can now plot maps of regionalized sea level changes averaged over about 18 years. One of these maps in Fig. 5 from NOAA (2010) is not only showing that in large regions sea level is rising with a rate well above 5 mm per year but also points to the peculiarities of oceanic and atmospheric circulation: strong mesoscale eddies along the major ocean currents lead to sea level rise or fall in adjacent regions, and also changed atmospheric circulation redistributes ocean water in major ocean basins (e.g., the Pacific). The mean sea level change rate of the recent 18 years lies at about 3 mm/year. During this period it is estimated that about a third stems from thermal expansion of sea water, the remaining part mainly from melting of mountain glaciers and mass losses from the land ice areas of Greenland and Antarctica. For details please see the contribution by Church and White (2011) in this Special Issue and book.

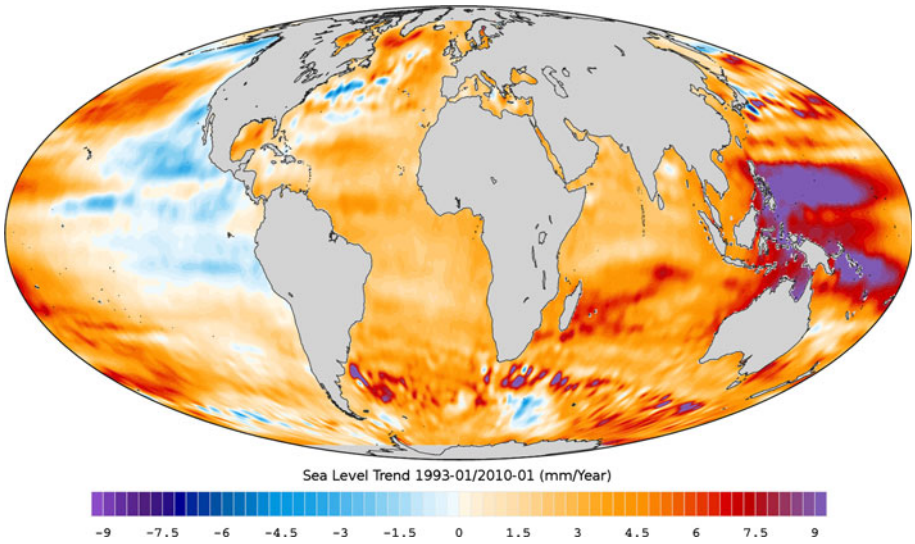

Fig. 5 Sea level change rate per year as derived from satellite altimeter measurements for the period from 1993 to early 2010; *Source*: NOAA (2010)

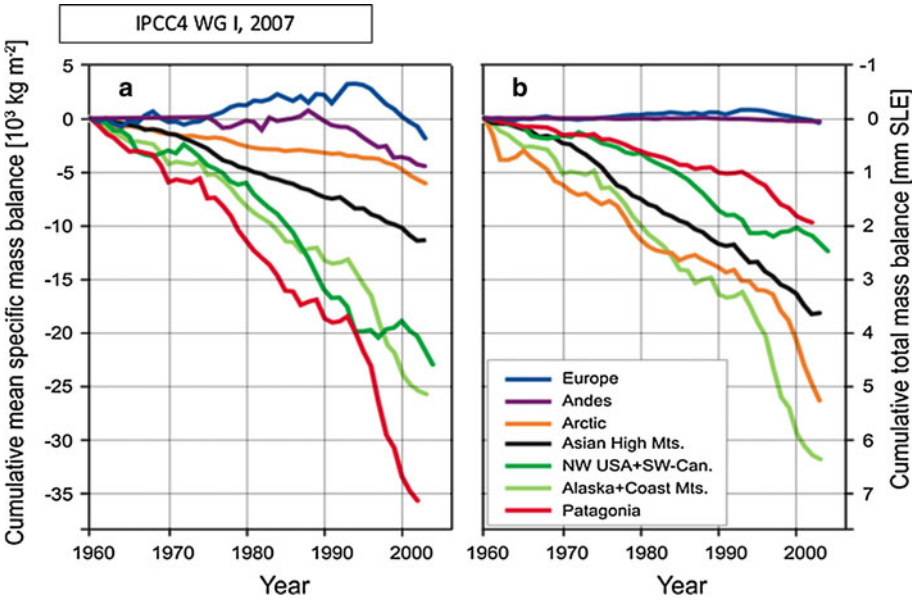

Fig. 6 Cumulative mean specific mass balances (**a**) and cumulative total mass balances (**b**) of glaciers and ice caps, calculated for large regions (Dyurgerov and Meier 2005). Mean specific mass balance shows the strength of climate change in the respective region. Total mass balance is the contribution from each region to sea level rise

5.3 Observed Melting of Mountain Glaciers

One of the most obvious impacts of mean global warming is the average mountain glacier retreat. Nearly all glaciers in all major mountain ranges shrink (see Fig. 6). Only in Europe did the retreat start rather late during the recent about 50 years, because major European glaciers are maritime glaciers in Iceland and Scandinavia whose mass loss by higher summer temperatures was until recently largely compensated by considerably higher wintertime snow accumulation in high latitudes (as a consequence of higher temperatures).

5.4 Mass Balance Changes of the Greenland Ice Sheet

Assessing the net mass balance of an ice sheet is very difficult, because melting occurs at the rim of the ice sheet, glaciers are calving into the sea and (additional) snow accumulates in the interior. For the Greenland ice sheet this means a very small difference between two large numbers. As it has become such a decisive topic for climate policy making and new studies are published with partly controversial results it is best to resort to the IPCC (2007) statement: Modelling studies as well as satellite observations, airborne altimeter surveys and other studies suggest a slight inland thickening and strong marginal thinning resulting in an overall negative Greenland Ice Sheet mass balance which has accelerated recently. It has reached 0.21 ± 0.07 mm/a for the 1993–2003 period.

For the Antarctic ice sheet the value is similar but the uncertainty of the mass balance estimates is much higher (0.21 ± 0.35 mm/a).

6 Impacts of Climate Change and Implications for Climate Policy

Climate is among the most important natural resources for all living beings, hence a rapid global climate change threatens entire life. Since the Third Full Assessment Report (TAR) of IPCC in 2001 research has shown that the vulnerability of natural and managed ecosystems as well as the economic system is higher than estimated so far. This is made clear by Fig. 7, taken from Smith et al. (2009).

In the most recent assessment report IPCC (2007a) has condensed the observations of global warming into the following sentence: The understanding of anthropogenic warming and cooling influences on climate has improved since the Third Assessment Report (TAR), leading to very high confidence that the global average net effect of human activities since the year 1750 has been one of warming, with a radiative forcing of +1.6 [+0.6 to +2.4] W/m^2. The very large range of radiative forcing is mainly due to very large uncertainties of the indirect aerosol effects on clouds. Mankind is thus confronted with a unique situation: Key challenges for policy makers following from this statement and the knowledge of the functioning of the climate system, e.g., with respect to turnover time of ocean circulation and rapid natural global climate change, are:

- Mankind has to make globally coordinated decisions in the coming decade for centuries to come.
- The global mean climate change rate is for the twenty-first century by a factor of at least 30 above the fastest natural global temperature change rate during the recent 800,000 years, if a globally coordinated climate policy does not exist. Can ecosystems adapt naturally to these rapid changes as stipulated by the UNFCCC in a side condition of its key goal?

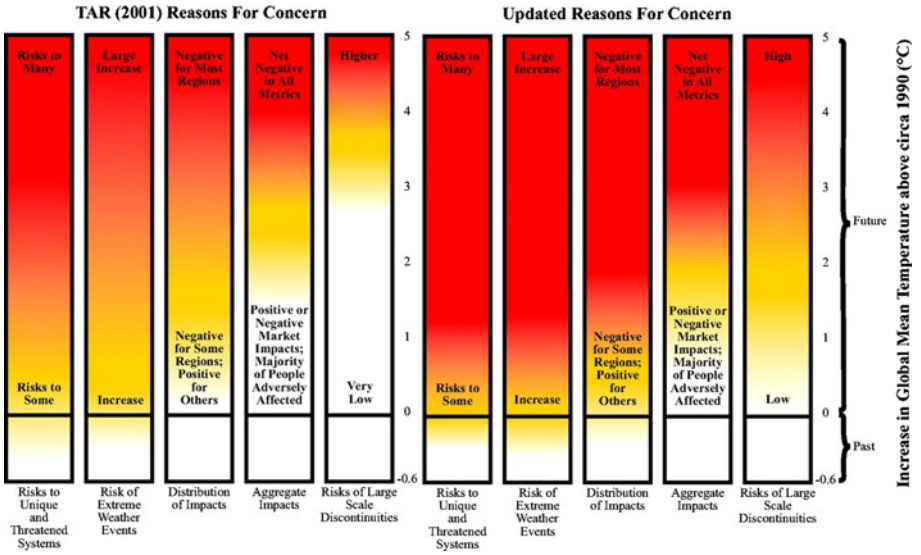

Fig. 7 Risks from climate change, by reason for concern—2001 compared with updated data. Climate change consequences are plotted against increases in global mean temperature (°C) after 1990. Each column corresponds to a specific reason for concern (RFC) and represents additional outcomes associated with increasing global mean temperature. The color scheme represents progressively increasing levels of risk and should not be interpreted as representing ''dangerous anthropogenic interference,'' which is a value judgment. The historical period 1900–2000 warmed by 0.6°C and led to some impacts. It should be noted that this figure addresses only how risks change as global mean temperature increases, not how risks might change at different rates of warming. Furthermore, it does not address when impacts might be realized, nor does it account for the effects of different development pathways on vulnerability. **a** RFCs from the IPCC TAR. **b** Updated RFCs derived from IPCC AR4

- Poor countries and poor parts of societies, not having caused significantly the changed composition of the atmosphere, will suffer more strongly from rapid anthropogenic climate change, thereby increasing injustice between the rich and the poor.
- Both major challenges of mankind, namely development of the developing countries and the dampening of the anthropogenic climate change rate can hamper each other, if the developed countries and those countries in the process of a strong industrialization of their economies (the latter encompassing roughly half of the world population) do not rapidly transform their energy supply systems into sustainable ones.

With the consensus reached at COP 16 in Cancun there is some hope for meeting these challenges.

References

Archer D (2006) Global warming: understanding the forecast. Blackwell Publishers, Oxford, UK

Arrhenius S (1896) On the influence of carbonic acid in the air upon the temperature of the ground. London, Edinburgh, and Dublin Philosophical Magazine and Journal of Science (fifth series) 41:237–275

Bengtsson L, Hodges KI, Roeckner E (2006) Storm tracks and climate change. J Climate 19:3518–3543

Bengtsson L, KI Hodges, N Keenlyside (2009) Will extra-tropical storms intensify in a warmer climate? J Climate 2276–2301

Callendar GS (1939) The composition of the atmosphere through the ages. Meteorol Mag 74:33–39
Church JA, White NJ (2011) Sea-level rise from the late 19th to the early 21st Century. Surveys in Geophysics (Accepted)
Dyurgerov M, Meier MF (2005) Glaciers and the changing earth system: a 2004 Snapshot. Occasional paper 58. Institute of Arctic and Alpine Research University of Colorado, Boulder, CO
Fourier J (1824) Remarques Générales sur les Températures du Globe Terrestre et des Espaces Planétaires. Annales de Chimie et de Physique 27:136–167
Fröhlich C (2010) Solar irradiance variations: what have we learned from the past three solar cycles? Lecture Notes for the Summer School in Alpbach 2010; World Radiation Center, CH-7260 Davos-Dorf, Switzerland
Hansen J, Sato M, Kharecha P, Russell G, Lea DW, Siddall M (2007) Climate change and trace gases. Phil Trans R Soc A 365:1925–1954. doi:10.1098/rsta.2007.2052
IPCC (2007a) Contribution of working group I to the fourth assessment report of the intergovernmental panel on climate change, 2007. In: Solomon S, Qin D, Manning M, Chen Z, Marquis M, Averyt KB, Tignor M, Miller HL (eds.) Cambridge University Press, Cambridge, United Kingdom and New York, NY, USA
IPCC (2007b) Summary for policymakers. In: Solomon S, Qin D, Manning M, Chen Z, Marquis M, Averyt KB, Tignor M, Miller HL (eds) Climate change 2007: the physical science basis. Contribution of working group I to the fourth assessment report of the intergovernmental panel on climate change. Cambridge University Press, Cambridge
NOAA (2010) File NOAA sea level trend 1993 2010.png assessed on 22 12 2010 from Wikipedia
Ridley JK, Huybrechts P, Gregory JM, Lowe JA (2005) Elimination of the Greenland ice sheet in a high CO_2 climate. J Climate 18:3409–3427. doi:10.1175/JCLI3482.1
Ridley J, Gregory JM, Huybrechts P, Lowe J (2010) Thresholds for irreversible decline of the Greenland ice sheet. Climate Dynamics 35:1065–1073. doi:10.1007/s00382-009-0646-0
Smith JB, Schneider SH, Oppenheimer M, Yohe GW, Hare W, Mastrandrea MD, Patwardhan A, Burton I, Corfee-Morlot J, Magadzaj CHD, Füssel H-M, Pittock AB, Rahman A, Suarez A, van Ypersele J-P (2009) Assessing dangerous climate change through an update of the Intergovernmental panel on climate change (IPCC) "reasons for concern". PNAS 106(11):4133–4137. doi:10.1073/pnas.0812355106
Svensmark H, Friis-Christensen E (1997) Variation of cosmic ray flux and global cloud coverage—a missing link in solar-climate relationships. J Atmos Sol Terr Phys 59:1225–1232
Tyndall J (1863) On the transmission of heat of different qualities through gases of different kinds. Proc Royal Inst Great Britain 3:158
WBGU (Global Change Advisory Council of the German Federal Government) (2006) The future oceans: warming up, rising high, turning sour. Berlin ISBN 3-936191-14-X

Surv Geophys (2011) 32:329–350
DOI 10.1007/s10712-011-9140-4

Climates of the Earth and Cryosphere Evolution

Gilles Ramstein

Received: 18 March 2011 / Accepted: 9 June 2011 / Published online: 8 September 2011

Abstract The interrelationship between the cryosphere and the climate is not always operating on Earth over a scale of billions or millions of years. Indeed, most of the time, the Earth is regulated at temperatures such that no ice sheet exists. Nevertheless, it is very fruitful to understand the conditions where and when ice sheets were triggered during the Earth's history. This paper deals with the paleoclimate and the cryosphere in the last 4.6 Ga and explains the different processes that make the climate of the first 4 billion years warm despite the weaker solar luminosity. We also describe the more recent evolution in the last 65 million years when a global decrease in atmospheric CO_2 from around 4 PAL to 1 PAL was associated with a global cooling (1 PAL present atmospheric level = 280 ppm). It is in this context that the Quaternary occurred characterized by low atmospheric CO_2 and the presence of two perennial ice sheets in Greenland and Antarctica. The last million years are certainly the most documented since direct and reliable CO_2 measurements are available. They are characterized by a complex climate/cryosphere dynamics leading to oscillations between long glacial periods with four ice sheets and shorter ones with only two ice sheets (interglacial). We are currently living in one of those interglacials, generally associated with a CO_2 level of 280 ppm. Presently, anthropogenic activities are seriously perturbing the carbon cycle and the atmospheric CO_2 content and therefore the climate. The last but not least question raised in this paper is to investigate whether the anthropogenic perturbation may lead to a melting of the ice sheets.

Keywords Paleoclimate · Thermal regulation · Onset of ice sheets · Climate/cryosphere modelling

G. Ramstein (✉)
Laboratoire des Sciences du Climat et de l'Environnement/CEA Saclay, IPSL UMR 8212, CNRS, l'Université de Versailles Saint-Quentin, 91191 Gif-sur-Yvette, France
e-mail: Gilles.ramstein@lsce.ipsl.fr

1 Introduction

We very often consider that we live in a warm climate. Through this travel in the deep ages of the Earth, we shall see that this idea is mostly wrong, depending on the timescale we are using. This paper aims at showing the relationships between the climate and the cryosphere during the Earth's history. A striking feature is that, most of the time, there is just no cryosphere at all. Periods when ice sheets developed are indeed very seldom (Frakes et al.

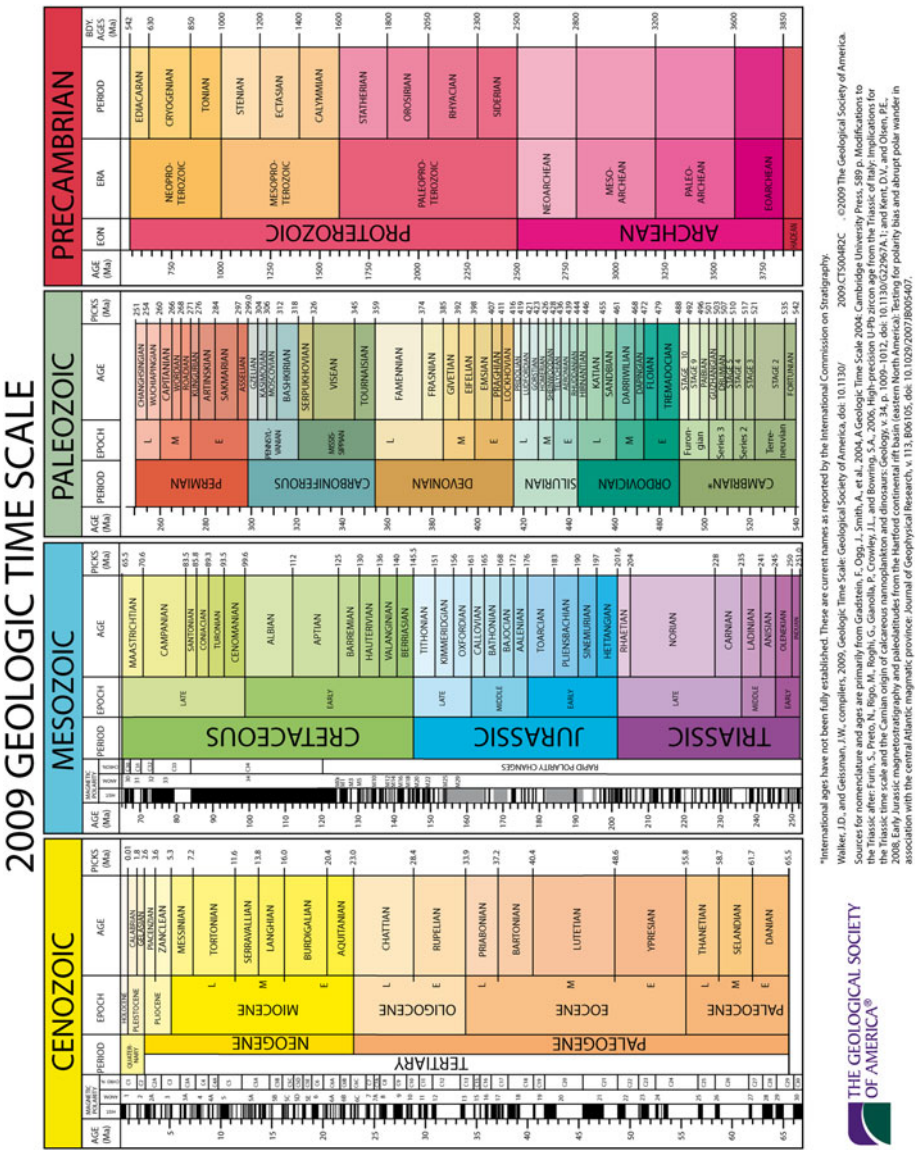

Fig. 1 Geological timetable in units of 1,000 years. From the Geological Society of America: http://www.geosociety.org/science/timescale/

1992). The most common climate state of our planet is in fact warm (see Fig. 1 for a geological timetable). Since the Precambrian explosion, 540 Ma ago (Ma = 10^6 years), the period that is best documented, the glacial periods are also very infrequent. For instance, the dinosaurs, which lasted very long (220–65 Ma), lived during warm climates without any ice sheet most of the time (Amiot et al. 2006). In contrast, the period where we presently live (the Quaternary) with two ice sheets (one in each hemisphere) in the last 2.6 Ma is indeed a cold period and one of the rare periods on the geological timescale where ice sheets did exist. Indeed, for more than 1 Ma, the climate has shifted from glacial (80%) to interglacial (20%). During the glacial period, four ice sheets existed. As well as Greenland and Antarctica, two extra ice sheets were located over the northern parts of North America (Laurentide) and over the north of Europe (Fennoscandia). In the most recent 14,000 years, we are in a warm interglacial climate (Holocene) during which human population has spread all over the world.

This paper not only considers the role of the cryosphere on past climate, but also deals with the future behaviour of the cryosphere under anthropogenic forcing. It discusses what we may infer as to the future evolution of Greenland and Antarctica beyond the twenty-first century, and whether the large and rapid increase in greenhouse gases may melt the ice sheets that normally survive during interglacial conditions. We shall also consider the thresholds and the scenarios that may lead to both the onset and decay of the ice sheets using coupled climate and cryosphere modelling.

2 Precambrian Climate

In the last 4.6 Ga (Ga = 10^9 years), solar radiation has represented an unparalleled forcing factor for providing energy to the Earth. The Sun—this is certainly not the most poetic definition—is 'just' a nuclear fusion reactor, which "burns" its hydrogen into helium and then helium itself. The resulting evolution of the Sun's luminosity is well modelled (Gough 1981; Fig. 2) and shows an increase of ~7% per each billion years (Ga). Therefore, 4.6 Ga ago, the young Sun was a 'weak' Sun as compared to its present status. The implications

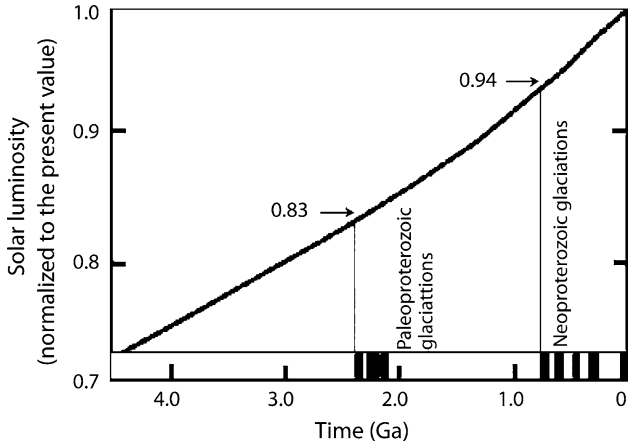

Fig. 2 Evolution of the Sun's luminosity with time in the last 4.6 Ga, as predicted by the computer model of Gough (1981). The increase is around 7% every Ga. The young Earth therefore experienced a fainter Sun ~30% less powerful 4.5 Ga ago than at present

for the Earth (but indeed also for Venus and Mars) are huge: first, because solar radiation is the main source of energy for the Earth system (>99%) and second because we know that even the weak variations in solar radiation at the top of the atmosphere (that can reach seasonally 15%), due to the orbital parameters of the Earth, have induced relatively large climatic variations during the Quaternary period (see Sect. 6 The last million year's climate). Consequently, the Earth should have experienced a drastic cooling due to this weak Sun: it should look like the frozen satellites of Jupiter and Saturn. In fact, geological and isotopic measurements demonstrate first that liquid water existed on the Earth's surface for at least 4 Ga, and second that during the Archaean (4.54–2.5 Ga) and the Proterozoic era (2.5–0.54 Ga) (Fig. 1), the Earth was warm with ocean temperatures ranging from 50 to 70°C (Robert and Chaussidon 2006). As to whether these temperatures really represent the Earth's surface temperature remains an open question. There are alternative views that question the temperatures deduced from isotopic values and suggest lower temperatures (Shields and Kasting 2007). This warm Earth situation raises an apparent contradiction: the so-called faint young Sun paradox. Although the greenhouse effect is accepted as the main process to counterbalance the weak young Sun, other interpretations (Rosing et al. 2010) do pinpoint the possibility of a rather cold Archaean climate. In that study, glaciation is avoided because of a lower Earth albedo resulting from the absence of continental mass (ocean albedos being much smaller than terrestrial ones) and because of biologically induced clouds (low-altitude clouds in the present day climate act as a cooling factor whereas this effect did not exist in the deep past). The linear increase in continental accretion results in a linear increase in the Earth's albedo all through the Archaean period. Both hypotheses (timing of the accretion and cloud properties) are puzzling (Flament et al. 2008). First they demonstrate that the relationship between continental accretion and albedo is not straightforward because the continents remain under the ocean surface during a very long period of time; their impact on albedo only becomes important after around 3Ga. Second, the cloud properties during the Achaean are totally unconstrained. Rosing et al. (2010) are still very controversial.

If the greenhouse effect is able to counteract the low forcing of the weak Sun, the next question is *to identify which greenhouse gas would be able to counterbalance the weak faint Sun.* Following the original suggestion of Sagan and Mullen (1972), who identified NH_4 as a possible candidate, most scientists agreed on identifying carbon dioxide as the most appropriate greenhouse gas. The volcanic source of CO_2 must have been enhanced during the early Earth, whereas the sink of CO_2, especially through silicate weathering, was much reduced because there was no or very little continental surface. Therefore, a high level of carbon dioxide in the atmosphere was very likely during the early Earth. However, large amounts of atmospheric carbon dioxide would have produced siderite ($FeCO_3$) on the continental surface (Rye et al. 1995). Unfortunately, none of the oldest rocks do show the presence of any siderite, which leads several authors (Kasting 2004) to suggest that CO_2, by itself, could not "do the job" alone and that another greenhouse gas should have been involved. Methane has been suggested as an appropriate candidate, but the next question is *what would be the possible sink and source of methane on Earth?*

Something often forgotten about the Earth's atmosphere is that during about half of the 4.6 billion years of the Earth's history, the atmosphere was anoxic (deficient in oxygen). An oxygen increase in the atmosphere only occurred 2.2–2.4 billion years ago (Catling and Claire 2005; Bertrand 2005). This feature is largely accepted by the community, even if there are still some controversies (Ohmoto et al. 2006). Several lines of evidence (Knoll 2004) pinpoint the fact that methanogene archae appeared very early in the Tree of Life. Kasting (2004) developed a scenario where the source of methane on Earth, in opposition

to the situation on Titan, can only be biological and most likely produced by these archae, which were very abundant in the ocean. Indeed, the surface temperature on the Earth is much higher than that of Titan, and the environmental conditions do not allow enough of the methane emitted by abiotic sources to be stored in the atmosphere at equilibrium.

What about the methane sink? Over the geological timescale, methane behaves as a "match". It can produce a strong warming because it is a powerful greenhouse gas (30 times more efficient than CO_2), but its residence time in the oxic atmosphere is very short: about 10 years. Methane is oxidized and transformed into carbon dioxide, which is a less powerful greenhouse gas but one that lasts much longer in the atmosphere: several hundreds of years. This is illustrated in the scenario that has been proposed to explain the brutal warming of the Paleocene/Eocene era boundary, 55 million years ago (Dickens and Francis 2004). Many authors invoked, to explain large ^{13}C variations, the huge methane emissions due to the enormous quantity of methane hydrates stored within oceanic sediments. These hydrates are a solid form of methane, in which the CH_4 molecules are inside a network of crystals as ice crystals. The phase diagram is such that a pressure decrease or a temperature increase can provoke a changing phase from solid hydrate CH_4 to gaseous CH_4 (Dickens 2003). The release of methane from the dissociation of the hydrate, highly depleted in $\delta^{13}C$[1] around -60 ‰, explains both the negative carbon excursion observed at the Paleocene/Eocene boundary and the subsequent abrupt warming (Zachos et al. 2001). This is the "match" effect of methane. Of course, in an anoxic atmosphere, the sink of methane is much less efficient. Therefore, both the methane source and sink processes discussed here support the possibility of a strong accumulation of methane in an anoxic atmosphere.

3 Regulation–Deregulation of the Earth's Surface Temperature

As described earlier, in a context where the Sun is fainter by a rather large amount (-30% at 4.6 Ga and -6% at 0.6 Ga with respect to the present—see Fig. 2), carbon dioxide most probably, and methane, would have helped to largely overcompensate the lower solar forcing and would explain the warm climates that the Earth enjoyed. Indeed, the Archaean and Proterozoic show very few evidences of glaciation. Recently, the existence of a Pongolian Glaciation ($\sim$2.7 Ga) has been pointed out (Crowell 1999; Young et al. 1998). Subsequent glaciations occurred, taking account of error bars, synchronously with the atmospheric oxygen rise at 2.4–2.2 Ga, during the so-called Huronian glaciation. This is supported by the evidence of glaciation that has been found in Canada (Fig. 3). The third glaciation occurred more than 1.5 Ga later during the Neoproterozoic. One can always argue that "the absence of evidence (of other glaciations) is not the evidence of absence". This remark is indeed valid when dealing with the deep past where we have only scarce data. Nevertheless, it appears that glaciations are only accidents on Earth, which is most of the time regulated by warm temperatures. *But how does this regulation work? And why did these accidents occur?*

[1] The ∂ notation is defined by the formula:

$$\partial‰ = 1000\left\{\frac{R\,\text{sample}}{R\,\text{standard}} - 1\right\}$$

where R stands for isotopic ratio, for example: $\frac{C^{13}}{C^{12}}$ or $\frac{O^{18}}{O^{16}}$.

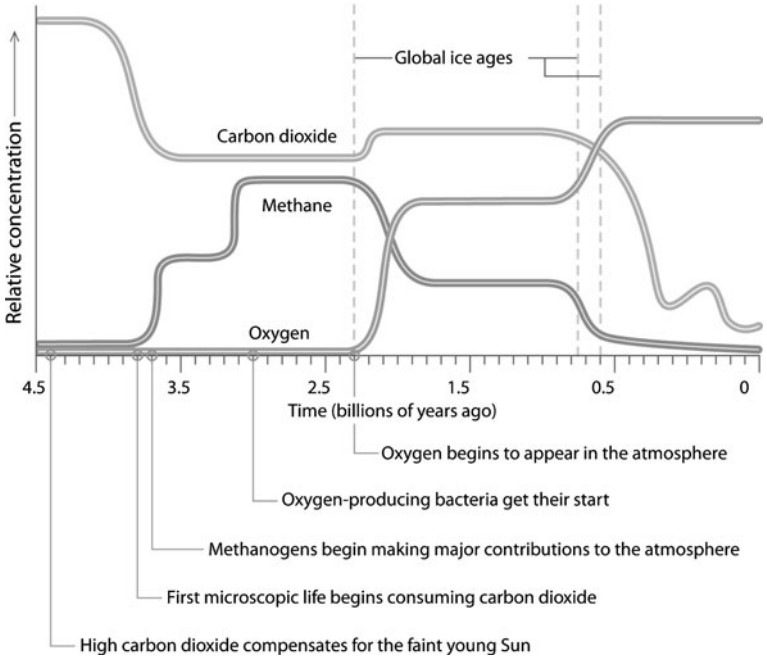

Fig. 3 Long-term evolution of the relative concentrations of CO_2 and CH_4, as well as of O_2. To be noticed are (1) the rapid decrease in methane coinciding with an O_2 rise, leading to the Huronian glaciation (2.2–2.4 Ga) and (2) the drop in CO_2 at the beginning of the Neoproterozoic leading to major glaciation (750 Ma). (From Kasting 2004)

This regulation is not a new idea. Lovelock performed pioneering work showing that many processes including biology make the Earth able to "protect" itself against perturbations (Lovelock 1979). Nevertheless, similar to Wegener, with his continental drift theory, as long as appropriate and well-quantified mechanisms were not found to explain and support this assumption, many scientists remain skeptical of its validity. Long-term interactions between the climate, tectonics, and the carbon cycle may therefore be invoked for supporting the regulation of the Earth system (Walker et al. 1981).

It is indeed difficult, if not impossible, to infer what the climate was before the Late Heavy Bombardment event (Morbidelli et al. 2001) but, through all the period extending between 3.8 Ga and the Precambrian (540 Ma), a regulation mechanism was powerful enough to maintain a warm climate despite a weaker Sun.

This mechanism is closely related to the carbon cycle at geological timescales. As to the source of carbon dioxide, recent publications (Cogné and Humler 2004) show that, for at least the last 100 Ma, there is no evidence that the quantity of carbon dioxide produced by volcanism has changed. It is indeed a very short time period as compared to 3 billion years but, in the absence of recorded variations for that period, we will be conservative and consider the source as constant and equal to the present day value. This hypothesis could be improved accounting for the variation in the heat flux at the Earth's surface (Mareschal and Jaupart 2006). In contrast, silicate weathering, which is the most powerful sink, is dependent on tectonics and therefore on paleogeography. If most of the continental mass is located in the equator/tropics area, the continents experience huge precipitation. The droplets including atmospheric carbon dioxide become acidic and dissolve silicate, which

is transported by runoff to the ocean, and then sink in the form of carbonates with sediments at the bottom of the ocean, resulting in the decrease in atmospheric carbon dioxide. In contrast, if most of the continental mass is located at high latitudes, it will experience a dry climate because of low precipitation, resulting in a weak alteration and little erosion. This low weathering context would logically correspond to an increase in atmospheric carbon dioxide.

More than 90 years ago, soon after Wegener (1915) proposed his tectonic plate drift theory, Köppen and Wegener (1924) showed how it would impact the Earth climate on the long term. However, one major piece of reasoning was missing in that analysis. Not only the climate but also the carbon dioxide content is modified by tectonics through the feedback loop produced by the triptych climate/carbon dioxide/tectonics, which remarkably explains the existence of a warm climate most of the time. When the temperature increases, weathering also increases and carbon dioxide decreases; this leads to a cooling and vice versa. Therefore, carbon dioxide is a powerful thermo-regulator (Walker et al. 1981).

In spite of this feedback and regulation phenomenon, *very rare deviations from this scenario do occur.* As previously discussed, the Earth depends on methane and carbon dioxide to maintain warm temperatures through the greenhouse effect, thereby overcoming the cooling effect of a faint young Sun; this makes the possible occurrence of major glaciations, if the concentration of one of these gases suddenly decreases (Fig. 3): the Earth would become a "snowball". A striking point in Kasting's scenario (Kasting 2004) is the occurrence of a methane drop and of a simultaneous oxygen atmospheric rise corresponding to the so-called Huronian glaciation (2.2–2.4 Ga) (Fig. 3).

What are the causes of these accidents, and what determines their timing? The first one, which occurred 2.2–2.4 Ga ago, could be related to biological activity. The methanogene archae, which prevailed in the surface ocean since about 3.5 Ga, contributed to methane production in the Earth's atmosphere, whereas oxygen producers (cyanobacterias) were totally marginal. On the other hand, because methanogene archae cannot survive in an oxic environment, they had to immigrate to anoxic refugia when the level of oxygen increased. A strong point in Kasting's theory is that when the oxygen concentration rises as a result of oxygen producers' shifts from marginal to prevailing, the archaes disappeared, with the consequence of a sudden drop of atmospheric methane, therefore, triggering a major glaciation. It can therefore be concluded following Kasting that the first large glaciation (Huronian) was driven by a biological crisis and was "instantaneous" on the geological timescale.

4 The Neoproterozoic Era Global Glaciation

Certainly, the most documented 'snowball Earth' episodes are those of the Neoproterozoic Era. They consist of three main glaciations: the two oldest ones, the Sturtian (715 Ma) and the Marinoan (635 Ma), are supposed to be global (Hoffman et al. 1998; Hoffman and Schrag 2002), whereas the third and most recent one, the Rapitan glaciation (550 Ma), appears to be essentially regional and linked to the Appalachian uplift (Donnadieu et al. 2004b). Such global glaciations result from a 'rapid' decrease in the atmospheric CO_2 content. Different lines of evidence are invoked in support of the existence of these temporary global glaciations: (1) paleomagnetism evidence for the presence of an ice sheet at low latitudes; (2) a strong decrease in $\delta^{13}C$; (3) the reappearance, after 1.5 Ga of absence

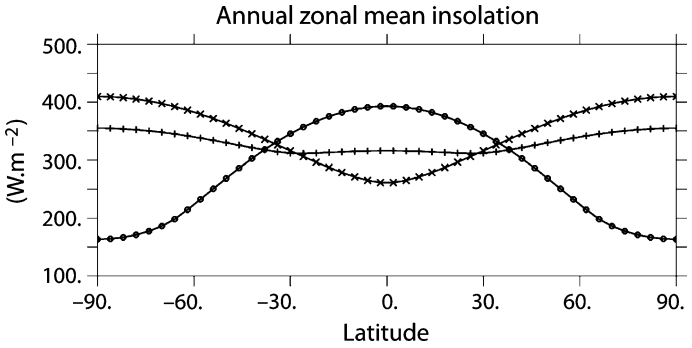

Fig. 4 Annual mean variation in insolation at the top of the atmosphere as a function of latitude, for different values of the Earth obliquity 90° (*crosses*), 60° (*plus signs*), and 23.5° (*dots*). For high-obliquity values, the coldest zones are in the equatorial regions, while for the present obliquity of 23.5°, the polar regions are the coldest. (From Donnadieu et al. (2002); Yannick.Donnadieu@lsce.ipsl.fr, LSCE, France)

of banded-iron formations (BIF[2]); and (4) huge cap carbonate formations overlaying glacial diamictites (tillites), which are typical glacial deposits. These observations were made by different research teams and, till the end of the last century, no reliable global explanation was available, which could help us to understand what was happening during the Neoproterozoic.

Concerning the unusual location of the ice sheet at equatorial latitudes and not in polar regions, a conclusion based on only few reliable paleomagnetic data, an attractive explanation was provided by Williams (1975) and, later on, theoretically demonstrated by Williams et al. (1998). Indeed, if the Earth did have at that time a much larger obliquity (>60°), it is easy to show (Fig. 4) that the lowest annual temperatures would have occurred over the equatorial regions. However, this simple explanation cannot be retained for two main reasons. First, Levrard and Laskar (2003) demonstrated that no realistic mechanism would be able to produce the large decrease in Earth's obliquity from a high value of >60° to its present-day low value of ~23°. Moreover, Donnadieu et al. (2002) showed that such a high obliquity would lead to a huge seasonal cycle, which would be inconsistent with a large mid-latitude ice sheet during the Marinoan glaciation.

Further pioneering work was triggered by the American geologist Harland (1964) who proposed that glaciations in the tropics (as observed through geological evidences) should in fact be global. However, that explanation was not accepted by modellers. A global glaciation would have resulted in an increased albedo on the Earth: instead of being a 'blue planet' with a global albedo of 0.3, the Earth would become a 'white planet' with a global albedo around 0.6–0.8. If such a snowball Earth did ever exist, it should still be here today because the only way to escape glaciation would be to increase the Sun's luminosity by a factor of 1.5, which is not possible. The solution to this conundrum came 30 years later when Kirschvink (1992) proposed that, during a snowball Earth episode, volcanism continues to be active and carbon dioxide continues to be emitted into the atmosphere. In contrast to the normal situation, where it interacts with the terrestrial biosphere and the

[2] In an anoxic environment, Fe^{2+} is soluble in ocean water, whereas Fe^{3+} is insoluble. Therefore due to Fe^{2+} the iron can accumulate in the ocean as it does today at the bottom of the Red Sea. In oxic conditions both oxides are insoluble and iron can no more accumulate i.e. BIF disappeared at 1.8 Ga.

ocean, CO_2 would remain in the atmosphere. Because continents were covered by ice sheets and oceans by sea ice, carbon dioxide was therefore accumulated in the atmospheric reservoir until it was able, through a super-greenhouse effect, to melt the snowball Earth. This scenario is consistent with the other three observations listed previously.

As sea ice and land ice sheets completely inhibit the carbon cycle, carbon is no longer fractionated and the $\delta^{13}C$ value remains very similar to its volcanic original value. As the ventilation of the ocean covered by sea ice completely declined, oxygenation of the ocean drastically decreased. Hence, the reappearance of banded iron formation that prevailed in the Archaean and in the early Proterozoic oceans when the ocean was anoxic and iron could accumulate and re-form the BIFs. Finally, after millions of years, the concentration of carbon dioxide reached a threshold value that resulted in a greenhouse effect strong enough to eventually produce a huge deglaciation, huge precipitation, and strong erosion. In such a very warm climate, a large amount of carbonates sunk into the oceans, explaining the paradox why tillite was overlaid by cap carbonates.

Hoffman's snowball Earth theory supported by these successes became very popular, in explaining most of the apparently paradoxical features that occurred during the Neoproterozoic Era. Nevertheless, many questions remained unsolved (Ramstein et al. 2004a). Why did carbon dioxide largely decrease after the Neoproterozoic perturbation and why was the Neoproterozoic not preceded by similar events during the first billion years of the Earth history? The answers to these questions were provided by Donnadieu et al. (2004a), thanks to a fruitful collaboration between geochemists and climate modellers (Goddéris et al. 2007).

Less than 10 years ago, the influence of paleogeography on CO_2 was suggested in order to explain the large decrease in carbon dioxide. It was known for a long time that continents were oscillating between the building-up of a large supercontinent that subsequently broke into several smaller continents drifting away from each other. The last of these supercontinents was called "Pangaea" that broke up in the period extending between the Triassic and the Cretaceous (Fig. 1). The preceding one, of interest to us here, was called "Rodinia". It was sitting on the equatorial band and spread to $\pm 40°$ (Fig. 5a); it was aggregated before 1 Ga and began to break up only around 800–750 Ma (Fig. 5b; Donnadieu 2004a).

Very peculiar characteristics of that breakup ought to be stressed. While the initial supercontinent extended to low latitudes (Fig. 5a), most of its fragments after break-up remained in the tropical belt (Fig. 5b). Referring to the preceding discussions on how CO_2–climate–tectonics act together to regulate the temperature at the surface of the Earth, it is understandable that this post break-up configuration, where all the fragments remained in the tropics, is the most favourable for producing large atmospheric CO_2 decreases, because these tropical continental masses experienced huge precipitation and massive erosion, creating a large sink of atmospheric CO_2 through silicate weathering as demonstrated by Donnadieu et al. (2004a). That major CO_2 decrease (Fig. 5) is consistent with a drastic cooling that finally shifted the Earth towards a snowball Earth. To escape such a situation, greenhouse warming from volcanic CO_2 stored during several million years in the atmosphere is certainly a robust countermechanism (Kirschvink 1992; Hoffman et al. 1998). Nevertheless, it has been shown recently (Le Hir et al. 2008a, b) that, first, the concept of no interaction of atmospheric CO_2 with oceans is difficult to maintain and, second, that the acidification of the surface oceans due to enormous quantities of CO_2 suddenly in contact with oceans depleted of CO_2 when the sea ice melts is inconsistent with biological evolution (Le Hir et al. 2008a). For these reasons, the behaviour of the carbon cycle during and after a snowball Earth has been substantially modified in the last few years. Le Hir et al. (2008c) showed that atmospheric CO_2 has to penetrate the ocean during a snowball Earth period, while Pierrehumbert (2004) showed that the threshold in CO_2 necessary to melt the

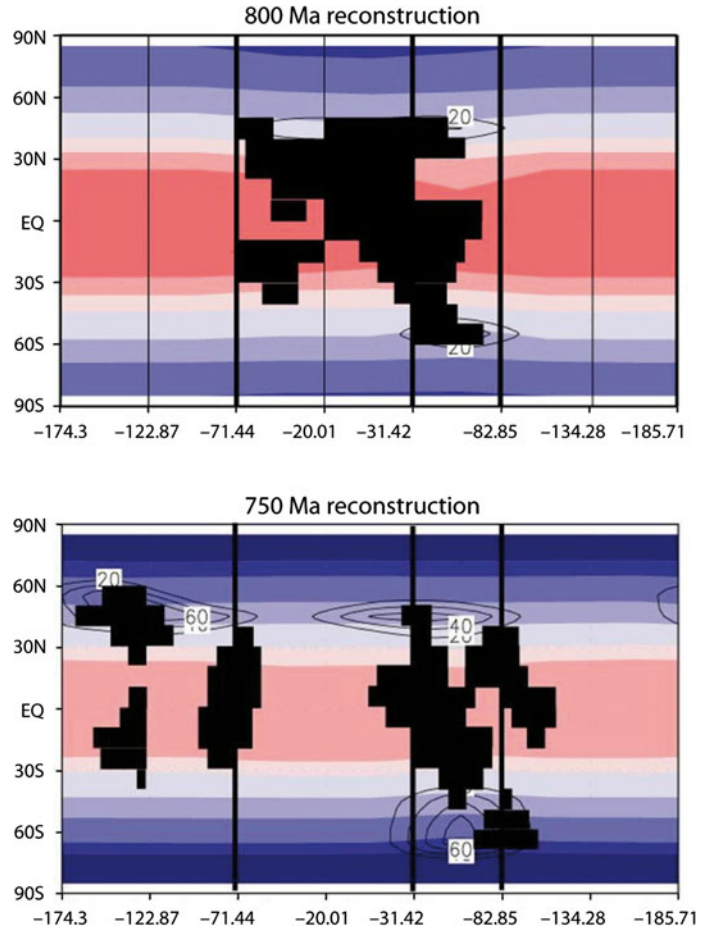

Fig. 5 *Top panel* annual mean temperature (degrees Celsius) reconstructed for the geological context of 800 Ma BP with the Rodinia supercontinent standing in the Equatorial region. The atmospheric CO_2 concentration introduced in the climate/CO_2 model is 1,800 ppm. *Bottom panel* Annual mean temperatures 50 Ma later, i.e., 750 Ma BP. Rodinia has broken into several plates, all of them lying in the tropical band. This configuration corresponds to optimal weathering, leading to a computed drop in CO_2 of 1,300 ppm, which corresponds to an equilibrium value of 500 ppm at 750 Ma (in the 750 Ma reconstruction, the isolines represent the temperature difference between 800 Ma and 750 Ma). (From Y. Donnadieu, Yannick.Donnadieu@lsce.ipsl.fr, LSCE, France)

ice was much higher than predicted. The amount of atmospheric carbon dioxide following these glaciations kept evolving with tectonic activity during the last 500 Ma. However, the Sun's luminosity that increased to a value of about 5% higher today than at the end of the Cambrian Period (Fig. 2) was able to compensate the decay of atmospheric CO_2, preventing the re-occurrence of a snowball Earth.

5 Climate Evolution Since the Precambrian (540 Ma)

The interrelationship between tectonics, climate, and the carbon cycle has played a major role in the regulation of and variation in atmospheric carbon dioxide most of the time. That

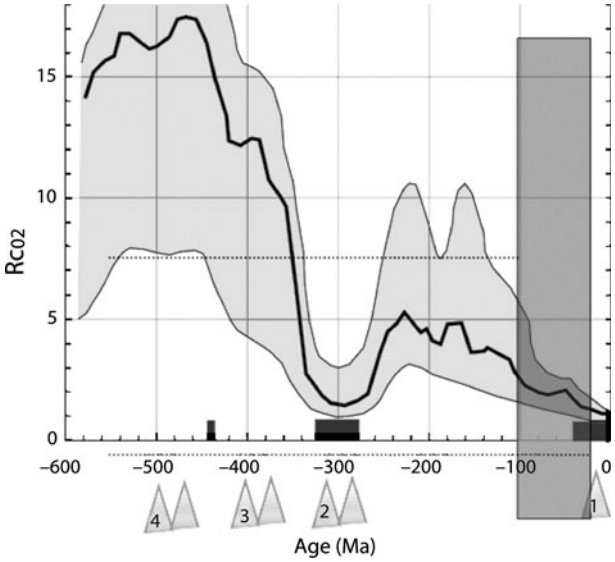

Fig. 6 This curve depicts the most recent results from the GEOCARB model of Berner for the evolution of CO_2 concentration in units of PAL (1 PAL = 280 ppm). The *grey* envelope shows the importance of uncertainties. The window inside the vertical lines corresponds to the Cretaceous–Palaeocene period. (From Berner 1994)

regulation tends to maintain a rather warm climate. Ice sheet build-ups are therefore rare events (Ramstein et al. 2004b). The Paleozoic era that follows the Cambrian (543–250 Ma) experienced a continuous but not linear decrease in temperature and in atmospheric CO_2. Whereas the reconstructions of atmospheric CO_2 concentrations are very scarce (Royer 2006; Knoll 2004), a decrease from 20 PAL to 10 PAL between the beginning and the end of the Paleozoic (Fig. 6) seems to be contemporaneous with the Hirnantian glaciation (Trotter et al. 2008). This glaciation has for long been difficult to explain because it occurred in a period of high concentration of atmospheric CO_2 over a long time (that spans from 500 ka to several Ma). The causes of the long-term cooling, which eventually led to glaciation, were not understood and are still discussed. Some hints of explanation (Kump et al. 1999) were proposed referring to phenomena associated with Taconic orogeny. The uplift of this mountain range that produced large areas covered with basalt had, as a consequence, an increase in orogenic precipitation and a decrease in atmospheric CO_2. As basalt erodes 5–10 times faster than granite, these phenomena resulted in a larger CO_2 sink and a long-term decrease in atmospheric CO_2 (Désert et al. 2003). Nevertheless, this hypothesis has been challenged by different authors and therefore is still an open question. Nardin et al. (2011) attributed the long-term CO_2 drawdown for one-third to fresh volcanic rocks (increased weathering) and two-third to tectonics. The drift in plate tectonics had, as a consequence, that a larger area of the continent was submitted to huge precipitation in the Inter-Tropical Convection Zone (ITCZ), resulting in drastically increased erosion and altogether in a decrease of atmospheric CO_2. This is the context in which at the late Ordovician, the so-called Hirnantian, a glaciation might have occurred (Le Heron et al. 2007). Therefore, it seems that the onset of glaciation did require a weak atmospheric CO_2 and the presence of continents at high latitude. The absolute value of atmospheric CO_2 generally given is 10 PAL, however, with large uncertainties (Boucot and Gray 2001). This

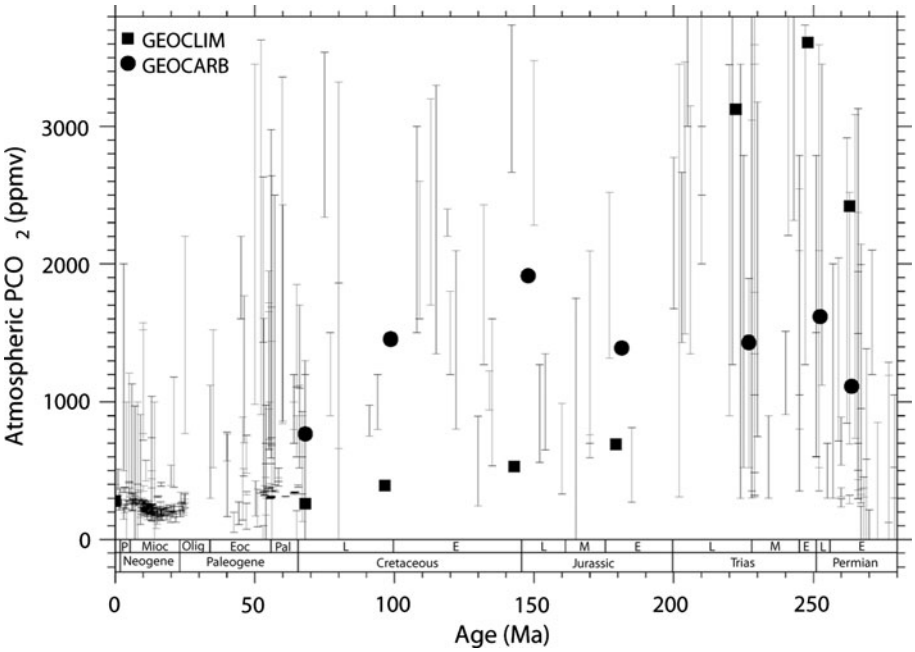

Fig. 7 Reconstruction of atmospheric CO_2 concentrations for the Mesozoic and the Cenozoic since 250 Ma, derived from two different models GEOCARB (*circles* Berner 1994) and GEOCLIM (*squares* Donnadieu et al. 2006). The major difference between these two models is the evaluation of the sink. Large uncertainties remain independently of the models used. (Reconstruction from compilation by Royer D.A. 2006)

value is rather large, but accounting for the lower insolation (−4% relative to present), the threshold for triggering the inception of ice sheets may have been even higher during the Paleozoic.

The last important glaciation occurred at the Permo-Carboniferous boundary at ≈300 Ma BP due to both a low atmospheric carbon dioxide content (Figs. 6, 7) and paleogeography, since a large fraction of the continental mass was located at high latitudes in the southern hemisphere (Fig. 8a). This Permo-Carboniferous glacial phase is quite well known in comparison with previous glaciations. Glacial deposits occurred first in South America 340 Ma ago, and the major phase of glaciation is from 320 to 285 Ma, with ultimate glacial proxy occurring at 270 Ma in Australia. These two forcing factors were introduced in the simulations of the Permo-Carboniferous glaciation. Figure 8 shows that annual temperatures reach negative values (in degrees Celsius) over the high southern latitudes of the Pangea continent. Also plotted in Fig. 8b are the albedo values corresponding to the summer seasons showing that perennial snow cover extended throughout the whole of South Gondwana (South Africa, South America, India, Australia, and Antarctica). This result is consistent with the moraine deposits found on these continents, an observation that led Wegener (1915) to imagine that all these areas were, at that time, placed in the same location. Later on, when the Pangea drifted towards the northern hemisphere, the continental mass slowly shifted from high to low latitudes and the alteration/erosion increased, implying a severe drop of atmospheric carbon dioxide, as simulated by the GEOCLIM (climate–carbon cycle) model of Donnadieu et al. (2006).

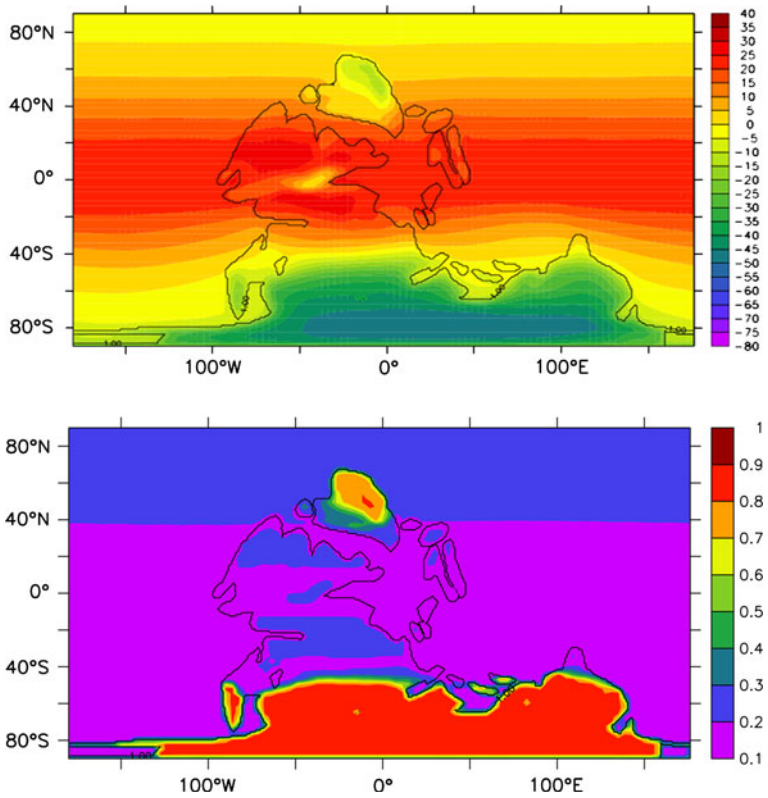

Fig. 8 During the Permo-Carboniferous, 300 Ma BP, a large glaciation occurred that covered the high latitudes of South Gondwana. The *top panel* shows the annual mean temperature in degrees C and the *bottom one* the summer albedo (December to February) for the southern hemisphere. A high albedo due to the large snow cover over south Gondwana prevailed even during the summer season, in good agreement with geological data. (From Gilles Schneiders, LSCE, 2005)

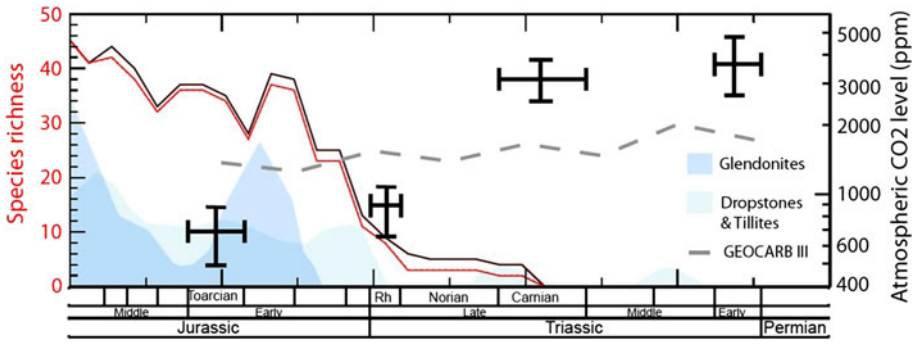

Fig. 9 Evolution of the biodiversity and of atmospheric CO_2 (*crosses*) during the Triassic and the Jurassic periods. The *red* and *black curves* correspond to calcareous plankton evolution during the same period. The *dashed curve* corresponds to the GEOCARB III model. (Goddéris et al. 2008)

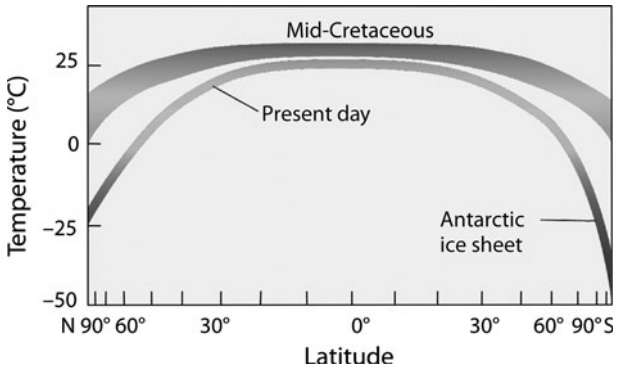

Fig. 10 Equator to pole temperature gradient derived from $\delta^{18}O$ data during the mid-Cretaceous and compared with that of present-day values showing that the mid-Cretaceous temperatures are higher and more flat than present ones. It should be noticed that most of the $\delta^{18}O$ data are derived from carbonate sediments resulting in rather smoother and more "flat" temperature changes with latitude. More recent $\delta^{18}O$ data derived from phosphates lead to a stronger equator to pole gradient

Interestingly, the appearance of calcareous plankton corresponds to the period of large carbon dioxide decrease at the Triassic-Jurassic Transition (Rhetian: 200 Ma) (Fig. 9), which is synchronous with an increase of carbonates in the ocean providing favourable conditions for the emergence of calcareous foraminifora.

Another interesting period is that of the Mid-Cretaceous Cenomanian period 100 Ma ago that coincided with a high level of carbon dioxide (Figs. 6, 7) and a high sea level, leading to a warm and uniform climate, with rather weak seasonal cycles and a large decrease in the equator-to-pole temperature gradient (Fluteau et al. 2007; Fig. 10). In contrast, however, to the good agreement obtained between the models and the available data for previous periods (Permo-Carboniferous and Rhaetian Periods), the rather low-temperature gradient deduced from $\delta^{18}O$ measurements in calcite cannot easily be reproduced (Barron and Washington 1982). That disagreement has been shown to be due to the data reconstruction process (Pucéat et al. 2007). Regional comparison of model results with data for different Cretaceous climates has depicted reliable features (Fluteau et al. 2007).

During the Cenozoic era (65–2.6 Ma), the atmospheric CO_2 decreases from 4 PAL to 1 PAL and the temperature tends to drop. A major shift from a warm to a cold climate did occur 34 Ma ago with the onset of the Antarctic glaciation. Different model simulations have shown that the most important feature that explains this shift is in fact a decrease in atmospheric carbon dioxide (DeConto and Pollard 2003; Pagani et al. 2005; Fig. 11). Moreover, the opening of the Drake Passage, between South America and Antarctica, also played a role in this transition. Greenland's glaciation occurred only 3 Ma ago. If the most recent evaluations of the different forcing factors (carbon dioxide drawdown, Rockies uplift, Panama Passage closure and changes in tropical ocean dynamics) show their contribution to explain the Pliocene climate; nevertheless, carbon dioxide alone is the major player in explaining Greenland's inception (Lunt 2008).

6 The Last Million Year's Climate

Since Greenland's glaciation 3 Ma ago, the climate in the northern hemisphere has changed drastically, with first a period of successive ice sheets build-ups and decays with a

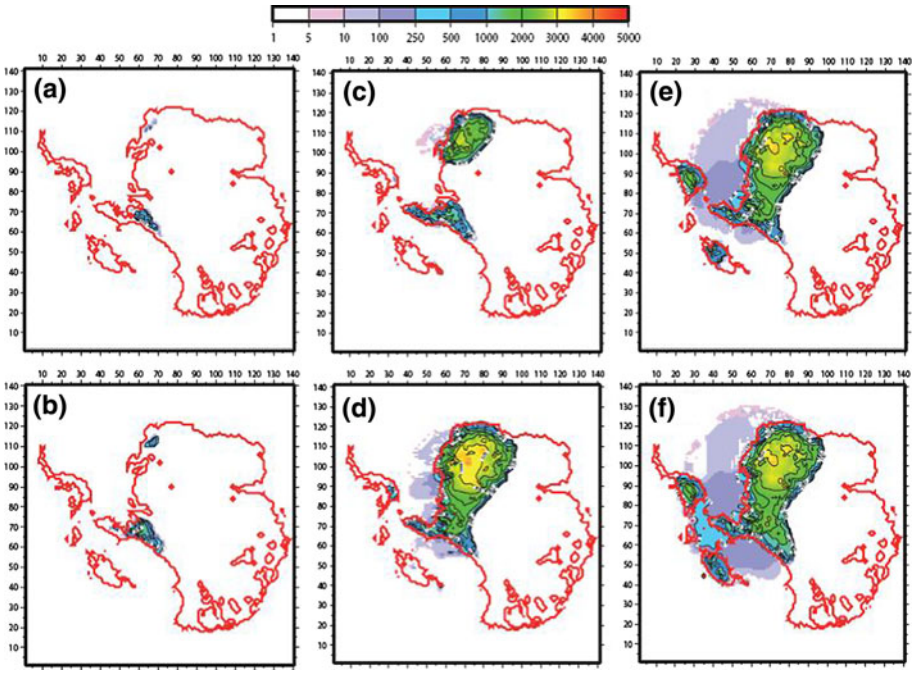

Fig. 11 Antarctic ice sheet (AIS) climate–cryosphere topography for different atmospheric CO_2 concentrations and different Drake Passage (DP) configurations (fully coupled CLIMBER-GRISLI experiments). The *two left panels* show the AIS derived using a pCO_2 set to 4 PAL in case of a closed DP (*top* **a**) and open DP (*bottom* **b**). The *middle panels* show the AIS topography for pCO_2 set to 4 PAL for the case of a closed DP (**c**) and *open* DP (**d**), respectively. The *right panels* represent the AIS obtained for pCO_2 set to 2 PAL, with closed DP (**e**) and open DP (**f**). The ice sheet thickness is expressed in [m]. The *red line* represents the grounding line; it is possible to note the presence of ice shelves for the simulations (**c**) to (**f**). (From Bonelli et al. 2009)

periodicity of 40 ka, and since around 1.2 Ma ago a periodicity of 100 ka (Paillard 2008). For that last period, hopefully, we can measure the temperature as well as methane and carbon dioxide levels through the analysis of successive layers of Antarctic ice cores—glaciologists even hope to be able to go back as far as 1.5 million years (Jouzel and Masson-Delmotte 2010). This is a huge progress in contrast to the long past, for which the partial pressure of carbon dioxide was indirectly deduced from various indicators such as boron isotopes or stomata with much larger uncertainties (Figs. 6, 7). As shown in Fig. 12, the different cycles are indeed not similar in terms of temperature and greenhouse gases, and there are still many unsolved questions to properly understand the climate of the Quaternary. The last glacial–interglacial cycle from 130 ka BP to present is certainly the best documented. Using a model of intermediate complexity (Petoukhov et al. 2000) that allows runs of long simulations coupled with ice sheet models, Ritz et al. (1997) and Bonelli et al. (2009) have succeeded in simulating altogether: the onset of glaciations (115 ka BP), the paroxysm at the last glacial maximum (21 ka BP), the fast decay of the ice sheets and the more stable climate of the Holocene Period (last 10 ka) (Waelbroeck et al. 2002). Figure 13 allows a comparison between the associated sea-level variations as reconstructed from data and from models (Bonelli et al. 2009).

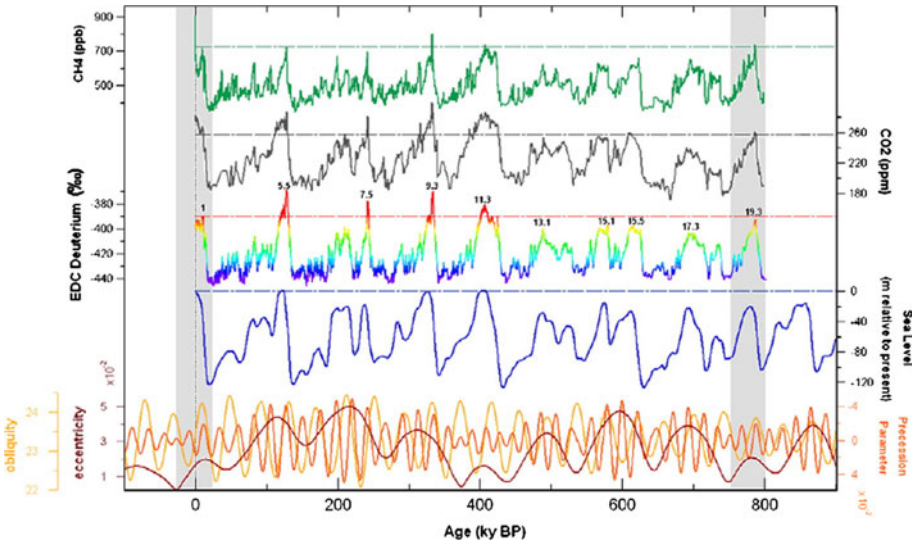

Fig. 12 From *top to bottom* Antarctic records of atmospheric methane concentration (ppb) (Loulergue et al. 2008), atmospheric carbon dioxide concentration (ppm) (Petit et al. 1999) (Siengenthaler et al. 2005) (Lüthi et al. 2008), and deuterium, a proxy for Antarctic temperature (Jouzel et al. 2007), (Masson-Delmotte et al. 2010). They are compared with the estimates of past changes in sea level (Bintanja et al. 2005) derived from a stack of marine records (Lisiecki and Raymo 2005) and with the past variations in the Earth's orbital parameters, eccentricity, precession parameter, and obliquity. Data are displayed as a function of time in thousands of years before 1950 (ka before present). (From Pol et al. 2010)

Indeed, being able to simulate a global cycle correctly leads to investigating the long-term behaviour of present-day ice sheets. Indeed, there is a natural variability induced by volcanic eruptions and high-frequency insolation variations but the anthropogenic forcing is, and will be, by far the major driver for long-term climate and consequently for ice sheet behaviour in the next few centuries. Using the same models and different scenarios, we stress that for accumulated carbon dioxide emission larger than 3,000 gigatons of cumulated carbon in the atmosphere (Fig. 14), the irreversible melting of Greenland may occur (Charbit et al. 2008; Fig. 15). Moreover, this 3,000 gigatons value is certainly overestimated because many processes are too coarsely parameterized in the model. For example, the spatial resolution of 40 km used in the models does not allow account to be taken of some explicit physical characteristics of ice streams, which are only 4 km large. Moreover, the nature of the different types of sediments that lie under the ice sheet and play an essential role in the sliding process is not accounted for yet in the models. Indeed, a comparison of this simulation with satellite data shows an underestimation of the ice streams' motion for present day.

7 Conclusions

During this travel through the Earth's past climate, we have shown that the presence of ice sheets, namely the existence of the cryosphere, is an infrequent component of the Earth's climate system. These periods are less than 5% of the Earth's history, but they are very exciting to document and simulate because there is strong evidence which describes them.

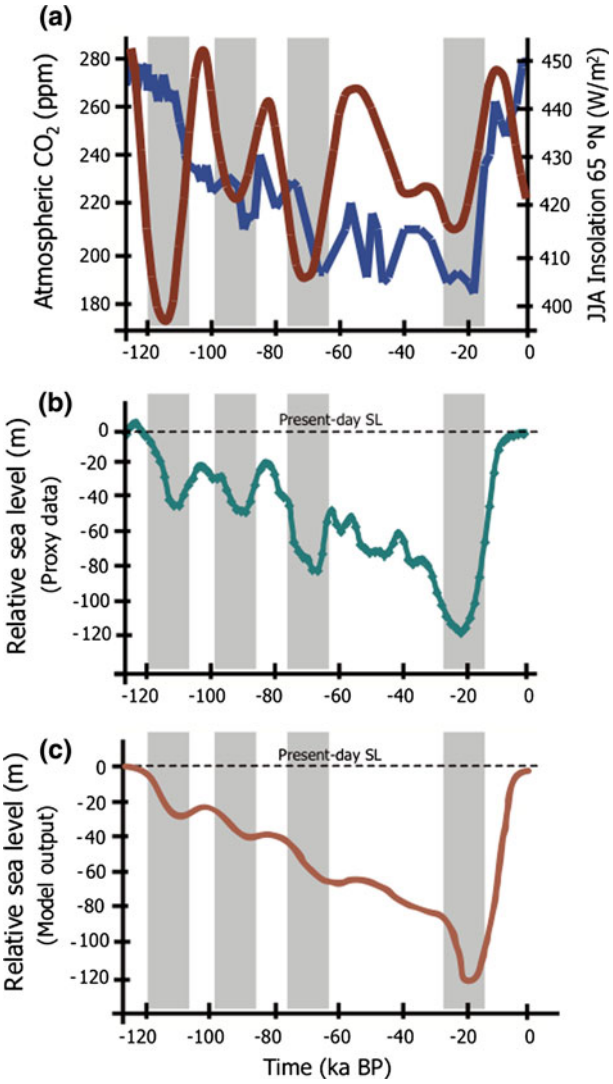

Fig. 13 Atmospheric CO_2 concentrations (in ppm) and estimated see levels relative to present (in m). Panel **a** forcing factors used for the simulation from 126 ka to present. (1) Summer insolation at 65°N (right), (2) CO_2 evolution as deduced from Antarctic ice cores (*left*). Panels **b** and **c** sea level evolution from proxy data (**b**) and from model simulations (**c**) evidencing a fairly good agreement between both estimations. (From Bonelli et al. 2009)

It is a challenging exercise for climate modellers to find the conditions under which the build-up of an ice sheet begins, is maintained and then decays.

In the long-term future, it would not be very surprising that human activity might lead to the melting of the ice sheet and later to its disappearance. This is what is foreseen in the short to mid term for Greenland and west Antarctica. First, this is because industrial development has induced extraordinarily fast and huge increases of concentrations of atmosphere. Secondly, as shown in this paper, the presence of ice sheets is not a very

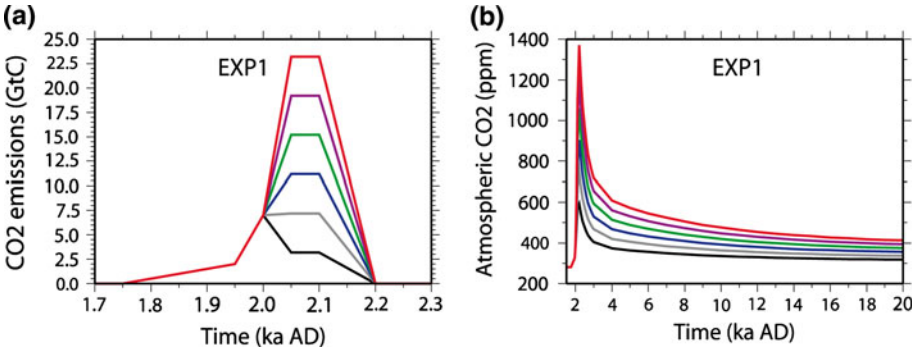

Fig. 14 CO_2 emission scenarios (**a**) and atmospheric CO_2 concentration (**b**). CO_2 emission scenarios used in the set of experiments (EXP1) (*left panel*) and the corresponding atmospheric CO_2 concentration accounting for the natural absorption of CO_2 (*right panel*). The cumulative emissions corresponding to all EXP 1 scenarios are 1,000 GtC (*black*), 1,500 GtC (*grey*), 2,000 GtC (*blue*), 2,500 GtC (*green*), 3,000 GtC (*purple*), and 3,500 GtC (*red*). These values are reached in the year 2200. At that time, the maximum CO_2 contents in the atmosphere are 592, 748, 904, 1,060, 1,215, and 1,371 ppm, respectively. (Charbit et al. 2008)

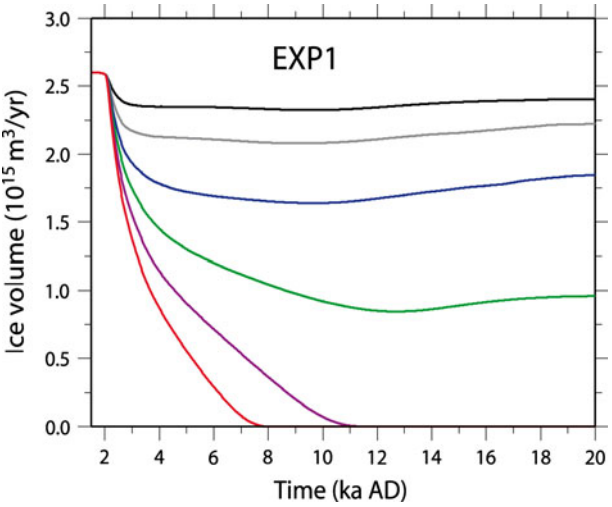

Fig. 15 Simulated ice volumes obtained with the six scenarios described in Fig. 14. Simulated ice volumes for the lowest value obtained for Greenland ice sheet show first a melting, then stabilization, whereas for a level larger than 3,000 GtC the total melting of Greenland is irreversible on the time scale of 10,000 years (10 ka). (Charbit et al. 2008)

frequent feature; they only exist under conditions of low concentartions of atmospheric carbon dioxide. Industrial development deeply perturbed the carbon cycle, rapidly transferring into the atmosphere huge amounts of carbon that was previously stored on the continents or underneath the ocean. This perturbation has been clearly evidenced by the measurements of CO_2 taken since 1950 in the Earth's atmosphere. The increased concentration from 280 ppm (preindustrial value) to 390 ppm as of 2010 is largely outside the range (180–280 ppm) of the last million years as deduced from Antarctic ice cores. In a

few decades, atmospheric CO_2 concentration will reach 420 ppm, a level that existed tens of Ma ago, when no Greenland ice sheet was present on the Earth.

The present ongoing climate change situation seems to be different from all climate transitions described in this paper that did occur over geological timescales (Ramstein 2011). Indeed, anthropogenic perturbations happen 'instantaneously' and most of the different reservoirs—ocean surface, vegetation, and ice sheet—are not in equilibrium. Because of its intensity and abruptness, that scenario is more reminiscent of a biodiversity crisis than to the 'smooth' climate evolution of the past described in this article. On the other hand, because the perturbation is associated with human activity, there is some hope that it may be brought under control, particularly because the greenhouse gas emission scenarios for the twenty-first century have not yet been written. Unfortunately, the residence time of CO_2 in the atmosphere is several hundred years (Fig. 14), and the consequences and effects of anthropogenic perturbations may still last for several centuries into the future.

Acknowledgments This chapter includes part of the recent work I did, thanks to my colleagues at LSCE: Y. Donnadieu, S. Charbit, S. Bonelli, G. Le Hir, C. Dumas and Y. Godderis at LMTG. I also want to thank JY Peterschmitt, P. Sepulchre and F. Gerry for text and illustrations. Most of the work on deep time has been funded through the ANR AccroEarth.

References

Amiot R, Lécuyer C, Buffetaut E, Escarguel G, Fluteau F, Martineau F (2006) Oxygen isotopes from biogenic apatites suggest widespread endothermy in Cretaceous dinosaurs. Earth Planet Sci Lett 246(1–2):41–54

Barron EJ, Washington WM (1982) Cretaceous climate: a comparison of atmospheric simulations with the geologic record. Palaeogeogr Palaeoclimatol Palaeoecol 40:103–133

Berner RA (1994) 3GEOCARB II: a revised model of atmosphere CO_2 over Phanerozoic time. Am J Sci 294:59–91

Bertrand P (2005) Chapitre "Vers une régulation planétaire" Des atomes aux planètes habitables de Gargaud M, Claeys P, MartinH PU Bordeaux. Collection: L'origine de la vie

Bintanja R, van de Wal R, Oerlemans J (2005) Modelled atmospheric temperatures and global sea levels over the past million years. Nature 437:125–128

Bonelli S, Charbit S, Ramstein G, Kageyama M, Woillez MN, Dumas C (2009) Investigating the evolution of major Northern hemisphere ice sheets during the last glacial-interglacial cycle. Clim Past 5:329–345

Boucot AJ, Gray J (2001) A critique of Phanerozoic climatic models involving changes in the CO_2 content of the atmosphere. Earth-Sci Rev 56:1–159

Catling DC, Claire MW (2005) How Earth's atmosphere evolved to an oxic state: a status report. Earth Planet Sci Lett 237:1–20

Charbit S, Paillard D, Ramstein G (2008) Amount of CO_2 emissions irreversibly leading to the total melting of Greenland. Geophys Res Lett 35:L12503. doi:10.1029/2008GL033472

Cogné JP, Humler E (2004) Temporal variation of oceanic spreading and crustal production rates during the last 180 My. Earth Planet Sci Lett 227:427–439

Crowell JC (1999) Pre-mesozoic ice ages: their bearing on understanding the climate system. Geological Society of America, Boulder. GSA Memoir, 192

DeConto R, Pollard D (2003) Rapid Cenozoic glaciation of Antarctica induced by declining atmospheric CO_2. Nature 421:245–249

Désert J-M, Vidal-Madjar A, Lecavelier des Étangs A, Hébrard G, Ballester G, Ferlet R, Mayor M (2003) The data analysis of HD209458 Ly-alpha transit occultation. In: Beaulieu J-P, Lecavelier des Etangs A,

Terquem C (eds) Proceedings of the XIXth IAP Colloquium "Extrasolar planets: today and tomorrow". ASP, San Francisco, 2 pp (arXiv:astro-ph/0312383)
Dickens GR (2003) Rethinking the global carbon cycle with a large, dynamic and microbially mediated gas hydrate capacitor. Earth Planet Sci Lett 213(3–4):169–183
Dickens GR, Francis JM (2004) Comment: a case for a comet impact trigger for the Paleocene/Eocene thermal maximum and carbon isotope excursion. Earth Planet Sci Lett 217:197–200
Donnadieu Y, Ramstein G, Fluteau F, Besse J, Meert J (2002) Is high obliquity a plausible cause for Neoproterozoic glaciations? Geophy Res Lett 29(23), Article number 2127. doi: 10.1029/2002GL015902
Donnadieu Y, Goddéris Y, Ramstein G, Nédelec A, Meert JG (2004a) Snowball Earth triggered by continental break-up through changes in runoff. Nature 428:303–306
Donnadieu Y, Ramstein G, Goddéris Y, Fluteau F (2004b) Global tectonic setting and climate of the Late Neoproterozoic: a climate-geochemical coupled study. In: Jenkins GS, McMenamin MAS, McKey CP, Sohl L (eds) The extreme proterozoic: geology, geochemistry, and climate, geophysical monograph 146. American Geophysical Union, Washington, DC, pp 79–89
Donnadieu Y, Godderis Y, Pierrehumbert R, Dromart G, Fluteau F, Jacob R (2006) A GEOCLIM simulation of climatic and biogeochemical consequences of Pangea breakup. Geochem Geophy Geosyst 7(Q11019):21. doi:10.1029/2006GC001278
Flament N, Coltice N, Reyb PF (2008) A case for late-Archaean continental emergence from thermal evolution models and hypsometry. Earth Planet Sci Lett 275:326–336
Fluteau F, Ramstein G, Besse J, Guiraud R, Masse JP (2007) Impacts of palaeogeography and sea level changes on Mid-Cretaceous climate. Palaeogeogr Palaeoclimatol Palaeoecol 247(3–4):357–381
Frakes LA, Francis JE, Syktus JI (1992) Climate modes of the phanerozoic: the history of the earth's climate over the past 600 million years. Cambridge University Press, 274 pp
Goddéris Y, Donnadieu Y, Dessert C, Dupré B, Fluteau F, François LM, Meert J, Nédélec A, Ramstein G (2007) Coupled modeling of global carbon cycle and climate in the Neoproterozoic: links between Rodinia breakup and major glaciations. Comptes Rendus Geosci 339(3–4):212–222
Goddéris Y, Donnadieu Y, De Vargas C, Pierrehumbert RT, Dromart G, Van de Schootbrugge B (2008) Causal or casual link between the rise of nannoplankton calcification and a tectonically-driven massive decrease in Late Triassic atmospheric CO_2? Earth Planet Sci Lett 267:247–255
Gough DO (1981) Solar interior structure and luminosity variations. Sol Phys 74:21–34
Harland WB (1964) Evidence of Late Precambrian glaciation and its significance. In: Nairn AEM (ed) Problems in palaeoclimatology, interscience. Wiley, London, pp 119–149
Hoffman PF, Schrag DP (2002) The snowball Earth hypothesis: testing the limits of global change. Terra Nova 14:129–155
Hoffman PF, Kaufman AJ, Halverson GP, Schrag DP (1998) A Neoproterozoic snowball Earth. Science 281(5381):1342–1346
Jouzel J, Masson-Delmotte V (2010) Deep ice cores: the need for going back in time. Quat Sci Rev 29(27–28), Elsevier Ltd, pp 3683–3689
Jouzel J, Masson-Delmotte V, Cattani O, Dreyfus G, Falourd S, Hoffmann G, Minster B, Nouet J, Barnola JM, Chappellaz J, Fischer H, Gallet JC, Johnsen S, Leuenberger M, Loulergue L, Luethi D, Oerter H, Parrenin F, Raisbeck G, Raynaud D, Schilt A, Schwander J, Selmo E, Souchez R, Spahni R, Stauffer B, Steffensen JP, Stenni BS, Tison JL, Werner M, Wolff E (2007) Orbital and millenial Antarctic climate variability over the past 800,000 years. Science 317:793–796
Kasting JF (2004) When methane made climate. Sci Am 291:78–85
Kirschvink JL (1992) Late proterozoic low-latitude global glaciation: the snowball earth. Section 2.3, In: Schopf JW, Klein C, Des Maris D (eds), The proterozoic biosphere: a multidisciplinary study. Cambridge University Press, pp 51–52
Knoll AH (2004) Life on a young planet: the first three billion years of evolution on earth. Princeton University Press, Princeton. ISBN-10: 0691120293 #; ISBN-13: 978-0691120294
Köppen W, Wegener A (1924) Die Klimate der Geologischen Vorzeit
Kump LR, Arthur MA, Patzkowsky ME, Gibbs MT, Pinkus DS, Sheehan PM (1999) A weathering hypothesis for glaciation at high atmospheric pCO2 during the Late Ordovician. Palaeogeogr Palaeoclimatol Palaeoecol 152(1, 15):173–187
Le Heron DP, Ghienne JF, El Houicha M, Khoukhi Y, Rubino JL (2007) Maximum extent of ice sheets in Morocco during the Late Ordovician glaciation. Palaeogeogr Palaeoclimatol Palaeoecol 245:200–226
Le Hir G, Goddéris Y, Donnadieu Y, Ramstein G (2008a) A geochemical modelling study of the evolution of the chemical composition of seawater linked to a "snowball" glaciation. Biogeoscience 5:253–267
Le Hir G, Goddéris Y, Donnadieu Y, Ramstein G (2008b) A scenario for the evolution of the atmopsheric pCO_2 during a snowball Earth. Geology 36(1):47–50

Le Hir G, Donnadieu Y, Goddéris Y, Pierrehumbert RT, Halverson GP, Macouin M, Nédélec A, Ramstein G (2008c) The snowball Earth aftermath: exploring the limits of continental weathering processes. Earth Planet Sci Lett 277(3–4):453–463

Levrard B, Laskar J (2003) Climate friction and the Earth's obliquity. Geophys J Int 154:970–990

Lisiecki LE, Raymo ME (2005) A Pliocene-Pleistocene stack of 57 globally distributed benthic d18O records: Paleoceanography 20:PA1003. doi:10.1029/2004PA001071

Loulergue L, Schilt A, Spahni R, Masson-Delmotte V, Blunier T, Lemieux B, Barnola JM, Raynaud D, Stocker T, Chappelaz J (2008) Orbital and millenial-scale features of atmospheric CH4 over the last 800000 years. Nature 453:383–386

Lovelock J (2000) [1979] Gaia: a new look at life on Earth, 3rd edn. Oxford University Press. ISBN: 0-19-286218-9

Lunt DJ, Foster GL, Haywood AM, Stone EJ (2008) Late Pliocene Greenland glaciation controlled by a decline in atmospheric CO_2 levels. Nature 454:1102–1105

Lüthi D, Floch ML, Bereiter B, Blunier T, Barnola JM, Siegenthaler U, Raynaud D, Jouzel J, Fischer H, Kawamura K, Stocker TF (2008) High resolution carbon dioxide concentration record 650,000–800,000 years before present. Nature 453:379–382

Mareschal J-C, Jaupart C (2006) Archean thermal regime and stabilization of the cratons, in Archean geodynamic processes and environments. Geophys. Mono. 164, In: Benn K, Mareschal J-C, Condie KC (eds), AGU, Washington (DC), pp 61–74

Masson-Delmotte V, Stenni B, Pol K, Braconnot P, Cattani O, Falourd S, Kageyama M, Jouzel J, Landais A, Minster B, Barnola JM, Chappellaz J, Krinner G, Johnsen S, Rothlisberger R, Hansen J, Mikolajewicz U, Otto-Bliesner B (2010) EPICA Dome C record of glacial and interglacial intensities. Quat Sci Rev 29:113–128

Morbidelli A, Petit J-M, Gladman B (2001) A plausible cause of the late heavy bombardment. Meteorit Planet Sci 36:371–380

Nardin E, Goddéris Y, Donnadieu Y, Le Hir G, Blakey Ronald C, Pucéat E, Markus A (2011) Modeling the early Paleozoic long-term climatic trend. GSA Bulletin

Ohmoto H, Watanabe Y, Ikemi H, Poulson SR, Taylor BE (2006) Sulphur isotope evidence for an oxic Archaean atmosphere. Nature 442:908–911

Pagani M, Zachos JC et al (2005) Marked decline in atmospheric carbon dioxide concentrations during the Paleogene. Science 309(5734):600–603

Paillard D (2008) From atmosphere, to climate, to Earth system science. Interdisc Sci Rev 33(1):25–35

Petit JR, Jouzel J, Raynaud D, Barkov NI, Barnola JM, Basile I, Bender M, Chappellaz J, Davis J, Delaygue G, Delmotte M, Kotlyakov VM, Legrand M, Lipenkov VM, Lorius C, Pépin L, Ritz C, Saltzman E, Stievenard M (1999) Climate and atmospheric history of the past 420,000 years from the Vostok ice core, Antarctica. Nature 399:429–436

Petoukhov V et al (2000) CLIMBER-2: a climate system model of intermediate complexity. Part I: model description and performance for present climate. Clim Dyn 16:1–17

Pierrehumbert RT (2004) High levels of atmospheric carbon dioxide necessary for the termination of global glaciation. Nature 429:646–649. doi:10.1038/nature02640

Pol K, Masson-Delmotte V, Johnsen S, Bigler M, Cattani O, Durand G, Falourd S, Jouzel J, Minster B, Parrenin F, Ritz C, Steen-Larsen HC, Stenni B (2010) New MIS 19 EPICA Dome C high resolution deuterium data: hints for a problematic preservation of climate variability at sub-millenial scale in the "oldest ice". Earth Planet Sci Lett 298:95–103

Pucéat E, Lécuyer C, Donnadieu Y, Naveau P, Cappetta H, Ramstein G, Huber BT, Kriwet J (2007) Fish tooth $\delta^{18}O$ revising Late Cretaceous meridional upper ocean water temperature gradients. Geology 35(2):107–110

Ramstein G (2011) Origins and evolution of life: an astrobiological perspective, chapter "Climate of the Earth", Cambridge Astrobiology. Cambridge University Press, Cambridge. doi: 10.1017/CBO9780511933875.014

Ramstein G, Donnadieu Y, Goddéris Y (2004a) Proterozoic glaciations. Comptes Rendus Geosci 336(7–8):639–646

Ramstein G, Khodri M, Donnadieu Y, Goddéris Y (2004b) Impact of the hydrological cycle on past climate changes: three illustrations at different time scales. Comptes Rendus Geosci 337(1–2):125–137

Ritz C et al (1997) Sensitivity of a Greenland ice sheet model to ice flow and ablation parameters: consequences for the evolution through the last climatic cycle. Clim Dyn 13:11–24

Robert F, Chaussidon M (2006) A Palaeotemperature curve for the Precambrian oceans based on silicon isotopes in cherts. Nature 443:969–972

Rosing MT, Bird DK, Sleep NH, Bjerrum CJ (2010) No climate paradox under the faint early Sun. Nat Lett 464:744–747

Royer DL (2006) CO_2-forced climate thresholds during the Phanerozoic. Geochim Cosmochim Acta 70:5665–5675
Rye R, Kuo P, Holland HD (1995) Atmospheric carbon dioxide concentrations before 2.2 billion years ago. Nature 378:603–605
Sagan C, Mullen G (1972) Earth and mars: evolution of atmospheres and temperatures. Science 177:52–56
Shields GA, Kasting JF (2007) Brief communication arising. Nature 447:E1
Siengenthaler U, Stocker TF, Monnin E, Lüthi D, Schwander J, Stauffer B, Raynaud D, Barnola J-M, Fischer H, Masson-Delmotte V, Jouzel J (2005) Stable carbon cycle–climate relationship during the last Pleistocene. Science 310:1313–1317
Trotter JA, Williams IS, Barnes CR, Lécuyer C, Nicoll RS (2008) Did cooling oceans trigger ordovician biodiversification? Evidence from conodont thermometry. Science 321(5888):550–554
Waelbroeck C, Labeyrie L et al (2002) Sea-level and deep water temperature changes 906 derived from benthic foraminifera isotopic records. Quat Sci Rev 21(1-3):907, 295–305
Walker JCG, Hays PB, Kasting JF (1981) A negative feedback mechanism for the long-term stabilization of Earth's surface temperature. J Geophys Res 86:9776–9978
Wegener A (1915) Die Entstehung der Kontinente und Oceane
Williams GE (1975) Late Precambrian glacial climate and the Earth's obliquity. Geol Mag 112:441–465
Williams DM, Kasting JF, Frakes LA (1998) Low-latitude glaciation and rapid changes in the Earth's obliquity explained by obliquity-oblateness feedback. Nature 396:453–455
Young GM, von Brunn V, Gold DJC, Minter WEL (1998) Earth's oldest reported glaciation; physical and chemical evidence from the Archean Mozaan Group ($\sim$2.9 Ga) of South Africa. J Geol 106:523–538
Zachos J, Pagani M, Sloan L, Thomas E, Billups K (2001) Trends, rhythms, and aberrations in global climate 65 Ma to Present. Science 292(5517):686–693. doi:10.1126/science.1059412

Surv Geophys (2011) 32:351–376
DOI 10.1007/s10712-011-9123-5

Overview and Assessment of Antarctic Ice-Sheet Mass Balance Estimates: 1992–2009

H. Jay Zwally · Mario B. Giovinetto

Received: 8 November 2010 / Accepted: 31 March 2011 / Published online: 13 May 2011

Abstract Mass balance estimates for the Antarctic Ice Sheet (AIS) in the 2007 report by the Intergovernmental Panel on Climate Change and in more recent reports lie between approximately +50 to −250 Gt/year for 1992 to 2009. The 300 Gt/year range is approximately 15% of the annual mass input and 0.8 mm/year Sea Level Equivalent (SLE). Two estimates from radar altimeter measurements of elevation change by European Remote-sensing Satellites (ERS) (+28 and −31 Gt/year) lie in the upper part, whereas estimates from the Input-minus-Output Method (IOM) and the Gravity Recovery and Climate Experiment (GRACE) lie in the lower part (−40 to −246 Gt/year). We compare the various estimates, discuss the methodology used, and critically assess the results. We also modify the IOM estimate using (1) an alternate extrapolation to estimate the discharge from the non-observed 15% of the periphery, and (2) substitution of input from a field data compilation for input from an atmospheric model in 6% of area. The modified IOM estimate reduces the loss from 136 Gt/year to 13 Gt/year. Two ERS-based estimates, the modified IOM, and a GRACE-based estimate for observations within 1992–2005 lie in a narrowed range of +27 to −40 Gt/year, which is about 3% of the annual mass input and only 0.2 mm/year SLE. Our preferred estimate for 1992–2001 is −47 Gt/year for West Antarctica, +16 Gt/year for East Antarctica, and −31 Gt/year overall (+0.1 mm/year SLE), not including part of the Antarctic Peninsula (1.07% of the AIS area). Although recent reports of large and increasing rates of mass loss with time from GRACE-based studies cite agreement with IOM results, our evaluation does not support that conclusion.

Keywords Antarctica · Ice sheet · Mass balance · ERS · GRACE · ICESat · Input output fluxes

H. J. Zwally (✉)
Cryospheric Sciences Branch Code 614. 1, NASA Goddard Space Flight Center,
Greenbelt, MD 20771, USA
e-mail: zwally@icesat2.gsfc.nasa.gov

M. B. Giovinetto
SGT Inc, Cryospheric Sciences Branch Code 614. 1, NASA Goddard Space Flight Center,
Greenbelt, MD 20771, USA

1 Introduction

A perspective on the contributions of ice sheets to sea-level rise relative to other sources and the different contributions of each ice sheet (Table 1, Figs. 1 and 2) emphasizes the necessity to discriminate on the role played by each ice sheet, as well as among the drainage regions in each ice sheet. Estimates of ice sheet contributions to the observed rise have practically doubled from 1961–2003 to 2003–2007. The overall contributions from each of Greenland and Antarctica were considered equal in 1993–2003 (Lemke et al. 2007 in Inter-Governmental Panel on Climate Change; IPCC07). Although reports of larger Antarctic contributions for 2002–2008 are assessed in this paper, the contribution of 0.24 mm/year from Antarctica listed in Table 1 from Wu et al. (2010) is smaller than the recent contribution of 0.38 mm/year (136 Gt/year) from southeast Greenland alone (c.f. Fig. 1a, b).

Table 1 Recent compilations of contributions to observed sea level rise (mm/year)

Origin/causes	1961–2003a[a]	1961–2003b[a]	1961–2003c[a]	1993–2003a[a]	1993–2003b[a]	Selected
Observed Sea Level	1.8 ± 0.5	1.6 ± 0.2	1.8 ± 0.3	3.1 ± 0.7	3.1 ± 0.4	3.3 ± 0.4[b]
Thermosteric	0.42 ± 0.12	0.7 ± 0.1	0.4 ± 0.06	1.6 ± 0.5	1.6 ± 0.25	0.75 ± 0.1[c]
Glaciers and Ice Caps	0.50 ± 0.18	0.5 ± 0.2	0.5 ± 0.1	0.77 ± 0.22	0.8 ± 0.11	1.1 ± 0.25[a]
Ice sheets:	–	–	0.2 ± 0.2	–	0.4 ± 0.2	0.72 ± ?[d]
Antarctica	0.14 ± 0.41	0.2 ± 0.4	–	0.21 ± 0.35	–	0.24 ± 0.12[d]
Greenland	0.05 ± 0.12	0.1 ± 0.1	–	0.21 ± 0.07	–	0.48 ± 0.01[d]
Unassigned	0.7 ± 0.7	0.1 ± ?	0.7 ± ?	0.3 ± 1.0	0.3 ± ?	0.73 ± ?

Selected data (last column) span 1993–2009 for the observed rise and 2002–2008 for the contributions (see notes [a, b, c, d] below), yielding a large unassigned residual

[a] Compilation of estimates: 1961–2003a, 1993–2003a, by Bindoff et al. (2007); 1961–2003b, by Domingues et al. (2008); 1961–2003c, 1993–2003b, 2003–2007, by Milly et al. (2010)

[b] Observed sea level rise 1993–2009; Ablain et al. (2009)

[c] Thermosteric 2003–2007; Domingues et al. (2008) updated in Church et al. (2010)

[d] Estimates derived from GRACE Antarctic data for 2002–2008 (Wu et al. 2010) and from ICESat Greenland data for 2003–2007 (Zwally et al. 2011) using 357 Gt/mm SLE (Sea Level Equivalent) for comparison with the other cited studies. Elsewhere in this study we use 362 Gt/mm SLE to account for the area of estuaries and tidal marshes over the commonly used 360 Gt/mm SLE

Fig. 1 **a** dI/dt map for Antarctica from Zwally et al. (2005) showing the distribution of mass losses or gains in combinations of drainage systems (DS) around the continent for 1992–2001. The largest mass loss is in the region of Pine Island, Thwaites, and Smith glaciers in DS 21 and DS 22 in West Antarctica. **b** dI/dt map for Greenland from Zwally et al. (2011) showing the distribution of mass losses or gains in eight major drainage systems for 2003–2007 with the values in parenthesis for 1992–2002 from Zwally et al. (2005). Note that the negative scale is 5 times as large as the negative scale for Antarctica. Large increases in mass loss occurred in DS 3 and DS 4 in the southeast and DS 7 and DS 8 in the west, and small increases in mass gain occurred in the northern DS 1 and DS 2. These changes occurred during a period of significant increases in temperature and acceleration of some outlet glaciers in Greenland as discussed in Zwally et al. (2011). dI/dt is an approximation to the change in thickness of the ice column defined by $dI/dt = dH/dt - dC_T/dt - dB/dt$, where dH/dt is the measured surface elevation change, dC_T/dt is the change in the rate of firn compaction induced by temperature changes, and dB/dt is the vertical motion of the underlying bedrock ▶

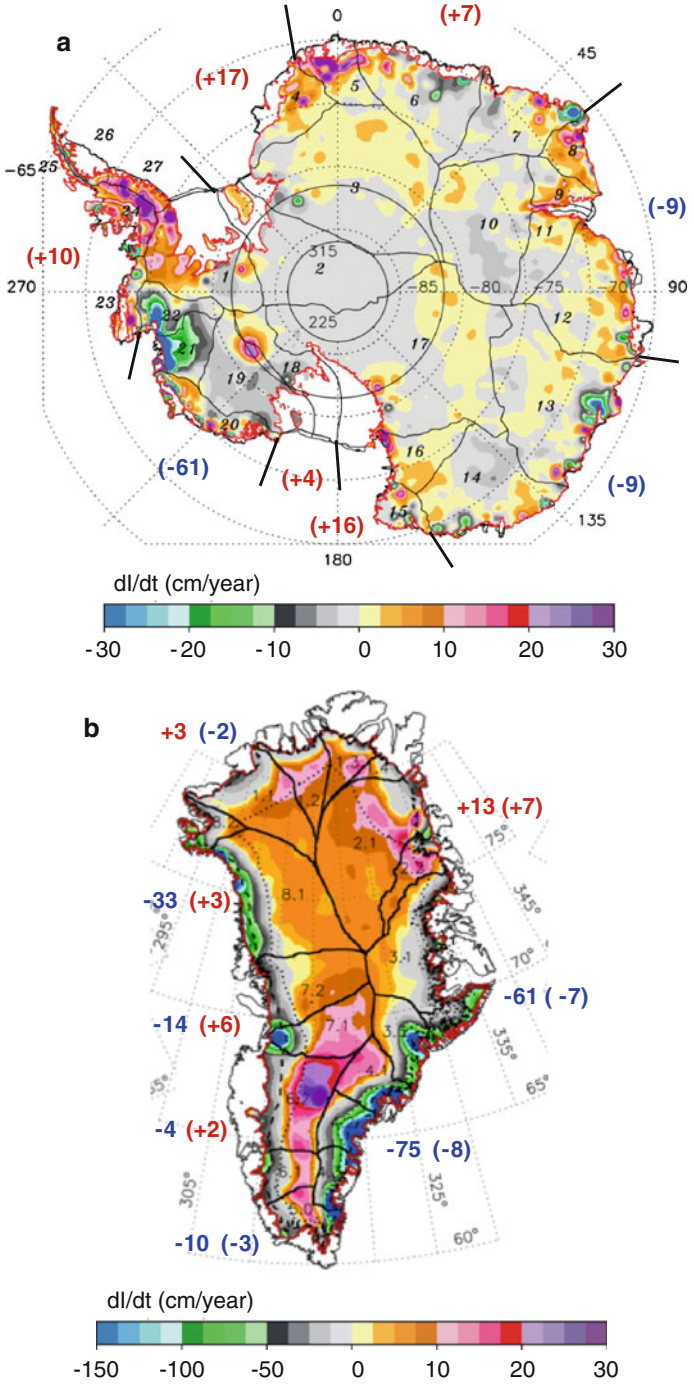
a
(+7)
(+17)
(-9)
(+10)
(-61)
(+4)
(+16)
(-9)
dl/dt (cm/year)
-30 -20 -10 0 10 20 30
b
+3 (-2)
+13 (+7)
-33 (+3)
-61 (-7)
-14 (+6)
-4 (+2)
-75 (-8)
-10 (-3)
dl/dt (cm/year)
-150 -100 -50 0 10 20 30

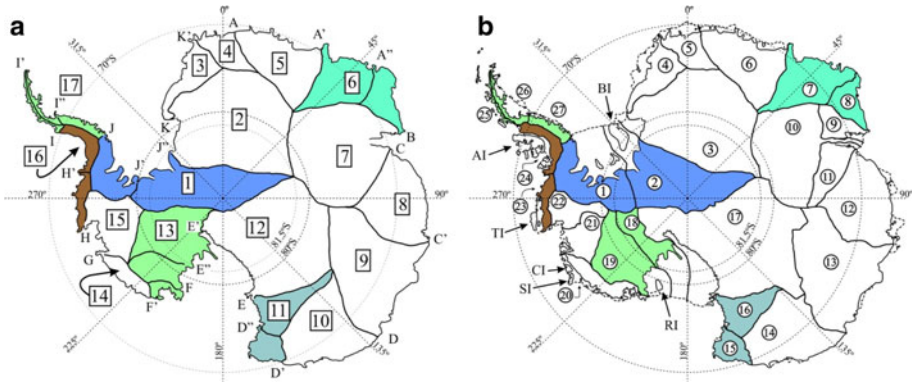

Fig. 2 Drainage entities (basins, sectors, systems, regions) of Antarctic grounded ice as identified in four sources cited in the text. **a** Drainage divides delineate twenty-five systems of the coterminous ice sheet with approximately the same pattern and sharing the same capital-letter designation of points at the coast or grounding line in three sources: Wingham et al. (2006) split the whole set in twenty-one basins, Rignot et al. (2008) in nineteen sectors, and Vaughan et al. (1999) in twenty-four basins. These entities are combined for comparison in seventeen regions (numbers shown in rectangles). The colored areas show where entities have been combined (regions 1, 6, 11, 13, 16, and 17). The drainage divides pattern shown, broadly similar in the three sources, is from Wingham et al. (2006).The boundary between East Antarctica and West Antarctica extends along the Trans-Antarctic Mountains, roughly from E to K. **b** Drainage divides in Zwally et al. (2005) delineate twenty-seven drainage systems (system numbers shown in circles). The budget estimates include all grounded ice (ice rises and on islands attached by ice, notably Berkner I. (BI) in 2, Roosevelt I. (RI) in 19, Siple I. (SI) and Carsey I. (CI) in 20, Thurston I. (TI) in 23, and Alexander I. (AI) in 24). The divides between systems 1, 2 and 17, 18 are drawn on the basis of ice provenance from either East or West Antarctica. The colored areas identify the regions as shown in **a** except for region 7 which includes systems 9–11. Applicable to **a** and **b**: (i) Large non-conformities between systems 1,2 and basins JJ′,J′J″ as well as between system 20 and basins FF′,F′G do not significantly affect the various area-normalized rate comparisons discussed in the text. (ii) Features and place names mentioned in the text: Antarctic Peninsula, roughly systems 24–27 (H′J); Graham Land, systems 25, 26 (II′,I′I″); western and eastern Palmer Land, system 24 (H′I) and 27 (I″J), respectively; northern Marie Byrd Land, broadly the northern zone of system 19 and southern zone of system 20, which overlap some parts of basins and sectors E″-G. (iii) The 81.5°S parallel shows the limit of ERS −1 and −2 radar altimeter coverage

The IPCC07 assessment of the Antarctic ice sheet (AIS) mass balance indicated a range between +50 and −200 Gt/year for the 1992–2003 period. Within the range assessed in IPCC07, the balance estimates closer to zero and either positive or negative are based on satellite radar altimetry from the European Remote-sensing Satellites (ERS). Estimates supporting the middle and lower half of the range are based on the Gravity Recovery and Climate Experiment (GRACE) data as well as on the Input-minus-Output Method (IOM). The ERS method is based on measurement of changes in ice thickness converted to changes in ice mass, the GRACE method is based on measurement of changes in gravity converted to changes in ice mass, and the IOM is based on the difference between surface balance and ice discharge at the grounding line. Generally, the range of estimates in IPCC07 encompassed the errors listed in the studies, but as noted in the report, a mid-range value does not indicate a more reliable estimate, and the composite errors listed in each study do not define confidence limits because important components lack formal statistical derivation. This caution on the error estimates applies to all studies regardless of methods of data collection and analyses.

The focus of this paper is a critical assessment of estimates of the AIS mass balance in IPCC07, along with more recent estimates as listed in Table 2. Our purposes are to find

Table 2 Antarctica. Mass budget estimates for grounded ice (values in parenthesis produced for this study)

Reference/modification	Database type	Period/year of application	Area ($\times 10^6$ km^2)		Original budget estimate				Adj. Estimate[a]
			Original[a]	Adjusted[a]	Bulk (Gt/year)		SFE(kg/m^2/year)		(Gt/year)
a	b	c	d	e	f	g	h	i	j
Velicogna and Wahr (2006)	GRACE[b]a	2004/2005–2007/2005		12.183	−139	±73	−11.4	±6.0	−139
Raimillen et al. (2006)	GRACE[b]b	2007/2004–2003/2005		12.183	−40	±36	−3.3	±3.0	−40
Velicogna (2009)	GRACE[b]a	2004/2004–2002/2009		12.183	−143	±73	−11.7	±6.0	−143
		2002–2006		12.183	−104		−8.5		
		2006–2009		12.183	−246		−20.2		
Chen et al. (2009)	GRACE[b]b	2004/2002–2001/2009		12.183	−190	±77	−15.6	±6.3	−190
〃 〃 〃 〃 : Supplementary Information		2002–2006		12.183	−144	±58	−11.8	±4.7	
〃 〃 〃 〃 : Supplementary Information		2006–2009		12.183	−220	±89	−18.1	±7.3	
〃 〃 〃 〃 : West Ant. and Ant. Pen.	GRACE[b]b	2004/2002–2001/2009		2.736	−132	±26	−48.2	±9.5	
〃 〃 〃 〃 : (East Antarctica)		2004/2002–2001/2009		9.447	(−58)	(±72)	−6.1	±7.6	
Wu et al. (2010)/East Ant.	GRACE[b]a	2004/2002–2012/2008		9.447	−23	±29	−2.4	±3.1	
Wu et al. (2010)/West Ant.	GRACE[b]a	2004/2002–2012/2008		2.736	−64	±32	−23.4	±11.7	
(East, West and Ant. Peninsula)		2004/2002–2012/2008		12.183	(−87)	(±43)	−7.1	±12.1	(−87)
Rignot et al. (2008) (R08)	IOM	2000 (?)[c]	12.183	12.183	−136	±92			
Modified Outflow only (T.3, col. r)	IOM_{Md}	(1996,1997)[c]	12.183	12.183	(+146)				
Modified Outflow and Input (T.3, col. t)	IOM_{Md}	(?)[c]	12.183	12.183	(−13.2)		−1.1		(−13.2)
Zwally et al. (2005) (Z05f)[d]	ERS	1904/1992–2004/2001	12.193	12.053	−13.6	±5.4	−1.1	±0.4	(−13.4)
Zwally et al. (2005) (Z05i)[d]		1904/1992–2004/2001	12.193	12.053	−30.3	±12.1	−2.5	±1.0	(−30.0)

Table 2 continued

Reference/modification	Database type	Period/year of application	Area ($\times 10^6$ km^2)		Original budget estimate				Adj. Estimate[a]
			Original[a]	Adjusted[a]	Bulk (Gt/year)		SFE(kg/m^2/year)		(Gt/year)
a	b	c	d	e	f	g	h	i	j
Wingham et al. (2006) (W06)[e]a	ERS	1910/1992–2002/2003	8.49	12.183	+27	±29	+3.2	±3.4	
Wingham et al. (2006) (W06)[e]b	ERS	1910/1992–2002/2003	11.71	12.183	+27	(±40)	+2.3	(±3.4)	(+28.0)
Wingham et al. (2006) (W06)[e]c	ERS	1910/1992–2002/2003	(11.9)	12.183	+37	(±40)	+3.1	(±3.4)	(+37.8)

[a] Area listed in the 'Original' reference used to derive the Surface Flux Equivalent (SFE), and 'Adjusted' to match the compilation in R08. 'Adj. estimate' is the SFE reintegrated for the Adjusted Area

[b] GRACE-based estimates used surface mass trend and GIA models IJ05 (b) or combinations of it and ICE5G-VM2 (a)

[c] The estimate in R08 is based on discharge (Output) data listed only once per basin and for a single year between 1992 and 2004; it cannot be assigned to 2000 or used to determine trend either from 1996 or to 2006. The surface balance estimate (Input), held constant, is the mean of atmospheric model products for 1980–2004

[d] Area of systems 25–27 (Graham Land and eastern Palmer Land) is excluded from Z05; the estimate includes the area of ice rises and grounded ice on islands attached by ice

[e] a The "best estimate" of +27 ± 29 Gt/year listed in W06 was for the observed area of 8.49 × 10^6 km^2

[e] b Following W06 p. 1633 (i.e. "*Our estimate of the mass gain of the unsurveyed Antarctic interior is comparable to our estimate of the mass loss of the unsurveyed coast*"), we take their best estimate to apply to the sum of basin area values listed in their Table 1 (11.71 × 10^6 km^2) and increase the error estimate in proportion to the respective areas

[e] c Alternatively, we apply +20 Gt/year for the interior following W06 p. 1633 (i.e. "*applying the average elevation rate (9 mm yr^{-1}) for the southernmost degree in latitude provides an estimated growth rate of 22 km^3/year for the omitted region*") and apply −10 Gt/year for the unsurveyed coastal areas following W06 p. 1633 (i.e. "*applying the average elevation rate for the coastal 200 km of the surveyed ice sheet (−14 mm yr^{-1}) to the unsurveyed coastal sector… provides an estimated 10 Gt/year source of ocean mass (assuming the change were to occur at the density of ice*")) and use their respective unobserved areas given on p. 1628 (interior 2.6 × 10^6 km^2 and coastal 0.8 × 10^6 km^2) for a total of 11.9 × 10^6 km^2

areas of agreement among the methods, to identify outliers, and to provide a rationale for a narrowed range of estimates and a preferred estimate. Table 2 includes two GRACE-based mass loss estimates of 104 Gt/year (Velicogna 2009) and 144 Gt/year (Chen et al. 2009) for the period 2002–2006 and two estimates of 246 Gt/year (Velicogna 2009) and of 220 Gt/year (Chen et al. 2009) for the period 2006–2009. These new GRACE estimates extend the IPCC07 range of AIS mass loss downward, and both papers cite results from the latest IOM estimate (Rignot et al. 2008; R08) in support of their findings, specifically the −136 Gt/year IOM estimate for 2000 and an increasingly negative balance toward 2006. In our evaluation of the IOM estimate of R08, we identify some issues regarding their methodology, and provide a modified IOM estimate. We compare two ERS estimates and our modified IOM estimate on a regional basis and find significant agreement over approximately one half of the AIS area.

Although this paper mainly addresses the AIS, we note results in a recent paper on the mass balance of the Greenland ice sheet for 2003–2007 and 1992–2002 (Zwally et al. 2011). The results for 2003–2007 are from Ice, Cloud, and land Elevation Satellite (ICESat) laser altimetry and the results for 1992–2002 are from a re-analyses of previous results from ERS radar altimetry complemented by airborne laser altimetry on outlet glaciers (Zwally et al. 2005; Z05). Particular relevant aspects include: (1) an improved treatment of firn compaction that enables separation of the elevation changes driven by accumulation changes from those driven by ablation and/or dynamic changes, (2) the calculation of appropriate firn/ice densities for those two elevation change components, and (3) the close agreement between the 171 Gt/year mass loss for the 2003–2007 period and two GRACE-based estimates (Wouters et al. 2008; Luthcke et al. 2009) for about the same time period. Those improved methods are being applied to new analyses of ICESat data over Antarctica for the period 2003–2009 and will be compared with other recent comparisons of ICESat and GRACE analyses (e.g. Gunter et al. 2009).

2 Assessment of Mass Balance Estimates from ERS Altimetry

One estimate (Z05) of AIS mass balance from ERS altimetry in IPCC07 gave a preferred estimate for 1992–2001 of -47 ± 4 Gt/year for West Antarctica (WA), $+ 16 \pm 11$ Gt/year for East Antarctica (EA), and -31 ± 12 Gt/year overall, not including Graham Land and eastern Palmer Land (1.07% of the AIS area) in the Antarctic Peninsula (AP). (In this and other references to relative area within the coterminous ice sheet, we use $100\% = 12.183 \times 10^6$ km^2 as compiled in R08.) Another estimate (Davis et al. 2005) gave + 45 Gt/year for EA for 1992–2003. A subsequent report (Wingham et al. 2006; W06) gave a preferred estimate of $+27 \pm 29$ Gt/year for AIS overall for 1992–2003. Direct comparison among these ERS-based estimates is affected by different interpolation/extrapolation procedures (IEP) to attain full area coverage for the area south of 81.5°S, differences in coverage over the relatively narrow zone of steep outer slopes at the ice sheet margin, and differences in analyses for the southwestern region of the AP. In addition, different approaches were used to estimate the appropriate firn/ice density (ρ_i) in the conversion of elevation changes (dH/dt) to mass changes (dM/dt), according to $dM/dt = \rho_i \, dH/dt$. Also, only one estimate (Z05) included a correction for variations in the rate of firn compaction caused by changes in surface temperature that do not involve changes in mass.

Regarding the choice of ρ_i, in their estimate for EA, Davis et al. (2005) used 350 kg/m^3, which is characteristic of near-surface firn and is appropriate if the dH/dt were caused

by very recent changes in precipitation and accumulation rate. In contrast, using ρ_i = 900 kg/m^3 would have increased their estimate of 45 Gt/year mass gain for EA to 115 Gt/year, which would be appropriate if the changes were caused by a long-term imbalance between accumulation and ice dynamics. The W06 analyses for October 1992–February 2003 lists a preferred estimate of +27 ± 29 Gt/year for AIS overall, with particular approaches showing results between −5 and +85 Gt/year. The W06 range includes the difference between restricting the change in elevation to the upper firn layers or attributing it to the whole firn/ice column, and incorporates corrections for accumulation anomalies in 1992–2001 determined from atmospheric modeling of Precipitation minus Evaporation (P-E) ("Appendix", Mass Balance Estimates of Wingham et al. (2006) (W06)). We believe arguments to attribute elevation change to changes in firn thickness on the basis of short-term trends in surface balance (e.g. on basins JJ′ and H-J; W'06) might have regional relevance, but overall there is no statistically significant trend for Antarctica as a whole either in the P-E products covering 1958–2002 (van de Berg et al. 2005) or in the field data collated for large areas since the 1950s (Monaghan et al. 2006a).

The preferred estimate given in Z05 was based on use of ρ_i = 900 kg/m^3 (Z05i) for the firn and ice column and arguments that the bulk of the changes were caused by a long-term (multi-decadal scale) imbalance given previously mentioned lack of evidence for recent overall trends in Antarctic precipitation and accumulation rate. For comparison purposes, Z05 also gave estimates using ρ_i = 400 kg/m^3 (Z05f) for the multi-annual upper firn layers that would reduce the overall AIS mass balance to −14 Gt/year. The dH/dt values from ERS data were also adjusted for changes in the rate of firn compaction (dC/dt) driven by changes in firn temperature. dI/dt = dH/dt−dC/dt−dB/dt was then used to calculate dM/dt using ρ_i dI/dt, where dB/dt is the bedrock motion. For WA, where a regional warming trend caused an increased rate of firn compaction and a surface lowering that did not involve a mass change, the average dC/dt on the grounded ice was −1.58 cm/year (28.4 Gt/year equivalent). In EA, the average dC/dt on the grounded ice was +0.21 cm/year (−19.3 Gt/year equivalent). The derived dH/dt data over 77.1% of the AIS were used applying the optimal-interpolation method (krig procedure) to provide nearly complete spatial coverage (99%) of the AIS including the area of grounded ice south of 81.5°S.

For Z05i, the average interpolated dH/dt south of 81.5° S was +1.6 cm/year, and the calculated average ice thickness and mass changes were relatively small (dI/dt = +0.64 cm/year and dM/dt = +14 Gt/year). Overall, their interpolation including the coastal areas lowered the dM/dt from near zero to −31 Gt/year, indicating that about 45 Gt/year of mass loss from grounded ice in the coastal areas (ice sheet periphery, ice rises, and islands) was included by their interpolation. The survey in W06 that provided a "*best estimate of the overall mass trend… of +27 ± 29 Gt/year"* included "*72% of the grounded ice sheet…, omitting just 6% of coastal sectors… where data are lost due to steep slopes, and 22% of the interior…, which lies beyond the latitudinal limit… of the satellite ground track"*. Although W06 also estimated a growth rate of +22 km^3/year (20 Gt/year) in the area south of 81.5°S and a loss of 10 Gt/year in their unsurveyed coastal area, they stated that the respective gain and loss were comparable (as noted in Table 2) and retained +27 ± 29 Gt/year as their overall estimate. In contrast, Davis et al. (2005) did not interpolate/extrapolate to areas not included in their ERS analyses.

Comparison of ERS-based estimates is also affected by selective use of Glacial Isostatic Adjustment (GIA) estimates, which are implemented singly or in combined values from GIA models in the range between +1.7 mm/year average over Antarctica in W06 and +5.4 mm/year average in Z05. Using the ice density of 900 kg/m^3, the corresponding GIA corrections are −19 Gt/year for W06 and 59 Gt/year for Z05i. Consideration of GIA in

ERS-based studies leads to smaller mass corrections than in GRACE-based studies (discussed in a following section), because the applicable densities of rock are at least three times larger.

3 Assessment of Mass Balance Estimates from IOM

The IOM essentially consists of calculating the difference between mass input values, obtained from estimates of accumulation rates, and outflow values, obtained from measurements of discharge velocities combined with estimates of ice thickness at the grounding line. The IOM study of R08 presents the most complete survey of discharge at the periphery to date and one of the latest combinations of atmospheric model products to estimate of surface balance. Although accumulation estimates are available for the entire area of grounded ice, discharge estimates have only been made for segments of the periphery. In Rignot and Thomas (2002), balance results were presented for 60% of the ice sheet area and in R08 for 85% of the periphery, which was also taken as 85% of the area. Therefore, a critical aspect of the IOM is the IEP used to derive estimates of the outflow for the non-observed (NOBS) parts of the ice sheet from the values obtained for the observed (OBS) parts.

The data for nineteen drainage sectors as published in R08 and combined into the three ice sheet entities (EA, WA, and AP) are reproduced in Table 3 (columns a to g). We abbreviate their notation of Input+, Net+, and Area+ for the total of OBS and NOBS values to I+, N+, and A+, and use O+ for the total outflow. We also abbreviate their notation of Input, Outflow, Net, and Area for OBS values to I_{ob}, O_{ob}, N_{ob}, and A_{ob}, and use I_{nob}, O_{nob}, N_{nob}, and A_{nob} for the corresponding NOBS values that are not listed in R08. We calculate $I_{nob} = I+ - I_{ob}$, A_{nob} (%) $= (A+ - A_{ob})/A+$, total discharge $O+ = N+ - I+$, and $O_{nob} = O+ - O_{ob}$ from their values, as listed in columns i to n. Some sums for WA, EA, and AP in Table 3 show differences of ± 1 Gt/year from the round-off values listed in R08, and the sum of N+ for EA is -2 Gt/year vs. -4 Gt/year in R08. We carry this difference to N+ for all of the AIS and use -136 Gt/year versus -138 Gt/year, and a total discharge of 2191 Gt/year versus 2193 Gt/year.

Four major issues arise from the R08 IOM analyses. The first issue is the implicit assumption equating the fractions of OBS drainage area to the fractions of OBS drainage-periphery length (i.e. "*we use satellite interferometric synthetic-aperture radar observations from 1992 to 2006 covering 85% of Antarctica's coastline to estimate the total mass flux into the ocean.*" (R08, page 106). Their values of $A_{ob} = 10.366 \times 10^6$ km^2 and $A+ = 12.183 \times 10^6$ km^2 show that their A_{ob} (%) for AIS is also 85%. Although equivalence of NOBS periphery and NOBS area is unlikely to be valid for most of the nineteen sectors, it is accepted here for the purpose of this assessment. However, it remains as a concern in the use of either the IOM results from R08 or our modified IOM results (IOM_{MD}). Since the fractions of perimeter with outflow measurements is known, a more appropriate assignment of the corresponding OBS areas could be made by inland mapping of flowlines from the OBS portions of the perimeter. As discussed below, however, the I_{ob} and I_{nob} may have been apportioned by inland mapping and calculation of input over the OBS and NOBS areas.

The second and most important issue is the IEP used in R08 to estimate the discharge from the NOBS periphery or from the NOBS area in each sector. Their IEP is described as "*To include non-surveyed areas, we apply a scaling factor on the mass fluxes of each large basin A-K" based on the percentage surveyed area versus total area to cover 100% of*

Table 3 IOM mass balance estimates from R08 for 2000 and modified estimate

	Values for 2000 from Table 1 in R08							Calculated from R08 values						
	Area A_{ob} 10^3 km^2	Input I_{ob} Gt/yr	Outflow O_{ob} Gt/yr	NET N_{ob} Gt/yr	NET+ N+ Gt/yr	Area+ A+ 10^3 km^2	Input+ I+ Gt/yr	$N + _{AS} = N_{ob} \cdot A + /A_{ob}$ Gt/yr	A_{nob} %	$I_{nob} = I + - I_{ob}$ Gt/yr	%	$O + = I + - N +$ Gt/yr	O_{nob} Gt/yr	%
Column	a	b	c	d	e	f	g	h	i	j	k	l	m	n
Col. calc.								d(f/a)	(f−a)/f	g−b	j/g	g−e	l−c	m/l
East ant														
J″K	1698	93	75	18	19	1780	100	19	5	7	7	81	6	7
KK′	218	42	45	−3	−3	246	50	−3	11	8	16	53	8	15
K′A	159	26	28	−1	−1	178	32	−1	11	6	19	33	5	15
AA′	615	60	60	0	0	622	62	0	1	2	3	62	2	3
A′B	354	39	40	−1	−1	645	115	−2	45	76	66	116	76	66
BC	1197	73	77	−4	−4	1332	87	−4	10	14	16	91	14	15
CC′	434	81	87	−7	−11	702	137	−11	38	56	41	148	61	41
C′D	1053	198	207	−8	−9	1162	261	−9	9	63	24	270	63	23
DD′	563	92	94	−2	−2	691	136	−2	19	44	32	138	44	32
D′E	267	20	22	−2	−3	450	62	−3	41	42	68	65	43	66
EE′	1441	61	49	11	13	1639	89	13	12	28	31	76	27	36
Sum	7999	785	784	1	−2	9447	1131	−5	15	346	31	1133	349	31
R08 sum	7998	786	785	1	−4	9447	1131	–	–	–	–	–	–	–
West ant														
E′F′	751	110	80	31	34	845	130	35	11	20	15	96	16	17
F′G	119	108	128	−19	−23	140	128	−22	15	20	16	151	23	15
GH	393	177	237	−61	−64	417	196	−65	6	19	10	260	23	9
HH′	55	51	86	−35	−49	78	71	−50	29	20	28	120	34	28
JJ″	933	142	145	−4	−4	1028	165	−4	9	23	14	169	24	14
Sum	2251	588	676	−88	−106	2508	690	−106	10	102	15	796	120	15

Table 3 continued

	Values for 2000 from Table 1 in R08							Calculated from R08 values							
	Area A_{ob} 10^3 km^2	Input I_{ob} Gt/yr	Outflow O_{ob} Gt/yr	NET N_{ob} Gt/yr	NET+ N+ Gt/yr	Area+ A+ 10^3 km^2	Input+ I+ Gt/yr	$N + _{AS} = N_{ob} \cdot A + /A_{ob}$ Gt/yr	A_{nob} %	$I_{nob} = I+ - I_{ob}$ Gt/yr	%	O +=I + −N + Gt/yr	O_{nob} Gt/yr	%
R08 sum	2251	588	676	−88	−106	2508	690	–	–	–	–	–	–	–
Ant pen														
H′I	92	71	78	−7	−7	98	77	−7	6	6	8	84	6	7
II″	13	15	20	−5	−15	78	125	−30	83	110	88	140	120	86
I″J	11	8	9	−1	−6	52	32	−5	79	24	75	38	29	76
Sum	116	94	107	−13	−28	228	234	−42	49	140	60	262	155	59
R08 sum	116	94	107	−13	−28	228	234	–	–	–	–	–	–	–
AIS														
Sum	10366	1467	1567	−100	−136	12183	2055	−154	15	588	29	2191	624	28
R08 sum	10365	1468	1568	−100	−138	12183	2055	–	–	–	–	–	–	–

		Modified O_{nob} and modified I+					R08 values		AS	Md
	OnobAS (area scaled)	O_{nobMd}	$O+_{Md}$	$N+_{MdO}$=I+−$O+_{Md}$	$I+_{Mod}$	$N+_{Md}$=$I+_{Md}$ −$O+_{Md}$	O_{ob} SFE	O_{nob}	O_{nobAS}	O_{nobMd}
	Gt/yr	Gt/yr	Gt/yr	Gt/yr	Gt/yr	Gt/yr	kg/m^2/yr			
Column	o	p	q	r	s	t	u	v	w	x
Col. calc.	c(f-a)/a	0.7 o	c+p	g−q		s−q	c/a	m/(f−a)	o/(f−a)	p/(f−a)
East ant										
J″K	4	3	78	22	100	22	44	73	44	31
KK′	6	4	49	1	50	1	206	286	206	144
K′A	3	2	30	2	32	2	176	263	176	123
AA′	1	0	60	2	62	2	98	286	98	68

Table 3 continued

	OnobAS (area scaled)	Modified O_{nob} and modified I+					R08 values		AS	Md
		O_{nobMd}	$O+_{Md}$	$N+_{MdO}=I+-O+_{Md}$	$I+_{Mod}$	$N+_{Md}=I+_{Md}-O+_{Md}$	O_{ob} SFE	O_{nob}	O_{nobAS}	O_{nobMd}
	Gt/yr	Gt/yr	Gt/yr	Gt/yr	Gt/yr	Gt/yr	kg/m^2/yr			
A′B	33	23	63	52	115	52	113	261	113	79
BC	9	6	83	4	87	4	64	104	64	45
CC′	54	38	125	12	137	12	200	228	200	140
C′D	21	15	222	39	261	39	197	578	197	138
DD′	21	15	109	27	136	27	167	344	167	117
D′E	15	11	33	29	62	29	82	235	82	58
EE′	7	5	54	35	89	35	34	136	34	24
Sum	173	121	905	226	1131	226	98	241	120	84
West ant										
E′F′	10	7	87	43	130	43	107	170	107	75
F′G	23	16	144	−16	44	−100	1076	1095	1076	753
GH	14	10	247	−51	159	−88	603	958	603	422
HH′	36	25	111	−40	53	−58	1564	1478	1564	1095
JJ″	15	10	155	10	165	10	155	253	155	109
Sum	98	68	744	−54	551	−194	300	467	381	266
Ant pen										
H′I	5	4	82	−5	57	−24	848	1000	848	593
II″	100	120	140	−15	125	−15	1538	1846	1538	1846
I″J	34	29	38	−6	32	−6	818	707	818	707
Sum	139	153	260	−26	214	−45	922	1384	1238	1362
AIS										
Sum	410	342	1909	146	1896	−13	151	343	226	188

Antarctica (Table 1)" (R08, page 107), and in their Table 1 as "*Net+: mass balance scaled on the basis of total area (Area+) versus surveyed (Area),…*". The first statement implies a scaling of both the input and output fluxes by the ratio of total area to OBS area (i.e. A+/A_{ob}) and the second statement indicates a scaling of the net flux by the same ratio. These scalings should be mathematically equivalent because the three terms are linearly related in a summation. According to the second statement, our calculation of net mass balance values as $N+ = N_{ob} \cdot A+/A_{ob}$ in column h agrees with the NET+ of R08 (column e), except for sector II″ (−30 versus −15 Gt/year) and roundoff differences in the other sectors. However, in contrast to the implication of the first statement, the input and outflow terms ($I_{ob,}$ I_{nob}, $O_{ob,}$ and O_{nob}) of the mass balance from R08 values in Table 3 are not separately consistent with this area scaling, as shown by comparisons of I_{nob}(%) and O_{nob} (%) in columns k and n with A_{nob} (%) in column i. A more explicit comparison is made below using the surface-flux equivalent (SFE) for each of the mass rate terms. The SFE (kg/m^2/year) is the ratio of bulk mass rate (Gt/year) to area (10^6 km^2), which normalizes the terms by their respective areas (Fig. 3a).

The inconsistency in scaling is illustrated by examination, for example, of the values for sector EE′ in Table 3 where a N+ of 13 Gt/year (column h) is obtained by scaling by A+/A_{ob} = 1.137, in agreement with the R08 N+ of 13 Gt/year (column e). However, separate scaling of the input and output terms by the same factor gives $I+_{AS}$ = 69.4 Gt/year and $O+_{AS}$ = 55.7 Gt/year, which are very different from respective R08 fluxes of I+ = 89 Gt/year (column g) and O+ = 76 Gt/year (column l). Since the input, output, and net terms are linearly related in a summation, and are not all scaled by the same factor, the input and output scaling factors must be somewhat different in a compensating manner. In fact, the values for sector EE′ show that input scaling (i.e. $I+/I_{ob}$ = 89/61 = 1.459) used by R08 was slightly different from the scaling factor applied to the output flux (i.e. $O+/O_{ob}$ = 76/49 = 1.551). Because a smaller scaling factor of 1.459 was applied to a larger OBS input flux of 61Gt/year, compared to a larger scaling factor of 1.551 that was applied to a smaller OBS output flux of 49 Gt/year, the differences compensated to give N+ of 13 Gt/year (i.e. 89–76) that is equal to the NET+ of R08.

The values of I_{nob} (%) (column k) calculated from R08 data range from a low of 3% in sector AA′ in EA to a high of 88% in sector II″ in the AP. For the AIS overall, the I_{nob}(%) value of 29% is almost twice as large as the A_{nob} (%) of 15%. Therefore, the R08 contributions to input per unit area from NOBS areas are significantly larger than those from the OBS areas, which is shown more clearly by the SFE of the respective mass terms (Fig. 3a). Using the values in Table 3, the I_{nobs} (SFE) is 324 kg/m^2/year for the overall AIS and the corresponding I_{ob} (SFE) is 142 kg/m^2/year, which are in a ratio of 2.3 to 1. A larger I_{nob} (SFE) than I_{ob} (SFE) seems appropriate, because the drainage areas corresponding to the periphery with the NOBS outflow tend to be more restricted to coastal areas (c.f. next paragraph) where the accumulation rates are generally larger, whereas the faster flowing OBS parts drain more of the interior where the accumulation rates are lower. Although the R08 method of apportionment is not stated, both I_{ob} and I_{nob} may have been calculated from their accumulation input maps, which cover the entire ice sheet, possibly using a tracing of the respective drainage areas inland from the periphery.

In contrast to the input, the outflow (O_{nob}) requires extrapolation, because it is not observed everywhere. However for the AIS overall, the O_{nob}(%) is 28%, or about twice the A_{nob} (%) of 15%. The values of O_{nob}(%) by sector in column n are closer to the values of I_{nob}(%) in column k than to the area ratio A_{nob} (%) in column I, but there are significant compensating differences as discussed above. Table 3 shows that the R08 value for O_{nob} (SFE) for the overall AIS is 343 kg/m^2/year (column v) and the corresponding O_{obs} (SFE)

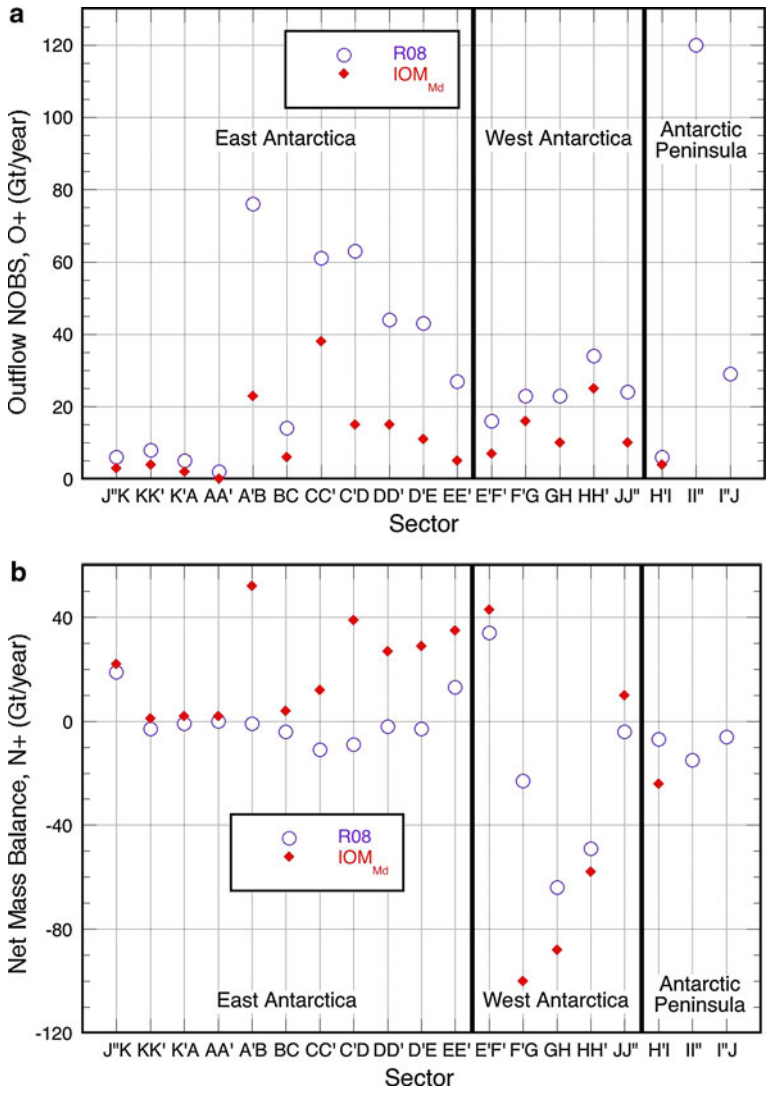

Fig. 3 **a** Difference in outflow from the non-observed (NOBS) area in each of the nineteen sectors in Rignot et al. 2008 (R08) and the modified estimate (IOM_{Md}) using alternate interpolation/extrapolation procedures (IEP). **b** Difference in Net+ for each of the nineteen sectors in R08 introduced by application of the alternate IEP to obtain Outflow from the NOBS area as shown in (a), and substitution of surface balance in sectors F′G, GH, HH′ and H′I from the compilation of Vaughan et al. (1999). There is no modification of Outflow from the NOBS area or of the Net+ statistics for sectors II″ and I″J, Graham Land and eastern Palmer Land, respectively, as cited in R08 from Rignot et al. (2005) and Pritchard and Vaughan (2007)

is 151 kg/m^2/year (column u), which are also in a ratio of 2.3 to 1. By sector, the R08 values of O_{nob} (SFE) are all greater than O_{obs} (SFE), except for sectors HH′ and I″J that together account for 1.07% of the AIS area. A larger SFE in the NOBS parts is not consistent with the fact that measured ice velocities used in the outflow calculations tend to be through the faster moving outlet glaciers and not through the slower moving parts of the

ice sheet periphery. Specifically, R08 noted that selection of OBS periphery "*covers all major outlet glaciers, ice streams and tributaries of importance for mass flux calculation*" (R08, page 106). This implies that the NOBS periphery should have a smaller rate of mass discharge per unit length than the OBS periphery, regardless of variable thickness at the grounding line, and that the corresponding O_{nob} (SFE) should be smaller than O_{ob} (SFE), not larger. Therefore, we believe the R08 scaling significantly overestimates the outflow (i.e. 28% of the total outflow from only 15% of the periphery that are the slower portions). For comparison, in columns o, p, and q of Table 3, we calculate the values of O_{nobAS} (column o) using a proportional area scaling of outflow, which gives equal O_{nob} (SFE) and O_{ob} (SFE) outflows (columns u and w). Compared to R08, area scaling reduces the NOBS outflow from 624 Gt/year to 410 Gt/year (columns m and o) and the total outflow (O+) by about 10% from 2191 Gt/year to 1977 Gt/year, which would change the net mass balance from a loss of 136 Gt/year of R08 to a gain of 78 Gt/year.

We present a modified IEP based on the assumption that the contributions to outflow per unit area in the NOBS areas are between 0.5 and 0.9 of that in the OBS areas. We apply a midpoint factor of 0.7 to the O_{ob} (SFE) (column u) to obtain O_{nobMd} (SFE) (column x), which is then multiplied by A_{nob} to obtain O_{nobMd} (Gt/year) (column p). Although applying a common factor is simplistic, a more elaborate IEP would require information such as periphery length, ice thickness at the grounding line, and velocities. In small sectors such as II″ and I″J, applying a common factor seems to introduce biases that would require a more detailed approach beyond the scope of this paper. Therefore for sectors (II″ and I″J), we use the Net+ values cited (Rignot et al. 2005; Pritchard and Vaughan 2007) and used by R08. The resulting modified values of O_{nobMd}, $O+_{Md}$, and $N+_{MdO}$ are in columns p, q, and r. For EA, the O_{nobMd} is reduced to 121 Gt/year (column p) from the 349 Gt/year of R08 (column m) and the corresponding O_{nobMd} (SFE) is reduced to 84 kg/m^2/year (column x) from 241 kg/m^2/year (column v), appropriately reducing the O_{nobMd} (SFE) to a value smaller than the O_{ob} (SFE) of 98 kg/m^2/year (column u). For WA, the O_{nobMd} is reduced to 68 Gt/year (column p) from the 120 Gt/year of R08 (column m) and the corresponding O_{nobMd} (SFE) is reduced to 266 kg/m^2/year (column x) from the 467 kg/m^2/year of R08 (column v), also appropriately reducing the O_{nobMd} (SFE) to a value smaller than the O_{ob} (SFE) of 300 kg/m^2/year (column u). For the seventeen sectors of WA, EA, and sector H′I in the AP, the O_{nobMd} is reduced by 282 Gt/year from the 475 Gt/year of R08 (column m) to 193 Gt/year (column p). Overall, our modification of the NOBS outflow would bring the overall $N+_{MdO}$ for Antarctica up to a mass gain 146 Gt/year (column r), if the input of R08 were used.

The third issue concerns the atmospheric model products used to obtain the surface balance input, generally referred to as P-E ("Appendix", Surface Balance Estimates in Rignot et al. (2008) (R08)). Among various surface balance inputs available, the P-E results used in R08 give the largest estimate of surface balance for most of northern WA and the AP. In these regions, the composite sector F′-H′ (5.2% of the area) includes three sectors in northwestern WA listing increases between 23 and 192% relative to the field data compilation of Vaughan et al. (1999; V99), which has been used as the benchmark for model products in van de Berg et al. (2006) and W06. One other composite sector H′-J (1.9% of the area) includes northeastern WA and the AP, for which the increases relative to the V'99 compilation range between 24 and 177%. These increases are well in excess of the overall increase in the surface balance of the AIS of "*up to 15%*" reported in van de Berg et al. (2006) where it is noted that it would require new field data to corroborate (c.f. van den Broeke et al. 2006b). Regardless of the soundness of the atmospheric models, product verification in sector F′-J is unconvincing. For example, in R08 disagreement between model product and field data sets led to their dismissal of reliable sets in

northeastern WA listed elsewhere (e.g. Turner et al. 2002) rather than to model-recalibration. Whereas some unreliable data sets are best ignored in the drawing of isopleths in compilations of field data (e.g. Giovinetto et al. 1989), the dismissal in R08 by claiming a bias toward reporting small accumulation rates in central-northern WA on the basis that field observations were made in shallow pits is not justified. Moreover, after acknowledging in earlier discussions of atmospheric model product that there are practically no data from the zone between the coast and an elevation of approximately 1200 m where most of the increase in precipitation is allocated (e.g. van de Berg et al. 2006), the citation in R08 of precipitation gauge data from Russkaya to support the model product in northwestern West Antarctica is questionable. Practically all gauge data everywhere in polar regions are grossly unreliable at wind speeds >10 m/s, particularly where there is ample supply of dry snow nearby, as is the case for Russkaya during at least nine months of the year. The Russkaya station (74°46′S, 136°52′W) lists wind speed >15 m/s for 264 days/year and >30 m/s for 136 day/year).

Substitution of the area adjusted V99 estimates of surface balance for the six sectors would reduce the I+ estimate for the whole ice sheet from 2055 to 1810 Gt/year. However, as mentioned in a preceding section the data cited in R08 for sectors II″ and I″J were from Rignot et al. (2005) and Pritchard and Vaughan (2007) and we retain those values. Therefore, we limit our surface balance substitution to four sectors from F′ to I (a combined 6.02% of the area) (Table 3). This substitution reduces the surface balance for the four sectors by 159 Gt/year from 472 to 313 Gt/year and reduces the R08 estimate of I+ from 2055 Gt/year (column g) to $I+_{Md}$ value of 1896 Gt/year (column s). This reduction of the I+, combined with the reduction of output from the 2191 Gt/year (column l) of R08 to the $O+_{Md}$ value of 1909 Gt/year (column q) brings the $N+_{Md}$ (column t) to a small overall loss of 13 Gt/year. The distribution of the differences between the NOBS outflow and the net mass balance from R08 and our IOM_{Md} are shown in Fig. 3b. The largest reductions in the NOBS outflow are in six of the seven sectors from A′B to EE′ of East Antarctica (Fig. 3a), resulting in more positive net balances (Fig. 3b). Two of the five sectors in WA also have more positive net balances in the IOM_{Md} as a result of the reduction in NOBS outflow, and the other three have a more negative balance as a result of our reduction in $I+_{Mod}$ in those sectors.

The fourth issue arises from the reported trend in the mass budget of Antarctica and particular regions and basins centered on the years 1996, 2000, and 2006 (Tables 1 and 2 in R08). An examination of Table S1 in the Supplementary Material of R08 shows estimates of discharge for each of the 66 basins comprising 85.10% of the area, but the estimate for each basin is based on a velocity measurement for only a single year distributed between 1992 and 2004. The number of basins and the fraction of OBS periphery (total observed area of 10.368×10^6 km^2) are: for single observations distributed between 1992 and 1997, 46 basins for 79.77% of the area; for single observations during 2000, 19 basins for 20.17% of the area; and for single observations during 2004, 1 basin for 0.05% of the area. There seem to be no acceptable assumptions that could be made to obtain discrete estimate values for 1996, 2000, and 2006 from these data, be it for all of Antarctica or for any region or basin. Therefore, additional measurements of discharge not listed in Table S1 in the Supplementary Material of R08 would be required for calculation of changes or trends in discharge during 1996–2006. Also, rather than assigning the finding in Table 1 of R08 to the single datum year of 2000, it seems that a more appropriate assignment would be 1996–1997, because the ice discharge data were compiled for 77.42% of the OBS periphery using observations made for 23 basins in 1996 for 33.23% of the periphery and 16 basins in 1997 for an additional 44.19% of the periphery.

The above four issues also affect the IOM results in Rignot et al. 2011 (R11) in a similar manner, both in regard to the magnitude of their estimates of I+, O+, and N+ and in regard to their conclusions about accelerations in these terms during 1992 through 2009. Using the trend lines (fitted through the illustrated interannual variability) for input (surface mass balance) and output (D*) in Fig. 1b of R11, the respective values I+, O+, and N+ are 2130, 2157, and −27 Gt/year for January 1992 and 2053, 2265, and −212 Gt/year for January 2006. For comparison, the respective IOM_{MdO} values from Table 3 are 1896, 1909, and −13 Gt/year. The R11 estimated accelerations in I+, O+, and N+ are respectively $I'+ = -5.5 \pm 2$ Gt/year^2, $O'+ = +9.0 \pm 1$ Gt/year^2, and $N'+ = -14.5 \pm 2$ Gt/year^2. Although the R11 discharge estimate includes corrections for grounding line retreat and thinning at the grounding line for two glaciers (Thwaites and Pine Island) in WA, the methodology otherwise appears to be that of R08 and subject to both the overestimate of discharge from the NOBS areas, as well as insufficient information on the time series of discharge velocities used to justify the estimated acceleration of O+.

In regard to the R11 estimate of a deceleration in I+ from 1992 through 2009, we again note that any conclusions regarding possible trends in precipitation, and therefore surface mass balance in Antarctica, are highly dependent on the model used and the time period (Bromwich et al. 2011; Nicolas and Bromwich 2011). The R11 estimated deceleration of 5.5 ± 2 Gt/year^2 for 1992 through 2009 is strongly influenced by the positive anomaly in 1992 to mid 1993. The corresponding linear trend for 1994 through 2009 following the anomaly is a statistically insignificant acceleration of 0.8 ± 2 Gt/year^2. Similarly, for a period beginning before the 1992 anomaly, the ERA-Interim reanalyses data set, considered to provide "*the most realistic depiction of precipitation changes in high southern latitudes during 1989 to 2009*", showed an insignificant change of 0.5 ± 2.7 mm/year/decade and four other reanalyses data sets showed positive trends in P-E (Bromwich et al. 2011). For a longer period, Monaghan et al. (2006b) found "*there has been no statistically significant change in snowfall since the 1950s,…*". Therefore, we believe there is insufficient evidence in the IOM results for either an acceleration or deceleration.

4 Comparison of Regional Distributions of Mass Balance Estimates from IOM and ERS

To assess the impact and distribution of balance estimates for particular drainage entities, we use seventeen regions (Fig. 2) approximately matching the twenty-one "basins" in W06, the nineteen "sectors" in R08, and the twenty-seven drainage "systems" in Z05 as combined in Table 4. These combinations aim to minimize boundary disparities, but several combinations require qualification. To match the sector E′F′ in R08 the basins E′E″, E″F, and FF′ from W06 are combined, but the area of FF′ common to both studies remains incorporated in system 20 of Z05; also, in Z05 the study includes grounded ice areas outside the coterminous ice sheet. However, no adjustments are made for these qualifications, because they do not alter the findings in a significant way.

Comparison of net SFE estimates in Table 4 (columns l–0) and re-integrated bulk estimates for the seventeen regions (columns p-r) show there is close agreement over most of the AIS between the ERS-based estimates of W06 and the two estimates in Z05 (as stated previously, Z05f used a density of 400 kg/m^3 and, for their preferred estimate, Z05i used a density of 900 kg/m^3). For comparison here, we use Z05i as the preferred estimate. Comparison of the estimates by region (Fig. 4a and Table 4), shows that the IOM_{Md} values are mostly the outliers (as it would be the case with the unmodified R08 values), even

Table 4 Antarctica. Comparison of net balance estimates for grounded ice compiled in seventeen regions

Region	Sector	Basin	System	Area (10^6 km^2 and (%) of total)			Net balance for original area (Gt/year)				Surface flux equivalent (kg/m^2/year)				Area adjusted net balance (Gt/year)		
Fig. 1 a[a]	R08 b	W06 c	Z05 d	R08 (%) e	W06 f	Z05 g	IOM^b_{Md} h	W06 i	Z05f j	Z05i k	IOM^b_{Md} l	W06 m	Z05f n	Z05i o	W06 p	Z05f q	Z05i r
1	JJ″	JJ′,J′J″	1, 2	1.028 (8.44)	1.04	1.3676	9.67	3.02	2.98	6.73	9.41	2.90	2.18	4.92	2.99	2.24	5.06
2	J″K	J″K	3	1.780 (14.61)	1.59	1.5181	22.47	5.72	5.00	11.25	12.62	3.60	3.29	7.41	6.40	5.86	13.19
3	KK′	KK′	4	0.246 (2.02)	0.24	0.2563	0.95	8.86	2.98	6.70	3.86	36.92	11.63	26.14	9.08	2.86	6.43
4	K′A	K′A	5	0.178 (1.46)	0.19	0.2065	1.66	10.26	6.12	13.78	9.33	54.00	29.64	66.73	9.61	5.28	11.88
5	AA′	AA′	6	0.622 (5.11)	0.59	0.6038	1.52	−1.59	−0.77	−1.73	2.44	−2.70	−1.28	−2.87	−1.68	−0.79	−1.78
6	A′B	A′A″,A″B	7, 8	0.645 (5.29)	0.64	0.6178	51.98	−7.02	−11.21	−25.24	80.59	−10.97	−18.15	−40.86	−7.08	−11.70	−26.35
7	BC	BC	9–11	1.332 (10.93)	1.29	1.3321	3.92	15.09	0.00	0.00	2.94	11.70	0.00	0.00	15.58	0.00	0.00
8	CC′	CC′	12	0.702 (5.76)	0.70	0.7163	12.39	19.53	4.82	10.86	17.65	27.90	6.73	15.16	19.59	4.72	19.64
9	C′D	C′D	13	1.162 (9.54)	1.15	1.1114	39.00	−34.16	−6.15	−13.85	33.56	−29.70	−5.53	−12.46	−34.52	−6.43	−14.48
10	DD′	DD′	14	0.691 (5.67)	0.74	0.6910	27.04	−9.99	−0.07	−0.15	39.13	−13.50	−0.10	−0.22	−9.33	−0.07	−0.15
11	D′E	D′D″,D″E	15, 16	0.450 (3.69)	0.41	0.4024	29.45	3.96	0.38	0.84	65.44	9.66	0.94	2.09	4.35	0.425	0.94
12	EE′	EE′	17	1.639 (13.45)	1.55	1.8481	35.29	2.79	6.56	14.77	21.53	1.80	3.55	7.99	2.95	5.82	13.10
13	E′F′	E′E″,E″F,FF′	18, 19	0.845 (6.94)	0.74	0.6414	42.99	4.15	1.91	4.30	50.88	5.61	2.98	6.70	4.74	2.52	5.67
14	F′G	F′G	20	0.140 (1.15)	0.13	0.2015	−100.01	7.61	1.00	2.25	−714.36	58.54	4.96	11.17	8.20	0.695	1.56
15	GH	GH	21, 22	0.417 (3.42)	0.43	0.4179	−88.03	−33.67	−27.86	−62.76	−211.10	−78.30	−66.67	−150.18	−32.65	−27.80	−62.63
16 (↓)[c]	HI (↓)	HJ (below)	23–24(↓)	0.176 (1.44)	0.28	0.2608	−82.44	32.76	0.85	1.91	−468.41	117.00	2.15	4.83	35.80	0.66	1.48
16.1	HH′	HH′[d]	23	0.078 (0.64)		0.0892	−58.18		−1.18	−2.67	−745.90		−13.23	−29.93		−1.03	−2.34

Table 4 continued

Region	Sector	Basin	System	Area (10^6 km^2 and (%) of total)			Net balance for original area (Gt/year)				Surface flux equivalent (kg/m^2/year)				Area adjusted net balance (Gt/year)		
Fig. 1 a[a]	R08 b	W06 c	Z05 d	R08 (%) e	W06 f	Z05 g	IOM^b_{Md} h	W06 i	Z05f j	Z05i k	IOM^b_{Md} l	W06 m	Z05f n	Z05i o	W06 p	Z05f q	Z05i r
16.2	H′I	H′I[d]	24	0.098 (0.80)		0.1716	−24.26		2.03	4.58	−247.55		11.83	26.69		1.16	2.62
17	II′,I′I″	I″J[d]	25–27	0.130 (1.07)		0.1350	−21.00				−161.54						
1–16	All	All	1–24	12.183 (100)	11.71	12.328	−13.15	27.32	−13.46	−30.34	−1.08	2.333	−1.092	−2.461	34.03[e]	−15.72[e]	−35.44[e]

[a] 1-Southwestern Filchner-Ronne I.S., 2-Eastern Filchner-Ronne I.S., 3-Coats Land/Risser-Larsen I.S., 4-Central-Western Fimbul I.S., 5-P. Astrid and P. Ragnhild Coasts, 6-Enderby Land., 7-Amery I.S., 8-Ingrid Christensen Coast/West and Shackleton I.S., 9-Wilkes Land, 10-George V and Adèlie Coasts, 11-Rennick Gl./Victoria Land, 12-Southwestern Ross I.S., 13-Eastern Ross I.S., 14-Ruppert Coast/Getz I.S., 15-Walgreen Coast., 16-Abbot I.S./Western Palmer Land, 17-Graham Land/Eastern Palmer Land

[b] Values for IOM_{Md} obtained from Table 3 after modifications of the IEP used to estimate discharge from the non-surveyed periphery in all sectors except II″(Region 17), and of the surface balance for sectors F′-H (Regions 14, 15) and sectors H–I (Region 16)

[c] Statistics for Region 16 are split to highlight the contrasts between 16.1 and 16.2 in net budget estimates and SFE

[d] No separate data are provided for these basins

[e] The sums of reintegrated values based on the generalization imposed by grouping sectors, basins, and systems are listed only to illustrate the numerical effects of the procedure and not as substitutes. The largest distortion affects the adjusted estimate of W06, from 28 to 34 Gt/year in the sum, mainly contributed to by change for basin HJ, from 33 to 36 Gt/year

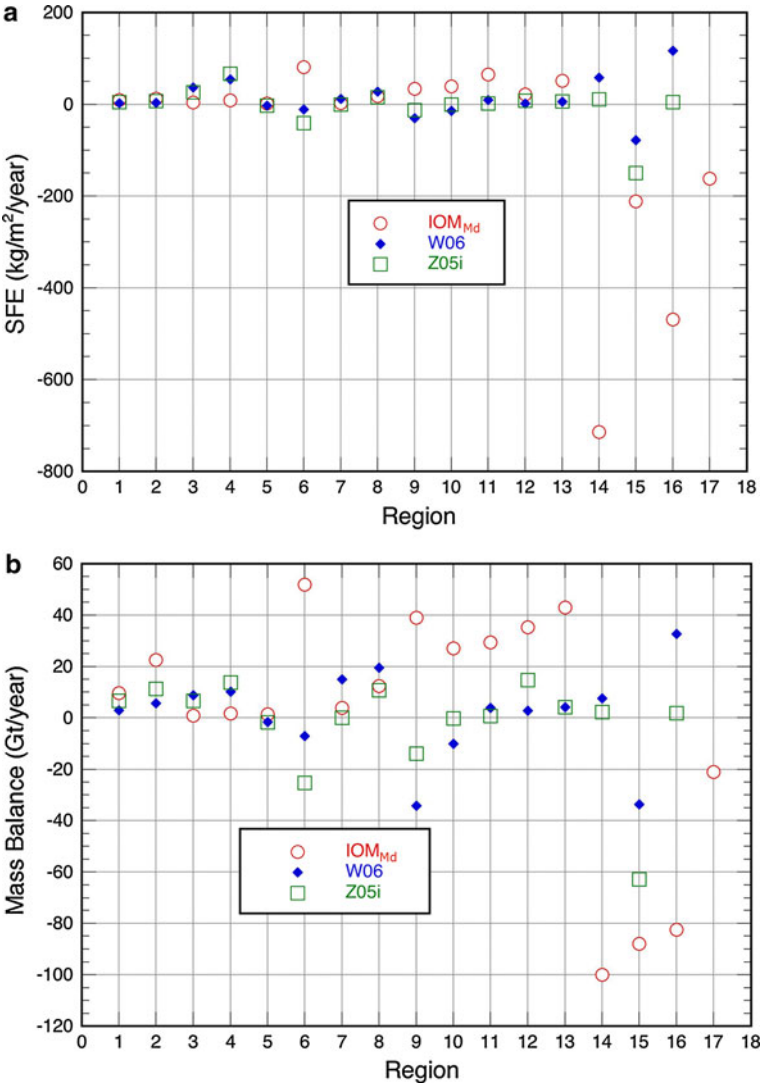

Fig. 4 Comparison of net budget estimates based on ERS radar altimetry data and the Input–Output Method (IOM) compiled for seventeen regions (Fig. 2, Table 4). ERS-based: Zwally et al. 2005 (Z05i), Wingham et al. 2006 (W06). IOM-based: Rignot et al. 2008 (R08) and the modified IOM (IOM_{Md}) presented in this study. **a** Comparison of surface flux equivalent (SFE) estimates in kg/m^2/year. **b** Comparison of bulk estimates in Gt/year

though the SFE for all regions for the IOM_{Md} and the ERS-based estimates are in closer agreement. The largest SFE difference (749 kg/m^2/year) is observed in region 14 (F′G, system 20; 1.15% of the AIS area) between the mean of the ERS-based estimates of W06 and Z05i (+35 kg/m^2/year) and the IOM_{Md} estimate (−714 kg/m^2/year). The second largest difference (529 kg/m^2/year) is observed in region 16 (HI in R08, HJ in W06, systems 23,24; 1.44% of the AIS area) between the mean of ERS-based estimates (+61 kg/m^2/year) and the modified IOM estimate (−468 kg/m^2/year). It should be noted that sector

HH′ (0.64% of the area) in the AP with an SFE of −746 kg/m^2/year is a principal contributor to the large mass loss in both IOM estimates, but not in ERS-based estimate. Elsewhere relatively small differences of approximately 100 kg/m^2/year are observed in regions 6 (A′B, systems 7,8; 5.29% of the AIS area: ERS mean of −26 kg/m^2/year c.f. the IOM_{Md} estimate of +81 kg/m^2/year) and region 15 (GH, systems 21,22; 3.42% of the area: ERS mean of −114 kg/m^2/year c.f. the IOM_{Md} estimate of −211 kg/m^2/year). All other SFE differences between the mean of the ERS estimates and the IOM_{Md} estimate are of approximately 50 kg/m^2/year or less over 88.63% of the area. Thus, our comparison covers most of the area (98.93%), except for sector IJ.

It follows that the re-integration of SFE values over the areas from the R08 compilation to obtain bulk net mass balance estimates would show a generally similar distribution of differences between the mean of the two ERS-based estimates (W06 and Z05i) and the IOM_{Md}, albeit enhanced in some regions of relative large area (Fig. 4b). The largest difference in net balance is observed in region 14 (105 Gt/year; ERS mean of +5 Gt/year c.f. IOM_{Md} estimate of −100 Gt/year). The second largest difference (101 Gt/year) is observed in region 16 between the ERS mean of +19 Gt/year and the IOM_{Md} estimate of −82 Gt/year. Three other relative large differences are observed in region 6 (69 Gt/year; ERS mean of −17 Gt/year cf. +52 Gt/year for the IOM_{Md} estimate), region 9 (C′D, system 13; 9.54% of the area: 63.5 Gt/year; ERS mean of −24.5 Gt/year cf. +39.0 Gt/year for the IOM_{Md} estimate), and region15 (40 Gt/year; ERS mean of −48 Gt/year cf. −88 Gt/year for the IOM_{Md} estimate). Smaller differences are noted in regions 10–13 (D-F′, systems 14–19; 29.75% of the area), where the IOM_{Md} estimates list values of approximately +40 Gt/year and the ERS mean values are in the range between −10 and +10 Gt/year. All other regions show differences smaller than 25 Gt/year over 48.34% of the area. Again, our comparison covers 98.93% of the area.

5 Overview of recent GRACE-based budget estimates

The GRACE-based estimates included in the IPCC07 report indicate −139 ± 73 Gt/year for April 2002–July 2005 (Velicogna and Wahr 2006) and −40 ± 36 Gt/year for July 2002 and March 2005 (Ramillien et al. 2006). More recently estimates based on longer series indicate an increase in the rate of mass loss. Based on April 2002–February 2009 data estimated at −143 ± 73 (Velicogna 2009) and on April 2002–January 2009 data at −190 ± 77 Gt/year (Chen et al. 2009). However, the latest estimate based on April 2002–December 2008 data list a mean of −87 Gt/year split at −64 ± 32 Gt/year for WA and −23 ± 29 Gt/year for EA (Table 2). These studies show improvement in the discussion of the composite error values assigned to the surface mass trend derived from geodynamic modeling and GIA that is highly dependent on ice sheet evolution (e.g. Gunter et al. 2009). Model selection denoted in Table 2 is important because the estimate introduced using either the IJ05 or ICE5G models can yield, e.g. either −190 or −250 Gt/year, respectively (Chen et al. 2009).

Implementation of particular GIA models produce mean postglacial rebound values for the AIS area between approximately 1.5 and 9 mm/year with a density of at least 2700 kg/m^3 implying adjustments ≥60 Gt/year, those actually applied being much larger by a factor of 3 (e.g. Velicogna and Wahr 2006; Velicogna 2009; Chen et al. 2009). The GIA is assumed to be constant for the period of analyses and GRACE series extending beyond 2005 allow observation of trend in changes of ice mass regardless of the large uncertainty in the mean value (e.g. Bromwich and Nicolas 2010). The studies by Velicogna (2009) and

Chen et al. (2009) identify 2006 as the year in which there is an acceleration of mass loss (from −104 Gt/year in 2002–2006 to −246 Gt/year in 2006–2009 or an increase of 137%, and from approximately −160 Gt/year in 2002–2006 to −220 Gt/year or an increase of 19%, respectively) and both cite the IOM results of R08 as part of the support for their findings. However, as discussed in a previous section the suggestion of an increasing rate of loss from IOM in R08 appears to be based on sets of single observations of discharge in particular years on part of the AIS, rather than a set of repeat observations that would support the identification of a trend in the mass loss.

The wide range of GRACE values reported for similar time periods indicates at least some of the GRACE values must be outliers. The issues affecting the derivation of ice mass changes from GRACE data include: uncertainties in the GIA correction from model and density errors, uncertainties in the various terms in the spherical-harmonic expression of the Earth′s gravity field, uncertainties in the corrections for variations in the atmospheric mass, errors in the calculations of the scaling factor ("kernel") to account for the effective size of the measurement region or limited spatial resolution of GRACE satellites, and "leakage" of signals from mass changes outside the measurement region. These issues are being addressed by various investigators and reported in the literature (e.g. Gunther et al. 2009). Also, the mass-concentration gravity solutions (Luthcke et al. 2006, 2008), which use the GRACE observations more directly and utilize the full inherent resolution of the gravity signal sensed by GRACE, have been providing higher-resolution results that avoid some of the limitations of the methods using the spherical-harmonic solutions of the gravity field. Also, as noted in Gunther et al. (2009) and elsewhere, comparing or jointly analyzing GRACE and ICESat derived mass changes for the same time period will, for example, enable the selection of an improved GIA correction for both data sets as well as help validate other corrections.

6 Conclusions

Additional estimates of mass balance reported after completion of the IPCC07 increased the range from +50 to −200 Gt/year for the period 1992–2003 to +50 to −250 Gt/year for the period 1992–2009. Some recent reports also suggested an increase in the rate of mass loss in recent years. A range of 300 Gt/year is approximately 15% of the annual mass input and 0.8 mm/year SLE. Our assessment reviews and evaluates those estimates, which are from three essentially different and mostly independent methods: (1) the volumetric method based on measurement of elevation changes by ERS radar altimetry, (2) the IOM that gives the difference between input and output mass fluxes using various measurements and calculations, and (3) the gravimetric method based on measurement of gravity changes by the GRACE satellites.

Assessment of the IOM estimate for overall AIS of -138 ± 92 Gt/year in R08 showed their extrapolation overestimated the discharge from the NOBS areas which are 15% of the total ice sheet area. We provide a modified IOM estimate (IOM_{Md}) that first reduces the outflow SFE for the NOBS areas to 0.7 of the SFE for the OBS areas, which would give a positive overall mass balance of 146 Gt/year. However, the IOM_{Md} estimate also substitutes lower mass input values from a compilation of accumulation data interpolated on the basis of microwave firn emissivity (V99) in place of the modeled P-E estimates in three sectors of WA and one in the AP (total of 6% of the AIS area). Our modification of the outflow changes the balance estimate by +282 Gt/year (15% of the annual output) and modification of the IOM input value changes the balance estimate by −159 Gt/year (8% of

the annual input), which together bring the net balance for overall AIS to a loss of 13 Gt/year.

Comparison between two ERS-based estimates shows that the difference between the preferred estimate for overall AIS of -31 ± 12 Gt/year for 1992 to 2001 given in Z05 and the preferred estimate of $+27 \pm 29$ Gt/year for 1992 to 2003 given in W06 are mainly due to different treatments of firn/ice density, corrections for the rate of upper firn compaction, differences in areal coverage, and IEP. The methodology in Z05 included an important correction for elevation changes caused by changes in the rate of firn compaction driven by changes in surface temperature, covered more AIS area with crossover analyses, and estimated the uncovered areas with optimal interpolation compared to the other analyses. Nevertheless, the difference between the two ERS estimates is only 3% of the annual mass input.

For all of the AIS, the IOM_{Md} estimate lies within the range of the two ERS estimates, which along with the GRACE-based estimate of Raimillen et al. (2006) gives a narrowed range of + 29 to −40 Gt/year that is only about 3.5% of the annual mass input. Our preferred estimate for 1992–2001 is −47 Gt/year for WA, + 16 Gt/year for EA, and −31 Gt/year overall (+0.1 mm/year SLE), not including part of the AP (1.07% of the AIS area) as taken from Z05. However, this narrowed range of estimates leaves the more negative GRACE-based estimates as outliers. Regarding the trend toward an increasing mass loss in some GRACE estimates, we also find that the evidence presented in R08, supporting an increase in mass loss from the IOM analyses, is insufficient as published.

A change of approximately 5% of the annual mass input or output to the AIS is approximately 100 Gt/year, which is 0.3 mm/year SLE and 10% of current sea level rise. Therefore, for the purpose of closing the sea level change budget to 10% or better, obtaining estimates of the AIS mass balance to an accuracy of several percent is required. Considering the state-of-art for determining the input and output fluxes, it is difficult to see how the IOM can achieve the required accuracy even for a snapshot in time. Furthermore, the problems with the IOM are even more difficult for determining trends.

Although the published GRACE estimates of mass change have a wide range and relatively large estimates of error, the methodology for deriving mass changes from GRACE data and correcting errors is improving significantly with time. The convergence of results from ICESat and GRACE within estimated errors for the recent mass loss from Greenland is a significant advance. However, the GIA is significantly larger in the Antarctic and the uncertainty of the modeled GIA is also larger, mainly because of uncertainty in the history of the glacial unloading and the sparsity of data for model calibration. The expansion of Global Positioning System (GPS) measurements of crustal motion in the Antarctic in recent years is providing new data that are being used for improving the modeled GIA estimates (e.g. King et al. 2010). Applying these improvements to GRACE data analyses, the recent improvements applied to the ICES at data analyses for Greenland, and the joint analyses of GRACE and ICESat data for the same time periods should significantly improve not only the estimates of the current mass balance of Antarctica, but also of its changes over time.

Acknowledgments This research was supported by NASA's ICESat Project Science funding. We thank Scott Luthcke for providing his insights on GRACE methodology, issues, and developments, and two anonymous reviewers for helpful suggestions and corrections.

Appendix

Mass Balance Estimates of Wingham et al. (2006) (W06)

The study of W06 collated ERS data in a 10 km grid format. Surface elevation change and accumulation anomaly values were given in mm/year (ice), and the accumulation mean for 1979–2001 was given in mm/year (snow). The P-E series were a product of the European Center for Medium-range Weather Forecasts model using boundary and initial conditions based on a 40 year re-analyses (ECMWF_ERA-40), which has a resolution of approximately 55 km. The study discussed the attribution of the observed change and of interpolated/extrapolated volume changes to either the upper firn layers with a density of 350 kg/m^3 or to the glacial column with a density of 917 kg/m^3. However, the area integration of their summarized surface elevation change and accumulation anomalies match the stated best balance estimate (a round off value of 27 Gt/year) using a density of 900 kg/m^3, which is actually closer to the mean density of firn and glacial ice columns than the often listed value of 917 kg/m^3. The mean snow accumulation values listed were factored by 0.35.

Surface Balance Estimates in Rignot et al. (2008) (R08)

The study of R08 compiles…*"the arithmetic average of the values given"*… by two atmospheric model products (van de Berg et al. 2006; van den Broeke et al. 2006a) to estimate surface balance for 1980–2004, obtained from a regional atmospheric climate model referred to as RAMCO2/ANT_E40 supplemented by the ECMWF_ERA-40 fields (E40 and ERA-40 refer to the same initial and boundary conditions). Surface balance estimates in studies using the IOM, from the least time-constrained field data compilations (e.g. V99), to the P-E obtained from atmospheric modeling products complemented with modeled melt losses (e.g. van de Berg et al. 2006; van den Broeke et al. 2006a) vary from study to study. In those using field data compilations mostly based on strata accumulated since ca. 1940, the difference in surface balance can be as large as 270 Gt/year, in approximately equal parts due to differences in the IEP and in the implementation of a deflation/ablation adjustment that is independent of the IEP (e.g. V99; Giovinetto and Zwally 2000; Z05). In studies using model products to estimate P-E in series generally starting ca. 1980, the difference in surface balance can be in excess of 600 Gt/year (discussed below) mainly due to different selection of initial and boundary conditions (e.g. Monaghan et al. 2006b; W06). There is no significant trend in the P-E statistic, in part due to the short series used (van den Berg et al. 2005). Clearly, in budget estimates based on the IOM the choice of model product determining the input is the principal consideration determining the result. A cursory review of the literature, ignoring the outlier estimates produced in many studies as part of the discussion of alternate initial and boundary conditions, and selecting the preferred results identified in each study, shows P-E estimates range between $130 \pm (7)$ and 180 ± 8 kg/m^2/year (W06, Monaghan et al. (2006b), respectively); the "$\pm(7)$" entry is assigned in this overview and it is an approximation based on similar estimates. Integrated for the area of 12.183×10^6 km^2 (from the latest compilation as reported in R08) the range is between 1584 and 2193 Gt/year, i.e. a difference of 609 Gt/year that could be deemed larger if the errors are considered. Ignoring the error, one half of the range between estimates implies that depending on the choice of model product, a difference of approximately 300 Gt/year (equivalent to 0.8 mm/year in sea level) could be introduced in practically any result obtained using the IOM. This half-

range difference is at least twice as large as that which could be introduced by selecting between different field data compilations each using a different IEP (say 135 Gt/year neglecting the optional use of the deflation/ablation adjustment), and is an order of magnitude larger than that which would result from choices such as attributing the observed change in surface elevation to either snow or ice.

References

Ablain M et al (2009) Ocean Sci 5:193

Bindoff NL et al (2007) Observations: oceanic climate change and sea level. In: Solomon S et al. (ed) Climate change 2007: the physical science basis. Fourth assessment report of the intergovernmental panel on climate change. Cambridge University Press, Cambridge UK, New York, USA

Bromwich DH, Nicolas JP (2010) Ice-sheet uncertainty. Nat Geosci 3:596–597

Bromwich DH, Nicolas JP, Monaghan AJ (2011) An assessment of precipitation changes over Antarctica and the southern ocean since 1989 in contemporary global reanalyses. J Clim (in press)

Chen JL et al (2009) Accelerated Antarctic ice loss from satellite gravity measurements. Nat Geosci 2:859. doi:10.1038/NGEO694

Church JA et al (2010) Ocean temperature and salinity contributions to global and regional sea-level change. In: Church JA et al (eds) Understanding sea-level rise and variability. Wiley-Blackwell, USA, pp 143–176

Davis CH et al (2005) Snowfall-driven growth in east Antarctic ice sheet mitigates recent sea-level rise. Science 308(5730):1898–1901

Domingues CM et al (2008) Improved estimates of upper-ocean warming and multi-decadal sea-level rise. Nature 453:1090–1093

Giovinetto MB, Zwally HJ (2000) Spatial distribution of net surface accumulation on the Antarctic ice sheet. Ann Glaciol 31:171–178

Giovinetto MB, Bentley CR, Bull CB (1989) Choosing between incompatible regional surface-mass-balance data sets in Antarctica. Antarct J US XXIV(1):7–13

Gunter B et al (2009) A comparison of coincident GRACE and ICESat data over Antarctica. J Geod 83:1051–1060

King MA et al (2010) Improved constraints on models of glacial isostatic adjustment: a review of the contribution of ground-based geodetic observations. Surv Geophys 31:465–507. doi:10.1007/s10712-010-9100-4

Lemke P et al (2007) Observations: changes in snow, ice and frozen ground. In: Solomon S et al (eds) Climate change 2007: the physical science basis. Fourth assessment report of the intergovernmental panel on climate change. Cambridge University Press, Cambridge, UK, New York, USA

Lutchke SB et al (2006) Recent greenland ice mass loss by drainage system from satellite gravity observations. Science 314:1286. doi:10.1126/science.1130776

Lutchke SB et al (2008) Recent glacier mass changes in the Gulf of Alaska region from GRACE mascon solutions. J Glaciol 54:188

Lutchke SB et al. (2009) Recent Changes of the earth's land ice from GRACE. Eos Trans AGU 90:52. Fall Meet. Suppl, Abstract H13G-02

Milly PCD et al (2010) Terrestrial water-storage contributions to sea-level rise and variability. In: Church JA et al (eds) Understanding sea-level rise and variability. Wiley-Blackwell, USA, pp 226–255

Monaghan AJ et al (2006a) Recent trends in Antarctic snow accumulation from Polar MM5 simulations. Philos Trans R Soc A364:1683–1708

Monaghan AJ et al (2006b) Insignificant change in Antarctic snowfall since the international geophysical year. Science 313(5788):827–831

Nicolas JP, Bromwich DH (2011) Precipitation changes in high southern latitudes from global reanalyses: a cautionary tale. Surv Geophys. In press (this issue)

Pritchard H, Vaughan D (2007) Widespread acceleration of tidewater glaciers on the Antarctic Peninsula. J Geophys Res 112: F03S29. doi:10.1029/2006JF000597

Ramillien G et al (2006) Interannual variations of the mass balance of the Antarctica and Greenland ice sheets from GRACE. Glob Planet Change 53:198–208

Rignot E, Thomas RH (2002) Mass balance of polar ice sheets. Science 297(5586):1502–1506

Rignot E et al. (2005) Recent ice loss from the fleming and other glaciers, Wordie Bay, West Antarctic Peninsula. Geophys Res Lett 32:L07502

Rignot E et al (2008) Recent Antarctic ice mass loss from radar interferometry and regional climate modelling. Nat Geosci 1:106–110
Rignot E et al (2011) Acceleration of the contribution of the Greenland and Antarctic ice sheets to sea level rise. Geophys Res Lett L05503. doi:10.1029/2011GL046583
Turner J et al (2002) Spatial variability of Antarctic Peninsula net surface mass balance. J Geophys Res 107(D13):4173–4190
van de Berg WJ et al (2005) Characteristics of the Antarctic surface mass balance (1958–2002) using a regional atmospheric climate model. Ann Glaciol 41:97–104
van de Berg WJ et al (2006) Reassessment of the Antarcitc surface mass balance using calibrated output of a regional atmospheric climate model. J Geophys Res 111:D11104–D11118
van den Broeke M et al (2006a) Identification of Antarctic ablation areas using a regional atmospheric climate model. J Geophys Res 111:D18110–D18123
van den Broeke M et al (2006b) Snowfall in coastal West Antarctica much greater than previously assumed. Geophys Res Lett 33:L02505–L02508
Vaughan DG et al (1999) Reassessment of net surface mass balance in Antarctica. J Clim 12:123–130
Velicogna I (2009) Increasing rates of ice mass loss from the Greenland and Antarctic ice sheets revealed by GRACE. Geophys Res Lett 36:L19503. doi:10.1029/2009GL040222
Velicogna I, Wahr J (2006) Measurements of time-variable gravity show mass loss in Antarctica. Science 311:1754–1756
Wingham DJ et al (2006) Mass balance of the Antarctic ice sheet. Phil Trans R Soc A364:1627–1635
Wouters B et al. (2008) GRACE observes small-scale mass loss in Greenland. Geophys Res Lett 35: L20501. doi:10.1029/2008GL034816
Wu Xiaoping et al (2010) Simultaneous estimation of global present-day water transport and glacial isostatic adjustment. Nat Geosci 3:642–646
Zwally HJ et al (2005) Mass changes of the Greenland and Antarctic ice sheets and shelves and contributions to sea-level rise: 1992–2002. J Glaciol 51(175):509–527
Zwally HJ et al (2011) Greenland ice sheet mass balance: distribution of increased mass loss with climate warming. J Glaciol 57(201):88–102

Surv Geophys (2011) 32:377–385
DOI 10.1007/s10712-011-9113-7

Present Day Regional Mass Loss of Greenland Observed with Satellite Gravimetry

E. Schrama · B. Wouters · B. Vermeersen

Received: 21 September 2010 / Accepted: 28 January 2011 / Published online: 15 March 2011

Abstract This paper summarizes results obtained for Greenland's mass balance observed with NASA's GRACE mission. We estimate a Greenland ice sheet mass loss at -201 ± 19 Gt/year including a discernible acceleration of -8 ± 7 Gt/year^2 between March 2003 and February 2010. The mass loss of glacier systems on the South East of Greenland has slowed down while the mass loss increases toward the North along the West side of Greenland. The mass balance can be compared with results obtained by a regional climate model of the Greenland system and ice sheet altimeter data obtained from NASA's ICEsat mission. Our GRACE-only results differ to within 15% from these independently calculated values; we will comment on the possible causes and the quality of the glacial isostatic adjustment model which is used to correct geodetic datasets.

Keywords Temporal gravity · Greenland ice sheet · Satellite gravimetry

1 Introduction

The Gravity Recovery and Climate Experiment (GRACE) was launched in March 2002. It consists of two satellites separated by $\approx$220 km orbiting at 450–500 km above the Earth's surface, see also Tapley et al. (2004). In this paper we rely on GRACE derived monthly sets of spherical harmonic coefficients that describe the gravity field of the Earth. The temporal variations in such gravity fields relative to a long term average gravity field provide the capability to calculate monthly maps of surface water thickness which come with a spatial resolution of $\approx$ 300 km.

With the help of the multi-basin estimation technique introduced in Wouters et al. (2008) we translate the observed water thickness variations into mass time series for 16

E. Schrama (✉) · B. Vermeersen
Delft University of Technology, Kluyverweg 1, 2629 JA, Delft, The Netherlands
e-mail: e.j.o.schrama@tudelft.nl

B. Wouters
The Royal Netherlands Meteorological Institute, Wilhelminalaan 10,
3732 GK, De Bilt, The Netherlands

basins defined within the Greenland system, see Fig. 1. There are four additional basins near Greenland (Ellesmere Island, Baffin Island, Iceland and Svalbard) where we also calculate mass time series. A sum of the estimated basin mass time signals yields a realistic estimate for the total mass change of the Greenland system. The motivation for writing this paper is to provide background information to a presentation with the same title at the workshop on the Earth's Cryosphere and Sea level Change held at the International Space Science Institute in Bern, Switzerland, March 22–27, 2010.

In Sect. 2 we show the results obtained with GRACE for Greenland's mass using a new implementation of the forward method discussed in Wouters et al. (2008), in Sect. 3.1 we compare the obtained solution with other solutions that only depend on GRACE, in Sect. 3.2 we compare our results to independent mass balances derived from satellite altimetry, in Sect. 3.3 we discuss a comparison with an independent mass balance calculation that does not depend on GRACE or satellite gravimetry, in Sect. 3.4 we discuss the possible consequences of a new glacial isostatic adjustment model that was recently published and in Sect. 4 we discuss the outlook for future research on Greenland's mass balance.

2 Mass Loss Trend and Acceleration of the Greenland Ice Sheet

The GRACE system described in Tapley et al. (2004) provides monthly estimates for the Earth's geoid up to a spatial resolution of approximately 300 km which is mostly governed by the height of the GRACE system above the Earth's surface. Under suitable conditions a sufficient number of GRACE measurements becomes available to compute degree and order 60 spherical harmonic coefficient sets at monthly intervals, whereby it should be remarked that the Centre Nationales de Etudes Spatiales (CNES) in Toulouse France produces GRACE gravity fields at 10 day intervals, cf. Bruinsma et al. (2010). Two standard GRACE spherical harmonic coeffient sets from the Center of Space Reseach at the University of Texas (CSR) and the Geo-Forschungs Zentrum in Potsdam (GFZ) are developed by the GRACE science team. These solutions can be downloaded from ftp://podaac.jpl.nasa.gov/grace/data/L2/.

The raw GRACE data consists of inter-satellite distance variations including GPS and accelerometer data collected on both spacecrafts. After processing this data we obtain a level-2 product that provides a monthly set of spherical harmonic coefficients that describe the gravity field of the Earth. During this process all high frequency mass variations that occur within the processing month are removed so that the produced monthly gravity fields are corrected for effects from ocean tides and atmospheric air pressure variations. The

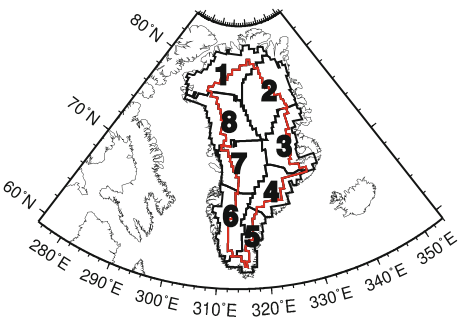

Fig. 1 Basin definitions and index numbers within the Greenland system, including, in red, the 2,000 m contour; for elevations above 2,000 m, the indices are increased by 8

latter both affect the Earth's crust through atmospheric pressure loading, but also play a role in a barotropic ocean model which is used to correct the GRACE gravity fields.

After removal of the static part of the geoid and correction for the glacial isostatic adjustment of the Earth, for which we initially use the models of Paulson et al. (2007) and Peltier (2004), a residual monthly geoid can be obtained from the GRACE system. If we assume that the resulting geoid variations after the GIA correction occur as a result of mass variations on the Earth's surface, and if we assume that the GRACE system is able to observe the signal with an infinite spatial resolution then an elastic loading theory can be used to compute monthly equivalent water thickness $y_t(x)$ where t is time and x the geographic location, for details see Wouters (2010) and Schrama and Wouters (2011).

In reality the spatial resolution of GRACE is limited for a number of reasons: (1) GRACE samples the gravity field from an orbit that occasionally experiences resonances resulting in unfavorable repeating ground track patterns, (2) the altitude of the GRACE satellites is between 450 and 500 km, and (3) the equivalent water thickness maps are convolved with an isotropic, homogeneous spherical Gaussian function G which assists in de-striping these maps.

A separate discussion is the use of a filter technique based on an empirical orthogonal function (EOF) approximation of the GRACE level-2 data or the computed water thickness maps. In the paper of Wouters et al. (2008) the spherical harmonic coefficients are freed from noise by means of an EOF approximation and in Schrama and Wouters (2011) an EOF approximation is used to identify noisy months in the GRACE level-2 series.

In the following GRACE observed water thickness maps are represented as $z_t(x) = G(y_t(x))$ and the task is to use this information to derive mass variations within basins as shown in Fig. 1. For this reason the defocussing method considers the linear system:

$$z_t(x) = \sum_{i=1}^{N} \alpha_{ti}\beta_i(x) + \epsilon_t(x) \tag{1}$$

where z is the convoluted water thickness observed by GRACE at month t at geographic location x. We define N basins in the model domain, the coefficients α_{ti} describe a uniform water thickness in basin i at month t and the functions $\beta_i(x)$ model the contribution of unit basin function i which is defined by the basin shape and the selected Gaussian smoothing radius, for details see Schrama and Wouters (2011). Equation (1) is solved by minimization of a cost function $\epsilon_t(x)'Q^{-1}\epsilon_t(x)$ where Q is the covariance matrix of the GRACE water thickness observations. The solved for coefficients α_{ti} are converted into a mass change per basin which results in a time series for basin i.

A first finding with the method described above is that the choice of the number of basins greatly affects Greenland's mass loss trend function which can be demonstrated by representing the ice sheet by one or more basins. If the Greenland ice sheet is modeled by a single basin being the overlap over compartments 1–16 in Fig. 1 then the mass change dM/dt becomes -146 ± 14 Gt/year where the error margin follows from a 95% confidence interval. If we use basins 1–8 within the coastal zone then we get -207 ± 18 Gt/year, when the system is fully described by all 16 basins as shown in Fig. 1 then we get -219 ± 19 Gt/year. Finally, if we include the four surrounding regions Ellismere Island, Baffin Island, Iceland and Svalbard (the EBIS region) then we get -250 ± 28 Gt/year. These mass change rates are computed with consideration of a 3 degree Gaussian smoothed radius. As input for the de-focussing method we used equivalent water thickness maps derived from monthly GRACE spherical harmonic coefficients provided by the CSR, the GFZ and the University of Bonn. GRACE data was used between March 2003 and Feb

2010 and we applied the glacial isostatic adjustment models from Paulson et al. (2007) and Peltier (2004) to obtain mass loss rates.

The difference between modeling the Greenland ice sheet with 1 or 8 basins hints to an approximation error of the here described de-focusing method. This problem may be avoided by defining a sufficient number of basins.

From the above results we conclude that there is a difference of approximately 12 Gt/year between a solution of 8 coastal basins and 16 Greenland basins, and a difference of approximately 31 Gt/year between a full 16 basin Greenland System (GS) solution and a 20 basin solution that includes the EBIS area. Since there are noticeable correlations in the solution one can not rely on differencing methods because mass changes that occur by adding a few basins to the system will propagate between the involved basins.

For numerical reasons discussed in Schrama and Wouters (2011) we decided to merge the GS above 2,000 m into one basin and to allow for mild a priori constraints, i.e. greater than 10^6 Gt^2 is assumed as a priori variance by modeled basin. This yields a 13-basin configuration where the mass change trend of the GS becomes -201 ± 19 Gt/year, below 2,000 m we find -250 ± 20 Gt/year, above 2000 m we see a mass gain of 49 ± 10 Gt/year, whereby we remark that the errors below and above 2,000 m are correlated by -0.89. For the EBIS region we find -51 ± 17 Gt/year and the correlation of errors to the rest of the solution is between -0.3 and 0.3. The full system consisting of the GS and the EBIS region experiences a mass loss of -252 ± 28 Gt/year and an acceleration of -22 ± 4 Gt/year^2 where more than half of the acceleration signal comes from the EBIS region. All reported values are obtained between from GRACE data collected between March 2003 and February 2010.

The time series by basin in the 13-basin solutions do not only show a linear trend; there are also unique accelerations and annual signals for each basin. The mass change rates and accelerations within the coastal zone of Greenland are shown in Figs. 2 and 3, respectively, for March 2003–February 2010. Any trend or acceleration of the Greenland system as a whole is by definition an approximation because it is the sum of mass changes that originate mostly from the coastal zone of the GS.

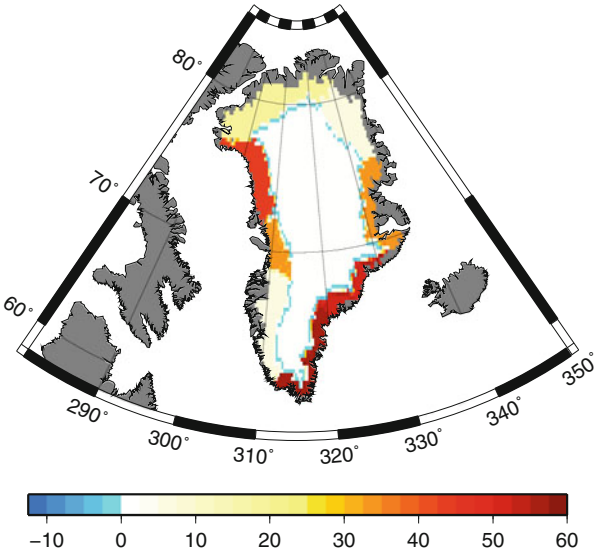

Fig. 2 Mass loss rates in Gt/year in the Greenland system derived by the de-focussing method. The *red zone* of the *color bar* is for negative mass change rates

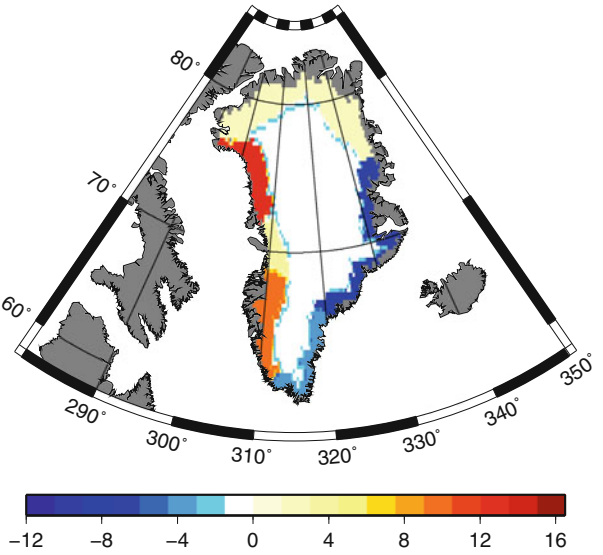

Fig. 3 Mass change accelerations in Gt/year^2 by compartment in the Greenland system. The *red zone* indicates that the mass change trends are becoming more negative

3 Discussion

In this section we will compare our obtained solution for the 13-basin configuration to existing GRACE-only mass balance estimates (MBE), altimeter derived MBEs, and climatologic MBEs of the Greenland ice sheet. Due to the recent developements in the Glacial Isostatic Adjustment (GIA) community we will also comment on Wu et al. (2010) who suggested that it may be necessary to develop a new GIA model for Greenland.

3.1 Comparison to "GRACE-Only" Solutions

When we compare our results to published mass balance estimates of Greenland we notice that Velicogna (2009) finds -137 Gt/year between 2002–2003 to -286 Gt/year in 2007–2009. Their suggestion is that one could interpret this result as a mass loss rate of -230 ± 33 Gt/year and an acceleration of -30 ± 11 Gt/year^2. In Wouters et al. (2008) we reported a mass change rate of -179 ± 25 Gt/year for the time period 2003–2008; the solution of Wouters et al. (2008) is compatible with the solution presented here because of the acceleration effect. For a 13-basin solution we find with the method described in Sect. 2 and with consideration of the gravity field solution provided by the CSR, the GFZ and the university of Bonn, including the GIA models of Paulson et al. (2007) and Peltier (2004), an acceleration of -8 ± 7 Gt/year^2 for the GS, and for the combination of the GS and the EBIS we get -22 ± 4 Gt/year^2.

A Greenland mass loss rate difference is observed between the methods of Wouters et al. (2008) and Velicogna (2009) because of the contribution of the EBIS region. The averaging kernel method used by Velicogna (2009) partly overlaps the neighborhood of Greenland so that this method is affected by mass loss processes in adjacent regions as explained in Wouters et al. (2008) and Wouters (2010).

Whereas both methods are based on monthly GRACE spherical harmonic coefficients provided by the Center of Space Research (CSR) at Austin the results of Luthcke et al. (2010) depend on their implementation of a mass concentration model (mascon model) as

reported in Luthcke et al. (2006) and Rowlands et al. (2005). At the European Geosciences Union meeting held in Vienna, Luthcke et al. (2010) showed that their Greenland mass loss rate stands at -177 ± 6 Gt/year during August 2003–August 2009. This mascon solution displays a large signal in the coastal zone of -242 ± 19 Gt/year while above 2,000 m a mass gain of 65 ± 9 Gt/year is observed; furthermore there is no evidence for an acceleration in the Goddard Space Flight Center (GSFC) mascon solution. In Schrama and Wouters (2011) it is reported that a significant anti-correlation occurs between the total mass variation in coastal zone and the area above 2,000 m on Greenland and that the separation of both signals obtained by the de-focussing method is difficult. Nevertheless for an unconstrained 13 basin solution we also find a mass gain of 49 ± 10 Gt/year over 2,000 m in the GS.

3.2 Comparison to Solutions from Satellite Altimetry

Any satellite altimetry mass balance estimate comes with the fundamental problem that it provides a volume estimate and that firn compaction affects the quality of the computed mass effects by basin. A second effect is that mass loss on Greenland occurs in the coastal margins where all altimeter systems face data interpretation problems because of a rugged topography. The MBE from radar altimetry is discussed in Zwally et al. (2005) for the period 1992–2002 with ERS-1 and ERS-2 data. Their conclusion is that the coastal margin of Greenland was losing -42 ± 2 Gt/year below the equilibrium line but that Greenland was gaining mass by a rate of $+53 \pm 2$ Gt/year inland. ICEsat provides estimates of the topographic change measured by a laser as is discussed in for instance Pritchard et al. (2009) who find thinning along the coastal margin and thickening above 2,000 m on Greenland. A recent Greenland MBE derived from ICEsat altimetry data is -171 ± 4 Gt/year during 2003–2007 as explained in Zwally et al. (2011), while Sørensen et al. (2010) mention -210 ± 21 Gt/year for October 2003–March 2008. In Zwally et al. (2011) the rate of mass gain above 2,000 m is compared between 1992–2002 and 2003–2007. Their conclusion is that the mass change in this area decreased from 44 to 28 Gt/year, while below 2,000 m the mass change increased from -51 to -198 Gt/year.

3.3 Comparison to Climatologic Mass Balance

The Greenland mass balance may also be obtained from regional climate models such as Regional Climate model for Greenland maintained by Michiel van den Broeke (RACMO/GL) which are an essential contribution in modeling the surface mass balance (SMB). In van den Broeke et al. (2009) the SMB follows from precipitation, evaporation and seepage of meltwater; another required component is the glacier discharge (D) which is measured with the help of satellite interferometry as is explained in Rignot and Kanagaratnam (2006). The mass balance for Greenland that should be compared to the values obtained from GRACE, ICEsat and ERS-1 and 2 is the difference SMB-D. This calculation results in -237 ± 20 Gt/year for the Greenland ice sheet according to van den Broeke et al. (2009). Their estimate is *entirely* independent of any assumption about the gravity field of the Earth including corrections to the gravity fields as a result of glacial isostatic adjustment of the Earth which must be applied to the monthly GRACE gravity fields to derive a surface mass balance.

The Greenland mass change rate reported in van den Broeke et al. (2009) is within 15 percent of the result obtained by Wouters et al. (2008), Velicogna (2009), Schrama and Wouters (2011), and Sørensen et al. (2010). Although the time window is nearly compatible it is not well understood why the results obtained by Luthcke et al. (2010) and

Table 1 Published mass balance estimates (MBEs) for Greenland based on various methods

Authors	MBE	Coastal	Inland	Period	Method
Zwally et al. (2005)	$+11 \pm 3$	-42 ± 2	53 ± 2	92–02	ERS-1/2
Zwally et al. (2011)	-171 ± 4	-198	28	03–07	ICEsat
Luthcke et al. (2010)	-177 ± 6	-242 ± 19	65 ± 9	03–09	GRACE
Wouters et al. (2008)	-179 ± 25	-186 ± 19	7 ± 18	03–07	GRACE
Schrama and Wouters (2011)	-201 ± 19	-250 ± 20	49 ± 10	03–09	GRACE
Sørensen et al. (2010)	-210 ± 21			03–08	ICEsat
Velicogna (2009)	-230 ± 33			02–09	GRACE
van den Broeke et al. (2009)	-237 ± 20			03–08	SMB-D

Zwally et al. (2011) deviate from the MBE published by van den Broeke et al. (2009) by more then the allowed confidence interval even if one would correct for known accelerations of the Greenland ice sheet, see also Table 1.

3.4 Consequences of a New Post Glacial Rebound Model

For the calculation of the Greenland ice sheet mass change trend and accelerations with the 13-basin approximation reported in Sect. 3.1 we tested two implementations of GIA models for Greenland, namely that of Peltier (2004) and Paulson et al. (2007). Both models are based on the same ice history model ICE-5G that originates from Peltier (2004). The GIA model of Paulson et al. (2007) is obtained by adjusting the viscosity structure within the Earth's crust to find a best match to the GRACE data. The conclusions with both used GIA models is that there are no significant differences in the obtained Greenland mass loss changes which was the status quo during the workshop in March 2010. Since the workshop Wu et al. (2010) suggested that a new GIA model should be constrained by a larger contribution to mass variations in Greenland.

In Wu et al. (2010) the authors use deformation vectors estimated from GPS data acquired from stations on the Greenland coast, including ocean bottom pressure predictions acquired from a data assimilation model and the CSR level-2 RL04 GRACE data from April 2002 to December 2008. One of the possibilities might be that the ICE-5G(VM2) model in Peltier (2004) underestimates GIA in the Greenland system. This was the a priori model that went into the simulations and the data-assimilation technique hinting at a -0.56 mm per year GIA geoid trend rather than the $+0.1$ mm per year trend that is associated with the ICE-5G(VM2) model. But uncertainties in Late-Pleistocene deglaciation is only one of the possibilities; another one is Late-Holocene glaciation. In Wu et al. (2010) the possibility is mentioned of more recent additional net past ice accumulation of about 100–300 m. The Earth starts to deform viscously typically on time scales of a few 100 years, so that additional recent ice mass accumulation between 6,000 years ago and the present might induce additional present-day crustal subsidence, cf. Sparrebom et al. (2006).

The conclusions of Wu et al. (2010) are that the Greenland Ice Sheet would experience about half of the present day mass loss, i.e. they find -104 ± 23 Gt/year between 2002 and 2008, which was later corrected to -130 Gt/year (X. Wu, personal communication). The consequence of the results in Wu et al. (2010) is that the difference widens between GRACE-based Greenland mass loss rates and the MBE obtained by climatologic studies, see Sect. 3.3 Also, the difference between altimeter derived MBEs and the climatologic studies would increase when an alternative GIA correction as suggested in Wu et al. (2010)

is used for correcting altimeter data. Whether the approach of Wu et al. (2010) should be adopted is a challenge for further studies, since the GIA correction is fundamental to all discussed gravimetry and altimeter methods shown in Table 1 except for the climatologic MBE as reported by van den Broeke et al. (2009).

4 Outlook

With the help of a de-focussing method reported in Sect. 3.1 applied to a 13-basin solution we find a Greenland system mass loss rate and acceleration that is consistent with the results published by Velicogna (2009), van den Broeke et al. (2009) and altimeter derived MBEs from Zwally et al. (2011) and Sørensen et al. (2010). As a result our Greenland mass balance estimates from GRACE agree to within 15% with independent mass balances derived from climatological studies and ICEsat altimetry studies.

The physical significance of an acceleration term as presently observed within the Greenland system is not well understood. The mass loss rate in Fig. 2 is for instance not uniform along the shore, neither is the acceleration of mass change as shown in Fig. 3. The glaciers along the South East of Greenland are still losing mass, but the acceleration map shows that this process is slowing down, whereas the basins on the West and North West of Greenland have increased their rate of mass loss. The GRACE derived regional climatologies within the coastal basins do resemble the results obtained by van den Broeke et al. (2009). Yet more research is necessary to refine the conclusions, and in particular the long term behaviour of the mass change on Greenland including its relation to known circulation pattern changes in the ocean and atmosphere related, e.g., to the North Atlantic oscillation and the El Niño Southern Oscillation.

The new GIA correction by Wu et al. (2010) provides a new direction in post glacial rebound research. The method uses GPS deformation vectors near Greenland, GRACE data, and an ocean model yielding ocean bottom pressure data. At the same time the GIA model developed by Wu et al. (2010) considerably widens the gap between the Greenland mass balance results of van den Broeke et al. (2009) and the GRACE mass loss estimates discussed in Velicogna (2009), Wouters et al. (2008), Schrama and Wouters (2011) and Luthcke et al. (2010). Whether the Greenland GIA model has converged may depend on further research focussing on the interpretation of geologic sea level records along the Greenland shore, such as discussed in Sparrebom et al. (2006).

Acknowledgments Bert Wouters was funded by the Netherlands Organisation for Scientific Research NWO; Paulo Stocchi at the Delft University of Technology provided helpful suggestions related to the role of the glacial isostatic adjustment in connection with GRACE.

References

Bruinsma S, Lemoine J-M, Biancale R, Valès N (2010) CNES/GRGS 10-day gravity field models (release 2) and their evaluation. Adv Space Res 45:587–601

Luthcke SB, Zwally HJ, Abdalati W, Rowlands DD, Ray RD, Nerem RS, Lemoine FG, McCarthy JJ, Chinn DS (2006) Recent Greenland ice mass loss by drainage system from satellite gravity observations. Sci Agric 314:1286–1289. doi:10.1126/Science.1130776

Luthcke SB, McCarthy JJ, Rowlands DD, Arendt A, Sabaka T, Boy JP, Lemoine FG (2010) Observing changes in the land ice from GRACE and future spaceborne multi-beam laser altimeters. EGU conference paper EGU2010-5576, Vienna, Austria

Paulson A, Zhong S, Wahr J (2007) Inference of mantle viscosity from GRACE and relative sea level data. Geophys J Int 171:497–508. doi:10.1111/j.1365-246X.2007.03556.x

Peltier WR (2004) Global glacial isostasy and the surface of the ice-age Earth: the ICE-5G (VM2) model and GRACE. Ann Rev Earth Planet Sci 32:111–149

Pritchard Hamish D, Arthern Robert J, Vaughan David G, Edwards Laura A (2009) Extensive dynamic thinning on the margins of the Greenland and Antarctic ice sheets. Nat Biotechnol 461:971–975. doi:10.1038/nature08471

Rignot E, Kanagaratnam P (2006) Changes in the velocity structure of the Greenland ice sheet. Science 311, 17 Feb 2006. doi:10.1126/science.1121381 (2006)

Rowlands DD, Luthcke SB, Klosko SM, Lemoine FGR, Chinn DS, McCarthy JJ, Cox CM, Anderson OB (2005) Resolving mass flux at high spatial and temporal resolution using GRACE intersatellite measurements. Geophys Res Lett 32:L04310. doi:10.1029/2004GL021908

Schrama EJO, Wouters B (2011) Revisiting Greenland ice sheet mass loss observed by GRACE, to appear in J Geophys Res 116. doi:10.1029/2009JB006847

Sørensen LS, Simonsen SB, Nielsen K, Lucas-Picher P, Spada G, Adalgeirsdottir G, Forsberg R, Hvidberg CS (2010) Mass balance of the Greenland ice sheet a study of ICESat data, surface density and firn compaction modelling. Cryosphere Discuss 4:2103–2141. doi:10.5194/tcd-4-2103-2010

Sparrenbom CJ, Bennike O, Björck S, Lambeck K (2006) Relative sea-level changes since 15,000 cal. year BP in the Nanortalik area, southern Greenland. J Quatern Sci 21(1):29–48. doi:10.1002/jqs.940

Tapley BD, Bettadpur S, Watkins M, Reigber C (2004) The gravity recovery and climate experiment: mission overview and early results. Geophys Res Lett 31:L09607. doi:10.1029/2004GL019920

van den Broeke M, Bamber J, Ettema J, Rignot E, Schrama E, Jan van de Berg W, van Meijgaard E, Velicogna I, Wouters B (2009) Partitioning of Greenland mass loss. Sci Agric 326:984–986. doi:10.1126/science.1178176

Velicogna I (2009) Increasing rates of ice mass loss from the Greenland and Antarctic ice sheets revealed by GRACE. Geophys Res Lett 36:L19503. doi:10.1029/2009GL040222

Wu X, Heflin MB, Schotman H, Vermeersen BLA, Dong D, Gross RS, Ivins ER, Moore AW, Owen SE (2010) Simultaneous estimation of global present-day water transport and glacial isostatic adjustment. Nat Geosci. Published online: 15-Aug-2010. doi:10.1038/NGEO938

Wouters B, Chambers D, Schrama EJO (2008) GRACE observes small-scale mass loss in Greenland. Geophys Res Lett 35:L20501. doi:10.1029/2008GL034816

Wouters B (2010) Identification and modelling of Sea level change contributors, on GRACE satellite gravity data and their application to climate monitoring, PhD. Thesis, Delft University of Technology, The Netherlands, http://www.ncg.knaw.nl/Publicaties/Geodesy/73Wouters.html

Zwally HJ, Giovinetto MB, Li J, Cornejo HG, Beckley MA, Brenner AC, Saba JL, Yi D (2005) Mass changes of the Greenland and Antarctic ice sheets and shelves and contributions to sea-level rise: 19922002. J Glaciol 51(175)

Zwally Jay H, Li J, Brenner AC, Beckley M, Cornejo HG, DiMarzio J, Giovinetto MB, Neumann TA, Robbins J, Saba JL, Yi D, Wang W (2011) Greenland ice sheet mass balance: distribution of increased mass loss with climate warming; 200307 versus 19922002. J Glaciol 57(201)

Surv Geophys (2011) 32:387–396
DOI 10.1007/s10712-011-9130-6

Interaction Between the Warm Subsurface Atlantic Water in the Sermilik Fjord and Helheim Glacier in Southeast Greenland

Ola M. Johannessen · Alexander Korablev · Victoria Miles · Martin W. Miles · Knut E. Solberg

Received: 21 January 2011 / Accepted: 13 May 2011 / Published online: 10 June 2011

Abstract Recent observations of ocean temperature in several Greenland fjords suggest that ocean warming can cause large changes in the outlet glaciers in these fjords. We have observed the Helheim outlet-glacier front in the Sermilik Fjord over the last three decades using satellite images, and the vertical fjord temperature and salinity during three summer expeditions, 2008–2010. We show that the subsurface water below 250 m depth is the warm saline Atlantic Water from the Irminger Sea penetrating into the fjord and exposing the lower part of the Helheim glacier to warm water up to 4°C. Lagged correlation analysis spanning the 30-year time series, using the subsurface Atlantic Water temperature off the coast as a proxy for the variability of the subsurface warm Atlantic Water in the fjord, indicates that 24% of the Helheim ice-front movement can be accounted for by ocean temperature. A strong correlation (–0.75) between the ice-front position and the surface air temperature from a nearby meteorological station suggests that the higher air temperature causes melting and subsequent downward percolation of meltwater through crevasses leading to basal lubrication; the correlation accounts for 56% of the ice-front movement. The precise contribution of air temperature versus ocean temperature however, remains an open question, as more oceanographic and meteorological measurements are needed close to the glacier terminus.

O. M. Johannessen (✉) · A. Korablev · V. Miles
Mohn Sverdrup Center for Global Ocean Research at Nansen Environmental and Remote Sensing Center, and Nansen Scientific Society, Thormøhlensgate 47, 5006 Bergen, Norway
e-mail: ola.johannessen@nersc.no

M. W. Miles
Uni Research—Bjerknes Centre for Climate Research, 5007 Bergen, Norway

M. W. Miles
Institute for Arctic and Alpine Research, University of Colorado, Boulder, CO 80309, USA

K. E. Solberg
Fotspor.org, Oslo, Norway

Keywords Greenland outlet glaciers · Ocean warming · Surface melting

1 Introduction

Recent observations suggest that major changes in the dynamics of Greenland outlet glaciers take place over time scales of years rather than several decades or centuries as previously believed (Truffer and Fahnestock 2007). Many studies have indicated that increased discharge rates of outlet glaciers are playing a significant role in mass loss from Greenland. For example, several large outlet glaciers doubled their discharge rates over 5 years, and in 1996, the annual ice loss was 91 km^3, but in 2005 it had risen to 224 km^3 (e.g., Rignot and Kanagaratnam 2006), though estimates depend on the period sampled. Satellite observations have also revealed apparent rapid changes in outlet-glacier discharge (Rignot and Kanagaratnam 2006), especially in southeast Greenland—e.g., Helheim and Kangerdlugssuaq glaciers (Howat et al. 2007, 2008; Joughin et al. 2008)—as well as Jakobshavn glacier in west Greenland (Joughin et al. 2004; Holland et al. 2008) and Petermann glacier in north Greenland (Johannessen et al. 2011). Differences in mass-balance estimates arise partly from uncertainties in changes near the ice sheet margins, largely due to limited temporal sampling that provides only 'snapshots' (e.g., Rignot and Kanagaratnam 2006; Howat et al. 2007) rather than the range of variability.

The underlying mechanisms of recent outlet-glacier behavior remain unclear, although it has been suggested that regional oceanic and/or atmospheric warming, as well as local effects of downward percolating meltwater (Zwally et al. 2002; Andersen et al. 2010; Schoof 2010) are responsible. Separating the influence and importance of these forcing is challenging (Bamber et al. 2007), although it has been suggested (Bindschadler 2006) that the ocean plays a critical role, at least for outlet glaciers such as Jakobshavn glacier (Holland et al. 2008), Petermann glacier (Rignot and Steffen 2008; Johnson et al. 2011) and southeast Greenland glaciers, e.g., Helheim (Murray et al. 2010; Straneo et al. 2010).

Despite its importance in this context, Greenland waters—especially in the inner shelf areas and fjords—have been sparsely sampled with oceanographic measurements, such that the spatial–temporal variability is scarcely known. Repeated oceanographic measurements that are highly-resolved spatially are needed from the locations near the dynamic outlet glaciers, in order to explore two-way interactions. This includes hypothesized triggering of ice discharge and retreat at the terminus (Nick et al. 2009), such as from warm water reaching the grounding line. Here we will explore this hypothesis by investigating the fjord-water variability and glacier linkages in addition to the impact of surface air temperature on the melting of the Helheim glacier. We take advantage of a comprehensive 30-year record of ice-front variations, together with long time series of air and ocean water temperature, as well as new oceanographic cruise data from the Sermilik Fjord during three consecutive summers.

Section 2 addresses the different data sets used, including the position of the Helheim ice-front over the last 30 years, oceanographic stations measuring temperature and salinities down to several hundred metres in the Sermilik Fjord during summers 2008–2010 and offshore of the fjord for the same 30-year period as for the movement of the Helheim ice-front, and surface air temperature in the region. In Sect. 3 we discuss the results and our preliminary conclusions.

2 Data

2.1 Helheim Glacier

We have analysed the position of the Helheim glacier, Fig. 1, from CORONA, Landsat, SPOT and ERS 1-2 satellite images and have produced a 30-year continuous time series from 1980 to 2010 for August/September, Fig. 2. This represents a longer continuous record of interannual variability than previously published for this glacier (e.g., Howat et al. 2008; Joughin et al. 2008).

During 1999, 2000 and 2001, there were no significant seasonal variations of the Helheim ice-front, but from 2002 to 2010 the seasonal variations were 3–4 km (not shown), reaching a maximum retreat in August/September. During the period from 1980 to 2001, the centre of the ice-front first moved 4 km forward and after that ±1–2 km back and forth, probably constrained by the sill depth of 550 m (Joughin et al. 2008). However, during the period from 2002 to 2005, a substantial retreat of 7–8 km took place, thereafter advancing 3 km from 2005 to 2006 and again stabilizing for the following period including 2010 (Fig. 2, see also Fig. 7a for movement). It should also be mentioned that the two other outlet glaciers in the same fjord: Midgård and Fenris glaciers (Fig. 1) showed similar

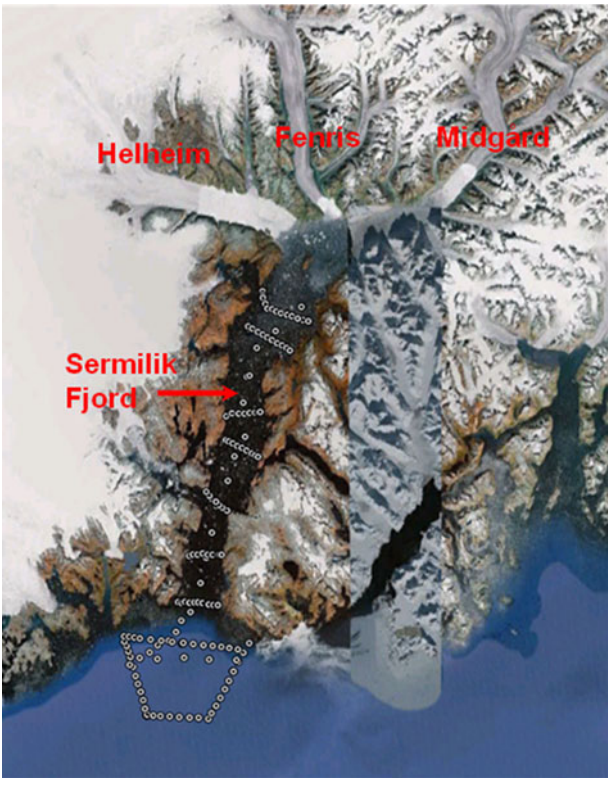

Fig. 1 Satellite image showing the outlet glaciers Helheim, Fenris and Midgård in the Sermilik Fjord. The CTD station positions in August 2009 are shown as *white circles*

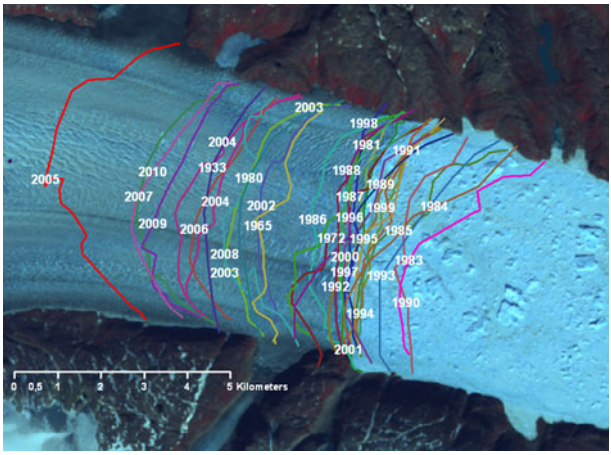

Fig. 2 Helheim glacier ice-front positions each year from 1980–2010, supplemented with a few earlier observations. The ice-front positions are derived from Corona, Landsat, SPOT and ERS 1–2 satellite images

movement, suggesting that the forcing was the same, although this is not addressed further here.

2.2 Fjord/Ocean Data

Our hypothesis is that the subsurface fjord water of warm Atlantic origin (Straneo et al. 2010) melts the deeper part of the ice-front and the bottom part of the floating Helheim glacier which penetrates vertically several hundred metres in the fjord (Joughin et al. 2008), causing some of the movement of the Helheim ice-front, in the addition to the effect of surface melting with downward percolating meltwater causing lubrication at the base of the glacier at the bedrock (Zwally et al. 2002, Schoof 2010).

We have therefore carried out a multi-year series of summer expeditions in August to the Sermilik Fjord, performing temperature and salinity, measurement from the sailboat *Jotun Arctic* using a conductivity temperature depth (CTD) recorder with an accuracy of 0.01°C for the temperature and 0.02 psu for the salinity down to 400 m in 2008 and to 600 m in 2009 and 2010. Navigation was done by using a GPS with accuracy of 5–10 m.

An example of the oceanographic stations is shown from 2009 in Fig. 1. As seen from Fig. 1, we were not able to penetrate all the way into the Sermilik Fjord to reach the Helheim ice-front, due to very heavy ice conditions caused by a large amount of drifting icebergs and seasonal fjord ice in the inner part of the fjord. The temperature and salinity sections from 2008, 2009 and 2010 (Fig. 3) show the fjord temperature and salinity structure. In general, a fjord circulation with a freshwater supply will have a low-salinity outflowing current in the surface layer of few metres thickness which requires an inflow further below, modified by wind, tides, internal waves (Johannessen 1968; Mernild et al. 2010) and offshore conditions on the shelf (Straneo et al. 2010). Our temperature and salinity sections from three summers, Fig. 3, show in general cold ($\sim$0°C) low-salinity water ($\sim$22 psu) in the surface layer, but below 200 m the water temperature was more than 2°C, increasing to more than 3°C below 250 m depth and to more than 4°C at 300 m caused by inflow of warm saline Atlantic water up to 34.80 psu.

In 2008 and 2010, the water temperature was $\sim$0.8–1.0°C higher at 400 m than in 2009. Because the Helheim glacier is up to 800 m deep (Joughin et al. 2008), this means that the

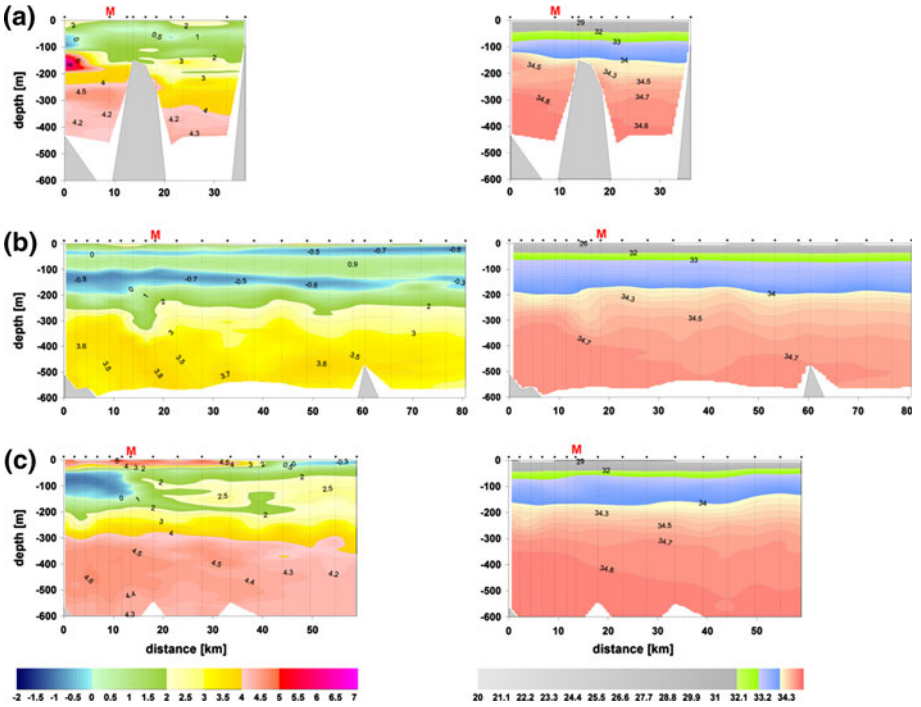

Fig. 3 Distributions of the potential temperature (°C, *left panel*) and salinity (psu, *right panel*) along the Sermilik Fjord longitudinal sections obtained in August 2008 (**a**), 2009 (**b**) and 2010 (**c**). The sections from different years had different starting points and different lengths but are centred to the fjord mouth marked with *red* 'M'

lower part of the glacier is exposed to warm water with a temperature of up to 4°C causing submarine melting from below. This "bathing" from warm Atlantic water has probably gone on for thousands of years, but what is important for the bottom melting of the glacier is that the temperature of the inflowing warm Atlantic water can change from year to year, as we have seen from our three sections.

However, in order to perform a robust statistical analysis, longer time series of the warm subsurface Atlantic water—as well as surface air temperature from a nearby meteorological station—are needed to compare with our 30-year time series of the movement of the Helheim ice-front.

2.3 Proxy for Warm Atlantic Water in the Fjord

Fortunately, Argo floats exist for the areas off the coast of the Sermilik Fjord. As an example, the drift of one of the Argo floats (http://www.argo.net) gives profiles of temperature and salinity from the surface to 2,000 m depth after 10 days of drifting at 1,000 m, as shown in Fig. 4.

This Argo float strongly indicates that it moves with the Atlantic water in the Irminger Current south of Iceland, then turns in the southern part of the Greenland–Iceland gap and thereafter hugging the Greenland continental shelf southwards (Fig. 4a). Thereafter it becomes grounded in the canyon across the shelf leading into the Sermilik Fjord. From the

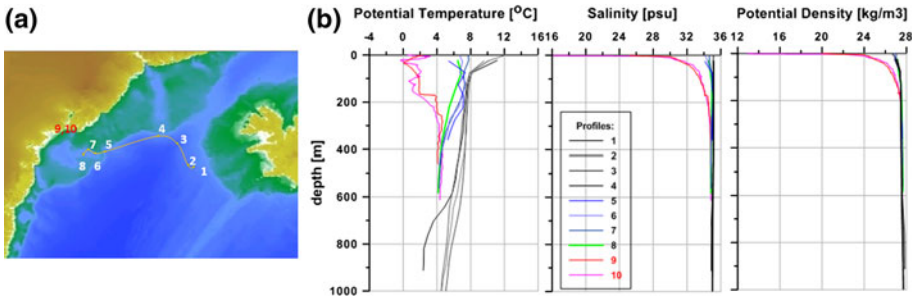

Fig. 4 **a** Consecutive position of the profiles (1–8) in the Irminger Sea and in a deep *canyon* over the Greenland shelf break as measured by Argo profiling float 6900452 from 04.07.2007 to 22.09.2007 and CTD stations (9, 10) in the Sermilik Fjord mouth. **b** Vertical profiles of the potential temperature, salinity and potential density for the positions numbered in a. Profiles for two CTD stations completed in the Sermilik Fjord mouth in August 2008 (*red*) and 2010 (*magenta*) inserted for comparison. Note that properties of the Atlantic Water were altered into fjord water below 300 m depth

vertical temperature and salinity profiles (Fig. 4b) it is seen that below 400 m the water in the canyon is more than 4°C, indicating that this is how the warm and saline water enters the fjord—note the similarity to the T-S measurements from the entrance of fjord (red lines in Fig. 4b). This implies that the warm, saline Atlantic water "dives" under the south-flowing East Greenland Current (EGC) and East Greenland Coastal Current (EGCC) because of its greater density (Fig. 4b). Therefore, Atlantic water in the Irminger Current is the source of the warm and saline subsurface water in the Sermilik Fjord, as shown schematically in Fig. 5.

We therefore assumed that the temporal variability of the temperature and salinity in the Irminger Current would also to some extent represent the temporal variability of the warm Atlantic water in the Sermilik Fjord. We therefore constructed a time series of all oceanographic stations back to 1970 (Fig. 6) and used this annual time series as a proxy for the variability of the fjord water at 400 m (Fig. 7b), albeit not as absolute values.

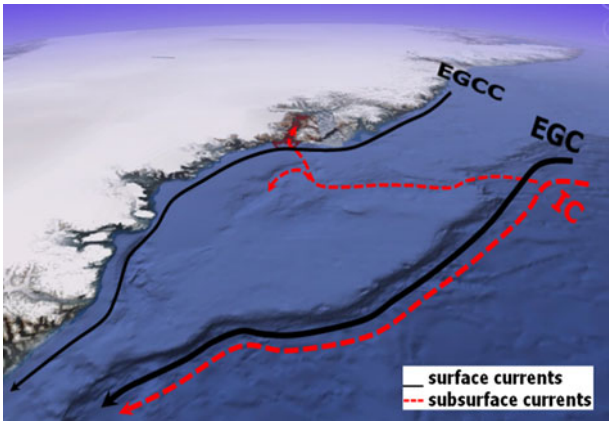

Fig. 5 Schematic of the major warm (*red*) and cold (*black*) currents over the Greenland shelf break and shelf including the East Greenland Current (EGC), East Greenland Coastal Current (EGCC) and Irminger Current (IC). The hypothesized trajectory of the Atlantic Water flowing from the shelf break through a canyon into the Sermilik Fjord is also shown

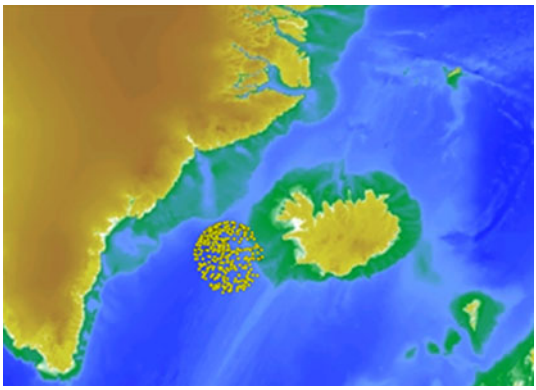

Fig. 6 Position of the oceanographic stations 1970–2010 selected to construct water temperature time series for the Irminger Sea shown in Fig. 7b

2.4 Surface Air Temperature

Surface air temperature (SAT) has been recorded at the Danish Meteorological Institute coastal station at Tasiilaq (http://climexp.knmi.nl) some 80–90 km east of the Helheim ice-front (Fig. 7c). This is the closest station to Helheim glacier that has a long record of measurements.

3 Results and Conclusions

3.1 Results

The long-term variability of the Helheim ice-front, as well as the variability of the fjord water temperature proxy and the SAT are shown in Fig. 7.

In studying the three curves qualitatively, it is clearly seen that when the Helheim ice-front retreated substantially during the period from 2001 to 2005 (Figs. 2, 7a), both the fjord water temperature proxy at 400 m (Fig. 7b) and the air temperature (Fig. 7c) were increasing, suggesting some linkage. Figure 7 also indicates that all three variables exhibit a shift to a new equilibrium state in the 2000s.

In order to study this more quantitatively, we carried out an exploratory statistical analysis. (We note that the proxy fjord temperature is about 2°C higher than observed in the fjord, but stress that in our analysis we are interested in the co-variability and not necessarily the absolute temperature values.) In our statistical analysis, we performed lagged cross-correlations between the ice-front movement with the proxy fjord temperature and found a maximum correlation of $r \sim -0.49$ when the temperature was lagged by 1 year, indicating that we can explain at least 24% ($r^2 \sim 0.24$) of the ice-front movement with the proxy variation of the warm Atlantic water. One caveat is that this is only a proxy for fjord temperature—if we had measurements of the actual temperature in the fjord near the Helheim glacier front over more than 30 years, the explanatory power may be substantially greater.

Then we also performed a similar cross-correlation analysis between the ice-front movement and SAT, finding a maximum correlation of -0.75 when lagged 2 years, thereby accounting for 56% of the ice-front movement ($r^2 \sim 0.56$). These statistics imply

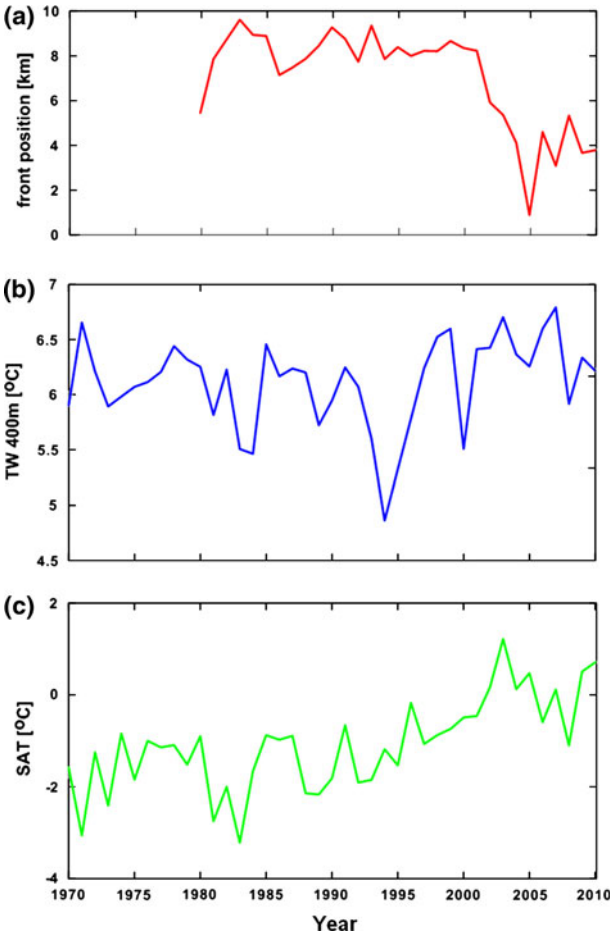

Fig. 7 Time series of the Helheim calving front position 1980–2010 in August/September (**a**), annual water temperature at 400 m depth in the Irminger Sea (**b**) and annual surface air temperature (SAT) 1970–2010 in Tasiilaq, southeast Greenland, 80–90 km east of the Helheim ice-front (**c**)

that the air temperature had more than twice the influence on the Helheim ice-front movement than did the ocean temperature. The effect of SAT on ice-front movement is through surface melting and subsequent downward percolation of meltwater through a huge number of crevasses in the Helheim glacier observed from a helicopter (Johannessen, pers. obs.), thereby leading to basal lubrication (e.g., Andersen et al. 2010; Schoof 2010) that may affect calving.

3.2 Preliminary Conclusions

1. The position of the Helheim glacier front appears to have been relatively stable from 1985 to 2001, varying only 1–2 km; after 2001, the variations were larger, with a 6–7 km retreat in 2005 compared to the pre-2001 position.
2. Sermilik Fjord is "filled up" with warm, saline Atlantic Water below 250 m depth with temperature ranging from 1–4.5°C, exposing the deeper part of Helheim glacier to warm water year-round.

3. The greater retreating of the Helheim ice-front after 2000 coincides both with local surface air warming and enhanced warming in the Irminger Current of warm, saline Atlantic Water, which is found to penetrate into the Sermilik Fjord. Correlation analysis indicates that the variation of the SAT is more important than the variability of the ocean temperature for the movement of the ice-front. The precise contribution of air temperature versus ocean temperature, however, remains an open question, as more oceanographic and meteorological measurements are needed close to the glacier terminus, together with modeling efforts.

Acknowledgments We acknowledge funding from a donation by Trond Mohn c/o Frank Mohn As, Bergen and from the Nansen Scientific Society. Furthermore, we acknowledge the excellent performance of the crew onboard the sailboat *Jotun Arctic*. The lead author (OMJ) worked on this paper while as a "Visiting Professor for Senior International Scientists of the Chinese Academy of Sciences (CAS)" in October–November 2010 at the Institute of Atmospheric Physics, CAS, in Beijing.

References

Andersen ML, Larsen TB, Nettles M, Elosegui P, van As D, Hamilton GS, Stearns LA, Davis JL, Ahlstrøm AP, de Juan J, Ekström G, Stenseng L, Khan SA, Forsberg R, Dahl-Jensen D (2010) Spatial and temporal melt variability at Helheim Glacier, East Greenland, and its effect on ice dynamics. J Geophys Res 115:F04041. doi:10.1029/2010JF001760

Bamber JL, Alley RB, Joughin I (2007) Rapid response of modern day ice sheets to external forcing. Earth Planet Sci Lett 257:1–13

Bindschadler R (2006) Hitting the ice sheets where it hurts. Science 311:1720–1721

Holland DM, Thomas RH, de Young B, Ribergaard MH, Lyberth B (2008) Acceleration of Jakobshavn Isbræ triggered by warm subsurface ocean waters. Nature Geosci 1:659–662

Howat IM, Joughin I, Scambos TA (2007) Rapid changes in ice discharge from Greenland outlet glaciers. Science 315:1559–1561

Howat IM, Joughin I, Fahnestock M, Smith BE, Scambos TA (2008) Synchronous retreat and acceleration of southeast Greenland outlet glaciers 2000–2006: ice dynamics and coupling to climate. J Glaciol 54:646–660

Johannessen OM (1968) Some current measurements in the Drøbak Sound, the narrow entrance to the Oslofjord. Hvalrådets skrifter. Det Norske Videnskaps-Akademi i Oslo. Oslo Universitetsforlaget: 38 p. ftp://ftp.nersc.no/OMJ/Joh68a.pdf

Johannessen OM, Babiker M, Miles MW (2011) Petermann Glacier, North Greenland: Massive calving in 2010 and the past half century. Cryosphere Discuss 5:169–181. www.the-cryosphere-discuss.net/5/169/2011

Johnson HL, Münchow A, Falkner KK, Melling H (2011) Ocean circulation and properties in Petermann Fjord, Greenland. J Geophys Res 116:C01003. doi:10.1029/2010JC006519

Joughin I, Abdulati W, Fahnestock M (2004) Large fluctuations in speed on Greenland's Jakobshavn Isbræ glacier. Nature 432:608–610

Joughin I, Howat I, Alley RB, Ekstrom G, Fahnestock M, Moon T, Nettles M, Truffer M, Tsai VC (2008) Ice-front variation and tidewater behavior on Helheim and Kangerdlugssuaq Glaciers, Greenland. J Geophys Res 113:F01004. doi:10.1029/2007JF000837

Mernild S, Howat IM, Ahn Y, Liston GE, Steffen K, Jakobsen BH, Hasholt B, Fog B, van As D (2010) Freshwater flux to Sermilik Fjord, SE Greenland. The Cryosphere 4:453–465

Murray T, Scharrer K, James TD, Dye SR, Hanna E, Booth AD, Selmes N, Luckman A, Hughes ALC, Cook S, Huybrechts P (2010) Ocean regulation hypothesis for glacier dynamics in southeast Greenland and implications for ice sheet mass changes. J Geophys Res 115:F03026. doi:10.1029/2009JF001522

Nick F, Vieli A, Howat IM, Joughin I (2009) Large-scale changes in Greenland outlet glacier dynamics triggered at the terminus. Nature Geosci 2:110–114

Rignot E, Kanagaratnam P (2006) Changes in the velocity structure of the Greenland Ice Sheet. Science 311:986–990

Rignot E, Steffen K (2008) Channelized bottom melting and stability of floating ice shelves. Geophys Res Lett 35:L02503. doi:10.1029/2007GL031765

Schoof C (2010) Ice-sheet acceleration driven by melt supply variability. Nature 468:803–806. doi:10.1038/nature09618

Straneo F, Hamilton GS, Sutherland DA, Stearns LA, Davidson F, Hammill MO, Stenson GB, Rosing-Asvid A (2010) Rapid circulation of warm subtropical waters in a major glacial fjord in East Greenland. Nature Geosci 3:182–186

Truffer M, Fahnestock M (2007) Rethinking ice sheet time scales. Science 315:1508–1510

Zwally HJ, Abdalati W, Herring T, Larson K, Saba J, Steffen K (2002) Surface melt–induced acceleration of Greenland ice-sheet flow. Science 297:218–222

Surv Geophys (2011) 32:397–416
DOI 10.1007/s10712-011-9131-5

Response of the Greenland and Antarctic Ice Sheets to Multi-Millennial Greenhouse Warming in the Earth System Model of Intermediate Complexity LOVECLIM

P. Huybrechts · H. Goelzer · I. Janssens · E. Driesschaert · T. Fichefet · H. Goosse · M.-F. Loutre

Received: 1 February 2011 / Accepted: 13 May 2011 / Published online: 9 June 2011

Abstract Calculations were performed with the Earth system model of intermediate complexity LOVECLIM to study the response of the Greenland and Antarctic ice sheets to sustained multi-millennial greenhouse warming. Use was made of fully dynamic 3D thermomechanical ice-sheet models bidirectionally coupled to an atmosphere and an ocean model. Two 3,000-year experiments were evaluated following forcing scenarios with atmospheric CO_2 concentration increased to two and four times the pre-industrial value, and held constant thereafter. In the high concentration scenario the model shows a sustained mean annual warming of up to 10°C in both polar regions. This leads to an almost complete disintegration of the Greenland ice sheet after 3,000 years, almost entirely caused by increased surface melting. Significant volume loss of the Antarctic ice sheet takes many centuries to initiate due to the thermal inertia of the Southern Ocean but is equivalent to more than 4 m of global sea-level rise by the end of simulation period. By that time, surface conditions along the East Antarctic ice sheet margin take on characteristics of the present-day Greenland ice sheet. West Antarctic ice shelves have thinned considerably from subshelf melting and grounding lines have retreated over distances of several 100 km, especially for the Ross ice shelf. In the low concentration scenario, corresponding to a local warming of 3–4°C, polar ice-sheet melting proceeds at a much lower rate. For the first 1,200 years, the Antarctic ice sheet is even slightly larger than today on account of increased accumulation rates but contributes positively to sea-level rise after that. The Greenland ice sheet loses mass at a rate equivalent to 35 cm of global sea level rise during the first 1,000 years increasing to 150 cm during the last 1,000 years. For both scenarios,

P. Huybrechts (✉) · H. Goelzer · I. Janssens
Earth System Sciences and Departement Geografie, Vrije Universiteit Brussel, Brussels, Belgium
e-mail: phuybrec@vub.ac.be

E. Driesschaert
Faculty of Sciences, Université Catholique de Louvain, Louvain-la-Neuve, Belgium

T. Fichefet · H. Goosse · M.-F. Loutre
Georges Lemaître Centre for Earth and Climate Research (TECLIM), Earth and Life Institute, Université Catholique de Louvain, Louvain-la-Neuve, Belgium

ice loss from the Antarctic ice sheet is still accelerating after 3,000 years despite a constant greenhouse gas forcing after the first 70–140 years of the simulation.

Keywords Ice sheets · Sea-level change · EMIC · Ice-climate interactions

1 Introduction

Sea-level changes are often mentioned as an important consequence of climate changes. Global temperatures have risen by about 0.8°C over the last 100 years concurrent with an average sea-level rise of about 20 cm (Solomon et al. 2007). By far the largest potential source for sea-level rise is made up by the Greenland and Antarctic ice sheets, which could raise global sea level by 70 m if melted entirely. Yet their current contribution to sea-level change is comparatively small and moreover prone to large uncertainties. Based on a variety of sources from remote sensing platforms and mass balance models, recent studies (Rignot et al. 2008a; Van den Broeke et al. 2009) estimate their combined total mass imbalance over the last decade at -433 ± 95 Gt/year. That is equivalent to 1.1 ± 0.2 mm/year of sea-level rise or 11 ± 2 cm if sustained over a whole century, but the error bar could be larger. Ongoing and past glacier accelerations may account for up to half or more of this total mass trend over the last decade (Rignot et al. 2008b) but a precise attribution to either surface mass balance changes or ice flow changes can not yet confidently be made. Available model projections for the 21st century stress the dominant role of surface mass balance changes and the mitigating role of increased Antarctic accumulation in a warmer atmosphere (e.g. Huybrechts et al. 2004). Fast ice-flow variations such as those observed over the last 10–15 years could possibly be a significant fraction in the sea-level contribution from the polar ice sheets on the centennial time scale but are not routinely included in model projections as their mechanisms are badly understood, and therefore cannot be projected with confidence (Meehl et al. 2007).

Longer-term projections of the response of the polar ice sheets to future warming are best addressed in the framework of fully dynamic ice sheet models incorporated in climate models. On time scales of centuries to millennia, the ice sheets themselves exert influences on the atmosphere and the ocean that in turn affect their surface mass balance and melting rates at places where the ice is in contact with the ocean. Changes in orographic height and slope of the ice sheets potentially alter atmospheric flow patterns through their effect on planetary vorticity and planetary waves (in the case of Greenland), and on a regional scale through the modification of the katabatic wind system (both Antarctica and Greenland) (Lunt et al. 2004; Ridley et al. 2005). A second effect relates to changes in surface reflectivity of thinning and receding ice sheets. This essentially constitutes the ice-albedo feedback, which, by changing the radiation regime of the surface, potentially leads to an amplification of the initial temperature perturbation. At any rate, changes in ice sheet geometry affect the distribution of ice thickness and surface slope (driving stress), altering the ice flow and thus also the shape of the ice sheet. This in turn affects surface temperatures on the ice sheet, giving rise to a positive elevation-temperature feedback. Moreover, modeling evidence suggests that freshwater input from Greenland ice sheet runoff could potentially slow down the Atlantic meridional overturning circulation (AMOC) by changing the density of the ocean surface water (Fichefet et al. 2003), but the effectiveness of this feedback is still under debate. Jungclaus et al. (2006), Mikolajewicz et al. (2007b), Driesschaert et al. (2007), Hu et al. (2009) found only a small transient effect of increased Greenland melting on the AMOC that was either small compared to the effect of enhanced

poleward atmospheric moisture transport or only noticeable in the most extreme scenarios. Ice-sheet ocean feedbacks in interactively coupled models have been found to slow down ice-sheet decay, but the effect is quite weak in most cases (Vizcaíno et al. 2008, 2010). By contrast, Swingedouw et al. (2008) and Goelzer et al. (2010) found that surface runoff and increased ice-shelf melting from the Antarctic ice sheet had a strong mitigating effect on the regional warming due to negative feedbacks arising from Antarctic Bottom Water formation and sea-ice formation.

Available model studies on the long-term fate of the polar ice sheets have mostly concentrated on the Greenland ice sheet, generally using a three-dimensional ice-sheet model coupled to climate models of varying complexity (e.g. Huybrechts and de Wolde 1999; Ridley et al. 2005; Charbit et al. 2008). These agree that the Greenland ice sheet will significantly decrease in area and volume in a warmer climate on account of increased melting outweighing increased accumulation. If the warming is maintained for a sufficiently long period, total decay of the ice sheet is predicted. Surface mass balance models suggest a threshold for the long-term viability of the ice sheet of between 1.9 and 4.6°C global mean annual warming (Gregory and Huybrechts 2006). Such a threshold is generally confirmed in coupled ice-sheet simulations. The temperature range may be larger when additional uncertainty from the melt model is included (Bougamont et al. 2007); however, Stone et al. (2010) find the threshold to be substantially lower using new boundary conditions for ice-sheet geometry, surface temperature and precipitation. For sustained 4× CO_2 forcing, corresponding to a mean Greenland warming of around 8°C, Ridley et al. (2005) find deglaciation to take around 3,000 years to complete using HadCM3. Similar rates of mass loss for comparable warmings were also obtained with the Hamburg Earth System Model (Mikolajewicz et al. 2007a, b; Vizcaíno et al. 2008, 2010), although they used a different set of climate scenarios.

Because of the positive climate feedbacks on ice-sheet decline, subsequent cooling below the threshold of sustainability may not regrow the ice sheet to its original size, indicative of hysteresis. This was investigated by Ridley et al. (2010) with a high-resolution ice-sheet model coupled to HadCM3. They found that the present-day ice sheet could be reformed only if the volume had not fallen below a threshold of irreversibility, which lay between 80 and 90% of the original value. Depending on the degree of warming, this threshold of irreversibility could be reached within several hundred years, sooner than global climate could revert to a pre-industrial state. Taking into account the long time it takes to remove atmospheric CO_2 by the Earth system, Charbit et al. (2008) linked irreversible decay of the Greenland ice sheet to a cumulative CO_2 emission above 3,000 GtC. For smaller emissions, the Greenland ice sheet could still recover over a period of several thousand years.

Compared to the mainly land-based Greenland ice sheet, the Antarctic ice sheet is surrounded by large ice shelves in contact with the ocean. The relevant quantities controlling sea-level changes therefore include changes in discharge from the grounded ice sheet into the ice shelves and grounding-line migration, which processes are affected by changes in melting below the ice shelves and buttressing effects from their shear margins (Huybrechts and de Wolde 1999). These mechanisms are missing from Earth System Models that include Antarctic models without ice shelf dynamics (Mikolajewicz et al. 2007a, b; Vizcaíno et al. 2008, 2010), and which find that the Antarctic ice sheet contributes negatively to global sea-level under a wide range of warming scenarios because of increased snowfall.

In this paper we discuss two 3,000-year simulations concentrating on the behavior of the Greenland and Antarctic ice sheets with the Earth System Model of Intermediate Complexity LOVECLIM (Goosse et al. 2010). Compared to other EMICs, this model includes fully dynamic 3-D ice-sheet models at high resolution (10 km horizontal grid size),

allowing a better representation of the ice flow at ice-sheet margins. The Antarctic ice sheet component additionally incorporates coupled ice-shelf flow, grounding-line migration and a parameterization for ice-shelf melt to account for ice-ocean interactions. All relevant mutual interactions between the various climate components (atmosphere, ocean, vegetation) are considered, except for the carbon cycle that is not active in this study. In the following we describe the LOVECLIM model (Sect. 2) and the experimental design (Sect. 3). The results are discussed separately for the Greenland and Antarctic ice sheets in Sect. 4, followed by a concluding section (Sect. 5). These results complement two other studies performed with the same model configuration (Driesschaert et al. 2007; Swingedouw et al. 2008) but which did not analyze the response of the ice sheets and their contribution to global sea level in detail.

2 Model Description

2.1 LOVECLIM

The results discussed in this paper are based on LOVECLIM version 1.0 in the same set up as described in Driesschaert et al. (2007) and Swingedouw et al. (2008). A slightly updated version of the model was recently released as version 1.2 (Goosse et al. 2010). Most of the modifications to the code were of a technical nature with no impact on the results and do not affect the details of the ice-climate interactions of interest here. Therefore only a brief overview of the model is given here. Figure 1 schematically shows all model components and their mutual interactions. The model includes components for the atmosphere (ECBilt), the ocean and sea-ice (CLIO), the terrestrial biosphere (VECODE), the carbon cycle (LOCH) and the Antarctic and Greenland ice sheets (AGISM). ECBilt (Opsteegh et al. 1998) is a spectral atmospheric model with truncation T21, which corresponds approximately to a horizontal resolution of 5.625° in longitude and latitude, and incorporates three vertical levels. It includes simple parameterizations of the diabatic heating processes and an explicit representation of the hydrological cycle. Cloud cover is prescribed according to the present-day climatology. CLIO—Coupled Large-scale Ice-Ocean model—is a global free-surface ocean general circulation model coupled to a thermodynamic sea-ice model (Fichefet and Morales Maqueda 1997; Goosse and Fichefet 1999; Goosse et al. 1999). The horizontal resolution of CLIO is 3° in longitude and latitude, and there are 20 unevenly spaced levels in the vertical. VECODE—VEgetation COntinuous DEscription model—is a reduced-form model of the vegetation dynamics and of the terrestrial carbon cycle (Brovkin et al. 1997). It is based on a continuous bioclimatic classification: every land grid cell is covered by a mixture of grass, forest and desert. LOCH—Liège Ocean Carbon Heteronomous model (Mouchet and François 1996) is a comprehensive, three-dimensional oceanic carbon cycle model subject to external controls. Since the evolution of CO_2 concentration was prescribed in the present simulations, the carbon cycle component of the model was used in diagnostic mode and its results are not discussed here.

2.2 The Ice Sheet Model

AGISM (Antarctic and Greenland Ice Sheet Model) consists of two three-dimensional thermomechanical ice-dynamic models for each of the polar ice sheets. Both models are based on the same physics and formulations, however with the major distinction that the Antarctic component incorporates a coupled ice shelf and grounding line dynamics. Ice

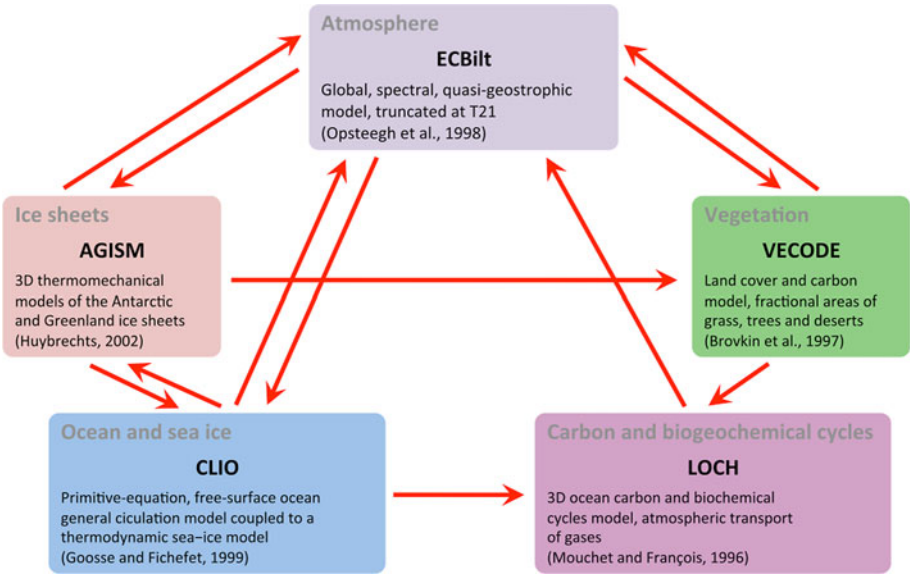

Fig. 1 Scheme of the LOVECLIM model showing the interactions between the five components. In this study, the LOCH component is not active

shelf dynamics is missing from the Greenland component as there is hardly any floating ice under present-day conditions, and this can be expected to disappear quickly under warmer conditions. Having a melt margin on land or a calving margin close to its coast for most of its glacial history, ice shelves probably played a minor role for Greenland also during colder conditions.

Both polar ice sheet models consist of three main components, which, respectively, describe the ice flow, the solid Earth response, and the mass balance at the ice-atmosphere and ice-ocean interfaces (Huybrechts and de Wolde 1999; Huybrechts 2002; Goosse et al. 2010; to which papers the interested reader is referred to for a full overview of all equations and model formulations). Figure 2 shows the structure of the models.

In the models, the flow is calculated both in grounded ice and, for Antarctica, in a coupled ice shelf to enable free migration of the grounding line. The flow is thermomechanically coupled by simultaneous solution of the heat equation with the velocity equations, using Glen's flow law and an Arrhenius-type dependence of the rate factor on temperature. In grounded ice, the flow results from both internal deformation and sliding over the bed in places where the temperature reaches the pressure melting point and a lubricating water layer is present. Longitudinal deviatoric stresses are disregarded according to the widely used 'Shallow Ice Approximation'. This does not treat the rapid component of the otherwise badly understood physics specific to fast-flowing outlet glaciers or ice streams. For the sliding velocity, a generalized Weertman relation is adopted, taking into account the effect of the subglacial water pressure. Ice shelves are included by iteratively solving a coupled set of elliptic equations for ice shelf spreading in two dimensions, including the effect of lateral shearing induced by sidewalls and ice rises. At the grounding line, longitudinal stresses are taken into account in the effective stress term of the flow law. These additional stress terms are found by iteratively solving three coupled equations for depth-averaged horizontal stress deviators.

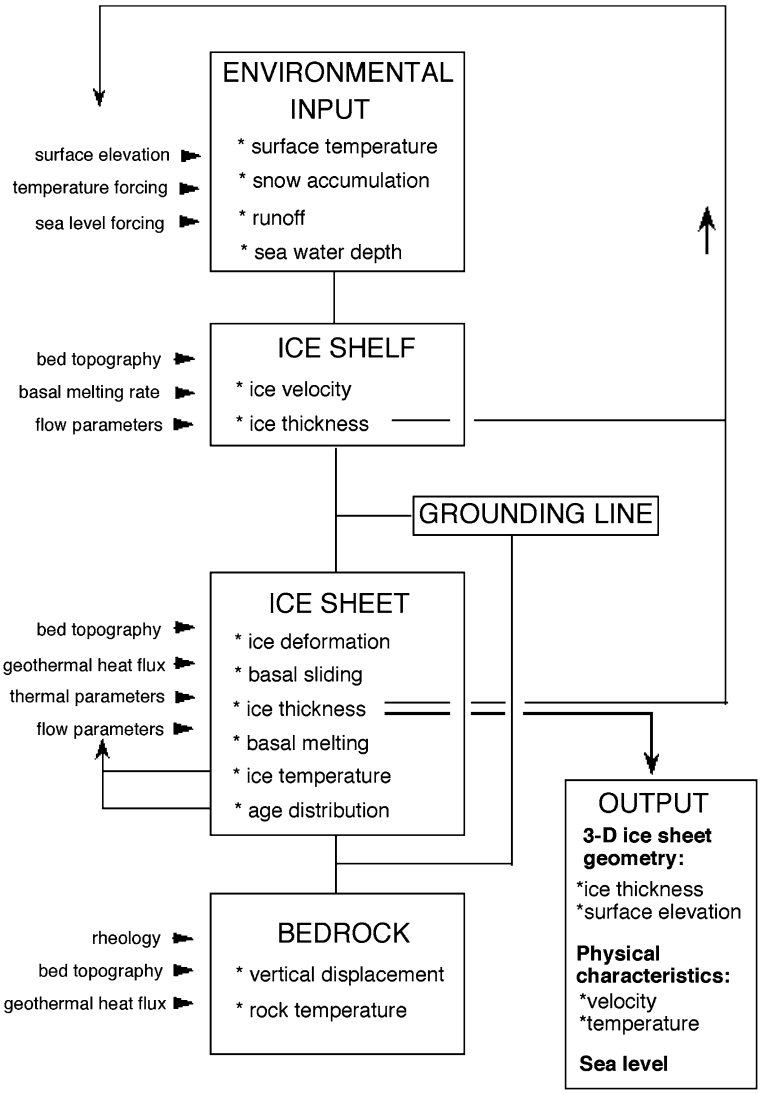

Fig. 2 Structure of the three-dimensional thermodynamic ice sheet model AGISM. The inputs are given at the left-hand side. Prescribed environmental variables drive the model, which incorporates ice shelves, grounded ice and bed adjustment as its major components. Regarding the Antarctic component, the position of the grounding line is not prescribed, but internally generated. The model essentially outputs the time-dependent ice sheet geometry and the associated temperature and velocity fields

Isostatic compensation of the bedrock is taken into account for its effect on bed elevation near grounding lines and marginal ablation zones, where it matters most for ice sheet dynamics, and because isostasy enables ice sheets to store 25–30% more ice than evident from their surface elevation alone. The bedrock adjustment model consists of a viscous asthenosphere, described by a single isostatic relaxation time, which underlies a rigid elastic plate (lithosphere). The crustal loading takes into account contributions from

both ice and ocean water within the respective numerical grids, but ignores any ice loading changes beyond the Greenland and Antarctic continental areas.

For both ice sheets, calculations are made on a 10 × 10 km horizontal resolution, with 31 vertical layers in the ice and another 9 layers in the bedrock for the calculation of the heat conduction in the crust. The vertical grid in the ice has a closer spacing near to the bedrock where the shear concentrates. Rock temperatures are calculated down to a depth of 4 km. This gives rise to between 1.85 and 12.6 × 10^6 grid nodes for Greenland and Antarctica, respectively. Geometric datasets for surface elevation, ice thickness and bed elevation incorporate most of the recent observations up to 2001, such as ERS-1 derived satellite heights, BEDMAP and EPICA pre-site survey Antarctic ice thicknesses and the University of Kansas collection of airborne radio-echo-sounding flight tracks over Greenland (Huybrechts and Miller 2005). The grids correspond to those discussed in Huybrechts and Miller (2005) and include modifications in marginal ice thickness around Greenland margins to remove known artefacts when subtracting an ice thickness field constructed for a more limited mask than the actual ice sheet surface elevation. Over-deepened fjord beds of important outlet glaciers were added manually when absent from the interpolated fields, both for Antarctica and Greenland. The 10 km horizontal resolution substantially improves the representation of the fast-flowing outlet glaciers and ice streams, which are responsible for the bulk of the ice transport towards the margin. Other physics specific to these features such as higher-order stress components or subglacial sediment characteristics are not included, in common with the current generation of three-dimensional ice-sheet models.

Interaction with the atmosphere and the ocean is effectuated by prescribing the climatic input, consisting of the surface mass balance (accumulation minus ablation), surface temperature and the basal melting rate below the ice shelves surrounding the Antarctic component. The mass balance model distinguishes between snow accumulation, rainfall and meltwater runoff, which components are all parameterized in terms of temperature. The melt- and runoff model is based on the positive degree-day method and is identical to the recalibrated version as described in Janssens and Huybrechts (2000) with a noticeable typing correction to the exponent in the calculation of the expected sum of positive degree days (Goosse et al. 2010). Meltwater is at first retained in the snowpack by refreezing and capillary forces until the pores are fully saturated with water, at which time runoff can occur. This method to calculate the melt has been shown to be sufficiently accurate for most practical purposes. It moreover ensures that the calculations can take place on the detailed grids of the ice-sheet models so that one can properly incorporate the feedback of local elevation changes on the melt rate, features which cannot be represented well on the generally much coarser grid of a climate model. The melt model is also implemented for Antarctica, but since current summer temperatures remain generally below freezing, melt amounts are currently negligible there. Because of their very low surface slopes, it is further assumed that melt water produced on the surface of the Antarctic ice shelves, if any, refreezes in situ at the end of the summer season, and therefore does not runoff to the ocean. Below the ice shelves, a uniform melting rate is applied which magnitude is linked to the heat input into the cavity, as explained in Sect. 2.3. For the experiments discussed in this paper, AGISM parameters are the same as those listed in Table 5 in Goosse et al. (2010).

2.3 Climate-Ice Sheet Interactions

The key atmospheric variables needed as input for AGISM are monthly surface temperature and annual precipitation. Because the details of the Greenland and Antarctica surface

climate are not well captured on the ECBilt coarse grid, these boundary conditions consist of present-day observations as represented on the much finer AGISM grid onto which climate change anomalies from ECBilt are superimposed. Monthly temperature differences and annual precipitation ratios, computed against a reference climate corresponding to the period 1970–2000 AD, are interpolated from the ECBilt grid onto the AGISM grid and added to and multiplied by the parameterized surface temperatures and observed precipitation rates, respectively. The anomaly approach avoids systematic errors in the absolute ECBilt fields and ensures that some processes, such as the melting taking place at the ice sheet margin over a spatial extent narrower than the atmospheric model resolution, can be adequately represented.

The ocean heat flux at the base of Antarctic ice shelves is also calculated in perturbation mode based on a parameterization proposed by Beckmann and Goosse (2003):

$$M(t) = \frac{Q^{net}(t)}{Q_0^{net}} \frac{A_0}{A(t)} M_0$$

where M is the basal melt rate, Q^{net} an estimate of the total heat flux entering the ice shelves integrated all along the perimeter of Antarctica, and A the total area of Antarctic ice shelves. Here the subscripts t and 0 refer to the actual model time and the reference time taken as 1500 AD, respectively. In this approach the melt rate below the ice shelves depends on the net heat input from the oceans into the cavity below the ice shelves. The total melt volume is proportional to changes in the net integrated ocean heat input but inversely proportional to the area of the ice shelves. The underlying assumption is that much of the water in the cavity is recycled locally forming a semi-closed circulation cell. Q^{net} is estimated directly from the mean ocean temperature around Antarctica.

After performing mass balance and ice dynamic computations, AGISM transmits the calculated changes in orography and land fraction covered by ice to ECBilt and VECODE, and the total freshwater flux to CLIO, as described further in Goosse et al. (2010). The anomaly coupling technique leads to heat and water losses/gains in the coupled model of the order of 10–25% maximally. Flux adjustments are applied to ensure strict conservation of heat and water. This ensures the closure of the heat and water balances in the coupled system.

3 Experimental Design

To illustrate the response of both polar ice sheets under global warming, we performed two idealized experiments sampling a plausible range of longer-term climate conditions. First the Greenland (Antarctic) ice sheet modules were integrated over the last two (four) glacial cycles up to 1500 AD with forcing from ice and sediment core data to derive initial conditions for coupling with the other components of LOVECLIM. Basal melting below the ice shelves was forced to follow the Vostok temperature forcing using the parameterization given in Huybrechts (2002) for a reference value of $M_0 = 0.25$ m year^{-1} for present-day conditions. The initialization experiments were first conducted on 20 km grid resolution to save computing time. At the time of the Last Glacial Maximum (19 kyr BP), all relevant data were interpolated on a 10 km resolution grid for the subsequent simulation of the glacial-interglacial transition and all of the Holocene. Hence, the outcome of the spin-up procedure are Greenland and Antarctic sheets at 1500 AD that are not in steady state as they carry the long term memory of their history with them, but are fully equilibrated (no model drift) to the model physics and the input data. These ice sheet

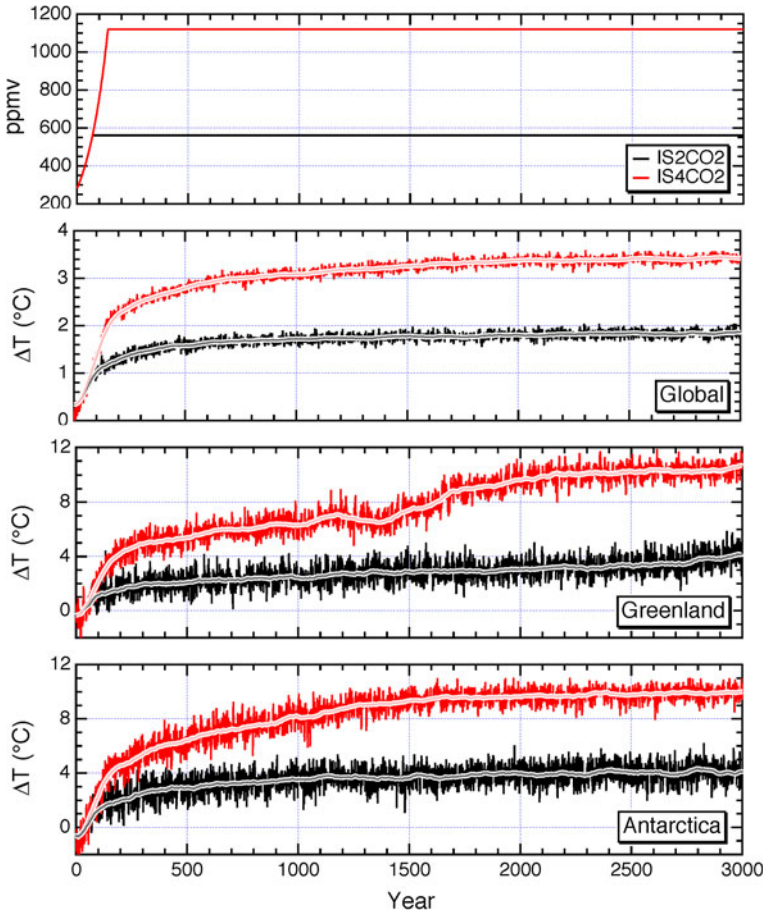

Fig. 3 The experiments employed two CO_2 forcing scenarios, respectively doubling (IS2CO2, *black lines*) and quadrupling (IS4CO2, *red lines*) the pre-industrial concentration of 280 ppmv. Shown are the corresponding time evolution of the CO_2 concentration, global mean annual temperature, and mean annual temperature over Greenland and Antarctica. The lower three *panels* display the full yearly variability of mean temperature around the 100 years running mean

configurations were used from 1500 AD onward in coupled mode. The resulting background evolution has been analyzed by means of a control experiment, conducted with LOVECLIM under forcing conditions corresponding to the year 1500 AD. The background trend of volume changes is, however, negligible compared to the strong changes imposed by the CO_2 forcing (not shown).

Two greenhouse warming experiments starting from the year 1500 conditions were performed. In IS2CO2 (IS4CO2), the CO2 concentration increases by 1% per year (compounded) until it reaches twice (four times) its initial value and remains unchanged for almost 3,000 years. The two forcing scenarios are illustrated in Fig. 3 along with the corresponding mean temperature changes over Greenland and Antarctica, and in the global mean. Global mean temperature changes are 1.8 and 3.4°C in IS2CO2 and IS4CO2, respectively, indicating a low climate sensitivity of our model compared to the IPCC AR4 best estimate of 3°C (Solomon et al. 2007). The change of mean annual temperature over

Greenland and Antarctica is around 4 and 10°C at the end of both simulations, respectively, half of which is reached within the first two to three centuries (Fig. 3). These temperature increases are about a factor 2.2 and 2.9 higher than the global average because of the polar amplification seen in LOVECLIM. Such a polar amplification is a robust characteristic of the climate system but is stronger in LOVECLIM than in most other models. Gregory and Huybrechts (2006) typically found a polar amplification of around 1.5 for a representative suite of IPCC AOGCMs. The higher polar amplification of LOVECLIM combines with its lower climate sensitivity to yield polar temperature changes for a given radiative forcing that are in line with more comprehensive AOGCMs. Interestingly, the simulated climate warming over Greenland in scenario IS4CO2 shows a small weakening between the year 1150 and 1400 followed by a stepwise increase to the year 1700. These features are linked to ice-sheet climate interactions. The first feature occurs shortly after the freshwater peak from Greenland, which induces a weakening of the AMOC by about 25% as discussed in similar experiments in Driesschaert et al. (2007) and Swingedouw et al. (2008). The subsequent stepwise warming is a direct response to the exposure of a critical amount of ice free land with a lower albedo when the ice sheet has lost about 65% of its volume and its area (see also further).

4 Results

The results are analyzed in most detail for the high scenario IS4CO2 as these span the full spectrum of expected behavior for a disintegrating ice sheet. Most attention is paid to the time evolution of relevant mass balance characteristics.

4.1 Greenland Ice Sheet

Figure 4 shows the implications for the Greenland ice sheet of a sustained warming averaging +8°C over a period of 3,000 years. Surface runoff from the ice sheet is affected most and rapidly dominates the total fresh water flux from Greenland. Critical is the ratio of total ablation to total accumulation over the ice sheet. Whereas for present-day conditions the total volume of melt water runoff is about half the volume of snow accumulation, a balanced surface mass budget (accumulation = ablation) is reached after 120 years of rising CO_2 concentrations at a time when the mean annual warming over Greenland is about +2.5°C. This threshold is fully in line with inferences from mass-balance models (e.g. Oerlemans 1991; Janssens and Huybrechts 2000), and approximately marks the limit of viability of the ice sheet. For a larger warming, the Greenland ice sheet can no longer be sustained, even when the calving flux were reduced to zero (Gregory et al. 2004). The latter effectively occurs later in the simulation after 500 years of warming when the ice sheet no longer borders the coastline in contact with ocean water. After 120 years, the calving rate is reduced by 50%. One of the implications is that marginal erosion of calving fronts by warmer ocean water, often considered a plausible explanation for the observed fast velocity changes in many outlet glaciers (e.g. Rignot and Kanagaratnam 2006), will gradually disappear as a potentially meaningful mechanism for ice loss in a warmer climate. Basal melting from below the Greenland ice sheet, on the other hand, always is a very minor contributor to the total freshwater budget from Greenland. Snow accumulation over the ice sheet remains almost constant for the first 1,000 years of the experiment (not shown) as the increased precipitation expected for a warmer climate is counterbalanced by both an increased fraction falling as rain and a decreasing ice-sheet area.

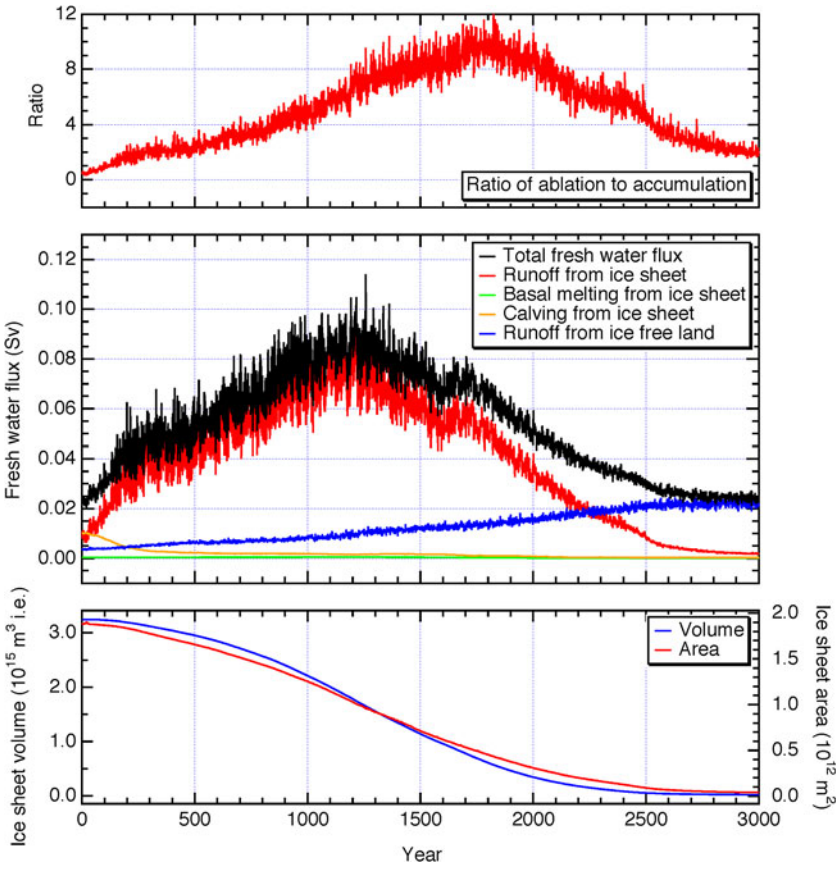

Fig. 4 Response characteristics of the Greenland ice sheet to scenario IS4CO2 during 3,000 years. Shown are changes in mass balance components and ice sheet size. The total freshwater flux derives from all of Greenland and is further divided in its components. Values are expressed in Sverdrup (1 Sv = 1×10^6 m^3 s^{-1})

The gradual melting of an ice reservoir containing enough ice to raise sea level by ~7.5 m causes peak runoff rates approaching 0.1 Sv after more than 1,000 years of sustained warming, corresponding to a tenfold increase. After that, the ice sheet becomes considerably smaller, and the runoff flux decreases rapidly. At the end of the 3,000 years of simulated Greenland ice sheet evolution, the ice sheet has almost completely melted away. Runoff from the remaining small cap is negligible and the total freshwater flux derives almost entirely from the yearly runoff from the ice-free tundra. The total freshwater flux originating from melting of the Greenland ice sheet induces a transient weakening of the AMOC strength by 10–25% that starts after 1,200 years and lasts for ~500 years (not shown). Such behavior is in line with previous results obtained with the same model but for a slightly different climate scenario (Driesschaert et al. 2007). The reduction of the associated meridional heat transport is visible in the mean annual temperature response over the Greenland ice sheet (Fig. 3) and therefore exemplifies a (transient) negative feedback mechanism.

Snapshots of the retreating Greenland ice sheet for IS4CO2 are shown in Fig. 5. The ice sheet retreat first occurs in the southwest, where already today a 300 km wide band of

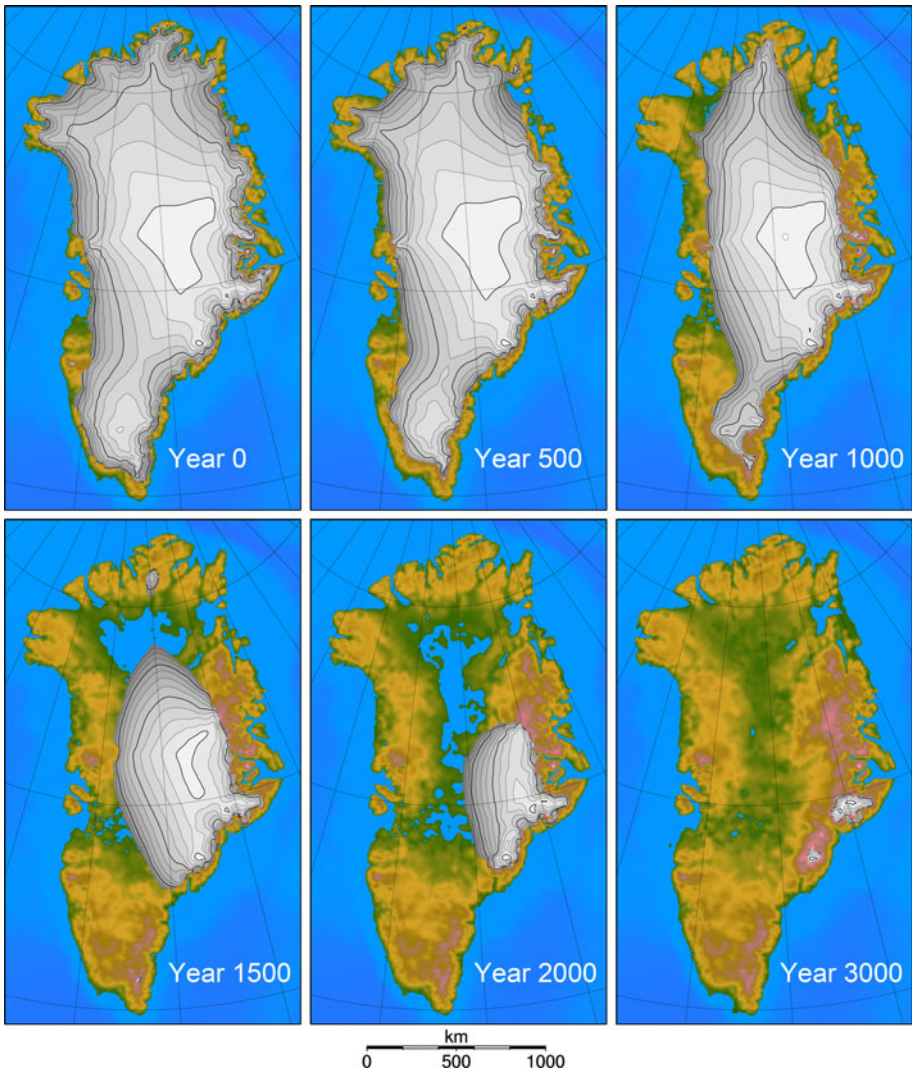

Fig. 5 Snapshots of Greenland ice sheet evolution under scenario IS4CO2. The ice sheet is represented by *grey shading*, ice-free land by *brown* and *green colours* and ocean and land below sea level in *blue*. Contour interval over the ice sheet is 250 m, with *thick lines* for every 1,000 m of surface elevation

tundra is present. After several centuries the Greenland ice sheet becomes fully land-based. The central dome survives longest at an almost constant elevation of around 3,000 m. This makes the ice sheet flanks steeper and the ice flow faster to accommodate for the higher mass balance gradients in a warmer climate. The steeper margins represent a counteracting effect on the ice sheet retreat. They dynamically reduce the area below the equilibrium line and thus reduce the area over which runoff can take place. Compared to experiments without this effect, the ensuing rate of ice sheet decay has been found in earlier studies to be about 20% smaller (Huybrechts and de Wolde 1999; Huybrechts et al. 2004). The ice sheet ultimately retreats to the easterly mountain range, gradually exposing bare land that

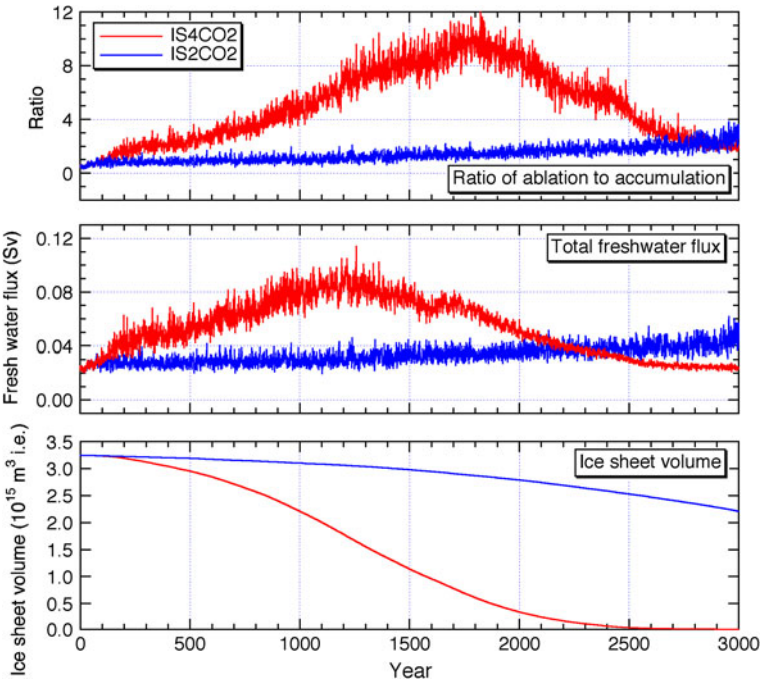

Fig. 6 Response of the Greenland ice sheet to scenario IS2CO2 (*blue lines*) compared to scenario IS4CO2 (*red lines*) during 3,000 years. Shown are changes in ice sheet volume and general mass balance characteristics. The total freshwater flux is expressed in Sverdrup (1 Sv = 1×10^6 m^3 s^{-1})

experiences more summer heating than the adjacent ice sheet because of its lower albedo. Initially, the retreating ice sheet unveils a series of large inland depressions on bed below sea level that are likely candidates for (proglacial) lakes. Most of them are shallow and have no direct connection to the ocean. However, the removal of ice enables the bedrock to slowly rebound with its characteristic millennial time scale. After 3,000 years of simulation, most initial sub-sea-level areas have risen above sea level.

As can be inferred from Fig. 6, the relation between the strength of the climate warming and the disintegration characteristics of the Greenland ice sheet is clearly non-linear. After 3,000 years in the IS2CO2 experiment, with approximately half of the temperature increase seen in IS4CO2, ice volume and mass balance characteristics are comparable to the situation for IS4CO2 after 1,000 years. Surface melting in IS2CO2 is steadily increasing throughout the whole experiment and even accelerating at the end, when temperatures over Greenland start rising again (Fig. 6). The reasons for this are positive ice-albedo and elevation-temperature feedbacks that lead to increasing surface temperatures long after the atmospheric CO_2 concentration has saturated.

4.2 Antarctic Ice Sheet

Surface runoff from the Antarctic ice sheet is a negligible component of the Antarctic mass balance in a pre-industrial climate and remains very small for the first 100 years of the IS4CO2 simulation as long as the warming does not exceed 2°C (Fig. 7). However, this component gradually becomes more important as temperature rises further at an almost

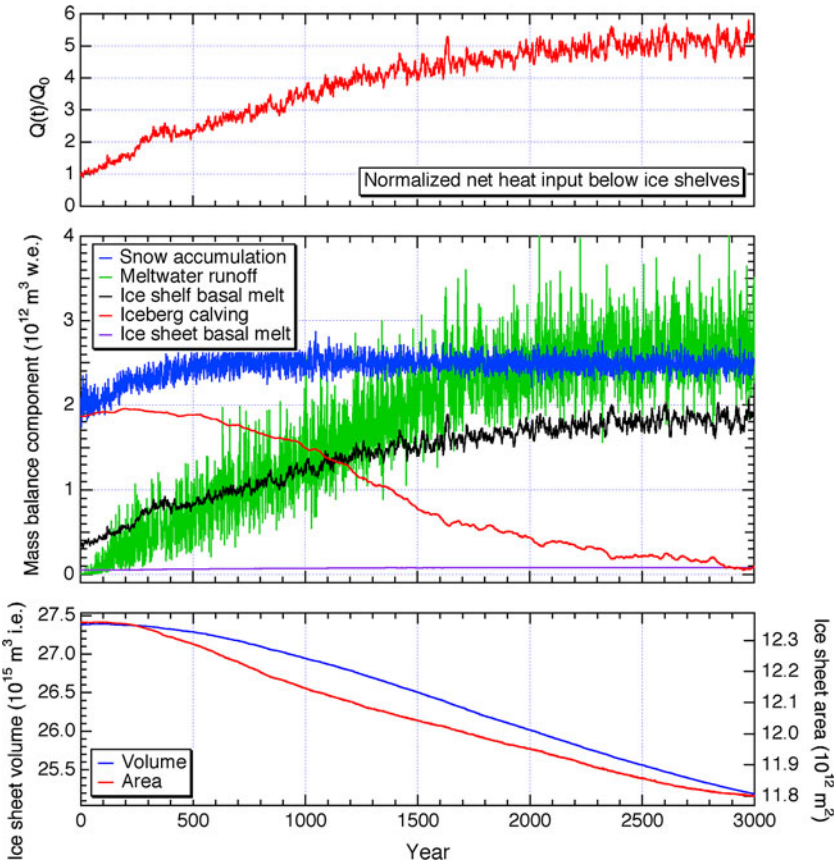

Fig. 7 Response characteristics of the Antarctic ice sheet to scenario IS4CO2 during 3,000 years. Shown are changes in mass balance components and the ensuing changes in ice sheet size

linear rate for about 1,500 years. An approximately balanced surface budget occurs after 2,000 years when the mean annual warming exceeds 10°C, in line with older studies (Huybrechts and de Wolde 1999). As a consequence, surface conditions along the Antarctic ice sheet margin eventually take on characteristics of the present-day Greenland ice sheet. Visual inspection of the associated mass-balance patterns brought to light that the ablation zone develops mainly around the low-lying perimeter of the East Antarctic ice sheet and along the Antarctic Peninsula but that the inland portions of the West Antarctic ice sheet (including the grounding zones of the large ice shelves) largely remain in the accumulation zone. The increase in snow accumulation by ~25% during the first 1,000 years when most of the precipitation falls as snow is weaker in LOVECLIM than dictated by the Clausius-Clapeyron relation and about half that obtained from time slice simulations with AOGCMs (Huybrechts et al. 2004).

A striking aspect of the melt curves shown in Fig. 7 is the gradual increase at an almost linear rate for the first 2,000 years of the simulation. This is explained by the thermal inertia of the Southern Ocean, which delays the warming around Antarctica on a multi-centennial time scale. This is an important aspect to consider when discussing the response of the Antarctic ice sheet to greenhouse gas warming. The effect is obvious in both the

increase of surface runoff, linked to coastal surface temperatures, and basal melting below the ice shelves. The latter is assumed proportional to the oceanic heat input integrated around Antarctica. The ocean warming continues long after greenhouse gas concentrations have stabilized, and is consistent with typical oceanic adjustment time scales.

The iceberg calving flux, calculated as the volume flux through a predefined dynamic ice shelf mask, is found to slightly increase during the first 200 years consistent with an increased accumulation rate and slightly higher ice shelf temperatures. After 500 years, ice shelf thinning from increased basal melting and reduced feeding of ice shelves from the grounded ice sheet as surface ablation increases, causes the iceberg flux to gradually decline to around 5% of its initial value by the year 3000. Taken together, the induced mass balance changes cause the Antarctic ice sheet to grow slightly during the first 100 years of experiment IS4CO2, whereafter grounding line retreat and marginal ice thinning set in. After 3,000 years in a +10°C climate, the Antarctic ice sheet has lost about 8% of its ice volume and 5% of its grounded ice sheet area (Fig. 7). The mechanisms responsible for grounding-line retreat in the Antarctic ice sheet model have been described elsewhere (Huybrechts and de Wolde 1999) and include strain softening near the grounding line, decreased ice fluxes from the grounded ice and a lower effective viscosity of a warmer ice shelf. Basal melting from below the grounded ice sheet is a negligible contributor to the mass balance of the Antarctic ice sheet at all times, as it is for the Greenland ice sheet.

Snapshots from Antarctic ice sheet evolution in scenario IS4CO2 are displayed in Fig. 8. The most important change is grounding-line retreat around the WAIS, especially in the Ross sector, and along overdeepened glaciers of the EAIS. On the millennial time scale considered here, elevations in central East Antarctica remain largely unaffected, although

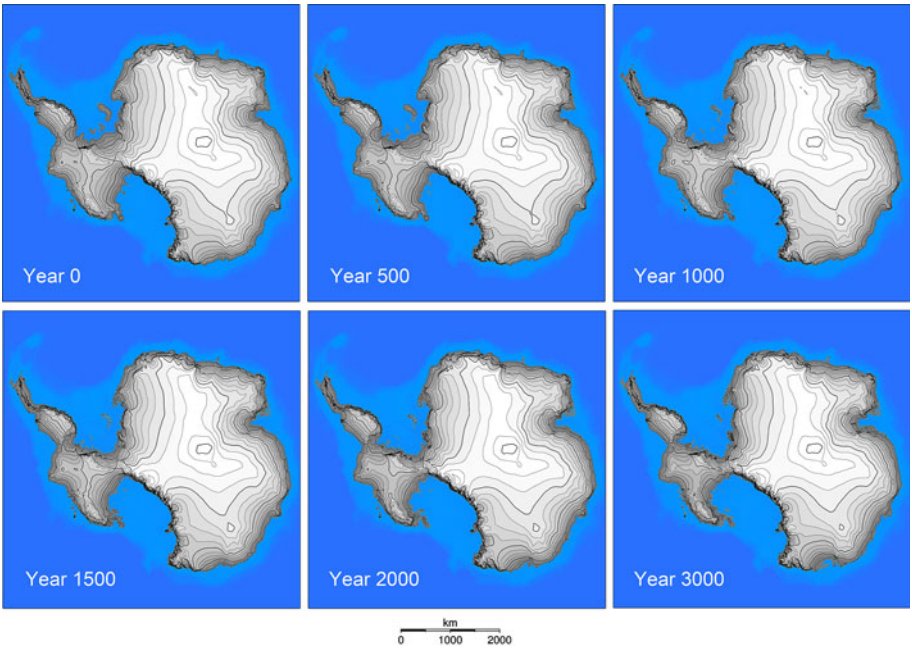

Fig. 8 Snapshots of Antarctic ice sheet evolution under scenario IS4CO2. Grey shading represents grounded ice. Contour interval is 250 m, with *thick lines* for every 1,000 m of surface elevation. The *blue colors* are for the ocean bathymetry below the floating ice shelves and the open ocean

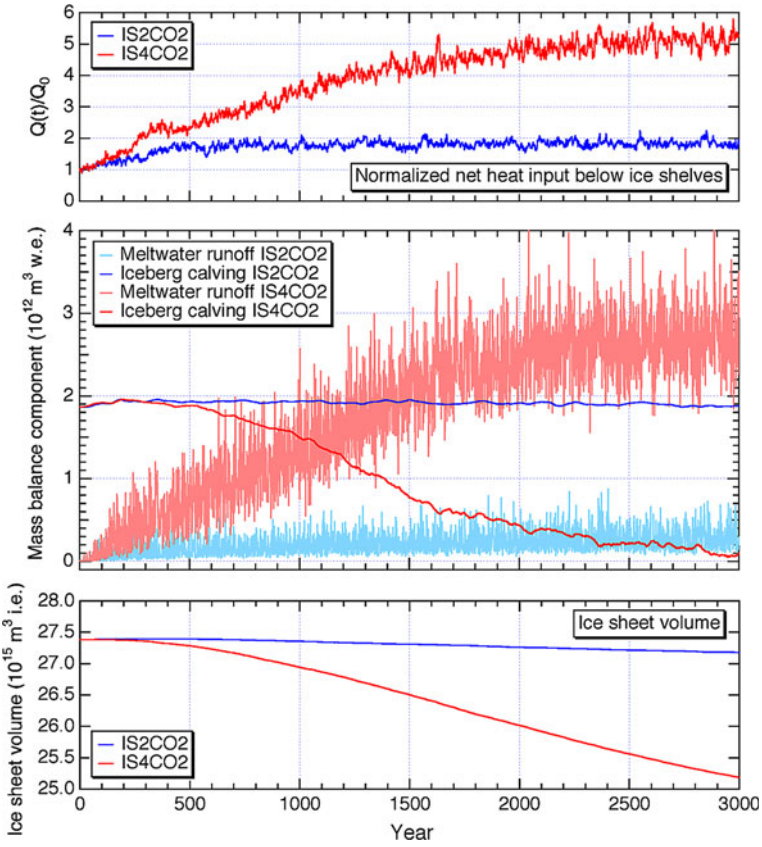

Fig. 9 Response of the Antarctic ice sheet to scenario IS2CO2 (*blue lines*) compared to scenario IS4CO2 (*red lines*) during 3,000 years. Shown are changes in ice sheet volume and general mass balance characteristics

significant thinning for elevations below 3,000 m can be detected from visual inspection of the surface contours.

The temperature increase over Antarctica in experiment IS2CO2 is generally not high enough to have a strong impact on the mass balance components of the Antarctic ice sheet (Fig. 9). For a mean annual warming gradually increasing to 4°C (Fig. 3), surface runoff from the grounded ice sheet never exceeds 20% of the snow accumulation. Ultimately, the average basal melting below the ice shelves almost doubles but iceberg calving remains almost constant for the whole duration of the experiment. As a result, Antarctic grounded ice volume increases somewhat during the first 300 years and by the end of the simulation is not more than 1% lower than the pre-industrial value, as shown in Fig. 9 together with the evolution of the same model characteristics of experiment IS4CO2.

4.3 Contribution to Global Sea-Level Change

The contribution of both ice sheets to global sea-level change in both experiments is displayed in Fig. 10. The curves mirror the evolution of ice sheet volume for the Greenland ice sheet but deviate from the grounded ice sheet volume for the Antarctic ice sheet as

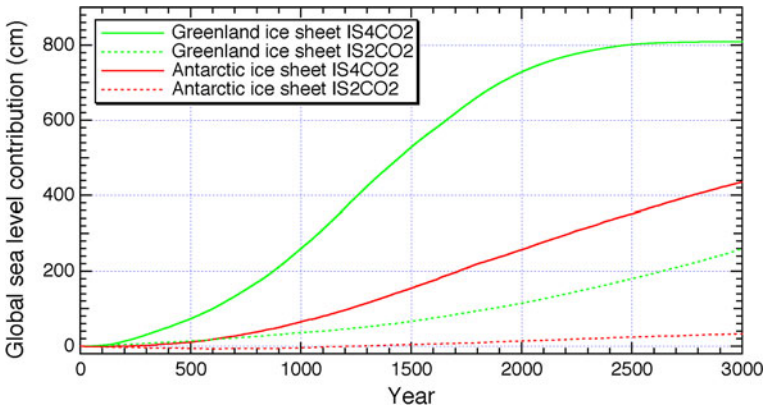

Fig. 10 Contributions to global sea level change from the Greenland (*green*) and Antarctic (*red*) ice sheet for scenarios IS4CO2 (*solid lines*) and IS2CO2 (*dashed lines*)

additional corrections have been made for isostatic depression and for ice displacing ocean water (Huybrechts 2002). The Greenland ice sheet always causes sea level to rise on account of the fast increase in surface runoff in a warmer climate. After 1,000 years, the ice sheet has lost ice volume equivalent to 35 cm in the low scenario IS2CO2 and more than 250 cm in the high scenario IS4CO2. In the low scenario, the Antarctic ice sheet actually lowers global sea level for the first 1,200 years with a maximum of 8 cm after 600 years. After 3,000 years in the high scenario, the Antarctic contribution is $\sim$400 cm, or about half of the Greenland ice sheet contribution of $\sim$8 m possible in our model. The more or less steady rate of 2 mm year^{-1} of sea level rise during the last 1,000 years of experiment IS4CO2 can be considered to bracket a maximum rate for a local warming of 10°C. It also indicates that the Antarctic ice sheet is still far from equilibrium with the imposed climate change. In effect, very long time scales of the order of 10^4 years are required before the Antarctic ice sheet eventually reaches a new steady state with less ice. Were the Antarctic ice sheet to continue to lose ice at this rate, its total melting would take $\sim$30,000 years more to complete.

In both scenarios, the combined contribution of both ice sheets to sea-level change is always positive, except for the first 200 years of experiment IS2CO2 when the negative contribution of the Antarctic ice sheet almost exactly counteracts the positive contribution from the Greenland ice sheet. That corroborates earlier results obtained with the same set of ice-sheet models.

5 Conclusion

LOVECLIM is a useful tool to study long-term ice-sheet and climate changes. Even when keeping in mind the rather coarse resolution of the atmosphere and ocean components, high-latitude climate changes are found to be similar to those obtained with more comprehensive AOGCMs, indicating that the climatic component of LOVECLIM is sufficiently detailed for the current application. Consequently, typical rates of ice-sheet and sea-level changes compare well with those found in earlier studies with more detailed climatic components or in offline experiments with the ice sheet model for similar prescribed temperature and precipitation changes.

An important conclusion is the long time scales associated with ice-sheet decay, partly caused by mitigating ice-climate interactions, and partly by the inertia of the ocean to the imposed greenhouse gas forcing, especially around Antarctica. On the millennial time scale, the results stress the dominant role of melting of the Greenland ice sheet at a rate in excess of 50 cm of sea level rise per century for a mean annual warming approaching 10°C. In the model, the ice loss is almost entirely due to increased surface runoff. An often mentioned accelerated ice dynamic process such as surface melt induced basal lubrication is not included in the model, but this mechanism is increasingly considered unlikely as an important process to speed up ice flow (van de Wal et al. 2008; Sundal et al. 2011). Another potential candidate for generating accelerated ice flow arises from increased melting at calving fronts of tidewater glaciers linked to penetration of warm ocean water. However, the effectiveness of this process is limited in time as the Greenland ice sheet is found to become almost entirely land-based after a few centuries of sustained warming.

The results for Antarctica provide a remarkable contrast. For a regional warming below 3–4°C, corresponding to a doubling of the CO_2 concentration in LOVECLIM, increased accumulation is projected to dominate the mass balance, leading to a slight growth of the ice sheet. Processes causing significant ice volume loss, such as increased basal melting of the ice shelves, grounding-line retreat, and surface runoff, only become significant for greenhouse gas concentrations more than twice the pre-industrial value, and moreover take several centuries to become fully effective. The experiments discussed here limit the maximum rate of the Antarctic ice sheet contribution to global sea level rise to about 20 cm per century for a $4\times$ CO_2 scenario corresponding to a regional warming of about 10°C. The long-term response could however be larger in case sub-ice shelf melting would be concentrated near grounding lines, the large West Antarctic ice shelves were to break up, and calving fronts would develop in deep waters, but such behavior cannot be investigated with the current model set up.

Acknowledgments This study was carried out in the framework of successive projects funded by the Belgian Federal Science Policy Office within its Research Program on Science for a Sustainable Development under contracts EV/03/9B (MILMO) and SD/CS/01A (ASTER).

References

Beckmann A, Goosse H (2003) A parameterization of ice shelf-ocean interaction for climate models. Ocean Mod 5(2):157–170. doi:10.1016/S1463-5003(02)00019-7

Bougamont M, Bamber JL, Ridley JK, Gladstone RM, Greuell W, Hanna E, Payne AJ, Rutt I (2007) Impact of model physics on estimating the surface mass balance of the Greenland ice sheet. Geophys Res Lett 34(17):5. doi:10.1029/2007gl030700

Brovkin V, Ganopolski A, Svirezhev Y (1997) A continuous climate-vegetation classification for use in climate-biosphere studies. Ecol Model 101(2–3):251–261. doi:10.1016/S0304-3800(97)00049-5

Charbit S, Paillard D, Ramstein G (2008) Amount of CO_2 emissions irreversibly leading to the total melting of Greenland. Geophys Res Lett 35(12):L12503. doi:10.1029/2008GL033472

Driesschaert E, Fichefet T, Goosse H, Huybrechts P, Janssens I, Mouchet A, Munhoven G, Brovkin V, Weber S (2007) Modeling the influence of Greenland ice sheet melting on the Atlantic meridional overturning circulation during the next millennia. Geophys Res Lett 34(10):10707. doi:10.1029/2007GL029516

Fichefet T, Maqueda MAM (1997) Sensitivity of a global sea ice model to the treatment of ice thermodynamics and dynamics. J Geophys Res 102(C6):12609–12646. doi:10.1029/97JC00480

Fichefet T, Poncin C, Goosse H, Huybrechts P, Janssens I, Le Treut H (2003) Implications of changes in freshwater flux from the Greenland ice sheet for the climate of the 21st century. Geophys Res Lett 30(17):1911. doi:1910.1029/2003GL017826

Goelzer H, Huybrechts P, Loutre MF, Goosse H, Fichefet T, Mouchet A (2010) Impact of Greenland and Antarctic ice sheet interactions on climate sensitivity. Clim Dyn online first. doi:10.1007/s00382-010-0885-0

Goosse H, Fichefet T (1999) Importance of ice-ocean interactions for the global ocean circulation: a model study. J Geophys Res 104(C10):23337–23355. doi:10.1029/1999JC900215

Goosse H, Deleersnijder E, Fichefet T, England MH (1999) Sensitivity of a global coupled ocean-sea ice model to the parameterization of vertical mixing. J Geophys Res 104(C6):13681–13695. doi:10.1029/1999JC900099

Goosse H, Brovkin V, Fichefet T, Haarsma R, Huybrechts P, Jongma J, Mouchet A, Selten F, Barriat PY, Campin JM, Deleersnijder E, Driesschaert E, Goelzer H, Janssens I, Loutre MF, Morales Maqueda M, Opsteegh T, Mathieu PP, Munhoven G, Pettersson E, Renssen H, Roche D, Schaeffer M, Tartinville B, Timmermann A, Weber S (2010) Description of the Earth system model of intermediate complexity LOVECLIM version 1.2 Geosci Model Dev 3:603–633. doi:10.5194/gmd-3-603-2010

Gregory J, Huybrechts P (2006) Ice-sheet contributions to future sea-level change. Phil Trans R Soc A 364(1844):1709–1731. doi:10.1098/rsta.2006.1796

Gregory JM, Huybrechts P, Raper SCB (2004) Threatened loss of the Greenland ice sheet. Nature 428:616. doi:10.1038/428616a

Hu AX, Meeh GA, Han WQ, Yin JJ (2009) Transient response of the MOC and climate to potential melting of the Greenland ice sheet in the 21st century. Geophys Res Lett 36:6. doi:10.1029/2009gl037998

Huybrechts P (2002) Sea-level changes at the LGM from ice-dynamic reconstructions of the Greenland and Antarctic ice sheets during the glacial cycles. Quat Sci Rev 21(1–3):203–231. doi:10.1016/S0277-3791(01)00082-8

Huybrechts P, de Wolde J (1999) The dynamic response of the Greenland and Antarctic ice sheets to multiple-century climatic warming. J Clim 12(8):2169–2188. doi:10.1175/1520-0442(1999)012<2169:TDROTG>2.0.CO;2

Huybrechts P, Miller H (2005) Flow and balance of the polar ice sheets. In: Hantel M (ed) Observed global climate. Landolt-Börnstein/New Series (Numerical data and functional relationships in science and technology), V/6 edn. Springer Verlag, Berlin, pp 13/1–13

Huybrechts P, Gregory J, Janssens I, Wild M (2004) Modelling Antarctic and Greenland volume changes during the 20th and 21st centuries forced by GCM time slice integrations. Global Planet Change 42(1–4):83–105. doi:10.1016/j.gloplacha.2003.11.011

Janssens I, Huybrechts P (2000) The treatment of meltwater retention in mass-balance parameterizations of the Greenland ice sheet. Ann Glaciol 31:133–140

Jungclaus JH, Haak H, Esch M, Roeckner E, Marotzke J (2006) Will Greenland melting halt the thermohaline circulation? Geophys Res Lett 33:L17708. doi:17710.11029/12006GL026815

Lunt D, de Noblet-Ducoudré N, Charbit S (2004) Effects of a melted Greenland ice sheet on climate, vegetation, and the cryosphere. Clim Dyn 23(7):679–694. doi:10.1007/s00382-004-0463-4

Meehl GA, Stocker TF, Collins WD, Friedlingstein P, Gaye AT, Gregory JM, Kitoh A, Knutti R, Murphy JM, Noda A, Raper SCB, Watterson IG, Weaver AJ, Zhao ZC (2007) Global climate projections. In: Qin D, Manning M, Chen Z et al (eds) Climate change 2007: the physical science basis Contribution of working group I to the fourth assessment report of the intergovernmental panel on climate change. Cambridge University Press, Cambridge, United Kingdom and New York, NY, USA

Mikolajewicz U, Groeger M, Maier-Reimer E, Schurgers G, Vizcaíno M, Winguth AME (2007a) Long-term effects of anthropogenic CO_2 emissions simulated with a complex Earth system model. Clim Dyn 28(6):599–631. doi:10.1007/s00382-006-0204-y

Mikolajewicz U, Vizcaíno M, Jungclaus J, Schurgers G (2007b) Effect of ice sheet interactions in anthropogenic climate change simulations. Geophys Res Lett 34(18):5. doi:10.1029/2007gl031173

Mouchet A, François LM (1997) Sensitivity of a global oceanic carbon cycle model to the circulation and to the fate of organic matter: preliminary results. Phys Chem Earth 21(5–6):511–516. doi:10.1016/s0079-1946(97)81150-0

Oerlemans J (1991) The mass balance of the Greenland ice sheet: sensitivity to climate change as revealed by energy-balance modelling. Holocene 1(1):40–49. doi:10.1177/095968369100100106

Opsteegh JD, Haarsma RJ, Selten FM, Kattenberg A (1998) ECBilt: a dynamic alternative to mixed boundary conditions in ocean models. Tellus 50(3):348–367. doi:10.1034/j.1600-0870.1998.t01-1-00007.x

Ridley J, Huybrechts P, Gregory J, Lowe J (2005) Elimination of the Greenland ice sheet in a high CO_2 climate. J Clim 18:3409–3427. doi:10.1175/JCLI3482.1

Ridley J, Gregory JM, Huybrechts P, Lowe J (2010) Thresholds for irreversible decline of the Greenland ice sheet. Clim Dyn 35(6):1065–1073. doi:10.1007/s00382-009-0646-0

Rignot E, Kanagaratnam P (2006) Changes in the velocity structure of the Greenland ice sheet. Science 311(5763):986–990. doi:10.1126/Science.1121381

Rignot E, Bamber JL, Van Den Broeke MR, Davis C, Li Y, Van De Berg WJ, Van Meijgaard E (2008a) Recent Antarctic ice mass loss from radar interferometry and regional climate modelling. Nat Geosci 1(2):106–110. doi:10.1038/ngeo102

Rignot E, Box J, Burgess E, Hanna E (2008b) Mass balance of the Greenland ice sheet from 1958 to 2007. Geophys Res Lett 35:L20502. doi:10.1029/2008GL035417

Solomon S, Qin D, Manning M, Chen Z, Marquis M, Averyt K, Tignor M, Miller H (eds) (2007) Contribution of Working Group I to the Fourth Assessment Report of the Intergovernmental Panel on Climate Change, 2007. Cambridge University Press, Cambridge. United Kingdom and New York, NY, USA

Stone E, Lunt D, Rutt I, Hanna E (2010) Investigating the sensitivity of numerical model simulations of the modern state of the Greenland ice-sheet and its future response to climate change. Cryosphere 4(3):397–417. doi:10.5194/tc-4-397-2010

Sundal AV, Shepherd A, Nienow P, Hanna E, Palmer S, Huybrechts P (2011) Melt induced speed-up of Greenland ice sheet offset by efficient subglacial drainage. Nature 469:521–524. doi:10.1038/nature09740

Swingedouw D, Fichefet T, Huybrechts P, Goosse H, Driesschaert E, Loutre M-F (2008) Antarctic ice-sheet melting provides negative feedbacks on future climate warming. Geophys Res Lett 35((17)):L17705. doi:10.1029/2008GL034410

Van de Wal RSW, Boot W, van den Broeke MR, Smeets CJPP, Reijmer CH, Donker JJA, Oerlemans J (2008) Large and rapid melt-induced velocity changes in the ablation zone of the Greenland ice sheet. Science 321:111–113. doi:10.1126/science.1158540

Van Den Broeke M, Bamber J, Ettema J, Rignot E, Schrama E, Van De Berg WJ, Van Meijgaard E, Velicogna I, Wouters B (2009) Partitioning recent Greenland mass loss. Science 326(5955):984–986. doi:10.1126/science.1178176

Vizcaíno M, Mikolajewicz U, Groeger M, Maier-Reimer E, Schurgers G, Winguth AME (2008) Long-term ice sheet-climate interactions under anthropogenic greenhouse forcing simulated with a complex Earth system model. Clim Dyn 31(6):665–690. doi:10.1007/s00382-008-0369-7

Vizcaíno M, Mikolajewicz U, Jungclaus J, Schurgers G (2010) Climate modification by future ice sheet changes and consequences for ice sheet mass balance. Clim Dyn 34(2–3):301–324. doi:10.1007/s00382-009-0591-y

Surv Geophys (2011) 32:417–435
DOI 10.1007/s10712-011-9133-3

Representing Grounding Line Dynamics in Numerical Ice Sheet Models: Recent Advances and Outlook

David Docquier · Laura Perichon · Frank Pattyn

Received: 18 February 2011 / Accepted: 16 May 2011 / Published online: 15 June 2011

Abstract Recent satellite observations of the Antarctic and Greenland ice sheets show accelerated ice flow and associated ice sheet thinning along coastal outlet glaciers in contact with the ocean. Both processes are the result of grounding line retreat due to melting at the grounding line (the grounding line is the contact of the ice sheet with the ocean, where it starts to float and forms an ice shelf or ice tongue). Such rapid ice loss is not yet included in large-scale ice sheet models used for IPCC projections, as most of the complex processes are poorly understood. Here we report on the state-of-the art of grounding line migration in marine ice sheets and address different ways in which grounding line migration can be attributed and represented in ice sheet models. Using one-dimensional ice flow models of the ice sheet/ice shelf system we carried out a number of sensitivity experiments with different spatial resolutions and stress approximations. These are verified with semi-analytical steady state solutions. Results show that, in large-scale finite-difference models, grounding line migration is dependent on the numerical treatment (e.g. staggered/non-staggered grid) and the level of physics involved (e.g. shallow-ice/shallow-shelf approximation).

Keywords Marine ice sheet instability · Grounding line · Ice sheet modeling · West Antarctic ice sheet

D. Docquier (✉) · L. Perichon · F. Pattyn
Laboratoire de Glaciologie, Université Libre de Bruxelles, CP160/03, Av. F.D. Roosevelt 50, 1050 Brussels, Belgium
e-mail: david.docquier@ulb.ac.be

L. Perichon
e-mail: lpericho@ulb.ac.be

F. Pattyn
e-mail: fpattyn@ulb.ac.be

1 Introduction

The West Antarctic Ice Sheet (WAIS) is currently losing ice at a considerable rate (Chen et al. 2009; Velicogna 2009; Rignot et al. 2008, 2011). Pine Island (PIG) and Thwaites Glaciers, situated in the Amundsen Sea Embayment, are the main contributors to this WAIS mass loss (Shepherd et al. 2001). PIG in particular has shown a nearly continuous acceleration (Joughin et al. 2003) and thinning (Wingham et al. 2009) during recent years. Recent evidence shows that this thinning is due to an inland grounding line migration from the 1970s to present by 30 km (Jenkins et al. 2010).

Due to its marine configuration, i.e. its bedrock mostly lying below sea level, the stability of the WAIS has been a subject of much debate. Marine ice sheet stability is mostly controlled by the dynamics of the grounding line, i.e. the junction between the grounded ice sheet and the floating ice shelf. This junction marks the change from inland ice sheet flow, dominated by vertical shear and basal friction, toward ice shelf flow, dominated by longitudinal stresses, and which is quintessential in understanding grounding line dynamics. Weertman (1974) and Thomas and Bentley (1978) proposed that ice discharge through the grounding line should increase with ice thickness. Therefore, a marine ice sheet lying on an upward-sloping bed (toward the ocean), such as WAIS, is unstable. A slight retreat in grounding line position could therefore lead to an increase in ice thickness, hence increased ice discharge at the grounding line. Ice sheet thinning is then initiated and further retreat of the grounding line potentially occurs.

Hindmarsh (1993, 1996) argued that ice shelves should have a limited impact on ice sheet dynamics, and that grounding line migration is governed by grounded ice flux. He advocated the concept of neutral equilibrium, i.e. that a perturbation in grounding line position should not lead to unstable retreat or advance for a foredeepened or upward-sloping bed, nor to a return to the original grounding line position for a downward-sloping bed.

However, Schoof (2007a, b) re-confirmed the instability hypothesis formulated by Weertman (1974) and Thomas and Bentley (1978), on the basis of a boundary layer theory for the ice sheet/ice shelf transition. He demonstrated that (1) marine ice sheets do not exhibit neutral equilibrium, but have well-defined, discrete equilibrium profiles; (2) steady grounding lines cannot be stable on upward-sloping beds; (3) marine ice sheets with overdeepened beds can undergo hysteresis under variations in sea level, accumulation rate, basal slipperiness and ice viscosity. Robison et al. (2009) confirmed the stability of the grounding line on a downward bed slope comparing fluid-mechanical experiments and model results (with time-dependent evolution of the grounding line), while Durand et al. (2009a) demonstrated the instability of marine ice sheets on upsloping beds with a Full Stokes (Elmer/Ice) model.

The aim of this paper is to address the state-of-the-art of modeling the processes affecting marine ice sheet stability and grounding line migration. To this end, we give an overview of different numerical approaches and approximations used in ice sheet models. A description is given for a simple model that copes with grounding line migration in a parameterized way. Numerical experiments are carried out to investigate the aspects of grid resolution and the time-dependent behavior and a discussion is given on the appropriate use of approximations and numerical approaches in large-scale ice sheet models.

2 Grounding Line Models: An Overview

2.1 Numerical Approaches

There are several numerical approaches in ice sheet models to simulate grounding line migration: fixed grid (FG), moving grid (MG) and adaptive techniques. They essentially differ in the way grounding lines are represented. The majority of models make use of the flotation criterion to separate grounded and floating ice:

$$\rho_i h = \rho_w (z_{sl} - b), \tag{1}$$

where ρ_i and ρ_w are ice and water densities, respectively, h is the ice thickness, z_{sl} is the sea level elevation, b is the bedrock elevation. In FG models, the grounding line position is not defined explicitly but must fall between grid points where ice is grounded and floating. Large-scale ice sheet models (Huybrechts 1990; Ritz et al. 2001) use this strategy to simulate grounding line migration. Moving grid (MG) models allow the grounding line position to be followed continuously, i.e. the grounding line coincides exactly with a grid point (Hindmarsh 1996; Hindmarsh and Le Meur 2001).

Vieli and Payne (2005) showed that there is a strong dependency of FG models on numerics, that—when perturbed—FG models exhibit large changes in grounding line migration, and that these changes are irreversible. Conversely, for MG models, changes in grounding line position are generally small and reversible. However, the models based on shallow-ice approximation used by Vieli and Payne lack a second independent boundary condition that is needed to accurately represent grounding line migration (see below; Schoof 2007a; Durand et al. 2009a), and although MG models generally produce more consistent results, a major drawback remains the complexity to implement in a three-dimensional ice sheet model (Vieli and Payne 2005).

Adaptive models are a trade-off between FG and MG models. Durand et al. (2009a) used the finite element code Elmer/Ice to couple the Stokes equations with the evolution of two free surfaces, i.e. the upper interface (air/ice) and the bottom interface (ice/bed or ice/sea). They applied a mesh refinement around the grounding line. With this method, the total number of nodes is constant and only the horizontal distribution of the nodes is modified. Durand et al. (2009a) need a grid size below 100 m at the grounding line in order to achieve consistent results.

Goldberg et al. (2009) used adaptive refinement, i.e. cells are divided into smaller cells where extra resolution is required and groups of cells are coarsened into larger cells in regions where lower resolution suffices. The grounding line is represented either as lying at the boundary between entirely grounded and entirely floating cells or by interpolating the flotation condition between grid lines according to Pattyn et al. (2006) (cells can be partially grounded in the latter case). Goldberg et al. (2009) found that buttressing was not always sufficient to stabilize an ice sheet, but the collapse of the grounded portion was greatly delayed.

Katz and Worster (2010) presented a theory for grounding line dynamics in three spatial dimensions. Although they incorporated internal shear and membrane stresses, a Newtonian viscosity was used and basal sliding neglected. They also used the 2D ice shelf proposed by Robison et al. (2009), which is valid only when the grounding line position is independent of the transverse direction.

Finally, FG models can be adapted in such a way that sub-grid grounding line position and migration can be achieved through local interpolations and approximations. Pattyn

et al. (2006) determined grounding line position at sub-grid resolution using the flotation criterion (1) and applied a basal friction function to mimic in a continuous way the transition zone between ice sheet and ice shelf. Gladstone et al. (2010) used several interpolation schemes in combination with locally increased resolution to suit the same purpose.

2.2 Physical Approximations

2.2.1 Linear Momentum

The flow of an ice body is described by the linear momentum balance equation:

$$\rho_i \frac{d\mathbf{v}}{dt} = \nabla \cdot \tau + \rho_i \mathbf{g}, \tag{2}$$

where $\mathbf{v}$ is the velocity field, $\boldsymbol{\tau}$ is the Cauchy stress tensor, and $\mathbf{g}$ is the gravitational acceleration. Neglecting acceleration terms and considering the gravitational acceleration only important in the vertical direction, we can write (2) in its component form (where x is the flow direction, y is the direction perpendicular to the flow and z is the vertical direction, positively upward):

$$\frac{\partial \tau_{xx}}{\partial x} + \frac{\partial \tau_{xy}}{\partial y} + \frac{\partial \tau_{xz}}{\partial z} = 0, \tag{3}$$

$$\frac{\partial \tau_{yx}}{\partial x} + \frac{\partial \tau_{yy}}{\partial y} + \frac{\partial \tau_{yz}}{\partial z} = 0, \tag{4}$$

$$\frac{\partial \tau_{zx}}{\partial x} + \frac{\partial \tau_{zy}}{\partial y} + \frac{\partial \tau_{zz}}{\partial z} = \rho_i g. \tag{5}$$

Full Stokes (FS) models (Durand et al. 2009a, b) solve the full system of linear momentum equations. Due to the considerable computational effort, approximations to these equations are often used, such as higher-order, shallow-shelf and shallow-ice approximations. They involve dropping terms from the momentum balance equations and simplifying the strain rate definitions.

Higher-order models (HOM) consider the hydrostatic approximation in the vertical direction by neglecting vertical resistive stresses, so that the linear momentum can be written (Herterich 1987; Blatter 1995; Pattyn 2003):

$$\frac{\partial \tau_{xx}}{\partial x} + \frac{\partial \tau_{xy}}{\partial y} + \frac{\partial \tau_{xz}}{\partial z} = 0, \tag{6}$$

$$\frac{\partial \tau_{yx}}{\partial x} + \frac{\partial \tau_{yy}}{\partial y} + \frac{\partial \tau_{yz}}{\partial z} = 0, \tag{7}$$

$$\frac{\partial \tau_{zz}}{\partial z} = \rho_i g. \tag{8}$$

A further approximation, known as the shallow-shelf approximation (SSA), is obtained by neglecting vertical shear (MacAyeal 1992; MacAyeal et al. 1996). This is valid for ice shelves and ice streams characterized by a low basal drag:

$$\frac{\partial \tau_{xx}}{\partial x} + \frac{\partial \tau_{xy}}{\partial y} = 0, \tag{9}$$

$$\frac{\partial \tau_{yx}}{\partial x} + \frac{\partial \tau_{yy}}{\partial y} = 0, \tag{10}$$

$$\frac{\partial \tau_{zz}}{\partial z} = \rho_i g. \tag{11}$$

For ice streams, an extra basal boundary condition is added, i.e. $\tau_b = \beta^2 u$, where τ_b is the basal shear stress, β^2 is a friction parameter, and u is the horizontal velocity ($\beta^2 = 0$ in ice shelves). The basal sliding law can also take a nonlinear form (see below).

The most common approximation is the shallow-ice approximation (SIA). This approximation incorporates only vertical shear stresses, which is valid for an ice mass with a small aspect ratio (i.e. thickness scale much smaller than length scale):

$$\frac{\partial \tau_{xz}}{\partial z} = \rho_i g \frac{\partial s}{\partial x}, \qquad \frac{\partial \tau_{yz}}{\partial z} = \rho_i g \frac{\partial s}{\partial y}, \tag{12}$$

where s is the surface elevation. Its main advantage is that all stress and velocity components are locally determined. However, the approximation is not valid for key areas such as ice divides and grounding lines (Hutter 1983; Baral et al. 2001).

2.2.2 *Transition Zones*

Besides being the limit of flotation, a grounding line is also the change from a shear-dominated ice flow to an ice flow dominated by longitudinal stretching.[1] The transition is never sharp, but gradual, and knowing the size of this transition zone is essential in understanding grounding line dynamics and inland ice response to sudden changes at the grounding line.

Herterich (1987) calculated the flow within a small transition zone, where the grounded ice sheet is frozen to the bed. The length of the transition zone was found to be of the order of the ice thickness and increased when basal sliding was incorporated. However, the geometry of these experiments was fixed (i.e. no change of the free surface) and the results obtained strongly dependent on this assumption.

Therefore, Lestringant (1994) took in account free-surface changes using a mixed[2] finite-element method to solve the flow equations within two-dimensional sharp transition zones. He concluded that it was *impossible* to use reduced Stokes equations in the transition zone and that the ice sheet and ice shelf could be linked by a jump-boundary condition for the horizontal velocity. However, he assumed no drag effect coming from the sides, which means that the ice shelf does not affect the upstream flow.

Similar conclusions were reached by Pattyn (2000), using a two-dimensional flowline model on a fixed finite-difference grid in order to evaluate the impact of model resolution on ice dynamics near the grounding line. He demonstrated that the transition zone is smaller than the grid size at coarse resolutions (i.e. grid sizes of 20–40 km). At finer resolutions, the transition zone is larger than the grid size, and hence all stress components

[1] This is less valid in the case of an ice stream, where upstream of the grounding line longitudinal stress gradients may be dominant.

[2] 'Mixed' means that the computed unknowns are the horizontal and vertical velocities as well as pressure (Lestringant 1994).

should be considered. As shown by Pattyn et al. (2006), the transition zone length scale is roughly inverse to basal friction as $0 < \beta^2 < +\infty$. Marine ice sheets with large transition zones (low β^2 values), such as ice streams, seem highly sensitive to perturbations at the grounding line or reduction in buttressing compared to ice sheets with small transition zones (high β^2).

Hindmarsh (2004) presented a computational analysis of the accuracy of different approximations to the Stokes equations. He showed that the inclusion of longitudinal (or membrane) stresses increases accuracy at smaller wavelengths compared with the SIA. From his analysis, two longitudinal stress schemes, namely L1L2 (a single-layer scheme, i.e. two-dimensional) and LMLa (multilayer scheme, i.e. three-dimensional; Pattyn 2003), are adequate approximations. LMLa is slightly more accurate than L1L2, but the latter has the advantage that it needs less computational effort since it is two-dimensional. Hindmarsh (2006) proposed a boundary layer in these membrane stresses extending about 10 km from the grounding line.

The flow of an ice sheet or a glacier is an example of free surface thin film flow, which can be described by two types of models. Lubrication models are appropriate when shear stresses are dominant in the force balance and in the absence of wall slip. Conversely, membrane models are used in the case of dominant normal stresses and rapid wall slip. However, both rapid and slow slip can occur within the same ice mass (e.g. surges, ice streams). Therefore, hybrid lubrication/membrane models, such as HOM (Blatter 1995; Pattyn 2003), have been developed. Schoof and Hindmarsh (2010) established a theory for such hybrid models, which was missing until now. They developed asymptotic expansions for the solution to the Blatter equations in order to obtain a depth-integrated model that describes both fast and slow sliding.

2.3 Grounding Line Migration

To accurately capture grounding line migration, it is necessary to resolve the transition zone at a sufficiently fine resolution. Furthermore, besides the flotation criterion (1), an extra boundary condition is needed, i.e. longitudinal stresses should be evaluated at both sides of the grounding line. Schoof (2007a) proposed a semi-analytical solution for the ice flux across the grounding line q_g obeying both boundary conditions:

$$q_g = \left[\frac{\overline{A}(\rho_i g)^{n+1}(1-\rho_i/\rho_w)^n}{4^n C} \right]^{\frac{1}{m+1}} \theta^{\frac{n}{m+1}} h_g^{\frac{m+n+3}{m+1}}, \tag{13}$$

where $\overline{A}$ is the depth-averaged parameter in Glen's flow law, n is the Glen's flow law exponent, C is the basal sliding parameter, m is the basal sliding exponent, θ is the buttressing factor ($\theta = 1$ in this study), and h_g is the ice thickness at the grounding line. This implies that ice flux at the grounding line is sensitive to changes in the ice shelf, contrary to earlier findings by Hindmarsh (1993).

Pollard and DeConto (2009) incorporated this solution in a numerical ice sheet model at coarse grid resolution by applying a heuristic rule: if the semi-analytical derived flux across the actual grounding line q_g from (13) is greater than the modeled flux through the last grounded grid point q_i, then q_g is imposed at that grid point. The velocity at the last grounded grid point u_i is calculated by dividing the analytical flux q_g by the ice thickness at that grid point h_i (derived from the numerical advection scheme). Otherwise, q_g is imposed one grid point further downstream (i.e. the first floating grid point) and the velocity at the

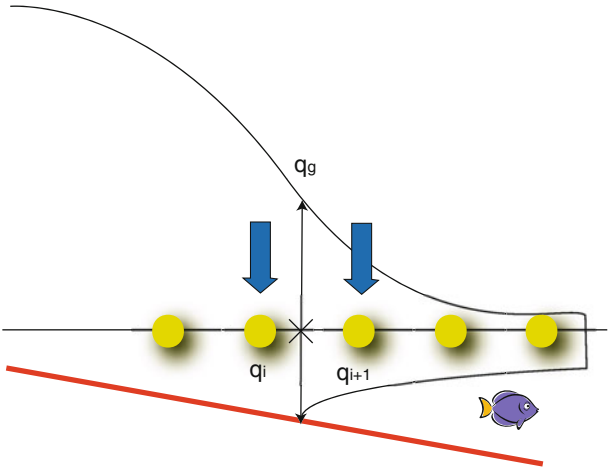

Fig. 1 Fixed grid heuristic rule adapted from Pollard and DeConto (2009)

first floating grid point u_{i+1} equals the analytical flux q_g divided by the ice thickness there h_{i+1}. The former is usually associated with grounding line retreat, and the latter usually with grounding line advance (Fig. 1):

$$q_g > q_i : q_i = q_g \quad \text{or} \quad u_i = \frac{q_g}{h_i}, \tag{14}$$

$$q_g < q_i : q_{i+1} = q_g \quad \text{or} \quad u_{i+1} = \frac{q_g}{h_{i+1}}. \tag{15}$$

The reason why the flux is imposed (and not the velocity) is that the equilibrated solutions in a finite-difference model have the same property as the semi-analytical Schoof solutions: namely, that the upstream snowfall integrated from the grounding line to the ice divide equals the flux across the grounding line. And since the latter is a function of the grounding line ice thickness (Schoof 2007a), which in turn depends on the grounding line position (for a given sea level and bed profile), the equilibrium grounding-line position is determined by the above balance, and is independent of all other model dynamics (as long as the model conserved mass).

Both principles (Schoof boundary condition and Pollard and DeConto heuristic rule) form the base of a simple ice sheet model developed in the next section.

3 A Simple Grounding Line Model

3.1 Model Description

The numerical ice sheet model used here is a one-dimensional (vertically integrated) finite-difference flowline model. The grounded part is either based on the shallow-ice approximation (thereby including vertical shear stresses) or the shallow-shelf model (with inclusion of basal friction, i.e. a so-called L1L2 model). In any case, the floating part is according to the shallow-shelf approximation. Therefore, two models are used here, namely SIA/SSA (SIA for the sheet and SSA for the shelf) and SSA (SSA for the whole domain). The depth-averaged horizontal velocity in the ice sheet is calculated as follows:

$$\overline{u} = u_b + \frac{2}{n+2}\overline{A}h|\tau_d|^{n-1}\tau_d, \tag{16}$$

where $\tau_d = -\rho_i\, g\, h\, \nabla s$ is the driving stress ($\tau_d \equiv \tau_b$ in the case of SIA). Basal velocity u_b is derived from a Weertman-type sliding law:

$$u_b = C^{-\frac{1}{m}}|\tau_d|^{\frac{1}{m}-1}\tau_d. \tag{17}$$

The shallow-shelf (SSA) model neglects vertical shearing and ice deformation is dominated by membrane stresses:

$$4\frac{\partial}{\partial x}\left\{\eta\frac{\partial \overline{u}}{\partial x}\right\} + \beta^2 u_b = \rho_i g\frac{\partial s}{\partial x}, \tag{18}$$

where

$$\eta = \frac{1}{2}\overline{A}^{-\frac{1}{n}}\left\{\frac{\partial \overline{u}}{\partial x}\right\}^{\frac{1-n}{n}} \tag{19}$$

is the effective viscosity. Due to its depth-integrated nature, it follows that $u_b \equiv \overline{u}$ in (18). The basal friction parameter β^2 is then defined as:

$$\beta^2 = \begin{cases} C|\overline{u}|^{m-1} & : \quad x < x_g \\ 0 & : \quad x \geq x_g, \end{cases}$$

where x_g is the position of the grounding line. A symmetric ice divide is considered at the upstream boundary:

$$\frac{\partial(h+b)}{\partial x} = 0; \qquad \overline{u} = 0.$$

At the downstream boundary (ice shelf/ocean), the longitudinal stress gradient is balanced by the hydrostatic pressure of the ocean water (Paterson 1994):

$$\frac{\partial \overline{u}}{\partial x} = \overline{A}\left[\frac{1}{4}\rho g h\left(1 - \frac{\rho_i}{\rho_w}\right)\right]^n. \tag{20}$$

The mass conservation equation is integrated along the vertical to obtain the ice thickness evolution:

$$\frac{\partial h}{\partial t} + \frac{\partial(\overline{u}h)}{\partial x} = \dot{a}, \tag{21}$$

where $\dot{a}$ is the accumulation rate.

There are several ways in which grounding line migration can be treated in a finite-difference model (Gladstone et al. 2010). One way is to determine the grounding line position x_g by linear interpolation between the last grounded grid point position x_i and the first floating point x_{i+1} using the flotation criterion expressed in terms of height above flotation h^*, i.e.

$$x_g = x_i - \frac{h_i^*}{\nabla h^*}, \tag{22}$$

where

$$h_i^* = b_i - z_{sl} + h_i \frac{\rho_i}{\rho_w}, \tag{23}$$

$$\nabla h^* = \frac{h_{i+1}^* - h_i^*}{\Delta x}, \tag{24}$$

and where Δx is the grid size. Ice thickness at the grounding line h_g is then linearly interpolated from its known position x_g. We enabled grounding line migration using (13) combined with the Pollard and DeConto heuristic rule (14) and (15).

3.2 Numerical Implementation

The model was implemented on a fixed finite-difference grid, both in a staggered and a non-staggered version. For the staggered model, velocities are determined between grid points (u-grid), while for the non-staggered version velocities are calculated on the grid points where the ice sheet geometry is available (h-grid). The mass conservation equation (21) is discretized using a semi-implicit scheme and coded as FTCS (forward in time, central in space). This gives for a staggered and a non-staggered grid, respectively

$$h_{i,t+1} + \frac{\Delta t}{2\Delta x}\left[u_{i+\frac{1}{2}}\left(h_{i+1,t+1} + h_{i,t+1}\right) - u_{i-\frac{1}{2}}\left(h_{i-1,t+1} + h_{i,t+1}\right)\right] = h_{i,t} + \dot{a}\Delta t \tag{25}$$

$$h_{i,t+1} + \frac{\Delta t}{2\Delta x}\left[u_{i+1}h_{i+1,t+1} - u_{i-1}h_{i-1,t+1}\right] = h_{i,t} + \dot{a}\Delta t \tag{26}$$

where indices $i = 1{:}N$ are the grid nodes along the flowline, and index t denotes time. For the SIA model, (25–26) are written as a diffusive equation [see Huybrechts et al (1996) for a more detailed description and discussion]. However, the combined diffusive-advective equations lead to mass loss across the grounding line with the non-staggered model, which is not the case with the staggered model, where mass is always conserved along the whole flowline irrespective of the physical model (SIA/SSA or SSA). The effect of mass loss across the grounding line is discussed in Pattyn et al. (2006) and has been shown to have no qualitative impact on grounding line migration.

3.3 Experiments

Vieli and Payne (2005) showed that marine ice sheet FG models were highly sensitive to horizontal grid size. Large grid sizes, for instance, prevent grounding line migration. Only small enough grid sizes lead to grounding line advance (Huybrechts et al. 1998; Vieli and Payne 2005; Durand et al. 2009b). To test the grid size sensitivity, we carried out model experiments with different grid sizes, i.e. 50, 25, 12.5, and 5 km as well as for different physical approximations (SIA/SSA and SSA) and numerical approaches (staggered and non-staggered grids). We compared our model results to the semi-analytical solution derived by Schoof (2007).

The first experiment is a MISMIP variant[3] (Schoof et al. 2007). A steady state geometry is developed on a linearly downward-sloping bedrock defined by

$$b(x) = -100 - x, \tag{27}$$

[3] MISMIP: Marine Ice Sheet Model Intercomparison Project; http://homepages.ulb.ac.be/~fpattyn/mismip/

Table 1 Constants and parameter settings for the first, third and fourth experiments

Parameter	Description	Value	Unit
ρ_i	Ice density	900	kg m^{-3}
ρ_w	Water density	1,000	kg m^{-3}
g	Gravitational acceleration	9.8	m s^{-2}
n	Glen's flow law exponent	3	
a	Accumulation rate	0.3	m a^{-1}
L	Domain length	1,000	km
C	Basal friction coefficient	10^7	Pa s^{m}m^{-m}
m	Basal friction exponent	1/3	

where b is bedrock elevation (m a.s.l.) and x is distance from the ice divide (km). Other parameters and constants are given in Table 1. In the standard experiment, a value for Glen's flow law parameter of $A = 10^{-25}$ Pa^{-n} s^{-1} is used. A steady state is achieved after $\sim$40,000 years of integration. Starting from this steady state configuration (further addressed to as *initial* state), the value for A is decreased (increasing viscosity), leading to an advance of the grounding line. This process is repeated for subsequent changes in A, ranging from 10^{-25} to 10^{-26} in steps of 2×10^{-26}, as well as the reverse process (starting from $A = 10^{-26}$ and decreasing the viscosity in steps of 2×10^{-26}). Each of these step changes takes $\sim$20,000 years to reach a steady state. What is referred to below as *final* state is the steady state after complete advance and retreat and for the value of $A = 10^{-25}$ Pa^{-n} s^{-1}.

The second experiment corresponds to MISMIP Experiment 3a, where a steady state geometry is allowed to develop on an overdeepened polynomial bedrock, defined by

$$b(x) = 729 - 2184.8 \times \left(\frac{x}{750\,\mathrm{km}}\right)^2 + 1031.72 \times \left(\frac{x}{750\,\mathrm{km}}\right)^4 - 151.72 \times \left(\frac{x}{750\,\mathrm{km}}\right)^6. \quad (28)$$

The flow parameter A is varied stepwise between 3×10^{-25} and 2.5×10^{-26} Pa^{-n} s^{-1}. Other parameters are similar to those of the previous experiment, except for the domain length, taken as $L = 1800$ km and the basal sliding parameter set to $C = 7.624 \times 10^6$ Pa s^m m^{-m}.

In the third experiment, we used the same linearly downward-sloping bed (27) and same constants as in the first experiment above (Table 1). We started from an initial steady state ice sheet with $A = 10^{-25}$ Pa^{-n} s^{-1}. The bulk viscosity of the ice sheet was increased by setting $A = 4 \times 10^{-26}$ Pa^{-n} s^{-1}, leading to a grounding line advance, until a new steady state was reached. Subsequently, the viscosity was decreased by setting $A = 10^{-25}$ Pa^{-n} s^{-1}, invoking a grounding line retreat to the initial state.

A major drawback of the Schoof solution is its validity restricted to steady state solutions and not to transient states. However, grounding line migration rate is a major issue when trying to understand marine ice sheet response over decadal time scales (as needed in IPCC projections). The transient response of the grounding line should therefore be independent of numerical parameters, such as grid resolution and time step, and should be coherent with theoretical developments. Therefore, we performed a fourth experiment to investigate the time-dependent response by evaluating ice fluxes across the grounding line with theoretical values (i.e. Schoof solution) and grounding line migration rate during grounding line advance and retreat for a staggered SSA model. We used the same setup and parameters as the third experiment above (i.e. linearly downward-sloping bed), except

that we used 5 values of rate factor A instead of 3 in order to compare the transient behavior with the same viscosity for the advance and the retreat. These values are, respectively, 10^{-25}, 4×10^{-26}, 10^{-26}, 4×10^{-26} and 10^{-25} $\mathrm{Pa}^{-n}\ \mathrm{s}^{-1}$.

4 Results

4.1 Effect of Grid Resolution on Steady State Grounding Line Position

4.1.1 Downward-Sloping Bed

Figure 2 shows the steady state profiles of the ice sheet and ice shelf along the flowline for both the linearly downward-sloping and the overdeepened bedrock profiles (staggered SSA model). Grounding line advance is obtained when decreasing the value of A, and a retreat is invoked when A is increased to its initial value. Advance and retreat steady state profiles are hardly discernible, as both are lying close together. According to theory (Schoof 2007a), they should overlap, which defies neutral equilibrium of grounding line positions.

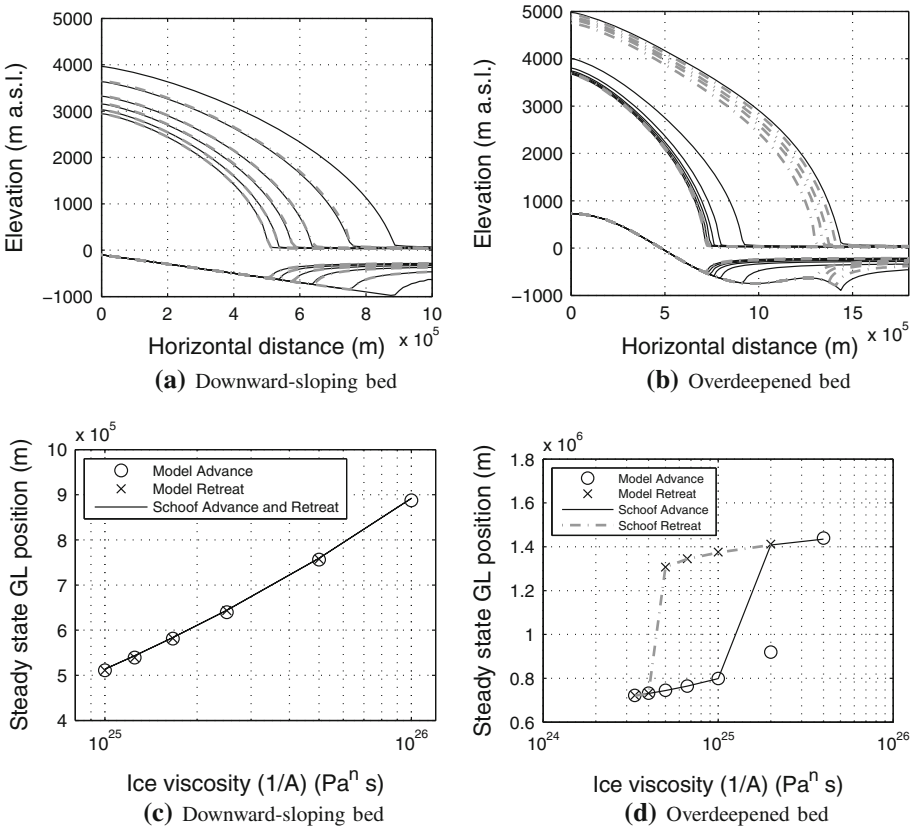

Fig. 2 Steady state profiles (*solid black curve* advance; *dashed gray curve* retreat) of the ice sheet on a downward-sloping bed (**a** and **c**) and on an overdeepened bed (**b** and **d**) for the SSA model on a staggered grid (first and second experiments). Grid size is 12.5 km in both cases. GL means 'grounding line'

When analyzing the differences between final (after perturbation of A) and initial steady state grounding line positions as well as the differences between final steady state grounding line positions and Schoof semi-analytical solution for the whole suite of grid resolutions as well as for the different physical and numerical approximations, it becomes clear that staggered grid models generally perform well in reproducing advance and retreat of the grounding line with high accuracy (Table 2). Especially the SSA staggered grid model displays differences between grounding line positions of the order of meters to tens of meters, which is a fraction of the grid size. Furthermore, there is no apparent relation between the accuracy and grid resolution. The same conclusions can be drawn for the SIA/SSA staggered grid model, albeit that differences are an order of magnitude larger, but still small compared to the grid size. The non-staggered grid model, on the contrary, shows the largest discrepancies in which differences are of the order of magnitude of the grid size (and therefore decreasing with decreasing grid size). Similar tests were also performed with staggered SSA and SIA/SSA models that do not include the Schoof boundary condition (not shown). They also reveal large discrepancies between the advance and retreat steady state positions and in the majority of the experiments the grounding line hardly retreats when A is set to its initial value.

In summary, all staggered grid models that are forced with the Schoof boundary condition converge to the same steady state grounding line position irrespective of the horizontal grid size used. Models that are either non-staggered or do not include the boundary condition converge only to the same advance-retreat position for sufficiently small grid sizes, which is considered a deficiency of fixed grid finite-difference models (Vieli and Payne 2005; Durand et al. 2009b; Gladstone et al. 2010). Results also depend on model type, i.e. the SSA model gives better results (difference between final and initial grounding line positions is less) compared to SIA/SSA (Table 2).

Table 2 Absolute differences between final (after perturbation of A) and initial steady state grounding line (GL) positions ($\Delta FI = |GL_{\text{Final}} - GL_{\text{Initial}}|$) and absolute differences between final steady state GL positions and Schoof semi-analytical solution ($\Delta FS = |GL_{\text{Final}} - GL_{\text{Schoof}}|$) as a function of grid size for the SSA staggered grid model, SIA/SSA staggered grid model and SIA/SSA non-staggered grid model

Physical approx.	Grid type	Grid size (m)	Runs	$\Delta FI(\sigma)$ (m)	$\Delta FS(\sigma)$ (m)
SSA	Staggered	50000	4	3.17 (3.74)	7020 (3018)
SSA	Staggered	25000	4	28.01 (38.05)	4567 (1287)
SSA	Staggered	12500	4	6.54 (9.27)	3194 (793)
SSA	Staggered	5000	2	0.94 (0.32)	2015 (231)
SIA/SSA	Staggered	50000	2	127.39 (116.48)	9616 (1405)
SIA/SSA	Staggered	25000	2	165.26 (36.83)	5750 (476)
SIA/SSA	Staggered	12500	1	65.57 (0)	2905 (0)
SIA/SSA	Non-staggered	50000	5	58610 (15388)	73243 (8378)
SIA/SSA	Non-staggered	25000	5	25901 (7974)	54154 (4602)
SIA/SSA	Non-staggered	12500	5	8983 (2367)	43904 (2365)
SIA/SSA	Non-staggered	5000	5	1413 (1144)	37529 (712)

Instead of performing only one model run per grid size, we performed a series of model runs for a 'nominal' grid size in which the initial grid size was slightly altered by adding/subtracting 1 or 2 grid points for the whole flowline, thereby keeping the flowline length constant. Standard deviation (σ) is indicated in brackets. These results correspond to the third experiment (linearly downward-sloping bedrock and 3 A values)

Even though modeled grounding line position is unique for each set of parameter values, deviations from the Schoof semi-analytical solution may occur. These differences decrease with decreasing grid size (Table 2). Since the Schoof semi-analytical solution is based on boundary layer theory, these positions do not necessarily have to coincide with the steady state positions for the different model types, as other physics are involved. Nevertheless, the difference is not more than a couple of kilometers for the staggered grid models, since all models are forced with the boundary condition from Schoof (2007a). In concordance with the above results, SIA/SSA models show a larger deviation from the Schoof solution and the non-staggered model deviates with several tens of kilometers.

4.1.2 Overdeepened Bed

For an overdeepened bed, multiple steady states occur for the same value of A as a function of the initial geometry of the ice sheet. This is due to the fact that no steady states are found on upward-sloping beds (Schoof 2007a), leading to hysteresis (Fig. 2b, d). In general, conclusions reached in "Subsect. 4.1.1" are also valid here, i.e. initial and final grounding line positions show differences of the order of meters to tens of meters with the staggered SSA model, while large deviations—also related to grid size, occur for either SIA/SSA and non-staggered grid models (not shown).

4.2 Grounding Line Migration Rate

Figure 3 displays the grounding line flux as a function of time during the advance (Fig. 3a) and the retreat (Fig. 3b) compared to the flux determined from (13). Since the value of rate factor A is the same for both advance and retreat, the ice flux converges towards the same value in Fig. 3a and b. Both solutions show a series of distinct jumps in time that are mainly due to the intrinsic discrete nature of the heuristic rule in (14–15), which causes flips between grid points for arbitrarily small changes of ice flux. These discrete steps cannot be removed despite the interpolating grounding line function (22). For an advancing ice sheet, the difference between the modeled and semi-analytical fluxes is relatively small. However, during retreat sudden high amplitude increases in grounding line flux occur with the SSA model. The peaks can be visualized in more detail in Fig. 3d, where ice fluxes are plotted against grounding line ice thickness. Nevertheless, after these jumps the modeled fluxes converge toward the fluxes determined from (13). Since the Schoof flux given by (13) is valid for steady state conditions and derived from boundary layer theory, deviations from this semi-analytical flux during a transient state do not indicate whether the model results are pertinent or not.

A sound way of evaluating grounding line migration rate is to compare the migration rate obtained with the model with the one calculated from differentiating the flotation criterion (Hindmarsh 1993), i.e.

$$\frac{dx_g}{dt} = -\frac{\dot{a} - \frac{\partial q}{\partial x}}{\frac{\partial h}{\partial x} + \frac{\rho_w}{\rho_i}\frac{\partial b}{\partial x}} \tag{29}$$

We solved (29) numerically by calculating both the flux divergence and the thickness gradient with a three-point upstream difference scheme centered on the sub-grid grounding line position x_g (Fig. 3e and f). A distinction is made based on the heuristic rule (14) or (15). Circles in the scatterplot correspond to the case where the grounding line flux is larger than the flux obtained from (13), generally leading to a grounding line advance. Crosses

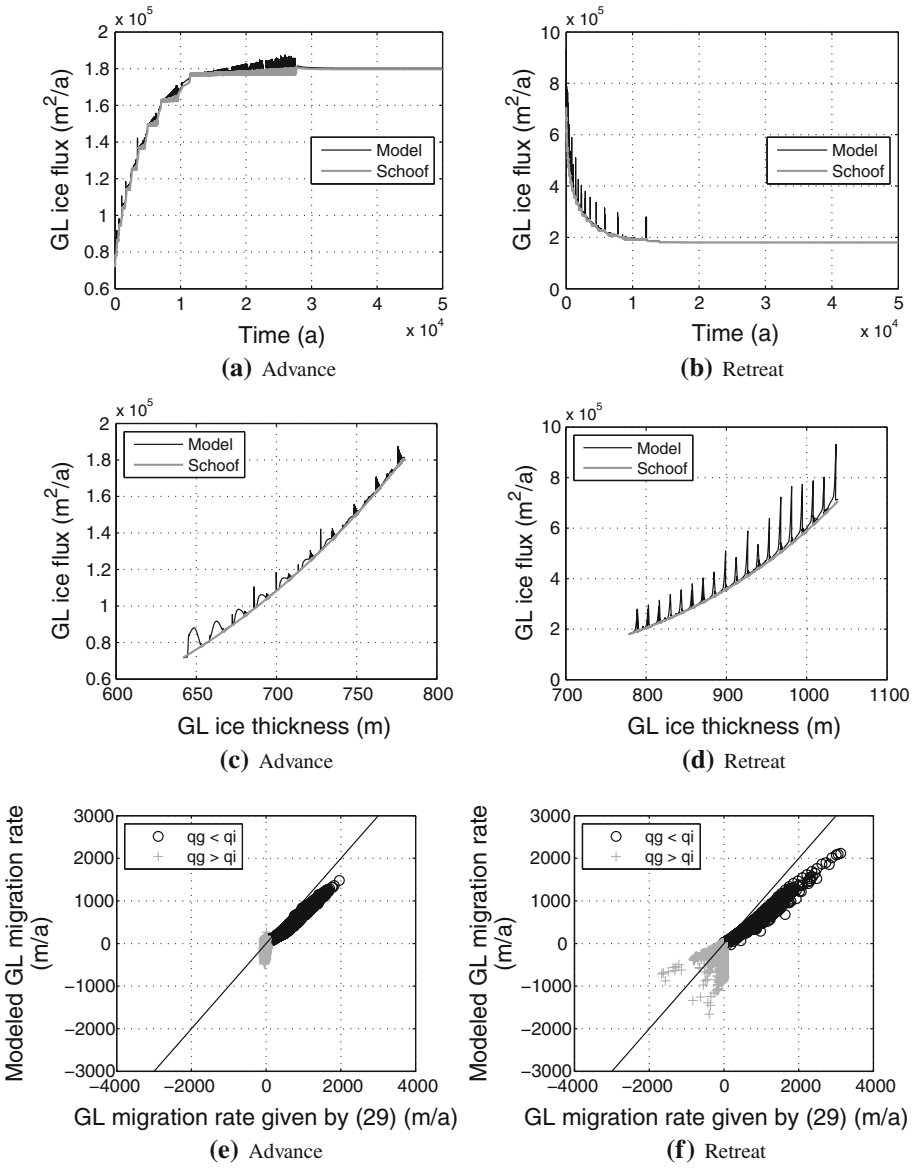

Fig. 3 Modeled grounding line (GL) flux compared to Schoof GL flux as a function of time (**a** and **b**) and GL ice thickness (**c** and **d**; fourth experiment). Modeled GL migration rate (dx_g/dt) is also plotted against GL migration rate given by (29). Left plots show the advance stage (A decreases from 10^{-25} to 4×10^{-26} $\mathrm{Pa}^{-n}\,\mathrm{s}^{-1}$), while right plots show the retreat stage (A increases from 10^{-26} to 4×10^{-26} $\mathrm{Pa}^{-n}\,\mathrm{s}^{-1}$). Grid size is 12.5 km

correspond to the inverse case [grounding line flux smaller than the flux obtained from (13)]. For both advance and retreat experiments, grounding line changes in either direction occur, albeit that negative migration rates are generally absent for the advancing case (Fig. 3e).

In general there are many more 'retreat' points (crosses) than there are 'advance' points (circles). The heuristic rule compares the modeled ice flux to the theoretical flux and adapts the modeled velocity field accordingly. Any 'advance' flux condition will alter the flow field considerably, and result in an important change in grounding line position as well as in glacier geometry. However, during the following time steps the flux at the grounding line will be too low compared to the theoretical one and slight adjustments to the jump in grounding line position are made (retreat), to compensate for the larger initial jump. These changes happen evidently on sub-grid level, leading to a negative migration rate. Therefore, during an advance phase, small 'retreat' changes can be observed, simply to counterbalance large changes due to the imposition of the grounding line flux. This also explains why during an advance phase small episodes of grounding line retreat can be observed, while according to theory, this should be zero (Fig. 3e). Both Fig. 3e and f show that modeled advance rates correspond well with the theoretical value, but are slightly underestimated, while the modeled retreat rates show a larger discrepancy, probably related to this so-called counterbalancing effect.

A similar experiment was carried out for a smaller grid size (6.25 km, Fig. 4). The behavior is coherent in the sense that, due to the higher resolution, jumps in grounding line flux occur more often, but they are of smaller amplitude. The comparison of modeled grounding line migration rates with the calculated ones leads to a similar graph as in the previous experiment. Migration rates are comparable and invariant for the grid size applied, albeit slightly lower than those determined from (29).

5 Discussion and Outlook

Representing grounding line migration in numerical ice sheet models remains an arduous task, not only because of the complexity of the physics involved (change from shear dominated flow to flow dominated by longitudinal pulling or stretching), the geometry of the problem (a grounding line is difficult to identify within a numerical model as it does not always coincide with a grid node), the computational challenge (solving a complex set of equations on a high-resolution mesh), but also the difficulty to observe and attribute the process of grounding line migration due to different interacting mechanisms, such as sub-shelf melting, loss of buttressing, inland ice flow acceleration due to basal sliding, ice thinning, etc. All these processes may cause grounding line retreat, but a number of them are at the same time a result of grounding line retreat as well, hence leading to a series of feedbacks. Therefore, observations alone are not sufficient to disentangle the mechanisms involved. Nowadays, the gap in our understanding has been filled by advances in time-dependent observations, numerical modeling and tools for model verification.

Only recently the debate on grounding line stability has moved onto the next level with the mathematical proof on grounding line steady state position as a function of ice flux and topography (Schoof 2007a), leading to a verification and intercomparison exercise for numerical ice sheet models (Schoof et al. 2007). In this paper we compared numerical results obtained with simple ice sheet models against the semi-analytical solutions proposed by Schoof et al. (2007), revealing the necessity of having numerical models with sound numerical treatments and proper physical approximations. Although the semi-analytical solution is only valid for steady states, the transient behavior of the model has been analyzed by different means.

The results presented in this paper are obtained with a couple of simple ice sheet/ice shelf models that capture the essence of grounding line migration by including the heuristic

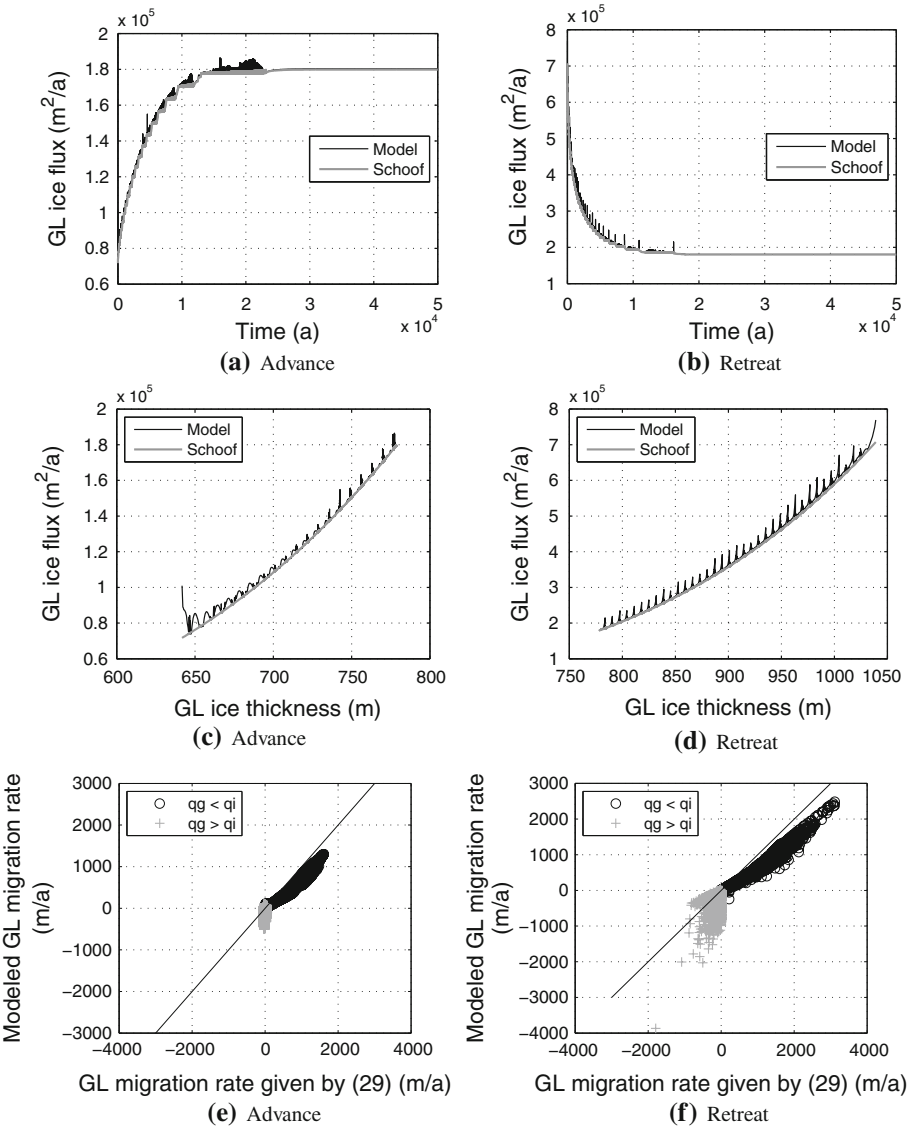

Fig. 4 Same as figure 3 with a grid size of 6.25 km

rule proposed by Pollard and DeConto (2009). The latter assures that modeled grounding line positions are in accord with the steady state grounding line positions given by Schoof (2007a). Ice sheet models on a staggered grid perform well and lead to high accuracy on steady state grounding line position (comparing advancing to retreating ice sheets). Non-staggered grid models lead to larger differences and accuracy increases with decreasing grid size. This poorer performance may be related to mass loss occurring at the grounding line while coupling a diffusive with an advective scheme, as discussed in Pattyn et al. (2006).

The time-dependent response of these models remains influenced by the parameterization scheme of grounding line migration, leading to sudden changes in grounding line ice flux whenever a jump from one grid point to another occurs, despite the sub-grid representation of grounding line position in the model. However, the bulk response in grounding line migration rate is coherent when compared with those expected from differentiating the flotation criterion at the grounding line (Hindmarsh 1993), albeit that modeled migration rates are generally underestimated.

A major drawback of the models presented in this paper is their limitation along a flowline. Although buttressing effects can be included in a parameterized way (Vieli and Payne 2005; Pattyn et al. 2006), real three-dimensional effects are lacking. A number of three-dimensional models that cope with grounding line migration in a verified way have been developed or are in the process of development (Pollard and DeConto 2009; Goldberg et al. 2009; Robison et al. 2009; Katz and Worster 2010), where the Pollard and DeConto model incorporates the heuristic rule as in the above experiments. A more detailed comparison with higher-order and Full Stokes models should be carried out in order to remove any bias towards the use of such types of models. International efforts, such as *ice2sea*[4] or *SeaRISE*,[5] are pushing the ice sheet model community to developing better and physically-based numerical ice sheet models for future sea-level change projections. Once such models are fully available, a physically-based assessment will be possible, making the use of selective grounding line migration scenarios obsolete.

Acknowledgments This work was supported by both the IceCube-Dyn project (Actions de recherche concertées) funded by the French Community of Belgium and the ice2sea project funded by the European Commission's 7th Framework Programme through grant 226375 (ice2sea manuscript No. 20). The authors are greatly indebted to Gael Durand for his constructive review and to David Pollard who pointed out an error in the initially submitted manuscript.

References

Baral DR, Hutter K, Greve R (2001) Asymptotic theories of large-scale motion, temperature, and moisture distribution in land-based polythermal ice sheets: a critical review and new developments. Appl Mech Rev 54(3):215–256

Blatter H (1995) Velocity and stress fields in grounded glaciers: a simple algorithm for including deviatoric stress gradients. J Glaciol 41(138):333–344

Chen JL, Wilson CR, Blankenship D, Tapley BD (2009) Accelerated Antarctic ice loss from satellite gravity measurements. Nat Geosci 2:859–862

Durand G, Gagliardini O, de Fleurian B, Zwinger T, Meur EL (2009a) Marine ice sheet dynamics: hysteresis and neutral equlibrium. J Geophys Res 114(F03009):170. doi:10.1029/2008JF001

Durand G, Zwinger T, Meur EL, Hindmarsh RCA (2009b) Full stokes modeling of marince ice sheets: influence of the grid size. Ann Glac 50(2)

Gladstone RM, Payne AJ, Cornford SL (2010) Parameterising the grounding line in ice sheet models. Cryosphere Discuss 4:1063–1105

Goldberg D, Holland DM, Schoof C (2009) Grounding line movement and ice shelf buttressing in marine ice sheets. J Geophys Res 114(F024026):227. doi:10.1029/2008JF001

[4] ice2sea is a science programme that is funded by the European Union Framework-7 scheme and will improve projections of the contribution of ice to future sea-level rise, http://www.ice2sea.eu.

[5] SeaRISE (Sea-level Response to Ice Sheet Evolution) is a community organized effort to estimate the upper bound of ice sheet contributions to sea level in the next 100–200 years, http://websrv.cs.umt.edu/isis/index.php/SeaRISE_Assessment.

Herterich K (1987) On the flow within the transition zone between ice sheet and ice shelf. In: Veen C, Oerlemans J (eds) Dynamics of the west Antarctic ice sheet. Kluwer Academic Publishers, Dordrecht, pp 185–202
Hindmarsh RCA (1993) Qualitative dynamics of marine ice sheets. In: Peltier W (ed) Ice in the climate system, NATO ASI series I , vol 12. Springer, Berlin, pp 67–99
Hindmarsh RCA (1996) Stability of ice rises and uncoupled marine ice sheets. Ann Glaciol 23:105–115
Hindmarsh RCA (2004) A numerical comparison of approximations to the Stokes equations used in ice sheet and glacier modeling. J Geophys Res 109(F01012):065. doi:10.1029/2003JF000
Hindmarsh RCA (2006) The role of membrane-like stresses in determining the stability and sensitivity of the Antarctic ice sheets: back pressure and grounding line motion. Phil Trans R Soc A 364:1733–1767
Hindmarsh RCA, Le Meur E (2001) Dynamical processes involved in the retreat of marine ice sheets. J Glaciol 47(157):271–282
Hutter K (1983) Theoretical glaciology. Kluwer Academic Publishers, Dordrecht
Huybrechts P (1990) A 3-D model for the Antarctic ice sheet: a sensitivity study on the glacial-interglacial contrast. Climate Dyn 5:79–92
Huybrechts P, Payne A, TheEISMINT Intercomparison Group (1996) The EISMINT benchmarks for testing ice-sheet models. Ann Glaciol 23:1–12
Huybrechts P, Abe-Ouchi A, Marsiat I, Pattyn F, Payne A, Ritz C, Rommelaere V (1998) Report of the third EISMINT workshop on model intercomparison. European Science Foundation, Strasbourg
Jenkins A, Dutrieux P, Jacobs S, McPhail S, Perrett J, Webb A, White D (2010) Observations beneath Pine Island Glacier in West Antarctica and implications for its retreat. Nat Geosci 3(7):468–472
Joughin I, Rignot E, Rosanova CE, Lucchitta BK, Bohlander J (2003) Timing of recent accelerations of Pine Island Glacier, Antarctica. Geophys Res Lett 30(13):609. doi:10.1029/2003GL017
Katz RF, Worster MG (2010) Stability of ice-sheet grounding lines. Proc R Soc A. doi:10.1098/rspa.2009.0434
Lestringant R (1994) A two-dimensional finite-element study of flow in the transition zone between an ice sheet and an ice shelf. Ann Glaciol 20:67–72
MacAyeal DR (1992) Irregular oscillations of the West Antarctic ice sheet. Nature 359:29–32
MacAyeal DR, Rommelaere V, Huybrechts P, Hulbe CL, Determann J, Ritz C (1996) An ice-shelf model test based on the Ross ice shelf. Ann Glaciol 23:46–51
Paterson WSB (1994) The physics of flaciers, 3rd edn. Pergamon Press, Oxford
Pattyn F (2000) Ice-sheet modelling at different spatial resolutions: focus on the grounding line. Ann Glaciol 31:211–216
Pattyn F (2003) A new 3D higher-order thermomechanical ice-sheet model: basic sensitivity, ice-stream development and ice flow across subglacial lakes. J Geophys Res 108(B8, 2382):329. doi:10.1029/2002JB002
Pattyn F, Huyghe A, De Brabander S, De Smedt B (2006) Role of transition zones in marine ice sheet dynamics. J Geophys Res 111(F02004):394. doi:10.1029/2005JF000
Pollard D, DeConto RM (2009) Modelling West Antarctic ice sheet growth and collapse through the past five million years. Nature 458:809. doi:10.1038/nature07
Rignot E, Bamber JL, van den Broeke MR, Davis C, Li Y, van de Berg WJ, van Meijgaard E (2008) Recent Antarctic ice mass loss from radar interferometry and regional climate modelling. Nat Geosci 1:106–110
Rignot E, Velicogna I, van den Broeke MR, Monaghan A, Lenaerts J (2011) Acceleration of the contribution of the Greenland and Antarctic ice sheets to sea level rise. Geophys Res Lett 38(L05503):583. doi:10.1029/2011GL046
Ritz C, Rommelaere V, Dumas C (2001) Modeling the evolution of the Antarctic ice sheet over the last 420000 years: implications for altitude changes in the Vostok region. J Geophys Res 106(D23):31943–31964
Robison RAV, Huppert HE, Worster MG (2009) Dynamics of viscous grounding lines. J Fluid Mech 648:363–380. doi:10.1017/S0022112009993119
Schoof C (2007a) Ice sheet grounding line dynamics: steady states, stability and hysteresis. J Geophys Res 112(F03S28):664. doi:10.1029/2006JF000
Schoof C (2007b) Marine ice sheet dynamics. Part I. The case of rapid sliding. J Fluid Mech 573:27–55
Schoof C, Hindmarsh R (2010) Thin-film flows with wall slip: an asymptotic analysis of higher order glacier flow models. Quart J Mech Appl Math 63(1):73–114
Schoof C, Pattyn F, Hindmarsh R (2007) Benchmarks and intercomparison program for marine ice sheet models. Geophysical Research Abstracts 9(EGU2007-A-04644)
Shepherd A, Wingham DJ, Mansley JAD, Corr HFJ (2001) Inland thinning of Pine Island Glacier, West Antarctica. Science 291:862–864

Thomas RH, Bentley CR (1978) A model for holocene retreat of the West Antarctic ice sheet. Quat Res 10:150–170

Velicogna I (2009) Increasing rates of ice mass loss from the Greenland and Antarctic ice sheets revealed by GRACE. Geophys Res Lett 36(L19503):222. doi:10.1029/2009GL040

Vieli A, Payne A (2005) Assessing the ability of numerical ice sheet models to simulate grounding line migration. J Geophys Res 110(F01003):202. doi:10.1029/2004JF000

Weertman J (1974) Stability of the junction of an ice sheet and an ice shelf. J Glaciol 13:3–11

Wingham DJ, Wallis DW, Shepherd A (2009) Spatial and temporal evolution of Pine Island Glacier thninning, 1995–2006. Geophys Res Lett 36(L17501):126. doi:10.1029/2009GL039

Surv Geophys (2011) 32:437–458
DOI 10.1007/s10712-011-9132-4

Understanding and Modelling Rapid Dynamic Changes of Tidewater Outlet Glaciers: Issues and Implications

Andreas Vieli · Faezeh M. Nick

Received: 5 November 2010 / Accepted: 16 May 2011 / Published online: 10 June 2011

Abstract Recent dramatic acceleration, thinning and retreat of tidewater outlet glaciers in Greenland raises concern regarding their contribution to future sea-level rise. These dynamic changes seem to be parallel to oceanic and climatic warming but the linking mechanisms and forcings are poorly understood and, furthermore, large-scale ice sheet models are currently unable to realistically simulate such changes which provides a major limitation in our ability to predict dynamic mass losses. In this paper we apply a specifically designed numerical flowband model to Jakobshavn Isbrae (JIB), a major marine outlet glacier of the Greenland ice sheet, and we explore and discuss the basic concepts and emerging issues in our understanding and modelling ability of the dynamics of tidewater outlet glaciers. The modelling demonstrates that enhanced ocean melt is able to trigger the observed dynamic changes of JIB but it heavily relies on the feedback between calving and terminus retreat and therefore the loss of buttressing. Through the same feedback, other forcings such as reduced winter sea-ice duration can produce similar rapid retreat. This highlights the need for a robust representation of the calving process and for improvements in the understanding and implementation of forcings at the marine boundary in predictive ice sheet models. Furthermore, the modelling uncovers high sensitivity and rapid adjustment of marine outlet glaciers to perturbations at their marine boundary implying that care should be taken in interpreting or extrapolating such rapid dynamic changes as recently observed in Greenland.

Keywords Tidewater outlet glaciers · Cryosphere · Greenland · Calving · Ice sheet modelling

A. Vieli (✉)
Department of Geography, Durham University, Durham DH1 3LE, United Kingdom
e-mail: andreas.vieli@durham.ac.uk

A. Vieli
Versuchsanstalt für Wasserbau, Hydrologie und Glaziologie, ETH Zürich, 8092 Zurich, Switzerland

F. M. Nick
Laboratoire de Glaciologie, Université Libre de Bruxelles, 1050 Bruxelles, Belgium
e-mail: fmnick@ulb.ac.be

1 Introduction

Tidewater outlet glaciers are narrow, fast flowing major drainage channels of ice sheets and polar ice caps that terminate in ocean fjords where the ice is calved off as icebergs. They flow through deep channels with beds well below sea-level and widths of only a few kilometers and they have speeds of several hundreds of meters to a few kilometers per year (Joughin et al. 2010a). In the recent decade many of such tidewater outlet glaciers in Greenland have strongly increased their flow speed (Rignot and Kanagaratnam 2006; Howat et al. 2007; Joughin et al. 2010a) and their surfaces started to thin rapidly (Pritchard et al. 2009; Thomas et al. 2009; Krabill et al. 2004; Abdalati et al. 2001). For example the three major Greenland outlet glaciers of Jakobshavn Isbrae (JIB) in the West and Helheim Glacier and Kangerdlugssuaq Glacier in the southeast have almost doubled their speed in recent years, they thinned dramatically with rates of tens of meters per year and their terminus retreated by several kilometers (Howat et al. 2007; Stearns and Hamilton 2007; Joughin et al. 2004, 2008a, 2008c, 2010a). The latter two, however, recently started to slow-down and readvance again (Howat et al. 2007; Murray et al. 2010).

These dramatic dynamic changes raised concern regarding Greenland's contribution to future sea level rise (IPCC 2007; Alley et al. 2005). Such dynamic mass loss has been estimated to contribute to sea level at a rate of 0.25 mm a^{-1} between 2003 and 2008 which is comparable with the mass loss through surface melt of the entire ice sheet and is significant in the sea level budget (Van den Broeke et al. 2009). Although oceanic warming has been suggested as the dominant trigger of such changes (Straneo et al. 2010; Holland et al. 2008; Rignot et al. 2010), the forcing mechanisms and controlling processes are not well understood and current large scale ice-sheet models are unable to realistically simulate these rapid dynamic changes (Alley et al. 2005; Bamber et al. 2007). In the Fourth IPCC Assessment Report, the contribution from dynamic mass loss have therefore been excluded and consequently sea-level projections appear to be underestimated but such dynamic change from marine outlet glaciers has been identified as a major limitation in our ability to assess future sea level (IPCC 2007).

Large scale ice sheet models that are typically used in prognostic assessments of Greenland's contribution to future sea-level have spatial resolutions of 5–10 km, with recent efforts pushing towards 1 km (Seddik et al. 2010; Gillet-Chaulet et al. 2011). This, is simply not enough to spatially resolve most of these very narrow and deep outlet glacier channels and, furthermore, the depth and detailed basal topography is still unknown for many of them. In recent years, clear advances have been made in terms of process representation within these models such as a more robust treatment of grounding line motion (Docquier et al. 2011; Pollard and DeConto 2009; Schoof 2007) and including fast ice flow and ice streaming by considering higher-order stresses to include longitudinal stress transfer (Bueler and Brown 2009; Pattyn 2003; Price et al. 2011; Pattyn et al. 2008), but most of these models are not yet fully operational on the required spatial resolution of outlet glaciers (Stone et al. 2010). And, importantly, major deficiencies remain in their representation of processes acting at the marine boundary such as calving and ocean melt. Some of these issues have been overcome in spatially reduced models that are specifically designed for single outlet glacier basins (Nick et al. 2009; Dupont and Alley 2005; Thomas 2004; Joughin et al. 2010b); however, such models cannot be generalized to an ice-sheet wide application and uncertainties in the forcing processes remain.

On the basis of such a reduced 1-dimensional flowband model applied to the example of JIB, this paper aims to explore and discuss the basic concepts and emerging issues in our understanding and predictive ability of the dynamics of tidewater outlet glaciers. We do

not attempt here to give a complete review on this topic but, rather, we will focus on issues and implications investigated and informed by our modelling experiments, and with a particular view on the recent rapid changes and their potential contribution to future sea level rise.

1.1 Jakobshavn Isbrae

JIB's acceleration was one of the earliest of the outlet glaciers in Greenland to be detected in the satellite era and was in parallel with the onset of a rapid retreat of its 15 km long floating ice tongue. Before, its flow of about 6 km a^{-1} near the grounding line (Fig. 1c) and its terminus position were relatively stable with only small seasonal fluctuations (Joughin et al. 2008c; Sohn et al. 1998; Echelmeyer et al. 1990; Luckman and Murray 2005). This changed in 1997 when a rapid retreat of the terminus set in, with some re-advance in 2001, and reaching almost complete disintegration of the floating ice tongue

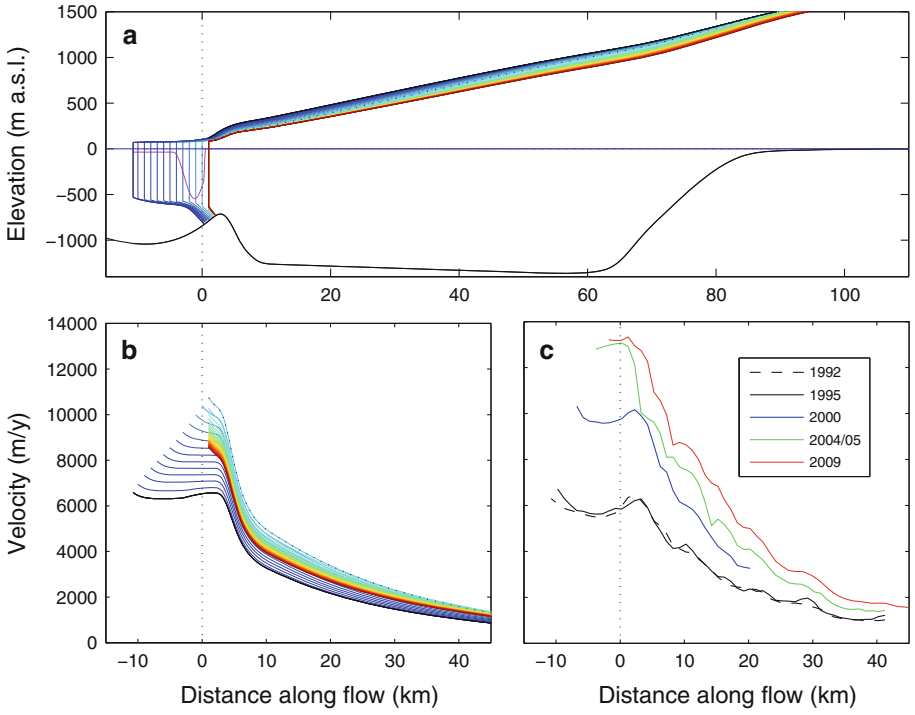

Fig. 1 **a** Profiles along the main channel of JIB showing **a** geometry and **b** modelled and **c** observed flow speed for a prescribed gradual retreat of 12 km over 6 years. The along flow distance is measured from the pre-retreat grounding line position. In **a** the *black line* shows the smoothed basal topography used in the model and the *coloured lines* show the modelled surface with time and go from *black* (initial unperturbed steady state surface) over *dark blue*, *light blue*, *green*, *yellow* to *red*, with time intervals of 0.5 years and over a total period of 20 years. The *dotted line* marks the time at 6 years when the retreat in the experiment was stopped. The *magenta line* indicates the prescribed basal melt rate pattern at the underside of the floating ice tongue in (m a^{-1}) with the origin at sea-level. **b** Profiles of modelled centreline flow speed over time using the same colour-coding as in **a**. **c** Observed profiles of along flow speed from satellite interferometry (from Joughin et al. 2004, 2010a and updated using recent TerraSAR-X observations, I. Joughin, personal comm.)

in 2004. During this retreat, JIB almost doubled its speed (Fig. 1c) and induced surface thinning with rates of up to 20 m a^{-1} near the terminus (Joughin et al. 2008c; Thomas et al. 2003, 2009). Further a strong seasonal variation in speed (Luckman and Murray 2005) and terminus position developed with summer retreat and winter re-advance in the order of 5–6 km (Joughin et al. 2008c). The thinning and speed-up have been observed to successively propagate and diffuse inland but is most pronounced in the main deep channel (Joughin et al. 2008c; Thomas et al. 2009). Currently the terminus position and grounding line is still near a relatively shallow sill but, behind, the bed deepens rapidly into a deep bedrock trough that reaches 70 km inland (Fig. 1a) and carries the potential for rapid unstable retreat in the near future (Hughes 1986; Weertman 1974; Vieli et al. 2001) As a trigger for its rapid retreat, ocean related processes such as changes in sea-ice concentration or subsurface melt at the ice ocean contact seem currently most plausible (Holland et al. 2008; Joughin et al. 2008c; Lloyd et al. 2011), but the linking processes at this marine boundary are still not well understood.

2 The Model

The model is described in detail in Nick et al. (2009, 2010) and is applied to an approximate case of the main channel of Jakobshavn Isbrae. It simulates the flow and surface evolution of JIB in a flowband along the main channel and includes basal and lateral resistance and transfer of stresses along the glacier through longitudinal stresses. The lateral resistance is parametrized by integrating the horizontal shear stress over the channel width (Van der Veen and Whillans 1996). For basal flow a non-linear Weertman-type sliding relation is assumed that includes effective pressure dependency (Fowler 2010). The model further includes a robust treatment of grounding line motion and a dynamic calving model based on a criterion of crevasse depth which in turn is a function of along flow strain rate (Nick et al. 2010; Benn et al. 2007). For basal topography a smoothed version of the high resolution dataset of CReSIS (https://www.cresis.ku.edu/plummer/jakob.html) is used and a fixed spatial basal melt pattern beneath the floating ice tongue is assumed based on estimates by Motyka et al. (2011) and outlined in Fig. 1a. A rate factor corresponding to −5 degree ice temperature has been assumed but has been softened by a factor of 2.5 in the side drag term to account for lateral shear softening. The model uses a moving grid that follows its ice front continuously and has an approximate along flow grid size of 250 m. The basal friction parameter has different values in the bed trough and upstream under the main ice sheet and additionally depends on effective pressure. It has been been tuned to correspond to the pre-1997 flow and surface geometry when the model is run to steady state. Thus, for the model experiments that follow below, the initial geometry (surface, ice front and grounding line position) is stable without any change in the boundary conditions.

3 Dynamic Adjustment

Recent rapid dynamic changes of marine based outlet glaciers around Greenland have the typical characteristics of calving front retreat in combination with strong flow acceleration and rapid surface thinning that propagates upstream with time (Joughin et al. 2008c, 2010a; Murray et al. 2010; Howat et al. 2007). Similarly, as a response to the collapse of the Larsen B ice shelf in the Antarctic Peninsula, strong acceleration and thinning have been observed for its former tributary glaciers (Rignot et al. 2004; Scambos et al. 2004).

This pattern of change suggests an initiation at the terminus with the most likely causing process being terminus retreat and the concurrent loss of buttressing from the terminus area (Nick et al. 2009; Howat et al. 2007; Joughin et al. 2008c; Thomas 2004). Recent research suggests that enhanced lubrication of the glacier bed from increased surface melt due to atmospheric warming is for fast-flowing outlet glaciers no major control (Joughin et al. 2008b; Nick et al. 2009; Murray et al. 2010; Schoof 2010), although it may be relevant for slower flowing grounded ice sheet margins (Zwally et al. 2002; Bartholomew et al. 2010) and therefore this process is in this paper not discussed much further. The observed acceleration and surface thinning that propagate upstream can in simple terms therefore be considered as a dynamic adjustment to a change in the boundary condition at the marine terminus. Regarding the abruptness in onset and the high rates of mass loss it is crucial in the wider context of potential sea-level contribution to discuss the process of dynamical adjustment and, importantly, the involved time scales.

Any retreat of the calving front leads to an instantaneous redistribution of stresses as the removed part of the terminus can no longer provide resistance to the upstream ice. This loss in buttressing induces an instantaneous acceleration in flow at the terminus which is transfered some distance upstream through longitudinal stresses. This longitudinal coupling distance is typically about 10 ice thicknesses and for outlet glaciers in the order of 5–20 km. The acceleration at the terminus increases the ice flux and initiates a thinning, which steepens the surface, increases the driving stress and leads to further acceleration. Through this feedback between acceleration and driving-stress the thinning is then propagating upstream with time (Payne et al. 2004; Joughin et al. 2003, 2008c). This thinning is a direct consequence of mass conservation and readjusts the flux back towards the pre-perturbation state in order to compensate for the mass loss. As a result, the flow and thinning start to slow down rapidly from the terminus after the retreat ceased whereas upstream it is still increasing although with reduced rates (Nick et al. 2009).

This dynamic adjustment is illustrated in Fig. 1 at the example of a prescribed gradual retreat of the floating ice tongue of JIB from its stable pre-1997 position by an annual rate of 2 km a^{-1} over a total period of 6 years. The successive retreat provides a gradual reduction of buttressing from the floating ice tongue and leads to a continuous increase in speed that is transferred upstream through longitudinal stresses and surface adjustment. The rapid slow down of flow and thinning at the terminus after stopping the retreat at 6 years illustrates well this rapid dynamic adjustment at the terminus and is supported by the modelled adjustment in flux and thinning rates with time (Fig. 2). Only 4 years after stopping the retreat, the mass loss decayed near the terminus more than a factor 2 from above 40 to 20% of its original balance flux of 24 km^3a^{-1} and the thinning rate drops there within half a year from around 20 m a^{-1} to almost zero. Upstream, where the flow speed is strongly reduced, the peak in flux change and thinning rate is delayed but also much wider and significantly reduced in magnitude (Fig. 2c+d). At 80 km behind the grounding line the peak in flux is reached about 8 years after ceasing the retreat and the amplitude is reduced to 7% of the initial balance flux at the grounding line, and both flux and thinning rates are maintained at such slightly enhanced levels for time-scales of decades.

Theoretical considerations and modelling suggest that the speed of upstream propagation of acceleration and thinning is a multiple of the flow-speed which is confirmed by our modelling experiment (Howat et al. 2007; Payne et al. 2004; Bindschadler 1997; Nye 1963). This is in simple terms explained by the fact that faster flowing systems can much quicker redistribute their mass, and it has important consequences regarding interpretation and assessment of rapid dynamic changes. It means that, although changes can propagate

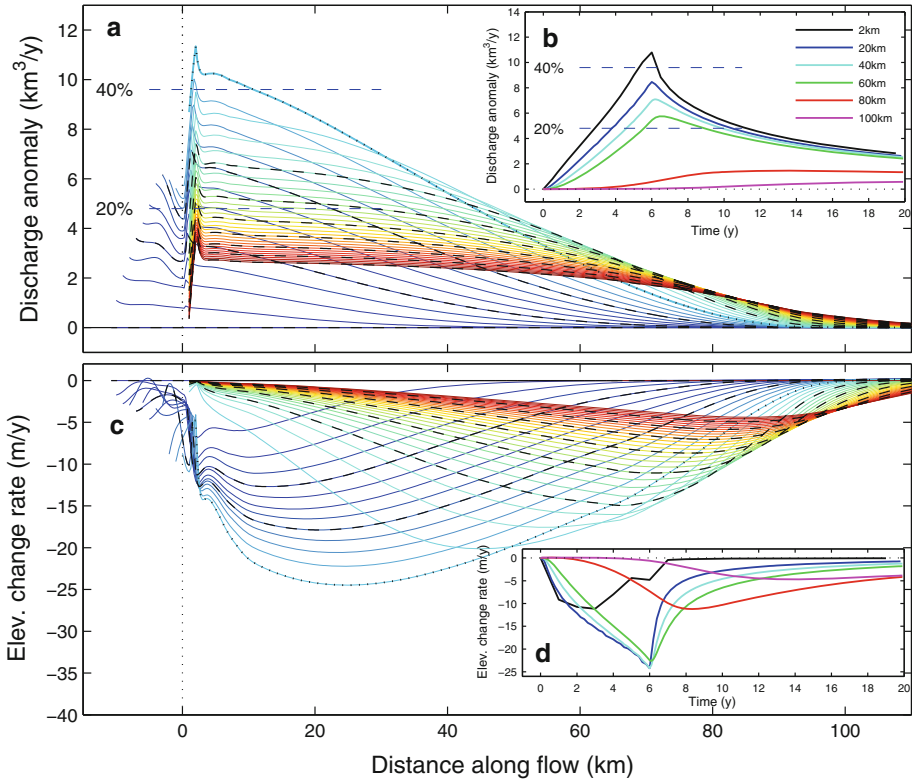

Fig. 2 Modelled along flow profiles of **a** ice discharge anomaly with reference to the pre-retreat discharge and **c** surface elevation change rates for the gradual retreat experiment corresponding to Fig 1. The *lines* are *colour-coded* as in Fig. 1 and are shown at 0.5 year time steps for *coloured lines* and 2 years for *dashed black lines* and span a total period of 20 years. The *dotted line* marks 6 years, the time when the retreat in the experiment was stopped. The *dashed blue lines* in **a** mark the relative percentage to the steady state pre-retreat grounding line discharge. The *insets* **b** and **d** show the evolution of the same quantities as in **a** and **c** but at fixed locations (legend in **c**) against time and again with the prescribed gradual retreat starting at time zero and stopping at year 6

upstream rapidly, they affect in the first few years only fast flowing areas whereas the slowly flowing inland ice acts almost as a buffer and changes will be much delayed and damped (see slowly flowing areas upstream of deep channel; Figs. 1a and 2). On the other hand, it also means slowly flowing upstream areas will continue to respond and contribute to mass loss at a reduced rate for the longer-term future as also demonstrated by Price et al. (2011) and further, that changes, currently observed upstream, may still be affected by terminus perturbations that happened several decades ago. This is important regarding interpretation of the present observations of thickness change in context of the longer-term terminus retreat of JIB since the Little Ice Age, when the terminus position was 35 km further advanced then at present (Csatho et al. 2008; Young et al. 2011).

Such rapid slow-down and readjustment at the terminus has been observed for many tidewater outlets around Greenland (Howat et al. 2007; Howat et al. 2008; Moon and Joughin 2008; Murray et al. 2010; Nick et al. 2009) and has several important consequences regarding the assessment of dynamic mass loss.

Firstly, it means that without any further perturbations, e.g., retreat or additional feedbacks at the terminus, such glaciers cannot keep their high speeds for long (more than a few years) and they start immediately readjusting and slowing down and thus the mass loss will decrease rapidly. However it is important to note that, after this initial adjustment phase, mass loss at a reduced level (order of few % of balance flux) may prolong for several decades as a result of the longer-term adjustment of slow flowing inland ice areas (Fig. 2; Price et al. 2011).

Secondly, estimations of mass loss through monitoring ice flux near the terminus are strongly affected by short-term perturbations and therefore may record outlet glacier *weather* rather than longer-term trends. Moving the flux gates somewhat upstream would provide more robust trends, but may not be practical, as relative observational errors increase significantly for reduced flow speeds (<100 ma^{-1}).

Thirdly, an obvious but important point in this context is that the flow speed will not go fully back to its initial pre-retreat level, even when as in our case the surface mass balance and consequently the steady state flux is kept the same, as the strong terminus thinning reduced the thickness significantly near the final grounding line and therefore higher flow speeds are needed to recover the pre-retreat flux. This effect is important in the interpretation of repeated flow speed observations and if neglected it may overestimate mass loss significantly. In our example, this overestimation in mass loss would be around 30% of the peak flux anomaly, as similarly determined for Helheim and Kangerdlugssuaq Glacier in SE-Greenland (Howat et al. 2007).

In our first prescribed retreat simulation, the patterns of flow acceleration and thinning are in good agreement with observations from the recent retreat phase of JIB (Figs. 1, 2; Joughin et al. 2004, 2008c; Thomas et al. 2009). The absolute increase in speed, however, is underestimated by the model and, more importantly, JIB has not been observed to slow down after the terminus ceased retreating in 2004, although the observed speed stagnated (Fig. 1c). This suggests that further feedbacks must be continuing to perturb this glacier which will be discussed in the section below.

4 Feedback Mechanisms

4.1 Grounding Line Retreat

A first major feedback is the retreat of the grounding line or grounded terminus as it removes areas of flow resistance at the base and if retreating into deeper water it may trigger unstable retreat as a result of increased ice flux with increasing water depth. This latter effect is well known from theoretical studies (Schoof 2007; Katz and Worster 2010) and studies on grounded tidewater glacier termini (Vieli et al. 2001; Meier and Post 1987) and has been observed for many tidewater glaciers such as Helheim (Howat et al. 2007) or Columbia Glacier (Van der Veen 1996). This effect can be enhanced by the positive feedback mechanism between subglacial motion and water pressure at the glacier bed. Any thinning brings the surface near the terminus closer to flotation and basal water pressure will approach the hydrostatic pressure of the overlying ice and therefore reduce frictional forces at the glacier bed (Pfeffer 2007; Vieli et al. 2000). It is important to note here that the effect of bed topography on grounding line stability is however significantly reduced in the case of a floating ice tongue or ice shelf through buttressing the upstream ice at their sides and stable positions are possible even on reversed slopes (Nick et al. 2010; Dupont and Alley 2006; Thomas 1978; Weertman 1974). This is particularly relevant for ice

tongues with a narrow width as in the case of outlet glaciers and makes their existence or disintegration a crucial control in outlet glacier stability. Recent modelling work also demonstrated that for calving criteria that are not directly water-depth dependent the stability of the grounding line is less sensitive to the sign of the bed slope (Nick et al. 2010).

The strong overdeepening behind the sill at JIB shows after removal of the floating tongue potential for such an instability; however, it is currently not clear whether the grounding line already retreated over the sill into deeper water or not, as basal topography there is not well known. Although in our model the grounding line retreats slightly (Fig. 1a), it is unable to retreat upstream over the shallow sill. An additional experiment with a more extreme and dynamic calving model that always removes all floating ice and therefore its buttressing (using a flotation criterion; Vieli et al. 2001) also showed stabilization of the grounding line downstream of the sill (Fig. 3). However, when we run the same experiment for an artificially lowered bed sill by 100 m, the grounding line eventually retreats over the bed sill and a catastrophic retreat through the basal trough is initiated before it stabilizes again on a shallower bed about 80 km upstream (Fig. 3). These rather extreme experiments illustrate the importance of detailed knowledge of basal topography of tidewater glaciers and how in any numerical model relatively small uncertainties in water depth around such a sill may decide between enhanced stability or catastrophic retreat. For few cases, including the major outlet glaciers Helheim, Kangerlugdlugssuaq and JIB, detailed basal topography of the marine based channels became recently available (Operation IceBridge; Koenig et al. 2010), but for many tidewater outlet glaciers in Greenland it is largely unknown and provides a major limitation in assessing and modelling their future behaviour. Another important point regarding basal topography is that the bed for most of these outlets eventually rises upstream to above sea-level and therefore limits this potential instability arising from reverse bed slopes for the longer-term

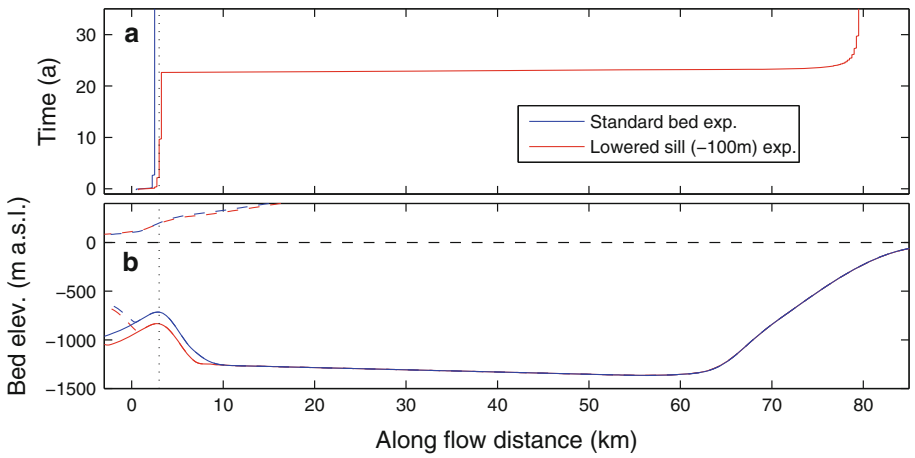

Fig. 3 **a** Modelled grounding line position against time for two retreat experiments with different basal topography (as shown in **b**) using a dynamic flotation criterion for which from time zero onwards any floating ice is always removed. The *black dotted line* refers to the location of the sill crest. **b** Basal topography showing the original bed (*blue line*) and the bed with a 100 m lower sill (*red line*). The *dashed coloured lines* in **b** refer to the initial *upper* and *lower* ice surface geometry before the removal of the floating ice tongue

future. This is, however, not the case for JIB and for a few other major outlets in the North and Northeast which have marine basins that extend inland by several tens of kilometres (Thomas et al. 2009).

There are further important issues in modelling grounding line motion which are largely of numerical nature and affect in particular large scale ice sheet models of relatively sparse resolutions and fixed grids (Schoof (2007); Vieli and Payne (2005); and see detailed discussion in this issue in Docquier et al. 2011). However, major advances have recently been made in the treatment of such grounding lines towards resolving these issues (Docquier et al. 2011; Gladstone et al. 2010; Pollard and DeConto 2009; Durand et al. 2009; Goldberg et al. 2009; Nowicki and Wingham 2008; Schoof 2007; Pattyn et al. 2006).

4.2 Calving Retreat Feedback

In the previous main experiment the retreat history of the terminus has been prescribed, however, in reality the position of the terminus is controlled by the interaction between the calving process and the flow dynamics and should be an output of a numerical model rather than an input.

The process of calving is still not well understood and rather poorly represented in numerical models (Benn et al. 2007; Bassis 2011). Most, larger scale ice sheet models prescribe calving rates using empirical relationships for calving flux which may constantly offset (over or underestimate) mass loss at the marine terminus or they do not evolve the terminus position with time and use a free flux condition and thereby ignore potential calving feedbacks. Recently, significant advances in calving model development have been made such as using strain rate criteria for determining terminus position (Benn et al. 2007; Nick et al. 2010) or calving rates (Alley et al. 2008; Albrecht et al. 2011; Amundson and Truffer 2010) or using a stochastic approach to calving (Bassis 2010). Implementation of such calving approaches in large scale 3-dimensional ice sheet models is, however, lacking behind and still in its infancy (Albrecht et al. 2011; Bassis 2011).

As explained above, after initiating retreat, the flow accelerates and leads to increased longitudinal stretching at the terminus which may enhance crevassing and therefore calving and further retreat. This positive feedback could therefore lead to rapid retreat of a terminus. We demonstrate this effect by including a dynamic, physically based calving criterion (Nick et al. 2010) that retreats the terminus back to a position up to where the longitudinal extension rate penetrates crevasses through the full depth. The initial retreat is here triggered by an increase in ocean melt beneath the floating tongue of 20% (corresponding to a warming of about 1°C, Motyka et al. 2011). This small increase in basal melt rate leads to a slight thinning which when applying the calving criteria triggers a continous retreat and initiates the strong acceleration and thinning as discussed above (Fig. 4). After 8.5 years the terminus retreat and flow start to slow down and stabilise automatically, probably as a result of the steepening of the surface in this location. Although in this case ocean melt triggered the retreat, the main work and cause for the dynamic changes is from the loss of buttressing as a result of a highly sensitive feedback between calving and retreat. Indeed, for an additional model run by keeping the terminus fixed but applying the same increase in ocean melt, the acceleration in flow is insignificant (below 1%). Thus, the feedback between calving and retreat seems crucial for the large scale dynamics and is therefore likely sensitive to the used calving parametrization. This implies that any prediction of dynamic changes of outlet glaciers hinges on a robust treatment of calving and thus there is an urgent need for development and validation of such calving models.

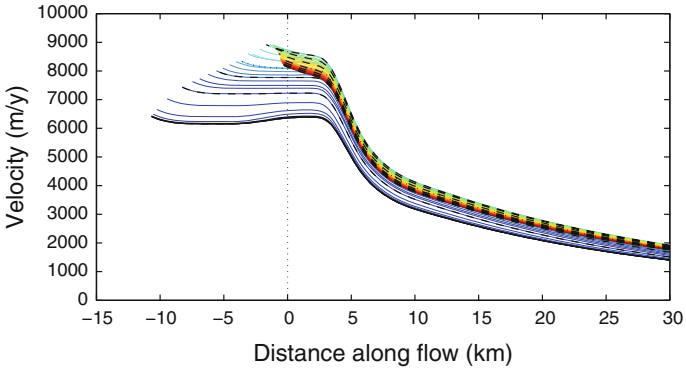

Fig. 4 Modelled along flow profiles of speed for an increase in ocean melt of 20% and using a dynamic calving model. The *lines* are colour-coded as in Fig. 2 (0.5 year time steps over 20 years). Note the automatic onset of slow down after 8.5 years

4.3 Lateral Shearing and Rifting

The very high flow speeds of such glaciers produce strong shearing along the lateral margins where shear stresses are highest. This shearing rheologically weakens the ice through strain heating (softening of ice by enhanced heat dissipation) and more effectively mechanically, through damaging the ice by fracture. This mechanical weakening then produces heavily crevassed bands along the lateral margins which are well visible in the field or on imagery and are characteristics of marine outlet glaciers. A further acceleration of the glacier will increase the shearing and therefore further breakup and weaken these margins. This weakening will therefore reduce the resistance provided by the sides (lateral drag) which in turn leads to further acceleration. This feedback has been suggested to play an important role in controlling Antarctic ice stream dynamics (Echelmeyer et al. 1994) and the pre-collapse changes of the Larsen B ice shelf (Vieli et al. 2007). At JIB shortly after the initiation of the recent retreat of the ice tongue, large rifts formed in these lateral shear margins and enhanced crevassing then propagated upstream (Joughin et al. 2008c). These rifts mechanically decouple the ice from its margin and the buttressing effect of the floating tongue is highly reduced. This may partly explain the continued acceleration between 1998 and 2001 despite a brief still stand of retreat or even slight re-advance of the terminus. With acceleration propagating upstream, this weakening of the margins will play a role some way upstream of the grounding line, as indicated in the case of JIB from imagery and in changed cross flow profiles in speed (Joughin et al. 2008c). Further, this feedback may explain the underestimated and continuing acceleration after the retreat ceased down.

In Fig. 5 we illustrate this potential effect in a very simple model experiment in which the softness of the ice is reduced proportionally to the excess of flow speed beyond an arbitrary critical speed of 7,500 m a^{-1} and additionally limiting this softening to a factor 20. For the same prescribed retreat as in the first experiment, this feedback triggers an earlier and far more abrupt acceleration and reaching higher speeds which are similar to those observed. However, the flow starts now to slow down even before the retreat ceases which is a simple consequence of the remaining floating terminus providing hardly any buttressing as the sides are very weak.

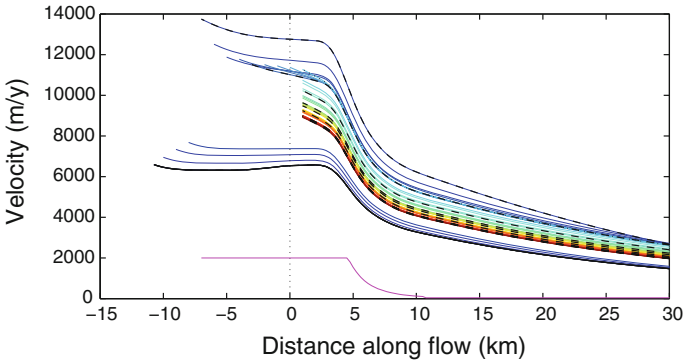

Fig. 5 Modelled along flow profiles of speed for the same prescribed retreat experiment as in Fig. 2 but including a feedback of lateral shear softening for flow above 7.5 km a^{-1}. The *lines* are colour-coded as in Fig. 1 (0.5 year time steps spanning 20 years). The *magenta line* indicates the factor of rheological lateral shear softening (100 times exaggerated) that is obtained 2 years after onset of the retreat

The example of JIB demonstrates the potential importance of this feedback in understanding and predicting the rapid mass loss from tidewater outlet glaciers, but also indicates the difficulties in including such effects into numerical flow models. The process of strain heating is relatively well understood and included in most thermo-mechanical ice sheet models. In the case of outlet glaciers, it is, however, the rheological damage through fracture such as rifting that is the dominant process which is not well understood in this context. Attempts of modelling the evolution of damage or rifting in ice have been undertaken (Pralong et al. 2003; Larour et al. 2004; Sandhaeger 2003), but they require high resolution and computational effort and are so far limited to small and well constrained cases. Larger scale models are unlikely to spatially resolve these narrow lateral shear zones sufficiently and therefore a more realistic approach may be to use a Coulomb-Plastic friction relation for side drag as similarly introduced for sliding at the glacier bed (Schoof 2005; Gagliardini et al. 2007). For 3-dimensionsal ice sheet models this parametrization would technically be included in the basal sliding boundary condition.

4.4 Vertical Deformation

A further mechanism that may explain the underestimation in flow acceleration by the model may be the neglect of vertical variations in horizontal stresses and flow. Our model and most existing large scale ice sheet models solve for vertically averaged flow and longitudinal stresses in areas of floating or rapidly flowing ice and thus vertical shear is ignored. However, preliminary experiments of ice tongue removal at JIB using a finite-element model that solves the full 3-D momentum equations indicate that even for an ice tongue with no lateral drag, terminus retreat resulted in flow acceleration (Luethi et al. 2009). Although this needs further investigation, this could imply that in order to include realistic boundary conditions at the marine terminus more sophisticated 3-D models that include the higher-order stresses (Blatter/Pattyn type models, Blatter 1995; Pattyn 2003) or solve the full-Stokes equation are needed. Such models are becoming readily available now (Pattyn et al. 2008) but are computationally far more expensive and therefore unlikely to be used for longer-term simulations on an full ice sheet scale in the near future. Thus, it will be crucial to rigorously test and assess the validity of different approximations of flow

physics such as the shallow-shelf approximation (MacAyeal (1989); Bueler and Brown (2009); and as used here), a depth-integrated hybrid approximation (Bassis 2010; Schoof and Hindmarsh 2010; Goldberg 2011) or the first-order Blatter/Pattyn type approximation (Blatter 1995; Pattyn 2003) against the full-Stokes case for a marine terminating boundary and in view of computational expense. Importantly, this requires also validation against real world data.

5 Forcing

As any natural system, tidewater outlet glaciers are constantly exposed to variations in climate and ocean conditions and, thus, they will dynamically respond to these external forcings. Indeed, the recent dynamic changes of tidewater outlet glacier coincide in rough terms with the general pattern of atmospheric and oceanic warming in Greenland and further such changes seem to be synchronous on a regional spatial scale (Howat et al. 2008; Murray et al. 2010; Moon and Joughin 2008; Rignot and Kanagaratnam 2006). The linking processes between the climate, oceanic forcing and dynamic changes are still not well understood and are only crudely represented in current ice flow models, including the model used in this study. This implies that even if we would have detailed knowledge of oceanic and atmospheric forcing we are still unable to predict accurately predict their impact and response in terms of outlet glacier dynamics. Below we outline our current understanding and issues related to these linking processes between forcing and ice dynamics.

5.1 Oceanic Forcing

In recent years enhanced oceanic melt at the glacier terminus has been suggested as a major trigger for dynamic changes of Greenland outlet glaciers. The onset of acceleration at JIB in the West and of several marine outlet glaciers in the Southeast time well with warmer subsurface waters from the Irminger current reaching these Greenland coasts (Holland et al. 2008; Lloyd et al. 2011; Murray et al. 2010). Recent observations of ocean conditions within the fjords of major outlet glaciers such as JIB, and Helheim and Kangerdluggssuaq Glacier in the Southeast show clear evidence of such warm waters and indicate that their ice termini are in contact with these warm water masses and that significant ice melt occurs at depth (Holland et al. 2008; Rignot et al. 2010; Straneo et al. 2010, 2011). Estimates of melt-rates beneath the floating ice termini of JIB (Motyka et al. 2011) and at vertical grounded calving fronts elsewhere (Rignot et al. 2010; Motyka et al. 2002) suggest melt rates in the order of several 100s of meters per year, in particular at depth near the grounding line. These high melt rates suggest that the increase in oceanic melt may be sufficient to trigger a dynamic acceleration through modifying terminus geometry. In case of a floating ice tongue, enhanced melt will lead to a thinning which then initiates the calving retreat feedback as demonstrated in our ocean melt experiment for JIB (Fig. 4). At JIB, the thinning may additionally have led to an ungrounding of a pinning point and further enhance acceleration (Thomas et al. 2003; Joughin et al. 2008c). An additional experiment with overlaying seasonal variations (sinusoidal) in oceanic melt, in addition to the step change (Fig. 6), indicates that higher melt rates beneath the grounding-line may explain the increased seasonal variation in flow speed after the major retreat of the ice tongue (Echelmeyer et al. 1990; Joughin et al. 2008c; Luckman and Murray 2005).

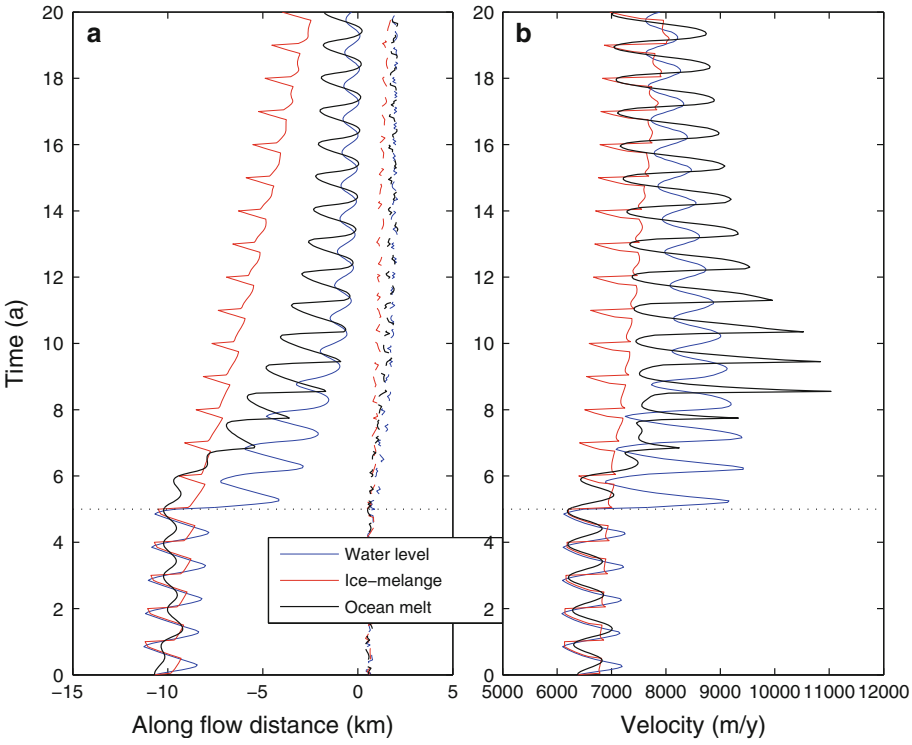

Fig. 6 **a** Position of the calving terminus (*solid*) and grounding line (*dashed*) with time for experiments of seasonal variations in water level within crevasses (*blue*), buttressing from ice-mélange (*red*) and ocean melt at the base of the floating ice tongue (*black*). After 5 years a step change in waterlevel (+1 m), in buttressing (reduction of ice-mélange season by 2 months) and in ocean melt (increase of 20%) has been applied. **b** Flow speed at pre-retreat grounding line position (0 km) with time

For grounded vertical calving faces which are most common for Greenland tidewater outlet glaciers, thinning of the terminus from underneath is not possible and ocean melt has to act in horizontal direction. Maximum rates, although high, are still several times below the typically observed calving rates, suggesting that basal melt must rather act through changing the shape of the front thereby influencing the stress field, such as through undercutting, and consequently affecting the calving rates (Rignot et al. 2010; Motyka et al. 2002; Vieli et al. 2002). This provides a major challenge for forcing ice flow models with ocean data as it is in this case unclear how to link ocean melt rates to the process of calving. Larger ice flow models use spatially fixed grids; thus directly applying ocean melt in horizontal direction is not possible and requires a sub-grid parametrization or a more sophisticated and high resolution treatment of the marine boundary. A further complication is added by the observation that melt rates are unlikely to be uniform along the width of a terminus as indicated by localised upwelling of freshwater plumes at many calving termini (Extreme Ice Survey: http://www.extremeicesurvey.org/).

Unlike prescribing a spatially fixed pattern of ocean melt as done in this study, a realistic oceanic forcing in a model should determine ice melt rates from the given conditions in temperature and salinity of the ambient fjord water and the given geometry. Although such ocean models are becoming available now (Thoma et al. 2010; Jenkins, in

review; Holland et al. 2010; Payne et al. 2007) their application is still limited and importantly they lack a direct coupling with dynamic ice flow models. Examples of such limitations are (1) the poorly known fjord bathymetry and vertical stratification of waters which are crucial for mixing the waters at the ice interface (Straneo et al. 2011), (2) lack of information of the ambient fjord water temperature and salinity, and, importantly, (3) the lack of understanding of the replacement of fjordwater with coastal ocean water. On the latter, the intensity of along shore winds has been suggested as a crucial control for the fjord circulation and transporting the warm subsurface waters to the ice face (Straneo et al. 2010) which in Greenland seems to be affected by atmospheric circulation in the North Atlantic (Holland et al. 2008). The effect of fresh water from ice melting at the terminus or icebergs and from surface melt water run off further adds to the complexity of fjord circulation (Straneo et al. 2011).

5.2 Atmospheric Forcing

The effect of atmospheric warming on surface melt and surface mass balance is well understood and reasonably well represented in large scale ice sheet models; however, its potential impact on ice dynamics is still uncertain and rather indirect through triggering some of the feedback mechanisms discussed above, with the calving-retreat feedback probably being the most effective.

As mentioned in Sect. 3 the effect of enhanced basal lubrication by increased surface melting appears in the context of fast flowing outlet glaciers of secondary importance, although it may on short time scales still be significant (Howat et al. 2010). The timescales of adjusting the drainge system at the base of a glacier to enhanced delivery of surface melt water are known to be extremely short (days to weeks) which means that enhanced surface melt may in the long-term not affect the flow much or even slow it down (Sundal et al. 2011; Schoof 2010; Van de Wal et al. 2008). In any case, the relationship between melt water input at the surface and basal lubrication at the glacier bed is far from straight forward and therefore linking atmospheric forcing with basal sliding conditions involves currently high uncertainties.

Enhanced surface melt in the terminus region may increase water delivery into crevasses and thereby enhance crevasse penetration though hydro-fracturing (Weertman 1973; Van der Veen 1998). This may weaken the ice and therefore ease calving at the terminus. This process has earlier been suggested for explaining the seasonal variations in calving rates and terminus positions of tidewater glaciers (Sohn et al. 1998); however, a quantitative assessment of its role is still lacking and requires detailed data and observations. The warming or enhanced melt acts in this case only as a trigger for calving retreat which then causes the actual dynamic changes. As our dynamic model for calving is based on a criterion of critical crevasse depth, we can directly force it with water level within crevasses.

This effect is illustrated by varying in our calving criterion the water level within the crevasses seasonally (sinusoidal), with an amplitude of 1 m and then performing a step increase in water level of 1 m after 5 years (Fig. 6). This produces seasonal variations in front position and flow speed, and the step change in water-level is able to initiate a rapid dynamic retreat and acceleration which is both in rough agreement with observations at JIB (Joughin et al. 2008b, 2008c; Sohn et al. 1998). This seems encouraging regarding prognostic modelling of such systems as it allows a direct forcing with atmospheric data. The very high sensitivity to small changes in water level, however, indicates a strong reliance on the calving model and any parameterization that link surface melt to water level within crevasses. Further, the onset of terminus retreat in spring observed at JIB is typically well

before surface temperatures reach above zero degrees and melting starts (Joughin et al. 2008b, 2008c).

Through a similar process, atmospheric warming may induce rheological weakening in lateral shear zones and thereby reduce buttressing from the sides, but this effect is probably of secondary importance. A further related effect could be rheological softening by warming up the ice from the surface through enhanced penetration of surface meltwater into the ice in crevassed areas. Although, this process has been suggested to be significant in slowly flowing ice sheet margins in Greenland (Phillips et al. 2010), its effect on outlet glacier dynamics remains speculative.

5.3 Sea-Ice and Ice-Mélange

A further potential forcing which is interlinked with both ocean and atmospheric forcing is the extent and duration of the seasonal *ice-mélange* in front of the calving terminus. At JIB, during winter when the sea-ice and icebergs freeze together to a rigid mass, calving activity has been observed to be highly reduced or even vanish and therefore the terminus advances in winter (Joughin et al. 2008c) at about the speed of ice flow. This ice-mélange is believed to exert a small force that is sufficient in preventing the already almost detached vertical ice-lamellas at the calving face from topping over and breaking off and therefore acts to reduce calving rates (Amundson et al. 2010). This effect provides a potential explanation of seasonal variations in calving rate (Joughin et al. 2008a, 2008c; Sohn et al. 1998; Howat et al. 2010; Reeh et al. 2001). The fact that for Greenland the onset of spring terminus retreat is correlated well with the disintegration of the ice-mélange supports this mechanism, in particular as the onset is well before surface melt starts. For JIB, a significantly reduced length of winter sea-ice in the outer fjord also seems to correlate well with the start of the terminus retreat in 1997 and the subsequent flow acceleration (Joughin et al. 2008c). A stabilizing effect of such ice-mélange on calving is also relevant for Antarctic outlet glaciers and ice shelves (Larour et al. 2004) where accretion of marine ice in rifts may act to strengthen such ice-mélange (Khazendar et al. 2009).

Including the stabilizing effect from ice-mélange is in our model implemented by adding a small longitudinal stress (40 kPa) at the marine boundary with a simple seasonal pattern of 6 months of ice free conditions (stress set to zero) followed by 6 months of compact ice-mélange (set to 40 kPa). After 5 years the duration of winter ice-mélange is reduced to 4 months. The resulting seasonal fluctuations in terminus position are again a consequence of changing calving rates from the ice-mélange forcing (Fig. 6). For the initial stable phase, our modelled terminus position and velocity variations at the grounding line are consistent with observations and we are able to trigger a rapid retreat by reducing the seasonal period of ice-mélange. However, the seasonal amplitude in terminus position variations is after the retreat far below the observed 5-6 km and the overall retreat is much less abrupt than observed which may both indicate a mis-representation of the ice-mélange forcing mechanism in our model. Further, it remains to be tested whether the longitudinal stress value of 40 kPa, required in our model to produce significant retreat and seasonal variations, is realistic or not.

5.4 Discussion on Forcing

All three different examples of seasonal forcings applied to our model above are able to produce similar patterns of seasonal front variations and abrupt retreat (Fig. 6). This is not surprising, given that they rely on the same calving retreat feedback and use the same

calving criteria. Further, atmosphere, ocean and sea-ice are not independent and temporal variability of these forcings will inherently be in phase. However, during the rapid retreat period we obtain some notable phase shifts in seasonal variations of speed and terminus position (Fig. 6), which may be used to identify controlling forcings. The above experiments also stress the need for further development and robust validation of parameterizations of atmospheric and in particular oceanic forcings within numerical ice flow models. The above forcings should of course not be considered in isolation. Sea-ice and ice-mélange are obviously placed right at the interface between ocean and atmosphere and fjord circulation seems to be controlled by along shore winds and therefore regional scale atmospheric circulation and surface runoff may further affect water exchange within the fjord (Holland et al. 2008; Straneo et al. 2010, 2011).

The high temporal variability in forcing is well reflected in observed outlet glacier dynamics and in our model results (Fig. 6) which underpins the extreme sensitivity of these systems to variation in external forcing. The dynamic feedbacks discussed, such as calving retreat, act here again as amplifiers for the applied forcing. The observed episodic nature in mass loss of such outlet glaciers can be interpreted as a non-linear threshold response to a fluctuating external forcing signal. The recent record of dynamic changes of Greenland outlet glaciers is therefore not a reliable measure of longer-term records of ice sheet mass balance.

Further, on longer time-scales of several decades to millenia, a longer-term deficit in surface mass balance leads to a general slow thinning trend which through interaction with basal topography can produce episodic rapid retreat phases, as similar suggested for valley tidewater glaciers (Meier and Post 1987; Vieli et al. 2001). For the recent rapid changes in Greenland this seems, however, unlikely to be a direct forcing as it would not explain the strongly synchronous behaviour of outlets on a regional scale. However, regarding the longer term trends involved in future projections of sea level, this effect may well be relevant. Even in the current example of JIB, 'hidden' within the current rapid retreat may still be a slow adjustment signal of retreat from the Little Ice Age (Csatho et al. 2008; Lloyd et al. 2011).

6 Implications and Conclusions

This paper explores and illustrates the major concepts and issues regarding our understanding and predictive ability of tidewater outlet glacier dynamics on the example of a numerical model application to the recent rapid changes of JIB. Our modelling shows that the dramatic dynamic changes at JIB are triggered from the marine terminus and supports the loss of buttressing from the disintegration of the floating ice tongue as a major cause. Furthermore, enhanced ocean melt is confirmed as a possible triggering mechanism for initiating retreat but other forcings such as reduced winter sea-ice coverage produce in our model similar dynamic behaviour. Importantly, we find that the modelled dynamic changes crucially depend on the calving-retreat feedback mechanism which implies a strong dependency of predictive outlet glacier models to the detailed treatment of calving. As demonstrated in our modelling, some advances have been made on this issue in recent years; however, the process of calving and importantly its link to atmospheric and oceanic forcing is still poorly understood and its representation and implementation remains a major limitation in current generation ice sheet models. In particular, regarding the likely oceanic warming as a trigger for outlet glacier acceleration, we still seem a long way away from being able to force dynamic ice sheet models with ocean data. Major efforts are

needed in monitoring and understanding fjord circulation and in numerical model development, in particular in the coupling of ocean melt with ice dynamics and calving.

This also includes the need for increased spatial resolution in ice sheet models in order to resolve the deep bedrock channels, but also the involved processes such as grounding line retreat or lateral shear weakening. Such increased resolution requires, however, accurate knowledge of basal topography which is for most Greenland outlet glaciers still rare but critical for the stability of grounding lines and calving termini. Therefore efforts in collecting basal data such as the recent Operation IceBridge (Koenig et al. 2010) are vital for improving predictions of future ice sheet change and should also include bathymetric data in ocean fjords as they are important for their circulation and therefore heat transport from the ocean to the ice contact.

Unlike in our modelling, JIB continues its high flow speed at peak-level even after the terminus stopped retreating which suggests that other feedback mechanisms than loss of buttressing may play an important role such as rheological weakening in lateral shear zones. Alternatively, this discrepancy may indicate that the assumption of negligible vertical shear at fast flowing marine termini, as commonly used in ice sheet models, requires careful re-consideration of its validity. This means that, for the calculation of flow, additional higher-order stress terms may have to be included or even the full-Stokes equations solved. Although such models are becoming available (Pattyn et al. 2008) they still lack a realistic dynamic treatment of marine boundaries (calving) and importantly their computational-time is dramatically increased which makes predictions on the required time scales of decades to centuries challenging.

Our modelling further confirms the extreme sensitivity of tidewater outlet glaciers to perturbations at their marine boundary and their ability to adjust rapidly as indicated by observations. This implies that the dramatic accelerations in speed as recently observed for many marine outlet glaciers in Greenland cannot be maintained for long without additional perturbations or feedback mechanisms, but also that on a reduced but significant level mass loss can continue for decades. Furthermore, these rapid changes reflect rather short-term fluctuations in climate and oceanic forcing that are amplified through feedback mechanisms such as calving retreat. This is crucial in interpreting the dynamic changes as it means we are recording outlet glacier *weather* rather than longer-term trends. Thus, assessments and projections of dynamic mass loss based on our existing relatively short observational record (Rignot et al. 2011) or based on scenarios such as doubling flow speed over decadal or century time-scales (Pfeffer et al. 2008) are unrealistic and may drastically overestimate the contribution to future sea-level rise.

Considering the limitations and issues outlined in this paper, it is not realistic to expect that ice sheet scale models will in the near future be able to predict the exact magnitude and timing of change of individual outlet glaciers around Greenland. Regarding projections for future sea-level rise, longer-term trends (decades, centuries) in mass loss should therefore strategically be considered in ice sheet model development and importantly their validation. This requires a better understanding of the involved processes and forcings and the development of more sophisticated models with full process representation and high spatial and temporal resolution that then can be reduced and simplified with confidence. Validation of such simplified models will therefore require data constraints that span time scales well beyond the recent decade and therefore should include reconstructions of past outlet glacier change (Roberts et al. 2008; Csatho et al. 2008; Alley et al. 2010; Young et al. 2011). In any case, such a longer time perspective from the palaeo-record would be beneficial for the interpretation and current discussion of dynamic mass loss from Greenland tidewater outlet glaciers.

Overall, the reasonable performance of our numerical model, despite being relatively simple, is encouraging for future development of full ice sheet models. However, its application to JIB also outlines some important limitations and issues that need addressing, of which implementation of ocean forcing, a robust calving model and an improved dataset of basal geometry being the most prominent ones. We should therefore in the near future not expect to fully solve this issue of rapid dynamic ice mass loss. The fact that most outlets have beds that are upstream eventually above sea-level indicates, however, that for longer-term future warming scenarios (centuries to millenia) the process of surface melt may dominate the overall mass loss from Greenland (Van den Broeke et al. 2009), which is reasonably well represented in existing ice sheet models, but introduces additional uncertainties (Stone et al. 2010).

Acknowledgments We would like to acknowledge M. Luethi for inspiring scientific discussions and G. J.-M. C. Leysinger Vieli and two anonymous reviewers for their useful comments. We further thank I. Joughin for providing the velocity data.

References

Abdalati W, Krabill W, Frederick E, Manizade S, Martin C, Sonntag J, Swift R, Thomas R, Wright W, Yungel J (2001) Outlet glacier and margin elevation changes: near-coastal thinning of the Greenland ice sheet. J Geophys Res 106(D24):33729–33742

Albrecht T, Martin MA, Winkelmann R, Haseloff M, Levermann A (2011) Parameterization for subgrid-scale motion of ice-shelf calving fronts. Cryosphere 5:35–44

Alley RB et al (2010) History of the Greenland ice sheet: paleoclimatic insights. Q Sci Rev 29:1728–1756

Alley RB, Clark PU, Huybrechts P, Joughin I (2005) Ice-sheet and sea-level change. Science 310:456–460

Alley RB, Horgan HJ, Joughin I, Cuffey KM, Dupont TK, Parizek BR, Anandakrishnan S, Bassis J (2008) A simple law for ice-shelf calving. Science 322(5906):1344

Amundson JM, Truffer M (2010) A unifying framework for iceberg-calving models. J Glaciol 56(199):822–830

Amundson JM, Fahnestock M, Truffer M, Brown J, Luethi MP, Motyka RJ (2010) Ice melange dynamics and implications for terminus stability, Jakobshavn Isbrae, Greenland. J Geophys Res 115(F01005). doi:10.1029/2009JF001405

Bamber JL, Alley RB, Joughin I (2007) Rapid response of modern day ice sheets to external forcing. Earth Plan Res Lett 257:1–13

Bartholomew I, Nienow P, Shepherd A (2010) Seasonal evolution of subglacial drainage and acceleration in a Greenland outlet glacier. Nat Geosci 3:408–411

Bassis J (2010) Hamilton-type principles applied to ice-sheet dynamics: new approximations for large-scale ice sheet flow. J Glaciol 56(197):497–513

Bassis J (2011) The statistical physics of iceberg calving and the emergence of universal calving laws. J Glaciol 57(201):3–16

Benn DI, Warren CR, Mottram RH (2007) Calving processes and the dynamics of calving glaciers. Earth Sci R 82:143–179

Bindschadler R (1997) Actively surging West Antarctic ice streams and their response characteristics. Ann Glaciol 24:409–414

Blatter H (1995) Velocity and stress fields in grounded glaciers: a simple algorithm for including deviatoric stresses. J Glaciol 41(138):333–344

Bueler E, Brown J (2009) Shallow shelf approximation as a 'sliding law' in a thermomechanically coupled ice sheet model. J Geophys Res 114(F03008). doi:10.1029/2008JF001179

Csatho B, Schenk T, van der Veen CJ, Krabill WB (2008) Intermittent thinning of Jakobshavn Isbrae, west Greenland, since Little Ice Age. J Glaciol 54(184):131–144

Docquier D, Perichon L, Pattyn F (2011) Representing grounding line dynamics in numerical models ice sheet models: recent advances and outlook. Surv Geophys. doi:10.1007/s10712-011-9133-3

Dupont TK, Alley RB (2005) Assessment of the importance of ice-shelf buttressing to ice-sheet flow. Geophys Res Lett 32:L04503. doi:10.1029/2004GL022024

Dupont TK, Alley RB (2006) Role of small ice shelves in sea-level rise. Geophys Res Lett 33:L09503. doi:10.1029/2005GL025665
Durand G, Gagliardini O, de Fleurina B, Zwinger T, Le Meur E (2009) Marine ice sheet dynamics: hysterisis and neutral equilibrium. J Geophys Res 114(F03009). doi:10.1029/2008JF001170
Echelmeyer K, Clarke TS, Harrison WD (1990) Jakobshavn Isbrae, west Greenland, seasonal variations in velocity or the lack of thereof. J Glaciol 36(122):82–88
Echelmeyer KA, Harrison W, Larsen C, Mitchell JE (1994) The role of the margins in the dynamics of an active ice stream. J Glaciol 40(136):527–538
Fowler AC (2010) Weertman, Lliboutry and the development of sliding. J Glaciol 56(200):965–972
Gagliardini O, Cohen D, Raback P, Zwinger T (2007) Finite-element modelling of subglacial cavities and related friction law. J Geophys Res 112(F02027). doi:10.1029/2006JF000576
Gillet-Chaulet F, Gagliardini O, Nodet M, Ritz C, Durand G, Zwinger T, Seddik H, Greve R (2011) Full-Stokes finite element modelling of the Greenland ice sheet using inverse methods. Geophys Res Abs 13(EGU2011-8399)
Gladstone R, Lee V, Vieli A, Payne AJ (2010) Grounding line migration in an adaptive mesh ice sheet model. J Geophys Res 115(F04014). doi:10.1029/2009JF001615
Goldberg D, Holland DM, Schoof C (2009) Grounding line movement and buttressing in marine ice sheets. J Geophys Res 114(F04026). doi:10.1029/2008JF001227
Goldberg D (2011) A variationally derived, depth-integrated approximation to a higher-order glaciological flow model. J Glaciol 57(201):157–170
Holland DM, Thomas TRH, deYoung B, Ribergaard MH, Lyberth B (2008) Acceleration of Jakobshavn Isbrae triggered by warm subsurface ocean waters. Nat Geosci 1:659–664
Holland PR, Jenkins A, Holland DM (2010) Ice ocean processes in the Bellingshausen Sea, Antarctica. J Geophys Res 115(C05020). doi:10.1029/2008JC005219
Howat I, Joughin I, Fahnestock M, Smith B, Scambos T (2008) Synchronous retreat and acceleration of southeast Greenland outlet glaciers 2000–06: ice dynamics and coupling to climate. J Glaciol 54:646–660
Howat IH, Joughin I, Scambos TA (2007) Rapid changes of ice discharge from Greenland outlet glaciers. Science 315:1559–1561
Howat IM, Box JE, Ahn Y, Herrington A, McFadden EM (2010) Seasonal variability in the dynamics of marine terminating outlet glaciers in Greenland. J Glaciol 56(198):601–613
Hughes T (1986) The Jacobshavn effect. Geophys Res Lett 13(1):46–48
IPCC (2007) Climate change, 2007: the physical basis. Contribution of working group I to the fourth assessment report of the intergovernmental panel on climate change
Joughin I, Rignot E, Rosanova CE, Luchitta BK, Bohlander J (2003) Timing of recent accelerations of Pine Island glacier, Antarctica. Geophys Res Lett 30(13):1706
Joughin I, Abdalati W, Fahnestock M (2004) Large fluctuations in speed on Greenland's Jakobhavn Isbrae glacier. Nature 432:608–610
Joughin I, Alley RB, Ekstroem G, Fahnestock M, Moon T, Nettles M, Truffer M, Tsai VC (2008a) Ice-front variation and tidewater behaviour on Helheim and Kangerdlugssuaq Glaciers, Greenland. J Geophys Res 113:F01004. doi:10.1029/2007JF000837
Joughin I, Das SB, King MA, Smith BE, Howat IH, Moon T (2008b) Seasonal speedup along the Western margin of the Greenland ice sheet. Science 320:781–783
Joughin I, Howat I, Fahnestock M, Smith B, Krabill W, Alley RB, Stern H, Truffer M (2008c) Continued evolution of Jakobshavn Isbrae following its rapid speedup. J Geophys Res 113:F04006. doi:10.1029/2008JF001023
Joughin I, Smith B, Howat IM, Scambos T, Moon T (2010a) Greenland flow variability from ice sheet wide velocity mapping. J Glaciol 56(197):415–430
Joughin I, Smith BE, Holland DM (2010b) Sensitivity of 21st century sea level to ocean-induced thinning of Pine Island Glacier, Antarctica. Geophys Res Lett 37(L20502)
Katz RF, Worster MG (2010) Stability of ice-sheet grounding lines. Proc R Soc Lond Ser A 466:1597–1620
Khazendar A, Rignot E, Larour E (2009) Roles of marine ice, rheology, and fracture in the flow and stability of the Brunt/Stancomb-Wills ice shelf. J Geophys Res 114(F04007). doi:10.1029/2008JF001124
Koenig L, Martin S, Stuedinger M, Sonntag J (2010) Polar airborne observations fill gap in satellite data. Eos 91(38):333–334
Krabill W, Hanna E, Huybrechts P, Abdalati W, Cappelen J, Csatho B, Frederick E, Manizade S, Martin C, Sonntag J, Swift R, Thomas R (2004) Greenland ice sheet: increased coastal thinning. Geophys Res Lett 31:L24402. doi:10.1029/2004GL021533
Larour E, Rignot E, Aubry D (2004) Modelling of rift propagation on Ronne ice shelf, Antarctica, and sensitivity to climate change. Geophys Res Lett 31:L16404. doi:10.1029/2004GL020077

Lloyd J, Moros M, Perner K, Telford RJ, Kuijpers A, Jansen E, McCarthy D (2011) A 100-year record of ocean temperature control on the stability of Jakobshavn Isbrae, West Greenland. Geology 39:131–139
Luckman A, Murray T (2005) Seasonal variation in velocity before retreat of Jakobshavn Isbrae, Greenland. Geophys Res Lett 32(L08501). doi:10.1029/2005GL022519
Luethi MP, Fahnestock MA, Truffer M, Motyka RJ (2009) Jakobshavn Isbrae: is there a speed limit? Eos Trans AGU, Fall Meet Suppl 90(52), meet. Suppl. Abstract C14A-03
MacAyeal DR (1989) Large-scale ice flow over a viscous basal sediment: theory and application to Ice Stream B, Antarctica. J Geophys Res 94(B4):4071–4087
Meier MF, Post A (1987) Fast tidewater glaciers. J Geophys Res 92(B9):9051–9058
Moon T, Joughin I (2008) Changes in ice front positions on Greenland's outlet glaciers from 1992 to 2007. J Geophys Res 113(F202022):415–430
Motyka R, Hunter L, Echelmeyer K, Conner C (2002) Submarine melting at the terminus of a temperate tidewater glacier, LeCont Glacier, Alaska, U.S.A. Ann Glaciol 36(1):57–65
Motyka RJ, Truffer M, Fahnestock MA, Mortesen J, Rysgaard S, Howat I (2011) Submarine melting of the 1985 Jakobshavn Isbrae floating tongue and the triggering of the current retreat. J Geophys Res 116(F01007). doi:10.1029/2009JF001632
Murray T, Scharrer K, James TD, Dye SR, Hanna E, Booth AD, Selems N, Luckman A, Hughes ALC, Cook S, Hybrechts P (2010) Ocean regulation hypothesis for glacier dynamics in southeast Greenland and implications ice sheet mass change. J Geophys Res 115(F03026). doi:10.1029/2009JF001522
Nick FN, Vieli A, Howat I, Joughin I (2009) Large-scale changes in Greenland outlet glacier dynamics triggered at the terminus. Nat Geosci 2:110–114
Nick FN, van der Veen CJ, Vieli A, Benn DI (2010) A physically based calving model applied to marine outlet glaciers and implications for their dynamics. J Glaciol 56(199):781–794
Nowicki SMJ, Wingham DJ (2008) Conditions for a steady ice sheet-ice shelf junction. Earth Plan Res Lett 265:246–255
Nye JF (1963) The response of a glacier to changes in the rate of nourishment and wastage. Proc R Soc Lond Ser A 275:87–112
Pattyn F (2003) A new three-dimensional higher-order thermomechanical ice sheet model: basic sensitivity, ice stream development, and ice flow across subglacial lakes. J Geophys Res 108(B8):2382–2395
Pattyn F, Huyghe A, de Brabander S, de Smedt B (2006) Role of transition zones in marine ice sheet dynamics. J Geophys Res 111(F02004). doi:10.1029/2005JF000394
Pattyn F, Perichon L, Aschwanden A et al (2008) Benchmark experiments for higher-order and full-Stokes ice sheet models (ISMIP-HOM). Cryosphere 2:95–108
Payne A, Holland PR, Shepherd A, Rutt IC, Jenkins A, Joughin I (2007) Numerical modelling of ocean -ice interactions under Pine Island Bay's ice shelf. J Geophys Res 112(C10019)
Payne AJ, Vieli A, Shepherd AP, Wingham DJ, Rignot E (2004) Recent dramatic thinning of largest West Antarctic ice stream triggered by oceans. Geophys Res Lett 31:L23401
Pfeffer WT (2007) A simple mechanism for irreversible tidewater glacier retreat. J Geophys Res 112:F03S25. doi:10.1029/2006JF000590
Pfeffer WT, Harper J, O'Neel S (2008) Kinematic constraints on glacier contributions to 21st-century sea-level rise. Science 321(5894):1340–1343
Phillips T, Rajaram H, Steffen K (2010) Cryo-hydrologic warming: a potential mechanism for rapid thermal response of ice sheets. Geophys Res Lett 37(L20503). doi:10.1029/2010GL044397
Pollard D, DeConto RM (2009) Modelling West Antarctic ice sheet growth and collapse through the past five million years. Nature 458:329–333
Pralong A, Funk M, Luthi MP (2003) A description of crevasse formation using continuum damage mechanics. Ann Glaciol 37:77–82
Price SF, Pane AJ, Howat IM, Smith B (2011) Commited sea-level rise for the next century from Greenland ice sheet dynamics during the past decade. Proc Nat Acad Sci (in press)
Pritchard HD, Arthern RJ, Vaughan DG, Edwards LA (2009) Extensive dynamic thinning on the margins of the Greenland and Antarctic ice sheets. Nature 461:971–975
Reeh N, Thompsen HH, Higgins AK, Weidick A (2001) Sea ice and the stability of north and northeast Greenland floating glaciers. Ann Glaciol 33(1):474–480
Rignot E, Kanagaratnam P (2006) Changes in velocity structure of the Greenland ice sheet. Science 311:986–990
Rignot E, Casassa G, Gogninenei P, Krabill W, Thomas R (2004) Accelerated ice discharge from the Antarctic Peninsula following the collapse of Larsen B ice shelf. Geophys Res Lett 31:L18401. doi:10.1029/2004GL020697
Rignot E, Koppes M, Velinconga I (2010) Rapid submarine melting of the calving faces of West Greenland glaciers. Nat Geosci 3:187–191

Rignot E, Veliconga I, van den Broeke MR, Monaghan A, Lenaerts J (2011) Acceleration of the contribution of the Greenland and Antarctic ice sheets to sea-level rise. Geophys Res Lett 38:L05503. doi: 10.1029/2011GL046583
Roberts D, Long AJ, Schnabel C, Freeman S, Simpson MJR (2008) The deglacial history of southeast sector of the Greenland ice sheet during the Last Glacial Maximum. Q Sci Rev 27:1505–1516
Sandhaeger H (2003) Numerical study on the influence of fractures and zones of weakness on the flow regime of Larsen Ice Shelf. Report 14, FRISP
Scambos TA, Bohlander JA, Shuman CA, Skvarca P (2004) Glacier acceleration and thinning after ice shelf collapse in the Larsen B embayment, Antarctica. Geophys Res Lett 31:L18402. doi:10.1029/2004GL020670
Schoof C (2005) The effect of cavitation on glacier sliding. Proc R Soc Lond Ser A 461:609–627
Schoof C (2007) Ice sheet grounding line dynamics: Steady states, stability and hysteresis. J Geophys Res 112:F03S28. doi:10.1029/2006JF000664
Schoof C (2010) Ice-sheet acceleration driven by melt supply variability. Nature 468:803–806
Schoof C, Hindmarsh RCA (2010) Thin-film flows with wall slip: an asymptotic analysis of higher order glacier flow models. Q J Mech Appl Math 63(1):73–114
Seddik H, Greve R, Zwinger T, Gagliardini O (2010) Steady-state simulations of the Greenland ice sheet using a three-dimensional full-Stokes model. Geophys Res Abs 12(EGU2010-8644)
Sohn HG, Jezek KC, Vander Veen CJ (1998) Jakobshavn glacier, West Greenland: 30 years of spaceborne observations. Geophys Res Lett 25:2699–2702
Stearns LA, Hamilton GS (2007) Rapid volume loss from two East Greenland outlet glaciers quantified using repeat strereo satellite imagery. Geophys Res Lett 34:L05503. doi:10.1029/2006GL028982
Stone EJ, Lunt DJ, Rutt IC, Hanna E (2010) Investigating the sensitivity of numerical model simulations of the modern state of the Greenland ice-sheet and its future response to climate change. Cryosphere 4:397–417
Straneo F, Hamilton GS, Sutherland DA, Stearns LA, Davidson F, Hammill MO, Stenson GB, Rosing-Asvid A (2010) Rapid circulation of warm subtropical waters in a major glacial fjord in Greenland. Nat Geosci 3:182–186
Straneo F, Curry RG, Sutherland DA, Hamilton GS, Cenedese C, Vage K, Stearns LA (2011) Impact of fjord dynamics and glacial runoff on the circulation near Helheim Glacier. Nat Geosci 4:322–327
Sundal AV, Shepherd A, Nienow P, Hanna E, Palmer S, Huybrechts P (2011) Melt-induced speed-up of Greenland ice sheet offset by efficient subglacial drainage. Nature 469:521–524
Thoma M, Grosfeld K, Makinson K, Lange MA (2010) Modelling the impact of ocean warming on melting and water masses of ice shelves in the Eastern Weddell Sea. Ocean Dyn 60:479–489
Thomas RB (2004) Force-perturbation analysis of recent thinning and acceleration of Jakobshavn Isbrae, Greenland. J Glaciol 50(168):57–66
Thomas RB, Abdalati W, Frederick E, Krabill WB, Manizade S, Steffen K (2003) Investigation of surface melting and dynamic thinning on Jakobshavn Isbrae, Greenland. J Glaciol 49(165):231–239
Thomas RB, Frederick E, Krabill W, Manizade S, Martin C (2009) Recent changes on Greenland outlet glaciers. J Glaciol 55(189):147–162
Thomas RH (1978) The dynamics of marine ice sheets. J Glaciol 24:167–177
Vande Wal RSW, Boot W, Vanden Broeke MR, Smeets CJPP, Reijmer CH, Donker JJA, Oerlemans J (2008) Large and rapid melt-induced velocity changes in the ablation zone of the Greenland ice sheet. Science 321:111–113
Vanden Broeke M, Bamber J, Etterna J, Rignot E, Schrama E, van de Berg WJ, van Meijgaard E, Velinconga I, Wouters B (2009) Partitioning recent Greenland mass loss. Science 326:984–986
Vander Veen CJ (1996) Tidewater calving. J Glaciol 42(141):375–385
Vander Veen CJ (1998) Fracture mechanics approach to penetration of surface crevasses. Cold Reg Sci Technol 27:31–47
Vander Veen CL, Whillans IM (1996) Model experiments on the evolution and stability of ice streams. Ann Glaciol 23:129–137
Vieli A, Payne AJ (2005) Assessing the ability of numerical ice sheet models to simulate grounding line migration. J Geophys Res 110:F01003. doi:10.1029/2004JF000202
Vieli A, Funk M, Blatter H (2000) Tidewater glaciers: frontal flow acceleration and basal sliding. Ann Glaciol 31:217–221
Vieli A, Funk M, Blatter H (2001) Flow dynamics of tidewater glaciers: a numerical modelling approach. J Glaciol 47(159):595–606
Vieli A, Jania J, Kolondra L (2002) The retreat of a tidewater glacier: observations and model calculations on Hansbreen. J Glaciol (in press)

Vieli A, Payne AJ, Shepherd A, Du S (2007) Causes of pre-collapse changes of the Larsen B ice shelf: numerical modelling and assimilation of satellite observations. Earth Plan Res Lett 259(3-4):297–306

Weertman J (1973) Can a water-filled crevasse reach the bottom surface of a glacier?. IAHS Pub 95:185–188

Weertman J (1974) Stability of the junction of an ice sheet and an ice shelf. J Glaciol 13(67):3–11

Young NE, Briner JP, Stewart HAM, Axford Y, Csatho B, Rood DH, Finkel RC (2011) Response of Jakobshavn Isbrae, Greenland, to Holocene climate change. Geology 39(2):131–134

Zwally HJ, Abdalati W, Herring T, Larson K, Saba J, Steffen K (2002) Surface melt-induced acceleration of Greenland ice-sheet flow. Science 297:218–222

Surv Geophys (2011) 32:459–474
DOI 10.1007/s10712-011-9120-8

Large-Scale Surface Mass Balance of Ice Sheets from a Comprehensive Atmospheric Model

Lennart Bengtsson · Symeon Koumoutsaris · Kevin Hodges

Received: 24 July 2010 / Accepted: 15 March 2011 / Published online: 20 April 2011

Abstract The surface mass balance for Greenland and Antarctica has been calculated using model data from an AMIP-type experiment for the period 1979–2001 using the ECHAM5 spectral transform model at different triangular truncations. There is a significant reduction in the calculated ablation for the highest model resolution, T319 with an equivalent grid distance of ca 40 km. As a consequence the T319 model has a positive surface mass balance for both ice sheets during the period. For Greenland, the models at lower resolution, T106 and T63, on the other hand, have a much stronger ablation leading to a negative surface mass balance. Calculations have also been undertaken for a climate change experiment using the IPCC scenario A1B, with a T213 resolution (corresponding to a grid distance of some 60 km) and comparing two 30-year periods from the end of the twentieth century and the end of the twenty-first century, respectively. For Greenland there is change of 495 km^3/year, going from a positive to a negative surface mass balance corresponding to a sea level rise of 1.4 mm/year. For Antarctica there is an increase in the positive surface mass balance of 285 km^3/year corresponding to a sea level fall by 0.8 mm/year. The surface mass balance changes of the two ice sheets lead to a sea level rise of 7 cm at the end of this century compared to end of the twentieth century. Other possible mass losses such as due to changes in the calving of icebergs are not considered. It appears that such changes must increase significantly, and several times more than the surface mass balance changes, if the ice sheets are to make a major contribution to sea level rise this century. The model calculations indicate large inter-annual variations in all relevant parameters making it impossible to identify robust trends from the examined periods at the end of the twentieth century. The calculated inter-annual variations are similar in magnitude to observations. The 30-year trend in SMB at the end of the twenty-first century is significant. The increase in precipitation on the ice sheets follows closely the Clausius-Clapeyron relation and is the main reason for the increase in the surface mass balance of Antarctica. On Greenland precipitation in the form of snow is gradually starting to decrease

L. Bengtsson (✉) · K. Hodges
Environmental Systems Science Centre, University of Reading, Reading, UK
e-mail: lennart.bengtsson@zmaw.de

L. Bengtsson · S. Koumoutsaris
International Space Science Institute, Hallerstrasse 6, 3012 Bern, Switzerland

and cannot compensate for the increase in ablation. Another factor is the proportionally higher temperature increase on Greenland leading to a larger ablation. It follows that a modest increase in temperature will not be sufficient to compensate for the increase in accumulation, but this will change when temperature increases go beyond any critical limit. Calculations show that such a limit for Greenland might well be passed during this century. For Antarctica this will take much longer and probably well into following centuries.

Keywords Mass balance · Ice sheets · Greenland · Antarctica · Atmospheric models

1 Introduction

The ice sheets on Antarctica and Greenland are exposed to a number of processes on a variety of time scales. These include long-term adjustments over millennia and fast changes driven by ice-dynamics related to processes in grounding lines or calving fronts. Several of these processes are incompletely understood. The net contribution to sea level change is a very complex process that requires a long-term integration including realistic, high-resolution land-ice models. However, in this study we restrict the investigation to the surface mass balance, SMB, and in particular how SMB is expected to change in a warmer climate. We determine the change in SMB from the difference in mass that is gained from solid precipitation and the losses that come from evaporation, sublimation or direct run-off of water. Consequently, we will ignore losses due to calving, as this has to be calculated using a dynamical model of the complete land ice. It has been suggested that the mass losses on Greenland due to calving is of the same order as SMB (Lemke et al. 2007; IPCC AR4). For Antarctica, on the other hand, iceberg calving or episodic losses of large part of the ice shelf are the overall dominating mechanisms for mass losses.

The sink terms are or the ablation is generally well estimated from routine meteorological observations such as surface temperature, cloudiness, etc., but the source term of solid precipitation requires the knowledge of the three-dimensional atmospheric circulation and is generally more difficult to estimate. There are several reasons for this. Firstly, precipitation varies widely in time and space and available observations, such as those that exist on the ice sheets, are insufficient to provide a satisfactory sampling. Secondly, precipitation is extremely difficult to measure accurately due to wind and similar problems making it difficult to accurately collect snow in the precipitation gauges (Bromwich et al. 2004). Generally there is a considerable underestimation of snow (Groisman et al. 1999; Allerup et al. 2000). Estimates from snow on the ground are also unreliable for several reasons including the problem with snowdrift leading to a very uneven deposition.

Precipitation on the Greenland ice sheet falls essentially as snow except in coastal regions. Over Antarctica practically all precipitation comes as snow. This is also likely to occur even if the climate is warming by some degrees Celsius towards the end of this century as suggested from the IPCC model simulations (Lemke et al. 2007; IPCC AR4). Even if precipitation occasionally comes as rain it is likely to subsequently freeze as the water percolates into the depth of the ice.

Simulation of the surface mass balance of glaciers and ice sheets has therefore been struggling with the difficulty of estimating precipitation (Oerlemans 1990) and in particular to estimate how future precipitation will evolve in conditions of higher surface and tropospheric temperatures. The methodology that has evolved during the last decades (e.g. Ohmura et al. 1996) is to make use of weather prediction models or similar models used for climate simulation. The principle is simple. The model calculates the temperature and the

surface energy balance from which the mass changes can be calculated. The net mass balance is obtained from the model's calculation of solid precipitation minus the net loss from melting and sublimation/evaporation. In the case of rain, the water is assumed to be drained away but might refreeze if percolated into the depth of the land ice. However, the refreezing is not normally considered in these kinds of studies and will not be included here.

As atmospheric models have improved in resolution and the handling of physical processes such as clouds, convection and radiation, they have increasingly been used to estimate the surface mass balance. The calculation of precipitation cannot be made from initial data but requires a short-time integration to avoid adjustment problems (Bengtsson et al. 2007b). Alternatively, one might also calculate the net divergence of water vapour over a region covering the ice sheets. Such estimates have been undertaken with increasingly realistic models during the last decade (Serreze et al. 2006; Jakobson and Vihma 2009). The advantage with this approach is that it can be calculated directly from analyses of horizontal winds and water vapour.

In a warmer climate the net water vapour transport increases rapidly as it scales with the Clausius-Clapeyron (C–C) relation as will be outlined below, the reason for this unexpected consequence, that will significantly influence the SMB, is the circumstance that different physical processes regulate the change in atmospheric water vapour and the change in evaporation. As a consequence, water vapour is expected to increase more rapidly than evaporation and consequently also faster than the global precipitation. Following the C–C relation the increase is some 6–7% for each degree of warming, while global mean precipitation increases only by about 1% per degree warming (Held and Soden 2006). It further follows that the change in the horizontal net transport of water vapour is also scaled by the C–C relation (Held and Soden 2006). This will have important consequences for the net mass accumulation on the ice sheets as precipitation over the ice sheets is expected to increase accordingly.

The result is sensitive to horizontal resolution. A high horizontal and vertical resolution will provide a better description of both physical and dynamical processes as well as a more realistic topographical mapping of the ice sheets that will affect both accumulation (solid precipitation) and ablation (evaporation, sublimation and run-off). We will exemplify this by analyzing a series of climate model integrations for the present as well as for a future climate.

In Sect. 2 we will first try to show the principal ideas by means of a simple *Gedankenexperiment* and demonstrate how temperature and precipitation are likely to influence SMB in a warmer climate. In Sect. 3 we show some results from SMB calculation from a high-resolution version of the ECHAM5 model. Section 4, finally, contains a general discussion and comparison with other recent studies.

2 Some General Consideration on the Mass Balance of Ice Sheets in a Warmer Climate

Let us undertake a simple *Gedankenexperiment* in addressing the following question:

What will happen to the Earth's ice sheets if the global temperature increases by some 3°C?

Let us assume at the outset that the ice sheets are in a quasi-equilibrium or that the imbalance is not caused by a temperature perturbation. This means that accumulation and ablation, at least when averaged over a period of time, are of the same magnitude.

Furthermore, we will not consider any changes in iceberg discharges, but simply assume that these at first order are either neutral or proportional to any changes in the net surface mass balance. We use here 1.75 and 13.92 Mkm^2 for the ice-covered area of Greenland and Antarctica, respectively.

According to observations and model studies (Ohmura 2001), ablation can be estimated from the mean summer temperature over the ice using the empirical formula

$$\begin{array}{ll} A = 514T_{JJA} + 930 & \text{if } T_{JJA} > -1.8°C \\ A = 0 & \text{if } T_{JJA} < -1.8°C \end{array} \quad (1)$$

Here A is the total annual ablation A (mm/year) and T_{JJA} is the mean summer temperature in °C. For the southern hemisphere we use DJF, December, January and February instead. As a first step we need to estimate the size of the area where the summer temperature is higher than −1.8°C. For Antarctica, preliminary studies (Wild et al. 2003) indicate that the −2°C isotherm for a comparative global warming to 3°C falls outside the Antarctic continent and consequently no significant ablation will occur. For Greenland on the other hand the area of ablation will increase. However, as has been shown by Wild et al. (2003) this must be estimated from detailed topographic data and not from low-resolution model topography.

The majority of present climate models, such as used in IPCC AR4, have a rather crude representation of the topography and are therefore in this respect highly misleading in representing steep slopes. A warming of some 3°C corresponds to a height difference of ca 400 m and using detailed topographic data that means that the melt zone of Greenland is increasing by some 10%. This would correspond to a total increase in ablation according to expression (1) by some 2.71×10^{14} kg or 271 km^3/year water. Using a topography representation (ca 100 km grid length) of a similar resolution as the climate model used in IPCC AR4 the melt zone area will lead to a higher ablation (Wild et al. 2003, their Figure 6).

As climate is warming the water vapour is increasing proportional to the Clausius-Clapeyron relation (Pierrehumbert et al. 2007). It also follows that the change in the transport or net convergence of water vapour also scales with the C–C relation, (Held and Soden 2006). For a 3°C warming the net transport of water vapour is expected to increase by 20–25%. Let us here use the lower value of 20%. The annual mass accumulation (precipitation-sublimation) of Greenland is estimated to 340 mm/year corresponding to some 600 km^3/year water. A 20% increase in net moisture convergence would then correspond to 120 km^3/year water. Together with the increase in ablation this will result in a mass loss for Greenland of 151 km^3/year corresponding to an increase in sea level rise by ca. 0.4 mm/year.

For Antarctica the situation is different. Here the ablation is insignificant and the corresponding mass increase of 20% (precipitation–sublimation) is equal to an increase in precipitation of ca 33 mm/year equal to 460 km^3/year water. The corresponding contribution to sea level would correspond to a fall of ca. 1.3 mm/year.

It is easily realized that the general issue is highly non-linear. If the warming were to increase further, the melt zone is likely to affect central areas of Greenland where the slope is much less and hence the melt zone would increase significantly faster. This would rapidly add to the negative mass balance leading to a further rise in sea level. Secondly, any further increase in warming is likely to extend ablation to some of the coastal regions of Antarctica. A more general interpretation can thus be done as follows.

For a modest warming we are likely to have a net mass accumulation as the source term increases more rapidly than the sink term. The ablation is further likely to be modest because the steep slopes of the glaciated areas. However, as soon as the warming has passed a critical value, that probably is higher than +3°C, the ablation will accelerate as

the area exposed to melting is rapidly growing as it starts to affect the region of modest slope on Greenland. Gregory and Huybrechts (2006) have estimated critical values for Greenland to 4.5°C ± 0.9°C. A similar development is likely to occur at the Antarctic continent but would require a much larger proportional temperature increase.

So a general conclusion might be that in a climate warming scenario ice sheets might initially increase and consequently sea level will fall due to the fact that accumulation will increase faster than ablation. However, for a more substantial warming this is likely to turn into another regime dominated by rapid mass losses. Needless to say, the estimate must be corrected for an additional mass loss due to calving that in its turn is influenced by higher temperatures both in the atmosphere and in the oceans. In the next section we will contrast these general observations with actual calculations from a comprehensive climate model.

3 Result of Recent Model Studies with the ECHAM5 Climate Model

To realistically and credibly calculate the surface mass balance with a numerical model it requires not only a model that is physically and dynamically capable of reproducing the key processes that determine the surface mass balance. It also requires a model with sufficient resolution to represent the 3-dimensional form of the ice sheets and the way the ice sheets are influenced by the weather patterns as well as the way the ice sheets influence the weather patterns in their turn. It is only recently that global models at sufficient resolution have become available for climate change studies such as computing the SMB of the ice sheets on Greenland and Antarctica. Most previous studies have made use of imbedded regional models using the lateral boundary values of a global general circulation model. The advantage of using a high-resolution global model is to avoid artificial circulation at the boundaries between the global and regional model that might influence the water flux. Furthermore, the results of limited area models depend also on the global model that controls the net transport of water vapour through the boundary.

We show here some recent studies with the Max Planck Institute for Meteorology (MPI-M) climate model ECHAM5 (Roeckner et al. 2003, 2006) but at a much higher resolution than was described in the original publications. Examples of high resolution studies by this model can be found in Bengtsson et al. (2007a) and (2009) and the reader is referred to these later publications for a description of the high resolution experiments. Data for precipitation, evaporation, ablation and SMB were calculated and systematically stored during the cause of the integrations. We have here used archived data for every month. Two kinds of studies are described.

The first study is a standardized numerical experiment using observed sea surface temperature, SST. Such experiments have been undertaken by the atmospheric modelling community to compare and evaluate models and are notified by the acronym, AMIP, Atmospheric Modelling Inter-comparison Project (AMIP 1996). To some degree AMIP experiments are constrained by the observed climate through the sea-surface-temperatures (SST) but only to a limited degree as the high and middle latitude circulation in particular is only weakly constrained by the SST.

The second study is a climate change experiment exploring how the ice sheets will respond to a warmer climate, in turn a consequence of an increasing greenhouse gas concentration and changing aerosols. Due to the use of different resolution in the experiments, the size of the ice sheets varies somewhat. In order to simplify the inter-comparison between the experiments undertaken here, as well as similar studies elsewhere, we have normalized the area size to 1.75 Mkm^2 for Greenland and 13.92 Mkm^2 for Antarctica.

3.1 Surface Mass Balance in the Present Climate

In the first experiment we use a very high-resolution version of the ECHAM5 spectral transform model at a triangular truncation of T319, corresponding to a Gaussian grid of ca 40 km. The model has been integrated through the 23 years (1979–2001) using observed sea surface temperatures, SST and other conditions, such as greenhouse gas concentration stipulated in the AMIP 2 protocol (AMIP 1996).

We compare the results with a similar integration at lower horizontal resolution. Figure 1 shows the topography of Greenland and Antarctica, respectively and for both T319 and T63. The T63 resolution is typical for the climate models used in IPCC AR4 (IPCC 2007). In Figure 2 we show a cross section in a West to East direction through Greenland at latitude 63°N and 73°N. We have also indicated in the cross section the topography calculated from a 1 × 1 km grid (DiMarzio et al. 2007). The cross section shows clearly that the T319 resolution follows the actual topography rather closely while the T63 is heavily smoothed.

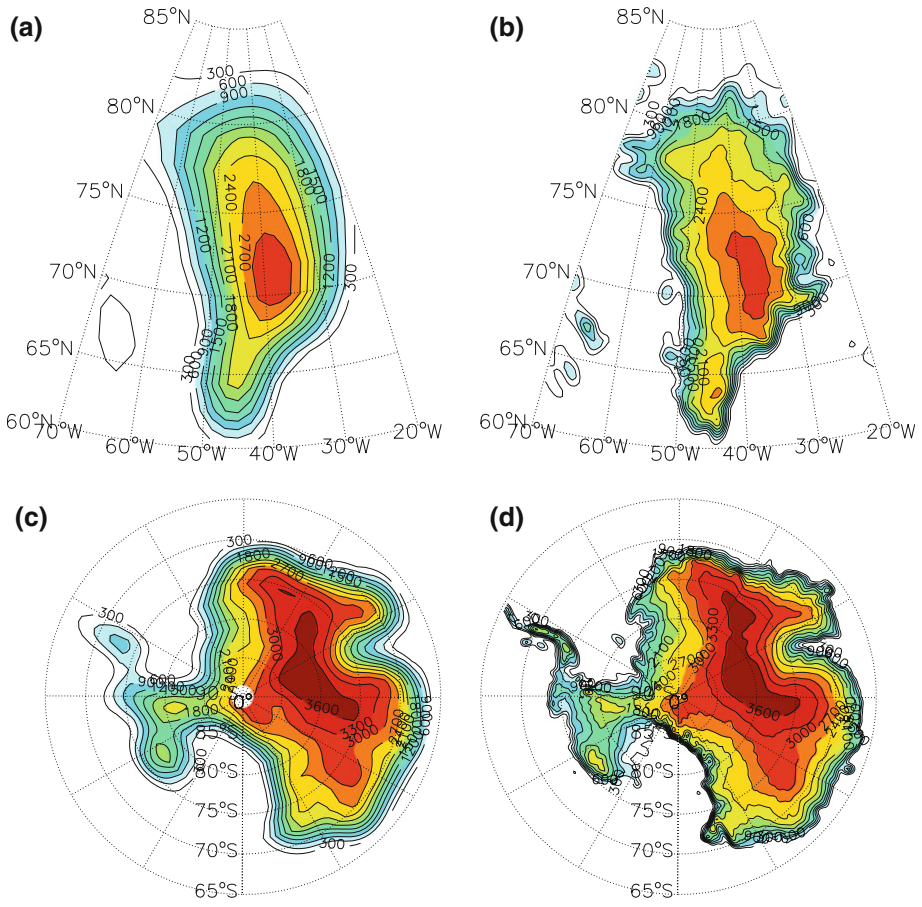

Fig. 1 Representation of the Greenland and Antarctica orography, for two model resolutions, T63 (**a**, **c**) and T319 (**b**, **d**). Values are expressed in meters (*contour lines* interval is 300 m). Colors towards red denote high elevation

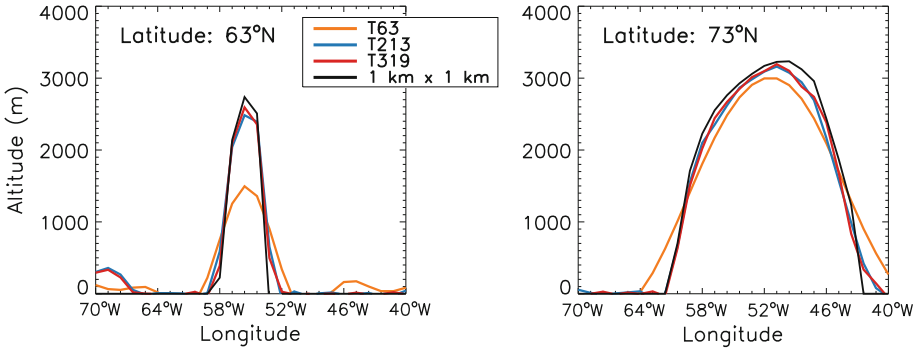

Fig. 2 Cross section in the West to East direction through Greenland at latitude 63°N (*left*) and 73°N (*right*), for various resolutions: T319 (*red line*), T213 (*blue line*), T63 (*orange line*) and 1 × 1 km (*black line*). Values are expressed in meters

Table 1 Greenland ice sheet; precipitation, ablation and surface mass budget (in km^3/year) for three horizontal resolutions

Parameter	T319[a]	T106[b]	T63[b]
Precipitation	746	778	861
Snow	626	660	723
Ablation	358	1,183	1,027
SMB	268	−523	−304
Sea level change mm/year	−0.7	1.4	0.8

[a] 1978–2000 average

[b] 1978–1998 average

We summarize the results for Greenland in Table 1 where we also for comparison include the results for the lower resolutions T106 and T63. Precipitation consists of some 85% of snow. It is larger for the lower resolutions presumably because the area of Greenland is distorted at the lower resolution due to the imperfect representation. Another explanation might be that synoptic weather systems that pass Greenland will be penetrating further inland in the lower resolution model. However, as can be seen, there is a considerable increase in the ablation at the lower resolution. We consider this to be a consequence of the artificial topography at the lower resolution as shown in Figure 2. This will strongly influence the SMB. The T319 resolution run shows a positive SMB of 268 km^2/year, implying a negative contribution to sea level height. The low-resolution runs on the other hand show a negative SMB because of a much larger ablation, and correspondingly a positive contribution to sea level change.

Table 2 shows similar results for Antarctica. At the T319 resolution 99% of the precipitation on Antarctica is snow. At this resolution the ablation is small leading to a SMB of 2,601 km^3. For the T63 resolution the ablation is significantly higher so in spite of higher precipitation, the SMB is reduced to 1,864 km^3. The effect on sea level height is strongly negative. For the T319 run the increased accumulation will reduce the sea level height by 7.2 mm/year and 2 mm/year less for the T63 resolutions. Again we must recall that these values do not include any mass losses due to calving or to long-term adjustment processes.

We have also investigated the annual variability of SMB for Greenland and Antarctica, respectively, Figure 3. There are considerable variations from year to year due to the natural variability of atmospheric circulation with considerable inter-annual variations making it virtually impossible to obtain robust trends. The magnitude of the internal

Table 2 Antarctica ice sheet; precipitation, ablation and surface mass budget (in km^3/year) for three model horizontal resolutions

Parameter	T319[a]	T106[b]	T63[b]
Precipitation	3,174	3,580	3,698
Snow	3,115	3,491	3,572
Ablation	514	1,627	1,778
SMB	2,601	1,864	1,794
Sea level change mm/year	−7.2	−5.2	−5.0

[a] 1978–2000 average

[b] 1978–1998 average

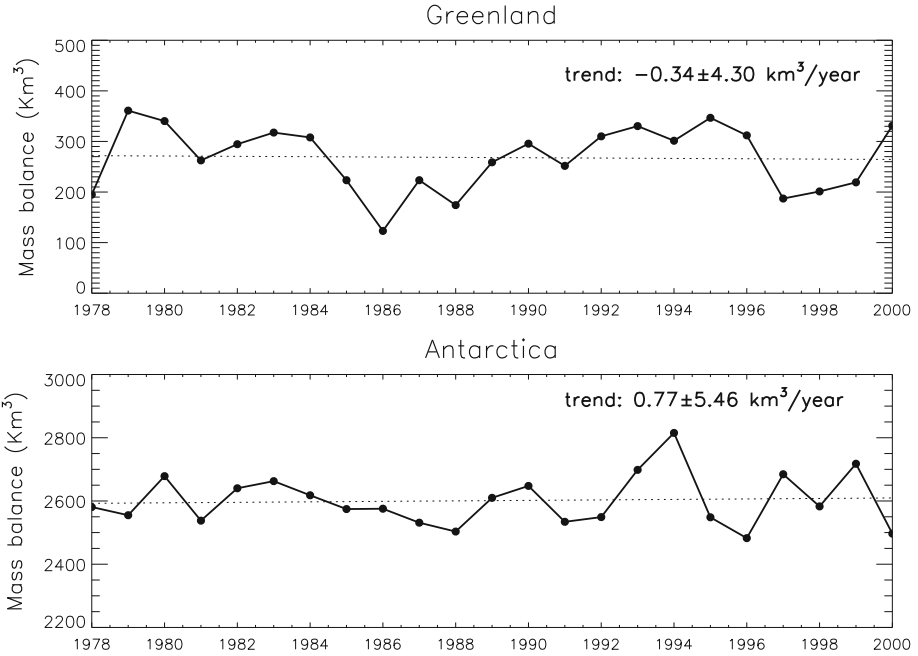

Fig. 3 Annual variability of SMB for Greenland and Antarctica. Values are in km^3/year

variability is close to the variability from observational assessment of SMB on Greenland (Johannessen et al. 2005). This must be kept in mind when interpreting observational records shorter than some 30 years.

3.2 The Effect of Climate Change

We will next consider results from the climate change experiment at T213 resolution (equivalent to ca 60 km grid). We compare two 30-year periods, one from the twentieth century (1960–1990), C20 and the other for the twenty-first century (2070–2100), C21 (Roeckner et al. 2006; Bengtsson et al. 2007a). For the period until year 2000 we have used

observed greenhouse gases and estimated aerosol concentrations. After year 2000 the calculation is based on the IPCC SRES scenario A1B (IPCC 2007).

A1B is a middle of the range scenario with a CO_2 increase growing to ca 60 Gton/year in 2050 (corresponding to an annual increase of 1.75%. The annual increase 2000–2007 was more than twice as high). The sulphate aerosol emission reaches a maximum in 2020 and decreases thereafter relatively fast. At the end of the twenty-first century it is only some 30% of its maximum value. The calculated global temperature change at C20 and C21 amounts to ca +3°C. The mean annual temperature change over Greenland increases by 5.2°C and over Antarctica by 3°C (Tables 3, 4).

Numerical experiments show that the transport of water vapour into areas of general convergence scales with the C–C relation. The increase in the net transport of moisture into the Arctic region (60°N–90°N) amounts to 27% between C20 and C21 with a similar increase in (P-E). The corresponding net transport into the Antarctic region (60°S–90°S) is slightly smaller, amounting to 22%. For further information see Bengtsson et al. (2011).

As discussed by Held and Soden (2006) regional precipitation in areas of convergence follows the transport. Specifically over Greenland calculation shows that precipitation is increasing by 33% (Table 3) and over Antarctica by 18% (Table 4).

The left panel of Figure 4 shows the annual precipitation for Greenland at C20 with the marked maximum precipitation in the southeastern part of the island, in agreement with different observational estimates (Ohmura et al. 1999). Figure 4 (right panel) shows the percentage change in precipitation between C21 and C20. Precipitation increases everywhere with the largest percentage contribution in the northeastern part. This is expected to be related to a change in cyclonic activity and reduced Arctic sea ice (Bengtsson et al. 2009).

Figure 5 shows the same for Antarctica. There are huge variations in precipitation between different parts of Antarctica, with comparatively high precipitation near the coast and at the western part of the Antarctic Peninsula. In the high altitude inner part of

Table 3 Greenland; mean temperature, precipitation, ablation and surface mass balance changes (in km^3/year) at C20 (1960–1990) and C21 (2070–2100) and the corresponding changes

Parameter	T213(C20)	T213(C21)	C21–C20
Temperature	−21.8°C	−16.6°C	5.2°C
Precipitation	714	946	232 (33%)
Snow	619	691	72 (12%)
Ablation	281	848	567
SMB	338	−157	−495
Sea level change mm/year	−0.9	+0.4	+1.4

Table 4 Antarctica; mean temperature, precipitation, ablation and surface mass balance changes (in km^3/year) at C20 (1960–1990) and C21 (2070–2100) and the corresponding changes

Parameter	T213(C20)	T213(C21)	C21–C20
Temperature	−38.5°C	−35.5°C	3°C
Precipitation	3,182	3,769	587 (18%)
Snow	3,137	3,624	487 (16%)
Ablation	583	785	202
SMB	2,554	2,839	285
Sea level change mm/year	−7.0	−7.9	−0.8

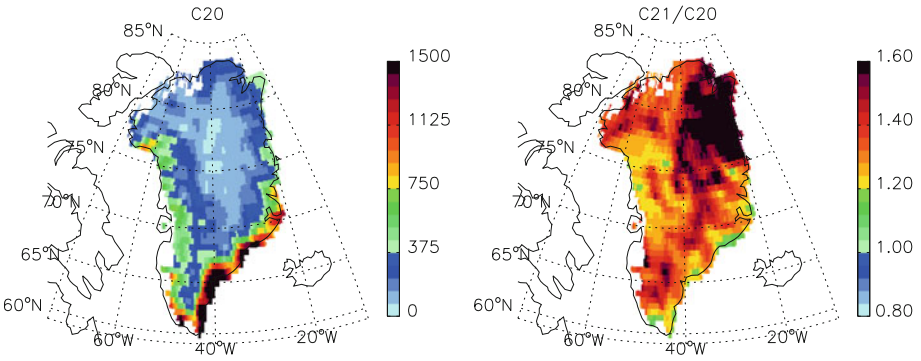

Fig. 4 Annual precipitation for Greenland for the C20 experiment (*left*) and percentage change between the C21 and C20 experiments (*right*). Values are in mm/year

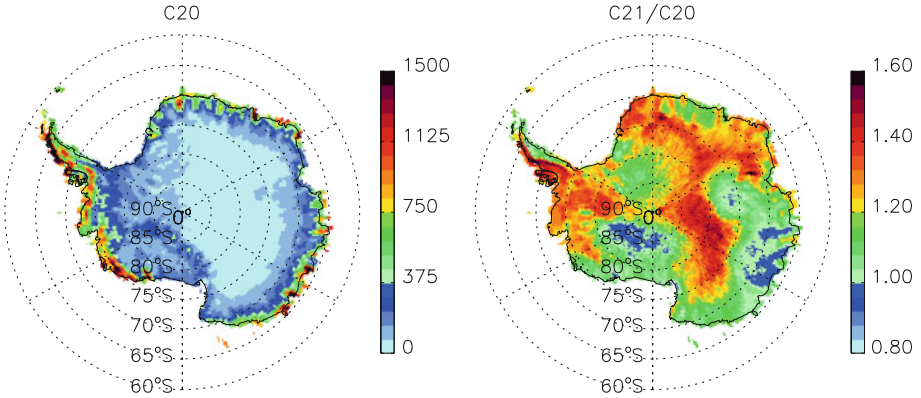

Fig. 5 Same as Figure 4 but for Antarctica

Antarctica, the precipitation is as low as 10–20 mm/year and difficult to estimate. Using recent re-analysis data from ECMWF ERA-Interim (Dee and Uppala 2009) we found a mean annual net moisture transport for an area over East Antarctica (a circular region of 8° radius in geodetic coordinates with its centre at 81°S, 60°E) as low as 2 mm/month. This is in general agreement with other estimates (Bromwich et al. 2004).

The somewhat irregular percentage change in precipitation between C20 and C21 (right panel of Figure 5) is probably a model artefact as we are comparing very low values in precipitation. As described in Bengtsson et al. (2006) the change in the climate of the southern polar region is a tendency for the storm tracks to move closer to the Antarctic continent. It was suggested that this is related to the poleward transition of the area of maximum SST gradient leading to a poleward transition of the area of maximum baroclinicity (Bengtsson et al. 2006).

Table 3 summarizes the mean mass balance for Greenland for C20 and C21. Precipitation increases by 33% while the increase for solid precipitation is much less by 12%. This indicates that an increasing amount of precipitation at C21 falls as rain on Greenland thus leading to a large increase in the ablation. The change in SMB is -495 km^3/year corresponding to a sea level rise of 1.4 mm/year. As shown in Figure 6a, the largest negative

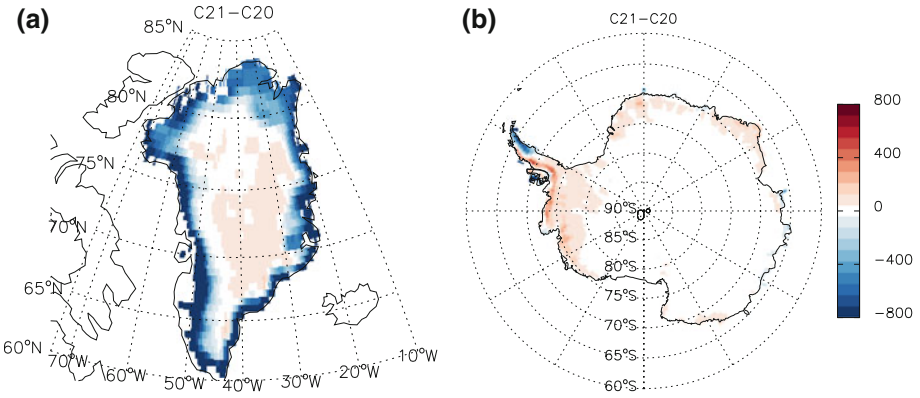

Fig. 6 **a** Shows the annual change in SMB for Greenland between C21 and C20 and **b** the same for Antarctica. Note the difference between the coastal regions (surface mass losses) and the interior (surface mass gains). Unit: mm/year

change in SMB is located at the ablation zones close to the ice sheet margin and, especially in the southern part, in agreement with Mernild et al. (2010). The inner parts of the ice sheets have a positive SMB.

Based on the GLAS/ICES at 1 km laser altimetry digital elevation model of Greenland (DiMarzio et al. 2007) and assuming that the upper limit of the ablation zone is increasing linearly from 850 to 1,500 m a.s.l. from the North to the South of Greenland, the mean width of the ablation zone is found to be 313 km, ranging from 6 km to 1,590 km. Consequently, the model may still overestimate the ablation zone even at the T213 resolution, which corresponds approximately to 60 km.

Table 4 shows the mass balance for Antarctica at C20 and C21. The increase in precipitation is less than for Greenland (18%) and the dominant part of precipitation at C21 will still fall as snow. The increase in ablation is less than the increase in solid precipitation so the SMB is positive. The change in SMB is $+285$ km^3/year corresponding to a sea level fall by 0.8 mm/year. At the northern and eastern part of the Antarctic Peninsula though, we find some increased net loss, as shown by the negative SMB (Figure 6b). Similar increases in melting over this region have also been found by Krinner et al. (2007) with the LMDZ4 model.

We have undertaken similar calculations with the T63-resolution model. Individual values differ as both precipitation and ablation are larger, but interestingly enough the change in SMB or sea level change is more or less the same. This suggests that the calculated change might be robust to resolution changes even if the data for each period differ significantly. Presently we do not know if this is a coincidence or an indication that climate change as a perturbation study can be accomplished with simpler models.

Figure 7 shows the inter-annual variation in SMB for both C20 and C21. The red lines show results for Greenland. While there is a distinct difference between the two curves it is not possible to identify a robust trend in the present climate run due to the dominance of strong inter-annual variations in the atmospheric circulation and hence in both temperature and precipitation. On the contrary, in the warmer climate scenario, the SMB trend over Greenland is strongly negative (around -10.7 km^3/year).

We have also included in Figure 7 the change in SMB for northern hemisphere (NH) glaciers outside Greenland. These glaciers cover an area equal to 550×10^3 km^2 (Ohmura

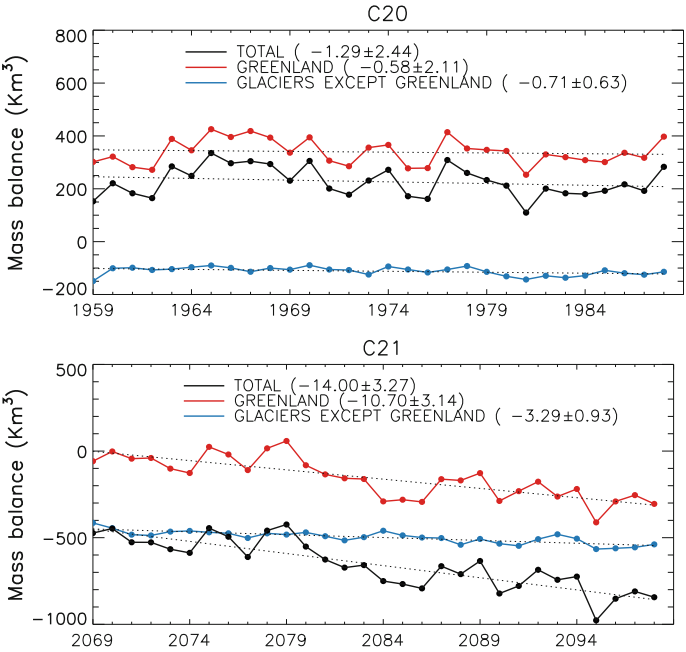

Fig. 7 Annual variability and linear trends of SMB for the C20 (*top panel*) and C21 (*bottom panel*) experiments for the Greenland ice sheet (*red line*), for the northern hemisphere glaciers outside Greenland (*blue line*) and the sum of the two (*black line*). Values are in km^3/year

2006). As previously, we normalize the simulated glaciated area to this value for comparison purposes. Over these glaciers, SMB is negative for the C20 as well with an indication of a slight negative trend. The average SMB for the C20 period (1959–1989) is −112 km^3/year, which is a bit lower than observational estimates, e.g., −140 km^3/year (Ohmura 2006).

The contribution of the NH glaciers outside Greenland to the total northern hemisphere SMB is significant, especially in the C21 run, reducing the SMB by 523 km^3/year on average (blue line, Figure 7). The change in SMB over these glaciers between C20 and C21 is equal to −404 km^3/year. This leads to a total NH SMB change of −900 km^3/year, which corresponds to a sea level rise of +2.7 mm/year.

4 Results from Other Model Studies

A series of papers during the last decade has undertaken different estimates of the total mass losses on Greenland (Mernild et al. 2010 and references therein). We summarize a number of these studies in Table 5. During the last decade or decades these data estimate the surface mass balance changes to between 200 and 400 km^3/year and generally smaller during the last 5–8 years. There are also estimates of changes in the surface melt area. According to Mote (2007) this was found to have increased by 1%/year during the period 1973–2007 corresponding to an increase in the melt area by some 35% of the whole of Greenland between 1973 and 2007. Other estimates are going even further. Tedesco (2007) for example suggests an increase in the melt area by some 32% for the period 1992–2005.

Table 5 Precipitation and SMB estimates (in km^3/year) for the Greenland ice sheet from recent studies. After Mernild et al. (2010)

Parameter (km^3/year) Studied period	Box et al. (2006) 1995–2004	Fettweis (2007) 1979–2006	Hanna et al. (2008) 1995–2007	Mernild et al. (2009) 1995–2007	This study T319 1978–2000
Precipitation	654 ± 61	641 ± 60	655 ± 54	636 ± 35	746 ± 76
SMB	160 ± 69	263 ± 138	316 ± 116	141 ± 85	268 ± 64

At the same time the longer term warming trend has been more modest. Box et al. (2009), combining meteorological stations' records and regional climate model output, have estimated the summertime temperature change over Greenland to be about 0.7°C from 1955 to 2007. This would correspond to a lifting of say the −2°C isotherm by ca 100 m. Using the methods by Wild et al. (2003) (see their Figure 6) this would correspond to a miniscule increase in the area of melting. How can we then explain this apparent inconsistency?

According to Box et al. (2009) and Hanna et al. (2008), the mean annual temperature was broadly constant from the 1950s to the mid 1990s and increased rapidly by 1–2°C thereafter. This suggests that according to Ohmura's empirical relation no ablation might be expected above some 1,200 m asl in the present climate. It is also clear that the many warm summers during the last 15 years are likely to have led to an increased ablation in levels generally below 1,200 m. However, there is no evidence from present climate models that the sharp warming trend over the last decade or so can be extrapolated. As can also be seen on both Figs. 3 and 6 there are considerable inter-annual variations that might create fortuitous trends on decadal time-scales.

We have compared our climate change results with other groups' results for Greenland and Antarctica, respectively, Tables 6 and 7. The results for Greenland is similar to Mernild et al. (2010) but cannot be exactly compared as the period of comparison differs. Wild et al. (2003) finds a positive SMB change with ECHAM4 (T106 grid), but with a $2 \times CO_2$ climate scenario. Over Antarctica, we find a somewhat lower increase in the

Table 6 Precipitation and SMB estimates comparison for the climate scenarios for Greenland

Reference	Precipitation			SMB		
	C20	C21	Change	C20	C21	Change
Wild et al. (2003) ($2 \times CO_2$)	670	873	203 (30%)	579	740	161 (28%)
Mernild et al. (2010) (C21: 2050–2080)	646	741	95 (15%)	219	−59	−278 (−127%)
This study (C21: 2070–2100)	714	946	232 (33%)	338	−157	−495 (−146%)

Table 7 Precipitation and SMB estimates comparison for the climate scenarios for Antarctica

Reference	Precipitation			SMB		
	C20	C21	Change	C20	C21	Change
Wild et al. (2003) ($2 \times CO_2$)	2,617	2,965	348 (13%)	2,311	2,617	+306 (13%)
Krinner et al. (2007) (C21: 2050–2080)	2,282	2,770	488 (21%)	2,102	2,547	+445 (21%)
This study (C21: 2070–2100)	3,182	3,769	587 (18%)	2,554	2,839	+285 (11%)

Antarctic SMB than Krinner et al. (2007). The reason for this is not clear but could be due to a tendency of the ECHAM5 model to simulate too high orographic precipitation as discussed by Hagemann et al. (2006). However, as pointed out previously, precipitation is to a large extent unknown in large parts of Antarctica. Present estimates from global models, reanalysis data and dynamical retrieval methods, range from 2,310 to 3,202 km^3/year (Bromwich et al. 2004) which means that the data from Krinner et al. (2007) is at the lower end, while the ECHAM5 used in our study is at the upper end.

5 Concluding Remarks

Mass changes on the ice sheets are due to processes covering a wide range of time scales from tens of thousand years to events such as massive losses of ice shelf that can occur in short time events such as the Larsen shelf ice in 2002 (De Angelis and Skvarca 2003). A realistic assessment of mass losses of the ice sheets must therefore take into consideration processes related to the internal dynamics of the ice. Considerable progress is taking place here as reported elsewhere (Mernild et al. 2009; Ridley et al. 2005; Gregory and Huybrechts 2006) and other publications in this issue.

Let us return to the simple theoretical estimate in Sect. 2 compared to the recent model results discussed in Sect. 3. The SMB results for Greenland are larger by a factor of three from the estimate of the *Gedankenexperiment*, Table 8. There are several reasons for this. The model shows a larger ablation than the empirical estimate. There are several explanations for this. First, we might expect that ablation in a warmer climate will occur outside the summer season implying a larger total ablation. An examination of the model experiment shows that this is the case. Secondly, we note that the temperature change for Greenland actually is larger that the global average of 3°C by more than 2°C. Thirdly, because of the higher temperature the area exposed to melting will increase more rapidly as we are entering a region with reduced slope. Finally, the accumulation is also slightly overestimated as the solid precipitation is increasing much less than the total precipitation.

For Antarctica the simple estimate in the *Gedankenexperiment* is in broad agreement with the model result except that the model calculation has a small ablation, giving rise to a reduction in the SMB. There is also a compensating effect in the accumulation as the model compared to our simple estimate has higher precipitation but a smaller percentage increase.

As discussed above the present result from the ECHAM5 model is close to what has been achieved with other general circulation models suggesting an accelerated mass loss at Greenland and a minor gain on Antarctica (Huybrechts et al. 2011). The contribution to sea level rise, if we assume a linear decrease in SMB during the twenty-first century, will amount to some 7.5 cm in sea level rise and from Antarctica a fall of some 4 cm. This

Table 8 Comparison of precipitation, ablation and SMB as estimated in Sect. 2 and model results from Sect. 3

Parameter/Mass changes in km^3/year	Estimate (Greenland)	Model (Greenland)	Estimate (Antarctica)	Model (Antarctica)
Precipitation	120	232	460	587
Ablation	271	567	0	202
SMB	−151	−495	460	285
Sea level change mm/years	+0.4	+1.4	−1.3	−0.8

result suggests that the problems for the twenty-first century are not the changes in SMB, that are likely to be minor, but rather other aspects of land ice losses such as a possible increase in calving caused by accelerating glaciers on the ice sheets. No doubt such questions will have to be addressed in a comprehensive way in future studies.

Acknowledgments The authors are most grateful to Noel Keenlyside of the Leibniz Institute of Marine Sciences at Kiel University for providing the ECHAM5 C20 and C21 climate simulation data.

References

Allerup P, Madsen H, Vejen F (2000) Correction of precipitation based on off-site weather information. Atmos Res 53(4):231–250

AMIP Project Office (1996) AMIP II Guidelines, AMIP newsletter, No. 8. Available online at http://www-pcmdi.llnl.gov/projects/amip/NEWS/amipnl8.php#2.%20AMIP%20II%20Experimental

Bengtsson L, Hodges KI, Roeckner E (2006) Storm tracks and climate change. J Climate 19(15):3518–3543

Bengtsson L, Hodges KI, Esch M, Keenlyside N, Kornblueh L, Luo J, Yamagata T (2007a) How may tropical cyclones change in a warmer climate? Tellus 59(4):539–561

Bengtsson L et al (2007b) The need for a dynamical climate reanalysis. Bull Amer Meteor Soc 88:495–501

Bengtsson L, Hodges KI, Keenlyside N (2009) Will extra-tropical storms intensify in a warmer climate? J Climate 2276–2301:2009

Bengtsson L, Hodges KI, Koumoutsaris S, Zahn M, Keenlyside N (2011) On the atmospheric water balance of the Polar Regions. Tellus, under review

Box JE, Bromwich DH, Veenhuis BA, Bai LS, Stroeve JC, Rogers JC, Steffen K, Haran T, Wang SH (2006) Greenland ice sheet surface mass balance variability (1988–2004) from calibrated Polar MM5 output. J Climate 19(12):2783–2800

Box JE, Yang L, Bromwich D, Bai L-S (2009) Greenland ice sheet surface air temperature variability: 1840–2007. J Climate 22(14):4029

Bromwich DH, Guo Z, Bai L, Chen Q-S (2004) Modeled Antarctic precipitation. Part I: spatial and temporal variability. J Climate 17:427–447

De Angelis H, Skvarca P (2003) Glacier surge after ice shelf collapse. Science 299(5612):1560–1562

Dee DP, Uppala S (2009) Variational bias correction of satellite radiance data in the era-interim reanalysis. Q J R Meteorol Soc 135(644):1830–1841

DiMarzio J, Brenner A, Schutz R, Shuman CA, Zwally HJ (2007) GLAS/ICESat 1 km laser altimetry digital elevation model of Greenland. National Snow and Ice Data Center. Digital media, Boulder, Colorado

Fettweis X (2007) Reconstruction of the 1979–2006 Greenland ice sheet surface mass balance using the regional climate model MAR. Cryosphere 1(1):21–40

Gregory JM, Huybrechts P (2006) Ice-sheet contributions to future sea-level change. Philos Trans R Soc A-Math Phys Eng Sci 364(1844):1709–1731

Groisman PY, Peck EL, Quayle RG (1999) Intercomparison of recording and standard nonrecording US Gauges. J Atm Ocean Tech 16(5):602–609

Hagemann S, Arpe K, Roeckner E (2006) Evaluation of the hydrological cycle in the ECHAM5 model. J Climate 19(16):3810–3827

Hanna E, Huybrechts P, Steffen K, Cappelen J, Huff R, Shuman C, Irvine-Fynn T, Wise S, Griffiths M (2008) Increased runoff from melt from the Greenland ice sheet: a response to global warming. J Climate 21(2):331–341

Held IM, Soden BJ (2006) Robust responses of the hydrological cycle to global warming. J Climate 19(21):5686–5699

Huybrechts P, Goelzer H, Janssens I, Driesschaert E, Fichefet T, Goosse H, Loutre M-F (2011) Response of the Greenland and Antarctic ice sheets to multi-millennial greenhouse warming in the Earth system model of intermediate complexity LOVECLIM. Surv Geophys (this issue)

Intergovernmental Panel on Climate Change (IPCC) (2007) Climate change 2007: the scientific basis. Cambridge University Press, Cambridge

Jakobson E, Vihma T (2009) Atmospheric moisture budget in the Arctic based on the ERA-40 reanalysis Int J Climatol. doi:10.1002/joc.2039

Johannessen OM, Khvorostovsky K, Miles MW, Bobylev LP (2005) Recent ice-sheet growth in the interior of Greenland. Science 310(5750):1013–1016

Krinner G, Magand O, Simmonds I, Genthon C, Dufrense J-L (2007) Simulated Antarctic precipitation and surface mass balance at the end of the twentieth and twenty-first centuries. Clim Dyn 28:215–230. doi: 10.1007/s00382-006-0177-x

Lemke P, Ren J, Alley RB, Allison I, Carrasco J, Flato G, Fujii Y, Kaser G, Mote P, Thomas RH, Zhang T (2007) Observations: changes in snow, ice and frozen ground. In: Solomon S, Qin D, Manning M, Chen Z, Marquis M, Averyt KB, Tignor M, Miller HL (eds) Climate change 2007: the physical science basis. Contribution of Working Group I to the fourth assessment report of the intergovernmental panel on climate change. Cambridge University Press, Cambridge, UK and New York

Mernild SH, Liston GE, Hiemstra CA, Steffen K, Hanna E, Christensen JH (2009) Greenland ice sheet surface mass-balance modelling and freshwater flux for 2007, and in a 1995–2007 perspective. Hydrol Process 23(17):2470–2484

Mernild SH, Liston GE, Hiemstra CA, Christensen JH (2010) Greenland ice sheet surface mass-balance modeling in a 131-yr perspective, 1950–2080. J Hydrometeorol 11(1):3–25

Mote TL (2007) Greenland surface melt trends 1973–2007: evidence of a large increase in 2007, Geophys Res Lett 34. doi:10.1029/2007GL031976

Oerlemans J (1990) A model for the surface balance of glaciers. Part 1: Alpine glaciers. Z Gletscherk Glazialgeol 27:63–83

Ohmura A (2001) Physical basis for the temperature-based melt-index method. J Appl Meteorol 40(4): 753–761

Ohmura A (2006) Changes in mountain glaciers and ice caps during the twentieth century. Ann Glaciol 43:361–368

Ohmura A, Wild M, Bengtsson L (1996) A possible change in mass balance of Greenland and antarctic ice sheets in the coming century. J Climate 9(9):2124–2135

Ohmura A, Calanca P, Wild M, Anklin M (1999) Precipitation, accumulation and mass balance of Greenland ice sheet (1999). Z Gletscherk Glazialgeol 35:1–20

Pierrehumbert RT, Brogniez H, Roca R (2007) On the relative humidity of the Earth's atmosphere. In: Schneider T, Sobel AH (eds) The global circulation of the atmosphere. Princeton University Press, Princeton, NJ, pp 143–185

Ridley JK, Huybrechts P, Gregory JM, Lowe JA (2005) Elimination of the Greenland ice sheet in a high CO_2 climate. J Climate 18(17):3409–3427

Roeckner E, Bauml G, Bonaventura L, Brokopf R, Esch M, Giorgetta M, Hagemann S, Kirchner I, Kornblueh L, Manzini E, Rhodin A, Schlese U, Schulzweida U, Tompkins A (2003) The atmospheric general circulation model ECHM5: Part 1, Tech Rep 349, Max Planck Institute for Meteorology, Hamburg

Roeckner E, Stier P, Feichter J, Kloster S, Esch M, Fischer-Bruns I (2006) Im-pact of carbonaceous aerosol emissions on regional climate change. Clim Dyn 27(6):553–571

Serreze MC, Barrett AP, Slater AG, Woodgate RA, Aagaard K, Lammers RB, Steele M, Moritz R, Meredith M, Lee CM (2006) The large-scale freshwater cycle of the arctic. J Geophys Res-Oceans 111(C11). doi:10.1029/2005JC003424

Tedesco M (2007) Snowmelt detection over the Greenland ice sheet from SSM/I brightness temperature daily variations. Geophys Res Lett 34. doi:10.1029/2006GL028466

Wild M, Calanca P, Scherrer SC, Ohmura A (2003) Effects of polar ice sheets on global sea level in high-resolution greenhouse scenarios. J Geophys Res-Atmos 108(D5). doi:10.1029/2002JD002451

Surv Geophys (2011) 32:475–494
DOI 10.1007/s10712-011-9114-6

Precipitation Changes in High Southern Latitudes from Global Reanalyses: A Cautionary Tale

Julien P. Nicolas · David H. Bromwich

Received: 30 October 2010 / Accepted: 4 February 2011 / Published online: 15 March 2011

Abstract The temporal consistency of the moisture fields (precipitation, evaporation and total precipitable water) from five global reanalyses is examined over Antarctica and the Southern Ocean during 1989–2009. This concern is important given that (1) global reanalyses are known to be prone to inhomogeneities and artificial trends caused by changes in the observing system, and (2) the period of study has seen a dramatic increase in the volume of satellite observations available for data assimilation. In particular, the study aims to determine whether the recent reanalyses are suitable for investigating changes in Antarctic surface mass balance. The datasets investigated consist of NCEP-2, JRA-25, ERA-Interim, MERRA and CFSR. Strong evidence of spurious changes is found in NCEP-2, JRA-25, MERRA and CFSR, although the magnitude, spatial patterns and timing of these artifacts vary between the reanalyses. MERRA exhibits a jump in Antarctic precipitation-minus-evaporation (P–E) and in Southern Ocean precipitation in the late 1990s. This jump is related to the introduction of sounding radiances from the Advanced Microwave Sounding Unit (AMSU). The impact of AMSU is also discernible, albeit less pronounced, in CFSR data. It is shown that ERA-Interim likely provides the most realistic depiction of the interannual variability and overall change in Antarctic P–E since 1989. We conclude that the presence of spurious changes is not a solved problem in recent global reanalyses. Caution should continue to be exercised when using these datasets for trend analyses in general, particularly in high southern latitudes.

Keywords Surface mass balance · Antarctica · Southern Ocean · Global reanalyses · Spurious trends · Hydrological cycle

Contribution of Byrd Polar Research Center number 1407.

J. P. Nicolas (✉) · D. H. Bromwich
Polar Meteorology Group, Byrd Polar Research Center and Atmospheric Sciences Program, Department of Geography, The Ohio State University, 1090 Carmack Rd, 108 Scott Hall, Columbus, OH 43210, USA
e-mail: nicolas.7@osu.edu

1 Introduction

The Antarctic Ice Sheet receives each year, on average, the equivalent of 6 mm of global mean sea level as snowfall. In light of the current 3.3 ± 0.4 mm year^{-1} rate of global mean sea level rise (Nicholls and Cazenave 2010), the temporal changes in this mass input, described as the surface mass balance (SMB), are of great climatic and societal interest (Meehl et al. 2007). Given the sparsity of accumulation measurements in Antarctica (Eisen et al. 2008) and the low spatial representativeness attached to these observations (Kaspari et al. 2004; Frezzotti et al. 2005), global reanalyses are instrumental for investigations of the changes in Antarctic SMB during recent decades.

In global reanalyses, a variety of historical observations are assimilated into a numerical weather prediction model, allowing the spatial and temporal observational gaps to be filled in a manner consistent with the model physics and dynamics (e.g., Uppala et al. 2008). Still, with meteorological observations restricted mainly to a few coastal Antarctic stations and isolated islands, the mid-high southern latitudes have long been an immense data void. Admittedly, the discrepancy with the observationally dense Northern Hemisphere has been considerably alleviated since 1979, the start of the modern satellite era. The observational coverage of high southern latitudes has been further improved through the launch of multiple polar-orbiting satellite missions in the late 1990s/early 2000s, especially as part of the Earth Observing System (EOS) Program of the National Aeronautics and Space Administration (NASA) (e.g., Parkinson 2003).

Nevertheless, in two respects, the Antarctic and Subantarctic regions can still be regarded as data-sparse areas. First, the benefits of spaceborne remote-sensing data remain uneven in these regions. While abundant satellite observations have become available over the Southern Ocean, the situation over the Antarctic continent has changed little: the difficult detection of clouds and uncertainties in surface emissivity still largely preclude the use of satellite radiances over the ice sheet (Rabier et al. 2010; Bouchard et al. 2010; Guedj et al. 2010). Second, direct meteorological observations such as from radiosondes remain essential to calibrate satellite radiances and ensure the temporal consistency of the geophysical quantities derived from them (Dee and Uppala 2009). This observational constraint is still largely absent over the Southern Ocean, making the reanalysis time series in this region prone to artificial trends and jumps (Hines et al. 2000; Marshall 2002; Bengtsson et al. 2004a, b; Van de Berg et al. 2005; Bromwich et al. 2007).

The paucity of observations, adding to the extreme conditions of the Antarctic climate, has made the mid-high southern latitudes an important challenge for the reanalysis projects carried out thus far. A review of the performance of the global reanalyses in the polar regions was first given by Bromwich et al. (2007), building in part on the results from Bromwich and Fogt (2004). The reanalysis datasets examined in this review included: the National Centers for Environmental Prediction (NCEP)-Department of Energy Atmospheric Model Intercomparison Project 2 reanalysis (NCEP-DOE AMIP-2, or NCEP-2; Kanamitsu et al. 2002); the European Centre for Medium-Range Weather Forecasts (ECMWF) 40-year Reanalysis (ERA-40; Uppala et al. 2005); and the Japan Meteorological Agency (JMA) 25 year Reanalysis (JRA-25; Onogi et al. 2007). Three new global reanalysis datasets have been recently released: the ECMWF 'Interim' reanalysis (ERA-Int; Simmons et al. 2006; Uppala et al. 2008); the NASA Modern Era Retrospective-analysis for Research and Applications (MERRA; Bosilovich et al. 2006); and the NCEP Climate Forecast System Reanalysis (CFSR; Saha et al. 2010).

The new reanalyses feature a number of improvements. Variational bias correction schemes have been developed to automatically and adaptively handle biases in satellite

radiances (Auligné et al. 2007; Dee and Uppala 2009). Observation error statistics from previous reanalysis experiments have served to bias correct radiosonde records (Haimberger 2007). Higher horizontal and vertical model resolutions have been implemented, a critical aspect for the modeling of Antarctic SMB because of the importance of orographic precipitation on the ice sheet's steep margins. Furthermore, the recent reanalyses have incorporated the wealth of satellite observations acquired since the late 1990s. These data have provided enhanced constraint on atmospheric temperature and moisture profiles, but have also generated a dramatic increase in the volume of satellite observations (Dee et al. 2009; Saha et al. 2010), the impact of which has not yet been investigated.

Bromwich et al. (2011, accepted) compared the changes in precipitation and precipitation-minus-evaporation (P–E) over Antarctica and the Southern Ocean simulated by five global reanalyses during 1989–2009, their period of overlap. They found marked differences in their respective depiction of the temporal changes in P and P–E. Spurious changes were identified in NCEP-2, JRA-25 and MERRA over Antarctica and the Southern Ocean. The present study aims to complement this first investigation by exploring additional variables and performing a finer temporal analysis.

The sections are organized as follows. Section 2 introduces the datasets and some methodological aspects. Section 3 describes the temporal variability and trends in Antarctic P–E. Section 4 explores the changes in precipitation and evaporation over the Southern Ocean. Section 5 investigates the changes in atmospheric precipitable water and meridional wind in an effort to further account for the trends in Antarctic P–E observed in the reanalyses. A synthesis table of our results and concluding remarks are given in Sect. 6.

2 Data and Methods

2.1 Reanalysis Datasets

The main characteristics of the six reanalysis datasets used in this study are summarized in Table 1. NCEP-2 and ERA-40 have been widely used in the literature and will therefore not be introduced here. The use of ERA-40 in our investigation is overall more secondary, as it does not provide data beyond August 2002.

JRA-25 is based on JMA's operational forecasting model and assimilation system as of April 2004. As such, it is the first reanalysis to assimilate observations from sensors onboard the constellation of EOS polar-orbiting satellites (e.g., QuikSCAT, *Terra* and

Table 1 Characteristics of the reanalyses

Reanalysis	Organization	Time coverage	Horizontal resolution	Vertical levels	Assimilation system
NCEP-2	NCEP/DOE	1979–present	T62, ~210 km	28	3D-Var
ERA-40	ECMWF	9/1957–8/2002[a]	T159, ~125 km	60	3D-Var
JRA-25	JMA/CRIEPI	1979–present	T106, ~125 km	40	3D-Var
ERA-Int	ECMWF	1979–present	T255, ~80 km	60	4D-Var
MERRA	NASA/GMAO	1979–present	1/2° × 2/3°, 55km[b]	72	3D-Var
CFSR	NCEP	1979–present	T382, ~38 km	64	3D-Var

[a] For ERA-40, only the 1979–2002 period is considered here

[b] Resolution in latitude

Aqua satellites). Evaluation of JRA-25 precipitation showed higher correlation with global precipitation analyses than NCEP-2 and ERA-40 (Onogi et al. 2007; Bosilovich et al. 2008).

ERA-Int starts in 1989 and, unique among current global reanalyses, uses a 4D-Var assimilation system. Biases in satellite radiances are corrected via a variational bias correction scheme (Dee and Uppala 2008, 2009). A similar approach is also used to handle biases in surface pressure observations (Vasiljevic et al. 2006). Thanks to improved model physics and moisture analysis, ERA-Int has eliminated some of the problems with the representation of the hydrological cycle in ERA-40 (Andersson et al. 2005; Uppala et al. 2008).

MERRA uses a 3D-Var assimilation system, the Grid-point Statistical Interpolation (GSI) scheme (Kleist et al. 2009); a variational bias correction of satellite radiances; and the Incremental Analysis Updates (IAU), a nudging technique allowing for a smooth transition from the model states toward the observed state (Rienecker et al. 2008; Cullather and Bosilovich 2011, accepted).

CFSR was completed in January 2010 and brings major improvements to NCEP-2, including a higher-resolution forecast model and intensive use of satellites observations. Similar to MERRA, observations are assimilated via the 3D-Var GSI system. CFSR is the only reanalysis using a coupled atmosphere–ocean-sea-ice-land model for its short-term forecasts.

The precipitation (P) and surface evaporation/sublimation (E) data are taken from the reanalysis forecast fields. Surface evaporation/sublimation fluxes are not available in NCEP-2 and JRA-25 and are calculated from the latent heat fluxes at the surface using a constant latent heat of sublimation of 2.838×10^6 J kg^{-1}.

2.2 The Antarctic Surface Mass Balance

The reanalysis SMB is calculated as precipitation minus surface evaporation/sublimation (P–E). This quantity neglects other relevant ablation processes such as melt/runoff, wind-induced snow transport and blowing-snow sublimation. Melt/runoff contributes negligibly to the overall SMB (Liston and Winther 2005; Tedesco and Monaghan 2009). The wind-related processes can be important, especially in the escarpment zone, and can produce net ablation in some areas (e.g., Frezzotti et al. 2007; Genthon et al. 2007; Scarchilli et al. 2010). Nevertheless, precipitation dominates the interannual variability of the Antarctic SMB (Cullather et al. 1998; Van de Berg et al. 2005; Monaghan et al. 2006a; Van den Broeke et al. 2006), supporting the use of P–E for our purposes. The contours of the grounded ice sheet and the floating ice shelves are taken from Vaughan et al. (1999), available at a $1° \times 1°$ latitude-longitude resolution (Fig. 1).

Bromwich et al. (2011, accepted) examined the skill of the reanalyses at simulating the long-term mean annual Antarctic SMB. The mean annual values for P, E and P–E are reported in Table 2. Their evaluation included a comparison with the observation-based accumulation map from Arthern et al. (2006). CFSR and, to a lesser extent, MERRA were found to agree particularly well with the observed accumulation. On the other hand, ERA-Int revealed a marked dry bias over the high-elevated East Antarctic plateau, already present (and more pronounced) in ERA-40, whereas JRA-25 substantially overestimated the accumulation over the same area. P–E was found to be excessively low in NCEP-2 because of unrealistically large sublimation fluxes. Bromwich et al. (2011, accepted) emphasized the caution required when using the Arthern et al. (2006) SMB estimates given their uncertainties and known biases.

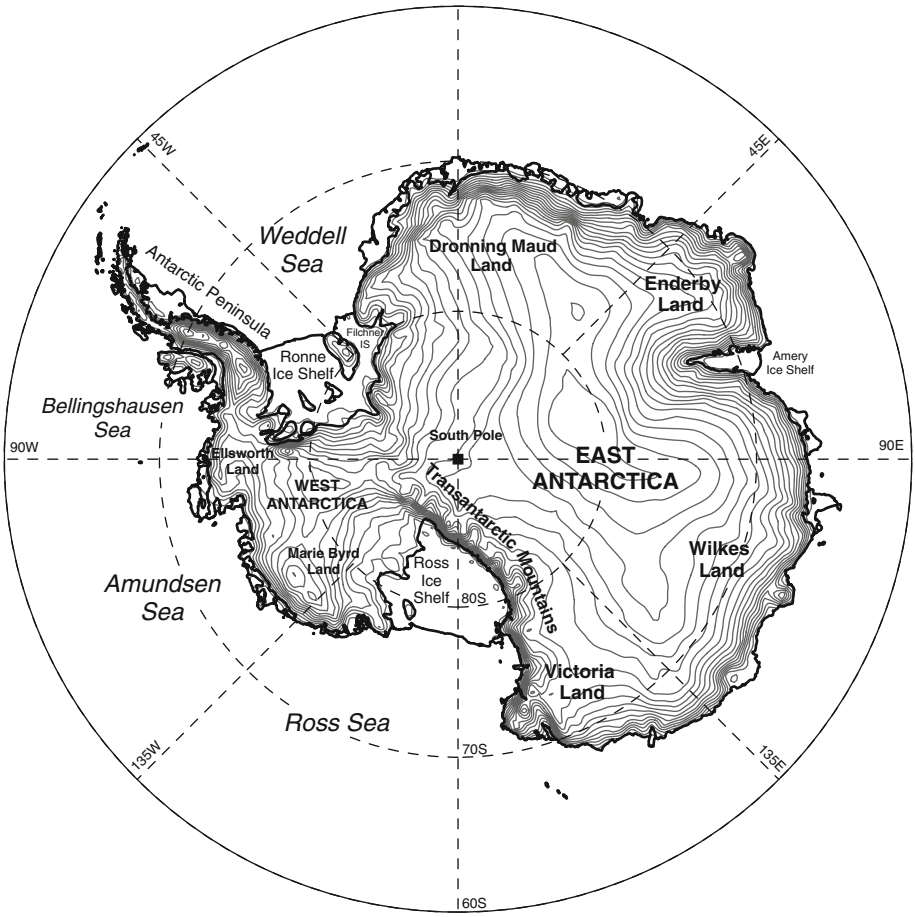

Fig. 1 Map of Antarctica showing elevation contours with 200-m intervals

Table 2 Mean total annual values for P, E, and P–E from the reanalyses during the 1989–2009 period (1989–2001 for ERA-40) in mm year^{-1} spatially averaged over the grounded Antarctic ice sheet (12.35×10^6 km^2)

	NCEP-2	JRA-25	ERA-40	ERA-Int	MERRA	CFSR	V99	A06
P	172	203	145	148	169	201	–	–
E	93	49	26	19	12	46	–	–
P–E	79	154	119	130	157	155	–	–
Accum.	–	–	–	–	–	–	149	143

For ERA-40, only the 1989–2001 period is considered. The observation-based accumulation estimates from Vaughan et al. (1999) and Arthern et al. (2006) are also shown

2.3 Caveats to the Evaluation of Reanalyses in High Southern Latitudes

The data sparsity characteristic of the high southern latitudes constitutes both a challenge for the reanalyses and a major obstacle to their evaluation. Our evaluation includes the use

of observation-based datasets of precipitation, evaporation and total atmospheric water vapor (described in Sect. 2.4). Caution is required when evaluating the reanalyses against these datasets because both utilize either similar satellite observations or observations from the same satellite sensors. The evaporation dataset even incorporates estimates of reanalysis surface variables. With few in situ measurements to anchor satellite data, the precipitation and evaporation datasets also face challenges similar to those faced by the reanalyses in the data-sparse regions.

The limited use of satellite data in NCEP-2 and its "frozen" assimilation system after 1998 would make this dataset, in theory, suitable for assessing the impact of satellite observations in the other reanalyses. Because of numerous issues in NCEP-2 (e.g., Bromwich et al. 2011, accepted) and the comparably good temporal consistency of ERA-Int data, this latter reanalysis is used here to compare with the other datasets (see Sects. 4 and 5). However, one must bear in mind the potential deficiencies of ERA-Int.

2.4 Observation-Based Datasets

Monthly mean precipitation data are taken from the satellite-gauge merged precipitation analyses from the Global Precipitation Climatology Project Version 2 (GPCP; Adler et al. 2003). This dataset provides globally gridded data at a 2.5° × 2.5° resolution. South of 50°S, this product incorporates in situ precipitation measurements from a few Antarctic stations but can otherwise be considered as exclusively satellite-based.

Monthly mean ocean surface evaporation estimates are obtained from the Objectively Analyzed air-sea Fluxes (OAFlux; Yu and Weller 2007) at a 1° × 1° resolution. This dataset results from a combination of multiple satellite retrievals (e.g., wind speed and near-surface specific humidity from QuikSCAT and SSM/I) and output data from the NCEP-2 and ERA-40 reanalyses.

SSM/I retrievals of total atmospheric water vapor—or total precipitable water (TPW)—are provided by Remote Sensing System (RSS) and available over ice-free ocean only at a 0.25° × 0.25° resolution. Monthly mean time series were produced using observations from six intercallibrated satellites (F08, F10, F11, F13, F14 and F15) of the Defense Meteorological Satellite Program (DMSP). Average values were used when the satellites overlap. F15/-SSM/I data were not used after July 2006 because of a discontinuity in the time series (note from RSS1).[1]

3 Temporal Variability and Trends in Antarctic P–E

The time series and trends in Antarctic P–E, examined in this section, reflect not only actual changes in the Antarctic climate but also the potential impact of changes in the observing system. Disentangling the two contributions is the primary objective of this study.

3.1 Changes in Total Antarctic P–E

Figure 2a shows the time series of annual P–E spatially averaged over the grounded Antarctic Ice Sheet and presented as anomalies from their respective values in 1989. The time series exhibit a large interannual variability, of the order of ±10% of the

[1] Warning note on RSS website: http://www.remss.com/ssmi/ssmi_browse.html.

21-year average. This variability is shared, to some extent, by all the reanalyses but they provide quite different depictions of the changes in P–E.

An upward shift in P–E occurs in MERRA in the late 1990s, concurrent with the start of the assimilation of radiances from the Advanced Microwave Sounding Unit (AMSU) (Cullather and Bosilovich 2011, accepted). From the late 1990s onward, the absence of apparent trend in P–E in CFSR and ERA-Int contrasts with the marked increase in P–E in NCEP-2 and JRA-25. Yet, CFSR and ERA-Int exhibit quite dissimilar P–E anomalies during ~1994–2004. It is noteworthy that, in late 2006, ERA-Int and CFSR start assimilating Global Positioning System radio-occultation (GPSRO) data from the Constellation Observing System for Meteorology Ionosphere and Climate (COSMIC) mission (Poli et al. 2010; Saha et al. 2010). These observations can be used without bias correction and provide temperature and moisture profiles over Antarctica. Such information is otherwise only available from the limited number of Antarctic radiosondes (e.g., Andersson 2007). Note, however, that the actual impact of the GPSRO data on Antarctic precipitation has not yet been demonstrated.

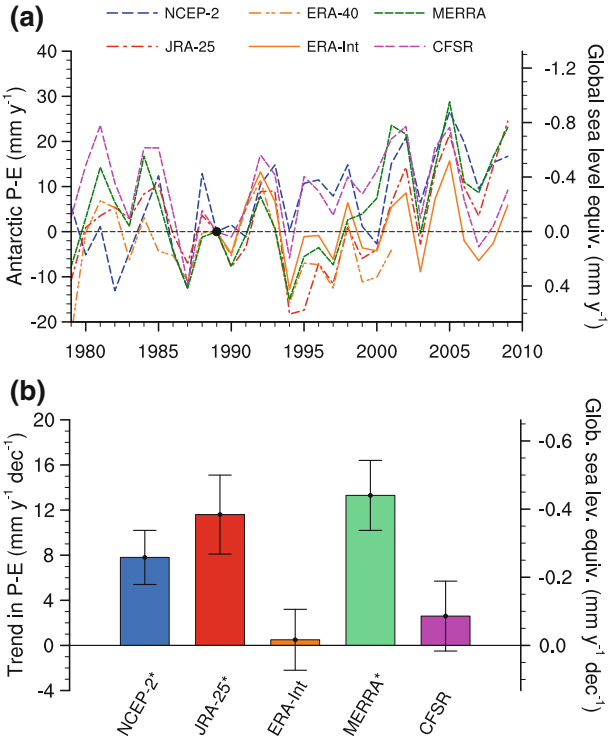

Fig. 2 **a** Time series of annual P–E in mm year^{-1} spatially averaged over the grounded Antarctic Ice Sheet from the six reanalyses. The series are presented as anomalies with respect to their respective value in 1989. **b** Corresponding linear trends in annual P–E in mm year^{-1} decade^{-1} and their standard error for the reanalyses except ERA-40 (because of time series ending in August 2002). The * symbol indicates datasets for which the trends are statistically different from zero at the 99% confidence level. The trends are otherwise not statistically significant. In **a** and **b**, the equivalent annual impact on global mean sea level is shown on the right-hand vertical axis. For this purpose, the trends in P–E are integrated over a grounded ice-sheet area of 12.35×10^6 km^2. Similar to Lemke et al. (2007), we assume a global oceanic area of 3.62×10^8 km^2 and a seawater density of 1028 kg m^{-3}

The linear trends of annual P–E from Fig. 2a during 1989–2009 are shown in Fig. 2b. The statistical significance of the trends is estimated from the p-value of a two-tailed Student's t test applied to the standard error of the trends. The 1989–2009 P–E trends in ERA-Int and CFSR are not significantly different from zero. In contrast, NCEP-2, JRA-25 and MERRA exhibit large positive trends, significant at the 99% confidence level. The largest increase rate is found in MERRA, a result from the jump in P–E mentioned above. For 1989–2009, the trends in Antarctic P–E from NCEP-2, JRA-25 and MERRA translate into a negative contribution to global mean sea level ranging between 0.26 and 0.44 mm year^{-1} decade^{-1}. Although there is strong indication that these trends are overestimated, they represent less than 2% of the global mean sea level rise measured from satellite altimetry for 1993–2009 (Nicholls and Cazenave 2010). It is notable that, regardless of their statistical significance, all trends in Antarctic P–E are positive.

3.2 Spatial Distribution of the P–E Trends

Figure 3 shows the spatial distribution of the P–E trends over Antarctica and the Southern Ocean (up to ~60°S) during 1989–2009 and provides a sense of the marked differences between the reanalyses. Over the Antarctic continent, ERA-Int exhibits smaller and less significant trends in P–E than the other reanalyses. NCEP-2, JRA-25 and MERRA show

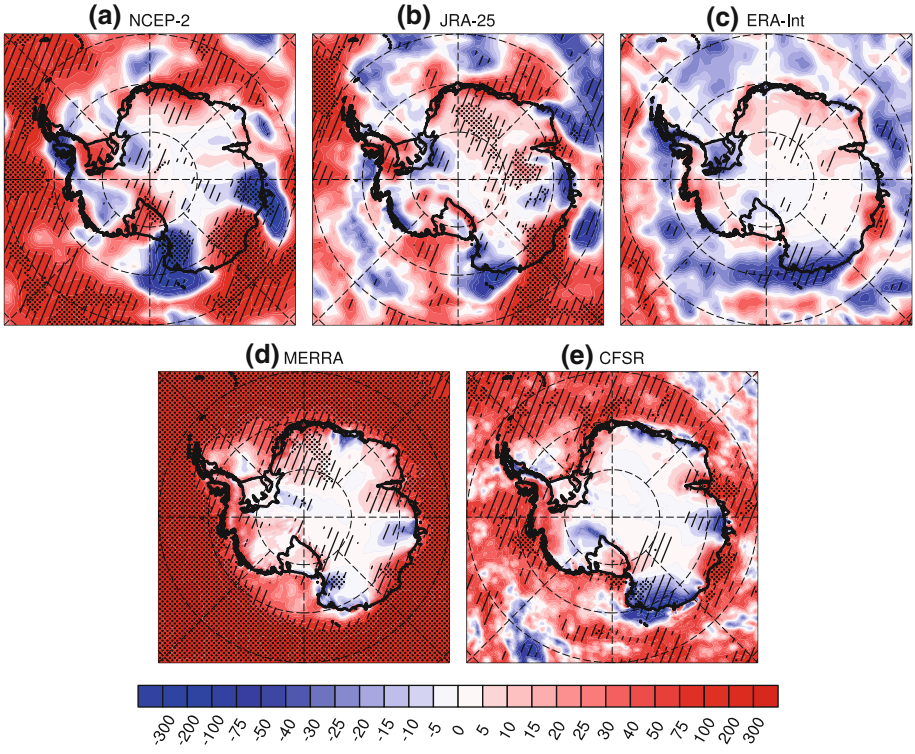

Fig. 3 1989–2009 linear trends in P–E from the global reanalyses in mm year^{-1} decade^{-1} over Antarctica and the Southern Ocean (south of 60°S). Hatched (dotted) areas denote trends that are statistically different from zero at the 90% (99%) confidence level

large areas with highly significant upward trends in Dronning Maud Land, although with rather dissimilar patterns. Some similarity is found in the five maps in the 70°–170°E sector, with alternating positive and negative trend patterns along the coast. Such patterns are suggestive of changes in the offshore atmospheric circulation and the associated moisture advection towards/off the coast (see Sect. 5.2). The magnitude and spatial extent of the patterns over Wilkes Land differ, however, greatly among the reanalyses. Notably, NCEP2 and JRA-25 exhibit trends in excess of 200 mm year^{-1} decade^{-1} over extensive areas in central Wilkes Land, casting doubts on the realism of the two datasets. We note that the pattern of large negative trends in P–E over Victoria Land—a common feature among the five reanalyses—is consistent with the observed increase in sea-ice cover in the Ross Sea (Stammerjohn et al. 2008; Turner et al. 2009), both resulting from enhanced off-continent winds. Little similarly between the reanalyses is found over West Antarctica where the trends in P–E are generally not statistically significant. Over the ocean, the contrasts among the datasets are again rather disconcerting. The spurious origin of the trends in MERRA becomes clearly apparent. These trends will be further discussed in Sect. 4.

4 Changes in P and E Over the Southern Ocean

In this section, we extend our analysis spatially to precipitation and evaporation changes over the Southern Ocean. Inconsistencies in the time series related to the assimilation of satellite observations are expected to be more apparent over the ocean than over Antarctica due to the paramount role of satellite observations over ocean areas.

4.1 Variability and Trends in Precipitation

Figure 4a shows the monthly precipitation anomalies from the reanalyses and GPCP, spatially averaged over the 50°–65°S latitude band. The anomalies are relative to the 1989–2009 period for the reanalyses, 1989–2008 for GPCP. The precipitation differences with respect to ERA-Int are shown in Fig. 4b.

Compared to GPCP, ERA-Int produces excessively low precipitation estimates. There remains, however, great uncertainty about the "true" value: over the same latitudes, the Climate Prediction Center Merged Analysis of Precipitation (CMAP; Xie and Arkin 1997) produces 40% less precipitation than GPCP, which places CMAP estimates below all reanalyses estimates (Yin et al. 2004; Bromwich et al. 2011, accepted). Artificial reductions in ERA-Int global precipitation have been associated with increases in the volume of SSM/I rain-affected radiances assimilated in this reanalysis (Uppala et al. 2008, Dick Dee, ECMWF, personal communication 2010). This does not seem to be an issue over the Southern Ocean as the precipitation differences between GPCP and ERA-Int remain relatively steady through 2004. The drop in GPCP precipitation after 2007 is not seen in any reanalysis and, thus, assumed to be spurious. This assumption is supported by the fact that post-2004 precipitation changes in GPCP account for the spatial discontinuities around 60°S seen in the 1989–2008 trend map (see Fig. 5f).

The drop in JRA-25 precipitation in mid-1987 coincides with the assimilation of SSM/I precipitable water observations (Bosilovich et al. 2006; Onogi et al. 2007). Between 1998 and 2001, MERRA precipitation anomalies and precipitation differences from ERA-Int follow a two-step upward shift. The first step is concurrent with the first use of AMSU observations in late 1998. The second step, in early 2001, may be related to the introduction of observations from a second AMSU unit (onboard NOAA-16). Except for a

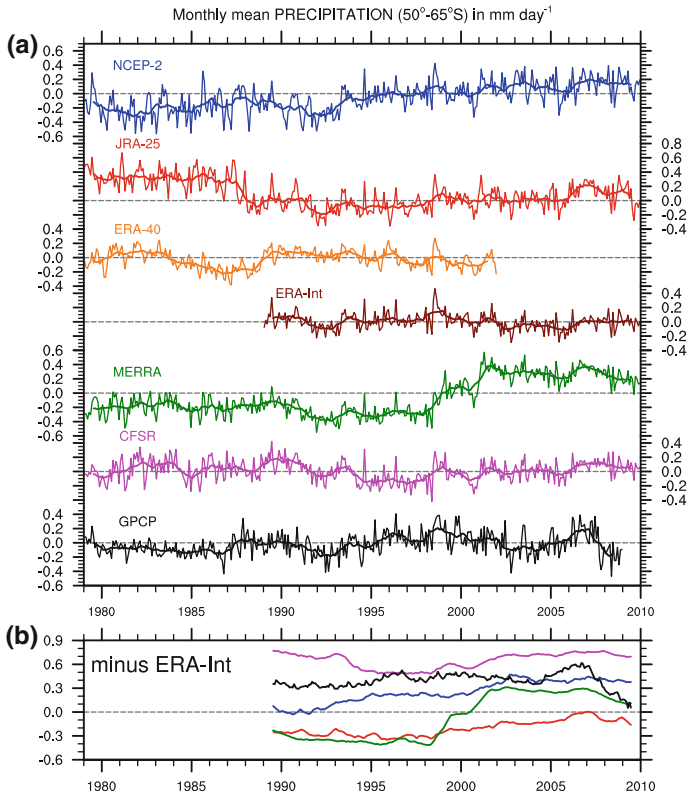

Fig. 4 **a** Monthly mean precipitation anomalies (*thin lines*) in mm day^{-1} spatially averaged between 50 and 65°S for the six global reanalyses and GPCP. The anomalies are relative to 1989–2009 for the reanalyses except ERA-40 (1989–2001), and 1989–2008 for GPCP. The thick line represents the 13-month running average. **b** Monthly mean precipitation differences from ERA-Int between 50 and 65°S smoothed with 13-month running average

decrease in CFSR in the early 1990s, the precipitation differences from NCEP-2, JRA-25 and CFSR all exhibit upward trends during 1989–2009, suggesting that the precipitation increase during the 2000 decade is probably not real. Saha et al. (2010, their Fig. 21) showed that a jump in CFSR global ocean precipitation occurs in late 1998 (related to AMSU), a reflection of which may be seen in Fig. 4b.

Figure 5 shows the 1989–2009 linear trends in annual precipitation south of 30°S. MERRA stands out among the reanalyses with a pattern of large positive and highly significant trends over the entire Southern Ocean poleward of 40°S, in direct relation to the jump seen in Fig. 4. Large positive precipitation trends are also found in NCEP-2, mainly in the Pacific sector of the Southern Ocean. The trends are generally small and insignificant in ERA-Int and CFSR south of 60°S. These two datasets differ, however, markedly in lower latitudes (e.g., South Atlantic), with a dominance of positive trends in CFSR and negative trends in ERAInt. Over the South Indian Ocean and south of Australia/New Zealand, the positive and significant trends in GPCP contrast with the insignificant or negative trends in ERA-Int.

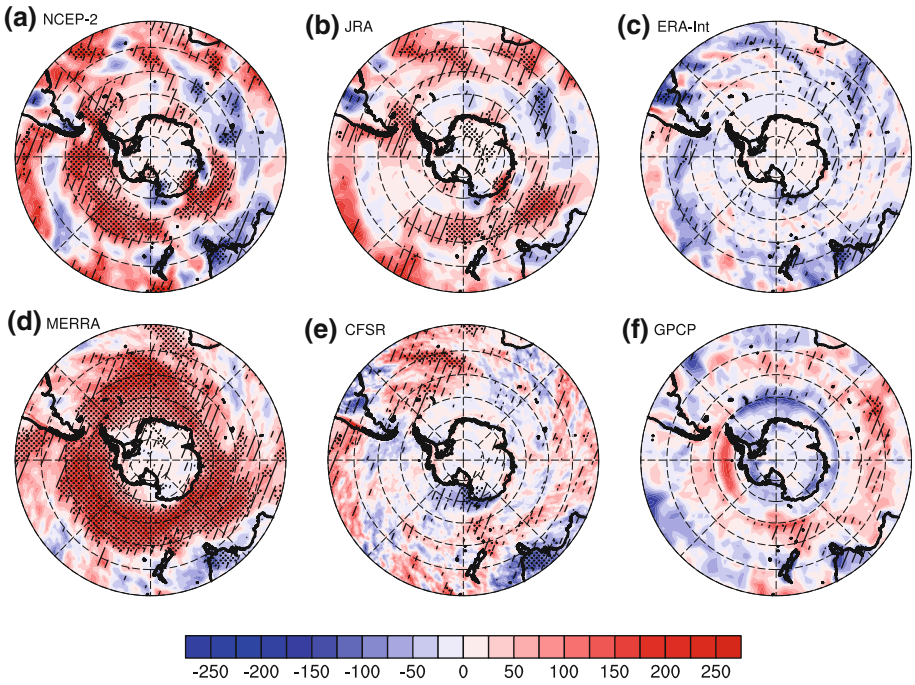

Fig. 5 1989–2009 linear trends in annual precipitation in mm day^{-1} decade^{-1} poleward of 30°S from the global reanalyses. For GPCP, the trends are calculated for 1989–2008. Hatched (dotted) areas denote trends that are statistically different from zero at the 90% (99%) confidence level

4.2 Variability and Trends in Evaporation

Surface conditions (e.g., sea surface temperature (SST), sea-ice concentration, near-surface wind) exert a major influence on evaporation fluxes over ocean, hence the merits of examining the latter separately from the precipitation. These fluxes affect the atmospheric moisture content that can be advected towards the Antarctic continent (e.g., Sodemann and Stohl 2009).

Figure 6a shows the monthly evaporation anomalies from the reanalyses and the OA-Flux dataset spatially averaged over 50°–65°S. The differences with respect to ERA-Int are shown in Fig. 6b. The reliability of OAFlux estimates is questionable because of the large temporal variations of the OAFlux-ERA-Int differences, and the fact that these differences do not show any consistency with any other curve in Fig. 6b. The drop in the evaporation differences for MERRA and CFSR in late 1998 likely reveals AMSU-related problems in these two datasets rather than in ERA-Int, which is confirmed by Fig. 7d and e.

The reduction in the magnitude of the differences between the reanalyses and ERA-Int in the early 2000s, especially in NCEP-2, may be associated with the use (from 2002 onward) of SST estimates based observations from the Advanced Microwave Scanning Radiometer-EOS (AMSRE). The use of AMSR-E microwave observations has considerably increased the spatial and temporal coverage of SST data over the Southern Ocean (Chelton and Wentz 2005). Prior to this, these estimates relied primarily on infrared measurements from the Advanced Very High Resolution Radiometer (AVHRR), available only for cloud-free areas.

Overall, three remarks pertaining to Fig. 6b support the reliability of ERA-Int evaporation estimates: (1) MERRA and CFSR show close agreement with ERA-Int until 1998;

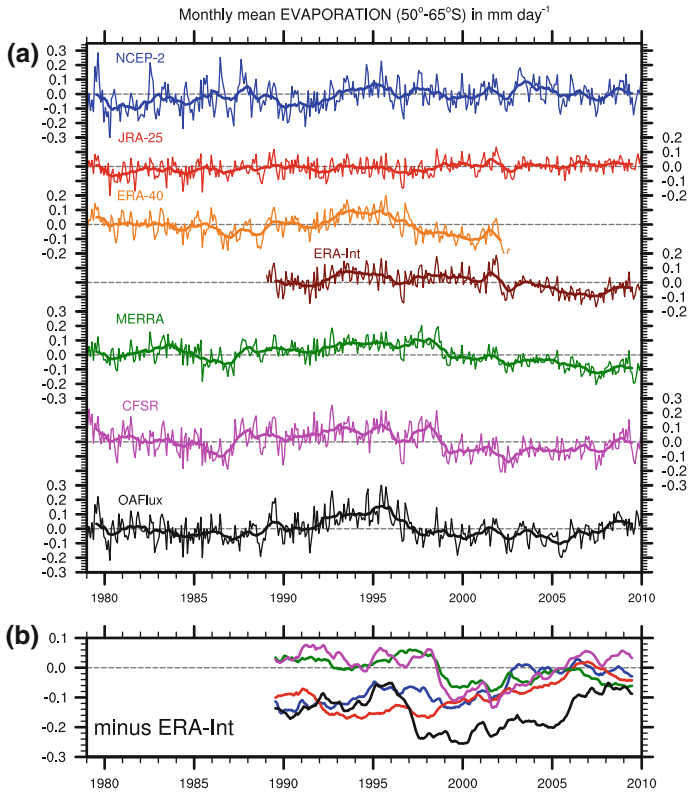

Fig. 6 Same as Fig. 4 but for **a** the monthly mean evaporation anomalies in mm day^{-1} from the reanalyses and OAFlux; and **b** the monthly mean evaporation differences with respect to ERA-Int

(2) the changes in surface evaporation fluxes in MERRA and CFSR after 1998 are presumably spurious; and (3) the differences between the four reanalyses and ERA-Int converge towards zero. The more gradual convergence of JRA-25 may be attributable to the absence of satellite observations in the SST dataset used by this reanalysis (Onogi et al. 2007).

The spatial distibution of the 1989–2009 trends in annual surface evaporation (Fig. 7) reveals notable differences among the reanalyses over the Southern Ocean. In MERRA, the pattern of highly significant negative trends covers an area very similar to the circumpolar pattern of large positive precipitation trends in Fig. 5. In CFSR, the most prominent pattern of negative trends in evaporation follows approximately the contours of the climatological maximum sea-ice extent. The reduction in evaporation fluxes in MERRA and CFSR may have acted to diminish the atmospheric moisture content, with a potentially negative impact on Antarctic precipitation. In MERRA, however, this effect is clearly offset by the enhanced precipitation.

5 Changes in Precipitable Water and Meridional Wind Over Antarctica and the Southern Ocean

In our effort to separate between real and artificial changes, we examine two variables more directly influenced by observations than precipitation and evaporation: total

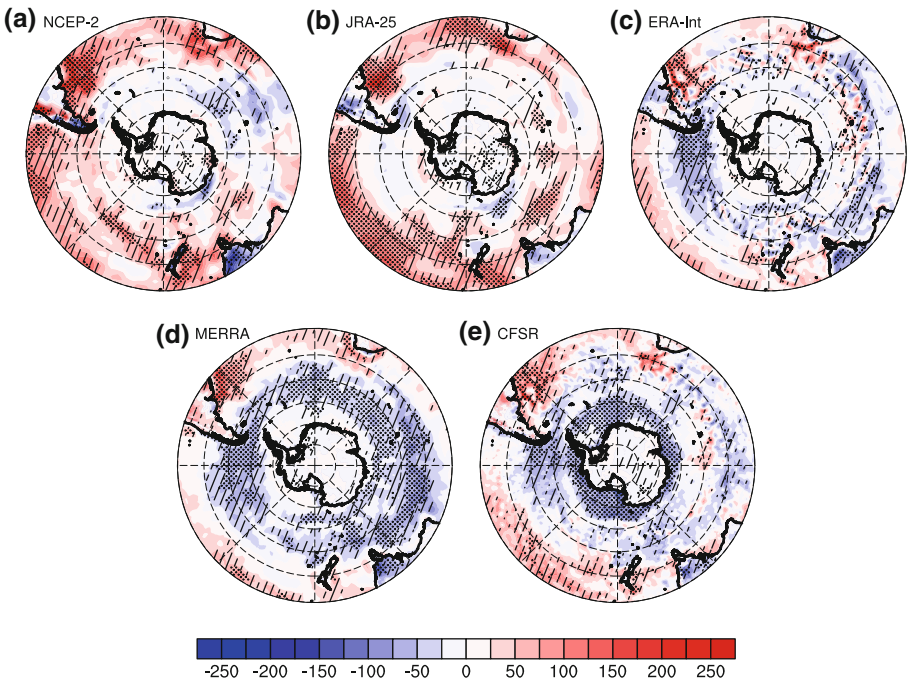

Fig. 7 Same as Fig. 5 but for the trends in annual evaporation in mm day^{-1} decade^{-1}

precipitable water (TPW) and the meridional wind component (Kalnay et al. 1996). These two variables are tightly related to precipitation changes as they determine either the moisture advection or the moisture reservoir available for precipitation.

5.1 Total Precipitable Water

The time series of monthly TPW anomalies from the reanalyses and SSM/I between 50 and 60°S are presented in Fig. 8a, while the differences with respect to ERA-Int are displayed in Fig. 8b. The TPW differences between SSM/I and ERA-Int remain close to 0.6 kg m^{-2} throughout the period, after a small increase around 1991. The fact that this increase is not reflected in the NCEP-2-ERA-Int differences (NCEP-2 does not use any SSM/I observations) leads one to conclude that the problem may lie with the SSM/I product (late 1991 corresponds to the transition between the F08 and F11 DMSP satellites).

The largest change in the TPW differences with respect to ERA-Int are found in MERRA and, to a lesser, CFSR, with a first upward shift in late 1998 and a second, smaller one in 2001, both likely related to the use of AMSU data (see Sect. 4.1). Note that the second jump occurs around the same time as, and must not be confused with, abnormally high TPW values captured by all datasets, including SSM/I (Fig. 8a). The TPW differences between NCEP-2, JRA-25 and ERA-Int remain relatively steady throughout the period, especially from 1999 onward in JRA-25. Note that, in Fig. 8b, the TPW differences between NCEP-2 and ERA-Int are shifted downward by 1.0 kg m^{-2} ($\sim$10% of the annual mean), which, despite good temporal consistency, highlights the poor representation of TPW in NCEP-2 already noted by Trenberth et al. (2005).

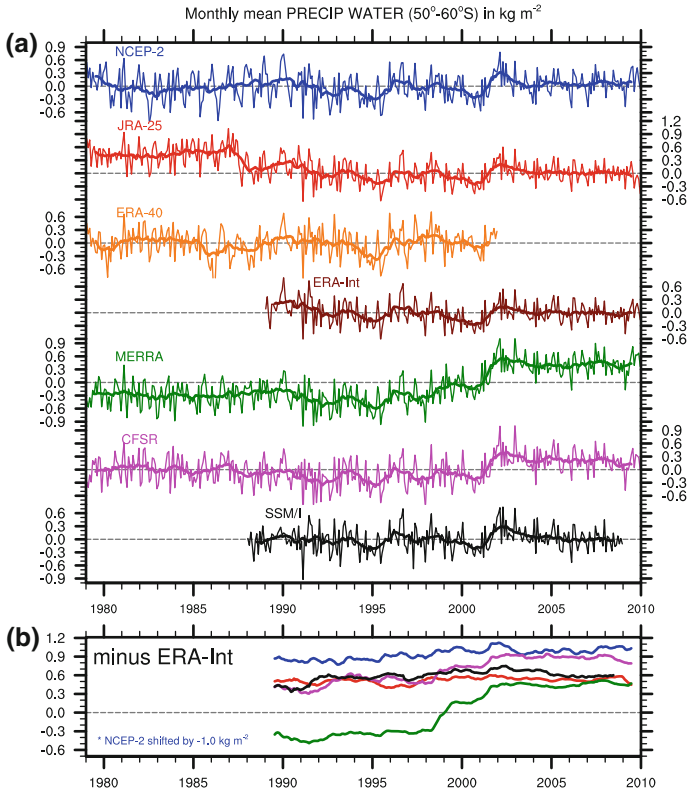

Fig. 8 Same as Fig. 4 but for **a** the monthly mean precipitable water anomalies in kg m^{-2} from the reanalyses and SSM/I; and **b** the monthly mean precipitable water differences with respect to ERA-Int

Figure 9 shows the spatial distribution of the 1989–2008 linear trends in TPW over the Southern Hemisphere. Some similarities with the precipitation trend map shown in Fig. 5 can be noted, such as the positive trend pattern over the West Pacific. Overall, NCEP-2, JRA-25 and ERA-Int agree well with SSM/I. MERRA and CFSR provide a picture that is markedly different from the other datasets, with widespread and highly significant positive trends over most of the Southern Hemisphere. However, compared to MERRA, CFSR exhibits smaller and less significant trends over the Southern Ocean, and larger and more significant trends in lower latitudes.

5.2 Meridional Wind

Because of the large contrast in atmospheric moisture content between Antarctica and the surrounding ocean (e.g., Tietäväinen and Vihma 2008), changes in the meridional wind component can greatly affect the moisture transport towards the ice sheet and the associated precipitation (e.g., Schlosser et al. 2010). Figure 10 shows the trends in V500 over Antarctica during 1989–2009. The largest trends (>0 or <0) are found in NCEP-2 and JRA-25 over Antarctica in the 90°–180°E quadrant. In particular, these two datasets exhibit large downward trends (revealing enhanced poleward moisture advection) in the vicinity of 125°–130°E, where the largest increases in P–E have been observed in Fig. 3.

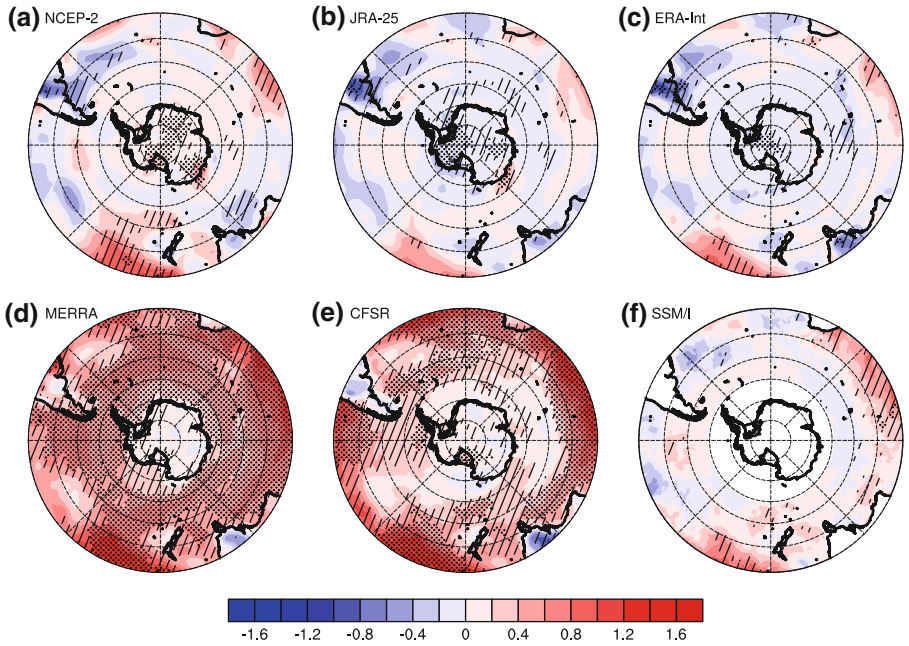

Fig. 9 Same as Fig. 5 but for the trends in mean annual precipitable water in kg m^{-2} $decade^{-1}$ for the global reanalyses and SSM/I. For SSM/I, only data over ocean are available. In this dataset, areas poleward of 60°S are masked out because of the presence of seasonal sea ice

In NCEP-2, the large negative trends in V500 in central Wilkes Land result from a strong equatorward wind anomaly from 1988–1991 turning into a gradually increasing poleward flow from 1992 onward (Fig. 11a). The reasons for this anomaly are still unclear. In JRA-25, the largest positive trends are found in the vicinity of the Russian Station, Vostok. They largely result from abnormally large negative values in 1992 (Fig. 11b). The radiosonde observation program at this station was terminated in early 1992. Aside from Amundsen-Scott SouthPole Station, they constituted the only observations available on the Plateau, until routine radiosoundings at Concordia-Dome C started in 2005. Further analysis of the trends in the reanalysis pressure and geopotential height fields can be found in Bromwich et al. (2011, accepted).

Overall, a clear correspondence can be established between the trends in V500 and the trends in P–E from Fig. 3. In NCEP-2 and JRA-25, the changes in V500 act to greatly enhance the poleward moisture advection and orographic precipitation over central Wilkes Land, where the two datasets exhibit the largest trends in P–E. We infer that the P–E changes in NCEP-2 and JRA-2 in this sector of Antarctica are likely spurious.

6 Conclusions

A tentative synthesis of our evaluation of the five reanalyses is given in Table 3. The datasets are ranked according to (1) the temporal consistency of the P–E, P, E and TPW series over Antarctica and/or the Southern Ocean; and (2) the realism of the spatial distribution of the 1989–2009 linear trends, as shown in Figs. 2, 3, 4, 5, 6, 7, 8, 9. As an

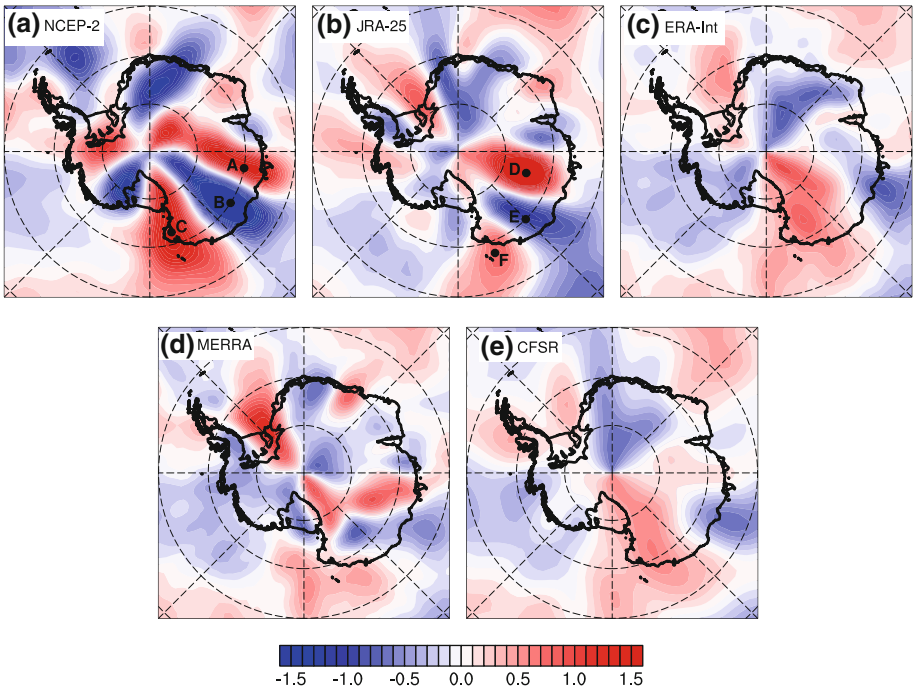

Fig. 10 1989–2009 linear trends in 500-hPa meridional wind in m s^{-1} $decade^{-1}$ from the global reanalyses. Points A to F correspond to local maxima/minima whose annual time series are displayed in Fig. 11

example, for the changes in Southern Ocean precipitation, MERRA is assigned the lowest rank (5), because of the magnitude of the late 1990s jump and the spatial extent of the spurious trends; NCEP-2 is assigned the second-lowest rank (4), because of the upward shift in the early 1990s (smaller than MERRA) and the spurious trend pattern in the South Pacific; ERA-Int is assigned the highest rank (1), because of the good temporal consistency with GPCP (at least prior to 2005). The actual degree of realism cannot always be differentiated between two reanalyses, in which case the datasets are assigned equal rank. The absence of observational records of the changes in Antarctic SMB during 1989–2009 and the unreliability of the precipitation and evaporation observation-based datasets over the Southern Ocean constitute important limitations to the objectivity of this assessment.

ERA-Int is found to provide the most realistic depiction of the interannual variability and overall change in P, E and TPW over Antarctica and the Southern Ocean during 1989–2009. MERRA contains a major disruption of its hydrological cycle over the Southern Ocean, manifested by a jump in precipitation in the late 1990s and related to the assimilation of AMSU sounding radiances. While the artificial changes are seemingly less important in CFSR in high southern latitudes, the hydrological cycle at lower latitudes in this dataset also reveal discontinuities concurrent with the introduction of AMSU data (see Saha et al. 2010). Most problematic in NCEP-2 and JRA-25 are unrealistically large changes in P–E in coastal East Antarctica, caused by spuriously enhanced meridional wind flow. While the two reanalyses are likely impacted by the end of radiosonde observations at Vostok in the early 1990s, spurious trends are also seen occurring well into the 2000

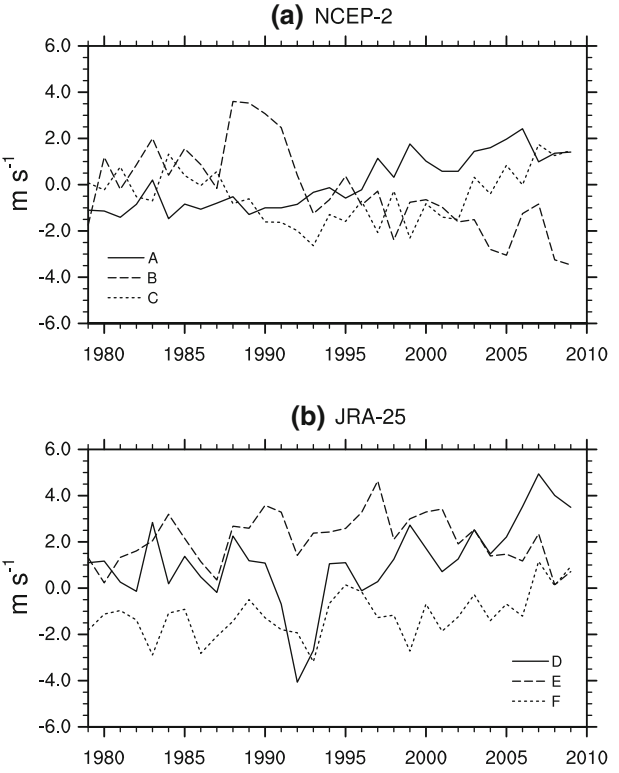

Fig. 11 Time series of the mean annual meridional wind component in m s^{-1} at 500 hPa in **a** NCEP-2 and **b** JRA-25, over points A to F shown in Fig. 10a and b

Table 3 Ranking of the reanalyses according to the reliability of the temporal changes in their hydrological cycle over Antarctica (Ant.) and the Southern Ocean (S.O.) during 1989–2009 (1 = highest reliability)

	NCEP-2	JRA-25	ERA-Int	MERRA	CFSR
Trends in P–E (Ant.)	4	3	1	5	2
Trends in P (S.O.)	4	3	1	5	2
Trends in E (S.O.)	2	2	1	4	4
Trends in TPW (S.O.)	3	2	1	5	4
Average ranking	3.25	2.5	1	4.75	3

These rankings are based on the results from Figs. 2, 3, 4, 5, 6, 7, 8, 9

decade and are still not fully comprehended. In addition, JRA-25 suffers from a major discontinuity in 1987 caused by the introduction of SSM/I observations.

Our first conclusion is that the presence of spurious changes is not a solved problem in recent global reanalyses, in spite of the implementation of improved data assimilation techniques. These artifacts still constitute major caveats to their application to trend analysis and climate change assessment. Our investigation cannot ascertain whether the better performance of ERA-Int must be attributed to the use of a 4D-Var assimilation system and/or to deficiencies in the variational bias correction of satellite radiances in MERRA and CFSR.

Tracing the causes of inhomogeneities in reanalyses is, however, a challenging task, if only because of the complexity of the assimilation process (e.g., Thorne and Vose 2010)

and the extreme variety of observations used for data assimilation. Furthermore, the response of the assimilation system is not always instantaneous (e.g., Bromwich and Fogt 2004). Indeed, while the variational bias correction technique should ensure smooth transitions between observations from successive satellites, it also carries along a potential drift towards the model bias (Dee and Uppala 2009), which is poorly assessed in data-sparse regions. Such potential drift remains an important unknown in ERA-Int.

Our second conclusion is that the higher reliability of the results from ERA-Int suggests the absence of significant change in Antarctic P–E, as previously reported by Van de Berg et al. (2005) and Monaghan et al. (2006a, b) for prior periods. Given the short time period investigated here (dictated by the overlapping time span between the datasets), our study does not claim to capture the long-term changes in Antarctic P–E and emphasizes the need for longer time series.

Acknowledgments This research was supported by Subcontract 20020793 from the University Corporation for Atmospheric Research, Grant ANT-0636523 from the National Science Foundation, and by the Center for Remote Sensing of Ice Sheets. The authors would like to thank Andrew Monaghan and Eric Rignot for preliminary discussions, Michael Bosilovich for information regarding MERRA, Dick Dee for information about ERA-Int, Richard Cullather for kindly providing his submitted manuscript, and Sheng-Hung Wang for his valuable help with the data processing. The authors are also grateful to the two anonymous reviewers whose comments improved the initial manuscript.

References

Adler R, Huffman G, Chang A, Ferraro R, Xie P, Janowiak J, Rudolf B, Schneider U, Curtis S, Bolvin D, Gruber A, Susskind J, Arkin P, Nelkin E (2003) The version-2 global precipitation climatology project (GPCP) monthly precipitation analysis (1979-present). J Hydrometeor 4:1147–1167

Andersson E (2007) Data assimilation in the polar regions. ECMWF Newslett 112:10–15

Andersson E, Bauer P, Beljaars A, Chevallier F, Hólm E, Janisková M, Kållberg P, Kelly G, Lopez P, Mcnally A, Moreau E, Simmons AJ, Thépaut JN, Tompkins AM (2005) Assimilation and modeling of the atmospheric hydrological cycle in the ECMWF forecasting system. Bull Amer Meteor Soc 86(3):387–402

Arthern RJ, Winebrenner DP, Vaughan DG (2006) Antarctic snow accumulation mapped using polarization of 4.3-cm wavelength microwave emission. J Geophys Res 111:D06107

Auligné T, McNally AP, Dee DP (2007) Adaptive bias correction for satellite data in a numerical weather prediction system. Q J Roy Meteor Soc 133(624):631–642

Bengtsson L, Hagemann S, Hodges KI (2004a) Can climate trends be calculated from reanalysis data? J Geophys Res 109(D11): D11111

Bengtsson L, Hodges KI, Hagemann S (2004b) Sensitivity of the ERA40 reanalysis to the observing system: determination of the global atmospheric circulation from reduced observations. Tellus Ser A 56: 456–471

Bosilovich MG, Schubert S, Rienecker M, Todling R, Suarez M, Bacmeister J, Gelaro R, Kim GK, Stajner I, Chen J (2006) NASA's Modern Era Retrospective-analysis for Research and Applications. US CLIVAR Variations 4(2): 5–8, http://www.usclivar.org/Newsletter/VariationsV4N2.pdf

Bosilovich MG, Chen J, Robertson FR, Adler RF (2008) Evaluation of precipitation in reanalyses. J Appl Meteor Climatol 47:2279–2299

Bouchard A, Rabier F, Guidard V, Karbou F (2010) Enhancements of satellite data assimilation over Antarctica. Mon Weather Rev 138(6):2149–2173

Bromwich DH, Fogt RL (2004) Strong trends in the skill of the ERA-40 and NCEP-NCAR reanalyses in the high and middle latitudes of the Southern Hemisphere, 1958–2001. J Climate 17:4603–4619

Bromwich DH, Fogt RL, Hodges KI, Walsh JE (2007) A tropospheric assessment of the ERA-40, NCEP, and JRA-25 global reanalyses in the polar regions. J Geophys Res 112(D10): D10111

Bromwich DH, Nicolas JP, Monaghan AJ (2011) An assessment of changes in Antarctic and Southern Ocean precipitation since 1989 in contemporary global reanalyses. J Climate Accepted

Chelton DB, Wentz FJ (2005) Global microwave satellite observations of sea surface temperature for numerical weather prediction and climate research. Bull Amer Meteor Soc 86(8):1097–1115

Cullather RI, Bosilovich MG (2011) The moisture budget of the polar atmosphere in MERRA. J Climate Accepted
Cullather RI, Bromwich DH, Van Woert ML (1998) Spatial and temporal variability of Antarctic precipitation from atmospheric methods. J Climate 11(3):334–367
Dee D, Uppala S (2008) Variational bias correction in ERA-Interim. ECMWF Tech Mem No 575
Dee DP, Uppala S (2009) Variational bias correction of satellite radiance data in the ERA-Interim reanalysis. Q J Roy Meteor Soc 135:1830–1841
Dee D, Berrisford P, Poli P, Fuentes M (2009) ERA-Interim for climate monitoring. ECMWF Newslett No 119 pp 5–6, http://www.ecmwf.int/publications/newsletters/pdf/119.pdf
Eisen O, Frezzotti M, Genthon C, Isaksson E, Magand O, van den Broeke MR, Dixon DA, Ekaykin A, Holmlund P, Kameda T, Karlo L, Kaspari S, Lipenkov VY, Oerter H, Takahashi S, Vaughan DG (2008) Ground-based measurements of spatial and temporal variability of snow accumulation in east antarctica. Rev Geophys 46:RG2001
Frezzotti M, Pourchet M, Flora O, Gandolfi S, Gay M, Urbini S, Vincent C, Becagli S, Gragnani R, Proposito M, Severi M, Traversi R, Udisti R, Fily M (2005) Spatial and temporal variability of snow accumulation in East Antarctica from traverse data. J Glaciol 51(172):113–124
Frezzotti M, Urbini S, Proposito M, Scarchilli C, Gandolfi S (2007) Spatial and temporal variability of surface mass balance near Talos Dome, East Antarctica. J Geophys Res 112(F2): F02032
Genthon C, Lardeux P, Krinner G (2007) The surface accumulation and ablation of a coastal blue-ice area near Cap Prudhomme, Terre Adelie, Antarctica. J Glaciol 53(183):635–645
Guedj S, Karbou F, Rabier F, Bouchard A (2010) Toward a better modelling of surface emissivity to improve AMSU data assimilation over Antarctica. IEEE Trans Geosci Remote Sens 48(4):1976–1985
Haimberger L (2007) Homogenization of radiosonde temperature time series using innovation statistics. J Climate 20(7):1377–1403
Hines KM, Bromwich DH, Marshall GJ (2000) Artificial surface pressure trends in the NCEP/NCAR reanalysis over the Southern Ocean and Antarctica. J Climate 13:39403952
Kalnay E et al (1996) The NCEP/NCAR 40-Year Reanalysis Project. Bull Amer Meteor Soc 77(3):437–471
Kanamitsu M, Ebisuzaki W, Woollen J, Yang SK, Hnilo JJ, Fiorino M, Potter GL (2002) NCEP-DOE AMIP-II Reanalysis (R-2). Bull Amer Meteor Soc 83:1631–1643
Kaspari S, Mayewski PA, Dixon DA, Spikes VB, Sneed SB, Handley MJ, Hamilton GS (2004) Climate variability in West Antarctica derived from annual accumulation-rate records from ITASE firn/ice cores. Ann Glaciol 39:585–594
Kleist DT, Parrish DF, Derber JC, Treadon R, Wu WS, Lord S (2009) Introduction of the GSI into the NCEP Global Data Assimilation System. Weather Forecast 24(6):1691–1705
Lemke P et al (2007) Observations: changes in snow, ice and frozen ground. In: Solomon S et al (eds) Climate change 2007: the physical science basis. Contribution of working group I to the fourth assessment report of the intergovernmental panel on climate change. Cambridge University Press, Cambridge
Liston GE, Winther JG (2005) Antarctic surface and subsurface snow and ice melt fluxes. J Climate 18(10):1469–1481
Marshall GJ (2002) Trends in Antarctic geopotential height and temperature: a comparison between radiosonde and NCEP-NCAR reanalysis data. J Climate 15:659–674
Meehl GA et al (2007) Global climate projections. In: Solomon S et al (eds) Climate change 2007: the physical science basis. Contribution of working group i to the fourth assessment report of the intergovernmental panel on climate change. Cambridge University Press, Cambridge
Monaghan AJ, Bromwich DH, Fogt RL, Wang SH, Mayewski PA, Dixon DA, Ekaykin A, Frezzotti M, Goodwin I, Isaksson E, Kaspari SD, Morgan VI, Oerter H, Van Ommen TD, Van der Veen CJ, Wen J (2006a) Insignificant change in Antarctic snowfall since the international geophysical year. Science 313(5788):827–831
Monaghan AJ, Bromwich DH, Wang SH (2006b) Recent trends in Antarctic snow accumulation from Polar MM5 simulations. Philos Trans R Soc Ser A 364:1683–1708
Nicholls RJ, Cazenave A (2010) Sea-level rise and its impact on coastal zones. Science 328(5985): 1517–1520
Onogi K, Tsutsui J, Koide H, Sakamoto M, Kobayashi S, Hatsushika H, Matsumoto T, Yamazaki N, Kamahori H, Takahashi K, Kadokura S, Wada K, Kato K, Oyama R, Ose T, Mannoji N, Taira R (2007) The JRA-25 reanalysis. J Met Soc Jpn 85(3):369–432
Parkinson C (2003) Aqua: an earth-observing satellite mission to examine water and other climate variables. IEEE Trans Geosci Remote Sens 41(2):173–183
Poli P, Healy SB, Dee DP (2010) Assimilation of global positioning system radio occultation data in the ECMWF ERA-Interim reanalysis. Q J Roy Meteor Soc 136(653):1972–1990

Rabier F et al (2010) The Concordiasi project in Antarctica. Bull Amer Meteor Soc 91(1):69–86
Rienecker MM, Suarez M, Todling R, Bacmeister J, Takacs L, Liu HC, Gu W, Sienkiewicz M, Koster R, Gelaro R, Stajner I, Nielsen J (2008) The GEOS-5 data assimilation system—documentation of versions 5.0.1, 5.1.0, and 5.2.0. Tech. rep., NASA, USA
Saha S et al (2010) The NCEP climate forecast system reanalysis. Bull Amer Meteor Soc 91(8):1015–1057
Scarchilli C, Frezzotti M, Grigioni P, De Silvestri L, Agnoletto L, Dolci S (2010) Extraordinary blowing snow transport events in East Antarctica. Climate Dyn 34(7):1195–1206
Schlosser E, Manning KW, Powers JG, Duda MG, Birnbaum G, Fujita K (2010) Characteristics of high-precipitation events in Dronning Maud Land, Antarctica. J Geophys Res 115(D14): D14107
Simmons A, Uppala S, Dee D, Kobayashi S (2006) ERA-Interim: New ECMWF reanalysis products from 1989 onwards. ECMWF Newslett No 110 pp 25–35, http://www.ecmwf.int/publications/newsletters/pdf/110rev.pdf
Sodemann H, Stohl A (2009) Asymmetries in the moisture origin of Antarctic precipitation. Geophys Res Lett 36: L22803
Stammerjohn SE, Martinson DG, Smith RC, Yuan X, Rind D (2008) Trends in Antarctic annual sea ice retreat and advance and their relation to El Nino-southern oscillation and southern annular mode variability. J Geophys Res 113: C03S90
Tedesco M, Monaghan AJ (2009) An updated Antarctic melt record through 2009 and its linkages to high-latitude and tropical climate variability. Geophys Res Lett 36(18): L18502
Thorne PW, Vose RS (2010) Reanalyses suitable for characterizing long-term trends. Bull Amer Meteor Soc 91:353–361
Tietäväinen H, Vihma T (2008) Atmospheric moisture budget over Antarctica and the southern ocean based on the ERA-40 reanalysis. Int J Climatol 28:1977–1995
Trenberth KE, Fasullo J, Smith L (2005) Trends and variability in column-integrated atmospheric water vapor. Climate Dyn 24:741–758
Turner J, Comiso JC, Marshall GJ, Lachlan-Cope TA, Bracegirdle T, Maksym T, Meredith MP, Wang Z, Orr A (2009) Non-annular atmospheric circulation change induced by stratospheric ozone depletion and its role in the recent increase of Antarctic sea ice extent. Geophys Res Lett 36(8): L08502
Uppala SM et al (2005) The ERA-40 re-analysis. Q J Roy Meteor Soc 131:2961–3012
Uppala S, Dee D, Kobayashi S, Berrisford P, Simmons A (2008) Towards a climate data assimilation system: status update of ERA-Interim. ECMWF Newslett No 115 pp 1218, http://www.ecmwf.int/publications/newsletters/pdf/115rev.pdf
Van de Berg WJ, van den Broeke MR, Reijmer CH, van Meijgaard E (2005) Characteristics of the Antarctic surface mass balance, 1958–2002, using a regional atmospheric climate model. Ann Glaciol 41:97–104
Van den Broeke M, van de Berg WJ, van Meijgaard E, Reijmer C (2006) Identification of Antarctic ablation areas using a regional atmospheric climate model. J Geophys Res 111: D18110
Vasiljevic D, Andersson E, Isaksen L, Garcia-Mendez A (2006) Surface pressure bias correction in data assimilation. ECMWF Newslett No 108 pp 20–27, http://www.ecmwf.int/publications/newsletters/pdf/108.pdf
Vaughan DG, Bamber JL, Giovinetto M, Russell J, Cooper APR (1999) Reassessment of net surface mass balance in Antarctica. J Climate 12:933–946
Xie P, Arkin P (1997) Global precipitation: a 17-year monthly analysis based on gauge observations, satellite estimates, and numerical model outputs. Bull Am Meteor Soc 78:2539–2558
Yin X, Gruber A, Arkin P (2004) Comparison of the GPCP and CMAP merged gauge-satellite monthly precipitation products for the period 1979–2001. J Hydrometeor 5(6):1207–1222
Yu L, Weller RA (2007) Objectively analyzed air-sea heat fluxes for the global ice-free oceans (1981–2005). Bull Am Meteor Soc 88(4):527–539

Surv Geophys (2011) 32:495–505
DOI 10.1007/s10712-011-9137-z

Ice Sheets and Sea Level: Thinking Outside the Box

Michiel R. Van den Broeke · Jonathan Bamber · Jan Lenaerts · Eric Rignot

Received: 14 January 2011 / Accepted: 31 May 2011 / Published online: 22 June 2011

Abstract Until quite recently, the mass balance (MB) of the great ice sheets of Greenland and Antarctica was poorly known and often treated as a residual in the budget of oceanic mass and sea level change. Recent developments in regional climate modelling and remote sensing, especially altimetry, gravimetry and InSAR feature tracking, have enabled us to specifically resolve the ice sheet mass balance components at a near-annual timescale. The results reveal significant mass losses for both ice sheets, caused by the acceleration of marine-terminating glaciers in southeast, west and northwest Greenland and coastal West Antarctica, and increased run-off in Greenland. At the same time, the data show that interannual variability is very significant, masking the underlying trends.

Keywords Greenland · Antarctica · Mass balance · Sea level

Surveys of Geophysics, proceedings of the ISSI workshop on the Earth's Cryosphere and Sea Level Change, March 22–26, Bern, Switzerland.

M. R. Van den Broeke (✉) · J. Lenaerts
Institute for Marine and Atmospheric Research, Utrecht University, Utrecht, The Netherlands
e-mail: m.r.vandenbroeke@uu.nl

J. Lenaerts
e-mail: j.lenaerts@uu.nl

J. Bamber
Bristol Glaciology Centre, School of Geographical Sciences, University of Bristol, Bristol, UK
e-mail: j.bamber@bristol.ac.uk

E. Rignot
Department of Earth System Science, University of California, Irvine, CA, USA
e-mail: erignot@uci.edu

E. Rignot
Jet Propulsion Laboratory, Pasadena, CA, USA

1 Introduction

The large ice sheets of Antarctica (AIS) and Greenland (GrIS) represent the largest freshwater sources on Earth, larger by two orders of magnitude than all other glaciers and ice caps combined, and sufficient to increase global sea level by about 70 m. Until quite recently, the mass balance (MB) of the AIS and GrIS and hence their contribution to sea level rise (SLR) was poorly known. Over the twentieth century, during which sea level rose by about 1.7 mm year^{-1}, their contribution to SLR was assumed to be small (Church et al. 2001).

For the period 1993–2003, based on satellite altimetry, Bindoff et al. (2007) estimated the rate of SLR to be 3.1 ± 0.4 mm year^{-1}, i.e. almost twice the rate of the twentieth century. Thermal expansion of the upper ocean layers amounted to 1.6 ± 0.3 mm year^{-1}. If for simplicity we neglect the contribution from other sources (e.g., deep ocean warming, storage of ground water and water in artificial basins), this leaves a land ice contribution of 1.5 ± 0.3 mm year^{-1}. Of this, 0.8 ± 0.2 mm year^{-1} is attributed to the melting of small glaciers and ice caps (GIC, Lemke et al. 2007). The residual of 0.7 ± 0.5 mm year^{-1} is ascribed to mass loss from the AIS and GrIS.

For the more recent period 2003–2008, for which many more data are available, considerable uncertainties remain with respect to the oceanic mass budget (Willis et al. 2008; Nicholls and Cazenave 2010). Using altimetry and satellite gravimetry data from GRACE over the period 2003–2008, Cazenave et al. (2009) estimate the rate of SLR to be 2.5 ± 0.4 mm year^{-1}, i.e. a 20% decrease compared to 1993–2003. This decrease was explained by a reduction in the contribution of thermal expansion, to 0.4 ± 0.1 mm year^{-1} (Willis et al. 2008), indicating that the contribution of land ice to SLR had increased to 2.1 ± 0.3 mm year^{-1}. Meier et al. (2007) estimate that GIC in 2006 contributed 1.1 ± 0.2 mm year^{-1} to SLR. If we assume this value to be the representative for 2003–2008, this leaves a contribution of 1.0 ± 0.4 mm year^{-1} for the AIS and GrIS. Both for GIC and the AIS/GrIS, this represents a $\approx$40% increase in mass loss compared to the period 1993–2003.

In spite of the insight it yields, it is unsatisfactory to treat the contribution of the AIS and GrIS to SLR as a residual. Firstly, all components of the sea level budget have large uncertainties, enhancing the uncertainty in the residual. Secondly, it is imperative that we partition the ice sheet mass loss into an ice dynamic (glacier acceleration) and surface (snowfall/run-off) component; only then will it be possible to model the physical processes responsible for ongoing mass losses and make predictions. Thirdly, we must resolve the temporal (interannual) variability of the AIS and GrIS mass balance, to explain interannual variations in SLR. In this survey, we present some recent advances and results in this field.

2 Methods to Determine Ice Sheet Mass Balance

The contributions of the AIS and GrIS to SLR depend on their mass balance (MB, Gt year^{-1}), defined as the temporal change of ice sheet mass ($\partial M/\partial t$). Neglecting basal melting of grounded ice, MB is governed by the difference between surface mass balance (SMB) and the ice discharge across the grounding line, including the effects of grounding line migration (D):

$$MB = \partial M/\partial t = SMB - D \tag{1}$$

Surface mass balance (SMB, Gt year^{-1}) is the sum of accumulation by precipitation (snow and rain) and ablation by sublimation and run-off. Run-off, in turn, is determined by

the liquid water balance (LWB), the sum of sources (water vapour condensation, rainfall and ice and snow melt) and sinks (refreezing and capillary retention) of liquid water. Recent developments in remote sensing and regional climate modelling offer three methods to estimate ice sheet MB, each with their advantages and disadvantages. These three methods are briefly discussed below.

2.1 Satellite Altimetry

Remotely sensed elevation changes from radar/laser altimetry yield changes in ice sheet volume, i.e. this technique does not discriminate between the different processes responsible for mass loss. Moreover, converting volume to mass changes can be problematic, because they are caused by changes in ice dynamics and firn densification rate as well as decadal changes in accumulation, the latter representing a major source for short-term ice sheet elevation changes (McConnell et al. 2000; Helsen et al. 2008). These processes cannot be isolated based on elevation change measurements alone, and a separate estimate must be made for firn densification and accumulation variability. This requires a firn densification model forced by high-resolution (in time and space) atmospheric re-analyses, which can only be done for the period with reliable atmospheric forcing data, i.e. after 1978 in Greenland and 1980 in Antarctica (Van de Berg et al. 2005). This excludes an assessment of the role of longer time scale variations in snowfall, which are known to exist. Radar altimeters have a penetration depth in snow that depends on (time varying) snow structure and density (Thomas et al. 2008). Until the launch of Cryosat-2 in 2010, the narrow, fast flowing outlet glaciers, which are expected to react most rapidly to environmental changes, were not adequately resolved. The laser altimeter onboard ICESat captures changes in these glaciers in detail (Pritchard et al. 2009), but unfortunately has limited coverage and life span and is sensitive to clouds, prohibiting continuous time series in high-accumulation (i.e. frequently overcast) areas.

2.2 Satellite Gravimetry

This method uses data of the Gravity Recovery and Climate Experiment (GRACE) satellites. GRACE has caused a small revolution in climate and sea level research by showing beyond a doubt that the large ice sheets are losing mass (Velicogna and Wahr 2006a, b; Wouters et al. 2008; Velicogna 2009; Chen et al. 2009). Moreover, the method is completely independent of the other two methods, making it a suitable verification and calibration tool. Drawbacks are that no distinction is made between the different processes responsible for mass loss, and the uncertainties arising from the short time period over which the trends have been calculated (2003–2009, i.e. 7 years). Moreover, multiple corrections must be applied to obtain mass changes, each introducing additional uncertainties. In Antarctica, the most important correction is that for upward motion of the Earth's crust following deglaciation (Glacial Isostatic Adjustment or GIA). The GIA correction is relatively small over Greenland, for which good agreement with the mass budget method is found (Van den Broeke et al. 2009) but large and relatively poorly constrained over Antarctica (Riva et al. 2009).

2.3 The Mass Budget Method

This method relies on an accurate determination of mass input (SMB) and mass output (D). The major advantage of the mass budget method is that individual MB components (SMB,

LWB and D) are quantified, per drainage basin and year, providing insight into the physical processes that determine ice sheet mass changes. Because MB represents the difference between two large terms (SMB and D), the method is very sensitive to uncertainties in the individual components. This prohibited its use over the full ice sheet surface until recently. Using remotely sensed ice velocities/thicknesses and elevation data, and improved SMB fields, ice sheet-wide MB assessments using the mass budget method are now feasible (Rignot and Kanagaratnam 2006; Rignot et al. 2008a, b; Van den Broeke et al. 2009; Rignot et al. 2011).

In addition to SMB compilations based on spatial interpolation of observations (Arthern et al. 2006; Bales et al. 2009; Burgess et al. 2010), regional climate models (RCMs) have recently also started to provide reliable SMB fields (Van de Berg, et al. 2006; Fettweis 2007; Ettema et al. 2009). RCMs explicitly resolve physical atmospheric processes leading to snowfall and melt, and run at higher resolution than global models, typically 10–30 km vs. 100–300 km. As an example, Fig. 1 shows recent results from the Regional Atmospheric Climate Model (RACMO2) for Antarctic and Greenland SMB. These fields represent the average SMB for a 21-year period (1989–2009), for which the regional model was forced at the boundaries by the European Centre for Medium-range Weather Forecasts interim re-analysis (ERA-Interim). These modelled SMB fields correlate very well with in situ observations from firn cores, stakes and snow pits (correlation coefficient $r = 0.87$ for the AIS, 0.95 for the GrIS).

Figure 1 shows that both ice sheets have coastal areas that are significantly wetter than the ice sheet interior. Coastal West Antarctica experiences accumulation rates in excess of 1500 kg m^{-2} $year^{-1}$, while peak values in excess of 3000 kg m^{-2} $year^{-1}$ occur in the western Antarctic Peninsula and coastal southeast Greenland. In contrast, northeast Greenland receives less than 100 kg m^{-2} $year^{-1}$ and interior East Antarctica even less than 50 kg m^{-2} $year^{-1}$. Due to strong summertime melt and run-off, Greenland has a well-defined marginal ablation zone, which is more than 100 km wide in the southwest, where ablation up to 3000 kg m^{-2} $year^{-1}$ occurs. Ablation in Antarctica is limited in area and magnitude. It is generally not caused by run-off, but rather by (snowdrift) sublimation and

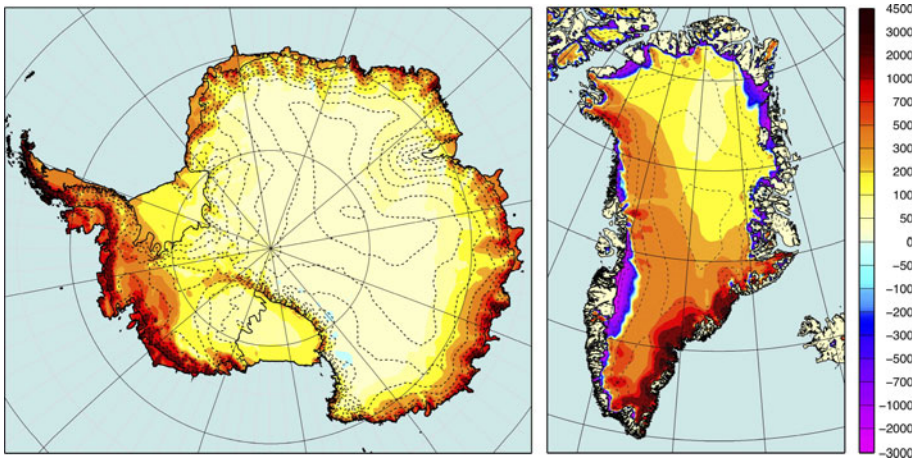

Fig. 1 Surface mass balance (SMB, 1989–2009) from RACMO2 of the AIS (*left*) and the GrIS (*right*) in kg m^{-2} $year^{-1}$. Contour levels (*dashed*) are shown every 500 m

erosion, limiting ablation to regions where these processes are active (Van den Broeke et al. 2006b; Lenaerts et al. 2010). Because observations are very sparse in coastal, high-accumulation/high-ablation areas (Van den Broeke et al. 2006a), compilations that rely on interpolation of available observations tend to under/overestimate SMB in coastal Antarctica/Greenland and therewith ice sheet SMB. This favours the use of modelled ('dynamically downscaled') SMB fields in the mass budget method. The SMB numbers presented in this paper refer to the conterminous, grounded ice sheet.

Ice discharge (D) is quantified using feature tracking from satellite imaging radar to obtain the flow speed of the narrow glaciers through the flux gates at the ice sheet grounding line (Rignot et al. 2008a, b). Satellite altimetry is used to accurately delineate the ice drainage basins as well as to obtain the elevation/thickness of the outlet glacier at the grounding line (Bamber et al. 2001, 2010). In Antarctica, where a floatation criterion is used to determine ice thickness at the grounding line for most glaciers (Rignot et al. 2008b), a correction must be applied for the density of the firn mantle that covers the ice. This can be achieved by using output of a regional atmospheric climate model in combination with a steady-state firn compaction model (Van den Broeke 2008; Van den Broeke et al. 2008). For the GrIS, where glacier tongues experience significant ablation in summer, this correction is less important. Finally, if the grounding line is migrating, as is currently the case in coastal West Antarctica, this represents a mass flux that must also be estimated (Rignot et al. 2011).

3 Application of the Mass Budget Method to the AIS and GrIS

Owing to the availability of improved SMB and D estimates, recent studies have applied the mass budget method to the AIS (Fig. 2a) and GrIS (Fig. 2b) for the period 1989–2009. Before 1980, re-analysis products are unreliable in the SH, and no SMB estimates are available for the AIS prior to that year (Van de Berg et al. 2005), while no accurate discharge observations are currently available before 1992 (Rignot et al. 2011). The SMB of the AIS does not show a significant trend, in line with earlier studies (Monaghan et al. 2006). A notable feature in Fig. 2a is the large interannual variability in SMB, with year-to-year changes as large as 300 Gt year^{-1}. However, the standard deviation of 121 Gt year^{-1} represents just 6% of the 1989–2009 average SMB over the grounded ice sheet (2083 Gt year^{-1}); this demonstrates that, even though the *relative* interannual variability is small, the variability in terms of *absolute mass* is very significant for the AIS, obscuring mass trends.

Estimates of total AIS discharge (D) are available for the years 1992, 1996, 2000, 2003, 2004 and annually since 2006 and include the estimated effect of inland migration of the grounding line in coastal West Antarctica (Rignot et al. 2011). For the years without discharge data, a linear interpolation between data points was applied, assuming slowly changing D. Here, we assume constant discharge between 1989 and 1992. The increase in discharge is mainly caused by the acceleration of glaciers in coastal West Antarctica, which still continues (Rignot 2008), and acceleration of glaciers in the Antarctic Peninsula mainly prior to 2005 (Pritchard and Vaughan 2007). Compared to 1992, discharge from the AIS has increased by 173 Gt year^{-1} or 8% in 2009; as a result, MB has been persistently negative since 1994, except for 3 years with high snowfall (1998, 2001 and 2005).

For the GrIS, reliable SMB time series date back as far as 1958, owing to much better observational coverage in the northern hemisphere (Ettema et al. 2009). However, reliable estimates of D are only available for years 1992, 1996, 2000 and annually since 2004

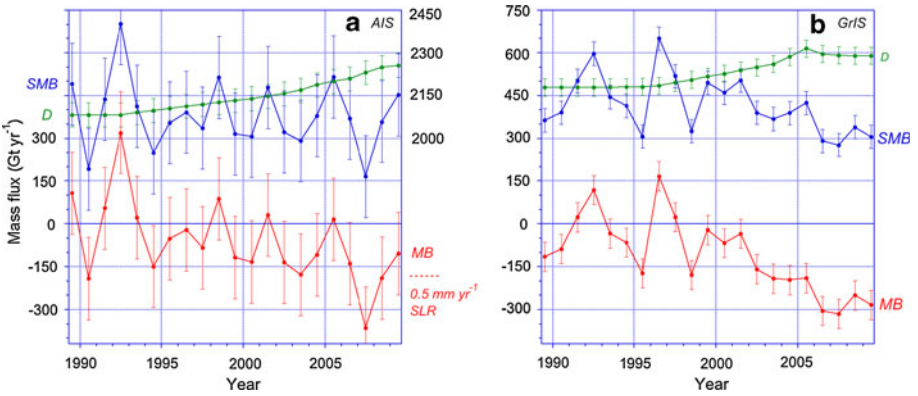

Fig. 2 Time series of surface mass balance (SMB, *blue*), solid ice discharge (D, *green*) and ice sheet mass balance (MB, *red*) for the AIS (*left*) and the GrIS (*right*) in Gt year^{-1}. For the AIS (*left*), scale for SMB and D has been shifted (*right ordinate*) to allow plotting on the same scale as for the GrIS (*right*). D is assumed constant before 1992

(Rignot et al. 2011). Both SMB and D time series are displayed in Fig. 2b for the period 1989–2009, once more assuming constant discharge between 1989 and 1992 and using a linear interpolation to obtain D data between years with observations. Unlike in Antarctica, where run-off is negligible, interannual SMB variability for the GrIS is also for an important part caused by run-off variability, which is anti-correlated with accumulation (little winter snowfall causes larger summer ablation through the lower albedo of bare ice); year-to-year variations in SMB can therefore be as large as 400 Gt year^{-1}. The average standard deviation is 100 Gt year^{-1}, 24% of the average SMB (417 Gt year^{-1}). Another contrast to the AIS is that the SMB shows a negative trend since about 2000, following atmospheric warming and increased run-off since the early 1990s (Hanna et al. 2008; Van den Broeke et al. 2009). In combination with an increase in D since about 1996, owing to glacier acceleration in southeast, west and northwest Greenland (Joughin et al. 2004; Howat et al. 2005, 2007; Rignot and Kanagaratnam 2006; Khan et al. 2010), this has resulted in a persistently negative MB since 1999.

4 Discussion and Conclusions

We can compare our ice sheet mass balance time series with results based on SLR residuals mentioned in the Introduction. The average 2003–2008 MB of the AIS is -161 ± 150 Gt year^{-1} and that of the GrIS -241 ± 51 Gt year^{-1}. This represents an average contribution of the ice sheets to SLR of 1.1 ± 0.4 mm year^{-1} over that six-year period, which agrees well with the estimate based on SLR residuals (1.0 ± 0.5 mm year^{-1}). The mass loss over this period is partitioned 40%/60% between the AIS and the GrIS. Acceleration of outlet glaciers is the only source of mass loss in Antarctica, and increased run-off (decreased SMB) is equally important in Greenland. For the period 1993–2003, the MB summed for both ice sheets averages -133 ± 158 Gt year^{-1}, equivalent to a SLR of 0.4 ± 0.4 mm year^{-1}, which agrees within error bars with the SLR residual of 0.7 ± 0.5 mm year^{-1}.

As important as time-averaged MB is its interannual variability. Figure 3 compares the MB time series of the AIS (Fig. 3a) and GrIS (Fig. 3b) with a (non-exhaustive) compilation of recent MB estimates using satellite altimetry (red), the mass budget method

(black) and GRACE (green). Until recently, review articles on ice sheet mass balance listed results of the above methods in a regular table (Rignot and Thomas 2002; Shepherd and Wingham 2007), but since the launch of GRACE in 2002, the number of mass balance estimates has grown rapidly. That is why the box plot has taken over as the preferred method to present estimates of ice sheet mass balance (Cazenave 2006). The box colour usually denotes the method used; the horizontal dimension covers the time period over which mass balance has been averaged, and the vertical dimension represents the uncertainty. If two boxes cover the same period but do not vertically overlap, the uncertainty has obviously been underestimated in one or both studies. The blue boxes represent 1993–2003 estimates as published in IPCC AR4 (Bindoff et al. 2007). Most MB estimates based on altimetry date from before 2003, and are based on ERS1/2 radar altimetry data, the exception being recent studies based on laser altimetry from GLAS onboard ICESat (2003–2009). Gravimetry estimates start in early 2003, following the launch of the GRACE satellites.

For both ice sheets, the general picture that emerges from the boxes in Fig. 3 is that of near balance to modest mass losses in the 1990s, increasing to more substantial mass losses after 2000. Annual MB values from Fig. 2 are plotted as black dashed lines. In general, these curves nicely connect the various boxes, confirming many of the earlier studies and partly explaining the differences among studies in terms of interannual MB variability. The black lines show that MB can vary substantially within a single box, which means that the choice of the averaging period is critical for the obtained average MB value and is not necessarily representative for a longer period. The box plot has the undesirable characteristic to hide the interannual variability, providing a too static picture of ice sheet mass balance. To do justice to the important interannual variability in MB, we suggest either to

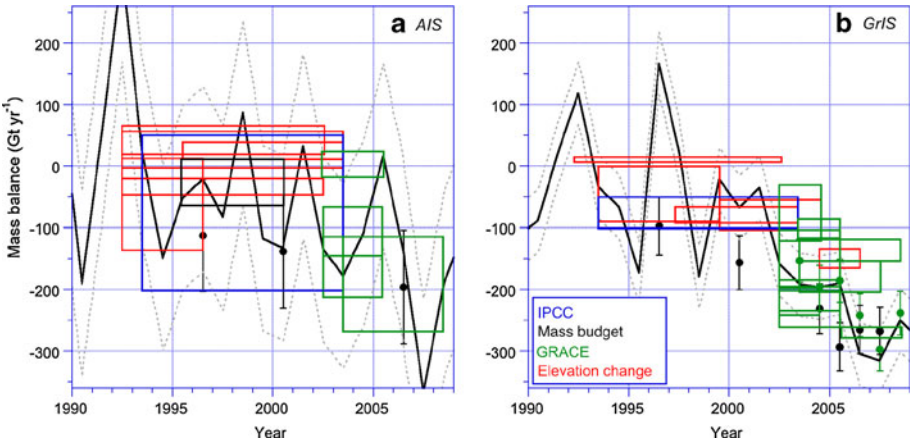

Fig. 3 Recent mass balance estimates (Gt year^{-1}) for the AIS (*left*) and the GrIS (*right*), based on altimetry (*red*), GRACE (*green*) and the mass budget method (*black*). MB data from Fig. 2 are plotted as *black dashed lines* with uncertainty margins. *Data sources* AIS (*left*): Wingham et al. (1998); Rignot and Thomas (2002); Davis et al. (2005); Zwally et al. (2005); Velicogna and Wahr (2006b); Ramillien et al. (2006); Wingham et al. (2006); Chen et al. (2006b); Bindoff et al. (2007); Helsen et al. (2008); Rignot et al. (2008b); Chen et al. (2009); *Data sources* GrIS (*right*): Krabill et al. (2000); Krabill et al. (2004); Velicogna and Wahr (2005); Thomas et al. (2006); Rignot and Kanagaratnam (2006); Ramillien et al. (2006); Chen et al. (2006a); Luthke et al. (2006); Bindoff et al. (2007); Wouters et al. (2008); Rignot et al. (2008a); Cazenave et al. (2009); Velicogna (2009); Schrama and Wouters (2011)

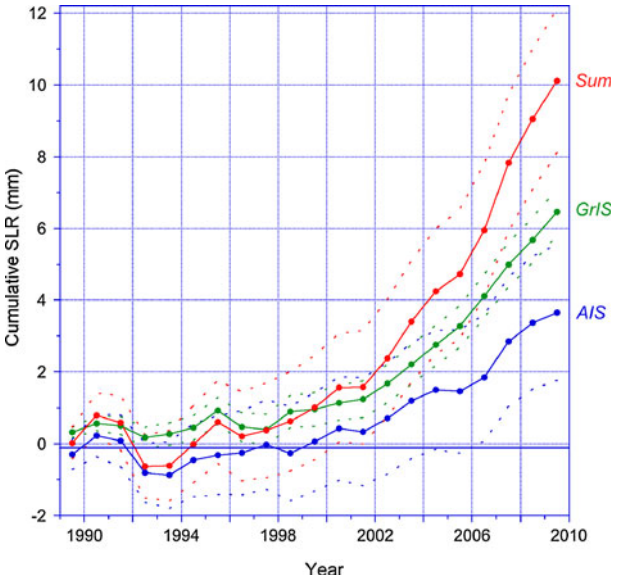

Fig. 4 Cumulative sea level rise contributions (1989–2009) from the AIS (*blue*) and the GrIS (*green*) and their sum (*red*). *Dashed lines* indicate uncertainty margins

calculate averages over a sufficiently long period (>10 years) or, better, to try to present MB at an annual resolution.

The latter is also the preferred option when closing the sea level budget. For example, our results show that the combined contribution of the AIS and GrIS to SLR was negative in 1992 (−1.2 mm) and 1996 (−0.4 mm), while in, e.g., 2007 it was positive and very large at almost 2 mm. Fig. 4 shows the cumulative contributions of the AIS and GrIS to SLR since 1989. Although the long-term trend is clearly positive and appears to be accelerating (Rignot et al. 2011), the year-to-year contributions to cumulative SLR are very variable. Taking these interannual variations into account will further help to explain and close the observed rate of global SLR.

References

Arthern RJ, Winebrenner DP, Vaughan DG (2006) Antarctic snow accumulation mapped using polarization of 4.3-cm wavelength microwave emission. J Geophys Res 111:D06107. doi:10.1029/2004JD005667

Bales RC, Guo Q, Shen D, McConnell JR, Du G, Burkhart JF, Spikes VB, Hanna E, Cappelen J (2009) Annual accumulation for Greenland updated using ice core data developed during 2000–2006 and analysis of daily coastal meteorological data. J Geophys Res 114:D06116. doi:10.1029/2008JD011208

Bamber JL, Ekholm S, Krabill WB (2001) A new, high-resolution digital elevation model of Greenland fully validated with airborne altimeter data. J Geophys Res 106:6733–6745

Bamber JL, Gomez-Dans JL, Griggs JA (2010) A new 1 km digital elevation model of the Antarctic derived from combined satellite radar and laser data, Part 1: data and methods. The Cryosphere 3:101–111

Bindoff NL, Willebrand J, Artale V, Cazenave A, Gregory JM, Gulev S, Hanawa K, Le Quéré KC, Levitus S, Nojiri Y, Shum CK, Talley LD, Unnikrishnan AS (2007) Observations: oceanic climate change and

sea level. In: Solomon S, Qin D, Manning M, Chen Z, Marquis M, Averyt KB, Tignor M, Miller HL (eds) Climate change 2007: the physical science basis. contribution of working group i to the fourth assessment report of the intergovernmental panel on climate change, Cambridge University Press, United Kingdom and New York, USA

Burgess EW, Forster RR, Box JE, Smith LC, Bromwich DH (2010) Greenland ice sheet annually-resolved accumulation rates (1958–2007), a spatially calibrated model. J Geophys Res 115:F02004. doi: 10.1029/2009JF001293

Cazenave A (2006) How fast are the ice sheets melting? Science 314:1250–1252

Cazenave A, Dominh K, Guinehut S, Berthier E, Llovel W, Ramillien G, Ablain M, Larnicol G (2009) Sea level budget over 2003–2008: a re-evaluation from GRACE space gravimetry, satellite altimetry and Argo. Glob Planet Change 65:83–88. doi:10.1016/j.gloplacha.2008.10.004

Chen JL, Wilson CR, Tapley BD (2006a) Satellite gravity measurements confirm accelerated melting of Greenland ice sheet. Science 313:1958. doi:10.1126/science.1129007

Chen JL, Wilson CR, Blankenship DD, Tapley BD (2006b) Antarctic mass rates from GRACE. Geophys Res Lett 33:L11502. doi:10.1029/2006GL026369

Chen JL, Wilson CR, Blankenship D, Tapley BD (2009) Accelerated Antarctic ice loss from satellite gravity measurements. Nature Geosci 2:859–862

Church JA, Gregory JM, Huybrechts P, Kuhn M, Lambeck K, Nhuan MT, Qin D, Woodworth PL (2001) Changes in sea level. In: Houghton JT, Ding Y, Griggs DJ, Noguer M, Van der Linden PJ, Xiaou D (eds) Climate change 2001: the scientific basis. Cambridge University Press, Cambridge and New York, pp 639–694

Davis CH, Li Y, McConnell JR, Frey MM, Hanna E (2005) Snowfall-driven growth in East Antarctic ice sheet mitigates recent sea-level rise. Science 308:1898–1901. 10.1126/science.1110662

Ettema J, Van den Broeke MR, van Meijgaard E, van de Berg WJ, Bamber JL, Box JE, Bales RC (2009) Higher surface mass balance of the Greenland ice sheet revealed by high-resolution climate modeling. Geophys Res Lett 36:L12501. doi:10.1029/2009GL038110

Fettweis X (2007) Reconstruction of the 1979–2006 Greenland ice sheet surface mass balance using the regional climate model MAR. The Cryosphere 1:21–40

Hanna E, Huybrechts P, Steffen K, Cappelen J, Huff R, Shuman C, Irvine-Fynn T, Wise S, Griffiths M (2008) Increased runoff from melt from the Greenland ice sheet: a response to global warming. J Climate 21:331–341

Helsen MM, van den Broeke MR, van de Wal RSW, van de Berg WJ, van Meijgaard E, Davis CH, Li Y, Goodwin I (2008) Elevation changes in Antarctica mainly determined by accumulation variability. Science 320:1626–1629. doi: 10.1126/science.1153894, 1626-1629

Howat IM, Joughin I, Tulaczyk S, Gogineni S (2005) Rapid retreat and acceleration of Helheim Glacier, east Greenland. Geophys Res Lett 32:L22502. doi:10.1029/2005GL024737

Howat IM, Joughin I, Scambos T (2007) Rapid changes in ice discharge from Greenland outlet glaciers. Science 315:1559. doi:10.1126/science.1138478

Joughin I, Abdalati W, Fahnestock M (2004) Large fluctuations in speed on Greenland's Jakobshavn Isbrae glacier. Nature 432:608–610

Khan SA, Wahr J, Bevis M, Velicogna I, Kendrick E (2010) Spread of ice mass loss into northwest Greenland observed by GRACE and GPS. Geophys Res Lett 37:L06501. doi:10.1029/2010GL042460.10

Krabill W, Abdalati W, Frederick E, Manizade S, Martin C, Sonntag J, Swift R, Thomas R, Wright W, Yungel J (2000) Greenland ice sheet: high-elevation balance and peripheral thinning. Science 289:428–429

Krabill W, Hanna E, Huybrechts P, Abdalati W, Cappelen J, Csatho B, Frederick E, Manizade S, Martin C, Sonntag J, Swift R, Thomas R, Yungel J (2004) Greenland ice sheet: increased coastal thinning. Geophys Res Lett 31:L24402. doi:10.1029/2004GL021533

Lemke P, Ren J, Alley RB, Allison I, Carrasco J, Flato G, Fujii Y, Kaser G, Mote P, Thomas RH, Zhang T (2007) Observations: changes in snow, ice and frozen ground. In: Solomon S, Qin D, Manning M, Chen Z, Marquis M, Averyt KB, Tignor M, Miller HL (eds) Climate change 2007: the physical science basis. contribution of working group i to the fourth assessment report of the intergovernmental panel on climate change, Cambridge University Press, United Kingdom and New York, USA

Lenaerts JTM, van den Broeke MR, Déry SJ, König-Langlo G, Ettema J, Kuipers Munneke P (2010) Modelling snowdrift sublimation on an Antarctic ice shelf. The Cryosphere 4:179–190

Luthke S, Zwally H, Abdalati W, Rowlands D, Ray R, Nerem R, Lemoine F, McCarthy J, Chinn D (2006) Recent Greenland mass loss by drainage system from satellite gravity observations. Science 314:1286–1289

McConnell JR, Arthern RJ, Mosley-Thompson E, Davis CH, Bales RC, Thomas R, Burkhart JF, Kyne JD (2000) Changes in Greenland ice sheet elevation attributed primarily to snow accumulation variability. Nature 406:877–879

Meier MF, Dyurgerov MB, Rick UK, O'Neel S, Pfeffer WT, Anderson RS, Anderson SP, Glazovsky AF (2007) Glaciers dominate eustatic sea-level rise in the twentyfirst century. Science 317:1064–1067

Monaghan AJ, Bromwich DH, Fogt RL, Wang S-H, Mayewski PA, Dixon DA, Ekaykin A, Frezzotti M, Goodwin I, Isaksson E, Kaspari SD, Morgan VI, Oerter H, Van Ommen TD, Van der Veen CJ, Wen J (2006) Insignificant change in Antarctic snowfall since the international geophysical year. Science 313:827–831

Nicholls RJ, Cazenave A (2010) Sea-level rise and its impact on coastal zones. Science 328:1517–1520

Pritchard HD, Vaughan DG (2007) Widespread acceleration of tidewater glaciers on the Antarctic Peninsula. J Geophys Res 112:F03S29. doi:10.1029/2006JF000597

Pritchard HD, Arthern RJ, Vaughan DG, Edwards LA (2009) Extensive dynamic thinning on the margins of the Greenland and Antarctic ice sheets. Nature 461:971–975

Ramillien G, Lombard A, Cazenave A, Ivins ER, Llubes M, Remy F, Biancale R (2006) Interannual variations of the mass balance of the Antarctica and Greenland ice sheets from GRACE. Global Planet Change 53:198–208

Rignot E (2008) Changes in West Antarctic ice stream dynamics observed with ALOS PALSAR data. Geophys Res Lett 35:L12505. doi:10.1029/2008GL033365

Rignot E, Kanagaratnam P (2006) Changes in the velocity structure of the Greenland ice sheet. Science 311:986–990

Rignot E, Thomas RH (2002) Mass balance of Polar ice sheets. Science 297:1502–1506

Rignot E, Box JE, Burgess E, Hanna E (2008a) Mass balance of the Greenland ice sheet from 1958 to 2007. Geophys Res Lett 35:L20502. doi:10.1029/2008GL035417

Rignot E, Bamber JL, van den Broeke MR, Davis C, Li Y, van de Berg WJ, van Meijgaard E (2008b) Recent Antarctic mass loss from radar interferometry and regional climate modeling. Nature Geosci 2:106–110

Rignot E, Velicogna I, van den Broeke MR, Monaghan A, Lenaerts J (2011) Acceleration of the contribution of the Greenland and Antarctic ice sheets to sea level rise. Geophys Res Lett 38:L05503. doi:10.1029/2011GL046583

Riva REM, Gunter BC, Urban TJ, Vermeersen BLA, Lindenbergh RC, Helsen MM, Bamber JL, van de Wal RSW, van den Broeke MR, Schutz BE (2009) Glacial isostatic adjustment over Antarctica from combined ICESat and GRACE satellite data. Earth Planet Sci Lett 288:516–523

Schrama EJO, Wouters B (2011) Revisiting Greenland ice sheet mass loss observed by GRACE. J Geophys Res 116:B02407. doi:10.1029/2009JB006847

Shepherd A, Wingham D (2007) Recent sea-level contributions of the Antarctic and Greenland ice sheets. Science 315:1529–1532

Thomas R, Frederick E, Krabill W, Manizade S, Martin C (2006) Progressive increase in ice loss from Greenland, Geophys Res Lett, L10503

Thomas R, Davis C, Frederick E, Krabill W, Li Y, Manizade S, Martin C (2008) A comparison of Greenland ice-sheet volume changes derived from altimetry measurements. J Glaciol 54: 203-212. 11

Van de Berg WJ, van den Broeke MR, Reijmer CH, van Meijgaard E (2005) Characteristics of the Antarctic surface mass balance, 1958–2002, using a regional atmospheric climate model. Ann Glaciol 41:97–104

Van den Broeke MR (2008) Depth and density of the Antarctic firn layer. Arct Antarct Alp Res 40:432–438

Van den Broeke MR, van de Berg WJ, van Meijgaard E (2006a) Snowfall in coastal West Antarctica much greater than previously assumed. Geophys Res Lett 33:L02505. doi:10.1029/2005GL025239

Van den Broeke MR, van de Berg WJ, van Meijgaard E, Reijmer CH (2006b) Identification of Antarctic ablation areas using a regional atmospheric climate model. J Geophys Res 111:D18110. doi:10.1029/2006JD007127

Van den Broeke MR, van de Berg WJ, van Meijgaard E (2008) Firn depth correction along the Antarctic grounding line. Antarctic Sci 20:513–517. doi: 10.1017/S095410200800148X

Van den Broeke MR, Bamber J, Ettema J, Rignot E, Schrama E, van de Berg WJ, van Meijgaard E, Velicogna I, Wouters B (2009) Partitioning recent Greenland mass loss. Science 326:984–986

Van de Berg WJ, van Den Broeke MR, van Meijgaard E (2006b) Reassessment of the Antarctic surface mass balance using calibrated output of a regional atmospheric climate model. J Geophys Res 111:D11104. doi:10.1029/2005JD006495

Velicogna I (2009) Increasing rates of ice mass loss from the Greenland and Antarctic ice sheets revealed by GRACE. Geophys Res Lett 36:L19503. doi:10.1029/2009GL040222

Velicogna I, Wahr J (2005) Greenland mass balance from GRACE. Geophys Res Lett 32(18):L18505. doi:10.1029/2005GL023955

Velicogna I, Wahr J (2006a) Acceleration of Greenland ice mass loss in spring 2004. Nature 443:329–331
Velicogna I, Wahr J (2006b) Measurements of time-variable gravity show mass loss in Antarctica. Science 311:1754. doi:10.1126/science.1123785
Willis JK, Chambers DP, Nerem RS (2008) Assessing the globally averaged sea level budget on seasonal to interannual timescales. J Geophys Res 113:C06015. doi:10.1029/2007JC004517
Wingham DJ, Ridout AJ, Scharroo R, Arthern RJ, Shum CK (1998) Antarctic elevation change from 1992 to 1996. Science 282:456. doi:10.1126/science.282.5388.456
Wingham DJ, Shepherd A, Muir A, Marshall GJ (2006) Mass balance of the Antarctic ice sheet. Phil Trans R Soc A 364:1627–1635. doi:10.1098/rsta.2006.1792
Wouters B, Chambers D, Schrama EJO (2008) GRACE observes small scale mass loss in Greenland. Geophys Res Lett 35:L20501. doi:10.1029/2008GL034816
Zwally HJ, Giovinetto MB, Li J, Cornejo HG, Beckley MA, Brenner AC, Saba JL, Yi D (2005) Mass changes of the Greenland and Antarctic ice sheets and shelves and contributions to sea-level rise: 1992–2002. J Glaciol 51:509–527

Surv Geophys (2011) 32:507–518
DOI 10.1007/s10712-011-9125-3

A Downscaling Approach Toward High-Resolution Surface Mass Balance Over Antarctica

Hubert Gallée · Cécile Agosta · Luc Gential · Vincent Favier · Gerhard Krinner

Received: 29 October 2010 / Accepted: 19 April 2011 / Published online: 28 May 2011

Abstract The Antarctic ice sheet surface mass balance shows high spatial variability over the coastal area. As state-of-the-art climate models usually require coarse resolutions to keep computational costs to a moderate level, they miss some local features that can be captured by field measurements. The downscaling approach adopted here consists of using a cascade of atmospheric models from large scale to meso-γ scale. A regional climate model (Modèle Atmosphérique Régional) forced by meteorological reanalyses provides a diagnostic physically-based rain- and snowfall downscaling model with meteorological fields at the regional scale. Although the parameterizations invoked by the downscaling model are fairly simple, the knowledge of small-scale topography significantly improves the representation of spatial variability of precipitation and therefore that of the surface mass balance. Model evaluation is carried out with the help of shallow firn cores and snow height measurements provided by automatic weather stations. Although downscaling of blowing snow still needs to be implemented in the model, the net accumulation gradient across Law Dome summit is shown to be induced mostly by orographic effects on precipitation.

Keywords Net accumulation · Downscaling · Antarctica · Law Dome

1 Introduction

Sea level rise is identified as one of the major impacts of climate change on populations. Changes in snow mass balance of polar ice sheets directly impact mean sea level through water budget of the Earth system.

Surface mass balance of the Antarctic ice sheet is listed in the IPCC WG1 4th assessment report as the only negative contribution to the twenty-first century sea level rise estimates (Meehl et al. 2007). As temperatures remain low, ablation is not expected to increase much nor the precipitation phase to evolve toward rain, whereas precipitation in a

H. Gallée (✉) · C. Agosta · L. Gential · V. Favier · G. Krinner
UJF-Grenoble 1/CNRS, LGGE UMR 5183, 54 rue Molière, BP 96, 38402,
Saint-Martin-d'Hères Cedex, France
e-mail: gallee@lgge.obs.ujf-grenoble.fr

moister context might increase more significantly (Krinner et al. 2006; Wild et al. 2003). On the other hand there are studies that show that precipitation has not increased in the past 50 years (e.g. Monaghan et al. 2006). To address the question of future evolution of the Antarctic ice sheet mass balance, modeling is a quite unique tool. However, the ability of current climate models to resolve small scale variability of net accumulation is facing the problem of computational costs.

To resolve the "computational cost versus spatial resolution" dilemma, many downscaling techniques have been proposed and used in the past 30 years, especially for hydrological purposes. Some approaches take advantage of the statistical properties of an observation data set of the target field. Others are based on the physics of orographic precipitation key processes which are supposed to govern small-scale variability (e.g. Goyette and Laprise 1996; Kuligowski and Barros 1999). While the former technique is well suited to complex processes in data-rich regions, the latter one is preferable in data-poor regions, especially when some simple physical law can explain most of the spatial features observed. In the case of Antarctica, a large continent with extreme weather, a physically-based downscaling model should improve the performance of cascades of models used to simulate the Antarctic surface mass balance (Bromwich et al. 2004). The small-scale topography is considered as one of the main forcings on accumulation in the coastal area (Goodwin et al. 2003). Consequently one can imagine that better results will be obtained when adding a downscaling model in the models' cascade than working with an atmospheric general circulation model and even a regional model only. Most of the existing physically-based downscaling models are developed on the basis of orographic precipitation modeling. To compute the airflow dynamics induced by the high-resolution topography, most of these models use results of the linear Boussinesq mountain wave theory (e.g. Smith 2002, Funk and Michaelsen 2004) that allows low computational costs. The most sophisticated models introduce time delays for the formation and the advection of hydrometeors. A further review of orographic precipitation models and their characteristics is given in Table 1 of Barstad and Smith (2005).

As coastal regions are those in Antarctica where small-scale orography shows the steepest slopes, they represent an appropriate domain for testing a physically-based precipitation downscaling model, especially since precipitation explains most of the measured net accumulation (Bromwich 1988). In particular, the area of Law Dome (Fig. 1) can be considered as a perfect laboratory for this kind of model validation. Indeed it is a coastal dome which weather is dominated by easterly flow associated with cyclones moving over the ocean. Consequently it is characterized by high accumulation rates on its eastern side and much lower accumulation rates on its western side. As for other east Antarctic coastal areas the fraction of liquid precipitation and runoff is not significant.

The present paper is organized as follows. In a first part we present the method, i.e. the models and data used. Then we share the results of model evaluation and draw some conclusions on the processes involved in coastal net accumulation. At the end, we discuss the results and conclude to the ability of the method to address the question of fine scale surface mass balance.

2 Methodology

2.1 Some Definitions

Snow accumulation is defined here as the sum of solid precipitation Ps and the result of the competition between blown snow particles deposition D and erosion E by the wind:

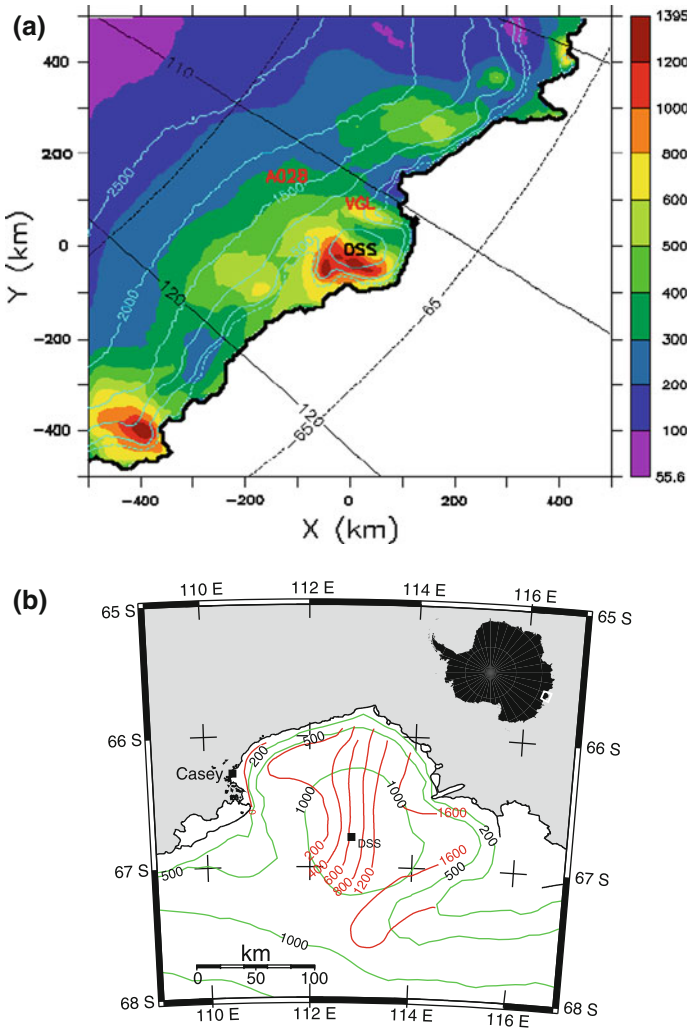

Fig. 1 **a** Annual-mean SMB over Law Dome area, for the 1998–2001 period (mm w.e. per year, see color scale). *Dashed* (*solid*) *lines* correspond to latitude (longitude E) contours and are drawn every 5 (10) degrees. The 200 (*dashed*), 500, 1,000, 1,500, 2,000 and 2,500 m surface elevation contours are shown in cyan. *VGL* Vanderford Glacier, *DSS* DSS AWS, *A028* A028 AWS. **b** SMB reconstruction over Law Dome made by van Ommen et al. (2004). *Red contours*: SMB (mm w.e. year^{-1}). *Green contours*: surface elevation (m). Adaptation by van de Berg et al. (2006). Copyright American Geophysical Union. Reproduced by permission of American Geophysical Union

$$\text{Snow accumulation} = (\text{Ps} + (\text{D} - \text{E})),$$

Surface mass balance (or net accumulation of snow/ice; hereinafter referred to as SMB) can be expressed as the balance between accumulation and ablation terms as follows:

$$\text{Surface mass balance SMB} = (\text{Ps} + \text{P1} + (\text{D} - \text{E}) - \text{Su} - \text{R}),$$

with Pl, Su and R denoting, respectively, liquid precipitation, sublimation and runoff. Units of these quantities are kg m^{-2} year^{-1} or mm water equivalent (mm w.e.) per year.

2.2 Model Description

Downscaling of precipitation was obtained with the use of a diagnostic model that computes total precipitation (solid plus liquid) on a fine grid given fine scale topography and large scale three-dimensional meteorological fields, i.e. pressure, temperature, wind, specific humidity, total water mixing ratio and total precipitation. The physics is based on the upslope model of Sinclair (1994) who assumes that the horizontal wind is not influenced by fine scale topography. The vertical wind component w_s at the surface is adjusted so that the surface wind vector follows the topography:

$$w_s = \mathbf{V_s}.\nabla z_s$$

where $\mathbf{V_s}$ is the horizontal component of the wind near the surface and ∇z_s is the surface slope. In Sinclair (1994) the vertical motion decreases with height at a specific rate. Here the importance of vertical stability over Antarctica is taken into account by replacing the initial empirical parameterization of Sinclair (1994) with a more explicit formulation based on the two-dimensional model of linearized internal gravity waves and proposed by Funk and Michaelsen (2004). Furthermore the vertical velocity near the surface is modified in order to take into account the vertical velocity provided by the host model and the influence of its topography on it, as in Goyette and Laprise (1996):

$$w_s = w_{sL} + \mathbf{V_{sL}}.\nabla(z_s - z_{sL})$$

where w_{sL}, $\mathbf{V_{sL}}$, and z_{sL} are provided by the host model and describe, respectively, its vertical and horizontal velocity, and its topography. Finally, we consider the case of a saturated baroclinic atmosphere when calculating the Scorer parameter (Durran and Klemp 1982). The Scorer parameter is obtained from the linear theory of mountain waves and describes the vertical wave number of lee waves induced by a single ridge.

Condensation occurs when adiabatic cooling of the rising water vapor leads to saturation (i.e. at the LCL—Lifting Condensation Level). Condensation rate above the LCL is calculated assuming that condensation arises by means of saturated ascent along the moist adiabatic. Unsaturated ambient conditions above the LCL are taken into account by multiplying the condensation factor by

$$\lambda(p) = [(r(p) - 0.6)/0.4]^{0.5}$$

where r(p) is the relative humidity and p is the pressure. $\lambda(p)$ is set equal to 0 when r(p) is smaller than 0.6.

Precipitation is then obtained by vertically integrating the condensation rate and by considering the efficiency of precipitation λ_s as a function of low-level relative humidity near the surface r_s

$$\lambda_s = [(r_s - 0.8)/0.2]^{0.25}$$

λ_s is set equal to 0 when r_s is smaller than 0.8.

Time delays for the formation of hydrometeors and their advection by the horizontal wind are considered, as well as fall speed of raindrops and snow particles, set to a constant value of 5 and 1 m s^{-1}, respectively, as in Collier (1975). We pay attention to the surface boundary condition and calculate a fictive surface horizontal wind speed extrapolated from two levels located above the katabatic layer (approximately 200 and 1,500 m a.g.l.—above ground level).

The Sinclair (1994) version of the model has been validated over the Alps by Brasseur et al. (2002) who found that such a simple model was able to improve the agreement between rain gauges and the 40-km resolution regional climate model MAR (Modèle Atmosphérique Régional) outputs.

2.3 Model Setup

2.3.1 Spatial and Temporal Domains

The downscaling model is run over a 1,000 km × 1,000 km domain centered over Law Dome and covering part of East Antarctica (Fig. 1). This region is chosen because of the supposed role of the orographic forcing on precipitation, the presence of high accumulation rates in the area and the availability of field data.

The 1998–2001 period is justified by the availability of AWS snow height measurements. We claim that 4 years are sufficient to address the climatological signature of the model, although measured annual-mean ENSO index is characterized during this period by near-neutral values (1998 and 2001) and moderately positive values (1999 and 2000). This leads to a wet anomaly of precipitation over Wilkes Land (Guo et al. 2004).

Note that the choice of horizontal domain size has very little influence on the results because the variables of the downscaling model do not depend on the horizontal distances.

2.3.2 Forcing

Model synopsis. Our downscaling model is forced every simulated 6 h by outputs from the regional climate model MAR, described in Gallée and Schayes (1994). MAR has been designed for polar studies and validated over Wilkes Land (Gallée et al. 2005) at the resolution of 40 km that was also used in the present study. The atmospheric part of MAR is coupled to a snow model and a parameterization of blowing snow is used. MAR is forced at its lateral boundaries by ECMWF reanalyses ERA-40.

Downscaling of the SMB. We derive two MAR experiments with blowing snow parameterization switched on and off (the last denoted by a « $|_{\mathrm{off}}$ »). The first one provided a regional SMB without runoff:

$$\mathrm{Ps} + \mathrm{P1} + (\mathrm{D} - \mathrm{E}) - \mathrm{Su}$$

Because runoff is overestimated in this simulation, it is replaced by an ensemble mean of a 1980–1982 MAR computation with a slightly different albedo parameterization (varying with the solar zenithal distance—labeled by a star): $\mathrm{R}|_{*}$. This only affects grid points that are located very close to the coast. When blowing snow is activated, precipitating snow Ps can't be distinguished from the contribution of drifting grains D–E within the microphysical scheme of MAR. Therefore, a second experiment is performed by switching off the blowing snow parameterization, in order to provide the downscaling model with the meteorological fields at the regional scale. Downscaled precipitation will be denoted by a $\ll\ |_{\mathrm{d}}\ \gg$: $Ps|_{\mathrm{d}} + PI|_{\mathrm{d}}$. Thus $\mathrm{Psl}_{\mathrm{d}} + \mathrm{Pll}_{\mathrm{d}} - (\mathrm{Psl}_{\mathrm{off}} + \mathrm{Pll}_{\mathrm{off}})$ represents the effects of fine scale topography on precipitation. Except otherwise stated conservation of water is performed by imposing that domain integral of $\mathrm{Psl}_{\mathrm{d}} + \mathrm{Pll}_{\mathrm{d}}$ is equal to domain integral of $\mathrm{Psl}_{\mathrm{off}} + \mathrm{Pll}_{\mathrm{off}}$.

Combined together, and after remapping X and $\mathrm{Xl}_{\mathrm{off}}$ fields onto the higher resolution grid using a bilinear interpolation method, the former components yielded a downscaled SMB:

$$\mathrm{Ps} + \mathrm{P1} + (\mathrm{D} - \mathrm{E}) + [\mathrm{Ps}|_{\mathrm{d}} + \mathrm{P1}|_{\mathrm{d}} - (\mathrm{Ps}|_{\mathrm{off}} + \mathrm{P1}|_{\mathrm{off}})] - \mathrm{Su} - \mathrm{R}|_{*}$$

Finally the sensitivity of the MAR to blowing snow at the regional scale (including non-linear processes) reads:

$$\mathrm{Ps} + (\mathrm{D} - \mathrm{E}) - \mathrm{Ps}|_{\mathrm{off}}$$

2.3.3 Spatial Resolution

Spatial resolution of our downscaled SMB is set to 5 km after verifying the convergence of the downscaling model for horizontal resolutions of 80, 40, 20, 10 and 5 km. The forcing of the downscaling model is obtained from MAR set up with an horizontal resolution of 80-km, for the year 1999. The 2.5 km solution, while not far from the 5-km solution, exceeded the asymptotic value; this behavior can be explained by the fact that one of our hypotheses is not valid for gravity waves whose horizontal wavelength is less than 6.3 km. Little variation was found between the resolutions of 5 and 10 km, in agreement with van de Berg et al. (2006) who noticed that both orographic and accumulation wavelengths were of the order of 10 km.

2.4 Field Data

2.4.1 Ice Cores

Figure 1 of van Ommen et al. (2004) was used to evaluate the model time mean spatial variability against observation-based data (see adaptation on Fig. 1b). The map showed actual net accumulation over Law Dome and had been obtained by combining dating constraints with an ice-flow model.

2.4.2 Automatic Weather Stations

Two automatic weather stations from the Australian Antarctic Division network (http://aws.acecrc.org.au) were used to compare local time series of modeled net accumulation with field measurements: DSS (66°46′09″ S, 112°48′38″ E, 1,376 m a.s.l. (above see level); date of installation: December 20, 1997), located very close to Law Dome Summit South, and A028-B (68°24′28″ S, 112°13′03″ E, 1,622 m a.s.l.; November 6, 1998), located about 300 km inland from Law Dome (see location of the AWS on Fig. 1.a).

To help for the comparison, snow heights were converted into their water equivalent using snow densities measured in the subsurface snow near the stations: 423.4 kg m^{-3} for DSS (McMorrow et al. 2001) and 420 ± 20 kg m^{-3} for A028-B (Goodwin et al. 2003). The choice of a constant value is responsible for an overestimation of snow mass balance during the snow densification process. After interpolating AWS data on the model time axis, we applied to the record data a 10-point (i.e. a 15-h) running-box smoothing to soften these artifacts.

As a resolution of 5 km is high enough for our purposes (see Sect. 2.3.3), field measurements were simply compared to the SMB calculated at the nearest model grid point. Model (observed) altitudes for DSS and A028-B were 1,280 m (1,376 m) and 1,628 m (1,622 m), respectively. The largest altitude error was obtained for DSS, although the area experiences gentle slopes. Two-thirds of this error appeared to be inherited from the 1-km resolution version of the Radarsat Antarctic Mapping Project Digital Elevation Model of

Fig. 2 Components of the SMB shown in Fig. 1 (mm w.e. per year, see *color scale*). *Dashed* (*solid*) *lines* correspond to latitude (longitude E) contours and are drawn every 5 (10) degrees. The 200 (*dashed*), 500, 1,000, 1,500, 2,000 and 2,500 m surface elevation contours are shown in cyan or in *blue*. **a** Accumulation defined as in 2.1 plus the marginal rainfall component. **b** Sublimation. **c** Runoff

Liu et al. (2001), whose vertical precision for the steeper ice sheet perimeter was estimated to about 35 m.

3 Results

3.1 Time-Integrated Results

Annual-mean snow mass balance for the years 1998–2001 is compared in Fig. 1 with observations made by van Ommen et al. (2004). The key features of the spatial variability are well captured by the model chain. Because runoff and sublimation remain low in absolute terms, net accumulation is dominated by the accumulation process (Fig. 2).

The simulated (Fig. 1a) and observation-based (Fig. 1b) (van Ommen et al. 2004) SMB gradients across Law Dome share the same main characteristics: west-east direction, homogeneity along a meridian, value over DSS (634 vs. 630 mm w.e. per year, respectively). However, the modeled SMB is underestimated on the eastern side (no more than 1,395 mm w.e. in place of 1,600 mm w.e.) and overestimated on the western side (no less than 300 mm w.e. in place of 200 mm w.e.). More striking discrepancies are the decrease of modeled SMB when approaching the eastern coast and the presence of a local maximum in the western side, over the Vanderford Glacier (Fig. 1a, x and $y = 20$ and 80 km, respectively).

3.2 Time Series at AWS Sites

More local model versus observations plots are shown in Fig. 3 for the two Australian AWS DSS and A028 (see location on Fig. 1a). Downscaled and observed SMB showed good agreement. Over DSS, where sublimation and runoff are negligible (see Fig. 2b, c) as well as the net effects of snow-drift processes (see Fig. 4a), modeled SMB increases more linearly with time than the observed one even when leaving aside compaction delays that add high-frequency artifacts to AWS series. Note that A028 is located farther inland than DSS, explaining why the net accumulation is much smaller there.

3.3 On the Origin of a Net Accumulation Gradient Across Law Dome Summit

Figure 4 shows the respective effects of snow drift and downscaling on modeled accumulation. The latter can be taken as an estimate of the fine scale orographic forcing on precipitation. None of these processes were found to have a significant impact on SMB over DSS. However, they are responsible for accumulation gradients across the summit, respectively, in the NW–SE and ENE–WSW directions. Snow-drift processes represent a difference of 230 mm w.e. per year within 165 km whereas fine-scale orography represents a difference of 708 mm w.e. per year within 73 km. Therefore, based on our model results we argue that the SMB gradient across DSS would be caused primarily by the orographic forcing on precipitation. The direction of the observed gradient is consistent with our conclusion.

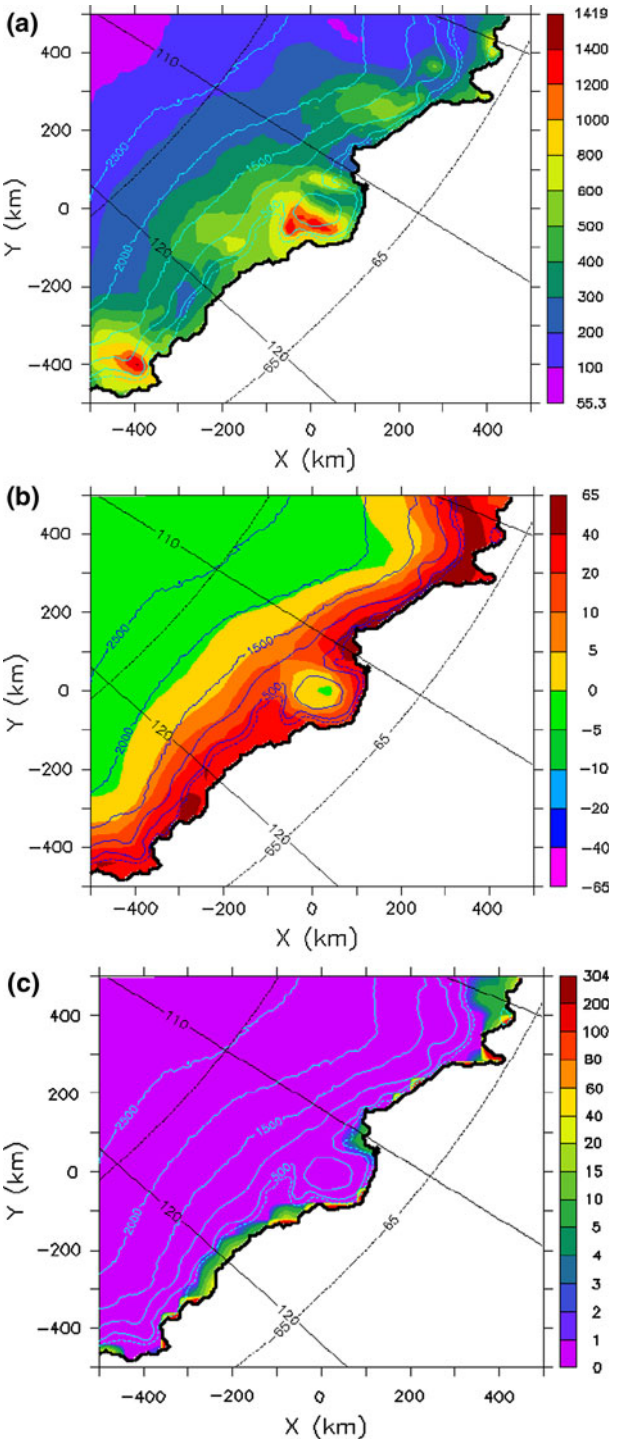
(a)
1419
1400
1200
1000
800
600
500
400
300
200
100
55.3
Y (km)
X (km)
(b)
65
40
20
10
5
0
−5
−10
−20
−40
−65
Y (km)
X (km)
(c)
304
200
100
80
60
40
20
15
10
5
4
3
2
1
0
Y (km)
X (km)

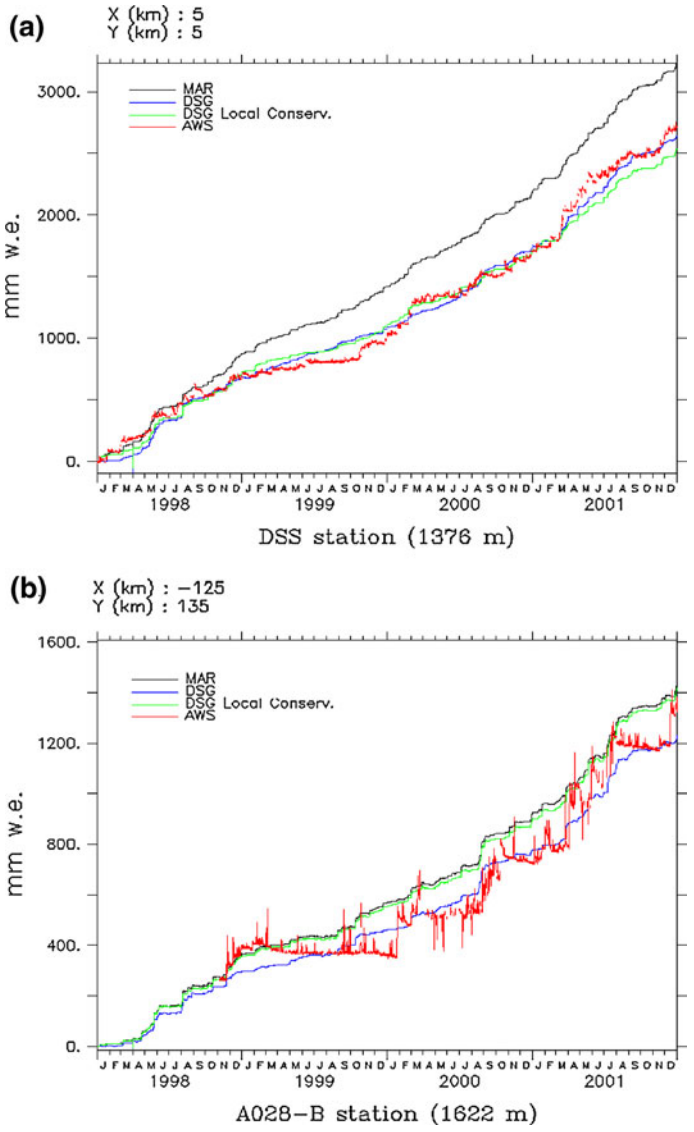

Fig. 3 Surface Mass Balance (mm w.e.): *black line*: regional climate model MAR; *blue line*: precipitation downscaled from MAR output (MAR → DSG) with domain conservation of water; *green line*: MAR → DSG with local conservation of water; *red line*: observations made at Automatic Weather Stations. *Top panel*: DSS; *bottom panel*: A028-B. Time interval is 6 h

4 Discussion and Conclusion

Capturing the small scale features of the surface mass balance becomes of primary importance when directly comparing model data to field measurements. For that purpose, we used a cascade of models from the synoptic scale to the meso-γ scale, based on the hypothesis that small scale features of SMB are induced by the orography through upslope

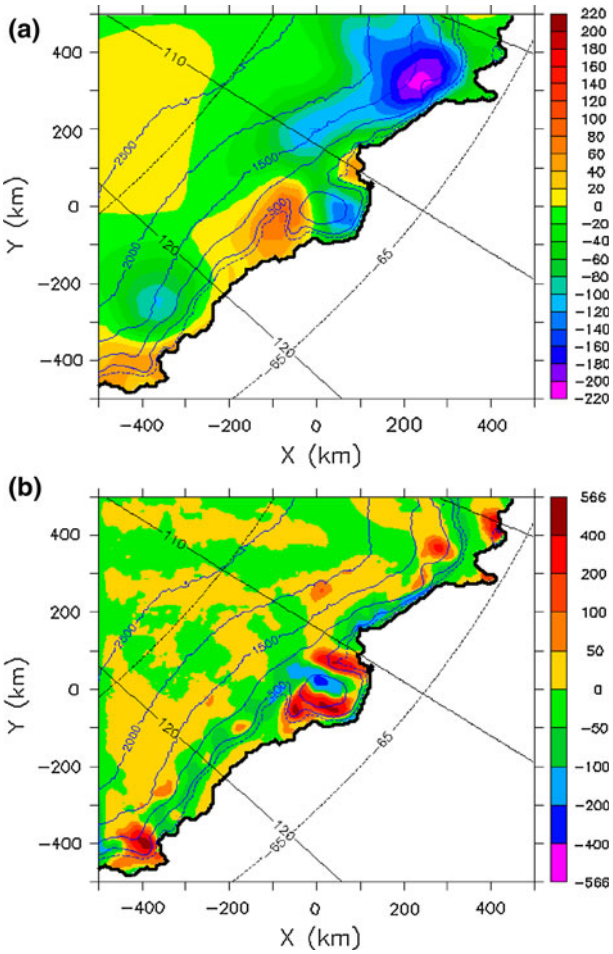

Fig. 4 **a** Effect of snow drift on accumulation: annual accumulation from the MAR simulation with blowing snow activated, minus annual accumulation from the MAR simulation without blowing snow. **b** Downscaled precipitation minus MAR precipitation. Unit: mm w.e. per year (see *colour scale*). *Dashed* (*solid*) *lines* correspond to latitude (longitude E) contours and are drawn every 5 (10) degrees. The 200 (*dashed*), 500, 1,000, 1,500, 2,000 and 2,500 m surface elevation contours are shown in *blue*

precipitation and snow-drift. Though it kept computational costs within reasonable levels, our method performed quite well when applied to the marked coastal topography of Law Dome. We were able to estimate roughly the roles of the different processes in the repartition of snow among the different slopes. The small scale variations of some SMB components of secondary importance at the regional scale (such as surface sublimation) were neglected in this study, but one should keep in mind that their local variations might be large near the coast (Frezzotti et al. 2004). Therefore, the downscaling of blowing snow, sublimation and melting, and more generally surface energy balance will be implemented in future versions of the downscaling model. The use of a mechanistic downscaling model, as opposed to a statistical one, must be limited to regions in which slopes are steep enough, so that precipitation rates are controlled by orographic processes. Moreover, though the

Antarctic Peninsula should appear as the ultimate region for downscaling applications, one should first consider implementing a representation of some of the föhn effects, such as lee drying and warming which are thought to be responsible for the lack of stability of the Larsen ice shelf (van den Broeke 2005). Aside from new developments and applications over other regions, downscaling of climatic scenarios will be performed in the frame of the European project ICE2SEA.

Acknowledgments We acknowledge the ice2sea project, funded by the European Commission's 7th Framework Programme through grant number 226375, ice2sea manuscript number 30. The MAR simulations were run on CNRS/IDRIS computers.

References

Barstad I, Smith RB (2005) Evaluation of orographic precipitation model. J Hydrometeor 6:85–99

Brasseur O, Gallée H, Creutin J-D, Lebel T, Marbaix P (2002) High resolution simulations of precipitation over the Alps with the perspective of coupling to hydrological models. Adv Global Change Res 10:75–100. M. Beniston, Ed

Bromwich DH (1988) Snowfall in high southern latitudes. Rev Geophys 20:149–168

Bromwich DH, Guo Z, Bai L, Chen Q (2004) Modeled antarctic precipitation. Part I: spatial and temporal variability. J Climate 17:427–447

Collier CG (1975) A representation of the effects of topography on surface rainfall within moving baroclinic disturbances. Quart J R Met Soc 101:407–422

Durran DR, Klemp JB (1982) On the effects of moisture on the brunt-Väisälä frequency. J Atmos Sci 39:2152–2158

Frezzotti M, Pourchet M, Flora O, Gandolfi S, Gay M, Urbini S, Vincent C, Becagli S, Gragnani R, Proposito M, Severi M, Traversi R, Udisti R, Fily M (2004) New estimations of precipitation and surface sublimation in East Antarctica from snow accumulation measurements. Clim Dyn 23:803–813

Funk C, Michaelsen J (2004) A simplified diagnostic model of orographic rainfall for enhancing satellite-based rainfall estimates in data-poor regions. J Appl Meteorol 43:1366–1378

Gallée H, Schayes G (1994) Development of a three-dimensional Meso-gamma primitive equation model: katabatic winds simulation in the area of Terra Nova Bay, Antarctica. Mon Weather Rev 122:671–685

Gallée H, Peyaud V, Goodwin I (2005) Simulation of the net snow accumulation along the Wilkes Land transect, Antarctica, with a regional climate model. Ann Glaciol 41:17–22

Goodwin ID, de Angelis M, Pook M, Young NW (2003) Snow accumulation variability in Wilkes Land, East Antarctica, and the relationship to atmospheric ridging in the 130°–170°E region since 1930. J Geophys Res 108:4673

Goyette S, Laprise JPR (1996) Numerical investigation with a physically based regional interpolator for off-line downscaling of GCMs: FIZR. J Climate 9:3464–3495

Guo Z, Bromwich DH, Hines KM (2004) Modeled antarctic precipitation. Part II: ENSO modulation over West Antarctica. J Climate 17:448–465

Krinner G, Guicherd B, Ox K, Genthon C, Magand O (2006) Simulated Antarctic precipitation and surface mass balance at the end of the twentieth and twenty-first centuries. Clim Dyn 28:215–230

Kuligowski RJ, Barros AP (1999) High-resolution short-term quantitative precipitation forecasting in mountainous regions using a nested model. J Geophys Res 194:31553–31564

Liu H, Jezek K, Li B, Zhao Z (2001) Radarsat Antarctic Mapping Project digital elevation model version 2. National Snow and Ice Data Center. Digital media, Boulder, CO

McMorrow AJ, Curran MAJ, van Ommen TD, Morgan V, Pook MJ, Allison I (2001) Intercomparison of firn core and meteorological data. Antarct Sci 13:329–337

Meehl GA, Stocker TF, Collins WD, Friedlingstein P, Gaye AT, Gregory JM, Kitoh A, Knutti R, Murphy JM, Noda A, Raper SCB, Watterson IG, Weaver AJ, Zhao Z-C (2007) Global climate projections. In: Solomon S, Qin D, Manning M, Chen Z, Marquis M, Averyt KB, Tignor M, Miller HL (eds) Climate change 2007: the physical science basis. Contribution of working group I to the fourth assessment report of the intergovernmental panel on climate change. Cambridge University Press, Cambridge

Monaghan AJ, Bromwich DH, Fogt RL, Wang S-H, Mayewski PA, Dixon DA, Ekaykin A, Frezzotti M, Goodwin I, Isaksson E, Kaspari SD, Morgan VI, Oerter H, Van Ommen TD, Van der Veen CJ, Wen J (2006) Insignificant change in Antarctic snowfall since the international geophysical year. Science 313(5788):827–831. doi:10.1126/science.1128243

Sinclair MR (1994) A diagnostic model for estimating orographic precipitation. J Appl Meteorol 33:1163–1175

Smith RB (2002) Stratified airflow over topography. Environmental stratified flows. In: Grimshaw R (ed) Topics in environmental fluid mechanics, vol 3. Kluwer, The Netherlands, pp 119–159

van de Berg WJ, van den Broeke MR, Reijmer CH, van Meijgaard E (2006) Reassessment of the Antarctic surface mass balance using calibrated output of a regional atmospheric climate model. J Geophys Res 111:D11104. doi:10.1029/2005JD006495

van den Broeke M (2005) Strong surface melting preceded collapse of Antarctic Peninsula ice shelf. Geophys Res Lett 32:L12815. doi:10.1029/2005GL023247

van Ommen TD, Morgan V, Curran MAJ (2004) Deglacial and Holocene changes in accumulation at Law Dome, East Antarctica. Ann Glaciol 39:359–365

Wild M, Calanca P, Scherrer SC, Ohmura A (2003) Effects of polar ice sheets on global sea level in high-resolution greenhouse scenarios. J Geophys Res 108:4165

Surv Geophys (2011) 32:519–535
DOI 10.1007/s10712-011-9121-7

Estimating the Glacier Contribution to Sea-Level Rise for the Period 1800–2005

P. W. Leclercq · J. Oerlemans · J. G. Cogley

Received: 16 December 2010 / Accepted: 28 March 2011 / Published online: 25 May 2011

Abstract In this study, a new estimate of the contribution of glaciers and ice caps to the sea-level rise over the period 1800–2005 is presented. We exploit the available information on changes in glacier length. Length records form the only direct evidence of glacier change that has potential global coverage before 1950. We calculate a globally representative signal from 349 glacier length records. By means of scaling, we deduce a global glacier volume signal, that is calibrated on the mass-balance and geodetic observations of the period 1950–2005. We find that the glacier contribution to sea-level rise was 8.4 ± 2.1 cm for the period 1800–2005 and 9.1 ± 2.3 cm for the period 1850–2005.

Keywords Sea-level rise · Glacier · Glacier length

List of symbols

L	Glacier length (m)
L_{1950}	Glacier length in 1950 (m)
L^*	Normalised glacier length change w.r.t. L_{1950}
$\bar{L}^*$	Mean of all normalised length change (w.r.t. L_{1950}) records
$\bar{L}^*_{13}$	Mean of the 13 regionally stacked normalised length change records
$\bar{L}^*_{w13}$	Weighted mean of the 13 regionally stacked normalised length change records
V^*	Normalised global glacier volume w.r.t. 1950

Electronic supplementary material The online version of this article (doi:10.1007/s10712-011-9121-7) contains supplementary material, which is available to authorized users.

P. W. Leclercq (✉) · J. Oerlemans
IMAU, Utrecht University, Princetonplein 5, 3584 CC Utrecht, The Netherlands
e-mail: p.w.leclercq@uu.nl

J. Oerlemans
e-mail: j.oerlemans@uu.nl

J. G. Cogley
Department of Geography, Trent University, 1600 West Bank Drive, Peterborough, ON K9J 7B8, Canada
e-mail: gcogley@trentu.ca

ΔV	Absolute change in global glacier volume (cm sea-level equivalent)
η	Exponent scaling length to volume
S_C	Cumulative contribution of glacier to sea-level change as determined by MB data Cogley (2009) (cm)
a, b	Regression coefficients
α, β	Scaling exponents relating glacier thickness and width to glacier length

1 Introduction

There is abundant evidence that eustatic sea level has been rising for at least the past two centuries (e.g. Church and White 2006; Jevrejeva et al. 2008; Cabanes et al. 2001; Warrick and Oerlemans 1990; Barnett 1983). Although the uncertainties are significant, the general view is that this rise has been between 15 and 25 cm for the period 1850–2000. This number is based on the analysis of tide gauge data, which do not provide a very good coverage of the oceans. Nevertheless, it appears that tide gauge and satellite data are broadly in agreement (e.g. Nicholls and Cazenave 2010), lending some credibility to the use of tide gauge data to infer sea levels further back in time. For the period 1993–2009, high precision altimetry from satellites shows that sea level rose by 3.3 ± 0.4 mm year^{-1} (Nerem et al. 2010). This suggests that sea level rise is accelerating.

Finding the causes for the current sea-level rise is crucial. Thermal expansion of ocean water, changes in terrestrial storage of water, mass loss of ice caps and glaciers, and possible long-term imbalances of the mass budgets of the Greenland and Antarctic ice sheets have been listed as the most important processes contributing to the observed sea-level rise. The pressure, both scientific and political, to make estimates of future sea-level change has led to the use of so-called semi-empirical approaches in which a simple relation between past sea-level rate and temperature or radiative forcing is determined, and then extrapolated through the twenty-first century (e.g. Rahmstorf 2007; Grinsted et al. 2009; Vermeer and Rahmstorf 2009). The uncertainties in such an approach are large and the resulting potential errors in projections enormous. For instance, if a long-term contribution from the Antarctic ice sheet to sea-level rise were to be erroneously attributed to the melt of glaciers and ice caps, an empirically determined sensitivity parameter could be very inaccurate. To constrain models in a better way, the processes that cause sea-level change have to be quantified in the best possible way. In this paper we attempt to estimate the contribution of glaciers and ice caps since 1800 AD. Throughout this paper we mean by glacier contribution the contribution to sea-level change from all glaciers and ice caps outside the large ice sheets of Greenland and Antarctica. Included are the glaciers and ice caps on Greenland and Antarctica which are not part of or attached to the main ice sheets.

There are basically two approaches to estimate the loss of glacier ice over longer periods of time. The first approach is to use modelled climate sensitivity of glacier mass balance in combination with instrumental meteorological records of temperature and/or precipitation. It is assumed that the glacierised area does not change, and that the effect of climate change can simply be calculated by the combination of mass-balance sensitivity and climate perturbations. This approach was applied by Zuo and Oerlemans (1997) to 100 glacierized regions, allowing for the fact that glaciers in different climatic settings have different sensitivities. A major problem in this procedure is the definition of an initial state. One cannot just assume that at a certain point in time the state of any glacier is in balance with the prevailing climate. Zuo and Oerlemans (1997) showed that a difference (‘climatic

imbalance') of only 0.3 K between the real climate and the climate in which glaciers would have been in equilibrium has a large effect on the calculated contribution to sea-level change.

In the second approach one uses data on geometric changes of glaciers directly. This is attractive, because climate data are not needed as input and the problem of defining an initial state does not exist. However, other difficulties have to be handled. When going back in time over a few centuries, the only available geometric parameter is glacier length. The step from glacier length to glacier volume is not a trivial one and depends on the geographic setting. Lüthi et al. (2010) showed for 12 Swiss glaciers that, with the use of a simple glacier model, information on glacier length change can be used to calculate glacier volume changes. They also showed strong coherence of recorded length changes across the Swiss Alps. However, this method requires an equilibrium line altitude history and at least two volume measurements for each of the glaciers used in the study. A different solution is to calibrate volume changes calculated from length records by in situ mass-balance observations over the past 50 years. This method was exploited by Oerlemans et al. (2007) and will be extended in the current paper, by using a significantly larger number of glacier length records, and by involving more extensive in-situ mass balance and geodetic measurements (Cogley 2009).

In Sect. 2 the data sets used in this study are presented. In Sect. 3 we discuss some basic statistics of the glacier length records, consider the significance of regional variability, and discuss methods of normalization. In Sect. 4 we discuss the method to obtain a proxy for global glacier volume. In Sect. 5 the glacier contribution to sea-level change is then presented. Section 6 provides a discussion about uncertainties, a comparison to other estimates, and a summary of the results.

2 Data

2.1 Glacier Length Variations

The dataset on glacier length used in this study is an extension of the one used in Oerlemans et al. (2007). A number of records has been updated, and 152 records were added, mostly from remote areas like Greenland, Alaska, Central Asia and the southern Andes. The total number of records is 349. Although there is a reasonable coverage of the land masses (Fig. 1), there are relatively few records from regions where much ice is found (Alaska, islands of the Arctic Ocean, Antarctica). There are no records from Antarctica or the arctic part of Canada and Russia, and only 8 from Greenland. In contrast, southern Europe (Pyrenees, Alps, Caucasus) has many records. Although there is an appreciable number of records from the Rocky Mountains, they are far from up-to-date: half of them have their last data points before 1990. Unlike North American records, most of the records in Patagonia continue up to 2005 at least, but 35 of the 54 records only start in 1945. The mean starting date of the 349 records is 1867, the mean end date 2001 (varying from 1534 to 1945 and from 1962 to 2009, respectively). The set of length records is divided into 13 regional subsets, following the division into regions by Radić and Hock (2010) (Table 1; Fig. 1). These subsets will be used to calculate a globally representative glacier signal.

The backbone of the data set is formed by Fluctuations of Glaciers data of the World Glacier Monitoring Service (WGMS 2008 and earlier volumes). Other sources are regular scientific publications, expedition reports, websites of glacier monitoring programs, and data supplied as personal communication. See the Supplementary Materials for details of

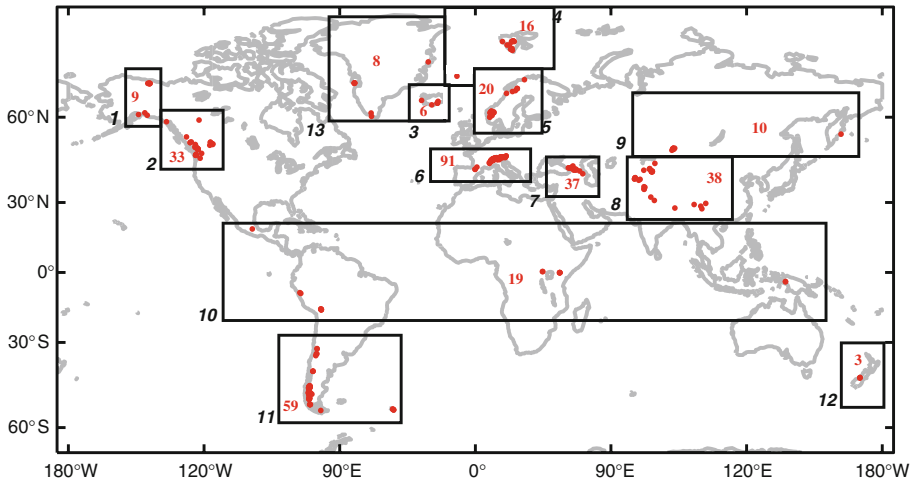

Fig. 1 Distribution of the glacier length records over the globe. In many cases the distance between glaciers is so small that the *red dots* overlap. The *boxes* depict the regions; the *red number* inside the *boxes* gives the number of records in the region; the *number outside the box* (*in italics*) gives the number of the region (cf. Table 1)

Table 1 The 13 regions from which glacier length records are available

	Region	# of records	Area (km^2)	Addition (km^2)	Weight	Comments
1	Alaska	9	79,260	–	0.1385	
2	Rocky Mountains	33	21,480	73,345	0.1656	Incl. half of Canadian Arctic
3	Iceland	6	11,005	–	0.0192	
4	Jan Mayen, Svalbard	16	36,506	37,384	0.1291	Incl. Novaya Zemlya and Franz Josef Land
5	Scandinavia	20	3,057	–	0.0053	
6	Alps and Pyrenees	91	3,045	–	0.0053	
7	Caucasus	37	1,397	–	0.0024	
8	Central Asia	38	114,330	–	0.1997	
9	N. and E. Asia	10	2,902	19,397	0.0390	Incl. Severnaya Zemlya
10	Tropics	19	7,069	–	0.0123	
11	Southern Andes	59	29,640	1,870	0.0550	Incl. half of sub-Antarctic islands
12	New Zealand	3	1,156	1,870	0.0053	Incl. half of sub-Antarctic islands
13	Greenland	8	54,400	73,345	0.2232	Incl. half of Canadian arctic
	Total	349	362,193	210,265	1	Glaciers and ice-caps on Antarctica not incl

Area is the total of ice-covered area within the region (Radić and Hock 2010), addition is the area that is added to this region, when we calculate the weight of the region. The total of added area is the area of glaciers and ice caps in regions in which we have no information on glacier length fluctuations

the individual records and references. Only records that start prior to 1945 are included in the data set. There are many more records available that start after 1950, but these were not included, because the main purpose of this study is to reconstruct the variations on a

centennial time scale. Furthermore, records of glaciers that are known to be surging were excluded. The proportion of glaciers that surge is small, implying that their exclusion will hardly affect the representativeness of the data set.

In Fig. 2, examples of glacier length records are shown. Most of the records have data points with varying spacing in time. Before 1900 most data points are reconstructed on the basis of geomorphological or historical evidence, e.g. paintings, drawings, and descriptions. For European glaciers there is plenty of historical information, resulting in some detailed records (e.g. Zumbühl 1980; Nussbaumer et al. 2007) but, mostly, records have sparse data prior to 1900. From 1900 onwards, there is more information available worldwide, even annually for regions like Iceland, Norway, the Alps, and New Zealand. All records are interpolated with Stineman interpolation (Stineman 1980; Johannesson et al. 2009) to get annual values for the entire period covered by the record.

With Stineman interpolation the interpolated values are calculated from the values of the data points and the slopes at the gives points. The slope at a point is calculated from the circle passing through the point itself, the point before and the point after it. This method works well for series with uneven spacing between the data points, as is the case with the glacier length records. Moreover, it has the advantage that it produces no spurious minima or maxima not prescribed by the data.

In this paper we consider glacier length changes relative to the glacier length in 1950 (L_{1950}), and we use normalised glacier length changes, defined as:

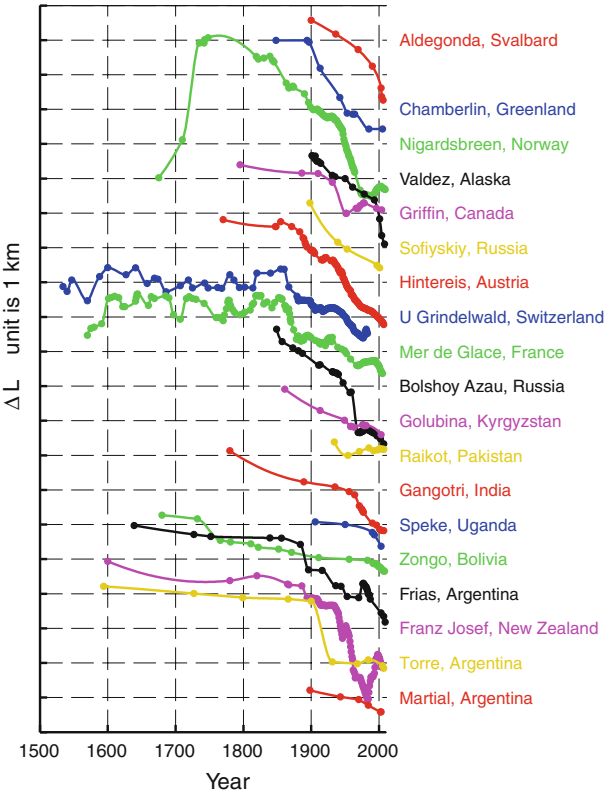

Fig. 2 Examples of glacier length records from different parts of the world. Each dot represents a data point. Data points are connected by means of Stineman interpolation. See Supplementary Material for references to the sources of the individual records

$$L^*(t) = \frac{L(t) - L_{1950}}{L_{1950}}. \quad (1)$$

The length of the glacier is taken from the WGMS, the World Glacier Inventory (National Snow and Ice Data Center 1999, update 2009), or the same source as the length record of the glacier. These glacier length measurements are made in different years for different glaciers. For all glaciers, L_{1950} is calculated from the measured glacier length and the length change between 1950 and the year of measurement. If the record has no data point in 1950, the length change is calculated from the interpolated length record. As we will show, the normalised length change can be used to reconstruct a globally coherent glacier length signal. Thus it will play a key role in the reconstruction of the volume change of all glaciers and small ice caps.

2.2 Global Glacier Mass Balance

Global averages of measured mass balances for 1950/1951 to 2008/2009 are taken from an update of the compilation of Cogley (2009). The dataset includes 2,905 balance-years of measurements by glaciological methods on 355 glaciers, and 13,671 balance-years of measurements by geodetic methods on 359 glaciers. Most of the glaciological measurements are of annual mass balance, while most of the geodetic measurements cover several to many years. The joint analysis of these disparate data, including a procedure for generating annual pseudo-series of geodetic mass balance with estimates of uncertainty, is explained by Cogley (2009).

The annual glaciological time series are serially uncorrelated. This finding is exploited by calculating pentadal averages of the annual estimates, which reduces uncertainty by a factor of $1/\sqrt{5} = 0.45$. To address the problem of spatial bias, with some ice-covered regions well represented while others have no measurements at all, the pentadal averages are interpolated to the centres of the 1301 glacierized cells of a $1^\circ \times 1^\circ$ grid.

The interpolation algorithm is explained in more detail by Cogley (2004). Briefly, the interpolation function is a polynomial, fitted by least squares, in the two horizontal coordinates of an azimuthal equidistant projection centred at each cell in turn. During the interpolation, the pentadal averages of the measurements are weighted by a suitable distance-decay function, which is derived from an analysis of the spatial autocorrelation of annual glaciological time series. The distance scale for loss of correlation between these time series is close to 600 km, as shown by Cogley and Adams (1998). For each cell, the interpolated estimate is the first coefficient of the polynomial (its intercept on the mass-balance axis) and its uncertainty is the standard error of that coefficient as estimated by the least-squares procedure. The global average for each pentad is the sum of the $1^\circ \times 1^\circ$ cell estimates, and its uncertainty is the root-sum-square of the cell uncertainties, each weighted by the glacierized area of each cell. The uncertainty of the glacierized areas is allowed for by conventional propagation of errors. Glacierized cells around the periphery of Antarctica are not included in the interpolation, and their contribution to the global average is obtained by upscaling the estimate for the rest of the world, following Kaser et al. (2006).

The total of the global glacierized area used in this paper amounts to 704,000 km^2 and is the glacierized area contained in the grid cells plus the glacierized area around the periphery of Antarctica. This total area is smaller than the 741,000 km^2 used in Radić and Hock (2010), who relied on an older estimate of the glacierized area in Antarctica outside the ice sheet proper.

3 Regional and Global Length Records

3.1 Regional Glacier Length Changes

As the examples in Fig. 2 show, the glacier records display a consistent signal over the globe. The curves differ in details like amplitude of the signal and fluctuations on decadal time scale, but the overall picture is rather uniform. There is a clear world-wide retreat of glaciers that started in the middle of the nineteenth century. The general retreat since this time is further illustrated by Fig. 3. Here the average rate of length change of the available records is shown for four different periods: 1801–1850, 1851–1900, 1901–1950, and 1951–2000. From 1801–1850, the majority of the glaciers had a small to moderate retreat, but a substantial proportion, 28%, of the glaciers advanced. Therefore the median retreat rate for this period is just slightly negative, namely -0.9 ma^{-1}. For all three periods after 1851, the median rate of change is more negative: -5.8, -10.3, and -8.9 ma^{-1} for the periods 1851–1900, 1901–1950, and 1951–2000, respectively. In these periods the number of average advances is very small, namely less than 5%.

For each of the 13 regions, we have calculated the average length change from the records within the region. Fig. 4a shows these regional glacier length records after smoothing with a weighted running average filter, with 21-year width. This smoothing is

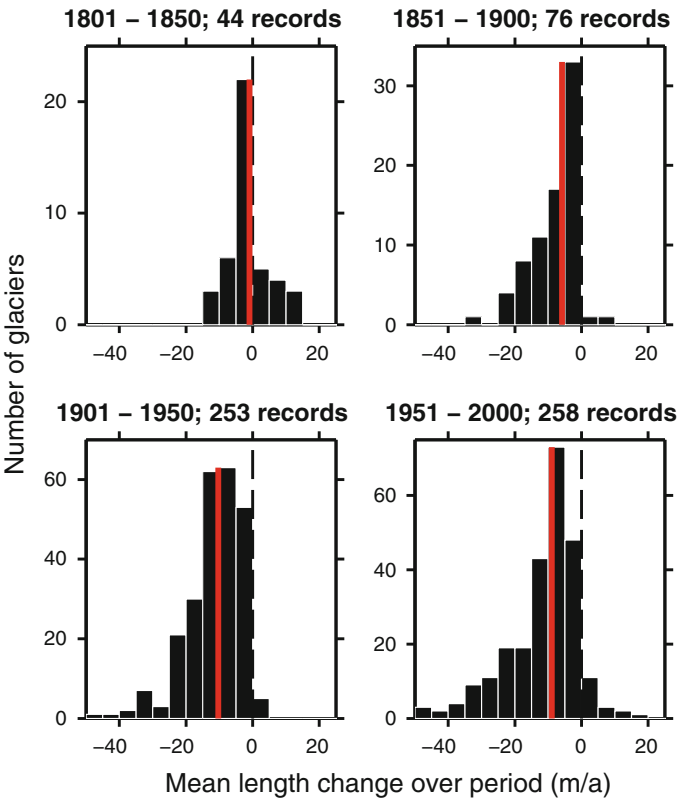

Fig. 3 Averaged rate of length change for four different periods. The *vertical red line* indicates the median rate of length change. Note the changing number of records for each period

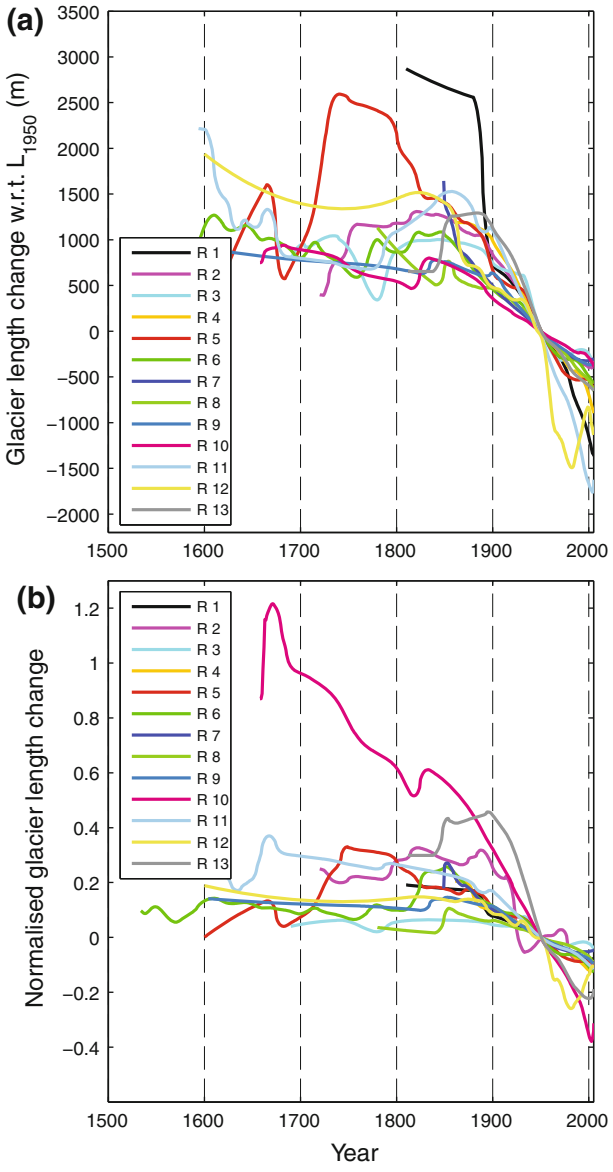

Fig. 4 **a** Stacked glacier length records for the different regions. The length change is with respect to the length in 1950. In **b** the *normalised* length records are shown. The clear outlier is the average of the tropical glaciers, region 10. See Table 1 and Fig. 1 for the further corresponding regions

necessary because jumps in the stacked record are created when a record enters the stack or when a record in the stack ends. The stacked records of the regions start at different years, varying from 1534 (Alps, region 6) to 1861 (Svalbard and Jan Mayen, region 4), but all stacked records continue to 2004 at least. Furthermore, the glacier retreat since the middle of the nineteenth century in all regions is clearly visible. However, the amount of length change over the covered period is variable.

We have also calculated the average normalised length change for each region, using Eq. 1. The resulting stacked records are shown in Fig. 4b, again smoothed with a 21-year weighted running average filter. The tropical glaciers (region 10) are a clear outlier, with a

large relative change. In general, the tropical glaciers are rather small, and they have significantly retreated over the past centuries. Especially the glaciers on Irian Jaya (Carstenz and Meren) have very large relative retreats (and have now almost disappeared), but also the glaciers in Central Africa and Bolivia have become much smaller. The smallest relative length changes have occurred in regions 3, 6, and 8 (Iceland, Alps, and Central Asia). In general the variability in the normalised stacked records is smaller than the variability in the stacked records, shown in Fig. 4a. This can be explained by the fact that larger glaciers are flatter and therefore more sensitive to climate change (Oerlemans 2005); the length and climate sensitivity compensate each other when we use the relative length change.

3.2 The Global Signal

The goal of this study is to develop a globally representative proxy for ice volume from the available glacier length records. This is done following the method of Oerlemans et al. (2007). As discussed above, the normalised length records have more coherency than the length records. Therefore, we use the normalised length records to construct a proxy for global ice volume. Moreover, most of the records come from regions where the ice cover is relatively small (notably the Alps and Caucasus). To obtain a globally representative length signal we have to apply a weighting procedure that reduces the effect of overrepresentation of regions with many records. We achieve this by averaging the stacked records of the 13 regions. The result is shown in Fig. 5a.

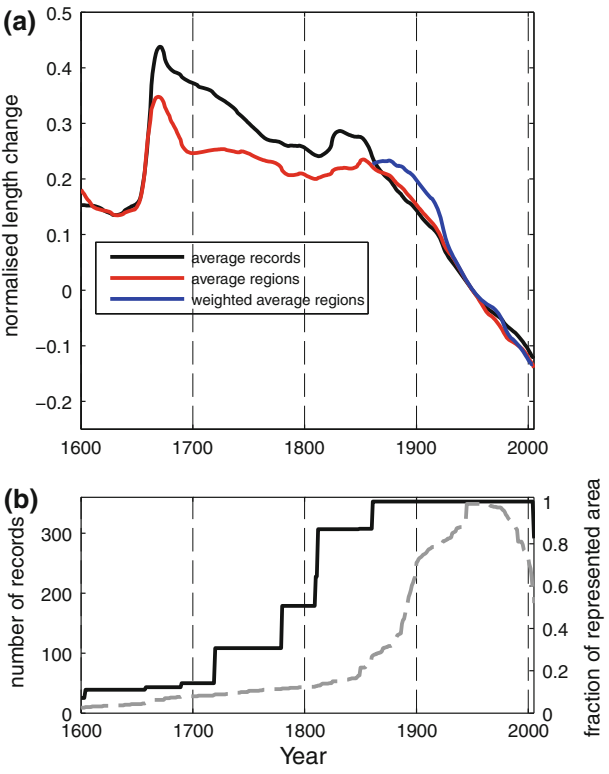

Fig. 5 **a** The global length signal from normalised glacier length records for three different averaging methods: mean of all records $\bar{L}^*$ (*black*), mean of the 13 regions $\bar{L}^*_{13}$ (*red*), and the weighted average of the 13 regions $\bar{L}^*_{w13}$ (*blue*). **b** Total number of available records (*dashed grey*), and cumulative weight of the regions that have at least one record (*black line*); the weights of the individual regions are given in Table 1

The black line is the average normalised length record of all available records ($\bar{L}^*$). In this average the large relative retreat of the tropical glaciers (see Fig. 4b) is clearly visible. The mean of all regions, with equal weights, ($\bar{L}^*_{13}$) then yields the red curve in Fig. 5a. After 1860, the two different averages are very similar, although $\bar{L}^*_{13}$ reveals a larger glacier retreat during the period 1960–2000. Before 1850, the records differ significantly due to the suppression of the tropical signal in the regional average.

A third approach ($\bar{L}^*_{w13}$) is to give the regions different weights, proportional to the area covered by glaciers in the regions. In principle, this is the best method to construct a proxy from the glacier length records that is representative for the ice volume. It removes the bias generated by the fact that we have more regions with smaller glaciers. The ice-covered area of the regions is taken from Radić and Hock (2010) (Table 1). To obtain weights, the ice-covered area not covered by the 13 regions is distributed over the regions that could plausibly represent the regions devoid of records (column labelled "addition" in Table 1). We have not included the area of Antarctic glaciers; we have no representative region with glacier length records. We have to assume that their behavior is similar to the behavior of the global signal we deduce from the other regions. In fact, this procedure reveals the weakness of the data set on glacier length fluctuations; little to nothing is known in regions with large amounts of ice, like the Canadian arctic and the Russian arctic islands. From Table 1 it is clear that the average is mainly determined by regions 1, 2, 4, 8, and 13. It only makes sense to construct $\bar{L}^*_{w13}$ for the period in which the sum of the represented area equals the total area, or is at least close to it. The fraction of the represented area, which equals the cumulative weight of the regions with records available in that year, is given in Fig. 5b. Before 1861 the total weight is less than 90%, so we have calculated $\bar{L}^*_{w13}$ for the period 1861–2004, shown with the blue line in Fig. 5a. However, we should keep in mind that the number of records in the dominating regions is limited until the beginning of the twentieth century.

$\bar{L}^*$, $\bar{L}^*_{13}$, and $\bar{L}^*_{w13}$ appear to be remarkably similar throughout the twentieth century. This finding reflects that (1) the relative change in glacier length has been comparable for smaller and larger glaciers and (2) the behavior of glaciers over the past century has been coherent over the globe. Before 1900, the similarity between the different averages is smaller, but we should keep in mind that here the number of records is limited, especially for the regions with a large weight. It would be most appropriate to base the proxy for world-wide glacier volume on $\bar{L}^*_{w13}$. However, this would limit the period of the reconstruction, and, in the second half of the nineteenth century, the reconstruction would rely heavily on just a few records. As $\bar{L}^*_{w13}$ and $\bar{L}^*_{13}$ are very similar, we base the glacier volume proxy on $\bar{L}^*_{13}$. This will be worked out in the next section.

4 Proxy for Glacier Volume

4.1 Scaling Glacier Volume to Glacier Length

To use the global glacier length signal to deduce the changes of glacier volume, we have to relate glacier length to glacier volume. There exist scaling theories relating the length of a single glacier to its volume (e.g. Bahr et al. 1997), but it is not entirely evident how this scaling of individual glaciers should be translated to a global average. Here, we follow the approach of Oerlemans et al. (2007). The ice volume scales with the ice thickness, the length and the width of a glacier (cf. Bahr et al. 1997):

$$[V] = [H][L][W]. \tag{2}$$

Based on results from analytical and numerical glacier modeling, we can assume a scaling relation between the normalised ice thickness and the glacier length:

$$\frac{H}{H_{\text{ref}}} = \left(\frac{L}{L_{\text{ref}}}\right)^{\alpha}, \tag{3}$$

where H is the mean ice thickness, L the glacier length or ice-cap radius and the subscript "ref" indicates a reference state. For a glacier on a flat bed with ice that deforms perfectly plastically the mean ice thickness is proportional to the square root of the glacier length, i.e. $\alpha = 0.5$ (Weertman 1961). From numerical models, using the shallow ice approximation, values in the range 0.40 to 0.44 are found, depending on the slope of the bed (Oerlemans 2001). Next we assume that the length and the width of a glacier are also related through a power law, with exponent β. Then it follows for the normalised volume:

$$\frac{V}{V_{\text{ref}}} = \left(\frac{L}{L_{\text{ref}}}\right)^{1+\alpha+\beta}. \tag{4}$$

We use L_{1950} as reference length, such that the normalised glacier volume can be written in terms of normalised length change L^* using Eq. 1:

$$\frac{V}{V_{1950}} = \left(\frac{L}{L_{1950}}\right)^{1+\alpha+\beta} = (1+L^*)^{1+\alpha+\beta}. \tag{5}$$

We assume a similar scaling as for individual glaciers can be used for the normalised global glacier length signal $\bar{L}^*_{13}$. Thus, the normalised global ice volume V^* can be expressed as:

$$V^* = \left(1+\bar{L}^*_{13}\right)^{\eta}, \tag{6}$$

where $\eta = 1 + \alpha + \beta$, and ranges from 1.4, for glaciers for which a change in volume does not affect the glacier width ($\beta = 0$), to 2.5, for ice caps that can expand freely in all directions ($\beta = 1$). Based on the analysis of the geometry of more than 300 glaciers by Bahr et al. (1997), the most likely average value for η is 2.0 to 2.1. Note that according to expressions 1 and 6 the non-dimensional volume equals unity in 1950, the reference year for the length changes. We consider V^* to be the best possible glacier volume proxy derived from the set of glacier length records, with η within the 1.4–2.5 range, but probably close to 2.0. V^* is again smoothed with a 21-year filter to smooth out jumps created in the volume when new regions enter the $\bar{L}^*_{13}$ average.

4.2 Calibration of Glacier Volume Proxy

To estimate the glacier contribution to sea-level rise, we need to translate the normalised glacier volume V^* into actual glacier volume change. Therefore, we calibrate the reconstructed glacier volume change on the compilation of mass balance data of Cogley (2009), that gives the changes in global ice mass for the period 1951–2009 (see Sect. 2.2). We denote the cumulative contribution to sea-level change as determined from the mass balance measurements by S_C. The calibration of V^* on S_C is simply done with a linear regression (least squares) such that:

$$\Delta V = a + bV^* = -S_C, \tag{7}$$

where ΔV is expressed in terms of sea-level equivalent. The regression is calculated for the period 1951–2005, because after 2005 the numbers of glacier length and mass-balance records are considered to be too small.

As explained in Sect. 2.2, the uncertainty in the total mass balance is calculated from the variance of the available measurements. However, although formally correct, this calculation underestimates the true uncertainty. Uncertainties due to the fact that not all regions are represented in the mass balance measurements, and in particular the uncertainty in the upscaling to Antarctica, are not taken into account. Furthermore, in the conversion of specific mass balance to ice volume change, the total ice-covered area is kept constant. In order to get a more realistic estimate of the uncertainty in the reconstructed contribution of glaciers to sea-level change, we have calculated upper and lower bounds of S_C by assuming that:

1. In 1950 about half of the ice-covered area is represented in the mass balance series, this fraction increases linearly to 75% in 1980, and stays constant after 1980.
2. The unrepresented ice has on average experienced half of the measured loss, which gives the lower bound, or,
3. the unrepresented area has experienced an average mass balance of 1.5 times that of the measured record, which gives the upper bound.

The resulting upper and lower bounds of the cumulative total mass balance are shown as dashed black lines in Fig. 6. The range in the cumulative total mass balance series is used to estimate an uncertainty band for ΔV. We recalculate ΔV, by calibrating it on the upper and lower estimate of S_C. The differences between ΔV_{upper} and ΔV_{lower} on the one hand and ΔV on the other (calculated while setting the difference in 2005 to zero), give an uncertainty range for the contribution of glaciers to sea-level change reconstructed from glacier length changes.

5 Results

After the calibration of ΔV on S_C, the glacier contribution to sea-level change can be extended backwards in time (Fig. 6). Since the number of records before 1800 and after

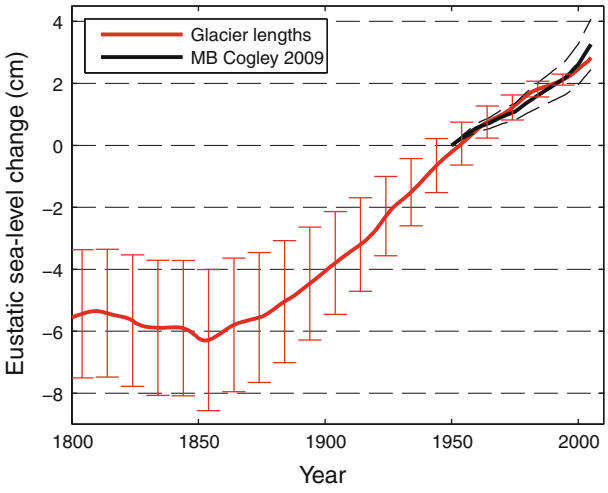

Fig. 6 Reconstructed contribution of glaciers and ice-caps to sea-level rise. The cumulative mass balance record is given in *black* (Cogley 2009); the reconstructed sea-level change from the glacier length records is shown in *red*. The range of the upper and lower estimates is indicated with *dashed black lines* for the mass balance record and with *red uncertainty bars* for the reconstruction from glacier lengths

2005 is very limited (Fig. 5b), the reconstruction is only shown for the period 1800–2005. We have found the contribution of glaciers to be 8.4 ± 2.1 for the period 1800–2005, with a maximum of 9.1 ± 2.3 cm between 1850 and 2005. The uncertainties in these estimates are derived from the result we obtain when we calibrate to the lower and upper estimate of the mass balance series. These uncertainties are substantial, following from the assumed range in the mass balance measurements. The cumulative total mass balance of all glaciers and ice-caps is calculated to be 3.2 ± 0.8 cm sea-level equivalent for the period 1950–2005.

As shown earlier by Oerlemans et al. (2007), the reconstructed contribution is hardly dependent on the choice of the scaling parameter η, as can be seen in Fig. 7a. The estimates of sea-level rise over the period 1850–2005 differ by about 1 cm for a range η from 1.4 to

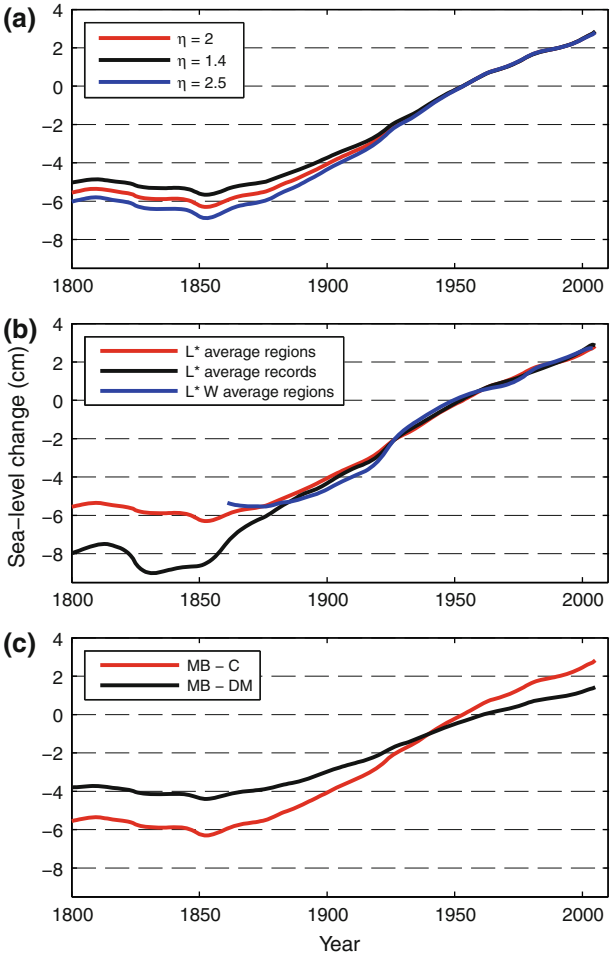

Fig. 7 Sensitivity of the reconstructed sea-level change to the choice of parameters; in each figure the best estimate shown in Fig. 6 is displayed in *red*. **a** Sensitivity to different values of the scaling constant η; **b** global ice volume change (sea-level equivalent) calculated from the different global length signals shown in Fig. 5a; **c** The global ice volume calibrated on the mass balance record of Cogley (2009) (MB-C, as used in this study) and of Dyurgerov and Meier (2005) [MB-DM, as used in Oerlemans et al. (2007)]

2.5. This is a wide range, covering the range of assumptions from the width of all glaciers being constant for any change of volume, to all glaciers being unbounded ice caps. Hence, the choice of the scaling parameter is not critical. It should be noted that for every choice of η the regression constants a and b in Eq. 7 are different.

The reconstructed sea-level change is more sensitive to the calculation of the global length signal (Fig. 7b) and the mass balance data (Fig. 7c). For the two global length signals derived from regional averages, $\bar{L}^*_{13}$ and $\bar{L}^*_{w13}$, the results are almost the same. If we use $\bar{L}^*_{w13}$ for the reconstruction of ΔV, the decrease in the ice volume seems to start later, at the end of the nineteenth century. Of course, this result is not conclusive as this record does not go far back in time and the number of records in the regions with large weight is limited (as was already stressed in Sect. 3.2, this is the reason we use $\bar{L}^*_{13}$). Using $\bar{L}^*$ gives a much larger contribution to sea-level change. Before the marked increase in the number of records in the second half of the nineteenth century, the relative contribution of the tropical glaciers to this global signal is much higher than in the other two averages. As the tropical glaciers are outliers in the normalised length change signal (see Fig. 4b), this results in an increased sea-level change.

If we calibrate ΔV on the mass balance data set compiled by Dyurgerov and Meier (2005), we get a substantially smaller estimate of the contribution of glaciers to sea-level change. The result is then very close to the 5–6 cm for the period 1850–1900 found by Oerlemans et al. (2007), who used this data set. This shows that our result is sensitive to the uncertainties in the global mass balance record on which ΔV is calibrated.

6 Conclusion and Discussion

6.1 Uncertainty

The data on glacier area, as summarized in Table 1, do not directly affect our estimate of the glacier contribution to sea-level rise. This information was only used to verify that L^*_{13} can be used as a proxy for global ice volume variations. The fact that the regional averages of normalised length change present a rather homogeneous picture, with the notable exception of the tropical glaciers, is a consequence of the coherent behavior of glaciers over the globe on a centennial time scale. This also explains the fact that, if we use the mass balance record of Dyurgerov and Meier (2005) (Fig. 7c), the reconstructed contribution based on the current data set of 349 glaciers is very similar to the results of Oerlemans et al. (2007), who used only 197 records. The difference between the results of this study and of Oerlemans et al. (2007) can thus mainly be attributed to the extended mass balance series of Cogley (2009), who noted that the newly-assimilated geodetic mass balances in this compilation were on average more negative than those in earlier compilations. However, this total mass balance, and thus the reconstruction of glacier sea-level contribution, is sensitive to the distribution of the global ice cover. In this study, the calculation of the total mass balance and the corresponding total ice-volume change is based on the gridded data set of Hock et al. (2009), with a total glacier area of 704,000 km^2, instead of the regional data set of Radić and Hock (2010) used for the weighted average of the global length signal.

As shown in Fig. 7a, our result is not very sensitive to the value of η used in the volume-length scaling. The difference in the calculated sea-level contribution is within 1 cm, for values of η ranging from 1.4 to 2.5. This is a very wide range. Therefore, we expect that assigning η and applying volume scaling to individual glaciers, rather than to the global

average length signal, will not substantially reduce the uncertainty in the reconstructed contribution. This would in addition require information on the geometry of all glaciers in the length data set. This information is not available at present.

Fundamental to our approach is the assumption that both the global length signal L^*_{13} and the global cumulative mass balance record S_C are truly globally representative. Several regions with large amounts of ice are not represented in the glacier length data set (Table 1; Fig. 1). This introduces an uncertainty in the global length signal, although we think that the glacier length signal is spatially rather coherent. The same holds for the mass balance measurements. The relative error in the reconstructed contribution of glaciers to sea-level change is approximately proportional to the error in the glacier contribution calculated from the mass balance series for the period 1950–2005. It is difficult to quantify these uncertainties, so we have shown (Fig. 6) the results with rather large uncertainty range of 25%. This gives a best estimate for the contribution of glaciers to sea-level change for the period 1850–2005 of 9.1 $\pm$ 2.3 cm eustatic sea-level equivalent. The best estimate shows a minimum in 1850, but as the uncertainty bars indicate, the significance of this minimum should not be overestimated. The number of length records as well as their global coverage is limited in the first half of the nineteenth century.

6.2 Comparison to Earlier Results

Earlier studies of the contribution of glaciers to sea-level change on a centennial timescale (Oerlemans et al. 2007; Gregory and Oerlemans 1998; Zuo and Oerlemans 1997; Meier 1984) all give smaller estimates than our results. Except for Oerlemans et al. (2007), all estimates are based on calculated mass balances. Meier (1984) calculated the contribution for the period 1900–1961. Based on very few measured volume changes and mass balance series he arrived at a contribution of 2.8 $\pm$ 1.6 cm, whereas we have calculated a contribution to sea-level rise of 4.7 $\pm$ 1.8 cm for the same period.

Zuo and Oerlemans (1997) and Gregory and Oerlemans (1998) calculated mass balance sensitivities for glaciers distributed over 100 different regions; the sensitivity was dependent on the characteristic precipitation (mean annual precipitation on the glaciers) in the region and a distinction was made between sensitivity to changes in summer temperatures and non-summer temperatures. Based on measured temperature data, Zuo and Oerlemans (1997) found a contribution of glaciers to sea-level rise of 2.7 $\pm$ 0.9 cm for the period 1865–1990. Based on the same mass balance sensitivities but using temperatures calculated with a general circulation model, Gregory and Oerlemans (1998) found a contribution of 1.9 or 3.3 cm for the period 1860–1990, depending on the climate scenario. These estimates are significantly lower than the estimate presented in this study; we have calculated a contribution to sea-level rise of 8.0 $\pm$ 2.2 cm for the period 1860–1990. Our twofold to fourfold greater estimate can partly be explained by the difference in the total area of all glaciers: Zuo and Oerlemans (1997) used 527,900 km^2, excluding the glaciers around Greenland (those were included in the contribution of the Greenland ice sheet) and Antarctica. Instead, we use the more recent estimate of 704,000 km^2, used in Cogley (2009), which includes glaciers in Greenland and Antarctica. Secondly, and more importantly, Zuo and Oerlemans (1997) have underestimated the characteristic precipitation in most of the 100 regions. This leads to lower values for the mass balance sensitivity, and thus to a too low estimate of the volume loss of glaciers. Slangen et al. (manuscript in preparation) show, with the use of the precipitation from an ensemble of twelve climate

models and accounting for the difference in total glacier area, that the results of the mass balance sensitivity approach are comparable to the results presented in this study.

Compared to our results, Oerlemans et al. (2007) estimated a smaller contribution for the period 1850–2000, and their best estimate showed a more pronounced minimum in the contribution around 1850. The difference in the reconstructed contribution for the period 1850–2000 is almost entirely due to the training data set S_C (see Sect. 5 and Fig. 7c). The disappearance of the pronounced maximum is due to the additional glacier length data.

6.3 Concluding Summary

In this study we have calculated the contribution of glaciers and ice caps to sea-level change of the last two centuries from geometric changes of glaciers. Length change is the only glacier property for which information goes far back in time. Hence, we have reconstructed a global volume signal from glacier length using a scaling relation. The global length signal is derived from the average of 13 regions. This can be done, because glaciers show a worldwide coherent signal. We have calibrated the thus derived glacier volume changes on the total mass balance of the period 1950–2005. This gives a maximum sea-level contribution for the period 1850–2005 of 9.1 $\pm$ 2.3 cm and a best estimate for the contribution over the period 1800–2005 of 8.4 $\pm$ 2.1 cm. This contribution is larger than previously estimated. According to our estimate, 35–50% of the observed sea-level rise since 1800 is due to melt of glaciers and ice caps.

Acknowledgments We would like to thank A. Slangen, R. van de Wal and two anonymous reviewers for their useful comments.

References

Bahr DB, Meier MF, Peckham SD (1997) The physical basis of glacier volume-area scaling. J Geophys Res 102(B9):20355–20362

Barnett TP (1983) Recent changes in sea level and their possible causes. Clim Change 5:15–38

Cabanes C, Cazenave A, Provost CL (2001) Sea level rise during past 40 years determined from satellite and in situ observations. Science 294(5543):840–842. doi:10.1126/science.1063556

Church JA, White NJ (2006) A 20th century acceleration in global sea-level rise. Geophys Res Lett 33(L01602). doi: 10.1029/2005GL024826

Cogley JG (2004) Greenland accumulation: an error model. J Geophys Res 109(D18101). doi: 10.1029/2003JD004449

Cogley JG (2009) Geodetic and direct mass-balance measurements: comparison and joint analysis. Ann Glaciol 50(50):96–100

Cogley JG, Adams WP (1998) Mass balance of glaciers other than the ice sheets. J Glaciol 44(147):315–325

Dyurgerov M, Meier MF (2005) Glaciers and the changing earth system: a 2004 snapshot. Occasional paper no. 58, INSTAAR. University of Colorado

Gregory JM, Oerlemans J (1998) Simulated future sea-level rise due to glacier melt based on regionally and seasonally resolved temperature changes. Nature 391:474–476

Grinsted A, Moore JC, Jevrejeva S (2009) Reconstructing sea level from paleo and projected temperatures 200 to 2100 AD. Clim Dyn 34(4):461–472. doi:10.1007/s00382-008-0507-2

Hock R, de Woul M, Radic V, Dyurgerov M (2009) Mountain glaciers and ice caps around Antarctica make large sea-level rise contribution. Geophys Res Lett 36. doi:10.1029/2008GL037020

Jevrejeva S, Moore J, Grinsted A, Woodworth P (2008) Recent global sea level started over 200 years ago? Geophys Res Lett 35(L08715). doi:10.1029/2008GL033611
Johannesson T, Bjornsson H, Grothendieck G (2009) Package 'stinepack'. Icelandic Meteorological Office
Kaser G, Cogley JG, Dyugerov MB, Meier MF, Ohmura A (2006) Mass balance of glaciers and ice caps: consensus estimates for 1961–2004. Geophys Res Lett 33(L19501). doi:10.1029/2006GL027511
Lüthi MP, Bauder A, Funk M (2010) Volume change reconstruction of Swiss glaciers from length change data. J Geophys Res 115(F0402). doi: 10.1029/2010JF001695
Meier MF (1984) Contribution of small glaciers to global sea level. Science 226(4681):1418–1421
National Snow and Ice Data Center (1999) World glacier inventory. World Glacier Monitoring Service and National Snow and Ice Data Center/World Data Center for Glaciology, Boulder (update 2009)
Nerem RS, Chambers DP, Choe C, Mitchum GT (2010) Estimating mean sea level change from the TOPEX and Jason altimeter missions. Mar Geodesy 33(1):435–446. doi:10.1080/0190419.2010.491031
Nicholls RJ, Cazenave A (2010) Sea-level rise and its impact on coastal zones. Science 328:1517. doi: 10.1126/science.1185782
Nussbaumer SU, Zumbühl HJ, Steiner D (2007) Fluctuations of the "Mer de Glace" (Mont Blanc area, France) AD 1500–2050: an interdisciplinary approach using new historical data and neural network simulations. Zeitschrift für Gletscherkunde und Glazialgeologie 40:1–183
Oerlemans J (2001) Glaciers and climate change. AA Balkema Publishers
Oerlemans J (2005) Extracting a climate signal from 169 glacier records. Science 308:675–677
Oerlemans J, Dyurgerov M, van de Wal RSW (2007) Reconstructing the glacier contribution to sea-level rise back to 1850. The Cryosphere 1(1):59–65
Radić V, Hock R (2010) Regional and global volumes of glaciers derived from statistical upscaling of glacier inventory data. J Geophys Res 115(F01010). doi:10.1029/2009JF001373
Rahmstorf S (2007) A semi-empirical approach to projecting future sea-level rise. Science 315:368. doi: 10.1126/science.1135456
Stineman RW (1980) A consistently well-behaved method of interpolation. Creative Comput 54–57
Vermeer M, Rahmstorf S (2009) Global sea level linked to global temperature. PNAS 106(51): 21527–21532. doi:10.1073/pnas.0907765106
Warrick RA, Oerlemans J (1990) Sea level rise. In: Climate change—IPCC scientific assessment. Cambridge University Press, Cambridge, pp 257–281
Weertman J (1961) Stability of ice-age ice-sheets. J Geophys Res 66:3783–3792
WGMS (2008) Fluctuations of glaciers, vol I–IX. ICSU (FAGS)/IUGG (IACS)/UNEP/UNESCO/WMO, World Glacier Monitoring Service, Zurich, Switzerland (earlier volumes)
Zumbühl HJ (1980) Die Schwankungen der Grindelwaldgletscher in den historischen Bild- und Schriftquellen des 12. bis 19. Jahrhunderts. Birkhäuser, Basel
Zuo Z, Oerlemans J (1997) Contribution of glacier melt to sea-level rise since AD 1865: a regionally differentiated calculation. Clim Dyn 13:835–845

Surv Geophys (2011) 32:537–554
DOI 10.1007/s10712-011-9124-4

Observed Mass Balance of Mountain Glaciers and Greenland Ice Sheet in the 20th Century and the Present Trends

Atsumu Ohmura

Received: 30 November 2010 / Accepted: 1 April 2011 / Published online: 12 May 2011

Abstract Glacier mass balance and secular changes in mountain glaciers and ice caps are evaluated from the annual net balance of 137 glaciers from 17 glacierized regions of the world. Further, the winter and summer balances for 35 glaciers in 11 glacierized regions are analyzed. The global means are calculated by weighting glacier and regional surface areas. The area-weighted global mean net balance for the period 1960–2000 is -270 ± 34 mm a^{-1} w.e. (water equivalent, in mm per year) or (-149 ± 19 km^3 a^{-1} w.e.), with a winter balance of 890 ± 24 mm a^{-1} w.e. (490 ± 13 km^3 a^{-1} w.e.) and a summer balance of $-1{,}175 \pm 24$ mm a^{-1} w.e. (-647 ± 13 km^3 a^{-1} w.e.). The linear-fitted global net balance is accelerating at a rate of -9 ± 2.1 mm a^{-2}. The main driving force behind this change is the summer balance with an acceleration of -10 ± 2.0 mm a^{-2}. The decadal balance, however, shows significant fluctuations: summer melt reached its peak around 1945, followed by a decrease. The negative trend in the annual net balance is interrupted by a period of stagnation from 1960s to 1980s. Some regions experienced a period of positive net balance during this time, for example, Europe. The balance has become strongly negative since the early 1990s. These decadal fluctuations correspond to periods of global dimming (for smaller melt) and global brightening (for larger melt). The total radiation at the surface changed as a result of an imbalance between steadily increasing greenhouse gases and fluctuating aerosol emissions. The mass balance of the Greenland ice sheet and the surrounding small glaciers, averaged for the period of 1950–2000, is negative at -74 ± 10 mm a^{-1} w.e. (-128 ± 18 km^3 a^{-1} w.e.) with an accumulation of 297 ± 33 mm a^{-1} w.e. (519 ± 58 km^3 a^{-1} w.e.), melt ablation -169 ± 18 mm a^{-1} w.e. (-296 ± 31 km^3 a^{-1} w.e.), calving ablation -181 ± 19 mm a^{-1} w.e. (-316 ± 33 km^3 a^{-1} w.e.) and the bottom melt-21 ± 2 mm a^{-1} w.e. (-35 ± 4 km^3 a^{-1} w.e.). Almost half (-60 ± 3 km^3 a^{-1}) of the net mass loss comes from mountain glaciers and ice caps around the ice sheet. At present, it is difficult to detect any statistically significant trends for these components. The total mass balance of the Antarctic ice sheet is considered to be too premature to evaluate. The estimated sea-level contributions in the twentieth

A. Ohmura (✉)
Institute for Atmospheric and Climate Science, Swiss Federal Institute of Technology (E.T.H.), Universitätsstrasse 16, 8092 Zürich, Switzerland
e-mail: ohmura@env.ethz.ch

Century are 5.7 ± 0.5 cm by mountain glaciers and ice caps outside Antarctica, 1.9 ± 0.5 cm by the Greenland ice sheet, and 2 cm by ocean thermal expansion. The difference of 7 cm between these components and the estimated value with tide-gage networks (17 cm) must result from other sources such as the mass balance of glaciers of Antarctica, especially small glaciers separated from the ice sheet.

Keywords Mass balance · Greenland · Mountain glaciers · Trends

1 Introduction

The net influx of mass from glaciers to the ocean is one of the major components of the sea level changes. Presently, about 200,000 glaciers (Ohmura 2009a) are estimated to exist outside Greenland and Antarctica. The total glacierized surface and the ice volume on the planet are estimated at 16.2×10^6 km^2 and 28.4×10^6 km^3 (Ohmura 2009a), respectively. The total glacier ice on the planet is 65 m sea level equivalent. With respect to the surface area, 86% is on Antarctica, 11% on Greenland and 3% in other regions. In terms of ice volume, 89% is on Antarctica, 10% on Greenland and less than 0.35% in other regions (Ohmura 2009a). The glacier ice distribution is newly evaluated and presented in Table 1.

The main data source is the World Glacier Inventory (WGI) as presented in Ohmura (2009a). About 110,000 glaciers archived in WGI are individually treated in the following calculations, instead of the gridded approach taken by Radic and Hock (2010). The main point of Table 1 is the new evaluation of the regional glacier area and ice volume for 27 regions outside Greenland and Antarctica. These 27 regions are defined to be associated with the WGI working groups. In 16 regions the regional inventories are completed. We have detailed information on all glaciers in these regions including the surface area. In the remaining 11 regions, the degree of the WGI completion rate varies from the half-done stage like Bhutan to zero like Mexico and Indonesia. The information for the untouched regions is due to literature of various regional studies (Ohmura 2009a). For partially completed regions, the total glacier areas of the regions are estimated by multiplying the inventoried area by the ratio of 100 to the percent of the completion rate. This approximation holds only when the area frequency distribution of the inventoried glaciers is identical to that of all glaciers. The global area of glaciers and ice caps is computed as 550×10^3 km^2. This result is practically identical to 546×10^3 km^2 by Dyurgerov and Meier (2005), but considerably smaller than 704×10^3 km^2 by Hock et al. (2009). This difference is due to the fact that Hock et al. (2009) includes glaciers and ice caps on Greenland (54×10^3 km^2) and Antarctica (132×10^3 km^2). The material in Hock et al. (2009) yields after calculation the global area of glaciers and ice caps outside Greenland and Antarctica as 518×10^3 km^2.

The glacier ice volume was estimated for individual glaciers with the area/depth equation by Chen and Ohmura (1990). For the partially completed regions, the total ice volume of inventoried glaciers was multiplied by the reciprocal of the completion rate, as for the total area. The global total ice volume of glaciers and ice caps outside Greenland and Antarctica by way of the Chen/Ohmura equation is 100.3×10^3 km^3 (28 cm sea level equivalent), while it is 131.8×10^3 km^3 (36 cm sea level equivalent) by the Bahr equation (Bahr et al. 1997). Comparing the computed volumes against the recent observations of actual glacier volumes with Ground Penetrating Radar, the Chen/Ohmura equation tends to underestimate the volume for smaller glaciers (area less than 100 km^2), but the Bahr equation tends to overestimate the volumes of larger glaciers. The reality may lie between

Table 1 Glacier area, ice volume, mean thickness and World Glacier Inventory completion rate (Antarctica is due to Fujii 2006)

Region	Surface area (10^3 km^2)	Ice volume (10^3 km^2)	Mean thickness (m)	WGI complete rate in %
Greenland	1,748	2,931	1,677	NA
Iceland	**11.200**	**3.65**	**326**	**100**
Scandinavia	**3.1**	**0.167**	**53.9**	**100**
Alps	**3.1**	**0.146**	**47.1**	**100**
Pyrenees and Cordillera Cantabrica	**0.011**	**10^{-4}**	**10**	**100**
Jan Mayen	0.116	10^{-2}	25	0.0
Svalbard	**33.7**	**7.66**	**227.3**	**100**
Zemlya Frantsa Yosifa	**13.759**	**1.907**	**138.6**	**100**
Novaya Zemlya	**23.645**	**11.133**	**470.8**	**100**
Severnaya Zemlya & Ostrov Ushakova	**19.366**	**6.603**	**341.0**	**100**
Ostrava de Longa, Novosibirskiye Ostrova	**0.081**	**0.007**	**86.4**	**100**
Ostrov Vrangelya	**0.004**	**0.000033**	**8.3**	**100**
Caucasus	**1.390**	**0.066**	**47.5**	**100**
Severniy Ural	**0.018**	**0.00037**	**20.6**	**100**
Ex-SU in Asia	**23.855**	**4.217**	**176.8**	**100**
Canadian Arctic Islands	151.758	27.56906	181.8	17.3
North America (continental,excl. Alaska)	49.609	4.5825	92.3	21.3
Alaska	74.722	20.45017	273.6	16.4
Mexico	0.011			0.0
Afganistan, Iran, Turkey	4. 044	0.14569	36.0	11.7
India, Pakistan	40.000	3.07622	76.9	4.7
Bhutan, Nepal	7.340	0.74046	100.9	40.7
China	**59.425**	**5.600**	**94.2**	**100**
Indonesia	0.007			0.0
Africa	0.011	10^{-4}	10	0.0
New Zealand	**1.158**	**0.062**	**53.5**	**100**
South America	25.855	1.9432	75.2	17.9
Sub-Antarctic islands	7	1.2	171.4	0.0
Antarctica	13,860	25,400	1,833	NA
Total	16,158	28,432	1,760	
Of which outside Antarctica & Greenland	550.241	100.926	183	

Bold figures are based on completed World Glacier Inventory (WGI), while regular figures are due to partially done WGI

these values. The main reason for this uncertainty is mainly due to the poor completion rate of WGI for regions of many glaciers, such as Alaska and Canadian Arctic Islands. The completion of the WGI will contribute tremendously to close the gap of our present knowledge. Although the glaciers outside Greenland and Antarctica are a minority in terms of surface area and ice volume, they are located mostly in mild climate zones, and respond rapidly to climate changes. The present article aims at presenting the mass balance and its variations during the last century for the glaciers and ice caps outside Greenland and Antarctica. Further, the mass balance variations will be explained with climatic conditions

of the last 100 years. The contemporary snapshot mass balance of Greenland glaciers is also estimated. It is considered premature to apply similar considerations to Antarctica at present.

2 The Method for Estimating the Global Mass Balance

The major portion of the glacier mass exchanges takes place at the surface. The surface mass balance of glaciers is evaluated commonly through three methods: a stake method, geodetic method and hydrological balance method. The stake method relies on the in situ measurement of the mass variation at stakes fixed on the glacier surface. The density of the stake network is preferred to be denser than 1 stake per one square kilometer (Funk 1985) for middle sized Alpine glaciers with area in the order of 10 km^2. This is the most direct approach and will remain the most trusted method. The geodetic method obtains the mass change by evaluating the elevation change of the entire glacier surface between two discrete times. A comparison of the stake and the geodetic methods (Haug et al. 2009; Huss et al. 2009) sometimes yields large differences, which helps finding errors efficiently in one or both of the measurements. This method is of increasing importance with the satellite data especially for larger glaciers. Further, the satellite-based geodetic method is suited for estimating calving rate, which is difficult to measure with the other methods. Under the hydrological method one measures precipitation, evaporation and discharge from a glacierized basin, and attributes the rest to the mass balance of the glacier. Ideally, all three methods should be applied for a glacier. Stake method and hydrological method are applied in most projects in the Alps and Scandinavia. All three methods have been used for more than 30 year only for Vernagtferner (data: personal communication by L. Braun) in the Austrian Alps.

If careful measurements are carried out with sufficient stake density, the estimated error of the mean specific net balance of a glacier could remain within 90–280 mm water equivalent (w.e.) a^{-1} (Huss et al. 2009). Dyurgerov (2002) quotes as a typical uncertainty 200 mm a^{-1}. Therefore, 200 mm $a^{-1}$is taken as a representative error by the stake measurement for an entire glacier. This estimation gives an error of 34 mm a^{-1} for the global mean net balance.

The present work is exclusively based on the mass balance measurements carried out with the stake method, and the stress is given to those glaciers, which have separate summer and winter balance observations. The data set is an updated version of the set that was made for the International Union of Geodesy and Geophysics (IUGG) Workshop on Changing Planet 2003 (Ohmura 2004). The data set of 2003 was made based on the World Glacier Monitoring Service (WGMS) mass balance archive, supplemented by the personal data collections by R. Braithwaite and A. Ohmura, and those glaciers in Dyurgerov (2002). All these four data files had glaciers, which were not included in the other collections. These glaciers were extracted from each collection and merged to the largest file of WGMS, to form the maximum mass balance data collection. This maximum data collection has been annually updated by the author, through the contributions by many mass balance observers and also by tracing individual publications where mass balance data are published. Presently, there are almost 400 glaciers where some form of mass balance measurement was carried out, including the measurement of only one hydrological year. In view of large year-to-year variations, it is necessary to continue the measurement at least for 5–10 years just to obtain a snapshot situation of the mass balance. There are about 160 glaciers, which satisfy this condition. To obtain a mass balance trend similar to that of the

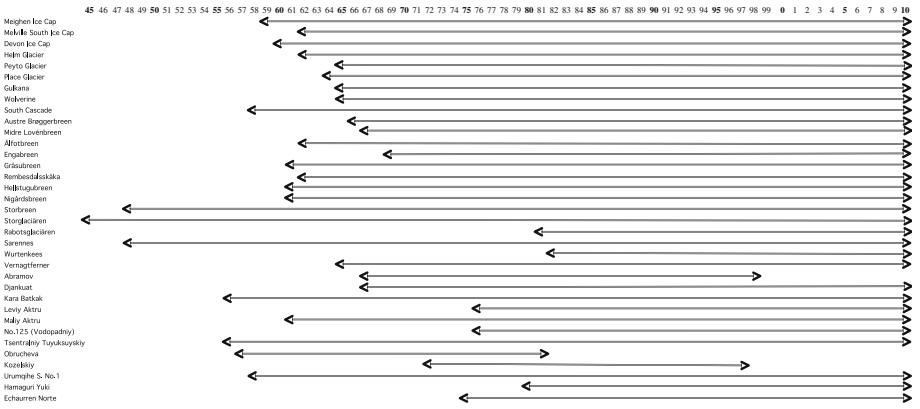

Fig. 1 Duration periods of 35 glaciers in the world, which kept annual observations of winter (Bw) and annual (Bn) mass balances for more than 30 years. Bs is usually calculated from Bw and Bn

climate, 30 years or longer observations are needed. There are slightly more than 50 glaciers with observation records longer than 30 years. Further, in order to understand the cause of the change of mass balance, the accumulation and the ablation must be separately determined for the same period. Except for the glaciers in the equatorial and monsoonal regions, the accumulation and the ablation can be substituted by the winter and summer balances which are easier to measure. There are presently 35 glaciers world wide with the observations of separate winter and summer balances lasting for more than 30 years. The duration periods of these important 35 glaciers are summarized in Fig. 1. All of these glaciers are located in the Northern Hemisphere. Further, most of these 35 glaciers have limited winter accumulation, a necessity to avoid an excessively long fieldwork in spring and also to avoid avalanche danger. None of these glaciers is calving glaciers. This selectiveness may introduce a certain sampling bias in calculating global total mass balance. Meier et al. (2007) discuss the role of the calving loss of glaciers and ice caps for some glaciers in Alaska and Russian Arctic islands, but the error due to the biased sampling at the global scale is at present hard to quantify.

Because of the data scarcity, the mass balance data are sometimes augmented with the estimated mass balance, usually expressed as functions of meteorological observations (e.g. Meier 1984). This approach has, however, not been taken in the present work, as one of the goals of the present work is to understand how the climatic conditions affect the mass balance changes. Only glacier mass balances determined with the stake method are used. The net balance will be compiled with respect to 17 glacierized regions of the world. The global mean mass balance will then be calculated by giving the weight of the surface areas of each region. For analyzing the winter and summer balances, the number of the glacierized regions is reduced to 11, as the other 6 regions do not have seasonal mass balance observations carried out for the necessary length of time.

3 Global Net Balance

From the 17 glacierized regions 137 glaciers were chosen to calculate the annual net balance. From necessity the glaciers with shorter observational records than 30 years are

also included for the region with poor data coverage. These glaciers are located in the Andes (7), North American Cordillera (24), Canadian Arctic Islands (8), Alaska (4), Kamchatka (2), the Himalayas (4), the Tienshians/Dzungaria (14), Altai (4), Pamir (1), Polar Ural (2), Caucasus (7), the Alps/Pyrenees (21), Iceland (9), Scandinavia (23), Svalbard (5), Severnaya Zemlya (1), and Africa (1). Since the density of the observed glaciers is very inhomogeneous, the surface areas of the glacierized regions were used as weights for calculating the global mean balance. Four regions hold 90% of the weight, the Canadian Arctic Islands, Alaska, the North American Cordillera, and Svalbard. In the previous section the likely error for the annual mass balance of a single glacier is taken as 50 mm a^{-1}. The major source of this error is not the measurement error at a single stake, but the sampling error due to the limited number of stakes. Assuming that a similar magnitude of errors might creep in when calculating regional means, and further for obtaining the area-weighted global mean, a rough estimate of the error for the global mass balance is set at 90 mm a^{-1}. Lemke et al. (2007) sets the error at 102 mm a^{-1}. The result of the regional and global mass balance estimation is presented in Fig. 2. Although the short-term variations of the annual net balance is large, all regions show a common trend for decadal intervals. The area-weighted global mean mass balance of the last half-century shows a negative balance with an accelerating trend. This type of analysis has become possible since the International Geophysical Year (IGY, 1957–1958). It appears that the end of the 1950s and the early 1960s captured the last stage of the large loss of mass.

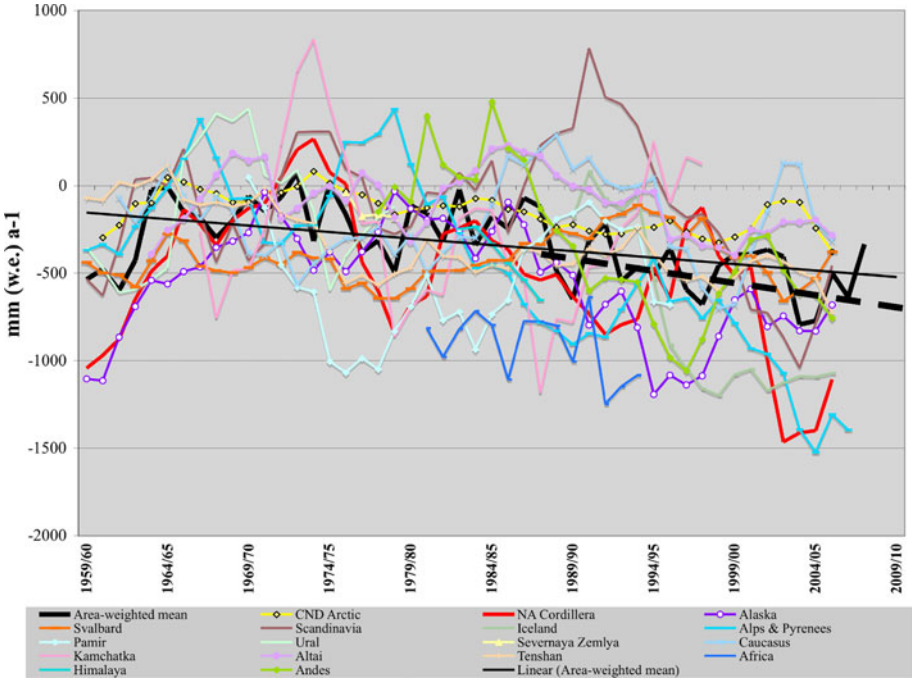

Fig. 2 5 year running means of the annual mean net balance for 50 years for the following 17 regions: Arctic Canada, North American Cordillera, Alaska, Svalbard, Scandinavia, Iceland, Alps, Pamir, Urals, Severnaya Zemlya, Caucasus, Kamchatka, Altaishan, Tienshan/Dzungaria, Africa, the Himalayas, the Andes. The *bold black line* indicates the area-weighted global mean, while the *two black straight lines* indicate the accelerations for the periods of the last 50 years 1961–2010 (*thin line*) and for the last 20 years 1991–2010 (*thick broken ilne*)

It is not certain if there was a period of global large mass loss before this period, as the global observational coverage did not exist before IGY. This problem will be reexamined later in this section with mass balance observations carried out in Europe. Starting in the mid-1960s until late 1980s the global mean mass balance became close to the equilibrium characterized with only a minor negative balance, -215 ± 34 mm (w.e.) a^{-1}. The end of the 1980s marks the transition to a large negative balance culminating at -605 ± 34 mm (w.e.) a^{-1} (mean of 2006–2008) after 2005. The half-century mean global net balance was -270 ± 34 mm (w.e.) a^{-1}. The pentade global mean net balance is summarized in Table 2 together with winter and summer balances, which are the theme of the following section. The mean global balance since 1960 can be compared with the most recent IPCC Assessment Report 4 (Lemke et al. 2007), which presents -283 mm (w.e.) a^{-1}.

Table 2 Area-weighted global mean winter (Bw), summer (Bs) and annual (Bn) mass balances of 35 glaciers from 11 regions, arranged for pentade means

Pentade period	Bw	Bs	Bn	Bn 137 glaciers
1960/1961–1964/1965	685	−848	−163	−131
1965/1966–1969/1970	835	−1,068	−233	−132
1970/1971–1974/1975	881	−1,048	−167	−140
1975/1976–1979/1980	944	−1,166	−222	−247
1980/1981–1984/1985	1,003	−1,144	−141	−232
1985/1986–1989/1990	914	−1,260	−346	−332
1990/1991–1994/1995	885	−1,353	−468	−317
1995/1996–1999/2000	984	−1,374	−389	−426
2000/2001–2004/2005	892	−1,292	−400	−444

The last column is the pentade means of the annual balance including the glaciers with only annual balance observations. Unit is mm w.e. a^{-1}. The range of uncertainty for Bw and Bs is estimated at 24 mm a^{-1}, and that for Bn is 34 mm a^{-1}

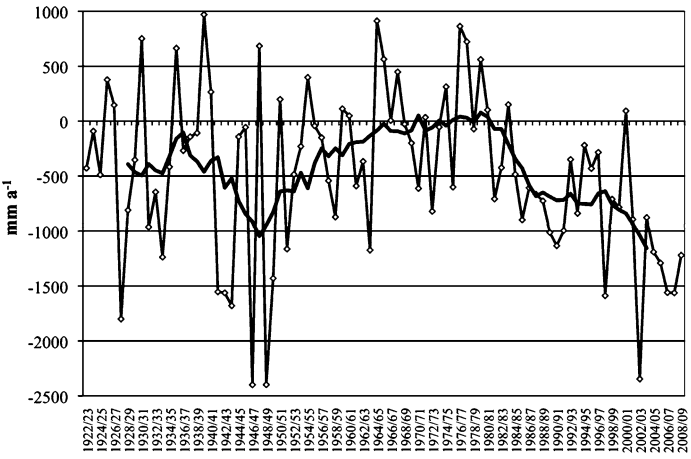

Fig. 3 Mean annual net balance of 20 glaciers in the Alps and the Pyrenees. The *black bold line* indicates a 11-year running mean. Unit in mm w.e. a^{-1}

The trend of the mass loss has been accelerating at a rate of -9 ± 2.1 mm a^{-2} during the last 50 years and -15 mm a^{-2} during the last 20 years. Meier et al. (2007) presents the acceleration of -22 mm (w.e.) a^{-2} for 10 years from 1996 to 2006.

To supplement the unavailable global information of the earlier period, the works on glaciers in Europe were used. The mean annual net balance for 19 glaciers from the Alps and 1 glacier from the Pyrenees is presented in Fig. 3. The figure shows a period of large mass loss starting in late 1930s, centered on 1948 and lasting until the late 1950s. It appears that the brief period of large negative balance depicted in the global mean at the end of 1950s in Fig. 2 probably captured the last glimpse of the large mass loss in the mid-century. It must be clarified how these variations were caused. To do this one needs seasonal mass balance in order to look at the accumulation and ablation separately.

4 Seasonal Mass Balance

There are 35 glaciers located in 11 regions for which winter and summer balances were measured for more than 30 years. The area-weighted winter, summer and annual balances are presented in Fig. 4 for the period of the last half-century. The upper line (blue) represents the winter balance, which is a good approximation of accumulation. The lower line (red) is the summer balance, an indicator of the melt. The black line in the middle is the annual net balance for the 35 glaciers. The annual net balance of the 35 glaciers is compared with the annual net balance (brown line) computed with 137 glaciers from the 17 glacierized regions. The closeness of the two lines representing the annual net balance indicates that the net balance computed with 35 glaciers represents fairly well the global

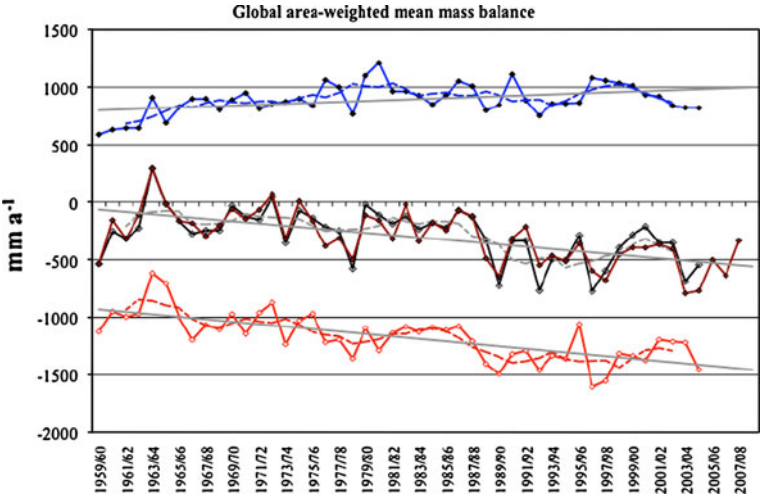

Fig. 4 Area-weighted global mean annual mass balance, based on 35 glaciers in 11 regions. *Blue*, *brown* and *red lines* indicate winter, annual and summer balances, respectively. *Broken lines* indicate 11 year running means in each category. Further, *black lines* in the *middle* indicating the mean annual net balance are those for 137 glaciers in 17 regions, for comparison. The closeness between the *brown* and *black lines* supports the global significance of the 35 glaciers from 11 regions, on which winter and summer balances are observed. These 11 regions are Arctic Canada, North American Cordillera, Alaska, Svalbard, Scandinavia, Alps, Pamir, Caucasus, Kamchatka, Altaishan, Tienshan/Dzungaria. Unit in mm w.e. a^{-1}

mean conditions. The broken lines accompanying the three lines are the 11-year running means, while the three grey straight lines indicate the linear trend of the 50 years.

The decrease in ablation in the late early 1960s, stagnation from the early 1960s to the mid-1980s, and the sudden increase in the late 1980s are the most important episodes in the decadal variation in the global summer balance. The winter balance (accumulation) indicates also a long-term variation, increasing from the late 1950s to the mid-1980s. Accumulation and melt appear weakly correlated until the mid-1980s. This tendency has been broken since the late 1980s and the accumulation has clearly been declining during the last decade. Overall, the range of variability for the accumulation is much smaller than that for the melt ablation. The 50-year trend as well as the decadal variation of the global annual net balance depicted in the previous section is to a great extent dictated by the change in the melt ablation. This analysis shows that globally averaged the decadal variation of the net balance is to 90% determined by the change in ablation. The mean annual net balance of the last half-century was -270 ± 34 mm (w.e.) a^{-1}. The mean accumulation and ablation were 890 ± 24 mm (w.e.) a^{-1} and $-1{,}175 \pm 24$ mm (w.e.) a^{-1}, respectively. The accelerations of net balance, accumulation and ablation are -9 ± 2.1 mm (w.e.) a^{-2}, $+ 0.7 \pm 2.0$ mm (w.e.) a^{-2} and -10 ± 2.0 mm (w.e.) a^{-2}, respectively.

5 Long-Term Mass Balance of Glaciers in the Alps and Scandinavia and its Causes

The longest observations of glacier mass balance and climate are available only in Europe. Two glaciers in Scandinavia, Storglaciären (mass balance observation starting in 1945/1946, data: personal communication by P. Jansson) and Storbreen (starting in 1948/1949, data: Kjøllmoen 2010) were chosen to represent Scandinavia, as these glaciers possess the longest seasonal mass balance observations. For the Alps, Glacier de Sarennes (starting in 1948/1949, data: personal communication by C. Vincent) was chosen. Further, annual net balance of the Aletchgletscher (starting in 1922/1923, data: personal communication by A. Bauder) and the summer mass balance of the Lower Stake of the Claridenfirn (starting in 1914/1915, data personal communication by H. Müller) are added. Fig. 5 presents the above-mentioned 5 curves with their 11 year running means. It appears that during the 1920s the annual mass balance was close to zero and the glaciers were at equilibrium with the climate. Summer ablation started to increase at the end of the 1910s and formed a period of strong ablation lasting for 20 year, centered on 1945. This period was the time of the largest mass loss that was only matched by the last decade of the twentieth century. After 1960, ablation decreased towards the beginning of the 1980s. At the beginning of the1980s the annual net balance approached zero. With the onset of the present century the ablation, hence negative annual net balance showed a rather sudden increase that was not matched by any other periods of the observation era. The decadal variation of the winter accumulation was small, but not insignificant. In the main it fluctuated proportional to the air temperature, except for the last decade, as the accumulation started to decrease. This was due to the decrease of solid precipitation under higher temperature. The period of the last 100 years can be characterized by the two periods of near equilibrium or slight positive balance (beginning of the twentieth century, and 1970s) and two periods of large mass loss (early 1940s to early 1950s, and the present day after 1995).

The general trend of the summer ablation can be interpreted in terms of air temperature. Fig. 6 represents the summer 3 months' (JJA) temperature measured in the glacier regions of Europe, three in Scandinavia and three in the Alps. The course of temperature in the

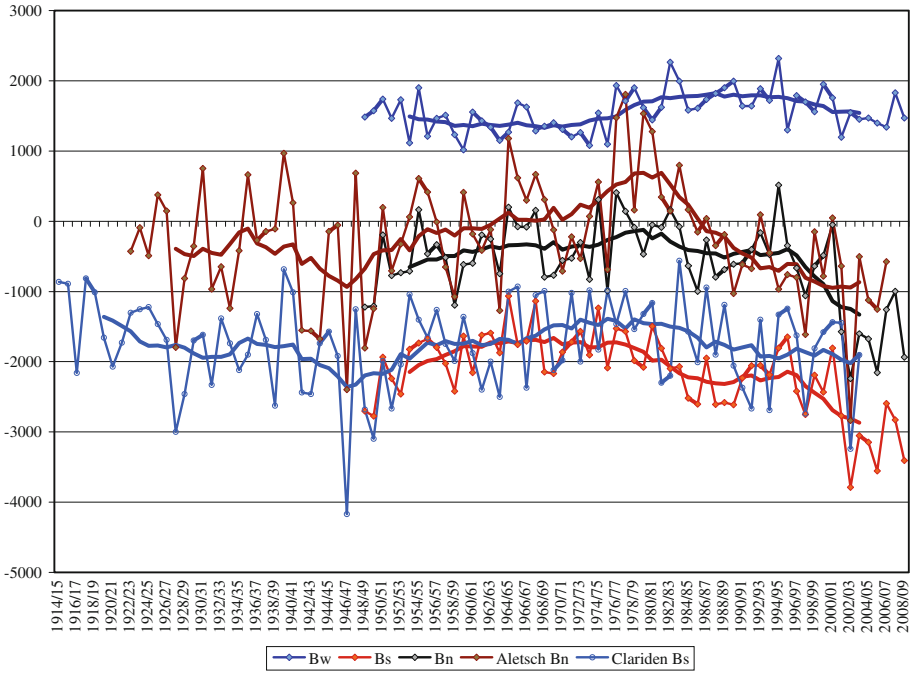

Fig. 5 Mean mass balance for the Alps and Scandinavia. The mean annual balances are the arithmetic means of the three glaciers, Storglaciären, Storbreen and Glacier de Sarennes. There are *three shorter lines* (for the period 1948/1949–2008/2009) marked with *diamonds*, from the *top* in *dark blue*, *black* and *red* indicating winter, annual and summer balances, respectively. The annual net balance for the Aletschgletscher is plotted for the period of 1922/1923–2005/2006 with a *brown curve*. The *light blue curve ticked* with *circles* is the summer balance at the lower stake on Claridenfirn, indicating the summer melt for the period of 1914/2005–2003/2004, near the equilibrium line. The *smooth curves* running through them in the same colours are 11 year running means. Unit in mm w.e. a^{-1}

glacierized regions of Europe resembles closely that of the global mean, except that the range of the temperature fluctuation is about three times larger in the glacierized areas. A close examination, however, shows that during the 1940s larger ablation was happening under lower temperature in comparison with the modern warm period. This can only be explained by considering the long-term change in solar radiation (Ohmura et al. 2007).

The decadal variability the solar radiation at the earth's surface in a continental and global scale has only recently been acknowledged. Fig. 7 illustrates the course of the global solar radiation observed at five sites in Europe. Solar radiation fluctuated over the range of 14 Wm^{-2} during the course of the last 90 years. Solar radiation was large during the 1940s and 1950s. Then, it decreased steadily during the following 30 years towards the late 1980s, which was followed by a rather sharp increase after late 1980s. These decreasing and increasing phases are often referred to as global dimming and brightening. One should, however, bear in mind that there was also an earlier brightening period during the 1940s and 1950s. The modern brightening period does not match the first brightening period of 1940s and 1950s. The change in the earth's surface global solar radiation was explained by Ohmura (2009b) through the direct and indirect effects of aerosol. Combining the incoming long-wave radiation and solar radiation, the change in the total incoming radiation was negative at least from 1955 until 1985, causing the climate cooling and small

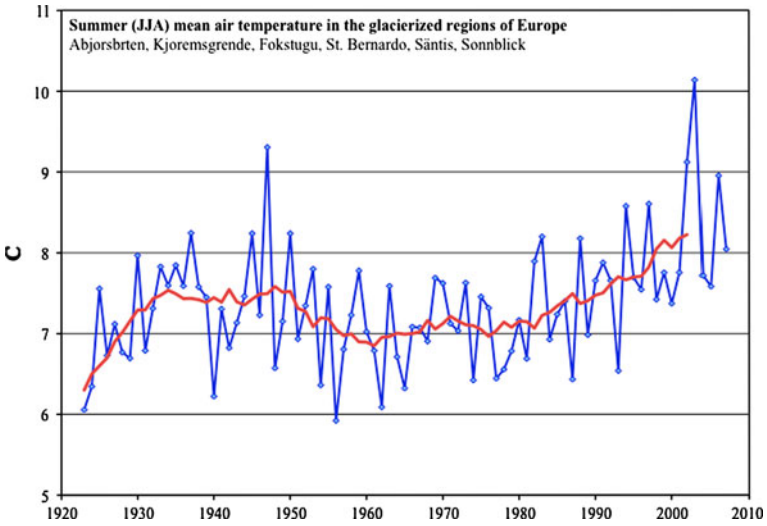

Fig. 6 Summer air temperature for the glacierized region of Europe. The *blue line* represents the mean values of the six stations, Abjorsbraten (601 m a.s.l.), Kjoremsgrende (626 m a.s.l.) and Fokstugu (972 m a.s.l.) of Norway, St. Bernardo (1,639 m a.s.l.) and Säntis (2,490 m a.s.l.) of Switzerland, and Sonnblick (3,105 m a.s.l.) of Austria for June, July and August. The *red line* is the 11-year running mean

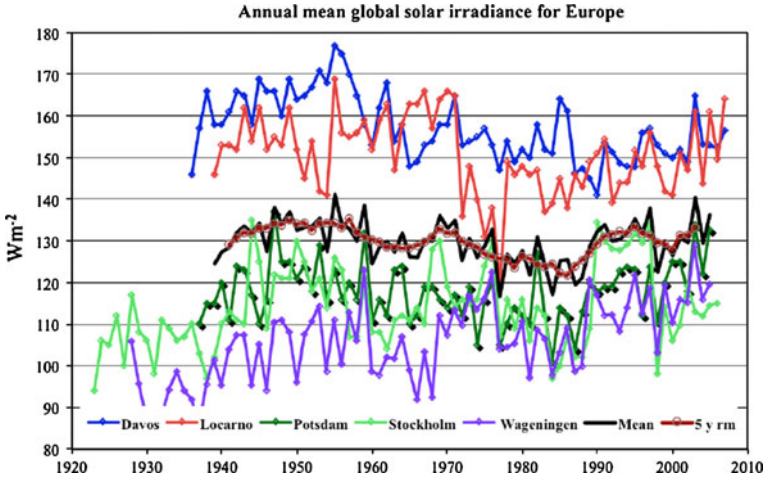

Fig. 7 Mean annual global solar radiation for 5 European sites (Stockholm, Wageningen, Davos, Potsdam and Locarno-Monti) with the longest observation records. The *black line* in the *middle* indicates the mean of the five stations, while the *brown line ticked* with *circles* is the 11-year running mean of the European mean curve

ablation. Increasing long-wave and solar radiation after 1985 is the reason for the rapid melt of the last two decades. The mass loss of the last decade took over that of the 1940s, not only due to the higher temperature, but also due to the decreasing accumulation and the rapidly increasing solar radiation (Ohmura et al. 2007; Huss et al. 2009).

There is an effort to relate the mass balance of European glaciers with respect to the fluctuation in the North Atlantic sea surface temperature (SST), which is referred to as Atlantic Multidecadal Oscillation (AMO). AMO was originally proposed by R. Newell (personal communication in 1985) indicating the SST fluctuation in the North Atlantic with about a 50-year periodicity. The cause of the fluctuation is explained by the ocean circulation fluctuation by Delworth and Mann (2000). The relationship between AMO, cloud amount and solar global radiation in Europe was reported earlier by Ohmura and Lang (1989). Recently Ohmura (2006, 2009a) found a similar variation of solar global radiation in North America and Northern Pacific. The correlation between AMO and negative glacier mass balance is not a cause and effect relationship, but both North Atlantic SST and larger glacier melt are caused by the same process, namely the change in solar global radiation as detailed in the present section.

6 Mass Balance of Greenland

The ice-covered area of Greenland ($1{,}748 \times 10^3$ km^2) comprises 82% of the total surface area of Greenland ($2{,}164 \times 10^3$ km^2). The total ice volume is estimated at $2{,}620 \times 10^3$ km^3 (Weidick 1995), which is equivalent to 6.7 m sea level without considering the effect of hydro-isostasy. About 97% of the surface area of glaciers on Greenland is made up by the ice sheet ($1{,}694 \times 10^3$ km^2), and the remaining 3% by mountain glaciers and ice caps (53.73×10^3 km^2) (Calanca et al. 2000; Hock et al. 2009). Most mountain glaciers and ice caps in Greenland occupy the regions near the coast and the lower altitudes. Consequently, the ablation from these small glaciers through melt and calving is large. The mass balance of these small glaciers is important for the mass balance of entire Greenland, as the ablation area (161×10^3 km^2) of the ice sheet accounts for only 9.5% of the ice sheet area (Ohmura et al. 1999). In the present section the snapshot mass balance of glaciers in Greenland will be estimated. The relevant period for this estimation is the second half of the twentieth century, as the main sources of the data are from investigations carried out since the IGY (e.g. Benson 1962).

The accumulation (substituted by winter balance) and ablation (substituted by summer balance) on Greenland glaciers have been rarely observed for more than 8 years consecutively at the same locations. The exceptions are GISP2/Summit (3,150 m a.s.l.), Swiss Camp (1,155 m a.s.l.) and 4 traverse lines of Geological Survey of Greenland and Denmark in the lower elevation sites (ranging from 200 to 1,100 m a.s.l.) in the southwest Greenland ice sheet. Although the annual and seasonal mass balance observations at these sites are valuable, other methods must be used to complete the full coverage of the ice sheet and glaciers. Snow pits and ice core studies offer useful information on accumulation in the dry snow and upper percolation zones of the accumulation area in accordance with the Benson (1961) and Müller (1962) definitions. The accumulation data obtained since Benson (1962) are much denser than those for Antarctica, and are used by various authors for estimation of the accumulation of the Greenland ice sheet (Reeh and Olesen 1986; Ohmura and Reeh 1991; Ohmura et al. 1999; Calanca et al. 2000; Bales et al. 2009). The accumulation in the lower percolation, superimposed ice and ablation zones must be estimated, as the ice core from these zones suffers at least from a partial loss of the mass. The estimation adopted in the present work is the interpolation between the accumulations observed in the lowest area of the upper percolation zone and the solid precipitation observed at meteorological stations outside the glaciers. In total monthly precipitation data from 42 meteorological stations were used. The observed precipitation values were

corrected against the observational errors with the Sevruk method (Sevruk 1986). The Sevruk correction method is a simple function expressing the rate of the snowfall underestimation as a function of wind speed, using the WMO absolute standard snow gauge (Busch precipitation gauge) as the standard. Actual mathematical forms are slightly different for each national standard snow gage. The merit of this method is that it does not over-correct the measured values, avoiding overestimations, a problem of many similar correction methods. There is a substantial investigation of the Danish standard Hellmann gauge behind the Sevruk method.

The melt ablation was calculated using the empirical relationship between the summer balance and the mean air temperature of the summer 3 months (JJA) proposed by Ohmura et al. (1996). The monthly temperature used for the calculation was taken from Ohmura (1987). The physical justification of the use of air temperature for the melt estimation is provided by Ohmura (2001). To ensure high accuracy it is essential to project the temperature distribution on a realistic topographic map, as the melt takes place in a narrow marginal zone where both contour lines and isothermal lines tend to be concentrated. The Ekholm 2 × 2 km digital topographic model (Ekholm 1996) was used as the base for the interpolation.

Ablation due to glacier calving is an important process of mass balance not only for the ice sheet but also for the mountain glaciers and ice caps, many of which are located near and on the coast. The only possibility to obtain the calving rate of the Greenland glaciers is to calculate all calving glaciers individually. Weidick (1995) completed such calculations for south-west coast of Greenland, south of 73° N. Higgins (1991) did a similar study for the northern shore of Greenland. The mid-east coast was studied by Reeh (1994). The compilation of calving by Reeh et al. (1999) by using all these results appears to this author as the most advanced study on the calving rate from Greenland glaciers and is adopted in the present study.

Error estimations for a continental scale glacier are difficult to quantify (Lemke et al. 2007). Nevertheless, Ohmura et al. (1999) adopted a half of the difference of maximum and minimum of the mean accumulation on EGIG-Line (Expédition Glaciologique Internationale au Groenland) measured by various authors (Benson 1962; Seckel 1977; Tober 1986; Anklin 1991, Anklin et al. 1998) as an indicator of the error. This is a zone with the richest scientific information in Greenland. For the Greenland ice sheet accumulation, it is 12% or 60 $km^3\ a^{-1}$. Hanna et al. (2005) estimates the accumulation error at 5%. In this work the larger error, 12% has been adopted. It is assumed that the other components, melt ablation and calving loss have an error range of the same order.

The estimation of the mass balance calculation based on the material presented above is summarized in Table 3. The most important conclusion of this evaluation is the fact that the mass balance of Greenland glaciers is already negative at the present time. The annual net balance of $-128 \pm 18\ km^3\ a^{-1}$ is equivalent to $+0.35 \pm 0.05\ mm\ a^{-1}$ in sea-level change. The present result can be compared with IPCC AR4 (Lemke et al. 2007) reporting the balance of +25 to $-60\ km^3\ a^{-1}$ for period from 1961 to 2003, and −50 to $-100\ km^3\ a^{-1}$ for 1993–2003. The work published after the last Assessment Report, for example Rignot et al. (2008) presents $-123 \pm 58\ km^3\ a^{-1}$ for the period of 50 years from 1958 to 2007, where the recent balance shows a bigger loss, $-212 \pm 41\ km^3\ a^{-1}$ for the period of 2001–2007.

Also important is the fact that almost half of this net discharge, $60 \pm 3\ km^3\ a^{-1}$ comes from mountain glaciers and ice caps. Hock et al. (2009) presents $22 \pm 59\ km^3\ a^{-1}$ for this component. These glaciers, which are not a part of the ice sheet, are located in a maritime climate of the coastal zone of Greenland, having usually larger mean specific accumulation

Table 3 Annual mass budget of the Greenland ice sheet and its marginal mountain glaciers and ice caps

	Greenland glaciers (total ice covered area: 1,747.7 × 10^3 km^2)						Source
	Ice sheet (1,694 × 10^3 km^2)		Glaciers and ice caps (53.725 × 10^3 km^2)		Total (1,747.7 × 10^3 km^2)		Weidick (1995); Bamber et al. (2004); Ohmura (2009a)
	km^3 a^{-1} w.e.	mm a^{-1} w.e.	km^3 a^{-1} w.e.	mm a^{-1} w.e.	km^3 a^{-1} w.e.	mm a^{-1} w.e.	
Accumulation	487 ± 58	288 ± 35	32 ± 4	600 ± 72	519 ± 58	297 ± 33	Ohmura et al. (1999); Wild et al. (2003)
Melt ablation	257 ± 31	152 ± 18	39 ± 5	723 ± 87	296 ± 31	169 ± 18	Calanca et al. (2000); Wild et al. (2003)
Calving	263 ± 32	154 ± 18	53 ± 6	987 ± 118	316 ± 33	181 ± 19	Reeh (1994); Reeh et al. (1999)
Bottom melt	35 ± 4	21 ± 3	0	0	35 ± 4	21 ± 2	Reeh et al. (1999)
Mass budget	−68 ± 18	−39 ± 13	−60 ± 3	−1,110 ± 54	−128 ± 18	−74 ± 10	This study

The budget is the mean condition for the second half of the twentieth century, 1951–2000

than the ice sheet. As many of these glaciers are located below 1,000 m a.s.l., specific melt is also large. Many of these glaciers are also calving glaciers, increasing further the total ablation rate. These low-altitude glaciers are also expected to respond quickly to the warming of the climate.

The next important point to investigate is the possibility of temporal variation of the mass balance on Greenland. There are some works reporting an accelerating net mass loss (e.g. Box et al. 2006). There are also reports on expanding melting zones (Abdalati and Steffen 2001). Some reports are directly concerned with the change in shape of the ice sheet (Krabill et al. 2000). These are remote sensing studies based on a relatively short period of investigations spanning from 10 to 15 years. A close examination of the existing direct mass balance measurements presented in the fifth paragraph of the present section shows that an observation period of about 10 years is too short to identify long-term trends. Although there is a possibility of promising advances in these directions, it may still be some time before the temporal change in Greenland's mass balance is numerically presented.

7 Effect on Sea-Level Change and Conclusion

The above findings are converted in terms of the sea level change and summarized in Table 4. The most important contribution to sea level rise is made by mountain glaciers and ice caps outside Greenland and Antarctica. These small glaciers occupy only 3.5 and 0.3% of the total glacier surface and ice volume, respectively. Nevertheless, the largest mass influx comes from these small glaciers, mainly because the ice sheets under the present climate are located in very cold climates, where a slight warming does not yet increase their melt significantly. A similar consideration applies to mountain glaciers and ice caps in Greenland. Their total surface area accounts for only 3% of the total ice-covered surface on Greenland. Owing mainly to their low altitudes and proximity to the sea, their net mass transfer to ocean almost matches that of the Greenland ice sheet. The total mass flow from all mountain glaciers and ice caps outside Antarctica is equivalent to 57 mm per century. This result suggests that possible contributions from mountain glaciers and ice caps on Antarctica may also be important.

Based on observations made during the second half of the twentieth century, the contributions to sea level can be accounted for as follows: 57 ± 5 mm per century by mountain glaciers and ice caps outside Antarctica; 19 ± 5 mm per century by the

Table 4 Estimated sea level changes of the twentieth century and its components

Components	Unit in mm	Source
Mountain glaciers and ice caps	41 ± 5	This study
Greenland ice sheet	19 ± 5	This study
Greenland glaciers and ice caps	16 ± 1	This study
Thermal expansion of ocean	20	Based on Levitus et al. (2005)
Antarctic ice sheet, glaciers and ice caps, and other sources	74	This study
Tide gauge interpretation	170	J. Church (personal communication)

Greenland ice sheet; 20 mm per century by thermal expansion of the sea water—totaling 96 ± 9 mm per century. Since the tide gauge-based sea-level rise during the twentieth century is 170 mm per century, the difference of 74 mm per century must still be accounted for. A part of this gap can be attributed to the mass balance of glaciers and ice caps on Antarctica as suggested by Hock et al. (2009). The small glaciers especially in the milder climatic zones of the Antarctic Peninsula and West Antarctica must be closely investigated.

Acknowledgments The author is indebted to the following colleagues for acquiring pre-publication mass balance data: Miguel Arenillas of Ingeniería 75, S.A., Andreas Bauder and Martin Funk of E.T.H. Zurich, Roger Braithwaite of the University of Manchester, Ludwig Braun of Bavarian Academy of Sciences, Graham Cogley of the University of Trent, Jon Ove Hagen of the University of Oslo, Peter Jansson of Stockholm University, Giovanni Kappenberger of Swiss Federal Office of Meteorology and Climatology, Bjarne Kjølloen of the Norwegian Water Resources and Energy Directorate, Jack Kohler of the Norwegian Polar Institute, Michael Kuhn and Andrea Fischer of the University of Innsbruck, Hans Müller of Tergeso A.G., Wolfgang Schöner of Central Institute for Meteorology and Geodynamics, Christian Vincent of the University of Grenoble, and Michael Zemp of the University of Zurich. The author received valuable help in computational methods for error estimations from Hans-Rudolf Künsch of the Department of Mathematics at E.T.H. Zurich.

References

Abdalati W, Steffen K (2001) Greenland ice sheet melt extent: 1979–1999. J Geophys Res 106(D24): 33983–33988

Anklin M (1991) CO_2-analyse an einem Eisbohrkern aus Zentralgrönland und Bestimmung von Niederschlagsraten entlang einer Fliesslinie mittels H_2O_2-analyse. Unpublished Lizentialarbeit, Division of Climate and Environment Physics, Institute of Physics, University of Berne

Anklin M, Bales RC, Mosley-Thompson E, Steffen K (1998) Annual accumulation at two sites in northwest Greenland during recent centuries. J Geophys Res 103(D22):28775–28783

Bahr DB, Meier MF, Peckham SD (1997) The physical basis of glacier volume-area scaling. J Geophys Res 102(B9):20355–20362

Bales RC, Guo Q, Shen D, McConnell JR, Du G, Burkhart JF, Spikes VB, Hanna E, Cappelen J (2009) Annual accumulation for Greenland updated using ice core data developed during 2000–2006 and analysis of daily coastal meteorological data. J Geophys Res 114:D06116. doi:10.1029/2008JD011208

Bamber JA, Payne AJ (eds) (2004) Mass balance of the cryosphere. Cambridge University Press, Cambridge

Benson CS (1961) Stratigraphic studies in the snow and firn of the Greenland Ice Sheet. Folia Geogr Dan 9:13–37

Benson CS (1962) Stratigraphic studies in the snow and firn of the Greenland Ice sheet. Research Report, No. 70, Snow, Ice, and Permafrost Research Establishment (SIPRE)

Box JE, Bromwich DH, Veenhuis LS, Bai L, Stroeve JC, Rogers JC, Steffen K, Haran T, Wang S (2006) Greenland ice sheet surface mass balance variability (1988–2004) from calibrated Polar MM5 output. J Clim 19:2783–2800

Calanca P, Gilgen H, Ekholm S, Ohmura A (2000) Gridded temperature and accumulation distributions for use in cryospheric models. Ann Glaciol 31:118–120

Chen J, Ohmura A (1990) Estimation of Alpine glacier water resources and their change since 1870s. In: Lang H, Musy A (eds) Hydrology in mountainous regions I. IAHS Publ., No. 193, pp 127–135

Delworth TL, Mann ME (2000) Observed and simulated multidecadal variability in the Northern Hemisphere. Clim Dynamics 16:661–676

Dyurgerov M (2002) Glacier mass balance and regime: data of measurements and analysis. Occasional Paper No.55, Institute of Arctic and Alpine Research, Univ. Colorado, Boulder

Dyurgerov M, Meier MF (2005) Glaciers and the changing earth system: a 2004 snapshot. Occasional Paper58, Occasional Paper 58, Institute of Arctic and Alpine Research, University of Colorado, Boulder, CO

Ekholm S (1996) A full coverage, high resolution, topographic model of Greenland computed from a variety of digital elevation data. J Geophys Res 101(B10):21961–21972

Funk M (1985) Räumliche Verteilung der Massenbilanz auf dem Rhonegletscher und Ihre Beziehung zu Klimaelementen. Geograph. Inst., Eidgenössische Techn. Hochsch. Zürich, Zürcher Geographische Schriften, p 24

Hanna E, Huybrechts P, Janssens I, Cappelen J, Steffen K, Stephens A (2005) Runoff and mass balance of the Greenland ice sheet: 1958–2003. J Geophys Res 110:D13108. doi:10.1029/2004JD005641
Haug T, Rolsrad C, Elvehøy H, Jackson M, Maalen-Johansen I (2009) Geodetic mass balance of the western Svartisen ice cap, Norway, in the periods 1968–1985 and 1985–2002. Ann Glaciol 50(50): 119–125
Higgins AK (1991) North Greenland glacier velocities and calf ice production. Polarforschung 60(1):1–23
Hock R, de Woul M, Radic V, Dyurgerov M (2009) Mountain glaciers and ice caps around Antarctica make a large sea-level rise contribution. Geophys Res Lett 36:L07501. doi:10.1029/2008GL037020
Huss M, Funk M, Ohmura A (2009) Strong Alpine glacier melt in the 1940s due to enhanced solar radiation. Geophys Res Lett 36:L23501. doi:10.1029/2009GL040789,2009
Kjøllmoen B (ed) (2010) Glaciological investigations in Norway 2009. Norwegian water resources and energy directorate, Oslo, pp. 94
Krabill W, Abdalati W, Frederick E, Manizade S, Martin C, Sonntag J, Swift R, Thomas R, Wright W, Yungel J (2000) Greenland ice sheet: high-elevation balance and peripheral thinning. Science 289: 428–430
Lemke P, Ren J, Alley RB, Allison I, Carrasco J, Flato G, Fujii Y, Kaser G, Mote P, Thomas RH, Zhang T (2007) Observations: changes in snow, ice and frozen ground. In: Solomon S, Qin D, Manning M, Chen Z, Marquis M, Averyt KB, Tignor M, Miller HL (eds) Climate change 2007: the physical science basis. contribution of working group I to the fourth assessment report of the intergovernmental panel on climate change. Cambridge University Press, Cambridge
Levitus S, Antonov J, Boyer T (2005) Warming of the world ocean. Geophys Res Lett 32:L02604. doi: 10.1029/2004GL021592
Meier MF (1984) Contribution of small glaciers to global sea level. Sci 226:1418–1421
Meier M, Dyurgerov MB, Rick UK, O'Neel S, Pfeffer WT, Anderson RS, Anderson SP, Glazovsky AF (2007) Glaciers dominates eustatic sea-level rise in the 21st century. Science 317:1064–1067
Müller F (1962) Zonation in the accumulation area of the glaciers of Axel Heiberg Island, N.W.T. Can J Glaciol 4:302–313
Ohmura A (1987) New temperature distribution maps for Greenland. Zeitschr Gletscherk Glazialgeol 23:1–45
Ohmura A (2001) Physical basis for the temperature/melt-index method. J Appl Meteor 40:753–761
Ohmura A (2004) Cryosphere during the twentieth century. Geophys Monogr 150:239–257 (Am Geophys Union)
Ohmura A (2006) Observed long-term variations of solar irradiance at the earth's surface. Space Sci Rev. doi:10.1007/s11214-006-9050-9 (special edition)
Ohmura A (2009a) Completing the world glacier inventory. Ann Glaciol 50(53):144–148
Ohmura A (2009b) Observed decadal variations in surface solar radiation and their causes. J Geophys Res 114(D00D13). doi:10.1029/2008JD011290
Ohmura A, Lang H (1989) Secular variation of global radiation in Europe. In: Lenoble J, Geleyn J-F (eds) IRS'88: current problems in atmospheric radiation. A. Deepak Publ., Hampton, pp 298–301
Ohmura A, Reeh N (1991) New precipitation and accumulation distribution maps for Greenland. J Glacial 37:140–148
Ohmura A, Wild M, Bengtsson L (1996) A possible change in mass balance of Greenland and Antarctic ice sheets in the coming century. J Clim 9:2124–2135
Ohmura A, Calanca P, Wild M, Anklin M (1999) Precipitation, accumulation and mass balance of the Greenland ice sheet. Zeitschr Gletscherk Glazialgeol 35:1–20
Ohmura A, Bauder A, Müller H, Kappenberger G (2007) Long-term change of mass balance and the role of radiation. Ann Glaciol 46:367–374
Radic V, Hock R (2010) Regional and global volumes of glaciers derived from statistical upscaling of glacier inventory data. J Geophys Res 115. doi:10.1029/2009JF001373
Reeh N (1994) Calving from Greenland glaciers: observations, balance estimates of calving rates, calving laws. In: Reeh N (ed) Workshop on the calving rate of West Greenland glaciers in response to climate change, 13–15 September 1993. Copenhagen, Danish Polar Center, pp 85–102
Reeh N, Olesen OB (1986) Velocity measurements on Daugaard-Jensen Gletscher, Scoresby Sund. East Greenland. Ann Glaciol 8:146–150
Reeh N, Mayer Christoph, Miller H, Thomsen HH, Weidick A (1999) Present and past climate control on fjord glaciations in Greenland: implications for IRD-deposition in the sea. Geophys Res Lett 26: c1039–1042
Rignot E, Box JE, Burgess E, Hanna E (2008) Mass balance of the Greenland ice sheet from 1958 to 2007. Geophy Res Lett 35. doi:10.1029/2008GL035417

Seckel H (1977) Höhenänderungen im grönländischen Inlandeis zwischen 1959 und 1968. EGIG 1967–1968 3(5):187, 194 (Medd. Gronland)
Sevruk B (1986) Correction of precipitation measurements: Swiss experience. In: Sevruk B (ed) Correction of precipitation measurements. Zürcher Geographische Schriften, No. 23, pp 187–196
Tober M (1986) Die deutschen geodätischen Arbeiten im Rahmen der internationalen glaziologischen Grönland Expedition (EGIG) 1959–1974. Deutsche Geodätische Kommission Reihe B, Nr. 281, Bayerische Akademie der Wissenschaften, München, pp 63–84
Weidick A (1995) Greenland. Satellite image atlas of glaciers of the world, professional paper, 1386-C, U.S. Geol. Survey, U.S. Gov. Printing Office, Washington, DC
Wild M, Calanca P, Scherrer SC, Ohmura A (2003) Effects of polar ice sheets on global sea level in high-resolution greenhouse scenarios. J Geophys Res 108(D5):4165, ACL 5-1-10

Surv Geophys (2011) 32:555–583
DOI 10.1007/s10712-011-9128-0

Present State and Prospects of Ice Sheet and Glacier Modelling

Heinz Blatter · Ralf Greve · Ayako Abe-Ouchi

Received: 14 October 2010 / Accepted: 12 May 2011 / Published online: 1 June 2011

Abstract Since the late 1970s, numerical modelling has become established as an important technique for the understanding of ice sheet and glacier dynamics, and several models have been developed over the years. Ice sheet models are particularly relevant for predicting the possible response of ice sheets to climate change. Recent observations suggest that ice dynamics could play a crucial role for the contribution of ice sheets to future sea level rise under global warming conditions, and the need for further research into the matter was explicitly stated in the Fourth Assessment Report (AR4) of the United Nations Intergovernmental Panel on Climate Change (IPCC). In this paper, we review the state of the art and current problems of ice sheet and glacier modelling. An outline of the underlying theory is given, and crucial processes (basal sliding, calving, interaction with the solid Earth) are discussed. We summarise recent progress in the development of ice sheet and glacier system models and their coupling to climate models, and point out directions for future work.

Keywords Glacier · Ice sheet · Numerical modeling

H. Blatter (✉)
Institute for Atmospheric and Climate Science, ETH Zurich,
Universitätstrasse 16, 8092 Zurich, Switzerland
e-mail: blatter@env.ethz.ch

R. Greve
Institute of Low Temperature Science, Hokkaido University, Kita-19,
Nishi-8, Kita-ku, Sapporo 060-0819, Japan
e-mail: greve@lowtem.hokudai.ac.jp

A. Abe-Ouchi
Atmosphere and Ocean Research Institute, The University of Tokyo,
5-1-5 Kashiwanoha, Kashiwa 277-8568, Japan
e-mail: abeouchi@aori.u-tokyo.ac.jp

1 Introduction

Ice sheets (with their attached ice shelves), ice caps and glaciers are an important dynamic part of the Earth's climate system on time scales of decades and more. Most of the terrestrial freshwater reserves are stored in these ice masses, and they amount to more than 60 m of sea level equivalent. Against the background of ongoing global warming, research into the behaviour of ice sheets and glaciers is of great relevance. Some basic observational data are summarised in Table 1.

In Chap. 10 ("Global Climate Projections") of the Fourth Assessment Report (AR4) of the United Nations Intergovernmental Panel on Climate Change (IPCC), an increase of the mean global sea level by 18–59 cm for the twentyfirst century is projected for the SRES (Special Report on Emissions Scenarios) marker scenarios (Meehl et al. 2007). The main causes are thermal expansion of ocean water and melting of glaciers and ice caps, and to a lesser extent changes of the surface mass balance of the Greenland and Antarctic ice sheets. However, recent observations suggest that ice flow dynamics could lead to significant additional sea level rise, as stated explicitly in the AR4: "Dynamical processes related to ice flow not included in current models but suggested by recent observations could increase the vulnerability of the ice sheets to warming, increasing future sea level rise. Understanding of these processes is limited and there is no consensus on their magnitude." (IPCC 2007). This illustrates the importance of ice sheet and glacier models, and further improvement of them, for assessing the impact of future climate change, and for that reason it is a very "hot topic".

Numerical models may be classified as *process models* (Fowler 2001) or *explanatory models* (Murray 2002) on the one hand, and *system models* (Fowler 2001) or *numerical simulations* (Murray 2002) on the other. The first are generally simplified models designed to focus specific processes. The latter are required to simulate the evolution of ice sheets in a given climate, as sketched in Fig. 1.

The large ice sheets constitute systems with complex interactions with bounding external systems such as the atmosphere, ocean and lithosphere. Smaller glaciers generally constitute a simpler system than the large ice sheets in terms of coupled external systems; however, the flow field is more demanding in terms of computational requirements.

The reason for this difference lies in the fact that the aspect ratio ε, ratio of vertical extent to horizontal extent of the ice mass, is of the order $\varepsilon = 10^{-3}$ for large ice sheets, but $\varepsilon = 10^{-1}$ for small glaciers. The shallowness of large ice sheets allows for a corresponding approximation that omits horizontal coupling. However, this *shallow ice approximation* has to be taken with caution if processes on smaller scales or with large horizontal gradients are considered, such as basal sliding/non-sliding transitions, rough bed topography or shear margins at ice sheet/ice stream transitions. The *process aspect ratio* ε_p, ratio of local ice

Table 1 Ice inventory on the present-day Earth (Lemke et al. 2007; Bindoff et al. 2007)

	Glaciers and ice caps	Greenland ice sheet	Antarctic ice sheet (+ice shelves)
Area (10^6 km^2)	0.51–0.54	1.7	12.3 (+1.5)
Volume (10^6 km^3)	0.05–0.13	2.9	24.7 (+0.7)
Sea level equivalent (m)	0.15–0.37	7.3	56.6 (+0)
Sea level rise 1993–2003 (mm a^{-1})	0.77 ± 0.22	0.21 ± 0.07	0.21 ± 0.35

Note the large contribution of glaciers and ice caps to current sea level rise despite their small volume

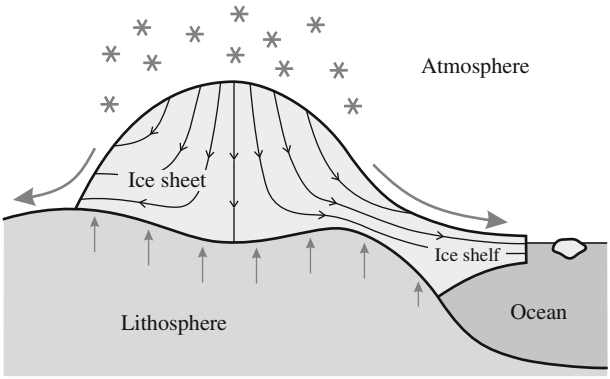

Fig. 1 Schematic of an ice sheet (with attached ice shelf) in the climate system. Gravity-driven glacial flow transports the ice from the central areas towards the margins. The ice sheet interacts with the atmosphere by precipitation (snowfall), surface temperature and surface melting. At the ice shelf-ocean interface, melting and freezing processes occur, and the ice shelf releases icebergs into the surrounding ocean ("calving"). Interaction with the lithosphere is by the geothermal heat flux entering the ice body from below, and by isostatic sinking and rebound. The vertical exaggeration factor is 200–500

thickness to horizontal scale length of the corresponding process, is generally larger, $\varepsilon_p \gg \varepsilon$, and thus the shallowness assumption no longer holds. A similar situation is given in models if the resolution of the horizontal grid becomes comparable to the local ice thickness. In this case, the *grid aspect ratio* ε_g, ratio of local thickness to horizontal grid spacing, may be of comparable magnitude to ε_p, and the shallowness assumption may also become unreliable.

Current ice sheet and glacier models are capable of simulating the continuous fields, velocity, temperature, surface and basal topography, to the correct magnitude. The accuracy, however, is critically affected by discontinuous processes such as sliding, calving, basal thermal and mechanical transitions, grounding lines, lateral margins. For long term simulations, the reliability of the model experiments also depends on the reliability of initial conditions and the transient boundary conditions.

Glacial systems may be considered stable if their change in volume is determined by the climatologically determined *mass flux time scale*, where the rate of volume changes is limited by the possible range of climatic accumulation and ablation rates. Internal discontinuous processes such as glacial hydraulics, sliding and calving, may lead to volume changes on much shorter time scales that may be referred to as *catastrophic time scale*. The latter processes will pose the greatest challenge for future ice sheet models, especially if the pressing question about the stability of the West Antarctic ice sheet must be answered.

This paper reviews the present state of ice sheet and glacier modelling and lists the present pressing questions concerning the dynamics of ice sheets and glaciers in the anticipated warming climate. The next section presents a summary of the Stokes problem of thermomechanically coupled ice flow, followed in Sect. 3 by a hierarchy of approximations presently in use. Discontinuities such as sliding, calving and the related issue of the stability of marine ice sheets are addressed in Sect. 4. Section 5 outlines the thermal and mechanical interaction of ice masses with the underlying solid Earth, which are relevant for the long term (10^5 years) dynamics of ice sheets during glacial cycles. In Sect. 6 we describe system models of ice sheets and glaciers, discuss the coupling with climate models of various sophistication and the possibilities to test the reliability of quantitative predictions. The concluding Sect. 7 outlines the currently pressing questions and topics, and the activities required to address them.

2 Full Stokes Flow Problem

Polycrystalline ice, as it occurs in ice sheets and glaciers, is described rheologically as an incompressible, nonlinear-viscous, heat-conducting fluid (e.g., Greve and Blatter 2009). The mass balance (continuity equation) thus reads

$$\operatorname{div} \mathbf{v} = 0, \tag{1}$$

where $\mathbf{v}$ is the velocity. Integration over the vertical coordinate z yields the evolution equation for the ice thickness $H(x, y, t)$ (horizontal coordinates x, y, time t)

$$\frac{\partial H}{\partial t} = -\operatorname{div} \mathbf{Q} + a_\mathrm{s} - a_\mathrm{b}, \tag{2}$$

where $\mathbf{Q}$ is the volume flux (vertically integrated horizontal velocity), and a_s and a_b are the mass balances at the surface (positive for supply) and the bottom (positive for loss), respectively. Equation (2) is the central evolution equation of glacier and ice sheet dynamics.

The deformation of ice is most commonly described by the nonlinear-viscous *Glen flow law*,

$$\mathsf{D} = \frac{1}{2\eta(T', \sigma_\mathrm{e})} \mathsf{t}^\mathrm{D}, \tag{3}$$

where $\mathsf{D} = \operatorname{sym} \operatorname{grad} \mathbf{v} = \frac{1}{2}(\operatorname{grad} \mathbf{v} + (\operatorname{grad} \mathbf{v})^T)$ is the strain-rate (stretching) tensor, t^D the deviatoric part of the Cauchy stress tensor t and η the shear viscosity. The fluidity (inverse viscosity) $1/\eta$ factorises as

$$\frac{1}{\eta(T', \sigma_\mathrm{e})} = 2EA(T')f(\sigma_\mathrm{e}), \tag{4}$$

where $T' = T - T_\mathrm{m} + T_0$ is the temperature relative to the pressure melting point T_m [$T_\mathrm{m} = T_0 - \beta\ p$; melting temperature at standard pressure $T_0 = 273.15$ K, Clausius–Clapeyron constant for air-saturated ice $\beta = 9.8 \times 10^{-8}$ K Pa^{-1}, pressure p], $A(T')$ the rate factor, $\sigma_\mathrm{e} = \sqrt{\frac{1}{2} \operatorname{tr}(\mathsf{t}^\mathrm{D})^2}$ the effective stress (square root of the second invariant of t^D), $f(\sigma_\mathrm{e})$ the creep function and E the flow enhancement factor (see below).

The rate factor and creep function are usually expressed in the form of an *Arrhenius law*

$$A(T') = A_0 e^{-Q/RT'} \tag{5}$$

(A_0: pre-exponential constant, Q: activation energy, $R = 8.314$ J mol^{-1} K^{-1}: universal gas constant), and a *power law*,

$$f(\sigma_\mathrm{e}) = \sigma_\mathrm{e}^{n-1} \tag{6}$$

(n: stress exponent), respectively (Table 2).

The inverse form of Glen's flow law (3) with the fluidity factorisation (4) and the power law (6) is

$$\mathsf{t}^\mathrm{D} = 2\eta(T', d_\mathrm{e})\mathsf{D}, \tag{7}$$

where $d_\mathrm{e} = \sqrt{\frac{1}{2} \operatorname{tr} \mathsf{D}^2}$ is the effective strain rate (square root of the second invariant of D). The viscosity η now factorises as

Table 2 Parameters for the Arrhenius law (5) and the power law (6) (Paterson 1994; Greve and Blatter 2009)

Parameter	Value	
Pre-exponential constant (A_0)	3.985×10^{-13} s^{-1} Pa^{-3}	(for $T' \leq 263.15$ K)
	1.916×10^{3} s^{-1} Pa^{-3}	(for $T' > 263.15$ K)
Activation energy (Q)	60 kJ mol^{-1}	(for $T' \leq 263.15$ K)
	139 kJ mol^{-1}	(for $T' > 263.15$ K)
Stress exponent (n)	3	

$$\eta(T', d_e) = \frac{1}{2} E_s B(T') d_e^{-(1-1/n)}, \tag{8}$$

where $B(T') = A(T')^{-1/n}$ is the associated rate factor and $E_s = E^{-1/n}$ the stress enhancement factor.

The flow enhancement factor E is equal to unity for *secondary creep* of pure, macroscopically isotropic polycrystalline ice (that is, the ice crystallites, a.k.a. grains, in the polycrystalline aggregate are randomly oriented). However, in regions of flowing ice sheets and glaciers with relatively high temperatures and/or stresses, *tertiary creep* may prevail, which goes along with the formation of an anisotropic fabric (non-uniform orientation distribution of the crystallites) favourable for the deformation regime at hand. A crude way of including this effect in the flow law is by multiplying the isotropic ice fluidity for secondary creep by a flow enhancement factor $E > 1$ chosen in an *ad-hoc* fashion (e.g., Hooke 2005). More sophisticated models attempt at describing the evolution of anisotropy and its effect on ice deformation macroscopically (phenomenologically) or even on the microscopic scale. This leads to modified flow laws that either provide a flow enhancement factor depending on the anisotropic fabric, or replace the scalar relation (collinearity) between the tensors t^D and D by a tensorial one (e.g., Gagliardini et al. 2009; Greve and Blatter 2009).

Another potential limitation of Glen's flow law lies in the use of the power law (6) with a single stress exponent. This is justified by the simplifying assumption that, under the stress, strain rate and temperature conditions typically prevailing in glaciers and ice sheets, a single microscopic creep mechanism (dislocation creep) is dominant. In reality, ice deformation results from a combination of creep mechanisms with different stress exponents (e.g., Alley 1992; Langdon 1996; Goldsby and Kohlstedt 2001; Pettit and Waddington, 2003), and thus the creep function may be expressed as a sum of different powers of the effective stress. However, there is no consensus about which additional terms should be considered, and because of that Cuffey and Paterson (2010) recommend to stick to the simple power law (6) with $n = 3$.

Scaling arguments show that, in contrast to atmosphere and ocean dynamics, the acceleration (inertia) term and the Coriolis force can be neglected in the momentum balance (e.g., Greve and Blatter 2009), so that it reduces to the force balance

$$\operatorname{div} \mathsf{t} + \rho \mathbf{g} = \mathbf{0}, \tag{9}$$

where $\rho = 910$ kg m^{-3} is the density of ice and $\mathbf{g}$ the downward-pointing gravitational acceleration with the value $g = |\mathbf{g}| = 9.81$ m s^{-2}. Combining the force balance (9) with the decomposition of the stress tensor

$$\mathsf{t} = -p\mathsf{I} + \mathsf{t}^{\mathrm{D}} \tag{10}$$

(where p is the pressure and I the unit tensor) and the flow law in the form of Eq. (7) yields the *Stokes equation*

$$-\mathrm{grad}\, p + \mathrm{div}\left[\eta(T', d_{\mathrm{e}})\left(\mathrm{grad}\mathbf{v} + (\mathrm{grad}\mathbf{v})^{\mathrm{T}}\right)\right] + \rho\mathbf{g} = \mathbf{0}, \tag{11}$$

which is the equation of motion for ice flow. Owing to the dependency of the viscosity η on the velocity $\mathbf{v}$ via the effective strain rate d_{e}, it is non-linear in $\mathbf{v}$.

From the general energy balance, Fourier's law of heat conduction

$$\mathbf{q} = -\kappa(T)\mathrm{grad}\, T \tag{12}$$

($\mathbf{q}$: heat flux, κ: heat conductivity, see Table 3) and the caloric equation of state

$$u = \int_{T_0}^{T} c(\bar{T})\mathrm{d}\bar{T} \tag{13}$$

(u: specific internal energy, c: specific heat, see Table 3), the temperature evolution equation

$$\rho c\left(\frac{\partial T}{\partial t} + \mathbf{v}\cdot\mathrm{grad}\, T\right) = \mathrm{div}(\kappa\mathrm{grad}\, T) + 4\eta d_{\mathrm{e}}^2 \tag{14}$$

results. In this relation, the production term $\mathrm{tr}(\mathsf{t}^{\mathrm{D}}\cdot\mathsf{D}) = 4\eta d_{\mathrm{e}}^2$ is the strain heating, and volumetric heating due to radiation has been neglected.

The above equations need to be complemented by dynamic and thermodynamic boundary conditions at the surface and the bottom of the respective ice body. Since the surface is in contact with the atmosphere, it can be described in good approximation as stress-free, that is,

$$\mathsf{t}\cdot\mathbf{n}\big|_{\mathrm{s}} = \mathbf{0}, \tag{15}$$

where $\mathbf{n}$ is the outer unit normal vector, and the subscript "s" denotes the surface. The surface temperature T_{s} can be prescribed directly as a Dirichlet condition.

If the bottom is a sufficiently cold ice/rock or ice/sediment interface, the basal ice is essentially frozen to the underlying substrate, and a no-slip condition can be employed,

$$\mathbf{v}_{\mathrm{b}} = \mathbf{0}, \tag{16}$$

where the subscript "b" stands for the ice base. By contrast, if the basal temperature is at or close to the pressure melting point, basal sliding will occur and must be parameterised by an empirical sliding law. This will be discussed in more detail below (Sect. 4.1).

Table 3 Heat conductivity κ and specific heat c (Ritz 1987; Greve and Blatter 2009)

Parameter	Value
Heat conductivity (κ)	$9.828\, e^{-0.0057\, T[\mathrm{K}]}$ W m$^{-1}K^{-1}$
Specific heat (c)	(146.3 + 7.253 T[K]) J kg^{-1}K^{-1}

As for the temperature field, let us assume that the geothermal heat flux that enters the ice body from below ($\mathbf{q}_{\mathrm{geo}}$) is known. Provided that the basal temperature is below the melting point and sliding is negligible, this yields the Neumann condition

$$\kappa \frac{\partial T}{\partial \mathbf{n}}\bigg|_{\mathrm{b}} = \mathbf{q}_{\mathrm{geo}}, \tag{17}$$

where $\mathbf{n}$ is again the outer unit normal vector. If the basal temperature is at pressure melting, this statement itself serves as a boundary condition,

$$T_{\mathrm{b}} = (T_{\mathrm{m}})_{\mathrm{b}} = T_0 - \beta p_{\mathrm{b}}, \tag{18}$$

where p_{b} is the basal pressure.

For the case of floating ice shelves, the basal boundary conditions must be changed. Instead of the no-slip condition (16) or an empirical sliding law, a stress condition holds that equals the basal stress $\mathbf{t} \cdot \mathbf{n}|_{\mathrm{b}}$ to the hydrostatic pressure of the sea water below the ice. The temperature conditions (17) or (18) are replaced by the statement that the basal temperature is equal to the freezing temperature of the sea water below the ice.

3 Hierarchy of Approximations

The full Stokes formulation is applicable to grounded ice sheets, ice caps and glaciers of all sizes as well as floating ice shelves. However, its numerical solution is demanding and computationally expensive. Therefore, it is desirable to derive suitable approximations that make use of the specific properties of the different systems. Specifically, the global geometric aspect ratio

$$\varepsilon = \frac{[H]}{[L]} \tag{19}$$

(where $[H]$ and $[L]$ are scales for the vertical and horizontal extents, respectively, of the ice body in question) can be used to truncate the Stokes equation in different order approximations. However, ice sheet and glacier dynamics are largely determined by other scale lengths such as smaller-scale variations in the bed topography or variations in the bed conditions, or even discontinuities. Thus, the applied approximation must be chosen to meet the requirements of the scales of the modelled processes. These global or local geometric aspect ratios, however, do not exclusively define the mode of operation of an ice mass, but the *slip ratio*, the ratio of the sliding velocity to the shear velocity, defines a second characteristic parameter:

$$\varepsilon_{\mathrm{s}} = \frac{[U_{\mathrm{b}}]}{[U_{\mathrm{d}}]} \tag{20}$$

(where $[U_{\mathrm{b}}]$ and $[U_{\mathrm{d}}]$ are scales for the basal sliding and internal deformation (shear) velocities, respectively). Of the two extreme cases, small aspect ratio and small slip ratio ($\varepsilon \ll 1$, $\varepsilon_{\mathrm{s}} \ll 1$) are well described by the *shallow ice approximation* (Sect. 3.2), whereas small aspect ratio and large slip ratio ($\varepsilon \ll 1$, $\varepsilon_{\mathrm{s}} \gg 1$) define a membrane flow, of which the *shallow shelf approximation* (Sect. 3.3) is a known example.

3.1 Higher Order Approximations

The largest portion of terrestrial ice is locked in ice sheets and glaciers with a horizontal extent [L] that is much larger than the vertical extent [H]. Thus, the geometric aspect ratio $\varepsilon \ll 1$, and this fact gives the motivation for a hierarchy of approximations. A detailed account of the approximations is given, for example, in Greve and Blatter (2009). Here, an overview is presented.

In Cartesian coordinates (x, y, z), where x, y and z are the two horizontal and the vertical coordinates, respectively, the components of the force balance (9) are

$$\begin{aligned} \frac{\partial t_{xx}}{\partial x} + \frac{\partial t_{xy}}{\partial y} + \frac{\partial t_{xz}}{\partial z} &= 0, \\ \frac{\partial t_{xy}}{\partial x} + \frac{\partial t_{yy}}{\partial y} + \frac{\partial t_{yz}}{\partial z} &= 0, \\ \frac{\partial t_{xz}}{\partial x} + \frac{\partial t_{yz}}{\partial y} + \frac{\partial t_{zz}}{\partial z} &= \rho g, \end{aligned} \tag{21}$$

where the $t_{\alpha\beta}$ are the corresponding components of the Cauchy stress tensor $\mathbf{t}$. Omitting the small horizontal derivatives of the shear stresses in Eq. $(21)_3$ results in the hydrostatic equation

$$t_{zz} = -\rho g(h - z). \tag{22}$$

Eliminating the non-deviatoric stress components yields the equations for the force balance written in deviatoric stress components (t^{D}_{xx}, t^{D}_{yy}) only,

$$\begin{aligned} 2\frac{\partial t^{\mathrm{D}}_{xx}}{\partial x} + \frac{\partial t^{\mathrm{D}}_{yy}}{\partial x} + \frac{\partial t_{xy}}{\partial y} + \frac{\partial t_{xz}}{\partial z} &= \rho g \frac{\partial h}{\partial x}, \\ 2\frac{\partial t^{\mathrm{D}}_{yy}}{\partial y} + \frac{\partial t^{\mathrm{D}}_{xx}}{\partial y} + \frac{\partial t_{xy}}{\partial x} + \frac{\partial t_{yz}}{\partial z} &= \rho g \frac{\partial h}{\partial y}. \end{aligned} \tag{23}$$

Substituting Glen's flow parameterisation, Eqs. (7) and (8), in the hydrostatic version of Eq. (21) results in two equations with the three velocity components v_x, v_y and v_z,

$$\begin{aligned} 4\frac{\partial}{\partial x}\left(\eta\frac{\partial v_x}{\partial x}\right) + 2\frac{\partial}{\partial x}\left(\eta\frac{\partial v_y}{\partial y}\right) + \frac{\partial}{\partial y}\left(\eta\left(\frac{\partial v_x}{\partial y} + \frac{\partial v_y}{\partial x}\right)\right) + \frac{\partial}{\partial z}\left(\eta\left(\frac{\partial v_x}{\partial z} + \frac{\partial v_z}{\partial x}\right)\right) &= \rho g \frac{\partial h}{\partial x}, \\ 4\frac{\partial}{\partial y}\left(\eta\frac{\partial v_y}{\partial y}\right) + 2\frac{\partial}{\partial y}\left(\eta\frac{\partial v_x}{\partial x}\right) + \frac{\partial}{\partial x}\left(\eta\left(\frac{\partial v_x}{\partial y} + \frac{\partial v_y}{\partial x}\right)\right) + \frac{\partial}{\partial z}\left(\eta\left(\frac{\partial v_y}{\partial z} + \frac{\partial v_z}{\partial y}\right)\right) &= \rho g \frac{\partial h}{\partial y}. \end{aligned} \tag{24}$$

Thus Eq. (24) must be solved simultaneously with the continuity equation (1). This *hydrostatic approximation* can be done for grounded ice sheets and floating ice shelves alike.

The next step of approximation is only valid for grounded ice sheets and glaciers, and applies the assumption that the vertical velocity component v_z scales with geometric aspect ratio to the horizontal velocity components v_x and v_y, thus the ratios of the horizontal gradients of v_z to the vertical gradients of the horizontal velocity components are order ε^2 (Greve and Blatter 2009). This approximation is sometimes called *first-order approximation* (Blatter 1995) and is shown to

reproduce the solution to the underlying Stokes equations to second order in the film's aspect ratio, regardless of the amount of slip at the base of the fluid (Schoof and Hindmarsh 2010).

With this assumption all terms in the hydrostatic approximation, Eq. (24), containing v_z are omitted. The resulting two equations contain only the two horizontal velocity components v_x and v_y, and can be solved independently of the continuity equation (1). There is no equivalent to this first-order approximation for floating ice shelves.

3.2 Shallow Ice Approximation

The above hydrostatic and first order approximations still consider horizontal derivatives of the velocity components, and thus consider all shear and deviatoric stress components. The *shallow ice approximation* (Hutter 1983; Morland 1984) omits the so called *membrane stresses* (Hindmarsh 2006b), and thus the deviatoric stresses t^{D}_{xx} and t^{D}_{yy}, and the shear stress component in the vertical plane, t_{xy}. The separation of *membrane stresses* and *horizontal shear stresses* defines the two extremes, the *shallow ice approximation* (SIA) and the *shallow shelf approximation* (SSA). The SIA omits the membrane stresses due to the shallowness assumption and large friction at the bed, the SSA omits the horizontal shear stresses due to shallowness and mostly free basal slip.

The assumption that the deviatoric components t^{D}_{xx} and t^{D}_{yy}, the shear stress component t_{xy} and their gradients are negligibly small in Eq. (23) yields

$$\begin{aligned} \frac{\partial t_{xz}}{\partial z} &= \rho g \frac{\partial h}{\partial x}, \\ \frac{\partial t_{yz}}{\partial z} &= \rho g \frac{\partial h}{\partial y}, \end{aligned} \tag{25}$$

and Glen's flow law reduces to

$$\begin{aligned} \frac{\partial v_x}{\partial z} &= 2A(T')\sigma_{\mathrm{e}}^{n-1} t_{xz}, \\ \frac{\partial v_y}{\partial z} &= 2A(T')\sigma_{\mathrm{e}}^{n-1} t_{yz}. \end{aligned} \tag{26}$$

This shallow ice approximation is widely used in present-day ice sheet models. Equations (25) and (26) reduce the dependencies of t_{xz}, t_{yz}, v_x and v_y to the depth below the ice surface and the inclination of the ice surface in the respective directions. The equations can be integrated such that the velocity components can be computed by quadratures,

$$\begin{aligned} v_x &= v_{\mathrm{bx}} - 2(\rho g)^n |\mathrm{grad}\, h|^{n-1} \frac{\partial h}{\partial x} \int_b^z A(T')(h-\bar{z})^n \mathrm{d}\bar{z}, \\ v_y &= v_{\mathrm{by}} - 2(\rho g)^n |\mathrm{grad}\, h|^{n-1} \frac{\partial h}{\partial y} \int_b^z A(T')(h-\bar{z})^n \mathrm{d}\bar{z}, \end{aligned} \tag{27}$$

where v_{bx} and v_{by} are the respective velocities at the ice base.

3.3 Shallow Shelf Approximation

For shallow ice shelves, the hydrostatic approximation follow the same arguments as those for the ice sheet flow and is also given by Eq. (24). The *shallow shelf approximation* (Morland 1987; Weis et al. 1999) assumes that a plug flow (very large slip ratio) approximates the velocity field closely in the membrane-type situation with almost vanishing shear tractions at both the upper and lower boundary of the plate,

$$\frac{\partial v_x}{\partial z} \approx 0, \quad \frac{\partial v_y}{\partial z} \approx 0. \tag{28}$$

With these assumptions, the vertically integrated force balance equation (23) becomes

$$\begin{aligned} 4\frac{\partial}{\partial x}\left(\bar{\eta}\frac{\partial v_x}{\partial x}\right) + 2\frac{\partial}{\partial x}\left(\bar{\eta}\frac{\partial v_y}{\partial y}\right) + \frac{\partial}{\partial y}\left(\bar{\eta}\left(\frac{\partial v_x}{\partial y} + \frac{\partial v_y}{\partial x}\right)\right) &= \rho g H \frac{\partial h}{\partial x}, \\ 4\frac{\partial}{\partial y}\left(\bar{\eta}\frac{\partial v_y}{\partial y}\right) + 2\frac{\partial}{\partial y}\left(\bar{\eta}\frac{\partial v_x}{\partial x}\right) + \frac{\partial}{\partial x}\left(\bar{\eta}\left(\frac{\partial v_x}{\partial y} + \frac{\partial v_y}{\partial x}\right)\right) &= \rho g H \frac{\partial h}{\partial y}, \end{aligned} \tag{29}$$

where $\bar{\eta}$ is the vertically integrated viscosity of the ice and H the local ice thickness. A detailed account of the derivation of these equations is given, for example, in Greve and Blatter (2009). Equation (29) is not *incompressible* in the horizontal plane since vertical ice flow determines the changes of the thickness of the ice plate. These equations must be complemented by the mass continuity equation and boundary conditions at the upper and lower surface, at the grounding line and at the calving front. The shallow shelf approximation allows for a simple formulation of the contact problem at the grounding line by using the *floating condition*.

3.4 Accuracy of Approximations

Approximations are mostly motivated by the limitations of computing power or the availability of efficient, stable and accurate numerical algorithms to solve the system of generally non-linear equations in question. The definition of the accuracy of approximations is essentially defined by the purpose of the model, either simulation (system) models or explanatory models (Fowler 2001). The primary goal of most system models is the computation of the evolution of the distributed ice thickness; thus the accuracy of the ice flow is most essential. In three-dimensional models, the ice flow ($\mathbf{Q}$ in Eq. 2) is computed by integration of the vertical profiles of the horizontal velocity component, whereas in vertically integrated models, the ice flow is a direct result of the vertically integrated model equations and the details of the velocity field are not explicitly computed. The determination of the accuracy of the latter models and their predictive power is thus more difficult.

In this section, we do not consider the verification of the numerical schemes. Considering the *accuracy* of approximations, the focus lies on a comparison of approximations to an *exact* solution of the equations such as the full Stokes equation. It must be ensured that in such a comparison neither the approximation nor the exact solution are *polluted* by significant errors in the numerical solutions.

Several studies investigated the accuracy of approximations of the Stokes equation at a range of wavelengths of the perturbations (Hindmarsh 2004, 2006a, b; Gudmundsson 2008; Schoof and Hindmarsh 2010); however, thus far only for isothermal ice flow. Since most of the approximations in consideration exploit the shallowness of the ice masses, the

approximations should be considered an expansion of the Stokes equations in terms of the global geometric aspect ratio.

The results of Hindmarsh (2004, 2006a) and Gudmundsson (2003) show a clear deviation of all approximations from the full Stokes solutions for shorter wavelength perturbations. The shallow ice approximation apparently starts to deviate from Stokes solutions at wavelengths shorter than 10^2 to 10^1, where the unit is given by the local ice thickness. Higher order solutions start to deviate at wavelengths below 5 to 10. This fact requires careful analysis of model results if dynamical or geometrical patterns of corresponding small scales are to be resolved. The possible accuracy is thus not only given by the *global* geometric aspect ratio ε, but, in realistic glacial systems, as well by *local* aspects ratios defined by local conditions. This may be expected to become a concern in shallow ice models if the resolution of horizontal grids is increased, such that the *grid* aspect ratio (ratio of vertical resolution to horizontal resolution) becomes substantially larger than the global geometric aspect ratio.

4 Discontinuous Processes

4.1 Basal Sliding

One difficulty in ice sheet modelling is the large range of possible sliding velocities such as between no sliding conditions at cold bases through slow sliding in the normal ice flow mode to fast sliding in ice streams. Basal friction may depend on largely different basal conditions such as rough hard beds to smoother sediment beds, or even perfect lubrication over subglacial lakes. Different types of sliding parameterisations stem from different underlying physical models of the sliding process itself; thus it is likely that one single sliding paramterisation may not be adequate for modelling the entire ice sheet.

The *Weertman-type sliding parameterisation* (Weertman 1957, 1964, 1971) is based on the assumption that the sole of the ice slides frictionlessly over a rough bed with a roughness with a wavelength considerably smaller than the local ice thickness. Thus, the sliding is described as the spatial mean velocity of the ice over a fictitious basal plane, averaged over a spatial area considerably larger than the roughness elements. This mean sliding velocity is determined by the resistance of the mean bed induced by the deformation of the ice across and around the roughness elements (Hutter 1983). The resulting resistance relates the mean sliding velocity to a power of the mean basal shear traction as can be anticipated from dimensional analysis (Gudmundsson 1994a; Greve and Blatter 2009) or determined by numerical modelling applying the Stokes equation for a fluid flowing over a wavy bed (Gudmundsson 1994a, b),

$$v_\mathrm{b} = C_1 \tau_\mathrm{b}^n, \tag{30}$$

where C_1 is a parameter defined by the roughness. The roughness can be modified by pressurised water at the bed such that the ice separates from the bed and sees a smaller effective amplitude of roughness, thus

$$v_\mathrm{b} = C_2 \frac{\tau_\mathrm{b}^n}{p_\mathrm{eff}}. \tag{31}$$

where the effective pressure $p_\mathrm{eff} = p_\mathrm{b} - p_\mathrm{w}$ is defined by the difference of the basal hydrostatic pressure p_b of the ice and the water pressure p_w in the basal hydraulic system,

and C_2 is a tunable coefficient. The direction of the basal velocity vector is always parallel to the basal shear traction, i.e., to the tangential component of the stress vector at the base.

Such Weertman-type sliding parameterisation has been implemented in many ice flow models of different approximations, in particular in shallow ice sheet models. The shallowness assumption implies that the stress field is a function of the local geometry alone and the velocity field additionally depends on the local temperature profile. Thus, sliding does not feedback on these fields except weakly through the slowly varying temperature field and the evolving geometry and its influence on the driving stress.

The fact that sliding in a SIA model does not feedback to the local nor the neighbouring stress profiles implies a singularity at the bed position where the criterion from non-sliding switches to sliding or vice versa, e.g., where the basal temperature has a cold/temperate transition (Fowler 2001). Stress only remains bounded if the velocity is continuous, which is a necessary condition for obvious reasons, and the second derivative of the horizontal velocity components with respect to the horizontal coordinates is finite (Blatter 1995). In numerical shallow ice sheet models, this singularity is hidden in the discretisation grids (Bueler and Brown 2009), especially at low resolution. With increasing computing power, higher resolution models become feasible and this issue may become a problem of accuracy and stability if processes with large gradients in the fields are resolved.

The *Weertman-type sliding parameterisation* has been implemented in higher order and full Stokes flow models in various ways. Direct implementations of the sliding parameterisation have been implemented through the discretisation scheme for basal grid point or mesh cells (Jouvet et al. 2009). One possibility is the inclusion of a homogeneous deforming shallow layer at the bottom of the ice, with no sliding between the ice sole and the layer and no sliding between the layer and the underlying bed (Vieli et al. 2001). The resulting relation between the tangential velocity component and the shear traction at the ice sole depends on the assumed rheology of the shallow layer. The Weertman-type power law with exponent n results if a power law stress strain-rate relation with exponent n for the layer is applied (Vieli et al. 2001; Greve and Blatter 2009).

In the above shallow layer implementation for sliding, the layer only shears in the horizontal plane; however, stress coupling in the horizontal direction is not included. If the shallow layer sliding model is coupled to higher order and full Stokes models, the membrane stresses are handled internally in the flow domain and the sliding parameterisation only handles the local stress strain-rate relation. If this sliding implementation is coupled to a SIA ice sheet model, it can not feedback to its shear velocity or handle the horizontal stress coupling.

A hybrid scheme is proposed by Bueler and Brown (2009) by implementing a similar idea for models in the shallow ice approximation: the ice sheet model yields the driving stress, a basal thin layer model handles the resistive basal shear stress, $\mathbf{t}_\mathrm{b}$, and a membrane balances the driving stress and the shear stress. To introduce the shallow shelf approximation as a sliding parameterisation, the shear stress is added to the right side of Eq. (29). The basal shear stress $\mathbf{t}_\mathrm{b}$ must be parameterised by a flow model for the basal thin layer corresponding to the envisaged basal sliding, and can depend on various physical quantities such as yield stress or water pressure in the layer.

This sliding parameterization does not feedback on the shear velocity in the local vertical profile of the shallow ice model. High sliding velocity corresponds to low friction and consequently to low basal shear stress. A weighted average of the velocities of the three-dimensional non-sliding shallow ice approximation and the velocities in the membrane was suggested by Bueler and Brown (2009) to consider the influence of basal sliding conditions on the velocity profile. However, the shallow ice approximation gives no

information on the weighting factor, except for non slip conditions the weight starts at one for the shear velocity and zero for sliding, and goes to zero for the shear velocity and to one for sliding for very large basal velocities. This scheme also avoids problems associated with the singularity at slip/no-slip transitions mentioned above and it allows for handling large ranges of sliding velocities as demonstrated with the Parallel Ice Sheet Model Greenland model for ice streams (Bueler et al. 2010).

Sliding remains a critical issue. One reason is the difficulty in observing sliding and the basal conditions directly. A second reason is that sliding can be highly variable on short temporal and spatial scales. Furthermore, sliding velocities can not be determined on a spatial resolution better than about one to two local ice thicknesses for objective reasons by inverse methods using surface observations (Bahr et al. 1994; Truffer 2004).

4.2 Calving

On the Greenland ice sheet, calving accounts to about 47% of the total annual mass loss besides surface and bottom melt (Ohmura 2010). The corresponding number seems to be somewhat larger for Antarctica but is more difficult to estimate. Calving is a process which is not directly coupled to the actual climatic conditions and may lead to mass loss on much shorter time scales than ablation through climate controlled melt. As a discontinuous process, calving is difficult to quantify in numerical models that can not resolve its temporal and spatial scales.

4.2.1 Grounded Ice

Glaciers may calve into freshwater lakes and into sea water. Due to the difference in the densities of fresh and salty water, calving may be slightly different due to processes such as frontal melt and convection in the water in front of the ice cliff. Especially glaciers with mostly temperate basal ice are resting entirely, including the calving front, on the solid bed.

A few grounded calving fronts have been observed over time periods of decades, such as Columbia Glacier, Alaska (Krimmel 2001) and Hansbreen, Spitsbergen (Vieli et al. 2002). These observations clearly reveal a connection between the calving rate and resulting advance or retreat rates and the bed geometry (Van der Veen 1996). Front positions on beds sloping downwards in the flow direction seem to be stable whereas, on upsloping beds, stable front positions may not be possible. One process that may explain this behaviour is buoyancy, which directly depends on the water depth at the calving front. However, buoyancy requires that the pressure of the sea water is transmitted below the ice at least to some distance, which is perhaps only possible over distributed areas if the glacier bed is temperate.

Model studies could reproduce these patterns of retreating and advancing grounded calving tongues over an undulating bed by applying a calving parameterisation related to an ice thickness above floatation (Vieli et al. 2000, 2001). For Hansbreen, Spitsbergen, the time scales of the modelled fast retreats over bed depressions correspond well with observed retreat rates (Vieli et al. 2002).

Nick et al. (2007) applied a simplified model to Columbia Glacier, Alaska, and confirmed the importance of bed geometry for calving rates, especially if moraines modify the bed topography near the calving front. Their results indicate that stable equilibria may not exist on backsloping beds; however, the results are not entirely conclusive.

Tidewater and freshwater glaciers may not become floating if only buoyancy would control the calving rate, such as applied in models with simple buoyancy related calving

parameterisations. A different approach has been taken by Benn et al. (2007). Following Nye (1957), the crevasse depths is parameterised with a depth

> where the longitudinal tensile strain rate exactly balances creep closure resulting from ice overburden pressure (Benn et al. 2007)

and the calving front is located where the crevasse depth reaches sea level. This may happen for both grounded and floating conditions.

The above model approaches to handle calving must be considered parameterisations. A novel suggestion to model calving may be given by *damage mechanics* (Pralong et al. 2003, 2006; Pralong and Funk 2005), which may be included into full Stokes flow models. Damage denotes a continuous field that is defined by source and sink terms related to the stress field, as formulated by Pralong and Funk (2005):

> The damage is described by a state variable D (called *damage variable*), which is defined through the change in rheological properties with increasing material deterioration (Kachanov 1999). The value of the damage variable is therefore determined with regard to the effects of the micro-defects on the mesoscopic response of the material (Krajcinovic 1996).

The magnitude of the damage defines the strength or weakness of the ice, a highly damaged zone is much less viscous and the density is small. Sources for damage are given by large stresses, sinks must be parameterised by additional conditions, which may be difficult to identify, to let ice recover to normal strength. Two-dimensional flow models including damage were successfully applied to crevasse opening and triggering ice avalanches (Pralong et al. 2003; Pralong and Funk 2005). One version of a two-dimensional model including the acceleration term in the force balance qualitatively reproduced the calving of a grounded terminus. When the viscosity in the damaged zone becomes small enough, the system becomes unstable and the calving piece of ice slides rapidly over the damaged zone (Jouvet 2010).

4.2.2 Floating Ice

In most ice sheet models, the floating ice shelves are treated with the shallow shelf approximation; however, the boundary conditions at the margins, (a) grounding line, (b) coastline, (c) ice rise margins and (d) calving front (Weis et al. 1999) require treatment that is beyond the possibilities of the approximation. In particular, the calving front is sometimes not treated explicitly and the ice shelf extends to the margin of the numerical grid (Huybrechts 1990) or the ice shelf is cut off at a given ice thickness (Ritz et al. 2001) or at the grounding line (Saito and Abe-Ouchi 2004; PISM, http://www.pism-docs.org/).

Ice shelves are the parts of ice sheets where the contact to ocean water establishes an important boundary that may control the dynamics and the stability of the larger glacial system. In view of this complexity, existing ice shelf models must be considered as *process models*. The ice shelf-ocean coupling involves not only the floating condition but may also contribute substantially to the mass budget at the ice base (Nøst and Foldvik 1994; Grosfeld and Sandhäger 2004). Depending on thermal conditions and flow of ocean water, the water-ice interaction may lead to both melting and freezing at the base. Melting at the ice base produces a layer of fresh water that may flow upwards towards the margin and become supercooled and form ice platelets with decreasing pressure. This ice may accumulate at the base and thus further contribute to the accumulation. The increased buoyancy due to the ice platelets in the ocean water, an *ice shelf plume* may form which feeds back to

the ocean circulation beneath the shelf (Lewis and Perkin 1986; Jenkins and Bombosch 1995; Smedsrud and Jenkins 2004).

Both grounded and floating calving thus far can only be handled by parameterisation. The primary problem lies in the fact that stress fields computed in models are only given at low resolution compared with the small scales on which the processes leading to calving work. This is especially true in shelves where fractures are triggered locally but progress over large distances and calve off large tabular ice bergs.

The Benn et al. (2007) calving law allows for both grounded and floating calving and the transition between both. Otero et al. (2010) extended the Benn et al. (2007) calving law to a three-dimensional glacier. They identified some weaknesses in the model related to basal sliding parameterisation and the parameterisation of crevasse depths; however, they also identified some possible improvement such as assuming a partial filling of crevasses with water, and the balancing at the crevasse bottom of the opening tensile deviatoric stress with the closing ice overburden pressure.

Several other observed processes may have to be considered in realistic floating calving models. Calving of tabular icebergs seems to be closely related to rift systems (Joughin and MacAyeal 2005), where rift widening seems to progress gradually but rift length increases episodically. A conceptual model, also related to rift formation, proposes rapid ice shelf disintegration due to bending stresses induced by calving along the shelf terminus (Scambos et al. 2009). The deepening of the new crevasses formed by the bending stress after the previous calving event is further supported by increased hydrostatic pressure due to increased amount of water in the crevasse (*hydro-fracture*) in a warming climate. Enhanced bottom melting in a warming climate may also carve substantial channels in the bottom of the ice shelf, thus may affect the mechanical strength of the shelf and support breaking of the ice (Rignot and Steffen 2008).

4.3 Stability of Marine Ice Sheets

Marine ice sheets or glaciers are in close contact with ocean water and are thus more exposed to possible instabilities than land based grounded glaciers. One possible situation of instability is related to grounding calving termini on reversely tilted glacier beds, where seemingly no stable equilibrium positions are possible (Vieli et al. 2001; 2002; Nick et al. 2007). Closely related to this is the situation of floating glacier tongues with a grounding line on a reversely tilted bed (Schoof 2007); however, this is under the assumption that the floating part only weakly feeds back on the dynamics of the grounding line. These results were found by using two-dimensional flowline models and do not consider other factors to be influencing the stability. There are indications that this partly applies to three-dimensional valley glaciers, e.g., Hansbreen, Spitsbergen (Vieli et al. 2002) and Columbia Glacier (Nick et al. 2007). However, Nick et al. (2010) show that stable equilibria may exist even if a grounded calving tongue or a grounding line lies on backsloping beds, if calving is determined by crevassing at the surface and at the bed, and not directly by buoyancy.

Thus far, the applied and presented full Stokes models of the ice sheet/ice shelf transition are two-dimensional (flowline) process models. Durand et al. (2009a) confirmed the hysteresis of Schoof (2007) in the grounding line dynamics; however, they also found a sensitivity of the grounding line position to the chosen horizontal grid resolution (Durand et al. 2009b), possibly making adaptive grid resolution a requirement for the modelling of the grounding line position and stability in large scale system models of Antarctica (Vieli and Payne 2005; Gladstone et al. 2009). The addition of melting below ice shelves and the

simulation of buttressing by including a lateral resistance to the force balances clearly demonstrate the strong influence of these additional factors to the grounding line dynamics (Walker et al. 2008; Goldberg et al. 2009; Gagliardini et al. 2010); however, also demonstrates the limitations of two-dimensional process models. They allow us to identify processes, such as basal melt, buttressing and basal flow conditions and topography, that are relevant for the dynamics and stability of marine ice sheets. For conclusive, quantitative and reliable predictions of the stability of West Antarctica, for example, considerably more complex models are required.

Large parts of the West Antarctic ice sheet are grounded well below sea level and laterally bounded by large floating ice shelves. This situation is certainly vulnerable to instabilities; however, despite the partly reverse tilt of the bed, additional features make it very difficult to conclusively judge the present day situation with respect to a possible runaway mass loss of the large ice shelves or even parts or the presently grounded West Antarctic ice sheet. Disintegration may mean break up of the floating parts of marine ice sheets as was observed in recent years on smaller ice shelves along the Antarctic peninsula. It may also mean that grounding lines move into critical regions where stable states are not possible. For large scale disintegration, both processes may have to work together such that floating parts break apart after grounding lines retreat inland, or vice versa, that ice shelf thinning due to bottom or surface melt or reduced advection leads to a migration of the grounding line into unstable positions. Thus, modelling of such breakup and retreat or collapse of marine ice sheets requires the treatment of these processes explicitly if a reliable prediction is to be obtained. The challenge is that these processes either act on small scales and must be treated by subgrid parameterisation (hydro-fracture, rift formation) or require the solution of the full equations without approximations, e.g., full Stokes for the force balance or plate bending stress (Scambos et al. 2009).

An additional feature that makes the interaction between ice sheet and ice shelf even more complex is the occurrence of ice streaming (Walker et al. 2009). Ice streams are dynamic systems, although their grounding lines seem to be relatively stable or moving only episodically between stable positions (Horgan and Anandakrishnan, 2006). A possible stabilising mechanism is the till deposition at the grounding line of ice streams (Anandakrishnan et al. 2007). There are also indications that ice streams are able to transmit changes in the floating part upstream on timescales of decades, i.e., more rapidly than at non-streaming parts (Payne et al. 2004). Thus the ice sheet/ocean coupling may become more important in ice streams. On the other hand, a shutdown of streaming may result from climatic warming, increased precipitation, resulting in larger advection rates (Verbitsky 2002). Thus, the response and stability of marine ice sheets in changing climates is not obvious, and

> Continued measurement of the evolving flow field, geophysical efforts to define the fjord geometry more precisely, and improved understanding of ocean/fjord/ice interactions will all improve our collective ability to model this (marine ice sheet) and similar systems (Joughin et al. 2008).

5 Interaction with the Solid Earth

5.1 Temperature Evolution in the Lithosphere

In time-dependent scenarios, the thermal inertia of the lithosphere dampens temperature changes in the deeper parts of a glacier or an ice sheet significantly. In order to account for

this effect, the temperature evolution in a thermal boundary layer of the lithosphere must be computed,

$$\rho_l c_l \left(\frac{\partial T}{\partial t} + \mathbf{v} \cdot \mathrm{grad}\, T \right) = \mathrm{div}(\kappa_l \mathrm{grad}\, T), \tag{32}$$

where ρ_l is the density, c_l the specific heat ($\rho_l c_l \sim 2,000$–$3,000\,\mathrm{kJ\,m^{-3}K^{-1}}$) and κ_l ($\sim 3\ \mathrm{Wm^{-1}\ K^{-1}}$) the heat conductivity of the lithospheric (crustal) material. This equation is similar to the temperature evolution equation (14) for ice; however, strain heating has been neglected. The horizontal component of the velocity $\mathbf{v}$ of the lithosphere is also negligible, whereas a vertical component arises from the displacement of the lithosphere due to glacial isostasy (see Sect. 5.2 below).

The thickness of the lithospheric thermal boundary layer to be considered depends on the time scale of imposed temperature changes at the surface. Ritz (1987) demonstrated that for climatological time scales $\leq$ 100 ka a thickness of 2 km is sufficient. If Eq. (32) is solved together with Eq. (14), the geothermal heat flux (Eq. 17) must be prescribed at the bottom of the lithospheric thermal boundary layer rather than at the ice base. Instead, temperature continuity is assumed between the ice and the lithosphere.

5.2 Glacial Isostasy

Glacial isostasy describes the process of restoring gravitational equilibrium between the Earth's lithosphere and the underlying asthenosphere under the influence of temporally and spatially varying ice loads. As a consequence, the lithosphere suffers an essentially vertical displacement $w(x, y, t)$ with respect to its unloaded equilibrium position (Fig. 2).

This process can be described in great detail by sophisticated self-gravitating, spherical, visco-elastic multi-layer (SGVE) models of the Earth (e.g., Lambeck et al. 1990; Le Meur 1996; Thoma and Wolf 1999; Le Meur and Huybrechts 2001; Tarasov and Peltier, 2002). However, in typical ice sheet modelling applications, such a level of complexity is not required, and a simpler treatment is feasible that models the lithosphere as a thin elastic plate and the asthenosphere as a viscous fluid, parameterised by a time-lag constant ("elastic lithosphere/relaxing asthenosphere" or ELRA model; Le Meur and Huybrechts 1996).

In the ELRA model, the steady-state displacement w_{ss} of the lithosphere under the influence of the ice load $\rho g H$ (downward) and the buoyancy $\rho_a g w_{ss}$ (upward) is governed by the biharmonic equation

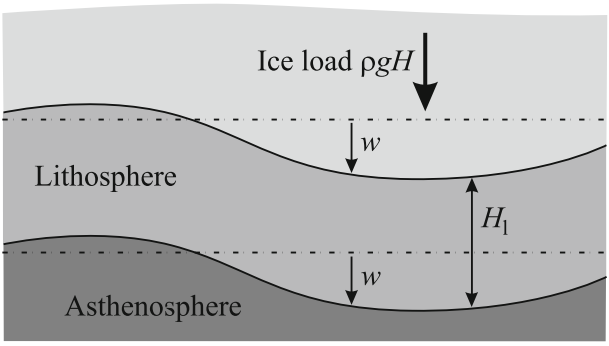

Fig. 2 Glacial isostasy: vertical displacement w of the lithosphere (thickness H_l) due to a temporally and spatially varying ice load $\rho\ gH$. The *dashed lines* mark the *top* and *bottom* of the lithosphere in unloaded equilibrium

$$K_l \Delta^2 w_{ss} + \rho_a g w_{ss} = \rho g H \tag{33}$$

(e.g., Marguerre and Woernle 1969), where K_l ($\sim 10^{25}$ N m) is the flexural stiffness of the lithosphere and $\rho_a = 3{,}300$ kg m^{-3} the density of the asthenosphere. The Green function G of Eq. (33) is given by

$$G(r) = G(x, \check{x}, y, \check{y}) = -\frac{L_r^2}{2\pi K_l} \operatorname{kei}\left(\frac{r}{L_r}\right), \tag{34}$$

with

$$r = \sqrt{(x-\check{x})^2 + (y-\check{y})^2}, \quad L_r = \left(\frac{K_l}{\rho_a g}\right)^{1/4} \tag{35}$$

(Brotchie and Silvester 1969). Here, kei$(\cdot)$ is a Kelvin function of zero order, which can be derived from the general Bessel function, and whose values are tabulated in mathematical handbooks (e.g., Abramowitz and Stegun 1970). It is shown in Fig. 3.

The Green function (34) allows to construct the solution of the biharmonic equation (33) for a general distribution of the ice load by superposition,

$$w_{ss}(x, y, t) = \int_{A_{ice}} \rho g H(\check{x}, \check{y}, t) G(x, \check{x}, y, \check{y}) \mathrm{d}\check{x}\mathrm{d}\check{y}, \tag{36}$$

where A_{ice} denotes the ice-covered area.

Due to the viscosity of the asthenosphere, the lithosphere cannot assume the steady-state displacement w_{ss} immediately. In the ELRA model, this is parameterised by the isostatic time lag τ_a (~ 3 ka), and the actual displacement $w(x, y, t)$ is determined by the simple relaxation equation

$$\frac{\partial w}{\partial t} = -\frac{1}{\tau_a}(w - w_{ss}). \tag{37}$$

The radius of relative stiffness L_r has a value of ~ 100 km. This is much smaller than the typical horizontal extent of a large ice sheet like Antarctica or Greenland. Therefore, the elastic term in Eq. (33) is sometimes neglected, which leads to the local balance between ice load and buoyancy

$$\rho_a g w_{ss} = \rho g H \quad \Rightarrow \quad w_{ss} = \frac{\rho}{\rho_a} H. \tag{38}$$

In combination with the relaxation equation (37), this model is referred to as the local lithosphere/relaxing asthenosphere or LLRA model.

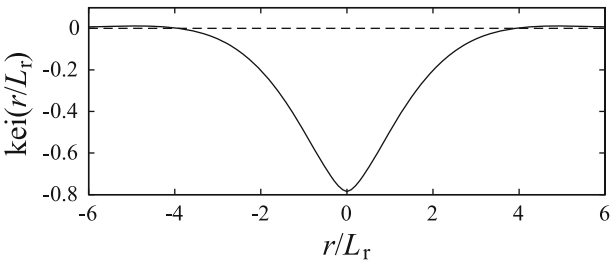

Fig. 3 The Kelvin function (normalised displacement of the elastic lithosphere under a point load)

For ice caps like Vatnajökull or Austfonna, the horizontal extent is similar to L_r, and the LLRA model cannot be used; the non-locality of the elastic lithosphere approach is then essential and must be accounted for. Glaciers are typically much smaller than L_r, which leads to an extreme spreading of the isostatic displacement and renders it negligible. Thus isostasy need not be considered for glaciers.

6 System Models

6.1 Ice Sheet Models

Although glaciers may contribute more to sea level changes on time scales of decades, the ice sheets of Greenland and Antarctica may be more important on longer time scales and in terms of large catastrophic contributions.

To study ice sheet dynamics, models of various degrees of sophistication are required, depending on the specific questions. These questions may concern the understanding of glacial cycles, the present state of the ice sheet or the future of the ice sheets for a range of possible climate scenarios.

Although the flow field is quasi-stationary, thermal inertia and the evolution of the geometry, both the basal isostatic relaxation and the surface evolution, are truly transient with a wide range of temporal scales. The long *memory* of the ice sheet requires accurate initial conditions in addition to accurate history of the boundary conditions. Furthermore, the extent, surface altitude and surface conditions may feedback to the conditions above and below the ice sheet. This may make it necessary to couple ice sheet models to models of the solid Earth, ocean and atmosphere bounding systems. Since these systems act on largely different scales, especially time scales, the coupling must apply specific techniques to maintain realistic process physics and computability.

The prediction of the future evolution of, e.g., the Greenland ice sheet depends primarily on the assumed scenarios of the future climate but also on the initial (present) conditions to start the model run. Observations provide the accurate surface and bedrock topography and information from the existing ice cores provides additional data such as ice temperature and rheology at given locations. The three-dimensional fields of present-day temperature and viscosity of the ice sheet can only be obtained by numerical ice sheet models.

The thermo-mechanical processes are slow in comparison with the temporal and spatial variability of the climatic states of the atmosphere and ocean. The long memory, over more than one glacial cycle (Calov and Hutter 1996) requires a correspondingly long *spin up* run of the model to establish the present-day conditions. Thus far, two distinct methods to compute present-day initial conditions were applied, (1) simulations driven by temperature reconstructions based on ice cores, and (2) steady state simulations with present-day climate conditions (Rogozhina et al. 2011 and references therein). Since the present state cannot possibly be a steady state to the present or any other climate condition, it must necessarily deviate from any transient state obtained by method 1). Seemingly, the steady state temperatures are too high and the domain of basal and near-basal temperate ice is too large (Huybrechts, 1996; Greve 1997; 2000). Also the present-day conditions obtained by transient model runs for some time in the past may depend on the chosen past initial conditions, unless the integration time is long enough for the ice sheet to forget those initial conditions. This, however, may be a problem since the paleo-climate reconstructions needed for the boundary conditions lose accuracy and reliability with increasing age.

Accurate initial conditions to start a model run for the next few millennia are crucial especially since basal thermal conditions determine whether there is sliding or non-sliding and large shearing of soft warmer ice or hard colder ice.

The problem becomes particularly serious if the evolution of ice sheets over the coming decades or few centuries must be predicted. Over this short time span, the initial conditions strongly influence the prognostic computations, and, if not accurate, produce poor predictions (Arthern and Gudmundsson 2010). To overcome this problem, combinations of observed data and model computations are applied, such as data assimilation techniques based on control methods (Vieli and Payne 2003; Vieli et al. 2006; Arthern and Hindmarsh 2006), or adjoint models that derive the sensitivities of ice sheets to boundary and initial conditions (Heimbach and Bugnion, 2009).

Three operational ice sheet models are currently available on the internet as free software:

- Glimmer-CISM (Community Ice Sheet Model, http://glimmer-cism.berlios.de/);
- PISM (Parallel Ice Sheet Model, http://www.pism-docs.org/);
- SICOPOLIS (SImulation COde for POLythermal Ice Sheets, http://sicopolis.greveweb.net/).

These models include three-dimensional coupling of temperature and velocity fields in the shallow ice approximation. They differ in the numerical grids and some numerical schemes, but also allow for various physical processes such as polythermal conditions (SICOPOLIS, PISM) or a novel type of sliding parameterisation (PISM). Glimmer-CISM is particularly designed to be interfaced to a range of global climate models. All three models are currently under rapid development, and in different stages towards implementation of higher-order dynamics (Sect. 3.1), ice shelf dynamics (Sect. 3.3) and discontinuous processes (Sect. 4). Figure 4 illustrates schematically the various components of the models.

6.2 Coupling to Climate Models

Glacial cycles constitute climate changes beyond the observed variations of the past few centuries. Thus, the reconstruction of the waxing and waning of the ice sheets is an essential component in studying the climate system, and, in particular, the dynamics of ice sheets. It is now well accepted that the Milankovitch cycles of orbital and rotational elements of the Earth play an essential role in the triggering and pacing of the growth and shrinkage of the ice sheets, especially in the northern hemisphere. However, a thorough understanding of internal processes and feedback mechanisms of the climate system is crucial to understand many details of the glacial cycles. It is thus necessary to couple, in some adequate way, a climate system model to a model of the ice sheets to capture the interactions between climate and ice sheets during entire glacial cycles. However, comprehensive global atmosphere ocean circulation models including sea ice and possible other sub-systems to handle CO_2 fluxes, land albedo and aerosols are prohibitively expensive in computational requirements. Thus, the integration over glacial cycles is still far beyond the reach of computer capacity presently and possibly for quite some time in the future.

To circumvent this obstacle, a whole palette of simplified methods for direct and indirect coupling of ice sheet models to climate models has been proposed. Since three-dimensional thermomechanically coupled ice sheet models can be run over several glacial cycles with present computers, the compromises always concern the climate models. Basically, three different types of approaches can be distinguished.

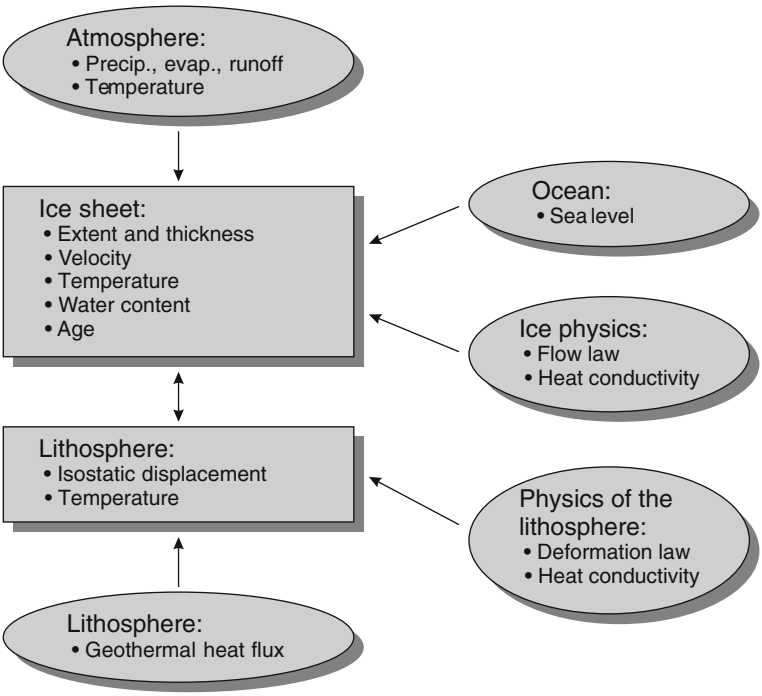

Fig. 4 Scheme of a modern, dynamic/thermodynamic ice sheet model. The *rectangular boxes* correspond to prognostic model components, the *oval boxes* to input quantities

The most commonly used approach uses the present-day observed climate and applies some perturbation to it derived from available proxy data such as isotopic composition and atmospheric greenhouse gas concentrations from ice cores (Ritz et al. 1997; Abe-Ouchi et al. 2007; and references therein).

A second approach couples ice sheet models to climate models reduced in dimension, resolution and physical processes. Recently, so called Earth Models of Intermediate Complexity (EMICs), see Clausen et al (2002), allow for long term climate simulations for a coarse zonal and sectorial resolution. The advantage of an EMIC is the possibility to couple several subsystems, such as the atmosphere, oceans, land surface types and energy and mass fluxes, atmospheric aerosols, and a comprehensive three-dimensional ice sheet model (Ganopolski et al. 2010). The low spatial resolution and limited physics, however, limit the possibility to take into account the feedback of variations in the ice sheet extent and altitude on the climate, in particular on atmospheric and oceanic circulation patterns.

A third possibility is the use of comprehensive three-dimensional global climate models, either atmosphere ocean general circulation models (AO-GCM) or atmosphere circulation models (A-GCM) with some idealised slab ocean. However, even at low spatial resolution, the computational requirement limits the time span to be modelled to few centuries. Therefore, time slices of a few decades for selected periods of glaciation extents, astronomical forcings or greenhouse gas concentrations may serve to parameterise climatic conditions, such as temperature and mass balance (Abe-Ouchi et al. 2007). Furthermore, A-GCM and AO-GCM experiments give the possibility to investigate the influence of the

ice sheet to general patterns of the atmospheric circulation and storm tracks, and thus have an influence back to the mass balance and ice sheet dynamics.

In coupled modelling of the ice age cycles, input from climate models is commonly given at low spatial resolution compared with the resolution of ice sheet models. However, one should not reduce the resolution of ice sheet models because, depending on the scheme to advance the ice sheet margin, a minimal resolution of the ice sheet models must be applied to avoid a failure of properly advancing the margin (Abe-Ouchi and Blatter 1993). To better match the resolutions of climate and ice sheet models, regional climate models are a possibility, see e.g. Box et al. (2006).

In contrast to glacial cycles, future global warming scenarios typically encompass time scales of decades to centuries. As mentioned above, for such time scales the coupling of AO-GCMs with ice sheet models has become feasible (see, e.g., Vizcaíno et al 2008; Ridley et al. 2009). The ongoing increase in computer performance will certainly allow improvements in time span covered and model resolution in the near future.

6.3 Testing Ice Sheet Models

System models of ice sheets consist of a coupled set of non-linear differential equations with boundary conditions on mass, momentum and energy fluxes, and initial conditions of geometry and thermodynamic fields. The complexity of the system requires simplifications of physical processes and the system components, and the computation of the evolution of the system requires numerical solutions of the equations.

Such a model requires the testing of its reliability in various ways. It may be reasonable to stick to a terminology that seems to be established in the community: *verification* refers to the test of the numerical solution process and *validation* refers to the test with observed information on a real system (Oreskes et al. 1994; Thompson 1995; Bueler 2008)

Although the word *verification* stems from the Latin word for truth, verification is a matter of accuracy rather than truth. The word *validation* in turn should be interpreted as a test of reliability. Taking the words too literally may tempt one to declare the corresponding control as *impossible* (Oreskes et al. 1994), instead of taking them more pragmatically.

A third testing possibility are *intercomparisons* of models for the same system. Intercomparison projects became popular in many Earth system modelling sciences, in particular in glacier and ice sheet modelling (Huybrechts et al. 1997). Model intercomparisons may contain elements of both verification and validation. Verification (or falsification) may result if the models in comparison solve the equations with essentially different numerical methods (Pattyn et al. 2007), or if a verified benchmark is available.

The European Ice Sheet Modelling Initiative intercomparison revealed a common feature of all ice sheet models, the breaking of the cylindrical symmetry in the internal fields despite the radial symmetry in the boundary conditions (Payne et al. 2000). Interestingly, such a symmetry breaking does not show in models of realistic ice sheets or, perhaps, it is disguised in the fields with more variability. The intercomparison shows that all models display this symmetry breaking; however, the patterns vary between the models. Higher order mechanics does not reduce the symmetry breaking (Saito et al. 2006) and the specific shapes may also depend on initial conditions. A persistent pattern is that the spokes follow the grid lines and grid symmetry, except for very cold ice sheets, where irregularities emerge that do not follow the grid symmetry (A. Aschwanden, personal communication, September 2009).

The EISMINT intercomparison discovered (Payne et al. 2000), described (Payne and Baldwin 2000) and compared the spokes in various different models; however, they did not

explain their physical or mathematical origin, except for some speculative interpretations (Payne and Dongelmans 1997). The emergence of the spoky patterns must be taken as an indication that the system of equations is vulnerable to ill condition and perhaps instability. Seemingly, the spokes only occur in the system with full thermomechanical coupling and free surface, and

> derivative with respect to temperature of the strain-heating term (can be identified) as the controlling quantity in the spokes ...
> ... local grid refinement near areas of maximum strain heating and/or smoothing of the strain heating term will ameliorate this problem (Bueler et al. 2005, 2006).

Recently, in the Heinrich Event INtercOmparison (HEINO) topic of the Ice-Sheet Model Intercomparison Project (ISMIP) internal large-scale ice sheet instabilities in different contemporary ice sheet models were explored (Calov et al. 2010). For the experiments, a simplified geometry that reproduces the main characteristics of the Laurentide ice sheet (including the sedimented region over Hudson Bay and Hudson Strait) and a temporally constant glacial climate were employed. It was found that all participating models (eight SIA models and one combined SIA/SSA model) are capable of producing Heinrich-type free oscillations if the boundary conditions are sufficiently favourable. However, the large differences between the results of different models (some are much more prone to produce oscillations than others) clearly showed that further model improvements are crucial for adequate, robust simulations of ice sheet instabilities.

6.4 Glacier Models

Land ice masses not connected to the Greenland and Antarctic ice sheets contribute less than 1% to the water locked in all ice sheets, ice caps and glaciers together (Table 1). Although glaciers may contribute to sea level rise by less than 0.5 m, their impact is on the short term, decades to centuries, and more local.

The strain softening property of ice limits the ice thickness as a function of the horizontal extent and steepness of the glacier. Thus the geometric aspect ratio of glaciers is one to two orders of magnitude larger than that of ice sheets, and requires more accurate models than the shallow ice approximation to reliably predict the long term evolution of its volume and geometry.

The application of higher order approximations or the full Stokes formulation of the ice flow make the implementation of a glacier model more demanding. The solution of the governing equations requires numerical algorithms that may be computationally expensive. Furthermore, the coupling of the ice flow in longitudinal and transverse directions due to the stress gradients makes the influence of boundary conditions non-local. Basal sliding feeds back to the velocity field both in vertical and horizontal directions and thus is not defined by local basal conditions alone, in contrast to the shallow ice approximation.

Various glacier models using the full Stokes scheme for the ice flow were implemented to study a range of processes, and recently to study glacial systems. Three-dimensional models were implemented to investigate the confluence of glaciers in the Swiss Alps (Gudmundsson 1994a, 1999). Full Stokes flow models including thermodynamics (Zwinger and Moore 2009) and in addition a compressible firn rheology (Lüthi and Funk 2000; Zwinger et al. 2007) were applied to high altitude firn areas for dating bore hole locations.

On a time scale of decades to centuries, for the predicted climate warming, glaciers and ice caps likely contribute more to sea level rise than the large ice sheets. Missing

information and prohibitive computation time prevents a reliable prediction of the change in ice volume in most glaciers with comprehensive models. However, the modelling of carefully chosen sample glaciers may give a background information for the behaviour of the multitude of glaciers.

The size of most glaciers falls short of the grid resolution of prognostic global climate models, but also of the resolution of local networks of meteorological stations. Furthermore, the local conditions in glacierised valleys or on ice caps may be influenced by the topography and the thermal conditions of the ice surface itself. Thus, downscaling of the projected climatic conditions is an important requirement.

A possible simplified downscaling is based on the assumption that in a changing climate the fields of temperature and precipitation have larger spatial variability than the fields of their corresponding changes over time. Thus, the observed present-day local conditions can be combined with the larger scale change of climatic conditions to generate a local climate scenario (Schneeberger et al. 2001, 2003). More sophisticated downscaling schemes range from statistical downscaling (see, e.g., Hofer et al. 2010, and references therein) to the nesting of comprehensive global and regional climate models (Christensen and Christensen 2007; Frei et al. 2007). The climate input can be transformed to a mass balance information using e.g. the temperature and radiation index model of Hock (1999), e.g., Jouvet et al. (2008) with measured meteorological data for the past decades or climate scenarios for the future.

7 Conclusions and Prospects

The seemingly high sensitivity of a glacial system is reflected in the high sensitivity of the combined problem of free surface flow and thermomechanical coupling. Thus, the prognostic power of ice sheet modelling depends crucially on reliable verification of the numerical methods used. However, the prognostic power may suffer from limited knowledge, either limited accuracy or even lack of information on internal processes (anisotropy, hydraulics, sliding, grounding line) and on the boundary conditions given from external systems (atmosphere, ocean, solid Earth). This is already the case for the ice sheet dynamics determined on the *mass flux time scale* by the smooth and continuous processes such as ice flow and climatological mass fluxes on the surface. Even more, this is true for processes determined by discontinuous processes that may lead to changes on the *catastrophic time scale* such as surges and ice shelf disintegration due to grounding line instabilities.

Computation power and efficiency of numerical methods have progressed to the point where full Stokes solutions for glaciers are obtainable on affordable computers. Three-dimensional flow fields were computed diagnostically for the Gorshkov crater glacier, Kamchatka (Zwinger et al. 2007), including thermomechanical coupling and firn, and prognostically for Midtre Lovénbreen, Svalbard (Zwinger and Moore 2009). A three-dimensional full Stokes model coupled to a novel scheme for solving the transport equation with a *volume of fluid* method was applied to Alpine glaciers (Jouvet et al. 2008; Jouvet et al. 2009). The above models apply a finite element method on unstructured grids. A three-dimensional full Stokes model solving the equations on a finite difference grid was applied to study the stability of subglacial lakes (Pattyn 2008).

The next logical steps in ice sheet model development may be anticipated by extrapolating recent developments and requirements for the future. The developments will likely include full Stokes solutions for entire ice sheets with adaptive grids to obtain high spatial

resolution where required. They will apply novel solvers and pre-conditioners to increase computational efficiency and certainly faster computers. Currently, at least three projects started to develop the next generation ice sheet models (http://www.elmerfem.org/wiki/index.php/Elmer_Ice_Sheet_modeling, http://issm.jpl.nasa.gov/, http://trac.mcs.anl.gov/projects/sisiphus). This kind of engineering work requires close collaboration between specialists in various fields: physicists, mathematicians, computer scientists. However, the challenge will also be the identification of the right processes and their relevant physics to obtain truly conclusive answers to the pressing questions of the future of the ice sheets and their stability.

Acknowledgments We thank Prof. Lennart Bengtsson (Director Earth Science, International Space Science Institute, Bern, Switzerland) for the kind invitation to submit this review paper to *Surveys in Geophysics*. Scientific editor Prof. Johannes Oerlemans (Institute for Marine and Atmospheric Research, Utrecht University, The Netherlands) and two anonymous reviewers provided useful comments for improving the paper. Dr. Tracy Ewen (Department of Geography, University of Zurich, Switzerland) proofread the manuscript.

References

Abe-Ouchi A, Blatter H (1993) On the initiation of ice sheets. Ann Glaciol 18:203–207

Abe-Ouchi A, Segawa T, Saito F (2007) Climatic conditions for modelling the northern hemisphere ice sheets through the ice age cycle. Clim Past 3:423–438

Abramowitz M, Stegun IA (1970) Handbook of mathematical functions with formulars, graphs, and mathematical tables. Dover Publications, New York

Alley RB (1992) Flow-law hypotheses for ice-sheet modeling. J Glaciol 38(129):245–256

Anandakrishnan S, Catania GA, Alley RB, Horgan HJ (2007) Theoretical limitations to englacial velocity calculations. Science 315:1835–1841

Arthern RJ, Gudmundsson GH (2010) Initialization of ice-sheet forecast viewed as an inverse Robin problem. J Glaciol 56(197):527–533

Arthern RJ, Hindmarsh RCA (2006) Determining the contribution of Antarctica to sea-level rise using data assimilation methods. Phil Trans R Soc A 364:1841–1865

Bahr DB, Pfeffer WT, Meier MF (1994) Theoretical limitations to englacial velocity calculations. J Glaciol 40(136):509–518

Benn DI, Hulton NRJ, Mottram R (2007) 'Calving laws', 'sliding laws' and the stability of tidewater glaciers. Ann Glaciol 46:123–130

Bindoff NL, Willebrand J, Artale V, Cazenave A, Gregory J, Gulev S, Hanawa K, Le Quéré C, Levitus S, Nojiri Y, Shum CK, Talley LD, Unnikrishnan A (2007) Observations: oceanic climate change and sea level. In: Solomon S, Qin D, Manning M, Chen Z, Marquis M, Averyt KB, Tignor M, Miller HL (eds) Climate change 2007: the physical science basis. Contribution of working group I to the fourth assessment report of the intergovernmental panel on climate change. Cambridge University Press, Cambridge, pp 385–432, http://ipcc-wg1.ucar.edu/wg1/wg1-report.html

Blatter H (1995) Velocity and stress fields in grounded glaciers: a simple algorithm for including deviatoric stress gradients. J Glaciol 41(138):333–344

Box JE, Bromwich DH, Veenhuis BA, Bai L, Stroeve JC, Rogers JC, Steffen K, Haran T, Wang S (2006) Greenland ice sheet surface mass balance variability (1988–2004) from calibrated polar MM5 output. J Clim 19:2783–2800

Brotchie JF, Silvester R (1969) On crustal flexure. J Geophys Res 74(22):5240–5252

Bueler E (2008) Lessons from the short history of ice sheet model intercomparison. Cryosphere Discuss 2:399–412

Bueler E, Brown J (2009) Shallow shelf approximation as a "sliding law" in a thermomechanically coupled ice sheet model. J Geophys Res 114:F03008. doi:10.1029/2008JF001179

Bueler E, Kallen-Brown JA, Lingle C (2005) Exact solutions and the verification of numerical models for ice sheets. Poster, EGU General Assembly, Vienna, Austria http://www.gi.alaska.edu/snowice/glaciers/iceflow/EGUposter.png

Bueler E, Brown J, Lingle C (2006) Verifying thermocoupled ice sheet models (and explaining the "warm spokes"). Presentation, 13th West Antarctic ice sheet workshop, Pack Forest, Washington http://www.gi.alaska.edu/snowice/glaciers/iceflow/Bueler_WAIS06.pdf

Bueler E, Khroulev C, Aschwanden A, Joughin I, Smith BE (2010) Modeled and observed fast flow in the Greenland ice sheet. Poster, EGU General Assembly, Vienna, Austria http://www.gi.alaska.edu/snowice/glaciers/iceflow/posterBKAJS.pdf

Calov R, Hutter K (1996) The thermomechanical response of the Greenland ice sheet to various climate scenarios. Clim Dyn 12:243–260

Calov R, Greve R, Abe-Ouchi A, Bueler E, Huybrechts P, Johnson JV, Pattyn F, Pollard D, Ritz C, Saito F, Tarasov L (2010) Results from the ice-sheet model intercomparison project—Heinrich event intercomparison (ISMIP HEINO). J Glaciol 56(197):371–383

Christensen JH, Christensen OB (2007) A summary of PRUDENCE model projection of changes in european climate by the end of theis century. Clim Change 81:7–30

Clausen M, Mysak LA, Weaver AJ, Crucifix M, Fichefet T, Loutre M, Weber SL, Alcamo J, Alexeev VA, Berger A, Calov R, Ganopolski A, Goosse H, Lohmann G, Lunkeit F, Mokhov II, Stone P, Wang Z (2002) Earth system models of intermediate complexity: closing the gap in the spectrum of climate system models. Clim Dyn 18:579–586

Cuffey KM, Paterson WSB (2010) The physics of glaciers, 4th edn. Elsevier, Amsterdam

Durand G, Gagliardini O, de Fleurian B, Zwinger T, Le Meur E (2009a) Marine ice sheet dynamics: hysteresis and neutral equilibrium. J Geophys Res 114(F3):F03009. doi:10.1029/2008JF001170

Durand G, Gagliardini O, Zwinger T, Le Meur E, Hindmarsh RCA (2009b) Full Stokes modeling of marine ice sheets: influence of the grid size. Ann Glaciol 50(52):109–114

Fowler AC (2001) Modelling the flow of glaciers and ice sheets. In: Straughan B, Greve R, Ehrentraut H, Wang Y (eds) Continuum mechanics and applications in geophysics and the environment. Springer, Berlin, pp 201–221

Frei C, Calanca P, Schär C, Wanner H, Schädler B, Haeberli W, Appenzeller C, Neu U, Thalmann E, Ritz C, Hohmann R (2007) Die Klimazukunft der Schweiz. In: Klimaänderung und die Schweiz 2050—Erwartete Auswirkungen auf Umwelt, Gesellschaft und Wirtschaft, Beratendes Organ für Fragen der Klimaänderung OcCC, pp 12–16. http://www.occc.ch

Gagliardini O, Gillet-Chaulet F, Montagnat M (2009) A review of anisotropic polar ice models: from crystal to ice-sheet flow models. Low Temp Sci 68(Suppl.):149–166

Gagliardini O, Durand G, Zwinger T, Hindmarsh RCA, Le Meur E (2010) Coupling of ice-shelf melting and buttressing is a key process in ice-sheet dynamics. Geophys Res Lett 37(L14501). doi:10.1029/2010GL043334

Ganopolski A, Calov R, Claussen M (2010) Simulation of the last glacial cycle with a coupled climate ice-sheet model of intermediate complexity. Clim Past 6:229–244

Gladstone RM, Lee V, Vieli A, Payne AJ (2009) Grounding line migration in an adaptive mesh ice sheet model. J Geophys Res 115(F04014). doi:10.1029/2009JF001615

Goldberg DN, Holland DM, Schoof CG (2009) Grounding line movement and ice shelf buttressing in marine ice sheets. J Geophys Res 114(F04026). doi:10.1029/2008JF001227

Goldsby DL, Kohlstedt DL (2001) Superplastic deformation of ice: experimental observations. J Geophys Res 106(B6):11017–11030

Greve R (1997) Application of a polythermal three-dimensional ice sheet model to the Greenland ice sheet: response to steady-state and transient climate scenarios. J Clim 10(5):901–918

Greve R (2000) On the response of the Greenland ice sheet to greenhouse climate change. Clim Change 46(3):289–303

Greve R, Blatter H (2009) Dynamics of ice sheets and glaciers. Advances in geophysical and environmental mechanics and mathematics. Springer, Berlin

Grosfeld K, Sandhäger H (2004) The evolution of a coupled ice shelf-ocean system under different climate states. Global Planet Change 42:107–132

Gudmundsson GH (1994a) Convergent glacier flow and perfect sliding over a sinusoidal bed. PhD thesis, ETH Zürich, no. 10711

Gudmundsson GH (1994b) Glacier sliding over sinusoidal bed and the characteristics of creeping flow over bedrock undulations. Mitteilung 130, Versuchsanstalt für Wasserbau, Hydrologie und Glaziologie der ETH Zürich

Gudmundsson GH (1999) A three-dimensional numerical model of the confluence area of unteraargletscher, bernese alps, switzerland. J Glaciol 45(150):219–230

Gudmundsson GH (2003) Transmission of basal variability to a glacier surface. J Geophys Res 108:B42253. doi:10.1029/2002JB002107

Gudmundsson GH (2008) Analytical analysis of small-amplitude perturbations in the shallow ice stream approximation. Cryosphere Discuss 2:23–74

Heimbach P, Bugnion V (2009) Greenland ice-sheet volume sensitivity to basal, surface and initial conditions derived from an adjoint model. Ann Glaciol 50(52):67–80

Hindmarsh RCA (2004) A numerical comparison of approximations to the Stokes equations used in ice sheet and glacier modeling. J Geophys Res 109:F01,012
Hindmarsh RCA (2006) Paradoxes and problems with the longitudinal stress approximations used in glacier mechanics. GAMM-Mitt 29(1):52–79
Hindmarsh RCA (2006) The role of membrane-like stresses in determining the stability and sensitivity of the Antarctic ice sheet: back pressure and grounding line motion. Phil Trans R Soc A 364:1733–1767
Hock R (1999) A distributed temperature-index ice and snowmelt model including potential direct solar radiation. J Glaciol 45(149):101–111
Hofer M, Mölg T, Marzeion B, Kaser G (2010) Empirical-statistical downscaling of reanalysis data to high-resolution air temperature and specific humidity above a glacier surface (Cordilliera Blanca, Peru). J Geophys Res D12120. doi:10.1029/2009JD012556
Hooke RL (2005) Principles of glacier mechanics, 2nd edn. Cambridge University Press, Cambridge
Horgan HJ, Anandakrishnan S (2006) Static grounding lines and dynamic ice streams: evidence from the Siple Coast, West Antarctica. Geophys Res Lett 33:L18502
Hutter K (1983) Theoretical glaciology; material science of ice and the mechanics of glaciers and ice sheets. D. Reidel Publishing Company, Dordrecht
Huybrechts P (1990) A 3-D model for the Antarctic ice sheet: a sensitivity study on the glacial-interglacial contrast. Clim Dyn 5:79–92
Huybrechts P (1996) Basal temperature conditions of the Greenland ice sheet during the glacial cycles. Ann Glaciol 23:226–236
Huybrechts P, Payne T, the EISMINT Intercomparison Group (1997) The EISMINT benchmarks for testing ice-sheet models. Annals Glaciol 23:1–12
IPCC (2007) Summary for policymakers. In: Solomon S, Qin D, Manning M, Chen Z, Marquis M, Averyt KB, Tignor M, Miller HL (eds) Climate change 2007: the physical science basis. Contribution of working group I to the fourth assessment report of the intergovernmental panel on climate change. Cambridge University Press, Cambridge, pp 1–18
Jenkins A, Bombosch A (1995) Modeling the effects of frazil ice crystals on the dynamics and thermodynamics of ice shelf water plumes. J Geophys Res 100:6967–6981
Joughin I, MacAyeal D (2005) Calving of large tabular icebergs from ice rift systems. Geophys Res Lett 32:L02, 501
Joughin I, Howat IM, Fahnestock M, Smith B, Krabill W, Alley RB, Stern H, Truffer M (2008) Continued evolution of Jakobshavn Isbrae following its rapid speedup. J Geophys Res 113:F04,006
Jouvet G (2010) Modélisation, analyse mathématique et simulation numérique de la dynamique des glaciers. PhD thesis, Ecole Polytechnique Fédérale de Lausanne
Jouvet G, Picasso M, Rappaz J, Blatter H (2008) A new algorithm to simulate the dynamics of a glacier: theory and applications. J Glaciol 54(188):801–811
Jouvet G, Huss M, Blatter H, Picasso M, Rappaz J (2009) Numerical simulations of Rhohnegletscher from 1874 to 2100. J Comp Phys 228:6426–6439
Kachanov LM (1999) Rupture time under creep conditions. Int J Fract 97(1–4):xi–xviii (translation from Izv. Akad. Nauk. SSSR, Itd. Tekh. Nauk. Metall. Topl., 8, 26–31, 1957)
Krajcinovic D (1996) Damage mechanics. Elsevier, New york
Krimmel RM (2001) Photogrammetric data set, 1957–2000, and bathymetric measurements for Columbia Glacier, Alaska. Water Resour. Invest. Rep. 014089, U.S. Geol. Surv
Lambeck K, Johnston P, Nakada M (1990) Holocene glacial rebound and sea-level change in NW Europe. Geophys J Int 103:451–468
Langdon TG (1996) Transitions in creep behavior. Mater Trans Jpn Inst Metal 37(3):359–362
Le Meur E (1996) Isostatic postglacial rebound over Fennoscandia with a self-gravitating spherical visco-elastic Earth model. Ann Glaciol 23:318–327
Le Meur E, Huybrechts P (1996) A comparison of different ways of dealing with isostasy: examples from modelling the Antarctic ice sheet during the last glacial cycle. Ann Glaciol 23:309–317
Le Meur E, Huybrechts P (2001) A model computation of the temporal changes of surface gravity and geoidal signal induced by the evolving Greenland ice sheet. Geophys J Int 145:835–849
Lemke P, Ren J, Alley RB, Allison I, Carrasco J, Flato G, Fujii Y, Kaser G, Mote P, Thomas RH, Zhang T (2007) Observations: changes in snow, ice and frozen ground. In: Solomon S, Qin D, Manning M, Chen Z, Marquis M, Averyt KB, Tignor M, Miller HL (eds) Climate change 2007: the physical science basis. Contribution of working group I to the fourth assessment report of the intergovernmental panel on climate change. Cambridge University Press, Cambridge, pp 337–383. http://ipcc-wg1.ucar.edu/wg1/wg1-report.html
Lewis EL, Perkin RG (1986) Ice pumps and their rates. J Geophys Res 91(C10):11756–11762

Lüthi M, Funk M (2000) Dating ice cores from a high Alpine glacier with a flow model for cold firn. Ann Glaciol 31:69–79
Marguerre K, Woernle HT (1969) Elastic plates. Blaisdell Publishing Company, Waltham
Meehl GA, Stocker TF, Collins WD, P F, Gaye AT, Gregory JM, Kitoh A, Knutti R, Murphy JM, Noda A, Raper SCB, Watterson IG, Weaver AJ, Zhao ZC (2007) Global climate projections. In: Solomon S, Qin D, Manning M, Chen Z, Marquis M, Averyt KB, Tignor M, Miller HL (eds) Climate change 2007: the physical science basis. Contribution of working group I to the fourth assessment report of the intergovernmental panel on climate change. Cambridge University Press, Cambridge, pp 747–845. http://ipcc-wg1.ucar.edu/wg1/wg1-report.html
Morland LW (1984) Thermomechanical balances of ice sheet flows. Geophys Astrophys Fluid Dyn 29:237–266
Morland LW (1987) Unconfined ice-shelf flow. In: Veen CJ, Oerlemans J (eds) Dynamics of the West Antarctic ice sheet. D. Reidel Publishing Company, Dordrecht, pp 99–116
Murray AB (2002) Seeking explanation affects numerical modeling strategies. EOS Trans AGU 83:418–419
Nick FM, van der Veen CJ, Oerlemans J (2007) Controls on advance of tidewater glaciers: results from numerical modeling applied to Columbia Glacier. J Geophys Res 112:F03S24. doi:10.1029/2006JF000551
Nick FM, van der Veen CJ, Vieli A, Benn DI (2010) A physically based calving model applied to marine outlet glaciers and implications for the glacier dynamics. J Glaciol 56(199):781–794
Nøst OA, Foldvik A (1994) A model of ice shelf-ocean interaction with application to the Filchner-Ronne and Ross ice shelves. J Geophys Res 99(C7):14243–14254
Nye JF (1957) The distribution of stress and velocity in glaciers and ice-sheets. Proc R Soc Lond Ser A 239(1216):113–133
Ohmura A (2010) Mass balance of glaciers and ice sheets during the observational period and climate change (in japanese). J Geogr Tokyo Geogr Soc 119(3):466–481
Oreskes N, Shrader-Frechette K, Belitz K (1994) Verification, validation, and confirmation of numerical models in the earth sciences. Science 263:641–646
Otero J, Navarro FJ, Martin C, Cuadrado ML, Corcuera MI (2010) A three-dimensional calving model: numerical experiments on Johnsons Glacier, Livingston Island, Antarctica. J Glaciol 56(196):200–214
Paterson WSB (1994) The physics of glaciers, 3rd edn. Pergamon Press, Oxford
Pattyn F (2008) Investigating the stability of subglacial lakes with a full Stokes ice-sheet model. J Glaciol 54(185):353–361
Pattyn F et al (2007) Benchmark experiments for higher-order and full Stokes ice sheet models (ISMIP-HOM). Cryophere 2:95–108. doi:10.5194/tc-2-95-2008
Payne AJ, Baldwin DJ (2000) Analysis of ice-flow instabilities identified in the EISMINT intercomparison exercise. Annals Glaciol 30:204–210
Payne AJ, Dongelmans PW (1997) Self-organization in the thermomechanical flow of ice sheets. J Geophys Res 102(B6):12219–12233
Payne AJ, Huybrechts P, Abe-Ouchi A, Calov R, Fastook JL, Greve R, Marshall S, Marsiat I, Ritz C, Tarasov L, Thomassen MPA (2000) Results from the EISMINT model intercomparison: the effects of thermomechanical coupling. J Glaciol 46(153):227–238
Payne AJ, Vieli A, Shepherd AP, Wingham DJ, Rignot E (2004) Recent dramatic thinning of largest West Antarctic ice stream triggered by oceans. Geophys Res Lett 31:L23, 401
Pettit EC, Waddington ED (2003) Ice flow at low deviatoric stress. J Glaciol 49(166):359–369
Pralong A, Funk M (2005) Dynamic damage model of crevasse opening and application to glacier calving. J Geophys Res 110:B01309. doi:10.1029/2004JB003104
Pralong A, Funk M, Lüthi MP (2003) A description of crevasse formation using continuum damage mechanics. Ann Glaciol 37:77–82
Pralong A, Hutter K, Funk M (2006) Anisotropic damage mechanics for viscoelastic ice. Cont Mech Thermodyn 17(5):387–408. doi:10.1007/s00161-005-0002-5
Ridley JK, Gregory JM, Huybrechts P, Lowe JA (2009) Thresholds for irreversible decline of the Greenland ice sheet. Clim Dyn. doi:10.1007/s00382-009-0646-0
Rignot E, Steffen K (2008) Channelized bottom melting and stability of floating ice shelves. Geophys Res Lett 35:L02,503
Ritz C (1987) Time dependent boundary conditions for calculation of temperature fields in ice sheets. In: Waddington ED, Walder JS (eds) The physical basis of ice sheet modelling. IAHS Publication No. 170, IAHS Press, Wallingford, pp 207–216
Ritz C, Fabre A, Letréguilly A (1997) Sensitivity of a Greenland ice sheet model to ice flow and ablation parameters: consequences for the evolution through the last climatic cycle. Clim Dyn 13(1):11–24

Ritz C, Rommelaere V, Dumas C (2001) Modeling the evolution of Antarctic ice sheet over the last 420,000 years: implications for altitude changes in the Vostik region. J Geophys Res 106(D23): 31943–31964
Rogozhina I, Martinec Z, Hagedorn JM, Thomas M (2011) On the long-term memory of the Greenland ice sheet. J Geophys Res 116:F01011. doi:10.1029/2010JF001787
Saito F, Abe-Ouchi A (2004) Thermal structure of Dome Fuji and east Dronning Maud Land, Antarctica, simulated by a three-dimensional ice-sheet model. Ann Glaciol 39:433–438
Saito F, Abe-Ouchi A, Blatter H (2006) European ice sheet modelling initiative (EISMINT) model intercomparison experiments with first order mechanics. J Geophys Res 111:F02012
Scambos T, Fricker HA, Liu C, Bohlander J, Fastook J, Sargent A, Massom R, Wu A (2009) Ice shelf disintegration by plate bending and hydro-fracture: satellite observations and model results of the 2008 Wilkins ice shelf break-up. Earth Planet Sci Lett 280:51–60
Schneeberger C, Albrecht O, Blatter H, Wild M, Hock R (2001) Modelling the response of glaciers to a doubling in atmospheric CO_2: a case study on Storglaciären, northern Sweden. Clim Dyn 17(11):825–834
Schneeberger C, Blatter H, Abe-Ouchi A, Wild M (2003) Modelling changes in the mass balance of glaciers of the northern hemisphere for a transient $2xCO_2$ scenario. J Hydrol 282(1-4):145–163
Schoof C (2007) Ice sheet grounding line dynamics: steady states, stability, and hysteresis. J Geophys Res 112:F03S28. doi:10.1029/2006JF000664
Schoof C, Hindmarsh RCA (2010) Thin-film flows with wall slip: an asymptotic analysis of higher order glacier flow. Q J Mech Appl Math 63(1):73–114. doi:10.1093/qjmam/hbp025
Smedsrud LH, Jenkins A (2004) Frazil ice formation in an ice shelf water plume. J Geophys Res 109:C03, 025
Tarasov L, Peltier WR (2002) Greenland glacial history and local geodynamic consequences. Geophys J Int 150(1):198–229
Thoma M, Wolf D (1999) Bestimmung der Mantelviskosität aus Beobachtungen der Landhebung und Schwere in Fennoskandien. Scientific Technical Report STR99/02, GeoForschungsZentrum Potsdam, Germany
Thompson DE (1995) Verification, validation, and solution quality in computational physics: Cfd methods applied to ice sheet physics. Tech. rep., NASA/TM-2005-213453, NASA, Ames Research Center
Truffer M (2004) The basal speed of valley glaciers: an inverse approach. J Glaciol 50(169):236–242
Vander Veen CJ (1996) Tidewater calving. J Glaciol 42:375–385
Verbitsky M (2002) Siple coast ice streams in a General Antarctic ice sheet model. J Clim 18:2194–2198
Vieli A, Payne AJ (2003) Application of control methods for modelling the flow of Pine Island Glacier, West Antarctica. Ann Glaciol 36:197–204
Vieli A, Payne AJ (2005) Assessing the ability of numerical ice sheet models to simulate grounding line migration. J Geophys Res 110:1815–1839. doi:10.1029/2004JF000202
Vieli A, Funk M, Blatter H (2000) Tidewater glaciers: frontal flow acceleration and basal sliding. Ann Glaciol 31:217–221
Vieli A, Funk M, Blatter H (2001) Flow dynamics of tidewater glaciers: a numerical modelling approach. J Glaciol 47(159):595–606
Vieli A, Jania J, Kolondra L (2002) The retreat of a tidewater glacier: observations and model calculations on Hansbreen, Spitsbergen. J Glaciol 48(163):592–600
Vieli A, Payne AJ, Du Z, Shepherd A (2006) Numerical modelling and data assimilation of the Larson B ice shelf, Antarctic Peninsula. Phil Trans R Soc A 364:F01003. doi:10.1098/rsta.2006.1800
Vizcaíno M, Mikolajewicz U, Gröger M, Maier-Reimer E, Schurgers G, Winguth AME (2008) Long-term ice sheet-climate interactions under anthropogenic greenhouse forcing simulated with a complex Earth System Model. Climate Dyn 31(6):665–690. doi:10.1007/s00382-008-0369-7
Walker RT, Dupont TK, Parizek BR, Alley RB (2008) Effect of basal-melting distribution on the retreat of ice-shelf grounding lines. Geophys Res Lett 35(L17503). doi:10.1029/2008GL034947
Walker RT, Dupont TK, Holland DM, Parizek BR, Alley RB (2009) Initial effects of oceanic warming on a coupled ocean-ice shelf-ice stream system. Earth Planet Sci Lett 287:483–487
Weertman J (1957) On the sliding of glaciers. J Glaciol 3(21):33–38
Weertman J (1964) The theory of glacier sliding. J Glaciol 5(39):287–303
Weertman J (1971) In defence of a simple model of glacier sliding. J Geophys Res 76(26):6485–6487
Weis M, Greve R, Hutter K (1999) Theory of shallow ice shelves. Continuum Mech Thermodyn 11(1):15–50
Zwinger T, Moore JC (2009) Diagnostic and prognostic simulations with a full Stokes model accounting for superimposed ice of Midtre Lovénbreen, Svalbard. Cryosphere 3:217–229
Zwinger T, Greve R, Gagliardini O, Shiraiwa T, Lyly M (2007) A full-Stokes thermo-mechanical model for firn and ice applied to the Gorshkov crate glacier, Kamchatka. Ann Glaciol 45:29–37

Surv Geophys (2011) 32:585–602
DOI 10.1007/s10712-011-9119-1

Sea-Level Rise from the Late 19th to the Early 21st Century

John A. Church · Neil J. White

Received: 2 November 2010 / Accepted: 7 March 2011 / Published online: 30 March 2011

Abstract We estimate the rise in global average sea level from satellite altimeter data for 1993–2009 and from coastal and island sea-level measurements from 1880 to 2009. For 1993–2009 and after correcting for glacial isostatic adjustment, the estimated rate of rise is 3.2 ± 0.4 mm year^{-1} from the satellite data and 2.8 ± 0.8 mm year^{-1} from the in situ data. The global average sea-level rise from 1880 to 2009 is about 210 mm. The linear trend from 1900 to 2009 is 1.7 ± 0.2 mm year^{-1} and since 1961 is 1.9 ± 0.4 mm year^{-1}. There is considerable variability in the rate of rise during the twentieth century but there has been a statistically significant acceleration since 1880 and 1900 of 0.009 ± 0.003 mm year^{-2} and 0.009 ± 0.004 mm year^{-2}, respectively. Since the start of the altimeter record in 1993, global average sea level rose at a rate near the upper end of the sea level projections of the Intergovernmental Panel on Climate Change's Third and Fourth Assessment Reports. However, the reconstruction indicates there was little net change in sea level from 1990 to 1993, most likely as a result of the volcanic eruption of Mount Pinatubo in 1991.

Keywords Sea level · Climate change · Satellite altimeter · Tide gauge

1 Introduction

Rising sea levels have important direct impacts on coastal and island regions where a substantial percentage of the world's population lives (Anthoff et al. 2006). Sea levels are rising now and are expected to continue rising for centuries, even if greenhouse gas emissions are curbed and their atmospheric concentrations stabilised. Rising ocean heat content (and hence ocean thermal expansion) is an important element of climate change and sea-level rise. The remaining contributions to sea-level rise come principally from the melting of land ice: glaciers and ice caps (which include the small glaciers and ice caps

J. A. Church (✉) · N. J. White
Centre for Australian Weather and Climate Research—A Partnership Between
CSIRO and the Australian Bureau of Meteorology, and CSIRO Wealth from Oceans Flagship,
CSIRO Marine and Atmospheric Research, GPO Box 1538, Hobart, TAS 7001, Australia
e-mail: john.church@csiro.au

fringing the major ice sheets) and the major ice sheets of Antarctica and Greenland, with additional contributions from changes in the storage of water on (or in) land. (See Church et al. 2010 for a summary of issues). Correctly estimating historical sea-level rise and representing global ocean heat uptake in climate models are both critical to projecting future climate change and its consequences. The largest uncertainty in projections of sea-level rise up to 2100 is the uncertainty in global mean sea level (GMSL) and thus improving estimates of GMSL rise (as well as regional variations in sea level) remains a high priority.

Since late 1992, high quality satellite altimeters (TOPEX/Poseidon, Jason-1, and OSTM/Jason-2) have provided near global measurements of sea level from which sea-level rise can be estimated. However, this altimeter record is still short (less than 20 years) and there is a need to know how sea level has varied over multi-decadal and longer time scales. Quantifying changes in the rate of sea-level rise and knowing the reasons for such changes are critical to improving our understanding of twentieth century sea-level rise and improving our projections of sea-level change for the twenty first century and beyond.

For the period prior to the altimeter record, estimates of sea-level change are dependent on a sparsely distributed network of coastal and island tide-gauge measurements (Woodworth and Player 2003). Even today, there are many gaps in the global network of coastal and island sea-level measurements and the network was sparser early in the twentieth century and in the nineteenth century. Many previous studies have used the individual sea-level records (corrected for vertical land motion) to estimate the local rate of sea-level rise (as a linear trend; e.g. Douglas 1991) and some studies attempted to detect an acceleration in the local rate of sea-level rise (Woodworth 1990; Woodworth et al. 2009; Douglas 1992). However, these individual records have considerable interannual and decadal variability and thus long records are required to get accurate estimates of the *local* trends in sea level (Douglas 2001). These authors assumed that these long-term trends are either representative of the global averaged rise or a number of records have been averaged, in some cases regionally and then globally, to estimate the global average rate of rise. However, the modern satellite record has made it clear that sea level is a dynamic quantity and it does not rise uniformly around the globe.

Sea level at any location contains the influences of local and regional meteorological effects (including storm surges), modes of climate variability (for example the El Niño-Southern Oscillation) and long-term trends (from both the ocean surface and land movements), including the impact of anthropogenic climate change. As the altimeter record has clearly demonstrated, GMSL has much less short term variability (more than an order of magnitude) than sea level at individual locations because while the volume of the oceans is nearly constant the distribution changes with time. While the variability at individual locations can be minimised by low pass filtering, there remains significant energy at yearly to decadal periods that may be either positively or negatively correlated between stations, thus confounding estimates of GMSL rise when few records are available.

To date, there have been two approaches to determining time series of GMSL from coastal and island tide gauges. The first and most straight forward approach averages the sea-level records (corrected for land motion) from individual locations. When there are only a small number of locations with continuous records, this approach is relatively straight forward, although care must be taken to remove data inhomogeneities. When more gauges are used, the records usually have different lengths and starting times. It is then necessary to average the rates of rise over some time step and integrate the results to get the sea-level change. Holgate and Woodworth (2004) used this approach and Jevrejeva et al. (2006) used a virtual station method of averaging neighbouring station sea-level changes in

several regions and then averaging to get the global mean sea-level change. No attempt was made to interpolate between the locations of observations and thus to estimate deep ocean sea level. Thus these are essentially estimates of coastal sea-level change. However, note that White et al. (2005) argued that over longer periods the rates of coastal and global rise are similar.

The second approach uses spatial functions which represent the large-scale patterns of variability to interpolate between the widely distributed coastal and island sea-level observations and thus to estimate global sea level (as distinct from coastal sea level). This technique was first developed by Chambers et al. (2002) for interannual sea-level variability and extended by Church et al. (2004) to examine sea-level trends. The Church et al. approach uses the Reduced Space Optimal Interpolation technique (Kaplan et al. 2000) developed for estimating changes in sea-surface temperature and atmospheric pressure. The spatial functions used are the empirical orthogonal functions (EOFs) of sea-level variability estimated from the satellite altimeter data set from TOPEX/Poseidon, Jason-1 and OSTM/Jason-2 satellite data, which now cover the period from January 1993 into 2011. We use data from January 1993 through December 2009 in this paper.

Here, we update previous estimates of GMSL rise for the period of the instrumental record using a longer (17 years) altimeter data set and an expanded in situ sea-level observational data set extending back to 1860. We use the Reduced Space Optimal Interpolation technique to quantify the rate of sea-level rise and the changes in the rate since 1880.

2 Methods and Data

2.1 In Situ Sea-Level Data

We use monthly sea-level data downloaded from the Permanent Service for Mean Sea Level (PSMSL; Woodworth and Player 2003) web site (http://www.psmsl.org) in August 2010. Careful selection and editing criteria, as given by Church et al. (2004) were used. The list of stations used in the reconstruction is available on our web site at http://www.cmar.csiro.au/sealevel/sl_data_cmar.html. Tide gauge records are assigned to the nearest locations (with good satellite altimeter data) on the $1^\circ \times 1^\circ$ grid of the satellite altimeter based EOFs. Where more than one record is assigned to a single grid point they are averaged. Changes in height from 1 month to the next are stored for use in the reconstruction.

The number of locations with sea-level data available for the reconstruction is larger than in our earlier 2004 (Church et al. 2004) and 2006 (Church and White 2006) studies, particularly prior to 1900 (Fig. 1). In the 1860s there are only 7–14 locations available, all North of 30°N. In the 1870s, there is one record available South of 30°N but still none in the southern hemisphere and it is only in the second half of the 1880s (Fort Denison, Sydney, Australia starts in January 1886) that the first southern hemisphere record becomes available. While we attempted the reconstruction back to 1860, the results showed greater sensitivity to details of the method prior to the 1880s when the first southern hemisphere record is available (see below for further discussion). As a result, while we show the reconstruction back to 1860, we restricted the subsequent analysis (computation of trends, etc.) to after 1880. The number of locations with data available increases to 38 in 1900 (from 71 individual gauges), including several in the southern hemisphere, to about 85 locations in 1940 (from 130 individual gauges but with still less than 10 in the southern

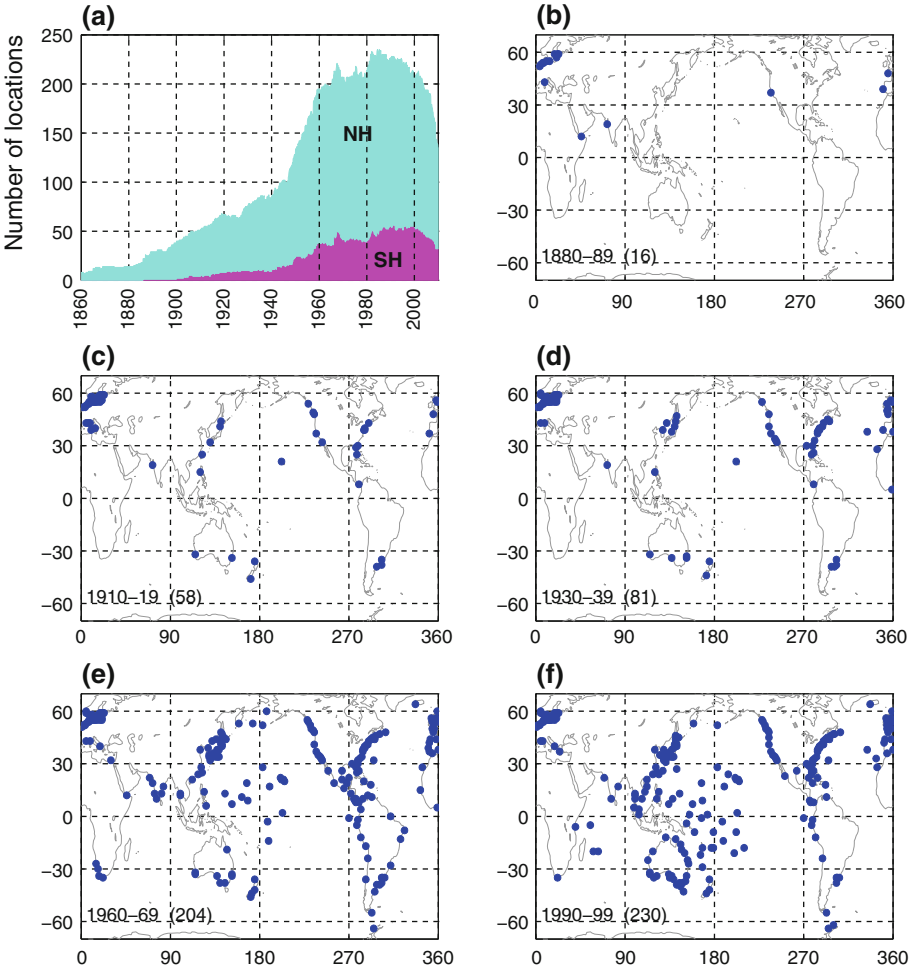

Fig. 1 The number and distribution of sea-level records available for the reconstruction. **a** The number of locations for the globe and the northern and southern hemispheres. **b–f** indicate the distribution of gauges in the 1880s, 1910s, 1930s, 1960s and 1990s. The locations indicated have at least 60 months of data in the decade and the number of records are indicated in *brackets*

hemisphere), and to about 190 in 1960 (from about 305 individual gauges with about 50 locations in the southern hemisphere). The number of locations peaks in May 1985 at 235 (from 399 individual gauges, with slightly less than one-third in the ocean-dominated southern hemisphere; Fig. 1). The largest gaps are in the Southern Ocean, the South Atlantic Ocean and around Africa (Fig. 1f). Through the 1990s there are at least 200 locations available from between 370 and 400 gauges. For the last few years there are fewer records available because of the unavoidable delay in the transmission by national authorities of monthly and annual mean information to the PSMSL. In December 2009, there are 135 locations available from 250 gauges.

Sea-level measurements are affected by vertical land motion. Corrections for local land motion can come from long-term geological observations of the rate of relative local

sea-level change (assuming the relative sea-level change on these longer times scales is from land motions rather than changing ocean volume), or from models of glacial isostatic adjustment, or more recently from direct measurements of land motion with respect to the centre of the Earth using Global Positioning System (GPS) observations. Here, the ongoing response of the Earth to changes in surface loading following the last glacial maximum were removed from the tide-gauge records using the same estimate of glacial isostatic adjustment (GIA; Davis and Mitrovica 1996; Milne et al. 2001) as in our earlier study (Church et al. 2004).

We completed the analysis with and without correction of the sea-level records for atmospheric pressure variations (the "inverse barometer" effect). The HadSLP2 global reconstructed atmospheric pressure data set (Allan and Ansell 2006) was used for this correction.

We tested the impact of correcting the tide-gauge measurements for terrestrial loading and gravitational changes resulting from dam storage (Fiedler and Conrad 2010). For the large number of tide gauges used in the period of major dam building after 1950 (mostly over 200), the impact on global mean sea level is only about 0.05 mm year^{-1} (smaller than the 0.2 mm year^{-1} quoted by Fiedler and Conrad, which is for a different less globally-distributed set of gauges). Tests of similar corrections for changes in the mass stored in glaciers and ice caps, and the Greenland and Antarctic Ice Sheets show that these effects have an even smaller impact on GMSL.

2.2 Satellite Altimeter Data Processing Techniques

The TOPEX/Poseidon, Jason-1 and OSTM/Jason-2 satellite altimeter missions measure sea surface height (SSH) relative to the centre of mass of the Earth along the satellite ground track. A number of instrumental and geophysical corrections must be applied. Every 10 days (one cycle) virtually global coverage of the world's ocean, between 66°N and S, is achieved. Our gridded data set as used here goes to 65°N and S.

Our satellite altimeter data processing mostly follows the procedures, and uses the edits and tests, recommended by the providers of the satellite altimeter data sets, and are similar to those described in Leuliette et al. (2004). The documents for the three missions used are Benada (1997) for TOPEX/Poseidon, Aviso (2003) for Jason-1 and CNES (2009) for OSTM/Jason-2.

Orbits from the most recent versions of the Geophysical Data Records (GDR files; MGDR-B for TOPEX/Poseidon, GDR-C for Jason-1 and GDR-T for OSTM/Jason-2) are used. GDR corrections from the same files for tides, wet troposphere, dry troposphere, ionosphere, sea-state bias (SSB), inverse barometer correction (when required) and the mean sea surface are applied in accordance with these manuals, except for some TOPEX/Poseidon corrections: firstly, the TOPEX/Poseidon wet troposphere correction has been corrected for drift in one of the brightness temperature channels (Ruf 2002) and offsets related to the yaw state of the satellite (Brown et al. 2002). Secondly, the inverse barometer correction (when used) has been recalculated using time-variable global-mean over-ocean atmospheric pressure, an improvement on the GDR-supplied correction which assumes a constant global-mean over-ocean atmospheric pressure. This approach makes the correction used for TOPEX/Poseidon consistent with the Jason-1 and OSTM/Jason-2 processing.

Calibrations of the TOPEX/Poseidon data against tide gauges have been performed by Gary Mitchum and colleagues (see, e.g., Nerem and Mitchum 2001). Here and in earlier publications, we have used the calibrations up to the end of 2001 (close to the end of the TOPEX/Poseidon mission). One of the problems these calibrations address is the

changeover to the redundant "side B" altimeter electronics in February 1999 (at the end of cycle 235) due to degradation of the "side A" altimeter electronics which had been in use since the start of the mission. An alternative processing approach to address the side A to side B discontinuity is to use the separate Chambers et al. (2003) SSB models for TOPEX sides A and B without any use of the Poseidon data, as this correction does not address the substantial drift in the Poseidon SSH measurements, especially later in the mission. No tide-gauge calibrations are applied to Jason-1 or OSTM/Jason-2 data. The altimeter data sets as used here are available on our web site at http://www.cmar.csiro.au/sealevel/sl_data_cmar.html.

2.3 The Analysis Approach

The full details of our approach to estimating historical sea level were reported in Church et al. (2004). Briefly, the reconstructed sea level $\boldsymbol{H^r}$ (x, y, t) is represented as

$$\boldsymbol{H^r}(x, y, t) = \boldsymbol{U^r}(x, y)\boldsymbol{\alpha}(t) + \boldsymbol{\varepsilon},$$

where $\boldsymbol{U^r}(x, y)$ is a matrix of the leading empirical orthogonal functions (EOFs) calculated from monthly satellite altimeter data mapped (using a Gaussian filter with a length scale of 300 km applied over a square with sides of 800 km) to a one degree by one degree grid for the ice free oceans between 65°S and 65°N, $\boldsymbol{\varepsilon}$ is the uncertainty, x and y are latitude and longitude and t is time. This matrix is augmented by an additional "mode" that is constant in space and used to represent any global average sea-level rise. In the reduced space optimal interpolation, the amplitude of the constant mode and these EOFs are calculated by minimising the cost function

$$\boldsymbol{S}(\boldsymbol{\alpha}) = (\boldsymbol{KU^r\alpha} - \boldsymbol{H^o})^T\boldsymbol{M}^{-1}(\boldsymbol{KU^r\alpha} - \boldsymbol{H^o}) + \boldsymbol{\alpha}^T\Lambda\boldsymbol{\alpha}.$$

This cost function minimises the difference between the reconstructed sea levels and the observed coastal and island sea levels $\boldsymbol{H^o}$, allowing for a weighting related to the observational uncertainties, omitted EOFs and also down-weights higher order EOFs. $\boldsymbol{K}$ is a sampling operator equal to 1 when there is observed sea-level data available and 0 otherwise, $\boldsymbol{\Lambda}$ is the diagonal matrix of the eigenvalues of the covariance matrix of the altimeter data and $\boldsymbol{M}$ is the error covariance matrix given by

$$\boldsymbol{M} = \boldsymbol{R} + \boldsymbol{KU'}\boldsymbol{\Lambda'}\boldsymbol{U'^T}\boldsymbol{K^T}$$

where $\boldsymbol{R}$ is the matrix of the covariance of the instrumental errors (assumed diagonal here) and the primes indicate the higher order EOFs not included in the reconstruction.

The EOFs are constructed from the covariances of the altimeter sea-level data after removal of the mean. Any overall increase in sea level as a result of ocean thermal expansion or the addition of mass to the ocean is difficult to represent by a finite number of EOFs. We therefore include an additional "mode" which is constant in space to represent this change in GMSL.

Because the sea-level measurements are not related to a common datum, we actually work with the change in sea level between time steps and then integrate over time to get the solution. The least squares solution provides an estimate of the amplitude of the leading EOFs, global average sea-level and error estimates.

Christiansen et al. (2010) tested the robustness of various reconstruction techniques, including an approach similar to that developed by Church et al. (2004) using thermosteric sea level calculated from climate model results. They used an ensemble of model results

(derived by randomising the phase of the principal components of the model sea level, see Christiansen et al. (2010) for details). For a method similar to that used here (including the additional "constant" mode and for a 20 year period for determining the EOFs), the trend in the ensemble mean reconstruction was within a few percent of the true value when 200 gauges were available (with about a 10% variation for the interquartile range of individual estimates, decreasing to about 5% when a 50 year period for determining the EOFs was available). When only 40 gauges were used, the ensemble mean trend was biased low by a little under 10% (with an interquartile range of about 15%). They further showed that the reconstructions tend to overestimate the interannual variability and that a longer period for determining the EOFs is important in increasing the correlation between the reconstructed and model year to year variability. Reconstructions that do not use the constant mode perform poorly compared to those that do. These results are similar to our own tests with climate model simulations, with the reconstruction tending to have a slightly smaller trend. Christiansen et al. also found a simple mean of the tide gauges reproduces the trend with little bias in the ensemble mean and about a 10% variation in the interquartile range. However, the simple mean has larger interannual variations and correlates less well with the model interannual variability.

The GMSL estimates are not sensitive to the number of EOFs (over the range 4–20 plus the constant mode) used in the reconstruction, although the average correlation between the observed and reconstructed signal increases and the residual variance decreases when a larger number of EOFs is used. For the long periods considered here and with only a small number of records available at the start of the reconstruction period, we used only four EOFs which explain 45% of the variance, after removal of the trend.

2.4 Computation of EOFs

For each altimeter mission the along-track data described above are smoothed onto a $1° \times 1° \times 1$ month grid for the permanently ice-free ocean from 65°S to 65°N. The smoothing uses an e-folding length of 300 km and covers 90% of the global oceans. The three data sets are combined by matching means *at each grid point* (rather than just the global average) over the common periods between TOPEX/Poseidon and Jason-1 and between Jason-1 and OSTM/Jason-2. This is an attempt to overcome the problem of different geographically correlated errors in the missions, for example due to different sea-state bias corrections. The overlap between TOPEX/Poseidon and Jason-1 was from 15-January-2002 to 21-August-2002 (T/P cycles 344-365, J-1 cycles 1-22) or, effectively, February to July 2002 in our monthly data sets. The overlap between Jason-1 and OSTM/Jason-2 was from 12-July-2008 to 26-January-2009 (J-1 cycles 240-259 and J-2 cycles 1-20) or, effectively, August to December 2008 in our monthly data sets.

Separate versions of the altimeter data sets with and without the inverse barometer correction and with and without the seasonal signal are produced, as follows:

- Only whole years (in this case 17 years) are used.
- Grid points with gaps in the time series (e.g. due to seasonal sea ice) are ignored.
- The data are area (cos(latitude)) weighted.
- The global-mean trend is removed.
- The GIA correction appropriate for this data is applied (Mark Tamisiea, NOC Liverpool, private communication).

In the original (Church et al. 2004; Church and White 2006) reconstructions, the EOFs were defined with the 9 and 12 years (respectively) of TOPEX/Poseidon and Jason-1 satellite altimeter data available at those times. There are now 17 years of monthly satellite altimeter data available, almost twice as long as the original series. This longer time series should be able to better represent the variability and result in an improved reconstruction of global average sea level, as found by Christiansen et al. (2010). After removing the global average trend and the seasonal (annual plus semi-annual) signal, the first four EOFs account for 29, 8, 5 and 4% of the variance (Fig. 2). If the seasonal signal is not removed, the first four EOFs account for 24, 18, 14 and 4% of the variance. These EOFs characterise the large-scale interannual variability, particularly that associated with the El Niño-Southern Oscillation phenomenon, and for the case where the seasonal signal has not been removed, also include the seasonal north/south oscillation of sea level.

2.5 Sensitivity of the Results

To complete the reconstruction, we need to specify two parameters: the instrumental error covariance matrix $\boldsymbol{R}$ and the relative weighting of the "constant" mode to the EOFs. Church and White (2006) used the first differences between sets of nearby sea-level records to compute an average error estimate of the first differences of 50 mm and assumed errors were independent of and between locations (i.e. the error covariance matrix was diagonal). When the seasonal signal was removed, tests indicated the residual variance increased when a smaller error estimate was used but was not sensitive to the selection of larger values. Similarly, the residual variance increased when the weighting of the "constant" mode was less than 1.5 times the first EOF but was not sensitive to larger values. The computed trends for the 1880–2009 increased slightly (0.06 mm year^{-1} or about 4%) when the relative weighting was increased by 33% from 1.5 to 2.0 or the error estimate was decreased by 40% to 30 mm. Prior to 1880 when there were less than 15 locations available and none in the southern hemisphere, there was considerably greater sensitivity to the parameter choice than for the rest of the record and hence we focus on results after 1880. When the seasonal signal was retained in the solution, a larger error estimate of 70 mm was appropriate. This solution also had a larger residual variance and a slightly greater sensitivity in the trend to the parameter choice and hence we focus on the solution with the seasonal signal removed, as in our earlier studies.

As a further test of the effectiveness of the EOFs to represent the interannual variability in GMSL, we computed EOFs using shorter periods of 9 and 12 years, similar to our earlier analyses (Church et al. 2004; Church and White 2006). The resulting estimates are well within the uncertainties.

The atmospheric pressure correction makes essentially no difference to the GMSL time series for the computations with the seasonal signal removed and no difference to the computations including the seasonal signal after about 1940. However, prior to 1940, the correction does make a significant difference to the GMSL calculated with the seasonal signal included. These results suggests some problem with the atmospheric correction prior to 1940 and as a result we decided not to include this correction in the results. This issue seems to be related to the HadSLP2 data set not resolving the annual cycle and, possibly, the spatial patterns well for the Southern Hemisphere south of 30°S for the 1920s and 1930s, presumably because of sparse and changing patterns of input data at this time and in this region. This is being investigated further.

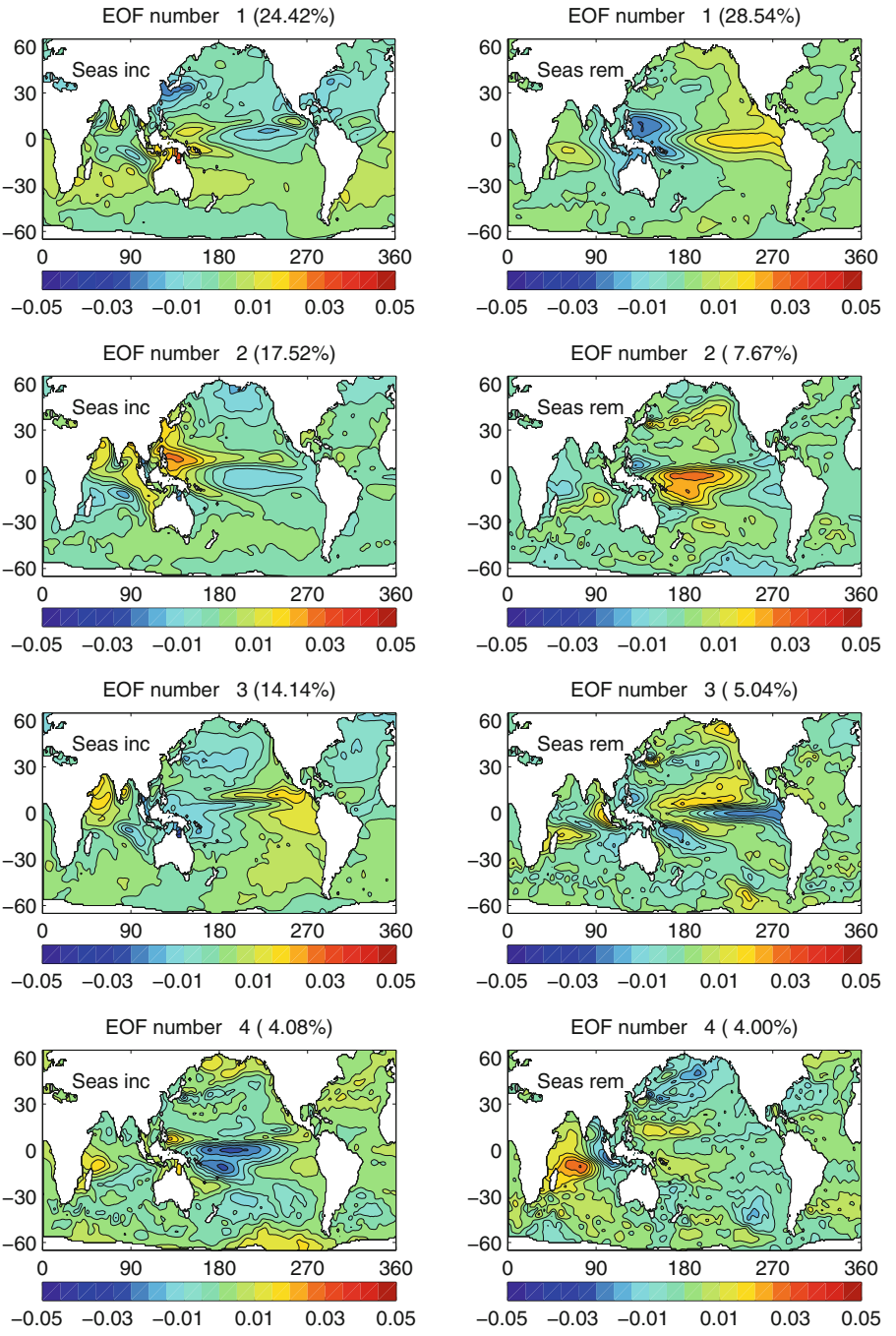

Fig. 2 The EOFs used in the sea-level construction. The four EOFs on the left include the seasonal signal and represent a combination of the seasonal signal and interannual variability. The corresponding four EOFs on the right are after the seasonal signal has been removed from the altimeter data. The EOFs are dimensionless and of unit length

3 Results

We present results for two periods: from 1880 to 2009 and the satellite altimeter period from January 1993 to December 2009. The latter is only a partial test of the reconstruction technique because the EOFs used were actually determined for this period.

The reconstructed and satellite estimates of GMSL have somewhat different error sources. The two largest uncertainties for the reconstructed sea level are the incomplete global coverage of sea-level measurements (particularly in the southern hemisphere), and uncertainties in land motions used to correct the sea-level records. The former contributes directly to the formal uncertainty estimates that are calculated on the basis that the sea-level records are independent. In estimating uncertainties on linear trends and accelerations, we recognise the series are autocorrelated and the number of effective degrees of freedom is only a quarter of the number of years of data. Previous tests using various GIA models suggest an additional uncertainty in trends of about ± 0.1 mm year^{-1} (Church et al. 2004) that should be added in quadrature to the uncertainty in the trend estimate from the time series (but not for estimates of the acceleration in the rate of rise). The annual time series of GMSL and the estimated uncertainty estimates are available at http://www.cmar.csiro.au/sealevel/sl_data_cmar.html.

3.1 1993–2009

The global mean sea level can be computed cycle-by-cycle (every 10 days) directly from the along track satellite data or from the mapped (monthly) satellite data. After averaging the cycle-by-cycle data set over 3 cycles these two estimates for the Jason-1 mission (February 2002 to January 2009; Fig. 3) are very similar; the differences have a standard deviation of 1.0 mm. The trends are different by only 0.2 mm year^{-1}, with the trend from the gridded data set being higher numerically, but not statistically different from the trend from the along-track data set.

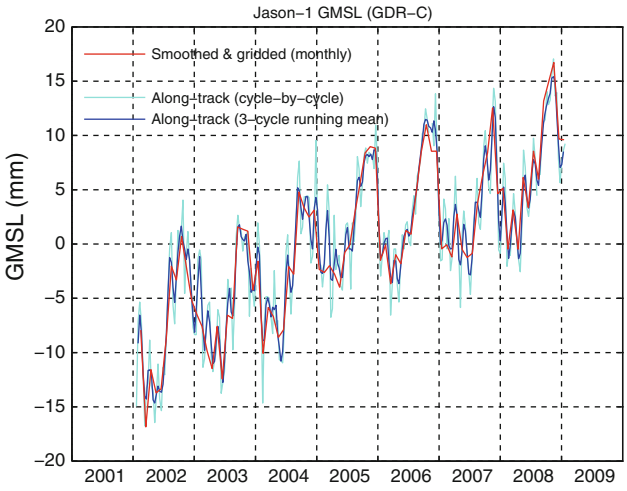

Fig. 3 Comparison of the satellite-altimeter estimates of GMSL from the along-track data (including all ocean areas where valid data are available) and the mapped data (for a fixed grid) for the duration of the Jason-1 altimeter mission

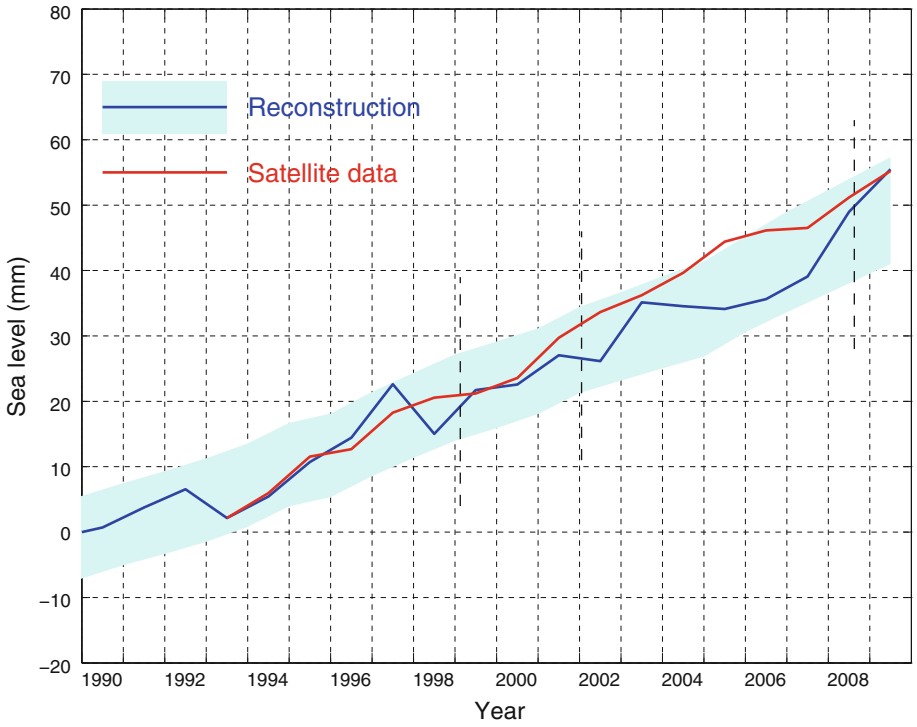

Fig. 4 Global average sea level from 1990 to 2009 as estimated from the coastal and island sea-level data (*blue* with one standard deviation uncertainty estimates) and as estimated from the satellite altimeter data from 1993 (*red*). The satellite and the in situ yearly averaged estimates have the same value in 1993 and the in situ data are zeroed in 1990. The *dashed vertical lines* indicate the transition from TOPEX Side A to TOPEX Side B, and the commencement of the Jason-1 and OSTM/Jason-2 records

The reconstructed and altimeter GMSL both increase from 1993 to the end of the record (Fig. 4). The larger year-to-year variability of the reconstructed signal (compared with the altimeter record) of ∼4–5 mm is less than the one standard deviation uncertainty estimates of about ±7 mm. For almost all of the record, the reconstruction is within the one standard deviation uncertainty estimate of the altimeter record. The uncertainty of the reconstruction increases slightly in the last couple of years because of the smaller number of tide gauge records available through the PSMSL.

After correcting for the GIA, the linear trend from the altimeter data from January 1993 to December 2009 is 3.2 ± 0.4 mm year^{-1} (note the GIA values appropriate for correcting the altimeter data are different to that necessary for the in situ data). The uncertainty range (1 standard deviation) comes from fitting a linear trend to the data using uncertainties on the annual averages of 5 mm and is consistent with an updated error budget of altimeter sea-level trend uncertainties (Ablain et al. 2009). They estimate the largest uncertainties are related to the wet tropospheric (atmospheric water vapour) correction, the bias uncertainty of successive missions, orbit uncertainty and the sea-state bias correction. These total to about 0.4 mm year^{-1}, similar to our uncertainty estimate. The reconstructed global average sea-level change over the same period is almost the same as for the altimeter data. However, as a result of different interannual variability, the trend of

2.8 ± 0.8 mm year^{-1} is smaller but not significantly different to the altimeter estimate after correction for glacial isostatic adjustment.

3.2 1880–2009

The GMSL time series (Fig. 5) are not significantly different from our earlier 2006 result (Church and White 2006). The total GMSL rise (Fig. 5) from January 1880 to December 2009 is about 210 mm over the 130 years. The trend over this period, not weighted by the uncertainty estimates, is 1.5 mm year^{-1} (1.6 mm year^{-1} when weighted by the uncertainty estimates). Although the period starts 10 years later in 1880 (rather than 1870), the total rise (Fig. 5) is larger than our 2006 estimate of 195 mm mostly because the series extends 8 years longer to 2009 (compared with 2001).

The interannual variability is mostly less than the one standard deviation uncertainty estimates, which range from ∼25 mm in 1880 to a minimum of ∼6 mm in 1988 (as shown in Fig. 5, where the yearly GMSL time series is plotted over the envelope of smoothed (±3 year boxcar) 1 standard deviation limits). However, there are a number of features which are comparable to/larger than the uncertainty estimates. Firstly, there is a clear increase in the trend from the first to the second half of the record; the linear trend

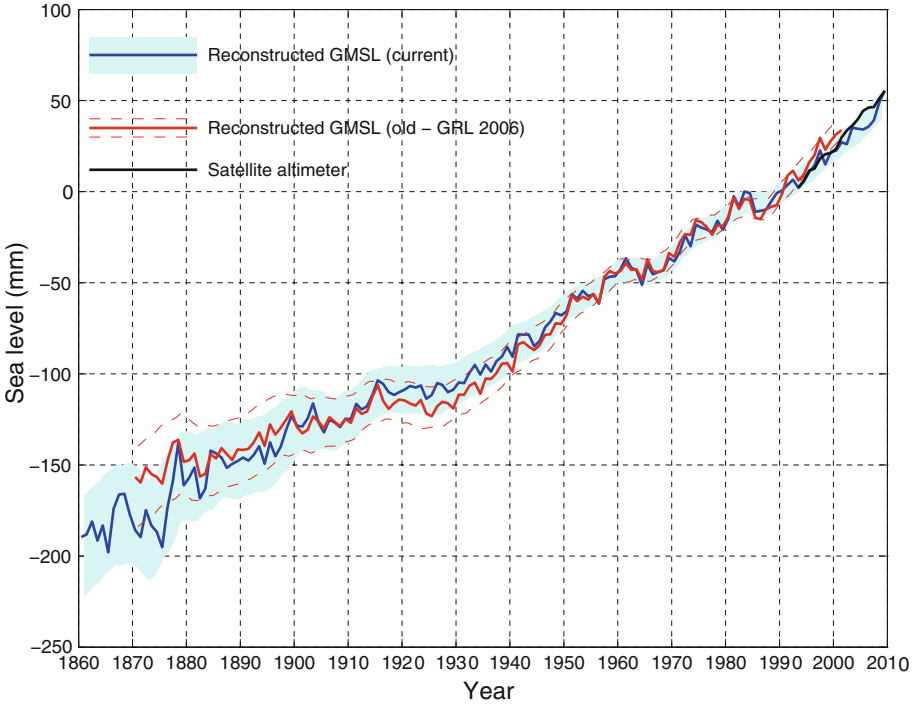

Fig. 5 Global average sea level from 1860 to 2009 as estimated from the coastal and island sea-level data (*blue*). The one standard deviation uncertainty estimates plotted about the low passed sea level are indicated by the *shading*. The Church and White (2006) estimates for 1870–2001 are shown by the *red solid line* and *dashed magenta lines* for the 1 standard deviation errors. The series are set to have the same average value over 1960–1990 and the new reconstruction is set to zero in 1990. The satellite altimeter data since 1993 is also shown in *black*

from 1880 to 1935 is 1.1 ± 0.7 mm year^{-1} and from 1936 to the end of the record the trend is 1.8 ± 0.3 mm year^{-1}. The period of relatively rapid sea-level rise commencing in the 1930s ceases abruptly in about 1962 after which there is a fall in sea level of over 10 mm over 5 years. Starting in the late 1960s, sea level rises at a rate of almost 2.4 mm year^{-1} for 15 years from 1967 and at a rate of 2.8 ± 0.8 mm year^{-1} from 1993 to the end of the record. There are brief interruptions in the rise in the mid 1980s and the early 1990s.

The linear trend from 1900 to 2009 is 1.7 ± 0.2 mm year^{-1} and from 1961 to 2009 is 1.9 ± 0.4 mm year^{-1}. However, there are significant departures from a linear trend. We estimate an acceleration in GMSL by fitting a quadratic to the time series, taking account of the time variable uncertainty estimates. From 1880 to 2009, the acceleration (twice the quadratic coefficient) is 0.009 ± 0.003 mm year^{-2} (one standard deviation). This estimate is slightly less than but not significantly different from the (one standard deviation) estimate of Church and White (2006) of 0.013 ± 0.003 mm year^{-2}, but still significantly different from zero at the 95% level. From 1900 to 2009, the acceleration is also 0.009 ± 0.004 mm year^{-2}. If the variable uncertainty estimates are ignored the equivalent accelerations are 0.010 and 0.012 mm year^{-2}.

4 Discussion

There are other recent estimates of changes in GMSL for this period widely available (Jevrejeva et al. 2006; Holgate and Woodworth, 2004; Fig. 6). They all agree approximately with our updated GMSL time series and the longer of these estimates (Jevrejeva et al. 2006) also has an acceleration in the 1930s and a pause in the rise commencing in the 1960s. These changes are also present in a number of individual sea-level records (Woodworth et al. 2009). However, note that the interannual variability in the Jevrejeva et al. series is unrealistically large in the early part of the record and larger than their uncertainty estimates. The Jevrejeva et al. estimate of sea level prior to 1850 (Jevrejeva et al. 2008) indicates an acceleration in the rate of rise commencing at the end of the eighteenth century. Note that their pre-1850 estimate uses only three-sea level records. We do not attempt to extend our construction back prior to 1860. If instead of the reconstruction technique, we employed a straight average of tide gauges, the overall trend back to 1910 is very similar but there is larger interannual variability (Fig. 6). Prior to 1910, the variability is even larger (consistent with the results of Christiansen et al. (2010), with unrealistic decadal trends of ±10 mm year^{-1}.

One source of error is the poor corrections for land motion. Bouin and Wöppelmann (2010) used GPS time series for correcting tide-gauge records for land motion from all sources and estimated a global average sea-level rise of 1.8 mm year^{-1} for the twentieth century, consistent with the present results and early studies (e.g. Douglas 1991). These GPS series are just now beginning to be long enough to provide useful constraints on land motion from all sources (not just GIA).

A significant non-climatic influence on sea level is the storage of water in dams and the depletion of ground water from aquifers, some of which makes it into the ocean. Chao et al. (2008) estimated that about 30 mm of sea-level equivalent is now stored in man-made dams and the surrounding soils; most of this storage occurred since the 1950s. Globally, the rate of dam entrapment has slowed significantly in the last decade or two. The depletion of ground water (Konikow et al. personal communication; Church et al. in preparation)

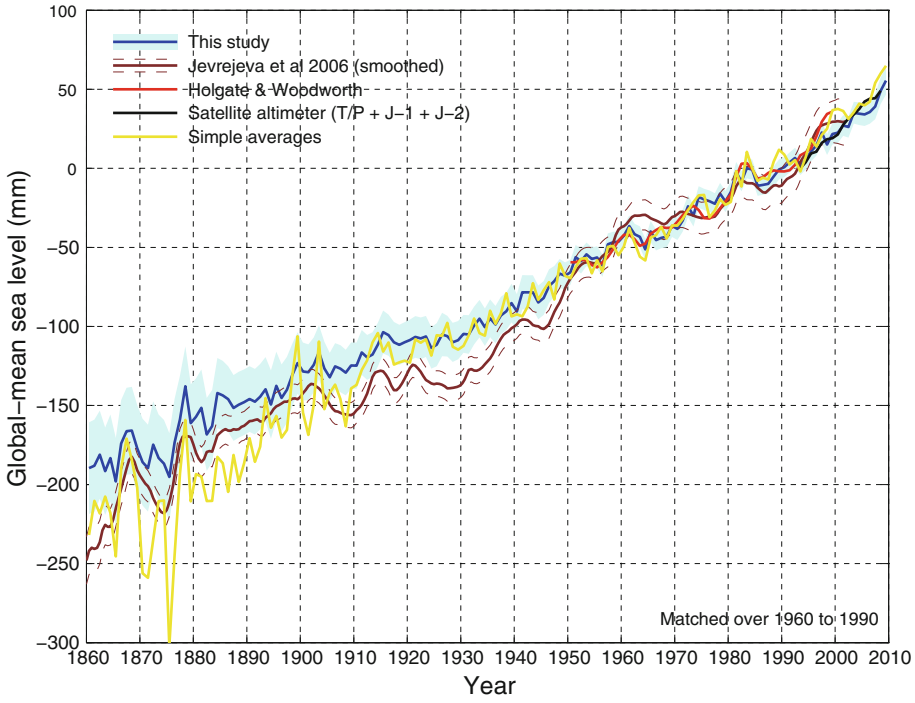

Fig. 6 Global average sea level from 1860 to 2009 as estimated from the coastal and island sea-level data (*blue*) compared with estimates of Jevrejeva et al. (2006, *brown*), Holgate and Woodworth (2004, *red*) and from a simple average of the gauges (*yellow*). All series are set to have the same average value over 1960–1990 and the reconstructions are set to zero in 1990. The satellite altimeter data since 1993 is also shown in *black*

offsets perhaps a third of this terrestrial storage over the last five decades and the rate of depletion has accelerated over the last two decades.

We remove this direct (non-climate) anthropogenic change in terrestrial water storage (both dam storage and aquifer depletion) from our observations to focus on the sea-level change related to climatic influences. The resulting time series (Fig. 7) shows a slightly faster rate of sea-level rise since about 1960 and a slightly larger acceleration for the periods since 1880 and 1900. Terrestrial storage contributed to the sea level fall in the 1960s but does not fully explain it. The volcanic eruptions of Mt Agung in 1963, El Chichon in 1982 and Mt Pinatubo in 1991 probably contribute to the small sea level falls in the few years following these eruptions (Church et al. 2005; Gregory et al. 2006; Domingues et al. 2008) but it has not yet been possible to quantitatively explain the mid 1960s fall in sea level (Church et al. in preparation).

The acceleration in the rate of sea-level rise since 1880 is in qualitative agreement with the few available long (mostly northern hemisphere) sea-level records and longer term estimates of sea level from geological (e.g. salt-marsh) data (for example Donnelly et al. 2004; Gehrels et al. 2006). These data mostly indicate an acceleration at the end of the nineteenth or start of the twentieth century (see Woodworth et al. 2011, this volume, for a summary and references).

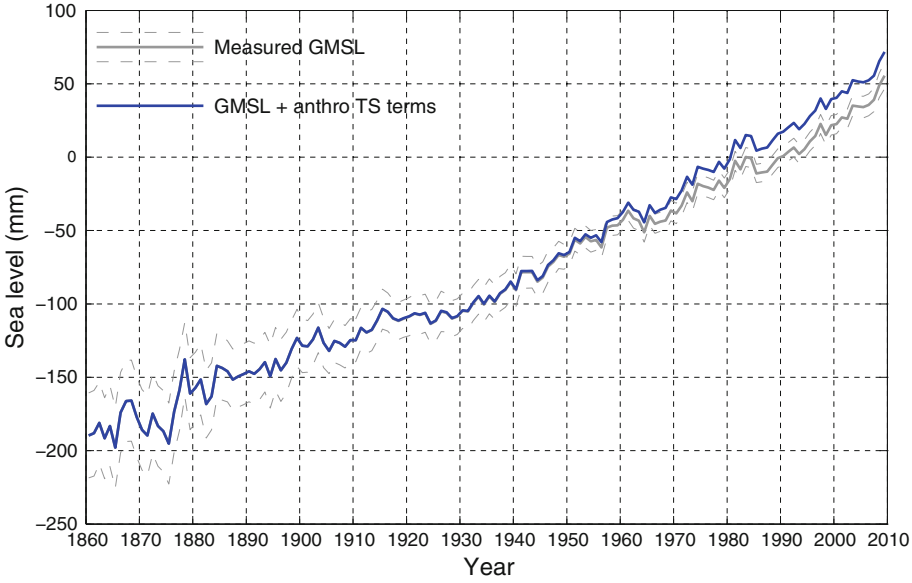

Fig. 7 Global average sea level from 1860 to 2009 as estimated from the coastal and island sea-level data (*grey*) and after correcting for the changes in terrestrial storage associated with the building of dams and the deletion of aquifers (*blue*). Note these series are virtually identical before 1950

In addition to the overall increase in the rate of sea-level rise, there is also considerable variability in the rate. Using the yearly average data, we computed trends for successive 16 year periods (close to the length of the altimeter data set) from 1880 to the present (Fig. 8). We find maxima in the rates of sea-level rise of over 2 mm year^{-1} in the 1940s and 1970s and nearly 3 mm year^{-1} in the 1990s (Fig. 8). As in earlier studies (using 10 and 20 year windows; Church and White 2006; Church et al. 2008), the most recent rate of rise over these short 16 year windows is at the upper end of a histogram of trends but is not statistically higher than the peaks during the 1940s and 1970s. Consistent with the findings of Christiansen et al. (2010), our computed variability in the rates of rise are almost a factor of two less than those where an average of tide gauges (Holgate and Woodworth 2004; Holgate 2007) is used to estimate GMSL. The rate of sea-level rise since 1970 has now been quantitatively explained (Church et al. in preparation) by a gradual increase in ocean thermal expansion, with fluctuations at least partly related to volcanic eruptions, and an increasing cryospheric contribution. The contribution from glaciers and ice caps (Cogley 2009), and the Greenland Ice Sheet (Rignot et al. 2008, 2011) both increased in the 1990s. There are also recent indications of an increasing contribution from the West Antarctic Ice Sheet (Rignot et al. 2011). The larger rate of rise in the 1940s may be related to larger glacier and ice-cap contributions (Oerlemanns et al. 2007) and higher temperatures over Greenland resulting in larger sea-level contributions at that time.

The rate of sea-level rise as measured both by the satellite altimeter record and the in situ reconstruction of about 3 mm year^{-1} since 1993 is near the upper end of the sea-level projections for both the Intergovernmental Panel on Climate Change's Third (Church et al. 2001) and Fourth (Meehl et al. 2007—see also Hunter 2010) Assessment Reports. However, note that the in situ data also indicates that there was little net change in GMSL from

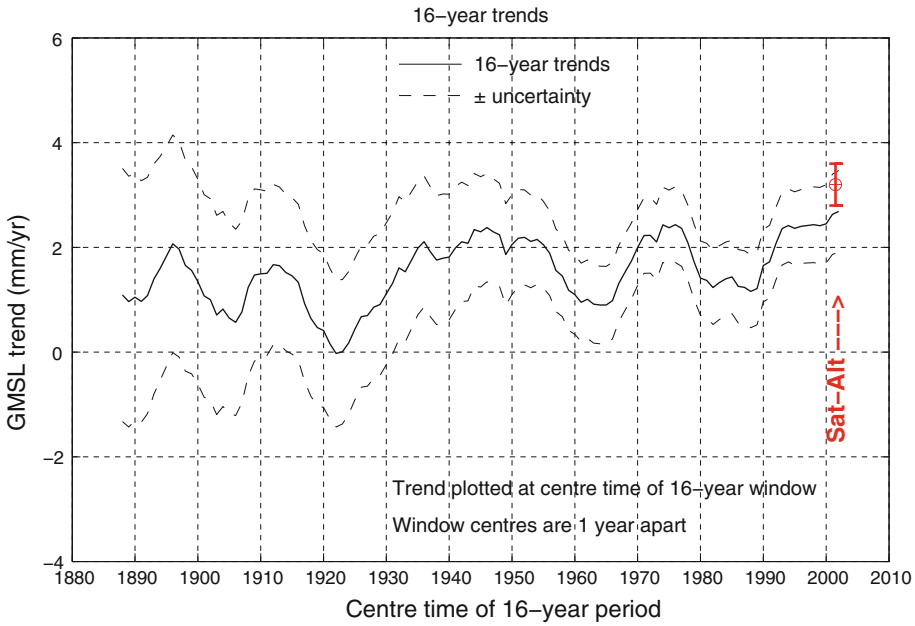

Fig. 8 Linear trends in sea level over successive 16 year periods for the yearly averaged reconstructed sea-level data. The trend from the satellite altimeter data are shown at the end of the time series

1990 to 1993, most likely as a result of the volcanic eruption of Mount Pinatubo in 1991 (Domingues et al. 2008; Church et al. in preparation).

Significant progress has been made during the last decade in estimating and understanding historical sea-level rise. However, much remains to be done. Of particular importance is the maintenance and continuation of the observing network and associated infrastructure such as the PSMSL archive. The in situ sea-level data set continues to provide a very valuable contribution to our understanding of late nineteenth, twentieth and early twenty first century sea-level rise. Data archaeology and paleo observations to extend the spatial and temporal coverage of in situ sea-level observations need to be vigorously pursued. Modern GPS measurements at tide-gauge locations, which are now beginning to provide valuable information on vertical land motion (e.g., Bouin and Wöppelmann 2010) should be continued and expanded. This applies in particular to the use of in situ data to monitor the accuracy of satellite altimeter measurement systems. Increasing the number and geographical distribution of these GPS observations is a priority. Of course a major priority is maintaining a continuous record of high-quality satellite-altimeter observations of the oceans and continuing to improve the International Terrestrial Reference Frame and maintaining and expanding the associated geodetic networks. These improved observations need to be combined with more elegant analysis of the observations, including, for example, considering changes in the gravitational field associated with evolving mass distributions on the Earth and using observations of sea-level rise, ocean thermal expansion and changes in the cryosphere in combined solutions.

Acknowledgments This paper is a contribution to the Commonwealth Scientific Industrial Research Organization (CSIRO) Climate Change Research Program. J. A. C. and N. J. W. were partly funded by the

Australian Climate Change Science Program. NASA & CNES provided the satellite altimeter data, PSMSL the tide-gauge data.

References

Ablain MA, Cazenave A, Valladeau G, Guinehut S (2009) A new assessment of the error budget of global mean sea level rate estimated by satellite altimetry over 1993–2008. Ocean Sci 5:193:2001

Allan R, Ansell T (2006) A new globally complete monthly historical gridded mean sea level pressure dataset (HadSLP2): 1850–2004. J Clim 19:5816–5842

Anthoff D, Nicholls RJ, Tol RSJ, Vafeidis AT (2006) Global and regional exposure to large rises in sea-level: a sensitivity analysis. Tyndall Centre for climate change Research Working paper 96

Aviso (2003) AVISO and PODAAC user handbook—IGDR and GDR jason products. Edition 2.0. SMM-MU-M5-OP-13184-CN

Benada JR (1997) PO.DAAC Merged GDR (TOPEX/POSEIDON) Generation B user's handbook, version 2.0, JPL D-11007

Bouin MN, Wöppelmann G (2010) Land motion estimates from GPS at tide gauges: a geophysical evaluation. Geophys J Int 180:193–209. doi:10.1111/j.1365-246X.2009.04411.x

Brown S, Ruf CS, Keihm SJ (2002) Brightness temperature and path delay correction for TOPEX microwave radiometer yaw state bias. Technical report to the TOPEX/Poseidon Science Working Team, 8 August 2002, University of Michigan

Chambers DP, Melhaff CA, Urban TJ, Fuji D, Nerem RS (2002) Low-frequency variations in global mean sea level: 1950–2000. J Geophys Res 107:3026. doi:10.129/2001JC001089

Chambers DP, Hayes SA, Reis JC, Urban TJ (2003) New TOPEX sea state bias models and their effect on global mean sea level. J Geophys Res 108:3305. doi:10.1029/2003JC001839

Chao BF, Wu YH, Li YS (2008) Impact of artificial reservoir water impoundment on global sea level. Science 320:212–214. doi:10.1126/science.1154580

Christiansen B, Schmith T, Thejll P (2010) A surrogate ensemble study of sea level reconstructions. J Clim 23:4306–4326. doi:10.1175/2010JCLI3014.1

Church JA, White NJ (2006) A 20th century acceleration in global sea-level rise. Geophys Res Lett 33:L10602. doi:10.1029/2005GL024826

Church JA, Gregory JM, Huybrechts P, Kuhn M, Lambeck K, Nhuan MT, Qin D, Woodworth PL (2001) Changes in Sea Level. In: Houghton JT, Ding Y, Griggs DJ, Noguer M, van der Linden P, Dai X, Maskell K, Johnson CI (eds) Climate change 2001: the scientific basis. Contribution of working group 1 to the third assessment report of the intergovernmental panel on climate change. Cambridge University Press, Cambridge

Church JA, White NJ, Coleman R, Lambeck K, Mitrovica JX (2004) Estimates of the regional distribution of sea-level rise over the 1950 to 2000 period. J Clim 17:2609–2625

Church JA, White NJ, Arblaster J (2005) Significant decadal-scale impact of volcanic eruptions on sea level and ocean heat content. Nature 438:74–77. doi:10.1038/nature04237

Church J, White N, Aarup T, Wilson SW, Woodworth P, Domingues C, Hunter J, Lambeck K (2008) Understanding global sea levels: past, present and future. Sustain Sci 3:9–22. doi:10.1007/s11625-008-0042-4

Church JA, Woodworth PL, Aarup T, Wilson SW (eds) (2010) Understanding sea-level rise and variability. Wiley-Blackwell Publishing, Chichester

CNES (2009) OSTM/Jason-2 Products Handbook. SALP-MU-M-OP-15815-CN

Cogley JG (2009) Geodetic and direct mass-balance measurements: comparison and joint analysis. Ann Glaciol 50:96–100

Davis JL, Mitrovica JX (1996) Glacial isostatic adjustment and the anomalous tide gauge record of eastern North America. Nature 379:331–333

Domingues CM, Church JA, White NJ, Gleckler PJ, Wijffels SE, Barker PM, Dunn JR (2008) Improved estimates of upper-ocean warming and multi-decadal sea-level rise. Nature 453:1090–1093. doi:10.1038/nature07080

Donnelly JP, Cleary P, Newby P, Ettinger R (2004) Coupling instrumental and geological records of sea level change: evidence from southern New England of an increase in the rate of sea level rise in the late 19th century. Geophys Res Lett 31:L05203. doi:10.1029/2003GL018933
Douglas BC (1991) Global sea level rise. J Geophys Res 96:6981–6992
Douglas BC (1992) Global sea level acceleration. J Geophys Res 97:12,699–12,706
Douglas BC (2001) Sea level change in the era of the recording tide gauge. In: Douglas BC, Michael S, Kearney MS, Leatherman SP (eds) Sea level rise. International Geophysical Series, vol 75, Academic Press, San Diego
Fiedler JW, Conrad CP (2010) Spatial variability of sea level rise due to water impoundment behind dams. Geophys Res Lett 37:L12603. doi:10.1029/2010GL043462
Gehrels WR, Marshall WA, Gehrels MJ, Larsen G, Kirby JR, Eirksson J, Heinemeier J, Shimmield T (2006) Rapid sea-level rise in the North Atlantic Ocean since the first half of the nineteenth century. The Holocene 16:949–965. doi:10.1177/0959683606hl986rp
Gregory JM, Lowe JA, Tett SFB (2006) Simulated global-mean sea-level changes over the last half-millenium. J Clim 19:4576–4591
Holgate SJ (2007) On the decadal rates of sea level change during the twentieth century. Geophys Res Lett 34:L01602. doi:10.1029/2006GL028492
Holgate SJ, Woodworth PL (2004) Evidence for enhanced coastal sea level rise during the 1990s. Geophys Res Lett 31:L07305. doi:10.1029/2004GL019626
Hunter J (2010) Estimating sea-level extremes under conditions of uncertain sea-level rise. Clim Chang 99:331–350. doi:10.1007/s10584-009-9671-6
Jevrejeva S, Grinsted A, Moore JC, Holgate S (2006) Nonlinear trends and multi-year cycles in sea level records. J Geophys Res 111:C09012. doi:10.1029/2005JC003229
Jevrejeva S, Moore JC, Grinsted A, Woodworth PL (2008) Recent global sea level acceleration started over 200 years ago. Geophys Res Lett 35:L08715. doi:08710.01029/02008GL033611
Kaplan A, Kushnir Y, Cane MA (2000) Reduced space optimal interpolation of historical marine sea level pressure. J Clim 13:2987–3002
Leuliette EW, Nerem RS, Mitchum GT (2004) Calibration of TOPEX/Poseidon and Jason Altimeter Data to construct a continuous record of mean sea level change. Mar Geodesy 27:79–94. doi:10.1080/01490410490465193
Meehl GA, Stocker TF, Collins WD, Friedlingstein P, Gaye AT, Gregory JM, Kitoh A, Knutti R, Murphy JM, Noda A, Raper SCB, Watterson IG, Weaver AJ, Zhao Z-C (2007) Global climate projections. In: Qin D, Solomon S, Manning M, Marquis M, Averyt K, Tignor MMB, Miller HL Jr, Chen Z (eds) Climate change 2007: the physical science basis. Contribution of working group 1 to the fourth assessment report of the intergovernmental panel on climate change. Cambridge University Press, Cambridge
Milne GA, Davis JL, Mitrovica JX, Scherneck H-G, Johansson JM, Vermeer M, Koivula H (2001) Space-geodetic constraints on glacial isostatic adjustment in Fennoscandia. Science 291:2381–2385
Nerem RS, Mitchum GT (2001) Chapter 6 of Sea level rise—history and consequences. In: Douglas BC, Kearney MS, Leatherman SP (eds) Academic Press, London
Oerlemanns J, Dyurgerov M, van de Wal RSW (2007) Reconstructing the glacier contribution to sea-level rise back to 1850. The Cryosphere 1:59–65
Rignot E, Box JE, Burgess E, Hanna E (2008) Mass balance of the Greenland Ice Sheet from 1958 to 2007. Geophys Res Lett 35:L20502. doi:10.1029/2008GL035417
Rignot E, Velicogna I, van den Broeke MR, Monaghan A, Lenaerts J (2011) Acceleration of the contribution of the Greenland and Antarctic ice sheets to sea level rise. Geophys Res Lett 38:L05503. doi:10.1029/2011GL046583
Ruf CS (2002) TMR drift correction to 18 GHz brightness temperatures, Revisited. Report to TOPEX Project, 3 June, 2002
White NJ, Church JA, Gregory JM (2005) Coastal and global averaged sea-level rise for 1950 to 2000. Geophys Res Lett 32:L01601. doi:10.1029/2004GL021391
Woodworth PL (1990) A search for accelerations in records of European mean sea level. Int J Climatol 10:129–143
Woodworth PL, Player R (2003) The permanent service for mean sea level: an update to the 21st century. J Coastal Res 19:287–295
Woodworth PL, White NJ, Jevrejeva S, Holgate SJ, Church JA, Gehrels WR (2009) Evidence for the accelerations of sea level on multi-decade and century timescales. Int J Climatol 29:777–789. doi:10.1002/joc.1771
Woodworth PL, Menendez M, Gehrels WR (2011) Evidence for Century-time scale Acceleration in mean sea levels and for recent changes in extreme sea levels. Surveys in Geophysics, This Volume

Surv Geophys (2011) 32:603–618
DOI 10.1007/s10712-011-9112-8

Evidence for Century-Timescale Acceleration in Mean Sea Levels and for Recent Changes in Extreme Sea Levels

Philip L. Woodworth · Melisa Menéndez · W. Roland Gehrels

Received: 25 August 2010 / Accepted: 18 January 2011 / Published online: 1 February 2011

Abstract Two of the most important topics in Sea Level Science are addressed in this paper. One is concerned with the evidence for the apparent acceleration in the rate of global sea level change between the nineteenth and twentieth centuries and, thereby, with the question of whether the twentieth century sea level rise was a consequence of an accelerated climate change of anthropogenic origin. An acceleration is indeed observed in both tide gauge and saltmarsh data at different locations around the world, yielding quadratic coefficients 'c' of order 0.005 mm/year^2, and with the most rapid changes of rate of sea level rise occurring around the end of the nineteenth century. The second topic refers to whether there is evidence that extreme sea levels have increased in recent decades at rates significantly different from those in mean levels. Recent results, which suggest that at most locations rates of change of extreme and mean sea levels are comparable, are presented. In addition, a short review is given of recent work on extreme sea levels by other authors. This body of work, which is focused primarily on Europe and the Mediterranean, also tends to support mean and extreme sea levels changing at similar rates at most locations.

Keywords Sea level accelerations · Extreme sea level changes · Tide gauge and saltmarsh measurements · Data archaeology

P. L. Woodworth (✉)
National Oceanography Centre, Joseph Proudman Building, 6 Brownlow Street,
Liverpool L3 5DA, UK
e-mail: plw@pol.ac.uk

M. Menéndez
Environmental Hydraulic Institute "IH Cantabria", Universidad de Cantabria,
39005 Santander, Spain

W. Roland Gehrels
School of Geography, Earth and Environmental Sciences, University of Plymouth,
Plymouth PL4 8AA, UK

1 Introduction

This paper addresses two of the most important questions in Sea Level Science. The first question is, given that global sea level has risen at a rate of approximately 1.7 mm/year during the twentieth century, was that value significantly larger than in previous centuries? If the twentieth century sea level rise was primarily a consequence of anthropogenic climate change, as suggested by the assessments of the Intergovernmental Panel on Climate Change (IPCC), then one would have expected there to have been a long-term acceleration in the rate of rise.

The second question concerns whether evidence exists for significant differences between rates of change of extreme and mean sea levels. Scientists usually focus on the latter, as changes in mean values are associated closely to climate-related processes including oceanic steric change, variations in ice sheet, ice cap and glacier mass balance, and hydrological exchanges between land and ocean. However, people more concerned with impacts of sea level change, including those people who live near to the coast, tend to be interested primarily in evidence for changes in extreme sea levels.

The understanding of historical mean sea level (MSL) change, and the accurate prediction of potential future MSL rise, is a difficult task (as demonstrated by other papers in this volume). However, if extremes were to be observed to change at different rates, on average, to mean levels, then their understanding and prediction would present us with an even more difficult problem.

2 Century-Timescale Acceleration in Sea Level

One advantage in the study of accelerations, rather than of linear trends, in MSL is that the vertical land movements (VLMs) of the land on which the tide gauges (sea level stations) are situated, and which contribute to the observed relative sea level changes, are in many cases much lower in frequency than the ocean-related signals of interest. Therefore, the quadratic (or higher order) time-dependence of a sea level record should be associated primarily with ocean change rather than land movement. This situation applies when the main geological process responsible for VLM is Glacial Isostatic Adjustment (GIA). However, it will clearly not be the case when the area around a tide gauge experiences earthquakes or when local groundwater pumping of water or hydrocarbons takes place (see Emery and Aubrey (1991) for many examples of contributions of VLMs to sea level records).

On the other hand, there is a difficulty in answering our first question (whether the sea level changes of the twentieth century were significantly larger than in previous centuries and, therefore, whether accelerations in sea level have taken place) due to the limited number of long term sea level records spanning two or three centuries. Most long tide gauge records are from northern Europe, constructed from measurements of high and low waters (or sometimes high waters alone) before the invention of automatic tide gauges in the mid-nineteenth century enabled the measurement of the full tidal curve and a computation of MSL. Figure 1a is adapted from a similar figure shown in Woodworth (1999) and the IPCC Third Assessment Report (TAR, Church et al. 2001). Important modifications are that the Amsterdam record has been extended with the use of data from Den Helder, the Brest time series has been extended back to the eighteenth century (Pouvreau 2008; Wöppelmann et al. 2008), the Liverpool time series now attempts to reflect MSL rather than mean high water change, and the Stockholm record of Ekman (1988) has been

updated using data from the Permanent Service for Mean Sea Level (PSMSL, www.psmsl.org, Woodworth and Player 2003). If one applies a second-order fit ($a + bt + ct^2$ where 't' is time and 'c' must be doubled to give acceleration) to each time series, then quadratic coefficients 'c' of order 0.005 mm/year^2 are obtained, all the records shown providing evidence for a long term acceleration in sea level, and suggesting that the acceleration commenced around the end of the nineteenth century or a little later. There is only one other northern European record of similar length known to us; that record is from Kronstadt, Russia, spanning 1773–1993 which had many difficulties in its construction (Bogdanov et al. 2000).

There are no records of similar length elsewhere. However, if one settles for somewhat shorter records and examines time series from the PSMSL Revised Local Reference data set which commence before 1871 and have at least 100 years of data since that time, then one obtains 4 records from the Baltic and North Sea coasts of Germany. These yield 'c' values between 0.0005 and 0.0062 mm/year^2 for the mid-nineteenth century onwards, those values for the German Baltic stations being essentially zero. Outside of Europe, the same selection criteria provide only two additional records from San Francisco and New York which yield 'c' values of 0.0069 and 0.0038 mm/year^2 respectively since the 1850s, consistent with the acceleration inferred by Maul and Martin (1993) for 1846 onwards for Key West, America's longest, if somewhat gappy, record. These six shorter records are shown in Fig. 1b, and have superimposed separate linear fits to their nineteenth and twentieth century data as a guide to any acceleration. Altogether, Fig. 1a, b suggests that a century-timescale acceleration applies to the northern hemisphere in general, a conclusion further confirmed by the study of saltmarsh information discussed below. However, the magnitude of the acceleration varies between stations. Furthermore, it can be seen that, for tide gauge records with start dates in the mid-nineteenth century or later, it is much more difficult to have confidence in the evidence for acceleration between the centuries, given the amount of interannual and decadal variability present in all records (as discussed by Douglas 1992 and other authors, as is evident visually from Fig. 1a, b, and from a comparison of the formal errors on 'c' values given in the captions to Fig. 1a, b).

Several studies have been published which have presented 'reconstructions' of 'global' sea level change, with the use of both long and short records combined in various ways (Church and White 2006, 2011; Jevrejeva et al. 2006). Results tend to support findings from the individual long records. Church and White (2011) have recently updated their 2006 reconstructions using Empirical Orthogonal Functions (EOFs) of ocean variability as observed by altimetry since 1993, together with coastal tide-gauge information. They obtained a global-average acceleration of sea level between 1880 and 2009 of 0.011 ± 0.004 mm/year^2 (quadratic coefficient 'c' $= 0.0055 \pm 0.002$ mm/year^2). Jevrejeva et al. (2006) derived time series of regional and global sea level by combining both short and long tide gauge records from the early part of the nineteenth century onwards with the use of a 'virtual station' technique, and demonstrated changes in global sea level trend between the nineteenth and twentieth centuries similar to those of Church and White (see comparisons of these analyses in Woodworth et al. 2009a). Jevrejeva et al. (2008) attempted to extend the reconstruction analysis over three centuries with the use of the small number of long records, concluding that the long-term acceleration could have started nearer to the beginning of the nineteenth century rather than at its end, as preferred by other studies.

As might be anticipated, such a period of long-term acceleration consists of shorter periods with greater acceleration, or even deceleration. In the review by Woodworth et al. (2009a), it was pointed out that most sea level data originate from Europe and N America and both sets display evidence for a positive acceleration, or 'inflexion', around 1920–1930

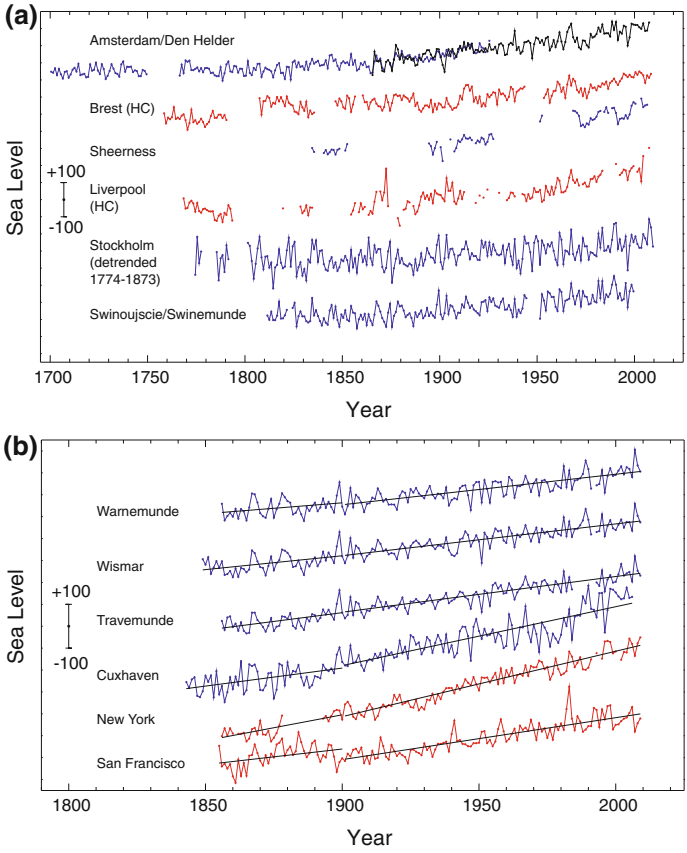

Fig. 1 **a** Long sea level records from northern Europe. The Brest record is a mean sea level time series derived from mean high waters as described by Pouvreau (2008) and Woodworth et al. (2010b). The Liverpool series has been derived in a similar manner using the 'adjusted mean high waters' of Woodworth (1999). These two records are denoted by 'HC' ('high water computation') and are shown in *red*. The Den Helder record shown in *black* has been adjusted to have the same mean value as Amsterdam for the period of overlap. The *vertical scale* is indicated by the ±100 mm error bars. The six time series yield 'c' coefficient values of 0.0037 ± 0.0002, 0.0015 ± 0.0005, 0.0091 ± 0.0015, 0.0057 ± 0.0008, 0.0036 ± 0.0010 and 0.0049 ± 0.0012 mm/year^2 respectively, top to bottom. **b** Records starting in the mid-nineteenth century for 4 stations in Germany (in *blue*) and 2 in North America (in *red*). The *vertical scale* is indicated by the ± 100 mm error bars. The six time series yield 'c' coefficient values of 0.0037 ± 0.0016, 0.0014 ± 0.0014, 0.0005 ± 0.0014, 0.0062 ± 0.0020, 0.0038 ± 0.0014 and 0.0069 ± 0.0019 mm/year^2 respectively, top to bottom. The *black lines* are separate linear fits to nineteenth and twentieth century data, as a guide to any acceleration between the centuries

and a negative one around 1960. These inflexions are the main contributors to the long-term accelerations mentioned above, and to the decelerations one tends to find using twentieth century data alone [as discussed by Woodworth (1990), Douglas (1992), and Holgate (2007)]. However, all of these characteristic features are not found in records from all parts of the world. For example, Raicich (2007) presented an extended (backwards) time series for Trieste spanning 1875 onwards which shows an overall secular trend of 1.3 ± 0.1 mm/year with little evidence for long-term acceleration, the downturn after the

1960s, seen particularly strongly in many Mediterranean records (Tsimplis and Baker 2000), being the single characteristic feature of the record.

Until the 1990s, the only evidence for accelerations came from tide gauge data and so could not be claimed to be necessarily 'global'. Since that time, precise radar altimeter data from space have become available (Fu and Cazenave 2001). One notes that the high rates during the 1990s, which represent an acceleration compared to those of the twentieth century as a whole, are of similar magnitude in both tide gauge and altimeter data. This recent acceleration has been reported by Holgate and Woodworth (2004), White et al. (2005) and Prandi et al. (2009), and has been discussed by Rahmstorf et al. (2007). Whether it represents the start of a long term increase in the rate of sea level rise, rather than decadal variability, remains to be seen.

If long, continuous records of sea level are not available from a region, then it becomes especially important to make maximum use of short periods of historical information where they exist. In particular, this applies to the relatively data-sparse southern hemisphere. The essential factor in such studies is that the historical tide gauge benchmarks must have survived to the present day. For example, Hunter et al. (2003) made use of measurements at Port Arthur, Tasmania from 1841 to 1842, together with more recent measurements, with the conclusion that sea level had risen at an average rate of 1.0 ± 0.3 mm/year, after a small correction for vertical land movement. Woodworth et al. (2010a) performed a similar analysis at Port Louis, Falkland Islands where James Clark Ross measured sea levels in 1842. The long-term rate of change of sea level was estimated to have been 0.75 ± 0.35 mm/year between 1842 and the mid-1980s, after correction for air pressure effects and for vertical land movement due to GIA.

These values of sea level change since the mid-nineteenth century do not provide insight into long term acceleration, but they do enable a baseline of change against which present day rates can be compared. For example, sea level has been rising at Spring Bay (near to Port Arthur) at a rate of 3.4 mm/year since 1991 (uncorrected for vertical land movement which is likely to be small, Table 5 of NTC 2009), while at Port Stanley (near to Port Louis) the rate of sea level rise observed since 1992, when the modern Stanley gauge was installed, has been 2.51 ± 0.58 mm/year, after correction for air pressure and GIA (Woodworth et al. 2010a). Figure 2 indicates this recent acceleration in the Falkland Islands. These larger rates over the last one or two decades are consistent with the picture of a general recent global acceleration with particular contributions from the tropics and from higher southern latitudes (Merrifield et al. 2009a). Other recent studies of southern hemisphere sea level change that have made use of sections of historical information include those of Watson et al. (2010) and Testut et al. (2006), although these investigations are limited to study of twentieth century changes. Testut et al. (2010) have recently studied changes at Saint Paul Island in the southern Indian Ocean, finding changes in sea level consistent with zero since 1874, although without a vertical land movement correction which is problematical at that location.

Alongside study of continuous tide gauge records, and of short sets of data separated by a long period of time, another important category to emphasise is that of gauges which once had sustained, continuous records but which were discontinued for one reason or other. Woodworth et al. (2009b) have shown how useful information on sea level trends can be obtained from the long historical records in Takoradi (Ghana), Aden (Yemen) and Karachi (Pakistan) separated by many decades from data obtained from newly installed instruments. Similar installations of new equipment at sites with long records must form a community priority.

It is well-known that the PSMSL data set is weighted considerably towards the northern hemisphere (see http://www.psmsl.org/products/data_coverage/). Although it is possible

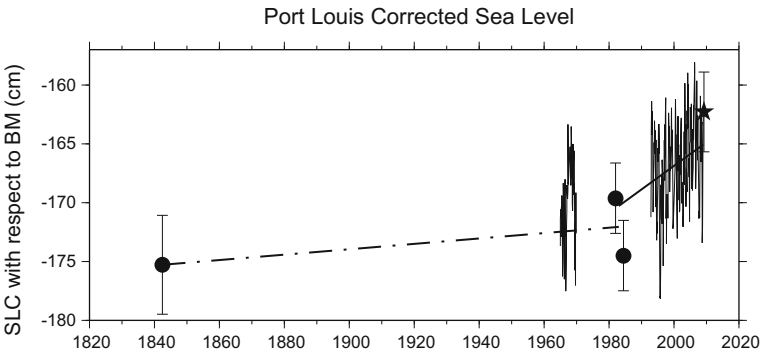

Fig. 2 *Large dots* indicate values of corrected sea level (SLC, i.e. sea level corrected for air pressure effects and for the seasonal cycle in SLC) at and near to Port Louis in the Falkland Islands. Values are shown relative to the height of the main ('Ross') benchmark. The *star* indicates SLC during a fortnight measurement period at Port Louis in February–March 2009. Also shown are monthly mean values of SLC from the permanent tide gauge station at Port Stanley that have been related to those at Port Louis with the use of overlapping data sets. The *dash-dotted trend line* connects the 1842 value to the 1981–1982 and 1984 values, while the *solid line* is a linear fit to the Port Stanley SLC data since 1992 extrapolated back to the early 1980s (adapted from Woodworth et al. 2010a)

that other historical tide gauge data of the types described above may be discovered in archives and analysed (a process called 'data archaeology'), thereby supplementing the PSMSL data set, it is clear that such information will always be limited, especially in the southern hemisphere. Consequently, other types of sea level information have to be investigated, and their data sets combined with those from tide gauges, thereby ensuring that our knowledge of sea level change over the past two or three centuries is more representative globally.

The complementary techniques might provide sea level time series which are either longer than those of tide gauges or come from regions where no gauge records exist. Possible techniques include the use of archaeological sources in areas such as the Mediterranean where tidal amplitudes are small and where Roman and other historical artifacts constructed at known heights relative to former sea levels still exist. In tropical areas, high-resolution information from corals can be used to deduce sea level changes over past centuries with sufficient precision to detect accelerations on multi-decadal timescales. Lambeck et al. (2010) provide a review of both areas of research.

Saltmarshes offer another source of sea level information and suitable marshes exist throughout the mid- to high-latitudes. Research has shown that in many circumstances the saltmarshes and nearby tide gauges provide similar information on timescales of decades to centuries, with the saltmarsh data appearing to a great extent to mimic a gauge record with a low-pass filter of approximately a decade depending on the location (Milne et al. 2009). The surface of a saltmarsh is close to the high tide level so that, when sea level rises over decades, sediments accumulate and the marsh surface builds up vertically. A history of sea level rise can then be reconstructed using micropalaeontological and sediment dating techniques, and the use of a 'transfer function' which depends on an assumption that the vertical distribution (relative to a chosen tide level) of fossil remains in the historical and modern marshes are the same. The need for continuous sedimentation means that marsh areas prone to erosion and highly fluctuating sedimentation rates, such as the lower saltmarsh and areas near tidal creeks, are to be avoided.

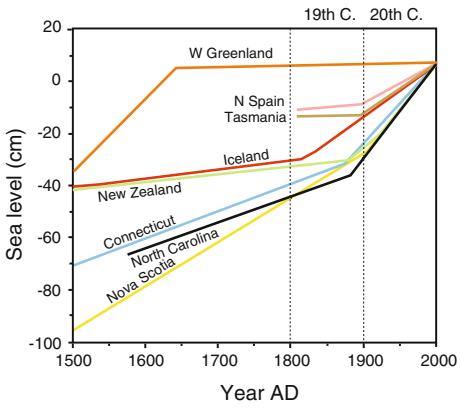

Fig. 3 A schematic compilation of sea level records obtained from saltmarshes demonstrating nineteenth to twentieth century accelerations in both hemispheres but with possibly different timing of 'inflexions' at different locations (Figure updated from that in Gehrels (2010). See the text for the individual references)

Figure 3 presents a compilation of findings from western Greenland (Long et al. 2010), northern Spain (Leorri et al. 2008), Tasmania (Gehrels et al. 2011), Iceland (Gehrels et al. 2006), New Zealand (Gehrels et al. 2008), Connecticut (Donnelly et al. 2004), North Carolina (Kemp et al. 2009) and Nova Scotia (Gehrels et al. 2005) (the individual papers may be consulted for analysis details, see also Woodworth et al. 2009a and Mitchum et al. 2010). Most of the saltmarsh records contain a rapid acceleration or 'inflexion' as indicated in this schematic compilation. The abruptness of the accelerations seen in the records has been often remarked upon and may be partly an artifact of the use of different dating methods at different points in the record. Nevertheless, the general character of acceleration seen in the northern European tide gauges can also be seen in the various saltmarsh data, although the changes of trend between the nineteenth and twentieth centuries suggested by Kemp et al. (2009), for the North American stations at least, would correspond to 'c' values of approximately 0.008–0.011 mm/year^2 which is approximately twice that inferred from the tide gauges. This may be due to the longer duration of these records and/or the 'filtering' effect mentioned above. However, if compaction has affected the sediments, the saltmarsh records may overestimate the sea level acceleration. Checks and, if required, corrections for compaction (e.g. through measurements of bulk density) are critical for establishing accurate sea level records from saltmarsh sediments (e.g. Gehrels et al. 2008). That said, the records in Fig. 3 are compaction-free or have been corrected for compaction.

All records, except Greenland and Iceland, show a clear inflexion at the end of the nineteenth century or the beginning of the twentieth century. The inflexion is most pronounced in the southern hemisphere records. This could be in line with the theory of sea level 'fingerprinting' (Mitrovica et al. 2001, 2010) if Greenland is a source of the excess sea level rise recorded in the twentieth century compared to preceding centuries. Similarly, this theory could provide an explanation why the inflexion is not present in the records close to the Greenland melt source (Iceland and western Greenland itself). On the other hand, it has been suggested that oceanic steric effects and changes in the ocean circulation may obscure any detectable sea level fingerprint signal (cf. Wake et al. 2006). This notwithstanding, the geographical pattern of the inflexion provides an interesting Greenland-melt working hypothesis which requires further testing. It is clearly important to use an expanded data set to study further the different timings of accelerations in different locations and by different methods (saltmarsh, corals, tide gauge, archaeology). Accelerations or inflexions which occur well before the twentieth century are of particular interest

as they suggest a natural rather than an anthropogenic cause. Those which have occurred in the more highly-instrumented modern era demand consistency between measurement techniques so as to have confidence in the various measurement methods.

What may have caused the long-term acceleration between the nineteenth and twentieth centuries seen in many parts of the world? Ultimately, an answer has to come from proper appreciation of the changing budget of oceanic steric, cryospheric and hydrological contributions due to natural (e.g. volcanic, solar) and anthropogenic forcings. Budgets have been discussed extensively recently (Domingues et al. 2008; Cazenave 2009; Church et al. 2010, 2011). Their findings are very encouraging. However, these discussions are from the perspective of the last few decades when most observational data sets have been of adequate quality. Consideration of budgets over longer timescales becomes more of a climate, glaciological and ocean circulation modelling exercise, and modelling undertaken so far has been unable to describe these features adequately.

One interesting (if speculative) relevant and recent study is that of Miller and Douglas (2007) who discussed evidence for a long-term deceleration in North Atlantic gyre strength (spin down), represented by decreasing air pressures near to the centre of the sub-tropical gyre, and for a connection to an acceleration in the rate of sea level change at the eastern boundary. A similar inference was made from the North Pacific data, although the poorer quality air pressure fields available for that ocean prevented as firm a set of conclusions as for the North Atlantic. Their analysis was limited to data sets from the late-nineteenth century onwards. However, Woodworth et al. (2010b) recently showed that the relationship holds, at a qualitative level for the North Atlantic, for the last two and a half centuries. Therefore, it is clear that a considerable amount of ocean and climate modelling remains to be performed in order to understand better the various contributors to global-average sea level rise and to the spatial redistribution of water.

3 Changes in Extreme Sea Levels

Similar considerations of data availability affect studies of extreme sea level changes. However, in this case the problems are much greater. For many years, most countries have contributed MSL information to the PSMSL. Such data were often regarded as having little commercial or national security importance, and hence could be shared internationally. However, the raw data (typically hourly values of sea level) were often restricted. Nowadays, the situation is much improved, standard formats for international data exchange have been agreed, and there are no technical reasons why data sets larger than the MSL ones cannot be submitted to, and quality controlled and archived by, data centres. Nevertheless, it remains the case that no raw data are shared by a number of countries with long coastlines (notably India, China and Russia).

A further factor related to data availability concerns the changes of tide gauge technology during the past half-century. Nowadays, most tide gauges have electronic data loggers with sea levels transmitted via telephone or satellite to data centres (although at different frequencies in different countries). In previous years, most tide gauges comprised stilling wells with floats connected to paper charts that required relatively simple inspection (for noting of high and low waters and thereby computation of Mean Tide Levels) or digitisation (for extraction of hourly values and computation of Mean Sea Levels). In some countries, charts remain undigitised, or worse have been destroyed. The consequence is that, while a small number of long records of hourly (or similar) sea levels exist, the vast majority of useful available records span the past few decades only. One

must recognise the excellent work of international programmes and data centres (notably the University of Hawaii Sea Level Center), the work of which through programmes such as TOGA (Tropical Ocean Global Atmosphere) and WOCE (World Ocean Circulation Experiment) has provided enhanced data sets for the latter part of the twentieth century (Woodworth et al. 2003).

When equipped with such a dataset of hourly sea levels from typically the 1970s onwards, one can ask if there is evidence for extremes having changed at different rates to MSL. A first attempt to address this question on a quasi-global basis was made by Woodworth and Blackman (2004) and has since been updated and extended by Menéndez and Woodworth (2010) who made use of a quasi-global sea level data set called GESLA (Global Extreme Sea Level Analysis) compiled through a collaborative activity of the Antarctic Climate and Ecosystems Cooperative Research Centre (ACE CRC), Australia and the National Oceanography Centre (NOC), Liverpool, UK.

They applied a non-stationary extreme value analysis to the monthly maxima of total elevations and surges for the period 1970 onwards, while a small subset of the data was used to study changes over the twentieth century. The analyses demonstrate the magnitude and timing of the seasonal cycle of extreme sea level occurrence, the magnitude of long-term trends in extreme sea levels, the evidence for perigean and nodal astronomical tidal components in the extremes, and the relationship of the interannual variability in high water levels to other ocean and atmosphere variations as represented by climate indices.

Extreme sea levels were found to have increased at most locations around the world, as suggested by many anecdotal reports of increased coastal flooding. However, the subtraction from the extreme sea levels of the corresponding annual median sea level was found to result in a reduction in the magnitude of trends at most stations, leading to the conclusion that much of the change in extremes is due to change in the mean values. This is clearly an important conclusion for coastal planners, if that conclusion applies also to the future, as predictions of MSL change are difficult and uncertain enough without additional uncertainties being introduced with regard to projected extremes.

This finding is illustrated in Fig. 4 which shows trends in the 99% percentiles of sea level, as measured (top) and with median sea level for each year removed (middle). The red dots at many tide gauge locations in the upper figure demonstrate the generally positive trends in extreme sea levels in recent decades. However, most red dots disappear in the middle figure when median sea levels are subtracted. Meanwhile, the bottom figure indicates that trends in 99% percentiles of non-tidal residuals (where mean residual is defined to be zero for each year and so 'residual' can be considered as a 'surge' component, see Menéndez and Woodworth 2010 for details) are negative at many locations, providing little or no evidence for increasing storminess in general and supporting the view that increases in measured extremes (top) have been due to MSL changes.

A related finding is demonstrated by Fig. 5. The upper figure indicates that extreme sea levels have become more frequent at most locations since the 1970s. However, when median sea level values are subtracted from the high percentiles, much smaller long-term changes in frequency of extreme events are found. Menéndez and Woodworth (2010) also pointed to the importance of climate variability on the extreme sea level trends, including in particular the El Niño—Southern Oscillation (ENSO) and North Atlantic Oscillation (NAO).

A large number of investigations have been made of changes in extreme sea levels by other authors. However, most studies have tended to concentrate on changes at particular locations. A problem in synthesising findings from this body of work stems from the fact that each analysis is made over different timescales and with the use of different methods

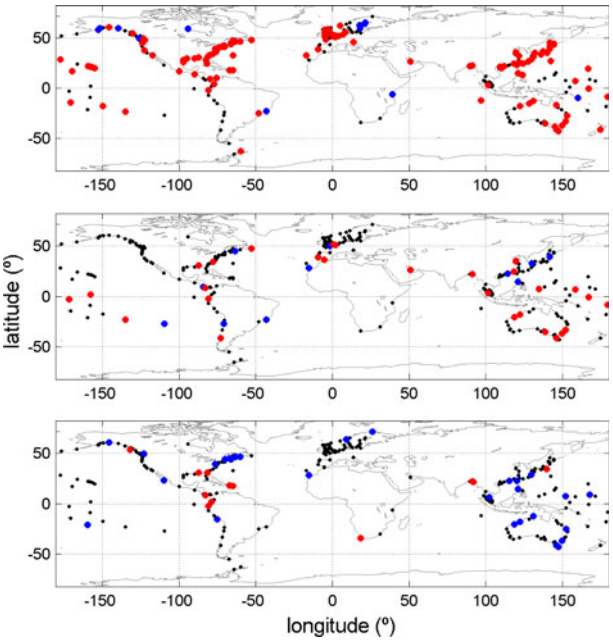

Fig. 4 Estimated trends in (*top*) annual 99th percentile of sea level, (*middle*) 99th percentile reduced to medians, and (*bottom*) 99th percentile of the non-tidal residual. Only trends at confidence level above 95% are shown by larger colour dots: *red* for positive and *blue* for negative trends [adapted from Menéndez and Woodworth (2010)]

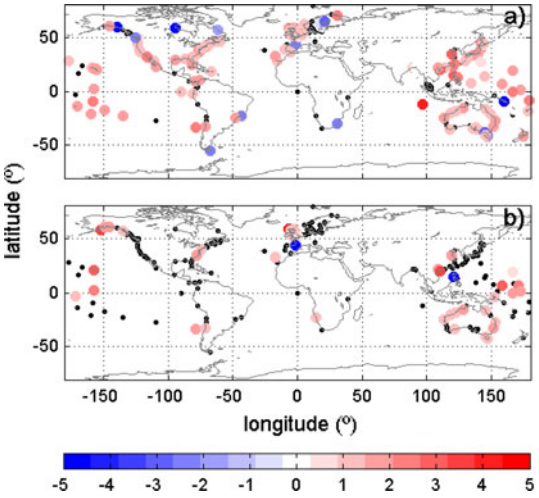

Fig. 5 Estimated changes in the frequency of extreme sea level events for **a** the measured sea level time series, and **b** for time series with annual median removed. Changes are the annual percentage of increase/decrease in the occurrence of extreme events relative to the average occurrence rate. *Small black dots* indicate trends with a confidence level below 95% [adapted from Menéndez and Woodworth (2010)]

(percentiles, peak over threshold, generalised extreme value, joint probably, revised joint probability, etc.) It is the nature of the problem when studying extremes that one is sensitive to the statistical properties of small samples, and each method employs the small amounts of data in different ways. A review of such publications has been made recently by Lowe et al. (2010), with the main conclusion once again that changes in extremes parallel those in MSL, although with exceptions to this general rule.

More recent publications, not contained in the Lowe et al. review, include the following papers, with a focus on Europe and the Mediterranean; we know of few recent papers on extreme sea levels from outside Europe since the review. Note that the following does not extend the Lowe et al. review of changes in waves, neither does it update discussion of the projected changes in twenty-first century extremes. Both latter topics will be covered extensively in an upcoming IPCC special report on extreme events (IPCC 2011).

Haigh et al. (2010) used a data set obtained from 18 tide gauges on the UK and French sides of the English Channel spanning 1900–2006. Changes in the surge, tide and MSL components in the records were analysed separately and in combination. Extreme sea levels were found to increase at all sites but at rates not significantly different from those in MSL. Ullmann and Monbaliu (2010) found that the wintertime 99th percentile of daily maximum sea level at Ostend in Belgium had increased at a rate of approximately 3 mm/year between 1925 and 2000, which can be largely understood as a combination of a rise in wintertime MSL of around 2 mm/year and of daily maximum sea surge of approximately +1 mm/year. Changes in the occurrence of large surges were further studied in terms of modifications of weather régimes over the North Atlantic.

Turning to southern Europe, Lowe et al. (2010) reported that Ullmann et al. (2007) had concluded that maximum annual sea levels had risen twice as fast as MSL during the twentieth century (4 rather than 2 mm/year) in the Camargue (Rhone Delta) region of southern France, largely due to changes in the wind field in recent decades. Related publications concerned with this particular locality include Moron and Ullmann (2005), Ullmann and Moron (2008) and Ullmann et al. (2008) who studied the relationships between air pressure, winds and storm surges in the area, and in particular the link between large surges and the negative phase of the NAO.

Marcos et al. (2009) employed data from 73 gauges covering the period 1940 onwards. The spatial distribution of extremes of tidal residuals (i.e. of non-tidal variability) was found to be well represented by those of a 2-D hydrodynamic model, although the model was found to underestimate the magnitude of the extremes. The interannual and decadal variability of extremes was found to be caused by MSL changes, with variability in both MSL and extremes being correlated negatively with the winter NAO index. Tsimplis et al. (2009) used data from 3 gauges in southern Europe (Coruña on the Atlantic coast of Spain, Malaga in the western Mediterranean and Trieste in the northern Adriatic) to study the effect of alteration of sampling frequency of the tide gauges on computed return periods of extremes. Differences of several centimeters were found in individual extremes obtained from hourly and 5-min sampling, resulting in differences in 50-year return period levels of decimeters (maximum difference of 38 cm at Trieste).

A seasonal climatology of extremes in southern Europe, including the Mediterranean, was presented by Tsimplis and Shaw (2010) who also found trends in high percentiles of hourly values to be largely removed when the 50% percentile (essentially the MSL) was removed. Letetrel et al. (2010) used hourly sea levels from Marseille for 1885–2008 and undertook a percentile analysis to investigate long-term trends of extremes. They concluded that secular variations in extreme sea levels are linked to MSL variations. However, decadal timescale variations in extremes showed differences to those in MSL. Changes in the return period levels of extremes were also studied, determining that an increase in levels had occurred since the 1970s.

In a study related to extremes but not discussing them per se, Vilibić and Šepić (2009) used data from 6 long records around Europe as representative of the region requiring each record to contain at least half a century of hourly or similar data. They investigated

variability in 4 frequency bands and considered how well the sea level variability was associated with storminess in the atmosphere and variation in storm tracks.

Outside of Europe, Lowe et al. (2010) referred to the study of Bromirski et al. (2003) who undertook a study of meteorologically-forced non-tidal residuals at San Francisco since 1858, concluding that winter non-tidal residuals had exhibited a significant increasing trend since about 1950. Cayan et al. (2008) have since complemented that work, concluding that the 99.99th percentile of measured sea level had increased considerably at San Francisco (by 20-fold since 1915) and at La Jolla (by 30-fold since 1933). Abeysirigunawardena and Walker (2008) discussed possible acceleration in MSL rise during the twentieth century at Prince Rupert in British Columbia, Canada. Sea level extremes were found to have risen at approximately 3.4 mm/year since 1945, which was twice the rate for MSL in that time, the additional amount of rise being suggested as due to ENSO-related regional interannual variability. This is one example of findings for which extremes appear to be rising faster than MSL.

Turning to South America, Fiore et al. (2009) found an increase in the number and height of positive surges at Mar del Plata in Argentina during the recent decade (1996–2005) compared to the previous half-century, consistent with findings from Buenos Aires by D'Onofrio et al. (2008). Both of these analyses were consistent with a rise in MSL being the responsible mechanism. Finally, from a more worldwide perspective of information on extremes, one can point to regular annual reporting of extreme levels published in the Bulletin of the American Meteorological Society (e.g. Merrifield et al. 2009b).

Advanced methods for studying extreme sea levels have also been published. For example, Mudersbach and Jensen (2010) developed a method which has some similarity to that described in Menéndez and Woodworth (2010). They developed a nonstationary extreme value analysis statistical approach, based on the generalized extreme value (GEV) distribution and an L-moment parameter estimation, which was employed to derive future design water levels. In addition, methods for best estimating extremes in the future have also been published since the Lowe et al. review. Thompson et al. (2009) considered two approaches for assessing the likely impact of changes in extremes in Atlantic Canada: a dynamical modelling approach, and a method based on statistical analysis of existing sea level data. Both methods provide a satisfactory description of present day flooding probabilities for regions with large tides, but both also have limitations with regard to the computation of future changes in the distribution of levels. Hunter (2010) described a method of combining observations of present sea level extremes with the (uncertain) projections for sea level rise during the twenty first century, with assumptions that most of the changes in extremes will be due to MSL rise and that changes in variability about the mean will be small. A method of estimating exceedance probability during the twenty first century was devised, using Australian data as an example.

A number of recent publications have pointed to long-term changes in the ocean tide which are larger than one would expect from simple changes in depth due to MSL rise (Jay 2009; Ray 2009; Woodworth 2010). At the least, these papers remind us that changes in extreme sea levels can originate from more than one source (i.e. changes in tides rather than, or as well as, storm surges or MSL).

4 Conclusions

Studies of long term changes in 'global' mean or extreme sea levels cannot be made without data sets of high quality and as good spatial and temporal coverage as possible. In

the past few years, one can point to general improvements in data sets due primarily to developments in the Global Sea Level Observing System (GLOSS) programme and to refurbishment in several ocean areas, notably in the Indian Ocean following the Andaman Tsunami in 2004. In addition, one can point to detailed 'data archaeology' exercises at a number of locations, especially in the southern hemisphere. However, it is clear that a lot of further effort in historical data acquisition and analysis is required.

A major conclusion from this body of work is that the global (or at least the northern hemisphere) ocean has experienced an acceleration in the rate of sea level change between the nineteenth and twentieth centuries, within which have been particular periods of greater or smaller acceleration. This conclusion was first obtained by inspection of the small number of long tide gauge records but has since been verified by the research into the use of saltmarsh data. An adequate explanation for the acceleration in terms of the budget of contributors to sea level change remains to be obtained. A second conclusion has particular practical as well as scientific importance but is applicable to a shorter period of decades rather than centuries. It appears that rates of change in extreme sea levels are similar to those in mean levels, although this general finding does not apply at every location. It is to be hoped that as data sets are enhanced, both spatially and temporally, that considerably greater insight will be obtained into the long term changes of extreme and mean sea levels and also the reasons for change.

Acknowledgments We thank Dr. Margot Saher of the University of Plymouth for assistance with the production of Fig. 3.

References

Abeysirigunawardena DS, Walker IJ (2008) Sea level responses to climatic variability and change in Northern British Columbia. Atmos-Ocean 46:277–296. doi:10.3137/ao.460301

Bogdanov VI, Medvedev MYu, Solodov VA, Trapeznikov YuA, Troshkov GA, Trubitsina AA (2000) Mean monthly series of sea level observations (1777–1993) at the Kronstadt gauge. Reports of the Finnish Geodetic Institute, No. 2000:1. Finnish Geodetic Institute, Kirkkonummi, Finland, p 34

Bromirski PD, Flick RE, Cayan DR (2003) Storminess variability along the California coast: 1858–2000. J Clim 16:982–993

Cayan DR, Bromirski PD, Hayhoe K, Tyree M, Dettinger MD, Flick RE (2008) Climate change projections of sea level extremes along the California coast. Clim Change 87(Suppl 1):S57–S73. doi:10.1007/s10584-007-9376-7

Cazenave A (2009) Sea level: regional and global trends. In: Hall J, Harrison DE, Stammer D (eds) Proceedings of OceanObs'09: sustained ocean observations and information for society, Venice, Italy, 21–25 September 2009, European Space Agency Publication WPP-306. Downloadable from http://www.oceanobs09.net/cwp/

Church JA, White NJ (2006) A 20th century acceleration in global sea-level rise. Geophys Res Lett 33:L01602. doi:10.1029/2005GL024826

Church JA, White NJ (2011) Changes in the rate of sea-level rise from the late 19th to the early 21st century. Surv Geophys (this volume)

Church JA, Gregory JM, Huybrechts P, Kuhn M, Lambeck K, Nhuan MT, Qin D, Woodworth PL (2001) Changes in sea level. In: Houghton JT, Ding Y, Griggs DJ, Noguer M, van der Linden PJ, Dai X, Maskell K, Johnson CA (eds) Climate change 2001: the scientific basis. Contribution of working group I to the third assessment report of the intergovernmental panel on climate change. Cambridge University Press, Cambridge, UK

Church JA, Aarup T, Woodworth PL, Wilson WS, Nicholls RJ, Rayner R, Lambeck K, Mitchum GT, Steffen K, Cazenave A, Blewitt G, Mitrovica JX, Lowe JA (2010) Sea-level rise and variability: synthesis and outlook for the future. Chapter 13. In: Church JA, Woodworth PL, Aarup T, Wilson WS (eds) Understanding sea-level rise and variability. Wiley-Blackwell, London

Church JA, White NJ, Konikow LF, Domingues CM, Cogley JG, Rignot E, Gregory JM, van den Broeke MR, Monaghan A, Velicogna I (2011) The Earth's sea-level and energy budgets from 1961 to 2008 (submitted for publication)

D'Onofrio EE, Fiore MME, Pousa JL (2008) Changes in the regime of storm surges in Buenos Aires, Argentina. J Coast Res 24:260–265. doi:10.2112/05-0588.1

Domingues CM, Church JA, White NJ, Gleckler PJ, Wijffels SE, Barker PM, Dunn JR (2008) Improved estimates of upper-ocean warming and multi-decadal sea-level rise. Nature 453:1090–1093. doi:10.1038/nature07080

Donnelly JP, Cleary P, Newby P, Ettinger R (2004) Coupling instrumental and geological records of sea level change: Evidence from southern New England of an increase in the rate of sea level rise in the late 19th century. Geophys Res Lett 31:L05203. doi:10.1029/2003GL018933

Douglas BC (1992) Global sea level acceleration. J Geophys Res 97(C8):12699–12706

Ekman M (1988) The world's longest continued series of sea level observations. Pure Appl Geophys 127:73–77

Emery KO, Aubrey DG (1991) Sea levels, land levels, and tide gauges. Springer, New York, 237 pp

Fiore MME, D'Onofrio EE, Pousa JL, Schnack EJ, Bertola GR (2009) Storm surges and coastal impacts at Mar del Plata, Argentina. Cont Shelf Res 29:1643–1649. doi:10.1016/j.csr.2009.05.004

Fu L-L, Cazenave A (eds) (2001) Satellite altimetry and Earth sciences. A handbook of techniques and applications. Academic Press, San Diego

Gehrels WR (2010) Sea-level changes since the Last Glacial Maximum: an appraisal of the IPCC Fourth Assessment Report. J Quat Sci 25:26–38. doi:10.1002/jqs.1273

Gehrels WR, Kirby J, Prokoph A, Newnham R, Achterberg E, Evans H, Black S, Scott D (2005) Onset of recent rapid sea level rise in the western Atlantic Ocean. Quat Sci Rev 24:2083–2100

Gehrels WR, Marshall WA, Gehrels MJ, Larsen G, Kirby JR, Eriksson J, Heinemeier J, Shimmield T (2006) Rapid sea level rise in the North Atlantic Ocean since the first half of the 19th century. The Holocene 16:948–964

Gehrels WR, Hayward BW, Newnham RM, Southall KE (2008) A 20th century sea-level acceleration in New Zealand. Geophys Res Lett 35:L02717. doi:10.1029/2007GL032632

Gehrels WR, Callard SL, Moss P, Marshall W, Milton A, Garnett M (2011) High rates of sea-level rise in the SW Pacific from the start of the 20th century (to be submitted for publication)

Haigh I, Nicholls R, Wells N (2010) Assessing changes in extreme sea levels: application to the English Channel, 1900–2006. Cont Shelf Res 30:1042–1055. doi:10.1016/j.csr.2010.02.002

Holgate SJ (2007) On the decadal rates of sea level change during the twentieth century. Geophys Res Lett 34:L01602. doi:10.1029/2006GL028492

Holgate SJ, Woodworth PL (2004) Evidence for enhanced coastal sea level rise during the 1990s. Geophys Res Lett 31:L07305. doi:10.1029/2004GL019626

Hunter J (2010) Estimating sea-level extremes under conditions of uncertain sea-level rise. Clim Change 99:331–350. doi:10.1007/s10584-009-9671-6

Hunter J, Coleman R, Pugh D (2003) The sea level at Port Arthur, Tasmania, from 1841 to the present. Geophys Res Lett 30:1401. doi:10.1029/2002GL016813

IPCC (2011) Special report of the "managing the risks of extreme events and disasters to advance climate change adaptation (SREX)" activity of Working Group 2 of the Intergovernmental Panel on Climate Change. To be published in 2011 (see http://ipcc-wg2.gov/AR5/extremes-sr/index.html)

Jay DA (2009) Evolution of tidal amplitudes in the eastern Pacific Ocean. Geophys Res Lett 36:L04603. doi:10.1029/2008GL036185

Jevrejeva S, Grinsted A, Moore JC, Holgate SJ (2006) Nonlinear trends and multiyear cycles in sea level records. J Geophys Res 111:C09012. doi:10.1029/2005JC003229

Jevrejeva S, Moore JC, Grinsted A, Woodworth PL (2008) Recent global sea level acceleration started over 200 years ago? Geophys Res Lett 35:L08715. doi:10.1029/2008GL033611

Kemp AC, Horton BP, Culver SJ, Corbett DR, van de Plassche O, Gehrels WR, Douglas BC, Parnell AC (2009) Timing and magnitude of recent accelerated sea-level rise (North Carolina, United States). Geology 37:1035–1038

Lambeck K, Woodroffe CD, Antonioli F, Anzidei M, Gehrels WR, Laborel J, Wright AJ (2010) Palaeo-environmental records, geophysical modelling and reconstruction of sea-level trends and variability on centennial and longer time scales. Chapter 4. In: Church JA, Woodworth PL, Aarup T, Wilson S (eds) Understanding sea-level rise and variability. Wiley-Blackwell, London

Leorri E, Horton BP, Cearetta A (2008) Development of a foraminifera-based transfer function in the Basque marshes, N. Spain: implications for sea-level studies in the Bay of Biscay. Mar Geol 251:60–74. doi:10.1016/j.margeo.2008.02.005

Letetrel C, Marcos M, Martín Míguez B, Wöppelmann G (2010) Sea level extremes in Marseille (NW Mediterranean) during 1885–2008. Cont Shelf Res 30:1267–1274. doi:10.1016/j.csr.2010.04.003

Long AJ, Woodroffe SA, Milne GA, Bryant CL, Wake LM (2010) Relative sea level change in west Greenland during the last millennium. Quat Sci Rev 29:367–383

Lowe JA, Woodworth PL, Knutson T, McDonald RE, McInnes K, Woth K, Von Storch H, Wolf J, Swail V, Bernier N, Gulev S, Horsburgh K, Unnikrishnan AS, Hunter J, Weisse R (2010) Past and future changes in extreme sea levels and waves. Chapter 11. In: Church JA, Woodworth PL, Aarup T, Wilson WS (eds) Understanding sea-level rise and variability. Wiley-Blackwell, London

Marcos M, Tsimplis MN, Shaw AGP (2009) Sea level extremes in southern Europe. J Geophys Res 114:C01007. doi:10.1029/2008JC004912

Maul GA, Martin DM (1993) Sea level rise at Key West, Florida, 1846–1992: America's longest instrument record? Geophys Res Lett 20:1955–1958

Menéndez M, Woodworth PL (2010) Changes in extreme high water levels based on a quasi-global tide-gauge dataset. J Geophys Res 115:C10011. doi:10.1029/2009JC005997

Merrifield MA, Merrifield ST, Mitchum GT (2009a) An anomalous recent acceleration of global sea level rise. J Clim 22:5772–5781. doi:10.1175/2009JCLI2985.1

Merrifield MA, Nerem RS, Mitchum GT, Miller L, Leuliette E, Gill S, Woodworth PL (2009b) Sea level variations, 2008 annual assessment. In: State of the Climate in 2008. Bull Am Meteorol Soc 90:S62–S65

Miller L, Douglas BC (2007) Gyre-scale atmospheric pressure variations and their relation to 19th and 20th century sea level rise. Geophys Res Lett 34:L16602. doi:10.1029/GL030862

Milne GA, Gehrels WR, Hughes CW, Tamisiea ME (2009) Identifying the causes of sea-level change. Nat Geosci 2:471–478. doi:10.1038/NGEO544

Mitchum GT, Nerem RS, Merrifield MA, Gehrels WR (2010) Modern sea-level-change estimates. Chapter 5. In: Church JA, Woodworth PL, Aarup T, Wilson WS (eds) Understanding sea-level rise and variability. Wiley-Blackwell, London

Mitrovica JX, Tamisiea ME, Milne GA, Davis JL (2001) Recent mass balance of polar ice sheets inferred from patterns of global sea-level change. Nature 409:1026–1029

Mitrovica JX, Tamisiea ME, Ivins ER, Vermeersen LLA, Milne GA, Lambeck K (2010) Surface mass loading on a dynamic Earth: complexity and contamination in the geodetic analysis of global sea-level trends. Chapter 10. In: Church JA, Woodworth PL, Aarup T, Wilson WS (eds) Understanding sea-level rise and variability. Wiley-Blackwell, London

Moron V, Ullmann A (2005) Relationship between sea-level pressure and sea-level height in the Camargue (French Mediterranean coast). Int J Climatol 25: 1531–1540. doi:10.1002/joc.1200.Erratum in 2006, Int J Climatol 26:987. doi:10.1002/joc.1320

Mudersbach C, Jensen J (2010) Nonstationary extreme value analysis of annual maximum water levels for designing coastal structures on the German North Sea coastline. J Flood Risk Manag 3:52–62. doi:10.1111/j.1753-318X.2009.01054.x

NTC (National Tidal Centre) (2009) The Australian baseline sea level monitoring project. Annual sea level data summary report, July 2008–June 2009. National Tidal Centre, Australian Bureau of Meteorology, Kent Town, South Australia, 41 pp. Available from http://www.bom.gov.au/ntc/IDO60202/IDO60202.2009.pdf

Pouvreau N (2008) Trois cents ans de mesures marégraphiques en France: outils, méthodes et tendances des composantes du niveau de la mer au port de Brest, PhD thesis, University of La Rochelle

Prandi P, Cazenave A, Becker M (2009) Is coastal mean sea level rising faster than the global mean? A comparison between tide gauges and satellite altimetry over 1993–2007. Geophys Res Lett 36:L05602. doi:10.1029/2008GL036564

Rahmstorf S, Cazenave A, Church JA, Hansen JE, Keeling RF, Parker DE, Somerville RCJ (2007) Recent climate observations compared to projections. Science 316:709. doi:10.1126/science.1136843

Raicich F (2007) A study of early Trieste sea level data (1875–1914). J Coast Res 23:1067–1073. doi:10.2112/04-0325.1

Ray RD (2009) Secular changes in the solar semidiurnal tide of the western North Atlantic Ocean. Geophys Res Lett 36:L19601. doi:10.1029/2009GL040217

Testut L, Wöppelmann G, Simon B, Téchiné P (2006) The sea level at Port-aux-Français, Kerguelen Island, from 1950 to the present. Ocean Dyn 56(5–6). doi:10.1007/s10236-005-0056-8

Testut L, Martin Miguez B, Wöppelmann G, Tiphaneau P, Pouvreau N, Karpytchev M (2010) Sea level at Saint Paul Island, Southern Indian Ocean, from 1874 to the present. J Geophys Res. doi:10.1029/2010JC006404

Thompson KR, Bernier NB, Chan P (2009) Extreme sea levels, coastal flooding and climate change with a focus on Atlantic Canada. Nat Hazards 51:139–150. doi:10.1007/s11069-009-9380-5

Tsimplis MN, Baker TF (2000) Sea level drop in the Mediterranean Sea: an indicator of deep water salinity and temperature changes? Geophys Res Lett 27:1731–1734
Tsimplis MN, Shaw AGP (2010) Seasonal sea level extremes in the Mediterranean Sea and at the Atlantic European coasts. Nat Hazards Earth Syst Sci 10:1457–1475. doi:10.5194/nhess-10-1457-2010
Tsimplis MN, Marcos M, Pérez B, Challenor P, Garcia-Fernandez MJ, Raicich F (2009) On the effect of the sampling frequency of sea level measurements on return period estimate of extremes—Southern European examples. Cont Shelf Res 29:2214–2221. doi:10.1016/j.csr.2009.08.015
Ullmann A, Monbaliu J (2010) Changes in atmospheric circulation over the North Atlantic and sea-surge variations along the Belgian coast during the twentieth century. Int J Climatol 30:558–568. doi:10.1002/joc.1904
Ullmann A, Moron V (2008) Weather regimes and sea surge variations over the Gulf of Lions (French Mediterranean coast) during the 20th century. Int J Climatol 28:159–171. doi:10.1002/joc.1527
Ullmann A, Pirazzoli PA, Tomasin A (2007) Sea surges in Camargue: trends over the 20th century. Cont Shelf Res 27:922–934. doi:10.1016/j.csr.2006.12.001
Ullmann A, Pirazzoli PA, Moron V (2008) Sea surges around the Gulf of Lions and atmospheric conditions. Glob Planet Change 63:203–214. doi:10.1016/j.gloplacha2007.10.002
Vilibić I, Šepić J (2009) Long-term variability and trends of sea level storminess and extremes in European Seas. Glob Planet Chang 71:1–12. doi:10.1016/j.gloplacha.2009.12.001
Wake LM, Milne GA, Leuliette E (2006) 20th Century sea-level change along the eastern US: unravelling the contributions from steric changes, Greenland ice sheet mass balance and Late Pleistocene glacial loading. Earth Planet Sci Lett 250:572–580. doi:10.1016/j.epsl.2006.08.006
Watson C, Burgette R, Tregoning P, White N, Hunter J, Coleman R, Handsworth R, Brolsma H (2010) Twentieth century constraints on sea level change and earthquake deformation at Macquarie Island. Geophys J Int 182:781–796. doi:10.1111/j.1365-246X.2010.04640.x
White NJ, Church JA, Gregory JM (2005) Coastal, global averaged sea level rise for 1950 to 2000. Geophys Res Lett 32:L01601. doi:10.1029/2004GL021391
Woodworth PL (1990) A search for accelerations in records of European mean sea level. Int J Climatol 10:129–143
Woodworth PL (1999) High waters at Liverpool since 1768: the UK's longest sea level record. Geophys Res Lett 26:1589–1592
Woodworth PL (2010) A survey of recent changes in the main components of the ocean tide. Cont Shelf Res 30:1680–1691. doi:10.1016/j.csr.2010.07.002
Woodworth PL, Blackman DL (2004) Evidence for systematic changes in extreme high waters since the mid-1970s. J Clim 17:1190–1197. doi:10.1175/1520-0442
Woodworth PL, Player R (2003) The permanent service for mean sea level: an update to the 21st century. J Coast Res 19:287–295
Woodworth PL, Aarup T, Merrifield M, Mitchum GT, Le Provost C (2003) Measuring progress of the global sea level observing system. EOS Trans Am Geophys Union 84(50):565. doi:10.1029/2003EO500009
Woodworth PL, White NJ, Jevrejeva S, Holgate SJ, Church JA, Gehrels WR (2009a) Evidence for the accelerations of sea level on multi-decade and century timescales. Int J Climatol 29:777–789. doi:10.1002/joc.1771
Woodworth P, Foden P, Pugh J, Mathews A, Aarup T, Aman A, Nkebi E, Odametey J, Facey R, Esmail MYA, Ashraf M (2009b) Insight into long term sea level change based on new tide gauge installations at Takoradi, Aden and Karachi. Int Hydrogr Rev No.1 (May 2009), 18–23. (http://www.iho-ohi.net/mtg_docs/IHReview/2009/IHR_May2009_Article02_1.pdf)
Woodworth PL, Pugh DT, Bingley RM (2010a) Long term and recent changes in sea level in the Falkland Islands. J Geophys Res 115:C09025. doi:10.1029/2010JC006113
Woodworth PL, Pouvreau N, Wöppelmann G (2010b) The gyre-scale circulation of the North Atlantic and sea level at Brest. Ocean Sci 6:185–190
Wöppelmann G, Pouvreau N, Coulomb A, Simon B, Woodworth P (2008) Tide gauge datum continuity at Brest since 1711: France's longest sea-level record. Geophys Res Lett 35:L22605. doi:10.1029/2008GL035783

Surv Geophys (2011) 32:619
DOI 10.1007/s10712-011-9116-4

ERRATUM

Erratum to: Evidence for Century-Timescale Acceleration in Mean Sea Levels and for Recent Changes in Extreme Sea Levels

Philip L. Woodworth · Melisa Menéndez · W. Roland Gehrels

Published online: 15 March 2011

Erratum to: Surv Geophys
DOI 10.1007/s10712-011-9112-8

The paper by Woodworth, P.L., Menéendez, M. and Gehrels, W.R. (2011) entitled "Evidence for century-timescale acceleration in mean sea levels and for recent changes in extreme sea levels" published in Surveys in Geophysics (doi:10.1007/s10712-011-9112-8) referred to the paper by Church, J.A. and White, N.J. (2011) entitled "Changes in the rate of sea-level rise from the late 19th to the early 21st century", submitted in the same volume of Surveys in Geophysics. It reported Church and White as having observed a global-average acceleration of sea level between 1880 and 2009 of 0.011 ± 0.004 mm/year^2 (quadratic coefficient 'c' $= 0.0055 \pm 0.001$ mm/year^2).

In fact, the title of the Church and White paper should have been given as "Sea-level rise from the late 19th to the early 21st century" and the acceleration of sea level between 1880 and 2009 should have been 0.009 ± 0.003 mm/year^2 (quadratic coefficient 'c' $= 0.0045 \pm 0.0015$ mm/year^2). These misquotes arose from papers being submitted at different times to the special issue of Surveys in Geophysics and from the inevitable updating of drafts during the review stages.

The online version of the original article can be found under doi:10.1007/s10712-011-9112-8.

P. L. Woodworth (✉)
National Oceanography Centre, Joseph Proudman Building, 6 Brownlow Street,
Liverpool L3 5DA, UK
e-mail: plw@pol.ac.uk

M. Menéndez
Environmental Hydraulic Institute "IH Cantabria", Universidad de Cantabria,
39005 Santander, Spain

W. Roland Gehrels
School of Geography, Earth and Environmental Sciences, University of Plymouth,
Plymouth PL4 8AA, UK

Surv Geophys (2011) 32:621–642
DOI 10.1007/s10712-011-9142-2

Response of a Coupled Ocean–Atmosphere Model to Greenland Ice Melting

D. Stammer · N. Agarwal · P. Herrmann · A. Köhl · C. R. Mechoso

Received: 21 December 2010 / Accepted: 5 July 2011 / Published online: 3 August 2011

Abstract We investigate the transient response of the global coupled ocean–atmosphere system to enhanced freshwater forcing representative of melting of the Greenland ice sheets. A 50-year long simulation by a coupled atmosphere–ocean general circulation model (CGCM) is compared with another of the same length in which Greenland melting is prescribed. To highlight the importance of coupled atmosphere–ocean processes, the CGCM results are compared with those of two other experiments carried out with the oceanic general circulation model (OGCM). In one of these OGCM experiments, the prescribed surface fluxes of heat, momentum and freshwater correspond to the unperturbed simulation by the CGCM; in the other experiment, Greenland melting is added to the freshwater flux. The responses by the CGCM and OGCM to the Greenland melting have similar patterns in the Atlantic, albeit the former having five times larger amplitudes in sea surface height anomalies. The CGCM shows likewise stronger variability in all state variables in all ocean basins because the impact of Greenland melting is quickly communicated to all ocean basins via atmospheric bridges. We conclude that the response of the global climate to Greenland ice melting is highly dependent on coupled atmosphere–ocean processes. These lead to reduced latent heat flux into the atmosphere and an associated increase in net freshwater flux into the ocean, especially in the subpolar North Atlantic. The combined result is a stronger response of the coupled system to Greenland ice sheet melting.

Keywords Greenland ice sheet melting · Sealevel rise · Coupled atmosphere–ocean experiments

D. Stammer (✉) · A. Köhl
Institut für Meereskunde, Universität Hamburg, Hamburg, Germany
e-mail: detlef.stammer@zmaw.de

N. Agarwal · P. Herrmann
Max-Planck-Institut für Meteorologie, Hamburg, Germany

C. R. Mechoso
University of California, Los Angeles, Los Angeles, CA, USA

1 Introduction

As a community, we are gradually coming closer to a better understanding of the present-day global sea level budget. However, many questions remain open on the subject of sea level variability and changes on regional scale and their future projection under climate change conditions. This situation is partly due to the large uncertainties of contemporary climate models in successfully reproducing the variability of the current climate. The lack of representation in the models of all forcing components of the climate system is an important contributor to such uncertainty. In this regard, a big deficit exists in the detailed knowledge of the impacts on regional sea level of freshwater input into the high-latitude oceans originating from the melting polar ice sheets.

Emerging knowledge suggests that sea level changes resulting from polar ice sheet melting are far from being intuitive. Instead, these changes seem to be associated with a strong regional dynamical response superimposed on contributions originating from the solid earth. For example, Stammer (2008), using an oceanic general circulation model (OGCM), highlighted the transient, steric (i.e., due to thermal expansion or haline contraction) response of the global ocean circulation to localized freshwater forcing around Greenland. In that study, increased freshwater runoff from Greenland resulted in a basin-wide steric response on timescales of a few years. The response was communicated remotely via oceanic processes including boundary waves, equatorial Kelvin waves, and propagating baroclinic Rossby waves. On the basis of those results, Stammer (2008) speculated that consideration of coupled atmosphere–ocean processes might significantly modify the insights obtained in an ocean-only framework. Hu et al. (2009) recently addressed some aspects of the coupled ocean–atmosphere response to potential Greenland ice sheet melting during the twenty-first century. In this case, the approach was based on the Community Climate System Model version 3 (CCSM3), and the transient response of the meridional overturning circulation (MOC) was emphasized. The paper suggests that only a strong ice sheet melting flux and associated net freshwater gain in the upper subpolar North Atlantic can weaken the MOC, but that the weakened MOC subsequently reduces the magnitude of the warming in the northern high latitudes by a few degrees, which in turn influences the regional sea level there. Using a different coupled atmosphere–ocean general circulation model (CGCM), Okumora et al. (2009) investigated the mechanisms by which a large freshwater input into the subarctic North Atlantic can influence the North Pacific climate via both oceanic and atmospheric pathways. The oceanic teleconnection contributes a large part of the North Pacific cooling through the Bering Strait throughflow by transporting colder, fresher water from the Arctic Ocean into the North Pacific. In addition, an atmospheric bridge originating from the North Atlantic leads to modified surface heat fluxes and southward Ekman transport in the Pacific, thereby playing a crucial role in the teleconnection between ocean basins.

Obviously, the subjects of regional sea level variability and change in response to Greenland ice sheet melting warrant more investigations and discussions. Of special concern are the feedback mechanisms and intrinsic timescales in the coupled climate system to freshwater input from polar ice sheets. In this context, the following questions need to be addressed:

1. What are the basin-wide responses of the ocean and atmosphere to increased melting of the polar ice sheets during the first decades after its onset?
2. How important are coupled atmosphere–ocean processes for the ocean's response to Greenland ice sheet melting, and what are those air–sea feedback mechanisms?

3. What is the role played by atmospheric and oceanic pathways in forcing the Pacific and Indian Oceans, what are the detailed paths, and how fast is the global response?

The present study addresses these questions by contrasting the oceanic response to increased melting of Greenland ice masses in a numerical model of the coupled atmosphere–ocean system with that obtained using the ocean component of the model with prescribed boundary conditions. The focus is on aspects related to changes in sea surface height (SSH). The special mechanisms at work in the response of the coupled system to perturbations in the ocean around Greenland and the pathways of anomalies in the atmosphere into the Pacific and Indian Ocean will be analyzed elsewhere (Agarwal et al. 2011).

The structure of the paper is as follows: Section 2 introduces the models used and describes the integrations performed. Section 3 compares the SSH response obtained in the model experiments. Section 4 discusses differences of the SSH responses obtained in the coupled framework relative to those emerging from the ocean-only run. Section 5 concentrates on changes of the MOC and polar heat transports in the Atlantic. Section 6 presents a discussion and the concluding remarks.

2 The Model Set-up and Experiments

Our study is based on the University of California, Los Angeles (UCLA) CGCM consisting of the UCLA atmospheric general circulation model (AGCM) coupled with the Massachusetts Institute of Technology (MIT) oceanic general circulation model (OGCM). Cazes-Boezio et al. (2008) describe the model's performance in the context of El Niño/Southern Oscillation (ENSO) forecasts. Details about the model are reported in Ma et al. (2010), and are also available online at http://www.atmos.ucla.edu/mechoso/esm/agcm.html.

The AGCM is a state-of-the-art model with advanced parameterizations of the major atmospheric physical processes. The parameterization of cumulus convection, including its interaction with the planetary boundary layer (PBL), follows the prognostic version of Arakawa and Schubert (1974) according to Pan and Randall (1998). The model includes parameterizations of prognostic cloud liquid water and ice (Köhler 1999). The parameterization of PBL processes is based on the mixed-layer approach of Suarez et al. (1983), as revised by Li et al. (2002), and upgraded to multi-layer by Konor et al. (2008). The parameterization of radiation processes is based on Harshvardhan et al. (1987, 1989), and includes the effects of cumulus, ice, and PBL clouds.

In the present study, we use AGCM version 7.1 with a horizontal resolution of 2.5° longitude and 2° latitude, and 29 layers in the vertical. Beginning with this version, the AGCM is coupled to the first-generation Simplified Simple Biosphere model (SSiB; Xue et al. 1991). In this model, several sources of data (Dorman and Sellers 1989; Xue et al. 1996a, b) are used to determine the vegetation types that specify monthly climatological land surface properties (e.g., leaf area index, green leaf fraction, and surface roughness length). The distributions of greenhouse gases, sea ice, and ocean surface albedo are all prescribed corresponding to a monthly mean observed climatology. SSiB has three soil layers and one vegetation layer.

The OGCM domain is quasi-global (80°S to 80°N) with all lateral boundary conditions closed. The sea-ice distribution is prescribed according to an observed monthly climatology. In our application, the zonal grid spacing in the MIT OGCM is 1° of longitude. The meridional ocean grid spacing is 0.3° of latitude within 10° of the Equator and increases to 1° latitude poleward of 22°N and 22°S. There are 46 ocean levels with thicknesses ranging

from 10 m in the top 150 m, and gradually increasing to 400 m thickness near the maximum model depth of 5,815 m. The model's bathymetry is based on ETOPO5 (Data Announcement 88MGG-02, Digital relief of the Surface of the Earth, NOAA, National Geophysical Data Center, Boulder, Colorado, 1988). The model employs the K-Profile Parameterization (KPP) vertical mixing scheme of Large et al. (1994) and the isopycnal mixing schemes of Redi (1982) and of Gent and McWilliams (1990) with surface tapering as per Large et al. (1997). Laplacian diffusion and friction are used except that horizontal friction is biharmonic. No-slip bottom, free-slip lateral, and free surface boundary conditions are employed. Surface freshwater fluxes are applied as virtual salt fluxes and heat and freshwater fluxes are exchanged between the ocean and the atmosphere at an interval of 1 day. Isopycnal diffusivity and isopycnal thickness diffusivity is 500 $m^2\ s^{-1}$. Vertical diffusivity is 5×10^{-6} $m^2\ s^{-1}$. Horizontal and vertical viscosities are 1,013 $m^4\ s^{-1}$ and 10^{-4} $m^2\ s^{-1}$, respectively.

As a preliminary step, the CGCM model was spun up for 30 years. The initial conditions for the AGCM correspond to November 1 in a long climate run with distribution of sea surface temperature (SST) corresponding to an observed climatology. The initial conditions for the OGCM correspond to the climatological temperature and salinity fields for November from Levitus et al. (1994). Initial conditions for all subsequent runs were taken from the end of the 30-year spin up. Using these initial conditions, the following set of experiments was performed, each lasting for 50 years:

1. The CGCM was integrated forward in time. This model integration will be referred to as the unperturbed coupled run.
2. The CGCM was integrated forward again, using exactly the same initial conditions as used in the unperturbed coupled run, but this time with a freshwater perturbation applied around Greenland as a virtual salt flux. This will be referred to as the perturbed coupled run.

The freshwater perturbation is 0.0275 Sv (1 Sv = $10^6 m^3/s$, equivalent to about 2 mm/year global sea level increase), five times the size of the present day estimated sea-ice melting rates (0.0055 Sv; Luthke et al. 2006), and its spatial distribution is shown in Fig. 1. The factor of five was applied to obtain a response with a magnitude larger than the model's internal variability. With this prescribed Greenland runoff, the ocean model response is comparable to that in Stammer (2008) in amplitude (see below). In contrast to that study, however, the surface temperature and salinity in our runs are not relaxed toward climatological fields. The magnitude of freshwater input obtained in this way is still an order of magnitude smaller than the hysteresis width reported by Rahmstorf et al. (2005), and more than 30 times smaller than the 1 Sv prescribed in typical water-hosing experiments (e.g., Timmermann et al. 2007; Stouffer et al. 2006).

To analyze the impact of coupling, two additional model integrations were performed, using the ocean component of the CGCM, again run over 50 years using the surface flux fields diagnosed from the unperturbed coupled run and starting from the same initial conditions as the coupled runs:

1. The OGCM was integrated forward in time, using the heat and freshwater fluxes obtained from the unperturbed coupled run. This model integration will be referred to as the ocean-only unperturbed run.
2. The OGCM was integrated forward in time again using the initial conditions of the ocean-only unperturbed run and with the same additional freshwater OGCM input around Greenland prescribed as a virtual salt flux in the coupled run. This model integration will be referred to as the ocean-only perturbed run.

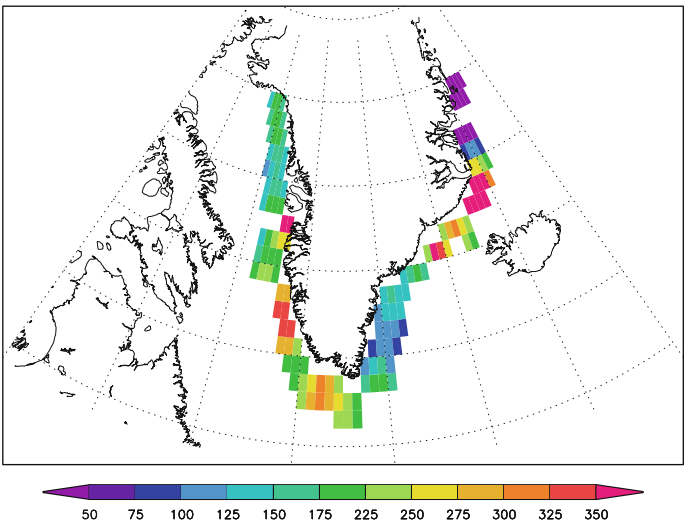

Fig. 1 Surface freshwater flux anomalies (in m^3/s) equivalent to 5 times the recent $\sim$170 GT per annum (Luthke et al. 2006) estimates of Greenland melt water loss

To investigate the response of the ocean-only or the coupled models to Greenland meltwater forcing, we focus the further analysis on the differences between perturbed and unperturbed coupled and ocean-only runs. For convenience, we will refer to those twin runs as the coupled experiments and the ocean-only experiments. However, to avoid analyzing climate noise originating from perturbations in the initial state rather than signals originating from the freshwater perturbations around Greenland, we will in the following analyze only lowpass filtered differences between the reference runs and the perturbed runs. In addition, we will average those differences in time and or space to further reduce any potential contamination from climate noise. To put later results into context, we show in Fig. 2 the standard deviation (SD) of the lowpass filtered SSH in the unperturbed coupled run. From the figure, it follows that the Atlantic and the Southern Ocean of the coupled reference run both show interannual to decadal variability of the order of 10 cm; respective numbers appear to be lower than 5 cm in the Indian Ocean and are even smaller over large parts of the Pacific.

A special feature of this paper is that the initial conditions in our experiments do not correspond to the model's long-term equilibrium state, since the 30-year spin-up of the CGCM is not long enough to achieve such a state. We can expect an extra model drift to be added resulting from the freshwater forcing. However, by not running the coupled model into equilibrium, we intend the ocean state to remain close to the observed climatology. In this way, the propagation of perturbations applied at the ocean's surface (such as freshening) into the interior basins will be more realistic than it would be through an equilibrium ocean state of the CGCM affected by the model's systematic errors.

3 Sea Surface Height Anomalies

Lowpass filtered SSH anomalies (i.e., differences between the values in the perturbed and the unperturbed runs) obtained in the ocean-only experiments are shown in left column of

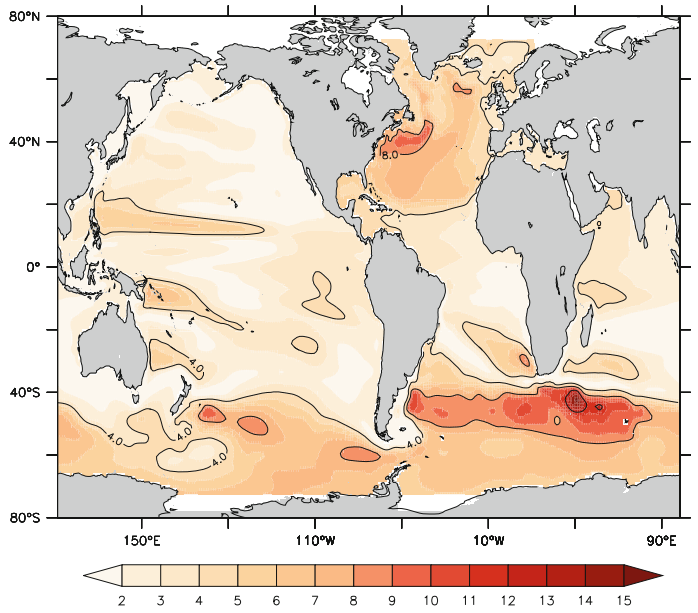

Fig. 2 Standard deviation (in cm) of the lowpass filtered (5-year running mean) SSH variations of the CGCM reference run over the 50-year integration period. *Solid contour lines* correspond to levels of 4 and 10 cm. The global mean is 3.97 cm

Fig. 3 after averaging them over the periods years 6–10, years 26–30, and years 41–45, respectively. Overall, the response agrees well with results obtained from Stammer (2008) (both in amplitude and pattern) and shows similar spatial patterns characterized by negative anomalies in the central North Atlantic and positive anomalies propagating southward. Associated steric anomalies reach amplitudes of about 4 cm along the western coast of the North Atlantic after just a few years, and basin-scale steric anomalies of about 1 cm in the North Atlantic after 30 years. In contrast, SSH anomalies are only about 1 mm in the Pacific (see also below).

For a comparison, we show in the right column of Fig. 3 similar SSH anomalies, but from the coupled experiment. There are several outstanding differences between the results in the experiments. Firstly, in the coupled experiment, clear SSH anomalies over the global ocean are evident in all three panels, with spatial patterns that are approximately the same scale and amplitude in the Indian Ocean and the Pacific. Moreover, in the Atlantic we find again structures similar to those obtained by Stammer (2008); however, the magnitude of the anomalies in the coupled experiment is substantially larger than in the ocean-only case. In the former experiment, the averaged steric increase in the Atlantic comes close to 1 cm in the first years and exceeds 10 cm in the lowest panel. We conclude from Fig. 3 that coupled processes do not significantly alter the SSH response in the Atlantic in terms of pattern but increase the magnitudes by a factor of about 5. In addition, the coupled experiment shows clear and statistically significant responses in all other ocean basins. These are of gyre-scale, suggesting that they essentially represent adjustments of the ocean circulation to changes of the atmospheric forcing in those basins. In particular, the negative SSH anomaly in the northern North Pacific has amplitudes that exceed the natural climate noise by several STDs.

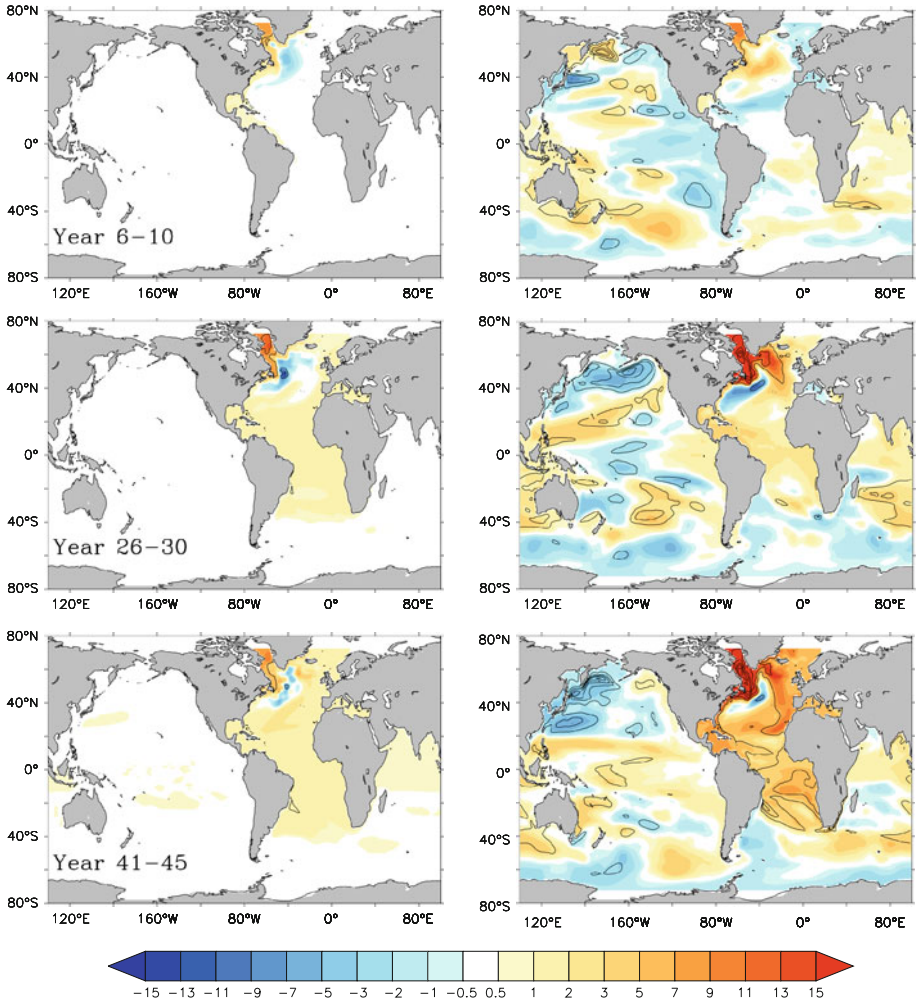

Fig. 3 Lowpass filtered SSH anomalies from the uncoupled (*left column*) and coupled (*right column*) experiments averaged over the years 6–10 (*top*), 26–30 (*middle*) and 41–45 (*bottom*), respectively. Units are cm, using a white-centred nonlinear colour-scale. In the *right column*, contours mark statistically significant areas (at a 65% confidence level and higher) using as a measure the quantity |SSH − anomaly|/STD with a contour interval of 1. The respective STD field is shown in Fig. 2

The time evolution of steric SSH anomalies averaged over the different ocean basins are shown in Fig. 4 for the coupled and ocean-only experiments. The values in Fig. 4 were corrected for the Boussinesq approximation effect on the global volume (Greatbatch 1994). According to Fig. 4, the SSH increase in the ocean-only experiment is largest in the North Atlantic, followed by the South Atlantic with about 50% of the amplitude. The increases in both the Indian Ocean and the Pacific are only about 25% of those in the North Atlantic. In all basins, the increase is smooth and almost monotonic in time, reaching about 1.5 cm in year 30 in the North Atlantic (2 cm in year 50) and about 0.5 cm in the North Pacific. In the coupled experiment, the largest SSH increase is also in the North Atlantic, while the

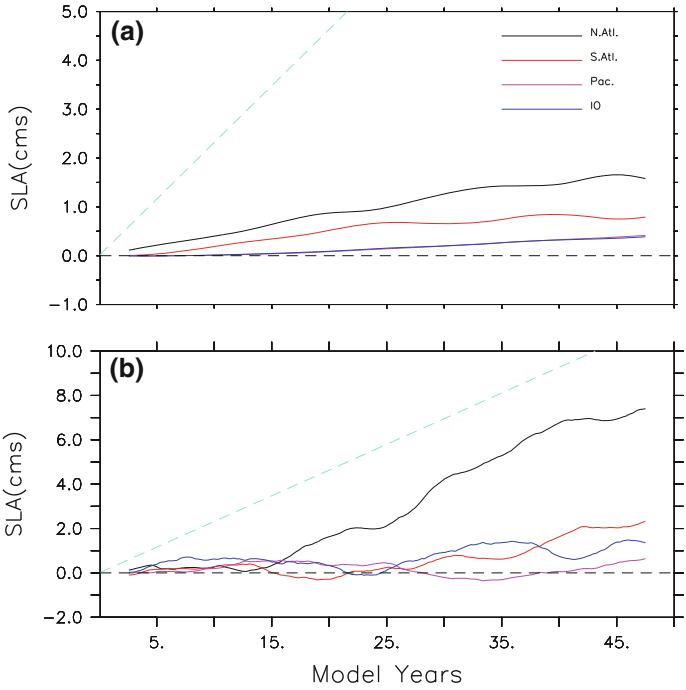

Fig. 4 Time series of lowpass filtered steric SSH anomalies (cm) (using a 5-year running mean) averaged over different ocean basins from ocean-only (*top*) and coupled (*bottom*) runs. *Dashed blue line* represents the non-steric sea level increase due to the meltwater addition. The *curves* labeled Pac. and IO represent the Pacific Ocean and the Indian Ocean respectively; they overlap in the *top panel*

increase in all other basins is substantially smaller, such that the long-term response in the South Atlantic is still larger than in the Pacific and the Indian Ocean. The increase in the North Atlantic reaches 8 cm during year 50, 3 cm in the South Atlantic, and about 1–2 cm in the North Pacific and Indian Ocean. Moreover, we note that the SSH varies strongly in all basins on interannual to decadal timescales, and that superimposed on those pronounced basin-scale oscillations in the coupled Pacific and Indian Ocean, both oceans show a net increase in steric sea level. In all basins and even as a global average, the SSH response in the coupled experiment is stronger than in the ocean-only one.

Figure 4 also shows in both panels as a blue dashed line the response of the global non-steric SSH increase due to the volume of melt water added to the ocean. These results illustrate that, in contrast to the ocean-only run experiment in which the non-steric SSH increase directly related to the Greenland melt is substantially larger than the steric response, the steric response in the coupled experiment has comparable order of magnitude in the North Atlantic. Two reasons as demonstrated below are responsible for this. Firstly, the atmospheric response contributes additional freshwater leading to a 76% larger halosteric increase (i.e., the volume increase due to freshening of the water column). Secondly, the associated heating and cooling patterns lead to a stronger heating in warm regions with relatively larger thermal expansion and stronger cooling in colder regions with smaller thermal expansion.

4 On the Different Responses in the Coupled and Ocean-Only Experiments

To investigate why steric responses are stronger both regionally, and globally (by a factor of about 2) in the coupled experiment, we compare in Fig. 5 the thermosteric and halosteric contributions to steric sea level change in the two experiments. The figure reveals that both contributions are larger in the coupled experiment as would result from enhanced surface heat and net freshwater input into the ocean. Nevertheless, the thermosteric component is still the main contributor to stronger steric SSH increase in the coupled experiment. The same component is also responsible for the pronounced temporal variability in the steric response. This result highlights again the coupled nature of the response of the climate system to Greenland meltwater forcing.

The time series of basin averaged SSH anomalies and the relative contributions from the thermosteric and halosteric components are shown in Figs. 6 and 7 for the ocean-only and coupled experiments, respectively. The results for the North Atlantic, the South Atlantic, the Pacific, and the Indian Ocean are shown separately. In both cases, thermosteric anomalies dominate the SSH increases in all basins, albeit with much larger amplitudes in the coupled experiment. An exception is the North Atlantic, however, where the net SSH response in the ocean-only experiment is smaller than that which would result from the halosteric component alone due to a negative thermosteric contribution. In contrast, the North Atlantic warms while becoming fresher in the coupled experiment, which leads to a much larger increase in basin-scale sea level. We also note the generally stronger, and temporally more variable halosteric response in all basins in the coupled experiment. We note that—in

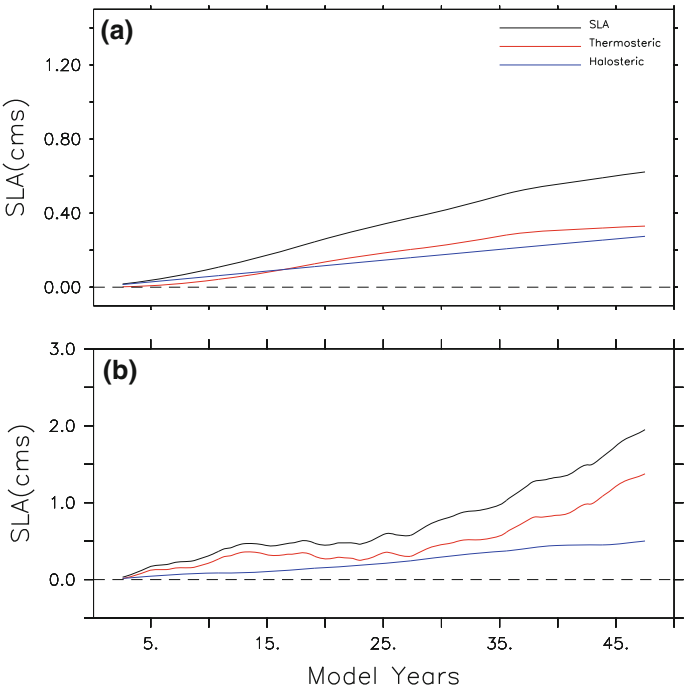

Fig. 5 Time series of globally averaged lowpass-filtered steric SSH anomalies (SLA; *black* in cm) and contributions from thermosteric (*red line*) and halosteric (*blue line*) effects ocean-only (*top*) and coupled (*bottom*)

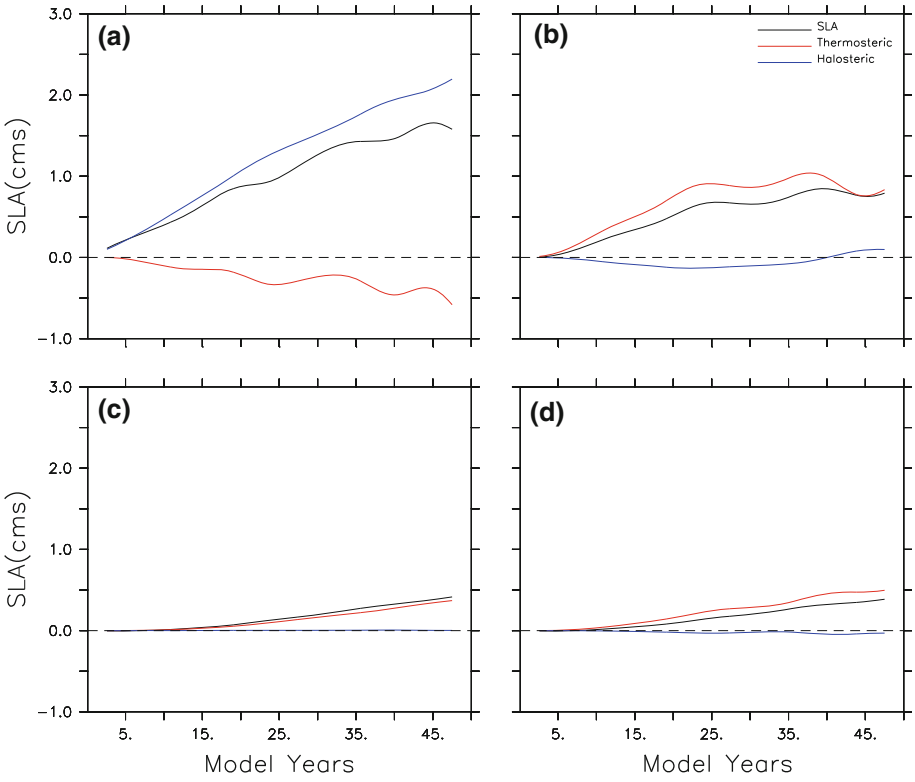

Fig. 6 Time series of basin averaged lowpass-filtered steric SSH anomalies(SLA, *black* in cm) and contributions from thermosteric (*red line*) and halosteric (*blue line*) effects in **a** North Atlantic, **b** South Atlantic, **c** Pacific and **d** Indian Ocean as seen in the uncoupled runs

the absence of any additional surface heat fluxes—the thermosteric effect in the ocean-only experiment can only result form the redistribution of heat by the changing circulation, the altered convection and the associated heating or cooling of near-surface water with different temperature than available in the unperturbed reference run.

To examine the causes for the enhanced steric response in the coupled experiment, we show in Fig. 8, as an example, the mean lowpass filtered salinity anomalies at 160 m depth from both experiments, averaged over the periods years 6–10, years 26–30, and years 41–45, respectively. The corresponding temperature anomalies are shown in Fig. 9. In the ocean-only experiment, the response has a similar pattern to that obtained by Stammer (2008); e.g., positive temperature anomalies appear around the coast of Greenland in year 1, subsequently move southward along the western coast of North America and later on spread across the equator via Kelvin waves. In the coupled experiment, the fields displayed in Figs. 8 and 9 show temperature and salinity perturbations stronger by an order of magnitude and include a pronounced remote response (in the Indian Ocean and Pacific) already during the first year. A remote response of comparable magnitude is totally absent in the ocean-only run. Such a quick and strong baroclinic response cannot be explained by ocean dynamics only. The signal must be transmitted by the atmosphere in response to the SST anomalies in the subpolar North Atlantic. We see that the subtropical gyres of all basins are dominated in the coupled run by basin-scale positive and negative anomalies

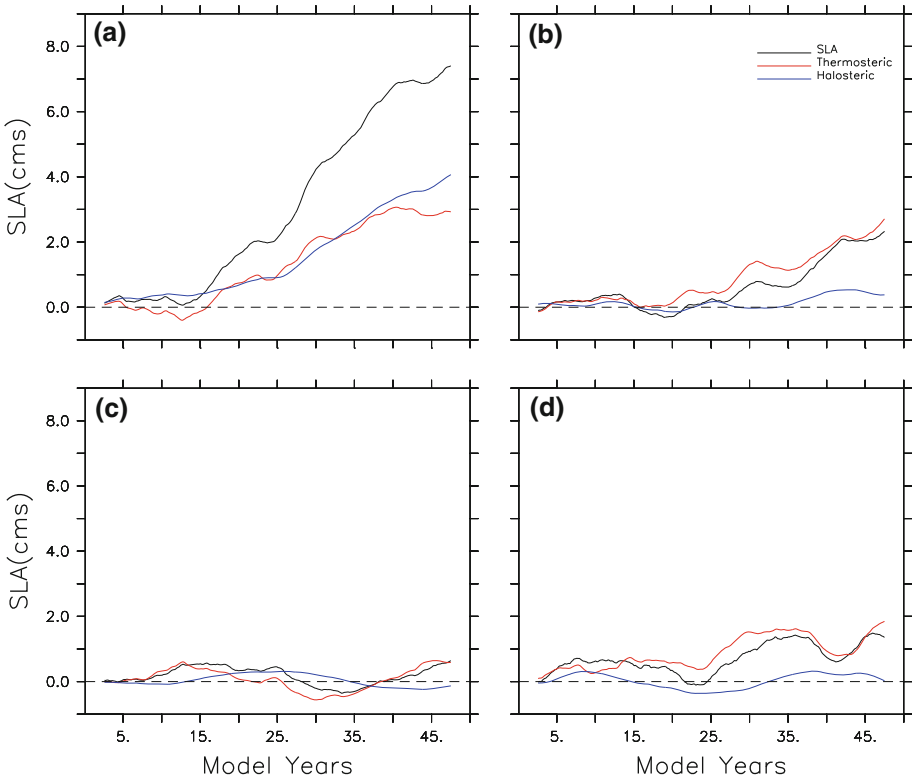

Fig. 7 Same as Fig. 6, but from coupled runs

that increase in amplitude and shift laterally with time. The pattern of the anomalies, however, does not change fundamentally with time, which is a typical forced ocean variability pattern.

The mean temperature anomalies averaged over the 50-year period of the ocean-only and coupled experiments are depicted in Figs. 10 and 11 along two meridional sections at 30°W and 180°E, respectively. In the ocean-only experiments, negative perturbations are maximum in the subpolar North Atlantic, where they extend throughout the entire ocean column. There are weaker negative anomalies over the Southern Ocean, while positive anomalies characterize the subtropics. Interestingly, a similar meridional distribution of temperature anomalies can be observed in the Pacific, albeit with much reduced amplitudes. The situation is again substantially different in the coupled experiments. Here, we find positive and negative anomalies with typically gyre scale in both hemispheres. Moreover, the surface layer has cooled in most of the two sections.

The temperature and salinity anomalies discussed in the previous paragraph are associated with anomalies in heat and freshwater contents. Averaged over the 50-year long run, the vertically integrated freshwater anomaly in the subpolar North Atlantic is generally positive (Fig. 12a), as expected since freshwater was added as runoff around Greenland. Other parts of the World Ocean also experience freshening, notably the South Atlantic and the South Pacific. In contrast, salinity increases in the tropical Atlantic, parts of the Indian Ocean, and in large areas of the Pacific and the Southern Ocean. Turning to the vertically

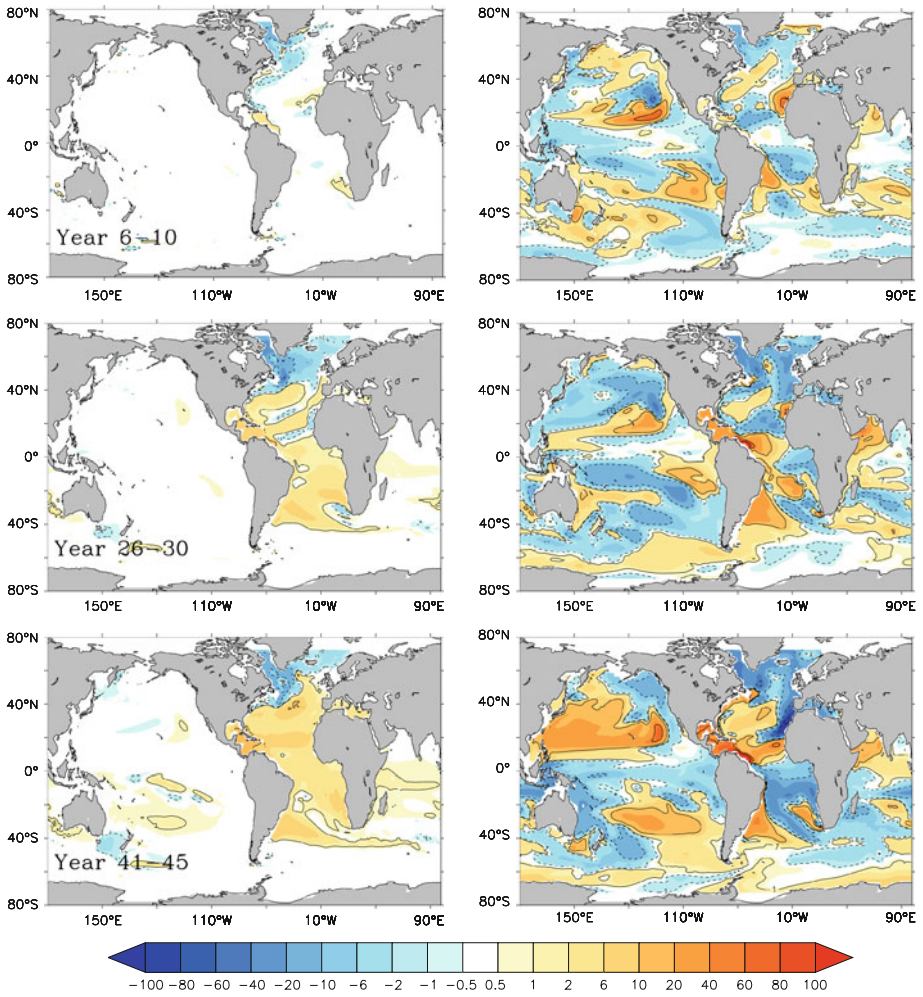

Fig. 8 Maps of mean salinity anomalies at 160 m depth resulting from the uncoupled (*left column*) and coupled (*right column*) experiments after lowpass-filtering (5-year running mean), each averaged over years 6–10 (top), 26–30 (middle) and 41–45 (bottom), respectively. Units are 0.01 PSU, using a white-centred nonlinear colour-scale. Contours on top are between $\pm 100 \times 10^{-2}$ psu at an interval of 50×10^{-2}, between $\pm 10 \times 10^{-2}$ at an interval of 10×10^{-2}, and between $\pm 1 \times 10^{-2}$ at an interval of 1×10^{-2}, excluding 0

integrated heat content (Fig. 12b), changes are to some extent consistent in pattern with density compensated freshwater changes as they would result from changes in the ocean circulation and an associated redistribution of heat and freshwater (see also Pardaens et al. 2010; and Landerer et al. 2007, for respective result in coupled climate scenario runs). A clear exception is the North Atlantic, where a positive heat anomaly is obvious along the entire western boundary.

The changes in freshwater and heat content shown in Fig. 12 are associated with, to some extent, changes in the net surface freshwater and heat fluxes shown in Fig. 13. According to this figure, on top of the addition of freshwater from Greenland melting, the

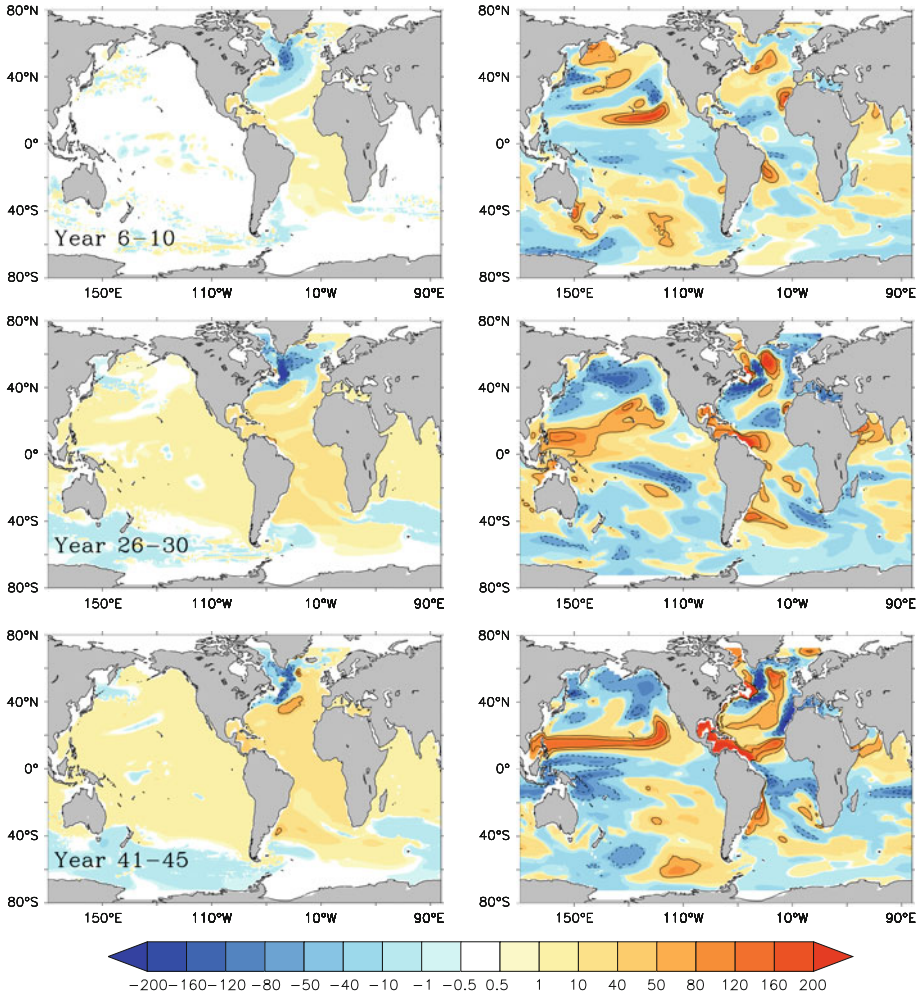

Fig. 9 Maps of mean temperature anomalies at 160m depth resulting from the uncoupled (*left column*) and coupled (*right column*) experiments after lowpass-filtering (5-year running mean), each averaged over years 6–10 (*top*), 26–30 (*middle*) and 41–45 (*bottom*), respectively. Units are 0.01°C, using a white-centred nonlinear colour-scale. Contours on *top* are between $\pm 100 \times 10^{-2}$°C at an interval of 50×10^{-2}°C, excluding 0

net surface freshwater flux into the ocean (Fig. 13a) is further enhanced along the western boundary of the North Atlantic as well as over large parts of the tropics. In contrast, the freshwater flux into the ocean is reduced in the Intertropical Convergence Zones (ITCZ) regions of all oceans. The changes in the net surface freshwater flux in the coupled experiment are largely related to surface temperature-dependent evaporation changes, which are directly related to changes in latent surface heat flux (Fig. 13b). This is especially clear in the western North Atlantic, where in response to the Greenland freshwater perturbation, the latent heat flux into the atmosphere is substantially reduced (Fig. 13c), resulting in enhanced freshwater input into the ocean. At the same time, sensible heat flux and long wave radiation into the atmosphere are reduced as well. Likewise, the net increase

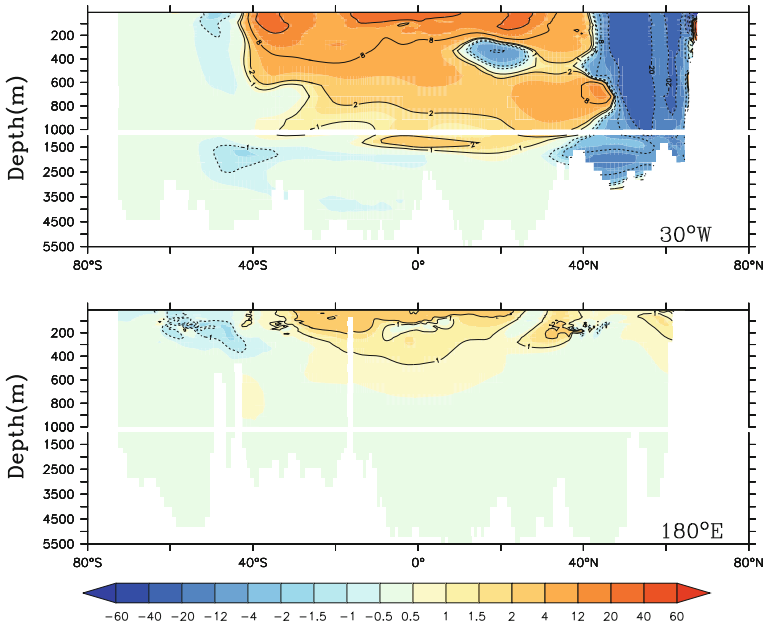

Fig. 10 Meridional cross section of lowpass filtered temperature anomalies (in 10^{-2}°C) at (*upper panel*) 30°W and (*lower panel*) 180°E, both averaged over the 50-year long uncoupled runs

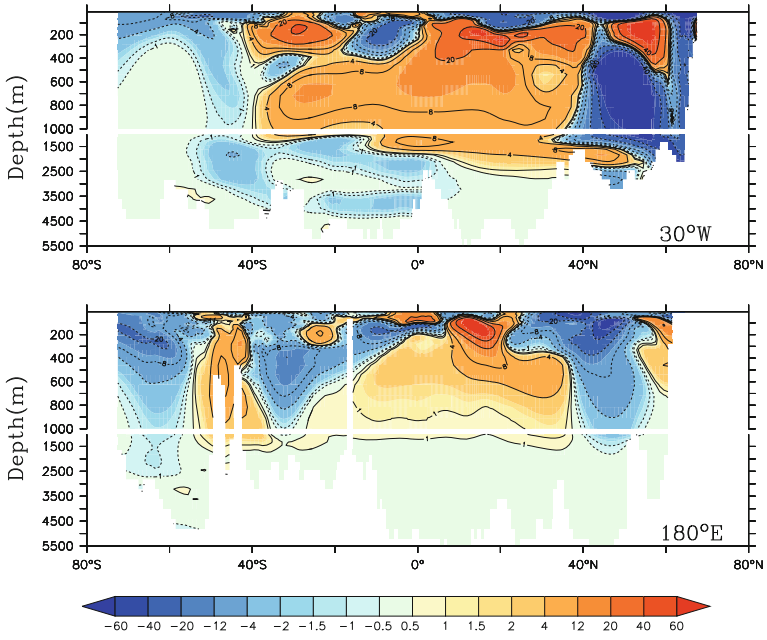

Fig. 11 Meridional cross section of lowpass filtered temperature anomalies (in 10^{-1}°C) at (*upper panel*) 30°W and (*lower panel*) 180°E averaged over the 50-year long coupled runs

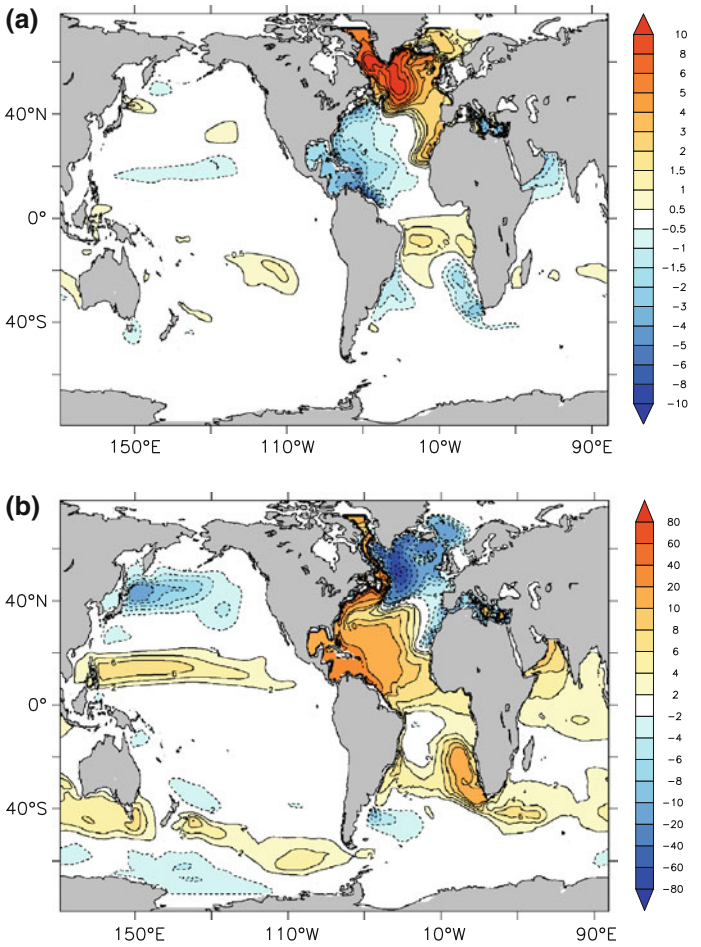

Fig. 12 Fifty-year mean anomalies of (*top*) freshwater content (m) and (*bottom*) heat content (10^8 J/m^2)

of heat flux into the atmosphere in the eastern North Atlantic (and the Kuroshio region) is also caused by changes in the latent and sensible heat flux. Finally, over the entire tropical oceans, changes in the latent heat are associated with local variations in net freshwater fluxes. However, we also observe changes in the shortwave radiation both in the tropics and in the North Atlantic, as they would result from changes in the cloud coverage.

Breaking down the global surface freshwater flux variations over the ocean in terms of changes in evaporation and precipitation, we find that these decrease by about 0.0116 and 0.0272 Sv, respectively. The two effects combined lead to a net increase in freshwater input into the ocean by 0.0156 Sv in the coupled experiment as compared to the ocean-only experiment. This is on top of the added 0.0275 Sv Greenland runoff, which leads to a global net reduction in freshwater flux (E-P-R) $= 0.0156 + 0.0275 = 0.0431$ in the coupled experiment. This net freshwater input results in an increase in the halosteric SSH anomaly, largely due to a reduction in evaporation rather than an increase in precipitation. At the same time, the reduced evaporation is a net heat source for the ocean, which again is consistent at least partially with the increased thermosteric increase in SSH. Both processes

Fig. 13 Mean changes in (*top*) net freshwater flux (cm/year), and (*middle*) net surface heat flux (W/m^2) in the coupled run averaged over the 50-year period. Contours on top of latent heatflux anomalies are −50 to 50 W/m^2 with an interval of 10, −10 to 10 with an increment of 5 and −1 to 1 with an increment of 2, all excluding the zero line. (*Bottom*) 50 year averaged difference in latent heatflux, using a contour interval of 2 W/m^2 over a range of ±30 W/m^2

are especially active in the North Atlantic, where they play an essential role in the larger steric SSH response of the coupled experiment. Acting concurrently, they provide an additional source of buoyancy in the subpolar North Atlantic in the coupled model with consequences for the ocean circulation.

We note that, in our model, the additional freshwater is being taken out of the soil moisture. Over a 50-year period, it appears as a plausible response of the coupled climate system given that it corresponds to only about 1% of the global river run-off into the ocean. However, such an additional freshwater source cannot be sustained in long climate scenario runs and it remains to be investigated how the global water cycle of the climate system would adjust in long climate scenario runs.

5 Impacts on the Atlantic Meridional Overturning Circulation and Meridional Heat Transport

Changes in the meridional overturning circulation (MOC), represented here by the meridional overturning streamfunction, and the meridional heat transport in the Atlantic illustrate both succinctly and in a dynamically compact way the complex ocean response to the Greenland freshwater forcing as expressed in the differences in the coupled and ocean-only experiments (Fig. 14). In the former case, the MOC weakens by about 1.5 Sv—i.e., by about 10%—at 50°N in year 8; the tendency to decrease is apparent over the entire North Atlantic. The coupled experiment shows a similar tendency to MOC decrease (Fig. 14b). However, in this case, there are also pronounced positive and negative values in low latitudes and over the Southern Ocean as they would result from changes in the regional circulation, which points again to a role for the atmosphere in generating remote responses in the gyre scale.

To illustrate the temporal behaviour of the MOC in the ocean-only and coupled experiments, we show in Fig. 15 time-latitude plots at 1000 m depth. The former case shows a clear oscillatory behaviour of the MOC strength with roughly decadal periodicity, superimposed on a longer-term decline. Anomalies tend to propagate southward from the subpolar Atlantic basin, as in the results of Stammer (2008). We recall that results shown in the present paper follow from a purely flux-driven run without a relaxation term included in the surface boundary conditions. The coupled experiment shows a far more complex evolution of MOC anomalies, which includes interannual fluctuations superimposed on decadal variations that appear somewhat weaker than in the ocean-only experiment. Both are superimposed on a quite pronounced longer-term reduction of the MOC by about 5 Sv over the 50-year length of the integrations.

The variations in the MOC shown in Fig. 15 are associated with variations in the meridional heat transport, which in the uncoupled experiment show a similar oscillatory behaviour with increasing amplitude but generally negative tendency (Fig. 16). In the coupled experiment, reduction of northward transport of heat is up to 0.2 PW over the 50-year period in the North Atlantic. Superimposed on these longer-term reductions are interannual to decadal variations.

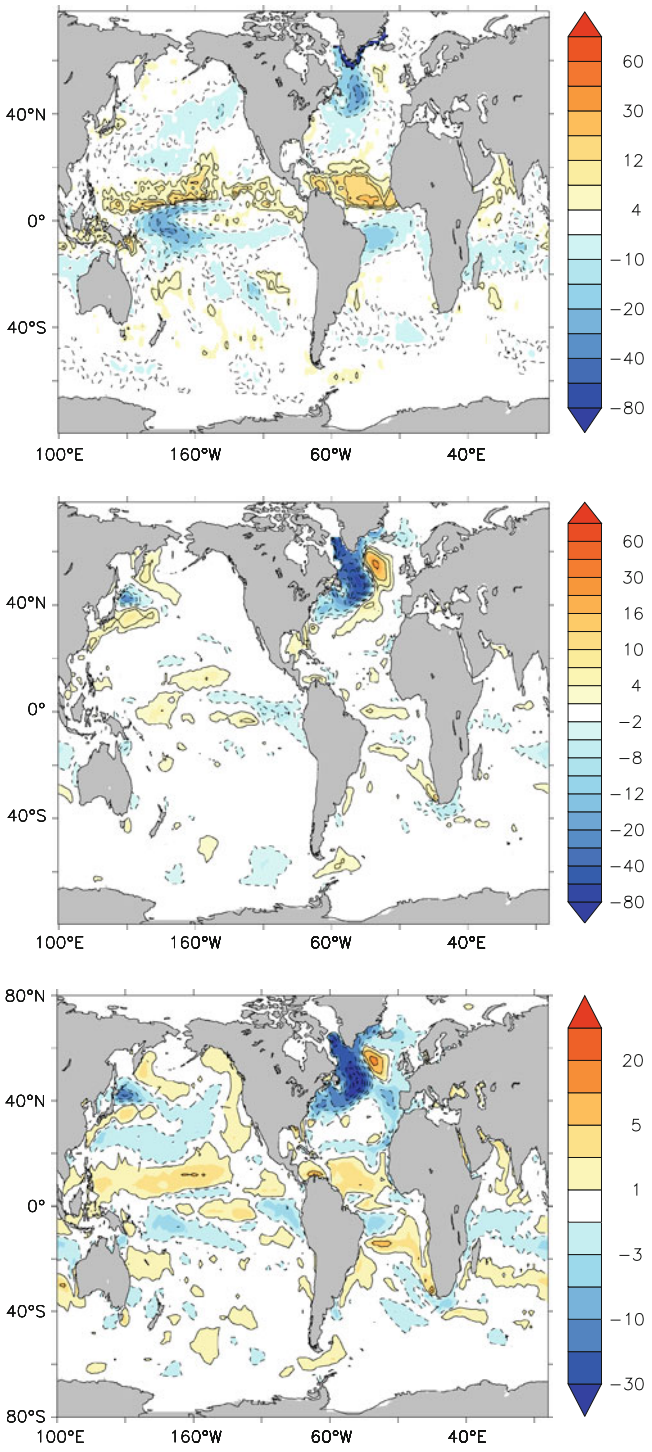
40°N
0°
40°S
100°E
160°W
60°W
40°E
60
30
12
4
−10
−20
−40
−80
40°N
0°
40°S
100°E
160°W
60°W
40°E
60
30
16
10
4
−2
−8
−12
−20
−40
−80
80°N
40°N
0°
40°S
80°S
100°E
160°W
60°W
40°E
20
5
1
−3
−10
−30

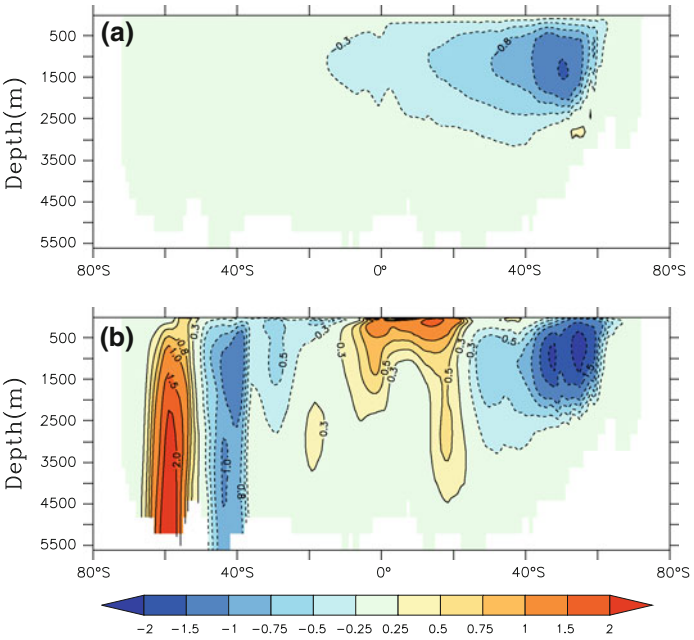

Fig. 14 Examples of annual mean anomalies of the MOC (Sv) taken randomly from year 8 from (*top*) uncoupled and (*bottom*) coupled runs

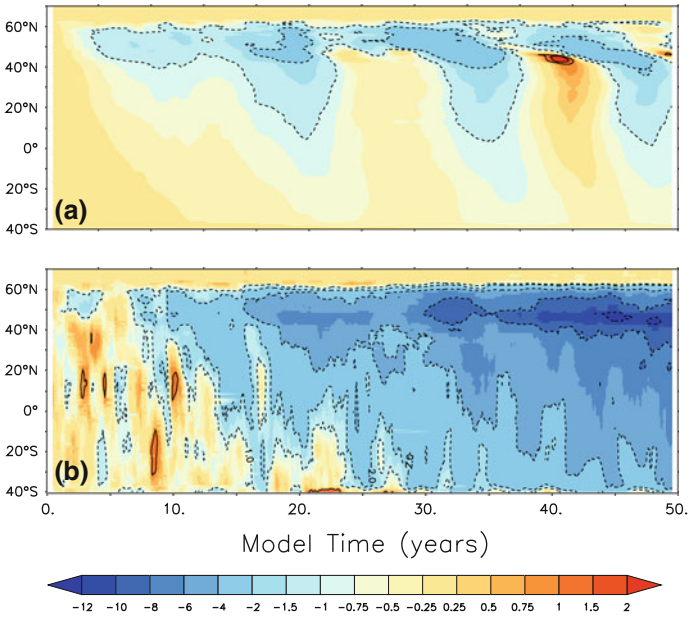

Fig. 15 Time-latitude plot of MOC anomaly (Sv) at 1,000 m depth from (*top*) uncoupled and (*bottom*) coupled runs

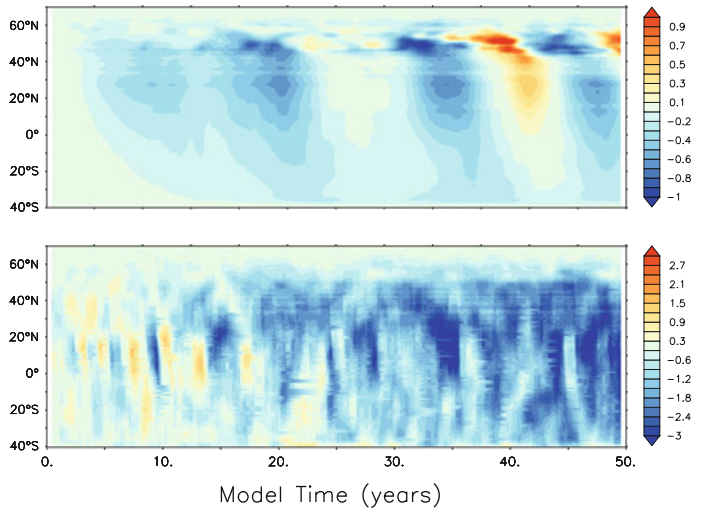

Fig. 16 Time-latitude plot of the meridional heat transport anomaly (PW) from (*top*) uncoupled and (*bottom*) coupled runs

Oscillations resembling those in Figs. 15 and 16 were found by Eden and Greatbatch (2003) in coupled and uncoupled model configurations, and were associated with patterns of a north–south temperature dipole, similar to those shown here in Fig. 12. These authors found stronger oscillations in the coupled configuration due to a positive feedback via the wind-driven circulation. A delayed negative feedback via the overturning circulation enables the oscillation. In the subpolar region north of 40°N, the propagation speed of the anomalies in heat transport anomalies in the ocean-only experiment appear to be much faster than those in the MOC, indicating a fast response of the subpolar gyre circulation. In year 40, for example, the positive heat transport anomaly is associated with a negative delayed response of the MOC anomaly similar to findings by Eden and Greatbatch (2003). In contrast to their results, however, our coupled experiment shows a weaker decadal oscillation than the ocean-only one, but a much stronger long-term trend. Due to a positive feedback with the atmosphere, the anomalies become more negative with time, reaching extremes of 11–14 Sv during the last 5 years of the integration.

In both experiments, the freshwater anomaly around Greenland causes a reduction in overturning, which in turn causes less transport of heat and salt from the Equator to the subpolar North Atlantic, resulting in a dipole for salinity and temperature. However, only in the coupled experiment, according to the temperature dependence of the heat flux terms, the local heat flux out of the ocean is reduced, especially through the latent heat flux. Along with marginal reduction in the wind speed, this causes also a lower rate of latent heat flux than that prescribed in the ocean-only experiment, which results in freshening and warming of the Labrador Sea (seen as stronger thermo- and halosteric responses above), which in turn provides a positive feedback in reducing the MOC.

This type of feedback is known to cause much larger responses in the ocean in terms of MOC changes as compared to a flux-driven ocean model (e.g., Rahmstorf and Willebrand 1995). The mechanism seems to be strong enough in our experiment (given the strength of the applied perturbation) to reduce the decadal oscillations. Instead, variations on a much

longer timescale become dominant which may cause the stronger trend in the coupled experiment. We note here that this trend is not continued beyond year 50 (not shown), suggesting it to be part of a longer- term oscillation. Whether this is the case or a result of the model not being in a statistical equilibrium is not clear at this point, and it will be addressed in the study of Agarwal et al. (2011).

6 Concluding Remarks

The present paper extends the earlier study of Stammer (2008) by investigating now regional sea level changes in response to enhanced Greenland ice mass loss using the same ocean model both uncoupled and coupled to a general circulation model of the atmosphere. Similar to the previous ocean-only results, we also find strong variations in regional sea level in the coupled system. However, in contrast to the ocean-only model experiment, the coupled one produces a stronger and faster response in steric height in the Pacific and Indian Ocean than that obtained by in the OGCM by considering ocean processes only. We find, therefore, that the atmosphere seems to play an additional and prominent role in causing sea level variations in all parts of the World Ocean on short timescale.

Okumora et al. (2009) reported the existence of an atmospheric bridge from the tropical Atlantic into the Pacific, leading to long-term changes in the Pacific and Indian Ocean. Here, we show that such a bridge is initially triggered by interactions between the atmosphere and ocean in the subpolar Atlantic, where SST anomalies develop. On both the global and basin scale, we see a stronger response of the steric SSH in the coupled system, which is primarily due to a stronger thermal response. This strengthening results from feedbacks between the perturbed ocean (by Greenland freshwater run-off) and the overlying atmosphere, which leads to reduced SSTs in the subpolar North Atlantic, less evaporation and less latent heat flux into the atmosphere. These processes then lead to a local increase in heat content and freshwater content and on global scale result in a steric SSH increase. In the North Atlantic, the steric increase is comparable to the non-steric increase caused by the addition of freshwater from Greenland ice mass loss. A detailed examination of these coupling processes will be performed in Agarwal et al. (2011) where we will also investigate the sensitivity of the response to the detailed state of the CGCM.

We note that the patterns obtained in the surface heat and freshwater fluxes of the North Atlantic resemble surprisingly well those reported by Hawkins and Sutton (2009) in terms of optimal perturbations in the Atlantic. Their optimal perturbation pattern showed that the HadCM3 CGCM is highly sensitive to small perturbations in temperature around Greenland, anticipating that any perturbation in SST resulting from Greenland freshwater pulses would have a substantial effect on the coupled system. We find a similar sensitivity in our results, suggesting the presence of strong and direct interaction mechanisms between the ocean and the atmosphere in response to SST changes in the subpolar North Atlantic. In our case, it is caused by the addition of Greenland freshwater melting; however, the mechanism should hold more generally for any SST anomaly present in the subpolar North Atlantic and potentially can have a large consequence for our understanding of the geographical distribution of air–sea coupling and the way the ocean is influencing the atmosphere.

Our results clearly support the notion that it is important to properly consider the effects of freshwater sources resulting from polar ice sheet melting in coupled climate models, so as to successfully simulate the feedback mechanisms between the ocean and the atmosphere thereby improving projections of the climate, including regional sea level. In our study, we limited our ocean-model domain to that used by Stammer (2008) to investigate

the extra effect on the solution resulting from the coupling with the atmosphere. Any future extensions will need to include also the Arctic and its addition bridging effect into the Pacific.

Acknowledgments While revising this paper, Peter Herrmann, a co-author of this paper, unexpectedly passed away and we are indebted for his contribution to this paper. We thank R. Ray and S. Luthke for providing the Greenland mass loss field. CRM acknowledges financial support through the Deutsche Forschungs Gemeinschaft (DFG) funded excellence initiative CliSAP during several research visits to the University of Hamburg. We also thank several anonymous referees who provided very constructive and helpful comments. Funded in part through a MPG (Max Planck Society) Fellowship, the Special Research Program (SPP 1257) "Mass transports and distribution in the Earth System" funded by the DFG, and the BMBF (Federal Ministery of Education and Sciencr) Project REAL-GOACE. Contribution to the CliSAP Excellence Cluster, also funded through the DFG.

References

Agarwal N, Köhl A, Stammer D, Mechoso CR (2011) Atmospheric response to high latitude perturbations in oceanic fresh-water forcing (in preparation)

Arakawa A, Schubert WH (1974) Interaction of a cumulus cloud ensemble with the large-scale environment, part I. J Atmos Sci 31:674–701

Cazes-Boezio G, Menemenlis D, Mechoso CR (2008) Impact of ECCO ocean-state estimates on the initialization of seasonal climate forecasts. J Clim 21:1929–1947

Dorman JL, Sellers PJ (1989) A global climatology of albedo, roughness length and stomatal resistance for atmospheric general circulation models as represented by the Simple Biosphere Model (SiB). J Appl Meteorol 28:833–855

Eden C, Greatbatch RJ (2003) A damped decadal oscillation in the North Atlantic climate system. J Clim 16:4043–4060

Gent PR, McWilliams JC (1990) Isopycnal mixing in ocean circulation models. J Phys Oceanogr 20: 150–155

Greatbatch RJ (1994) A note on the representation of steric sea-level in models that conserve volume rather than mass. J Geophys Res 99:12767–12771

Harshvardhan RD, Randall DA, Corsetti TG (1987) A fast radiation parameterization for atmospheric circulation models. J Geophys Res 92:1009–1016

Harshvardhan RD, Corsetti TG, Dazlich DA (1989) Earth radiation budget and cloudiness simulations with a general circulation model. J Atmos Sci 46:1922–1942

Hawkins E, Sutton R (2009) Decadal predictability of the Atlantic Ocean in a coupled GCM: forecast skill and optimal perturbations using linear inverse modelling. J Clim. doi:10.1175/2009JCLI2720.1

Hu A, Meehl GA, Han W, Yin J (2009) Transient response of the MOC and climate to potential melting of the Greenland Ice Sheet in the 21st century. Geophys Res Lett. doi:10.1029/2009GL037998

Köhler M (1999) Explicit prediction of ice clouds in general circulation models. Ph.D. dissertation, Department of Atmospheric Sciences, University of California, Los Angeles

Konor CS, Cazes-Boezio G, Mechoso CR, Arakawa A (2008) Parameterization of PBL processes in an atmospheric general circulation model: description and preliminary assessment. Mon Weather Rev 137(3):1061

Large WG, McWilliams JC, Doney S (1994) Oceanic vertical mixing: a review and a model with a nonlocal boundary layer parameterization. Rev Geophys 32:363–403

Landerer FW, JH Jungclaus, L Marotzke (2007) Regional dynamic and steric sea level change in response to the IPCC-A1B scenario. J Phys Oceanogr 37:296–312

Large WG, Danabasoglu G, Doney SC, McWilliams JC (1997) Sensitivity to surface forcing and boundary layer mixing in a global ocean model: annual-mean climatology. J Phys Oceanogr 27:2418–2447

Li JL, Köhler M, Farrara JD, Mechoso CR (2002) The impact of stratocumulus cloud radiative properties on surface heat fluxes simulated with a general circulation model. Mon Weather Rev 130:1433–1441

Luthke S, Zwally H, Abdalati W, Rowlands DD, Ray RD, Nerem RS, Lemoine FG, McCarthy JJ, Chinn DS (2006) Recent Greenland mass loss by drainage system from satellite gravity observations. Science 314(5803):1286–1289

Ma HY, Mechoso CR, Xue Y, Xiao H, Wu CM, Li JL, DeSales F (2010) Impact of land surface processes on the South American warm season climate. Clim Dyn. doi:10.1007/s00382-010-0813-3

Okumora YM, Deser C, Hu A (2009) North Pacific climate response to freshwater focring in the subarctic North Atlantic: oceanic and atmospheric pathways. J Clim. doi:10.1175/2008JCLI2511.1

Pan DM, Randall DA (1998) A cumulus parameterization with a prognostic closure. Q J R Meteorol Soc 124:949–981

Pardaens A, Gregory JM, Lowe J (2010) A model study of factors influencing projected changes in regional sea level over the twenty-first century. Clim Dyn. doi:10.1007/s00382-009-0738-x

Rahmstorf S, Willebrand J (1995) The role of temperature feedback in stabilizing the thermohaline circulation. J Phys Oceanogr 25:787–805

Rahmstorf S, Crucifix M, Ganopolski A, Goosse H, Kamenkovich I, Knutti R, Lohmann G, Marsh R, Mysak LA, Wang Z, Weaver AJ (2005) Thermohaline circulation hysteresis: a model intercomparison. Geophys Res Lett. doi:10.1029/2005GL023655

Redi MH (1982) Oceanic isopycnical mixing by coordinate rotation. J Phys Oceanogr 12:1154–1158

Stammer D (2008) Response of the global ocean to Greenland and Antarctic ice melting. J Geophys Res. doi:10.1029/2006JC004079

Stouffer RJ, Yin J, Gregory JM, Dixon KW, Spelman MJ et al (2006) Investigating the causes of the response of the thermohaline circulation to past and future climate changes. J Clim 19:698–722

Suarez M, Arakawa A, Randall D (1983) The parameterization of the planetary boundary layer in the UCLA general circulation model: formulation and results. Mon Weather Rev 111:2224–2243

Timmermann A, Okumura Y, An SI, Clement A, Dong B, Guilyardi E, Hu A, Jungclaus JH, Renold M, Stocker TF, Stouffer RJ, Sutton R, Xie SP, Yin J (2007) The Influence of a weakening of the Atlantic meridional overturning circulation on ENSO. J Clim. doi:10.1175/JCLI4283.1

Xue Y, Sellers PJ, Kinter JL III, Shukla J (1991) A simplified biosphere model for global climate studies. J Clim 4:345–364

Xue Y, Bastable HG, Dirmeyer PA, Sellers PJ (1996) Sensitivity of simulated surface fluxes to changes in land surface parameterization—a study using ABRACOS data. J Appl Meteorol 35:386–400

Xue Y, Fennessy MJ, Sellers PJ (1996) Impact of vegetation properties on US summer weather prediction. J Geophys Res 101:7419–7430

Surv Geophys (2011) 32:643–657
DOI 10.1007/s10712-011-9115-5

GOCE, Satellite Gravimetry and Antarctic Mass Transports

Reiner Rummel · Martin Horwath · Weiyong Yi · Alberta Albertella · Wolfgang Bosch · Roger Haagmans

Received: 3 December 2010 / Accepted: 4 February 2011 / Published online: 19 March 2011

Abstract In 2009 the European Space Agency satellite mission GOCE (Gravity Field and Steady-State Ocean Circulation Explorer) was launched. Its objectives are the precise and detailed determination of the Earth's gravity field and geoid. Its core instrument, a three axis gravitational gradiometer, measures the gravity gradient components V_{xx}, V_{yy}, V_{zz} and V_{xz} (second-order derivatives of the gravity potential V) with high precision and V_{xy}, V_{yz} with low precision, all in the instrument reference frame. The long wavelength gravity field is recovered from the orbit, measured by GPS (Global Positioning System). Characteristic elements of the mission are precise star tracking, a Sun-synchronous and very low (260 km) orbit, angular control by magnetic torquing and an extremely stiff and thermally stable instrument environment. GOCE is complementary to GRACE (Gravity Recovery and Climate Experiment), another satellite gravity mission, launched in 2002. While GRACE is designed to measure temporal gravity variations, albeit with limited spatial resolution, GOCE is aiming at maximum spatial resolution, at the expense of accuracy at large spatial scales. Thus, GOCE will not provide temporal variations but is tailored to the recovery of the fine scales of the stationary field. GRACE is very successful in delivering time series of large-scale mass changes of the Antarctic ice sheet, among other things. Currently, emphasis of respective GRACE analyses is on regional refinement and on changes of temporal trends. One of the challenges is the separation of ice mass changes from glacial isostatic adjustment. Already from a few months of GOCE data, detailed gravity gradients can be recovered. They are presented here for the area of

R. Rummel · M. Horwath (✉) · W. Yi · A. Albertella
Institute of Astronomical and Physical Geodesy (IAPG), Technische Universität München, 80290 München, Germany
e-mail: martin.horwath@bv.tum.de

R. Rummel
e-mail: rummel@bv.tum.de
URL: http://www.iapg.bv.tum.de/iapg.html

W. Bosch
Deutsches Geodätisches Forschungsinstitut (DGFI), Alfons-Goppel-Str.11, 80539 München, Germany

R. Haagmans
ESA-ESTEC, Keplerlaan 1, 2201 AZ Noordwijk, The Netherlands

Antarctica. As one application, GOCE gravity gradients are an important addition to the sparse gravity data of Antarctica. They will help studies of the crustal and lithospheric field. A second area of application is ocean circulation. The geoid surface from the gravity field model GOCO01S allows us now to generate rather detailed maps of the mean dynamic ocean topography and of geostrophic flow velocities in the region of the Antarctic Circumpolar Current.

Keywords GOCE · Satellite gravimetry · GRACE · Antarctica · Ice mass balance · Mean dynamic topography · Geostrophic flow velocity

1 Introduction

In 2001, Thomas (2001) reported on NASA's Program for Arctic Regional Climate Assessment (PARCA) and its results on the shrinking Greenland ice sheet. In this work the idea of a comprehensive observing system is introduced dedicated to the determination of ice mass gain, transport, loss, and balance. It was published before the laser ice altimetry mission ICESat (Ice, Cloud, and land Elevation Satellite) (Zwally et al. 2002) and the satellite gravimetry mission GRACE (Gravity Recovery and Climate Experiment) (Tapley et al. 2004) both launched in 2002. Since then, estimates of ice mass balance in Greenland and Antarctica have been improved significantly, with decisive contributions coming from geodetic space techniques (see, e.g., Plag and Pearlman 2009, ch. 3.4). Recently, another satellite gravimetry mission, GOCE (Gravity Field and Steady-State Ocean Circulation Explorer), was launched on March 17, 2009. The purpose of this article is to introduce the reader into the principle and role of GOCE and to show some first results, where we focus on the region of Antarctica. The complementarity between GOCE and GRACE is explained and, in this context, GRACE results for Antarctica are summarized.

The GOCE mission objective is the detailed and accurate measurement of the Earth's gravity field and geoid surface. Its core instrument is a gravity gradiometer, which is the first instrument of this kind on board a satellite. The high precision of the instrument requires complementary sensors and a perfectly controlled and stable space laboratory. The principle of the gradiometer and the characteristics of the sensor system will be described in Sect. 2.

The two missions GOCE and GRACE are complementary. While GOCE is designed to measure, with high spatial resolution, the stationary part of the gravity field, GRACE observes its temporal variations. Section 3 discusses this complementarity.

GRACE is the first satellite mission capable of measuring the details of large scale temporal gravity field variations due to, e.g., melting ice sheets, changes in ocean water mass and continental hydrology. Thus, GRACE provides a new and very important set of climate parameters, as pointed out in a recent White House Office of Science and Technology Policy (OSTP) document (2010). A review of recent GRACE achievements with respect to the Antarctic ice mass balance is given in Sect. 4.

The benefit of GOCE in the field of ice mass balance and sea level research will be twofold. On the one hand the measured gradients will reveal the topographic and crustal structure underneath the ice covers of Antarctica and Greenland. On the other hand the high precision geoid surface derived from GOCE will serve as global physical reference surface for sea level research as well as for the determination of mean ocean topography in global ocean circulation studies. In Sect. 5 we show first GOCE results based on data from

the first few months of the mission. These results demonstrate the high spatial resolution of GOCE. In Sect. 6 we draw some conclusions.

2 GOCE Gravitational Sensor System

The GOCE gravitational sensor system is described, e.g., by Drinkwater et al. (2007), Rummel (2010), or Rummel and Gruber (2010). Here we follow Rummel (2010). Actually, there are two gravity sensor systems on board GOCE and they complement each other: the satellite orbit motion "in gravitational free fall" measured by GPS and the gravity gradiometer. The orbit is determined by GPS (Global Positioning System) using a newly developed European receiver. From GPS code and phase measurements the orbit trajectory is computed with an accuracy of 1–2 cm. This is done either purely geometrically, that is, using kinematic orbits, or by the method of reduced dynamic orbit determination (compare Švehla and Rothacher 2004; Jäggi 2007). The latter approach is based on a combination of orbit mechanics and additional stochastic parameters. As the spacecraft is kept free of drag in the along-track direction (see below), the recovered orbit trajectory is describing the free fall of the satellite as determined by the gravitational field of the Earth, and to a lesser extent, by the direct and indirect tidal attraction of the Sun, Moon and planets, as well as some other small cross-track effects. This allows reconstruction of the long-wavelength part of the Earth's gravity field.The details of the field come from the gravity gradiometer.

Gravity gradiometry is the measurement of the second-order derivatives of the gravitational potential, V. There exist altogether nine second-order derivatives, $M = \frac{\partial^2 V}{\partial x^i \partial x^j}$, with $i, j = 1, 2, 3$. In the case of GOCE these nine elements are derived from acceleration differences measured along the baselines of the gradiometer instrument. The instrument consists of three orthogonally mounted one-axis gradiometers. Each of them is made of a pair of accelerometers mounted at the end of a 50 cm rigid axis. The accelerometers have two ultra-precise axes and one less sensitive axis. The most precise components have a precision of 10^{-12} m/s^2 per square-root of Hz. The measurement principle is differential accelerometry. As an example, the component V_{xz} is derived from the difference of the z-component of the two accelerometers taken over the x-axis, while V_{zx} is derived from the difference of the x-components over the z-axis. Taking only the ultra-precise components, a precision of approximately 10^{-11} s^{-2} or 10 mE per square-root of Hz can be attained (1 E $= 10^{-9}$ s$^{-2} = 1$ Eötvös Unit). This means that in the case of GOCE, from the arrangement of precise and less sensitive axes, the gradiometer components V_{xx}, V_{yy}, V_{zz} and V_{xz} are measured with high precision, while the components V_{xy} and V_{yz} are less accurate. The instrument is rigidly mounted in the satellite with its center approximately at the center of mass of the satellite and with the x-axis pointing in the in-flight direction, the y-axis normal to the orbit plane and the z-axis approximately radial toward the Earth, the so-called gradiometer reference frame (GRF). The extremely high measurement performance is only achieved in a measurement bandwith, between 5×10^{-3} Hz and 0.1 Hz; at frequencies below this bandwidth the noise is approximately proportional to $1/f$.

The gradiometer is embedded in an almost perfect spaceborne laboratory, compare Fig. 1. The orientation of the gradiometer axes in inertial space is measured by a set of three star trackers. Since the satellite in orbit carries out a rotational motion in inertial space, the accelerometers pick up angular velocities and accelerations apart from the gravitational signal. The angular acceleration part can be isolated by a separation of the symmetric from the skew-symmetric part of the matrix of nine measured acceleration

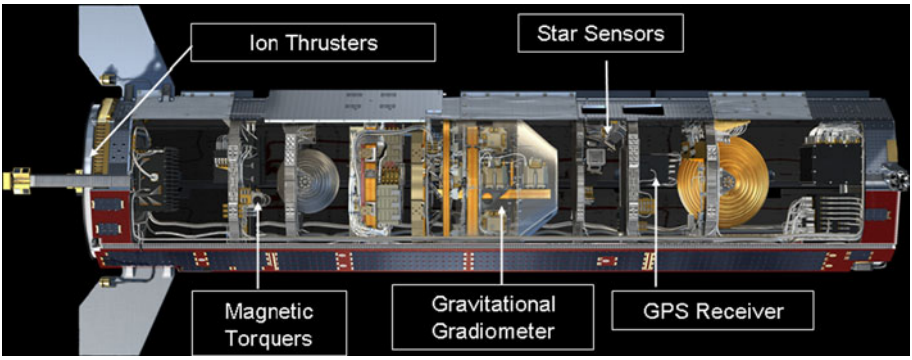

Fig. 1 GOCE sensor system, consisting of the three core instruments, gravity gradiometer, geodetic GPS receiver and star trackers, the ion thrusters for drag compensation, and magnetic torquers for angular control

differences. They are then employed, in combination with the star tracking, for the elimination of the angular velocity part. The accelerometry applied in common mode, i.e. measuring the common acceleration in x, y and z direction, delivers the necessary control signal for the drag-free control of the spacecraft. Air drag in the in-flight direction is compensated by proportional ion-thrusting. This allows the very low orbit altitude of 260 km to be maintained. The angular control is done by magnetic torquing. This method implies that only two instead of all three angular degrees-of-freedom are controlled at any moment. Control can therefore only be maintained in a range of a few angular degrees. The gradiometer measurements require all accelerometers to be perfectly consistent in terms of scale and orientation. In-flight calibration is therefore required at regular intervals. Random shaking by cold gas thrusters provides the necessary calibration signal. Finally, any time-variable gravitational signal stemming from the satellite itself needs to be avoided. For GOCE this involves a design which includes no moving parts, the use of carbon sandwich structures and a very accurate thermal control. In summary, the GOCE sensor system is a very sophisticated gravitational laboratory in space, containing several novelties. Some of its sensors are similar to those intended to be used for future fundamental physics missions such as LISA (Laser Interferometry Space Antenna) (Vitale 2009), LISA-Pathfinder (Armano et al. 2009), STEP (Sumner 2009), or Microscope (Touboul 2009).

3 GOCE versus GRACE

The GRACE mission (Tapley et al. 2004; Schmidt et al. 2008) consists of a pair of satellites following each other at a 200 km distance on a near-polar low-altitude orbit. A K-band microwave ranging system measures the inter-satellite distance at micrometer precision. In this way, the orbit effect of gravity field variations is observed in a differential manner. An on-board GPS receiver and a three-axis accelerometer enable precise orbit determination and the observation of non-gravitational accelerations, respectively.

Both GOCE and GRACE are satellite missions dedicated to gravimetry. The two missions are complementary. While GOCE is designed to measure the stationary field with maximum spatial detail and precision, the focus of GRACE is on the recovery of the temporal variations of the Earth's gravitational field. How is it possible that one system can be focussed on temporal variations while the other one measures spatial details?

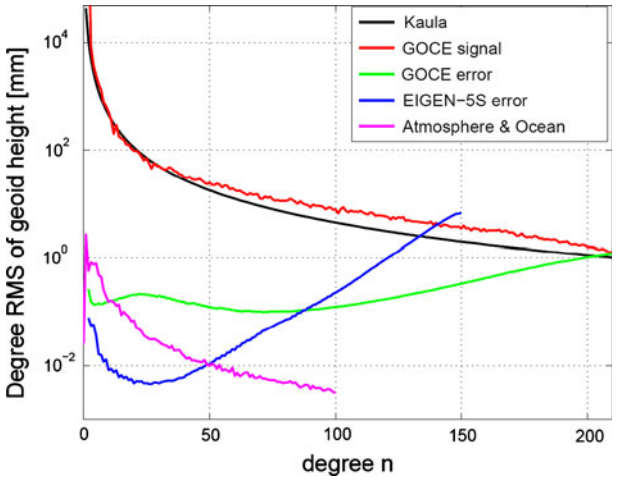

Fig. 2 Comparison of GRACE and GOCE error structure: Shown are signal degree RMS per spherical harmonic degree n according to the Kaula rule (*black*) and as derived from GOCE (*red*), the error degree medians for GRACE (*blue*) and GOCE (*green*) and signal degree RMS of temporal variations of ocean and atmosphere (*violet*)

This question had to be addressed already before the launch of both missions, (compare Balmino et al. 1998, 1999). It is most easily explained here in terms of the signal and noise characteristics of both missions. For one-dimensional time series such analysis is commonly done in the Fourier domain by comparing power-spectral densities of signal and noise. On the sphere, root-mean-square values per spherical harmonic degree (degree RMS; e.g. Pail and Wermuth 2003) of signal and noise are compared. Figure 2 shows degree RMS curves. The spherical harmonic degrees n of the horizontal axis correspond to spatial length scales (=half wavelength s) on the Earth's surface according to $s = 20{,}000\ \text{km}/n$. The vertical axis is expressed in terms of geoid heights in mm and is logarithmic. The smooth black curve is considered to approximate the average power of the stationary Earth gravity signal, the Kaula rule-of-thumb (Kaula 1966). It shows that the degree RMS between degrees 2 and 200 spans about four orders of magnitude. The red curve represents the signal curve as measured by GOCE. Its power at high degrees is slightly higher than that suggested by Kaula 40 years ago. The blue line gives the estimation error of one of the best gravity field models based purely on GRACE measurements, the model EIGEN-5S (Förste et al. 2008a, b). The green line is a formal error curve of GOCE based on a preliminary analysis of the first 2 months of data and a quick-look processing. The two error curves are not exactly degree RMS but instead degree medians. This way, it is avoided that the high error contribution from the zonal spherical harmonic coefficients dominates the curve. The zonals are not well determined because with an inclination of 96.5° the orbit is not exactly polar. However, on the sphere this effect is almost perfectly confined to the two polar caps, the areas not covered by orbit tracks.

It can be seen that at low degrees the GRACE error curve is more than one order of magnitude lower than the GOCE error curve. The two curves intersect at degree 90, and at degrees above 90 GOCE exhibits a much lower error level than GRACE. The resolution of GOCE, as indicated by the intersection with the signal curve, is about $n = 205$, or 98 km half wavelength in the spatial domain. With more GOCE observations becoming available

the error curve will be somewhat lowered; however, the overall picture will remain the same.

The high precision of GRACE at low degrees is essentially determined by the fantastic precision of the K-band link between the two spacecrafts. In a certain way GRACE can be regarded as a one-axis gradiometer with a baseline of 200 km, the distance between the two satellites (compare Rummel 2003). The dependence of the error curves on altitude, instrument precision and measurement principle is discussed by Balmino et al. (1998).

The signal of the stationary gravity field is represented by the Kaula curve. All temporal variations are much smaller. Apart from long-term core and glacial isostatic adjustment (GIA) processes, short-term solid Earth tides and singular tectonic events, the temporal variations are due to mass variations of geophysical fluids (Chao 2003), such as atmospheric mass variations, continental hydrology, ocean mass variations, glacier mass balance and ocean tides. Temporal variations follow a power law analogous to Kaula's rule of thumb, but with a maximum value somewhere at the mm-level and a steep decrease to a level below 10^{-2} mm at $n = 50$. As an illustration, the violet curve in Fig. 2 shows the degree RMS curve of temporal gravity field variations calculated from modelled atmospheric and oceanic mass variations. The low errors of GRACE at lower degrees explain why GRACE can monitor temporal variations. In the case of GOCE they hardly exceed the error curve and the major part of them is even removed from the observations by models in the standard processing.

More detailed simulation studies have confirmed that temporal gravity field variations generally remain far below the GOCE noise level (Jarecki et al. 2005; Han et al. 2006; Moore and King 2010). The extended mission duration now foreseen will hardly change this situation. Nonetheless, GOCE might aid to improve the spatial resolution of time-variable results from GRACE when, in a combination approach, the higher-order components that are poorly determined by GRACE are stabilized towards the accurate GOCE solution.

It is somewhat misleading to discuss time-variable geophysical signals in terms of degree RMS. Degree RMS represent global averages, i.e. the RMS value of variations is taken over the entire globe. In reality, some of these processes are confined to land, some to ocean and some to the large ice sheets. Their signal variation, being confined to the respective domain, may be higher there than expressed by "global" signal degree RMS.

4 GRACE and Mass Changes in Antarctica

As far as Antarctica and Southern Ocean applications of GRACE are concerned, GRACE has observed bottom pressure variations in the Southern Ocean and, by this means, has elucidated the variability of barotropic transport in the Antarctic Circumpolar Current (Rietbroek et al. 2006; Zlotnicky et al. 2007; Böning et al. 2010). Moreover, GRACE has revolutionized our knowledge of Antarctic Ice Sheet mass balance since 2002 (Velicogna and Wahr 2006; Ramillien et al. 2006; Chen et al. 2009; Horwath and Dietrich. 2009; Sasgen et al. 2010b). Here we address this ice sheet application of GRACE.

Using GRACE data, the integral mass change of the ice sheet can be detemined from its gravitational effect. Almost all GRACE-based studies conclude a significant negative trend of the integral Antarctic ice mass since 2002. Still, large uncertainties persist, and results of different studies differ considerably not only due to the different underlying time intervals but also due to methodological differences in the adopted GRACE processing and analysis (Allison et al. 2009; Horwath and Dietrich 2009).

Most commonly, GRACE inferences on ice mass changes are based on GRACE period solutions, such as monthly solutions, of the global gravity field. Gravity field changes may be converted into equivalent changes of surface mass (Wahr et al. 1998). Those changes are further analyzed, typically aiming at integrated mass change estimates over a certain area (Swenson and Wahr 2002). Alternatively, the GRACE observations can be analyzed more directly in the mascon approach to infer mass changes (Sabaka et al. 2010).

Principally, from variations of the gravity field outside the masses one cannot uniquely deduce the spatial distribution of mass changes inside and on the surface of the Earth, unless one assumes that mass changes are confined to a thin surface layer. For the case of Antarctica, masses in the Earth interior are displaced by the glacial isostatic adjustment in reaction to ice load changes since the last glacial maximum (Ivins and James 2005). It is therefore an intrinsic problem of GRACE mass change inferences to separate the vertically superimposed signals of ice mass changes and of GIA (and, less severely but still importantly, of atmospheric mass changes) (Wahr et al. 2000). In fact, for linear, pan-Antarctic ice mass trends from GRACE, the uncertainty of the superimposed GIA signal is the predominant source of uncertainty (Velicogna and Wahr 2006).

In addition to the problem of vertical separation, GRACE is insensitive to important parts of the spherical harmonic spectrum of time-variable signals (degree one and degree higher than about 60). Therefore, a compromise has to be found between errors of the mass change estimates propagated from GRACE solution errors (GRACE error effects) and an imperfect spatial separation (leakage effects) (Swenson and Wahr 2002). The situation may be improved by relying on a priori information on the geographic mass change patterns (Horwath and Dietrich 2009; Sasgen et al. 2010b; Sabaka et al. 2010), which is, however, a compromise again.

As an example of ice mass balance results from GRACE, Fig. 3a shows a map of surface mass trends expressed in terms of the thickness of an equivalent water layer and filtered in a way adapted for their regional integration (see Horwath and Dietrich 2009). Figure 3b, c shows time series of estimated ice mass changes integrated over the entire grounded ice sheet and over a large, near-coastal part of West Antarctica, respectively. These results are updates of the analysis of Horwath and Dietrich (2009) by their Method II, an amended regional integration approach with an ocean-ward widening of the region function and an eventual rescaling depending on forward-modeling experiments. The results are based on the Release-4 monthly GRACE solutions by GFZ (GeoForschungs-Zentrum Potsdam) (Schmidt et al. 2008) and now cover the 8 years from 08/2002 to 07/2010. The IJ05 GIA model (Ivins and James 2005) is subtracted from the GRACE trends in an attempt to isolate ice mass changes.

In agreement with previous GRACE analyses (e.g. Chen et al. 2009; Horwath and Dietrich 2009), prominent features may be identified: strong mass loss in the Amundsen Sea Sector related to a dynamic imbalance (Bindschadler 2006) with partly ongoing accelerations of ice flow (Rignot et al. 2008; Wingham et al. 2009); mass loss at the Antarctic Peninsula likewise attributable to glacier acceleration (Rignot et al. 2008); mass gain at Siple Coast, associated with the stagnation of Kamb Ice Stream (Joughin and Tulaczyk 2002); mass loss in Wilkes Land, dominated by the unbalanced outflow of Totten Glacier (Pritchard et al. 2009). From the map and the time series it is evident that current ice losses are dominated by the coastal regions of West Antarctica (in particular the Amundsen Sea Sector) and the Antarctic Peninsula.

The time series for the entire ice sheet shows a strong negative trend (-108 Gt/year, corresponding to a $+0.30$ mm/year mean eustatic sea level rise) superimposed by a considerable scatter which contains apparent interannual signals. The noted one-sigma

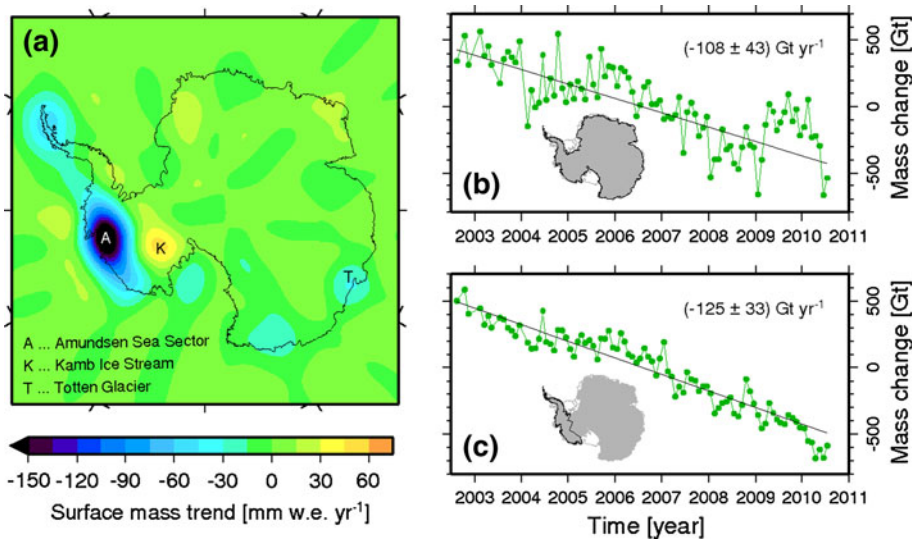

Fig. 3 GRACE-based estimates of Antarctic ice mass changes. **a** map of surface mass trends for the period 08/2002–07/2010. **b** estimated time series of mass changes integrated over the entire grounded ice sheet (*green*) and their linear component (*black*). **c** same as (**b**) but for the coastal regions of West Antarctica and the Antarctic Peninsula (see map *inset*). The effect of the IJ05 GIA model (Ivins and James 2005) is reduced from the GRACE solutions. See the main text and Horwath and Dietrich (2009) for more methodological details

uncertainties of the trends are not the formal uncertainties of the fit but include assessments of the uncertainty of the GIA correction and of other systematic effects (Horwath and Dietrich 2009).

As a matter of fact, the pan-Antarctic trend largely depends on the applied GIA correction. Without this correction, this trend would be virtually zero (−7 Gt/year). The GIA uncertainty, assessed to be ±40 Gt/year for the pan-Antarctic trend, largely dominates the uncertainty of the linear ice mass trend from GRACE. Due to the limited constraints on both the glaciation history and the solid Earth rheological parameters, present GIA models for Antarctica, such as IJ05 (Ivins and James 2005) or ICE-5G (Peltier 2004) differ enormously. GPS observations of the related crustal deformations lend themselves as geodetic constraints (Rülke et al. 2008; Bevis et al. 2009; King et al. 2010). The network of GPS observations has been enlarged considerably in recent years but remains constrained by the sparsity of rock outcrops and by the difficult logistics. From preliminary GPS-based vertical crustal displacement rates, Bevis et al. (2009) concluded that neither of the considered GIA models (including the widely used IJ05 and ICE-5G models) was consistent with the observations. Global inversions of GRACE and GPS results (and more complementary data) for GIA and present-day surface mass changes (e.g. Wu et al. 2010) are a theoretically more rigorous approach than the GIA correction from models, but may be practically more adventurous. A very promising approach to disentangle GIA and ice mass signals consists in the combination of satellite altimetry over the ice sheet with GRACE, owing to the different relative sensitivities of the two techniques to the two phenomena (Wahr et al. 2000). Riva et al. (2009) presented important initial results using surface height trends from ICESat laser altimetry. Despite the persisting limitations (limited ICESat temporal and spatial sampling, ambiguity of converting ice sheet thickness changes

to ice mass changes) they conclude that the combined geodetic observations favour the IJ05 GIA model as compared to ICE-5G. Clearly, the continuation of efforts to integrate GRACE within a system of complementary geodetic observations and modeling is the way to address the problem of GIA-versus-ice mass separation and other persisting challenges.

Beyond linear, large-scale trends from GRACE, research has been more recently oriented towards a finer partitioning of the geographic structure of changes and their geophysical character and towards the understanding of nonlinear interannual signals. This has become possible by the longer time series, by the continuous improvement of GRACE processing and by the ongoing development of analysis methods. As for the spatial partitioning of mass changes, a priori information on the spatial patterns has been employed, e.g. derived from visual inspection of GRACE trend maps (Chen et al. 2009), simple basin-wise mathematical shapes (Horwath and Dietrich 2009, their Method III), ice flow velocity fields (Sasgen et al. 2010b), or neighbor constraints between adjacent surface compartments (Sabaka et al. 2010). As for the nonlinearity of changes, an acceleration of ice mass loss has been stated (Chen et al. 2009; Velicogna 2009) based on GRACE time series up to January/February 2009. While from visual inspection of Fig. 3c such an acceleration might persist in West Antarctica where there is independent evidence for flow acceleration (Rignot et al. 2008; Wingham et al. 2009), the most recent 1.5 years in the pan-Antarctic time series (Fig. 3b) suggest a deviation from an acceleration scheme. Sasgen et al. (2010a) related interannual variations from GRACE to variations of net precipitation from ECMWF atmospheric modeling. Horwath et al. (2010) demonstrate good correlation between nonlinear interannual variations in GRACE mass changes and ENVISAT radar altimetry height changes, thus confirming the geophysical origin of these signals and suggesting (based on high-resolution radar altimetry patterns of change) surface mass balance variations as their primary origin.

In conclusion, GRACE has become a central element in an evolving geodetic observing system for the ongoing mass changes in Antarctica.

5 GOCE and First Results in the Antarctic Region

As discussed in Sects. 3 and 4, GRACE measures temporal variations of gravity. In the Antarctic region it is likely to be the most reliable method to assess ice mass gain and loss. The use of GOCE is twofold. On the one hand the geoid surface derived from GOCE establishes a consistent height reference for sea level estimates and ocean circulation studies as well as for calculating freeboard heights of the floating ice shelves. On the other hand GOCE gravitational gradients reflect the topographic relief and its state of isostatic balance. First results from GOCE related to geophysical studies and to the determination of ocean circulation are discussed in the following.

Level-2 processing is done by ESA's high-level processing facility. The first measurement cycle of 61 days from November and December 2009 is now available. Currently data are evaluated for the period from January to June 2010 with a large gap in February caused by a failure of one of the on-board processors. The gravitational gradients constitute a symmetric and trace-less 3×3 matrix, the so-called Marussi tensor (compare Rummel 2010):

$$M = \frac{\partial^2 V}{\partial x^i \partial x^j} = \begin{pmatrix} V_{xx} & V_{xy} & V_{xz} \\ V_{yx} & V_{yy} & V_{yz} \\ V_{zx} & V_{zy} & V_{zz} \end{pmatrix} \quad (1)$$

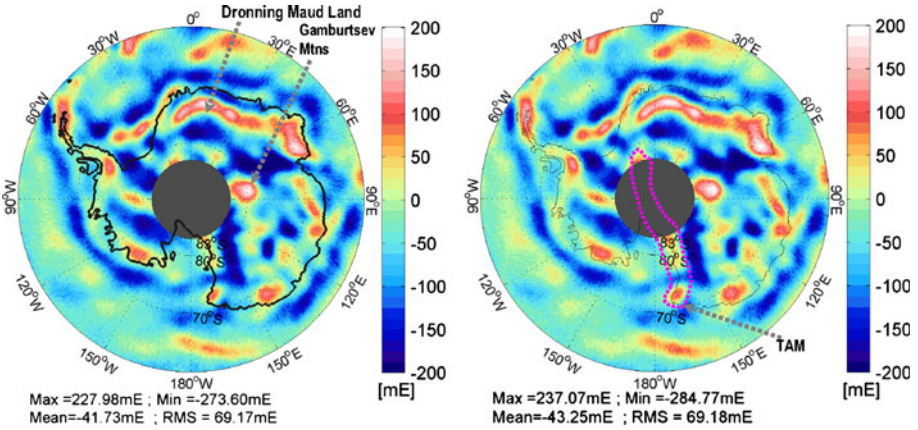

Fig. 4 Band-pass filtered vertical, i.e. radial, gravity gradients for the area of Antarctica as derived from GOCE: left for the first measurements cycle (November and December 2009) and right for the period (March to June 2010 with an interruption in February) for ascending arcs. The gradients reflect some prominent tectonic features of Antarctica. The polar data gap is marked in *gray*

The components of M are measured in the gradiometer reference frame. The gradiometer, being fixed to the satellite, is following the attitude motion of the spacecraft. A finite impulse response filter was applied to the measured gradients. Thus the signal content is confined to the measurement bandwidth. Figure 4 shows the resulting band-pass filtered vertical gradients V_{zz} in the Antarctic region, at the left for the period November and December 2009 and at the right for March through June 2010. The polar gap, the area not covered with observations, is marked in gray. One observes a good agreement between the two maps. The signal RMS value is 70 mE with a range between −270 and +230 mE. The RMS difference of the two data sets is 15 mE and not completely random. There is still room for improvement. It will be an important addition to the continental Antarctic gravity data base. An overview of available terrestrial and airborne gravity surveys of Antarctica is given by Scheinert et al. (2007). The gradient map reflects well all prominent tectonic features such as Dronning Maud Land, Gamburtsev mountains and the Transantarctic mountains (TAM). GOCE gradients may also be suitable to further investigate the question about meteor impact craters under the ice. The new data set will serve tectonic and crustal studies, such as von Frese et al. (1999).

Analogous gradients are available now for all measured gradient components and for both measurement periods. Since the gradients are given in the GRF, i.e., in a local frame following the orbit, data from ascending and descending tracks have to be mapped separately. As an example, Fig. 5 shows the V_{yy}-component of all ascending arcs. Again, data from the time span November and December 2009 are given at the left and from March to June 2010 on the right. Next steps will be the joint processing of the entire data span, comparison with GRACE for various spectral bands and gravimetric inversion. From the GOCE data of November and December 2009 and 7 years of GRACE data the combined gravity field model GOCO01S was derived (Pail et al. 2010; GOCO stands for "Combination of GOCE data with complementary gravity field information"). The set of spherical harmonic coefficients is complete up to maximum degree and order 224 and is provided together with its complete variance–covariance error matrix.

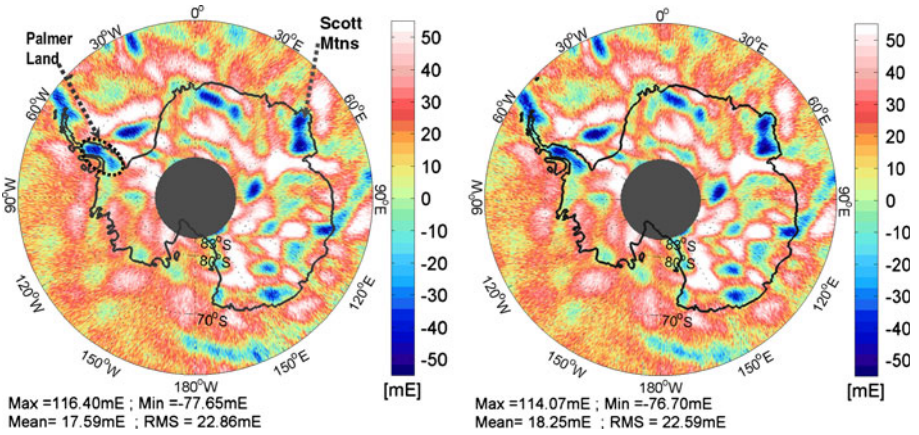

Fig. 5 As Fig. 4 but now for the gravity gradient component V_{yy} along the ascending arcs

Table 1 Mean and RMS values of differences among recent mean sea surface models for non-coastal ocean areas

MSS—DTU10	MSS—CLS10	DTU10—CLS10
-2 ± 3 (11) cm	1 ± 2 (15) cm	3 ± 4 (15) cm

MSS mean sea surface of this paper, DTU10 (Andersen et al. 2008), CLS10 (Schaeffer et al. 2010). If coastal areas are included the RMS values increase to the values given in brackets—basically due to different strategies to average data over the half space of coastal oceans

This model is applied here for the determination of the mean dynamic ocean topography (MDT) from the difference between a 17.5-year average altimetric mean ocean surface, h, and the geoid surface, N, from the GOCE01S gravity model:

$$H = \mathrm{MDT} = h - N \tag{2}$$

The altimetric mean sea surface (MSS) represents a mean for the period October 1992 to April 2010 and was derived from satellite track data of ERS-1 & 2, Topex/Poseidon, ENVISAT, and Jason 1 & 2 after a multi-mission cross-calibration (Bosch and Savcenko 2007; Dettmering and Bosch 2010a, b). Although the averaging period is different this MSS is very close to other recently published mean sea surfaces like DTU10 and CLS10, cf. Table 1. The altimetric surface and the geoid refer to the same coordinate system, reference ellipsoid and mean tide system. The altimetric surface and the geoid were made spectrally consistent by applying a Gauss filter. For this purpose, the altimetric surface was extended to land areas using a geoid model and, in an iteration process, expanded into spherical harmonics (see Albertella and Rummel 2009). Several spatial resolutions were tested. A resolution up to spherical harmonic degree 150 is used here.

Assuming geostrophic balance, ocean surface circulation velocities follow from the mean dynamic topography, as

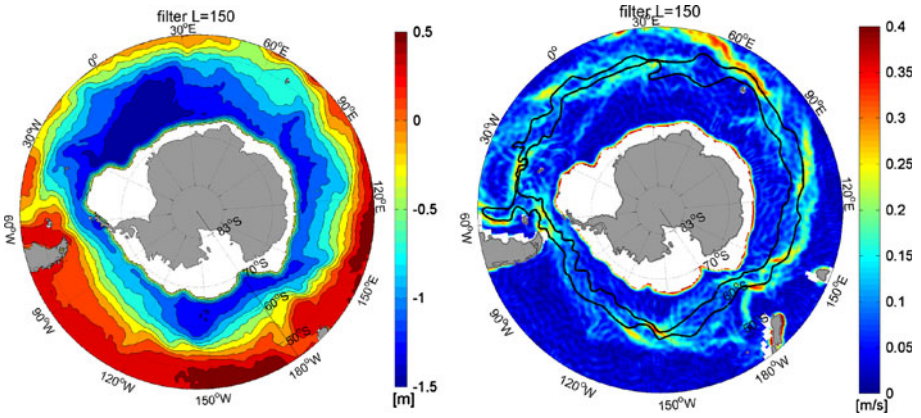

Fig. 6 (*left*) the mean dynamic topography of the Antarctic Circumpolar Current (ACC) as derived from the difference of a multi-year and multi-mission altimetric mean sea surface and the GOCE geoid (based on model GOCO), spatial resolution corresponding to degree and order 150; (*right*) geostrophic velocities calculated based on the mean dynamic ocean topography on the *left*. Fronts are shown as *black lines*

$$u = -\frac{g}{f}\frac{\partial H}{\partial y}$$
$$v = \frac{g}{f}\frac{\partial H}{\partial x} \qquad (3a, b)$$

with x and y the East and North direction, respectively, and u and v the corresponding East and North components of the surface velocity vector, g gravity and f the Coriolis Parameter $f = 2\omega \sin B$ (ω = Earth's angular velocity and B = geographic latitude, compare Stewart 2003, ch. 10.3). Figure 6 shows on the left the mean dynamic topography in the area of the Antarctic Circumpolar Current (ACC) and on the right the geostrophic surface velocities. The ACC is the most dynamic ocean area, globally (Stewart 2003). It is also one of the two areas of downwelling and fresh water generation. There are still artifacts visible in the maps of velocity and dynamic ocean topography. They may be either related to the altimetric analysis which has still problems in areas with seasonal ice cover or to residual errors in the satellite gradiometry analysis. They are currently being investigated.

6 Conclusions

Through the observation of temporal gravity field variations, GRACE is producing more and more detailed and accurate estimates of the temporal changes of Antarctic ice masses. It thereby benefits from the increasing length of the time series, continuous improvements of processing, a better understanding of the sensor system and the combination with complementary data. A challenge remains in separating the effect of ice mass changes from glacial isostatic adjustment.

GOCE is providing gradients of the stationary gravity field with high spatial resolution. Two measurement periods (November/December 2009 and March–June 2010) have now been processed. The gravity gradients provide detailed gravity information for geophysical studies in Antarctica. The higher spatial resolution of GOCE adds significant spatial detail

to the determination of the mean dynamic ocean topography and geostrophic ocean flow velocities. This was illustrated for the example of the Antarctic Circumplolar Current.

Acknowledgments The work of the first and third author is supported by the Institute for Advanced Study of Technische Universität München. Additional support of the work of the third author comes from Institute of Geodesy and Geophysics, Chinese Academy of Sciences. The work of the second author was supported by a research fellowship of the Deutsche Forschungsgemeinschaft (DFG). Roman Savcenko (German Geodetic Research Institute, DGFI) together with the fifth author provided the altimetric mean surface from the multi-mission analysis.

References

Andersen OB et al (2008) The DTU10 global Mean sea surface and Bathymetry. Presented EGU-2008, Vienna, Austria, April, 2008

Albertella A, Rummel R (2009) On the spectral consistency of the altimetric ocean and geoid surface, a one-dimensional example. J Geod 83:805–815. doi:10.1007/s00190-008-02999-5

Allison I, Alley R, Fricker H, Thomas R, Warner R (2009) Ice sheet mass balance and sea level. Antarct Sci 21(5):413–426. doi:10.1017/S0954102009990137

Armano M et al (2009) LISA Pathfinder: the experiment and the route to LISA. Class Quantum Grav 26:094001. doi:10.1088/0264-9381/26/9/094001

Balmino G, Perosanz F, Rummel R, Sneeuw N, Sünkel H (1999) CHAMP, GRACE and GOCE: mission concepts and simulations. Boll Geof Teor Appl 40(3–4):309–319

Balmino G, Perosanz F, Rummel R, Sneeuw N, Sünkel H, Woodworth PL (1998) European views on dedicated gravity field missions: GRACE and GOCE. European Space Agency, ESD-MAG-REP-COW-01

Bevis M, Kendrick E, Smalley Jr R, Dalziel I, Caccamise D, Sasgen I, Helsen M, Taylor FW, Zhou H, Brown A, Raleigh D, Willis M, Wilson T, Konfal S (2009) Geodetic measurements of vertical crustal velocity in West Antarctica and the implications for ice mass balance. Geochem Geophys Geosystems 10(10):Q10005. doi:10.1029/2009GC002642

Bindschadler R (2006) The environment and evolution of the West Antarctic ice sheet: setting the stage. Phil Trans R Soc A 364(1844):1583–1605. doi:10.1098/rsta.2006.1790

Böning C, Timmermann R, Danilov S, Schröter J (2010) Antarctic circumpolar current transport variability in GRACE gravity solutions and numerical ocean model simulations. In: Flechtner FM, Gruber T, Güntner A, Mandea M, Rothacher M, Schöne T, Wickert T (eds) System earth via geodetic-geophysical space techniques. Springer, Berlin, pp 187–199. doi:10.1007/978-3-642-10228-8_15

Bosch W, Savcenko R (2007) Satellite altimetry: multi-mission cross calibration. In: Tregoning P, Ch Rizos (eds) Dynamic planet 2005. IAG symposia 130:51–56. Springer, Berlin

Chao BF (2003) Geodesy is not just for static measurements anymore. Eos Trans AGU 84(16). doi:10.1029/2003EO160001

Chen JL, Wilson CR, Blankenship D, Tapley BD (2009) Accelerated Antarctic ice loss from satellite gravity measurements. Nat Geosci 2:859–864. doi:10.1038/ngeo694

Dettmering D, Bosch W (2010a) Global calibration of Jason-2 by multi-mission crossover analysis. Marine Geod 33(S1):150–161. doi:10.1080/01490419.2010.487779

Dettmering D, Bosch W (2010b) Envisat radar altimeter calibration by multi-mission crossover analysis. In: Proceedings of ESA living planet symposium, SP-686, ESA ESTEC, Noordwijk, The Netherlands, ISBN 978-92-9221-250-6

Drinkwater M, Haagmans R, Muzi D, Popescu A, Floberghagen R, Kern M, Fehringer M (2007) The GOCE Gravity Mission: ESA's first core earth explorer. In: Proceedings of 3rd International GOCE User Workshop, ESA SP-627, Frascati

Förste C, Flechtner F, Schmidt R, Stubenvoll R, Rothacher M, Kusche J, Neumayer H, Biancale R, Lemoine J-M, Barthelmes F, Bruinsma S, König R, Meyer U (2008a) EIGEN-GL05C–A new global combined high-resolution GRACE-based gravity field model of the GFZ-GRGS cooperation. Geophys Res Abstr 10:EGU2008-A-03426

Förste C, Schmidt R, Stubenvoll R, Flechtner F, Meyer U, König R, Neumayer H, Biancale R, Lemoine J-M, Bruinsma S, Loyer S, Barthelmes F, Esselborn S (2008b) The GeoForschungsZentrum Potsdam/Groupe de Recherche de Gèodésie Spatiale satellite-only and combined gravity field models: EIGEN-GL04S1 and EIGEN-GL04C. J Geod 82:331–346. doi:10.1007/s00190-007-0183-8

Han S-C, Shum CK, Ditmar P, Visser P, van Beelen C, Schrama EJO (2006) Aliasing effect of high-frequency mass variations on GOCE recovery of the Earth's gravity field. J Geodyn 41:69–76

Horwath M, Dietrich R (2009) Signal and error in mass change inferences from GRACE: the case of Antarctica. Geophys J Int 177(3):849–864. doi:10.1111/j.1365-246X.2009.04139.x

Horwath M, Legrésy B, Rémy F, Blarel F, Lemoine J-M (2010) Consistent patterns of Antarctic ice sheet interannual variations from ENVISAT radar altimetry and GRACE satellite gravimetry. Geophys Res Abstr 12:EGU2010-4972

Ivins ER, James TJ (2005) Antarctic glacial isostatic adjustment: a new assessment. Antarct Sci 17(4): 541–553

Jäggi A (2007) Pseudo stochastic orbit modelling of low earth satellites using the global positioning system. Geodätisch-geophysikalische Arbeiten in der Schweiz, 73, Schweizerische Geodätische Kommission, ISBN 978–3–908440–17–8

Jarecki F, Müller J, Petrovic S, Schwintzer P (2005) Temporal gravity variations in GOCE gradiometric data. In: Jekeli C, Bastos C, Fernandes J (eds) Gravity, geoid and space missions: GGSM 2004. IAG International Symposium Porto, Portugal, August 30–September 3, 2004. Springer, Berlin, pp 333–338

Joughin I, Tulaczyk S (2002) Positive mass balance of the Ross ice streams, West Antarctica. Science 295:476–480

Kaula WA (1966) Theory of satellite geodesy. Blaisdell Publishing Group, Waltham

King MA, Altamimi Z, Boehm J, Bos M, Dach R, Elosegui P, Fund F, Hernandez-Pajares M, Lavallee D, Cerveira PJM, Penna N, Riva REM, Steigenberger P, van Dam T, Vittuari L, Williams S, Willis P (2010) Improved constraints on models of glacial isostatic adjustment: a review of the contribution of ground-based geodetic observations. Surv Geophys 31:465507. doi:10.1007/s10712-010-9100-4

Moore P, King MA (2010) Satellite gravity gradiometry: secular gravity field change over polar Regions. J Geodyn 49:247–253. doi:10.1016/j.jog.2010.01.007

Office of Science and Technology Policy (2010) Achieving and sustaining earth observations: a preliminary plan based on a strategic assessment by the US group on earth observations. Washington DC. http://www.whitehouse.gov/sites/default/files/microsites/ostp/ostp-usgeo-report-earth-obs.pdf. Accessed 5 Jan 2011

Pail R, Wermuth M (2003) GOCE SGG and SST quick-look gravity field analysis. Adv Geosci 1:5–9

Pail R, Goiginger H, Schuh W-D, Höck E, Brockmann JM, Fecher T, Gruber T, Mayer-Gürr T, Kusche J, Jäggi A, Rieser D (2010) Combined satellite gravity field model GOCO01S derived from GOCE and GRACE. Geophys Res Lett 37:L20314. doi:10.1029/2010GL044906

Peltier WR (2004) Global glacial isostasy and the surface of the ice-age earth: the ICE-5G (VM2) Model and GRACE. Ann Rev Earth Planet Sci 32(1):111–149. doi:10.1146/annurev.earth.32.082503.144359; (AN 13161612)

Plag H-P, Pearlman M (eds) (2009) Global geodetic observing system–meeting the requirements of a global society on a changing planet in 2020. Springer, Berlin

Pritchard HD, Arthern RJ, Vaughan DG, Edwards LA (2009) Extensive dynamic thinning on the margins of the Greenland and Antarctic ice sheets. Nature 461:971–975. doi:10.1038/nature08471

Ramillien G, Lombard A, Cazenave A, Ivins ER, Llubes M, Rémy F, Biancale R (2006) Interannual variations of the mass balance of the Antarctica and Greenland ice sheets from GRACE. Glob Planet Change 53:198–208

Rietbroek R, LeGrand P, Wouters B, Lemoine J-M, Ramillien G, Hughes CW (2006) Comparison of in situ bottom pressure data with GRACE gravimetry in the Crozet-Kerguelen region. Geophys Res Lett 33:L21601. doi:10.1029/2006GL027452

Rignot E, Bamber J, van den Broeke MR, Davis C, Li Y, van de Berg WJ, van Meijgaard E (2008) Recent Antarctic ice mass loss from radar interferometry and regional climate modelling. Nat Geosci 1(13Jan 2008):106–110. doi:10.1038/ngeo102

Riva REM, Gunter BC, Urban TJ, Vermeersen BLA, Lindenbergh RC, Helsen MM, Bamber JL, van de Wal RSW, van den Broeke MR, Schutz BE (2009) Glacial Isostatic Adjustment over Antarctica from combined ICESat and GRACE satellite data. Earth Planet Sci Lett 288:516–523. doi:10.1016/j.epsl.2009.10.013

Rülke A, Dietrich R, Fritsche M, Rothacher M, Steigenberger P (2008) Realization of the Terrestrial Reference System by a reprocessed global GPS network. J Geophys Res 113:B08403. doi:10.1029/2007JB005231

Rummel R (2003) How to climb the gravity wall. In: Beutler G, Rummel R, Drinkwater MR, von Steiger R (eds) Earth gravity field from space–from sensors to earth sciences, Space Science Reviews, 108:1–14

Rummel R (2010) GOCE: gravitational gradiometry in a satellite, handbook of geo-mathematics, ch. 22. Springer, Heidelberg, Berlin

Rummel R, Gruber T (2010) Gravity and steady-state ocean circulation explorer GOCE. In: Flechtner F, Gruber T, Güntner A, Mandea M, Rothacher M, Schöne T, Wickert J (eds) System earth via geodetic–geophysical space techniques. Springer, Heidelberg, Berlin, pp 203–212

Sabaka TJ, Rowlands DD, Luthcke SB, Boy JP (2010) Improving global mass flux solutions from Gravity Recovery and Climate Experiment (GRACE) through forward modeling and continuous time correlation. J Geophys Res 115(B11403). doi:10.1029/2010JB007533

Sasgen I, Dobslaw H, Martinec Z, Thomas M (2010a) Satellite gravimetry observation of Antarctic snow accumulation related to ENSO. Earth Plan Sci Lett. doi:10.1016/j.epsl.2010.09.015

Sasgen I, Martinec Z, Bamber J (2010b) Combined GRACE and InSAR estimate of West Antarctic ice-mass loss. J Geophys Res. doi:10.1029/2009JF001543

Schaeffer P, Ollivier A, Faugere Y, Bronner E, Picot N (2010) The new CNES CLS 2010 Mean Sea Surface. Oral presentation at OSTST 2010 meeting: http://www.aviso.oceanobs.com/fileadmin/documents/OSTST/2010/oral/Schaeffer.pdf

Scheinert M, Müller J, Dietrich R, Damaske D, Damm V (2007) Regional geoid determination in Antarctica utilizing airborne gravity and topography data. J Geod. doi:10.1007/s00190-007-0189-2

Schmidt R, Flechtner F, Meyer U, Neumayer K-H, Dahle C, König R, Kusche J (2008) Hydrological signals observed by the GRACE satellites. Surv Geophys 29:319–334. doi:10.1007/s10712-008-9033-3

Stewart, RH (2003) Introduction to physical oceanography. Department of Oceanography, Texas A&M University

Sumner TJ (2009) The STEP and GAUGE missions. Space Sci Rev 148(1–4):475–487. doi:10.1007/s11214-009-9558-x

Švehla D, Rothacher M (2004) Kinematic precise orbit determination for gravity field determination. In: Sansò F (ed) The proceedings of the international association of geodesy: a window on the future of geodesy. Springer, Berlin, pp 181–188

Swenson S, Wahr J (2002) Methods for inferring regional surface-mass anomalies from Gravity Recovery and Climate Experiment (GRACE) measurements of time-variable gravity. J Geophys Res 107(B9): 2193. doi:10.1029/2001B000576

Tapley BD, Bettadpur S, Ries JC, Thompson PF, Watkins M (2004) GRACE measurements of mass variability in the earth system. Science 305(5683):503–505. doi:10.1126/science.1099192

Thomas RH (2001) Program for Arctic Regional Climate Assessment (PARCA): goals, key findings, and future directions. J Geophys Res 106(D24):33691–33705

Touboul P (2009) The microscope mission and its uncertainty analysis. Space Sci Rev 148(1–4):455–474. doi:10.1007/s11214-009-9565-y

Velicogna I (2009) Increasing rates of ice mass loss from the Greenland and Antarctic ice sheets revealed by GRACE. Geophys Res Lett 36:L19503. doi:10.1029/2009GL040222

Velicogna I, Wahr J (2006) Measurements of time-variable gravity show mass loss in Antarctica. Science 311(5768):1754–1756

Vitale S (2009) Space-time metrology for the LISA gravitational wave observatory, and its demonstration on LISA pathfinder. Space Sci Rev 148(1–4):441–454. doi:10.1007/s11214-009-9521-x

von Frese RRB, Tan L, Kim JW, Bentley CR (1999) Antarctic crustal modeling from the spectral correlation of free-air gravity anomalies with the terrain. J Geophys Res 104(B11):25,275–25,296. doi:10.1029/1999JB900232

Wahr J, Molenaar M, Bryan F (1998) Time variablity of the Earth's gravity field: hydrological and oceanic effects and their possible detection using GRACE. J Geophys Res 103(B12):30205–30229

Wahr J, Wingham D, Bentley C (2000) A method of combining ICESat and GRACE satellite data to constrain Antarctic mass balance. J Geophys Res 105(B7):16,279–16,294

Wingham DJ, Wallis DW, Shepherd A (2009) Spatial and temporal evolution of Pine Island Glacier thinning 1995–2006. Geophys Res Lett 36:L17501. doi:10.1029/2009GL039126

Wu X, Heflin MB, Schotman H, Vermeersen BLA, Dong D, Gross RS, Ivins ER, Moore AW, Owen SE (2010) Simultaneous estimation of global present-day water transport and glacial isostatic adjustment. Nat Geosci 3:642–646. doi:10.1038/NGEO938

Zlotnicki V, Wahr J, Fukumori E, Zong YT (2007) Antarctic circumpolar current transport variability during 2003–05 from GRACE. J Phys Oceanogr 37:230–244. doi:10.1175/JPO3009.1

Zwally HJ, Schutz B et al (2002) ICESat's laser measurements of polar ice, atmosphere, ocean, and land. J Geodyn 34(3–4):405–445